FUNDAMENTAL STUDY OF NANOSTRUCTURED ELECTRO-CATALYSTS WITH REDUCED NOBLE METAL CONTENT FOR PEM BASED WATER ELECTROLYSIS

by

Karan Sandeep Kadakia

B.S. in Chemical Engineering

Institute of Chemical Technology (formerly U.D.C.T.), Mumbai, India, 2008

Submitted to the Graduate Faculty of

Swanson School of Engineering in partial fulfillment

of the requirements for the degree of

Doctor of Philosophy

University of Pittsburgh

2014

UNIVERSITY OF PITTSBURGH

SWANSON SCHOOL OF ENGINEERING

This dissertation was presented

by

Karan Sandeep Kadakia

It was defended on

March 17, 2014

and approved by

Robert M. Enick, PhD, Bayer Professor, Department of Chemical and Petroleum Engineering

Di Gao, PhD, Associate Professor, Department of Chemical and Petroleum Engineering

Ayyakkannu Manivannan, PhD, US Department of Energy / National Energy Technology Laboratory

Dissertation Director: Prashant N. Kumta, PhD, Edward R. Weidlein Chair Professor, Department of Chemical and Petroleum Engineering

FUNDAMENTAL STUDY OF NANOSTRUCTURED ELECTRO-CATALYSTS WITH REDUCED NOBLE METAL CONTENT FOR PEM BASED WATER ELECTROLYSIS

Karan Sandeep Kadakia, PhD

University of Pittsburgh, 2014

Identification and development of non-noble metal based electro-catalysts or electro-catalysts with significant reduction of expensive noble metal contents (*E.g.* IrO_2, Pt) with comparable electrochemical performance as the standard noble metal/metal oxide for proton exchange membrane (PEM) based water electrolysis would constitute a major breakthrough in the generation of hydrogen by water electrolysis. Accomplishing such a system would not only result reduction of the overall capital costs of PEM based water electrolyzers, but also help attain the targeted hydrogen production cost [< $ 3.0 / gallon gasoline equivalent (gge)] comparable to conventional liquid fuels.

In line with these goals, it was demonstrated that fluorine doped IrO_2 thin films and nanostructured high surface area powders display remarkably higher electrochemical activity, and comparable durability as pure IrO_2 electro-catalyst for the oxygen evolution reaction (OER) in PEM based water electrolysis. Furthermore, corrosion resistant SnO_2 and NbO_2 support has been doped with F and coupled with IrO_2 or RuO_2 for use as an OER electro-catalyst. A solid solution of SnO_2:F or NbO_2:F with only 20 - 30 mol.% IrO_2 or RuO_2 yielding a rutile structure in the form of thin films and bulk nanoparticles displays similar electrochemical activity and stability as pure IrO_2/RuO_2. This would lead to more than 70 mol.% reduction in the noble metal

oxide content. Novel nanostructured ternary (Ir,Sn,Nb)O_2 thin films of different compositions have also been studied. It has been shown that ($Ir_{0.40}Sn_{0.30}Nb_{0.30}$)$O_2$ shows similar electrochemical activity and enhanced chemical robustness as compared to pure IrO_2. F doping of the ternary (Ir,Sn,Nb)O_2 catalyst helps in further decreasing the noble metal oxide content of the catalyst.

As a result, these reduced noble metal oxide catalyst systems would potentially be preferred as OER electro-catalysts for PEM electrolysis. The excellent performance of the catalysts coupled with its robustness would make them great candidates for contributing to significant reduction in the overall capital costs of PEM based water electrolyzers. This thesis provides a detailed fundamental study of the synthesis, materials, characterization, theoretical studies and detailed electrochemical response and potential mechanisms of these novel electro-catalysts for OER processes.

TABLE OF CONTENTS

ACKNOWLEDGEMENTS XXVI

1.0 INTRODUCTION 1

1.1 HYDROGEN 1

1.2 HYDROGEN PRODUCTION TECHNOLOGIES 2

1.3 WATER ELECTROLYSIS 5

2.0 BACKGROUND 8

2.1 TYPES OF ELECTROLYZERS 8

2.1.1 Alkaline Electrolysis 8

2.1.2 Solid Oxide Electrolysis 9

2.1.3 PEM based Water Electrolysis 11

2.2 FUNDAMENTALS 13

2.2.1 Thermodynamics and Kinetics 13

2.2.2 Reaction Mechanism 15

3.0 GOALS AND OBJECTIVES 16

3.1 MOTIVATION 16

3.2 ELECTRO-CATALYST SYSTEMS 17

3.3 PROPOSED NOVEL STRATEGY 19

3.3.1 Fluorine doped IrO_2 20

3.3.2 Binary SnO_2 based electro-catalysts 20
3.3.3 Binary Nb_2O_5 based electro-catalysts 21
3.3.4 Ternary metal oxide electro-catalysts 22
4.0 EXPERIMENTAL DETAILS 24
4.1 THIN FILM ELECTRO-CATALYST PREPARATION 24
4.1.1 F doped IrO_2 24
4.1.2 Binary F doped $(Ir,Sn)O_2$ 25
4.1.3 Binary F doped $(Ru,Sn)O_2$ 26
4.1.4 Ternary $(Ir,Sn,Nb)O_2$ 27
4.1.5 Ternary F doped $(Ir,Sn,Nb)O_2$ 28
4.2 NANOPARTICULATE CATALYST SYNTHESIS 29
4.2.1 F doped IrO_2 29
4.2.2 Binary F doped $(Ir,Sn)O_2$ 30
4.2.3 Binary F doped $(Ir,Nb)O_2$ 31
4.3 PHYSICAL AND CHEMICAL CHARACTERIZATION 32
4.3.1 X-ray Characterization 32
4.3.2 Specific surface area Determination 33
4.3.3 Thermogravimetric Analysis 33
4.3.4 Microstructure Analysis 34
4.3.5 X-ray Photoelectron Spectroscopy 34
4.4 ELECTROCHEMICAL CHARACTERIZATION 35
4.4.1 Set-up 35
4.4.2 Polarization Testing 37

4.4.3 Electrochemical Impedance Spectroscopy (EIS) 37

4.4.4 Kinetic Studies 38

4.4.5 Chronoamperometry 40

4.4.6 Single full cell test Analysis 40

5.0 RESULTS AND DISCUSSION 42

5.1 THIN FILMS 42

5.1.1 F doped IrO_2 42

5.1.1.1 Structural Analysis 42

5.1.1.2 Electrochemical Testing 44

5.1.2 Binary F doped $(Ir,Sn)O_2$ 49

5.1.2.1 Structural Analysis 49

5.1.2.2 Electrochemical Testing 53

5.1.3 Binary F doped $(Ru,Sn)O_2$ 70

5.1.3.1 Structural Analysis 70

5.1.3.2 Electrochemical Testing 74

5.1.4 Ternary $(Ir,Sn,Nb)O_2$ 92

5.1.4.1 Structural Analysis 92

5.1.4.2 Electrochemical Testing 107

5.1.5 Ternary F doped $(Ir,Sn,Nb)O_2$ 117

5.1.5.1 Structural Analysis 117

5.1.5.2 Electrochemical Testing 121

5.2 NANOSTRUCTURED POWDERS 143

5.2.1 F doped IrO_2 143

5.2.1.1 Structural Analysis 143
5.2.1.2 Electrochemical Testing 147
5.2.2 Binary F doped (Ir,Sn)O_2 182
5.2.2.1 Structural Analysis 182
5.2.2.2 Electrochemical Testing 192
5.2.3 Binary F doped (Ir,Nb)O_2 207
5.2.3.1 Structural Analysis 207
5.2.3.2 Electrochemical Testing 217
6.0 FIRST PRINCIPLES CALCULATIONS 232
6.1 F DOPED IRIDIUM OXIDE 234
6.1.1 Computational Methodology 235
6.1.2 Theoretical Discussion 239
6.2 F DOPED IRIDIUM - TIN OXIDE 245
6.2.1 Computational Methodology 245
6.2.2 Theoretical Discussion 248
6.3 F DOPED RUTHENIUM - TIN OXIDE 257
6.3.1 Computational Methodology 257
6.3.2 Theoretical Discussion 258
6.4 F DOPED IRIDIUM - NIOBIUM OXIDE 263
6.4.1 Computational Methodology 263
6.4.2 Theoretical Discussion 265
6.5 IRIDIUM - TIN - NIOBIUM OXIDE 271
6.5.1 Computational Methodology 271

6.5.2 Theoretical Discussion 273
6.6 F DOPED IRIDIUM - TIN - NIOBIUM OXIDE 282
6.6.1 Computational Methodology 282
6.6.2 Theoretical Discussion 283
7.0 SUMMARY 295
7.1 THIN FILM CATALYSTS 296
7.2 NANOPARTICULATE CATALYSTS 297
APPENDIX A. DIRECT METHANOL FUEL CELLS 300
APPENDIX B. QUATERNARY ANODE CATALYSTS FOR DMFC 336
APPENDIX C. PEM WATER ELECTROLYSIS SUPPORTS 372
APPENDIX D. SUPERCAPACITORS 398
APPENDIX E. BATTERIES 450
APPENDIX F. PERMISSIONS 486
BIBLIOGRAPHY 490

LIST OF TABLES

Table 1. Impedance parameters and Tafel slope of IrO_2 and (Ir,Sn)O_2:F thin film..... 54

Table 2. Impedance parameters and Tafel slope of RuO_2 and (Ru,Sn)O_2:F..... 75

Table 3. Lattice parameter, molar volumes and crystallite size of (Ir,Sn,Nb)O_2 compositions ... 94

Table 4. Starting compositions compared to compositions determined by EDX analysis for (Ir,Sn,Nb)O_2..... 102

Table 5. Impedance parameters and Tafel slope of IrO_2 and (Ir,Sn,Nb)O_2:F thin film..... 127

Table 6. Impedance parameters of IrO_2:F powder catalyst..... 153

Table 7. The Tafel slope, number of electrons transferred in the OER and the kinetic rate constant from the Koutecky - Levich plots for IrO_2:F..... 162

Table 8. Impedance parameters of nanoparticulate (Ir,Sn)O_2:F and commercial IrO_2..... 194

Table 9. Impedance parameters of nanoparticulate (Ir,Nb)O_2:F and commercial IrO_2 219

Table 10. Bader charges of the terminated oxygen ions *O adsorbed to the pure and F doped surfaces for *OH, *O and *OOH..... 243

Table 11. Calculated values of density of electronic states at Fermi level n(E_F), positions of the Ir d-band center εd, and the cohesive energy - Ecoh for the catalysts..... 268

Table 12. Lattice parameters, cohesive energy and density of electronic states at Fermi level for IrO_2, SnO_2 and (Ir,Sn,Nb)O_2..... 275

Table 13. Segregation energies of Pt and Ru to (1 1 1) surface and Pt only to (1 0 0) surface for two corresponding Pt and Ru atoms exchange steps. Surface energies for pure Pt, Ru and Pt-Ru are also presented for (1 1 1) and (1 0 0) crystallographic orientations 312

Table 14. The current and power density obtained at 0.2 V for CSG-Pt(Ru) and JM-Pt(Ru).... 332

Table 15. The maximum power density obtained at various temperatures for CSG-Pt(Ru) and JM-Pt(Ru) along with the corresponding voltage and current densities..... 332

Table 16. Intermetallic sodium stannide (zintl phases) with hteir molar volume, volume expansion and theoretical capacity 454

Table 17. Reaction potential and associated specific capacity of different intermetallics (zintl phases) form during alloying of Na ion with pure Sn..... 459

LIST OF FIGURES

Figure 1. Schematic of a water electrolysis cell 7

Figure 2. PEM electrolysis schematic diagram..... 12

Figure 3. Molar ratio of (Ir,Sn,Nb)O_2 chosen to investigate as an anode electro-catalyst in PEM water electrolysis 28

Figure 4. Three electrode cell set-up for electrochemical testing..... 36

Figure 5. XRD patterns of thin film IrO_2:F with 10, 20 and 30 wt.% F coated on Ti foil..... 43

Figure 6. The SEM micrograph (a) along with EDAX (b) of IrO_2:F film with 10wt.% F 44

Figure 7. The polarization curve with iR correction of IrO_2:F films conducted in the presence of 1 N H_2SO_4 solution at 40°C with a scan rate of 1 mV/sec 45

Figure 8. The variation of current density at ~ 1.65 V (vs. NHE) with F content of the doped IrO_2:F anode electro-catalyst 47

Figure 9. Variation of current vs. time in the accelerated life test of IrO_2:F performed in a 1 N H_2SO_4 solution under ~ 1.65 V at 40°C..... 48

Figure 10. XRD patterns of ($Ir_{0.20}Sn_{0.80}$)O_2:F of different compositions coated on Ti foil 51

Figure 11. The SEM micrograph along with x-ray mapping of Ir, Sn and O (a), and EDAX (b) of ($Ir_{0.20}Sn_{0.80}$)O_2:F film 52

Figure 12. The bright field TEM image ($Ir_{0.2}Sn_{0.8}$)O_2:10F film shows the presence of fine particles in the nanometer range (~ 10 - 15 nm)..... 53

Figure 13. The EIS plot obtained at 1.6 V at 40°C in the presence of 1 N H_2SO_4 solution in the frequency range of 100 mHz - 100 kHz..... 55

Figure 14. The EIS plot obtained at open circuit potential and different voltages for pure IrO_2 (a), and (Ir,Sn)O_2:10F (b) in the frequency range of 100 mHz - 100 kHz..... 56

Figure 15. The polarization curve of pure IrO_2 and SnO_2:10F film before and after iR correction, and the inset shows the Tafel plot of pure IrO_2 before and after iR correction 57

Figure 16. The polarization curve of (Ir,Sn)O_2:F film conducted in the presence of 1 N H_2SO_4 solution at 40°C with a scan rate of 1 mV/sec before and after iR correction..... 58

Figure 17. The polarization curve for high F doping of (Ir,Sn)O_2:F film conducted in the presence of 1 N H_2SO_4 solution at 40°C before and after iR correction 60

Figure 18. The Tafel plot of ($Ir_{0.2}Sn_{0.8}$)O_2 (a), ($Ir_{0.2}Sn_{0.8}$)O_2:5F (b), and ($Ir_{0.2}Sn_{0.8}$)O_2:10F (c), before and after iR correction, showing the Tafel slope 61

Figure 19. Koutecky - Levich plot in PEM based water electrolysis at 1.55 V, 1.65 V and 1.75 V (vs. NHE) in 1 N H_2SO_4 at 25°C for ($Ir_{0.2}Sn_{0.8}$)O_2:10 wt.% F 63

Figure 20. Arrhenius plot for ($Ir_{0.2}Sn_{0.8}$)O_2:10 wt.% F at 1.55 V, 1.65 V and 1.75 V (vs. NHE) over a temperature range of 25°C to 70°C..... 64

Figure 21. Variation of current vs. time in the accelerated life test of pure IrO_2 and ($Ir_{0.2}Sn_{0.8}$)O_2:10F performed in a 1 N H_2SO_4 solution under ~ 1.65 V at 40°C 66

Figure 22. Polarization curve of IrO_2 and (Ir,Sn)O_2:10 wt.% F thin film after the CA test 67

Figure 23. The Tafel plot of pure IrO_2 after the CA test..... 68

Figure 24. The Tafel plot of (Ir,Sn)O_2:10 wt.% F thin film after the CA test 69

Figure 25. XRD patterns of thin film RuO_2 and SnO_2 coated on a Ti foil 71

Figure 26. XRD patterns of thin film ($Ru_{0.2}Sn_{0.8}$)O_2:F for different F compositions coated on Ti foil 72

Figure 27. The SEM micrograph along with x-ray mapping of Ru, Sn and O 73

Figure 28. The EDX (a), and TEM imaging (b) of (Ru,Sn)O_2:10F thin film 74

Figure 29. The EIS plot of (Ru,Sn)O_2:F and RuO_2 obtained at 1.6 V in the presence of 1 N H_2SO_4 solution in the frequency range of 100 mHz - 100 kHz 77

Figure 30. The polarization curve of pure RuO_2, SnO_2 and SnO_2:10F film conducted in the presence of 1 N H_2SO_4 solution at 40°C with a scan rate of 1mV/sec 79

Figure 31. The polarization curve of (Ru,Sn)O_2:F film of different F compositions conducted in 1 N H_2SO_4 at 40°C with a scan rate of 1mV/sec before and after iR correction 80

Figure 32. The polarization curve for high F doping of (Ru,Sn)O_2:F film conducted in 1 N H_2SO_4 solution at 40°C before and after iR correction with a scan rate of 1mV/sec..... 81

Figure 33. Variation of current density at ~ 1.75V (vs. NHE) with compositions of undoped and F doped $(Ru,Sn)O_2$ anode electro-catalyst 82

Figure 34. The Tafel plot of pure RuO_2 before and after iR correction 83

Figure 35. The Tafel plot of $(Ru_{0.2}Sn_{0.8})O_2$ before and after iR correction 84

Figure 36. The Tafel plot of $(Ru_{0.2}Sn_{0.8})O_2$:5 wt.% F before and after iR correction 85

Figure 37. The Tafel plot of $(Ru_{0.2}Sn_{0.8})O_2$:10 wt.% F before and after iR correction 86

Figure 38. The variation of current vs. time in the durability test of pure RuO_2 and $(Ru,Sn)O_2$:F performed in a 1 N H_2SO_4 solution under ~ 1.5 V at 40°C 87

Figure 39. Polarization curve of RuO_2 and $(Ru,Sn)O_2$:10 wt.% F thin film after the CA test 89

Figure 40. The Tafel plot of RuO_2 thin film after the CA test 90

Figure 41. The Tafel plot of $(Ru,Sn)O_2$:10 wt.% F thin film after the CA test 91

Figure 42. XRD patterns of thin film IrO_2, SnO_2 and $(Sn_{0.50}Nb_{0.50})O_2$ coated on Ti foil 93

Figure 43. XRD patterns of $(Ir_{1-2x}Sn_xNb_x)O_2$ with x = 0.125, 0.20, 0.25, 0.30 coated on a Ti foil 96

Figure 44. XRD patterns of $(Ir_{1-2x}Sn_xNb_x)O_2$ with x = 0.35, 0.40 and 0.425 coated on Ti foil 97

Figure 45. The SEM micrograph (a), and EDAX spectra (b) of $(Ir_{0.2}Sn_{0.4}Nb_{0.4})O_2$ film 99

Figure 46. The SEM micrograph (a), EDAX (b), and high magnification SEM image (c) of $(Ir_{0.75}Sn_{0.125}Nb_{0.125})O_2$ film showing the presence of fine nano-particles. 100

Figure 47. The nominal and EDAX determined molar ratio of $(Ir,Sn,Nb)O_2$ anode electro-catalyst for PEM based water electrolysis 101

Figure 48. The XPS spectra of Ir $4f_{7/2}$ and $4f_{5/2}$ doublet of pure IrO_2 and $(Ir,Sn,Nb)O_2$ thin film 104

Figure 49. The XPS spectra of O1s of pure IrO_2, SnO_2 and $(Ir,Sn,Nb)O_2$ thin film 105

Figure 50. The XPS spectra of Sn $3d_{5/2}$ and Sn $3d_{3/2}$ doublet of pure SnO_2 and $(Ir,Sn,Nb)O_2$ thin film 106

Figure 51. The XPS spectra of Nb $3d_{7/2}$ and Nb $3d_{5/2}$ doublet of $(Ir,Sn,Nb)O_2$ thin films 107

Figure 52. The polarization curve of pure IrO_2 and $(Sn_{0.50}Nb_{0.50})O_2$ film conducted in the presence of 1 N H_2SO_4 solution at 40°C 109

Figure 53. The polarization curve with iR correction of $(Ir_{1-2x}Sn_xNb_x)O_2$ films conducted in the presence of 1 N H_2SO_4 solution at 40°C..... 110

Figure 54. Variation of current density at ~ 1.65V (vs. NHE) for various compositions of $(Ir,Sn,Nb)O_2$ thin film electro-catalyst..... 111

Figure 55. Variation of current vs. time in the accelerated life test of pure IrO_2 and $(Ir_{0.4}Sn_{0.3}Nb_{0.3})O_2$ performed in 1 N H_2SO_4 at 40°C at ~ 1.65 V 113

Figure 56. Polarization curve of $(Ir,Sn,Nb)O_2$ thin film after the CA test..... 115

Figure 57. The Tafel plot of $(Ir,Sn,Nb)O_2$ thin film after the CA test 116

Figure 58. XRD patterns of thin film $(Ir_{0.30}Sn_{0.35}Nb_{0.35})O_2$:F of different compositions coated on Ti foil 118

Figure 59. The x-ray mapping of Ir, Sn, Nb, O and Ti of the SEM micrograph of $(Ir_{0.30}Sn_{0.35}Nb_{0.35})O_2$:10 wt.% F film..... 120

Figure 60. EDX of $(Ir_{0.30}Sn_{0.35}Nb_{0.35})O_2$:10 wt.% F coated on a Ti thin film..... 121

Figure 61. EIS spectra of pure IrO_2 obtained at OCP, 1.5 V, 1.6 V and 1.8 V in 1 N H_2SO_4.... 123

Figure 62. EIS spectra of $(Ir,Sn,Nb)O_2$ obtained at OCP, 1.5 V, 1.6 V and 1.8 V in 1 N H_2SO_4 124

Figure 63. EIS spectra of $(Ir,Sn,Nb)O_2$:5 wt.% F obtained at OCP, 1.5 V, 1.6 V and 1.8 V in 1 N H_2SO_4..... 125

Figure 64. EIS spectra of $(Ir,Sn,Nb)O_2$:10 wt.% F obtained at OCP, 1.5 V, 1.6 V and 1.8 V in 1 N H_2SO_4..... 126

Figure 65. The polarization curve of pure IrO_2 and $(Ir,Sn,Nb)O_2$:F with 0, 5 and 10 wt.% F before and after iR correction conducted at a scan rate of 1 mV/sec 128

Figure 66. The Tafel plot of IrO_2 before and after iR correction..... 129

Figure 67. The polarization curve of $(Ir,Sn,Nb)O_2$:F with 10, 15 and 20 wt.% F before and after iR correction conducted at a scan rate of 1 mV/sec..... 131

Figure 68. Variation of current density at ~ 1.75V (vs. NHE) for $(Ir,Sn,Nb)O_2$:F anode electro-catalyst 132

Figure 69. The Tafel plot of $(Ir,Sn,Nb)O_2$ before and after iR correction..... 133

Figure 70. The Tafel plot of $(Ir,Sn,Nb)O_2$:5 wt.% F before and after iR correction 134

Figure 71. The Tafel plot of $(Ir,Sn,Nb)O_2$:10 wt.% F before and after iR correction 135

Figure 72. The Tafel plot of (Ir,Sn,Nb)O_2:15 wt.% F before and after iR correction 136

Figure 73. The Tafel plot of (Ir,Sn,Nb)O_2:20 wt.% F before and after iR correction 137

Figure 74. The variation of current vs. time measurement of pure IrO_2 and ($Ir_{0.30}Sn_{0.35}Nb_{0.35}$)$O_2$:F performed in a 1 N H_2SO_4 solution under ~ 1.65 V at 40°C 139

Figure 75. Polarization curve of (Ir,Sn,Nb)O_2:10 wt.% F thin film after the CA test 141

Figure 76. The Tafel plot of (Ir,Sn,Nb)O_2:10 wt.% F thin film after the CA test 142

Figure 77. The XRD pattern of the nanostructured IrO_2:F of different compositions..... 144

Figure 78. The bright field TEM image of nanostructured IrO_2:10 wt.% F electro-catalyst..... 145

Figure 79. The HRTEM image of IrO_2:10 wt.% F confirming the nanoparticulate nature of the electro-catalyst 146

Figure 80. EIS spectra of undoped IrO_2 in a solution of 1 N H_2SO_4 at 40°C 148

Figure 81. EIS spectra of IrO_2:5 wt.% F in a solution of 1 N H_2SO_4 at 40°C 149

Figure 82. EIS spectra of IrO_2:10 wt.% F in a solution of 1 N H_2SO_4 at 40°C 150

Figure 83. EIS spectra of IrO_2:15 wt.% F in a solution of 1 N H_2SO_4 at 40°C 151

Figure 84. EIS spectra of IrO_2:20 wt.% F in a solution of 1 N H_2SO_4 at 40°C 152

Figure 85. Polarization testing of undoped IrO_2, IrO_2:5 wt.% F and IrO_2:10 wt.% F conducted at a scan rate of 1 mV/sec in 1 N H_2SO_4 at 40°C 155

Figure 86. Polarization testing of IrO_2:10 wt.% F, IrO_2:15 wt.% F and IrO_2:20 wt.% F conducted at a scan rate of 1 mV/sec in 1 N H_2SO_4 at 40°C 156

Figure 87. The Tafel plot of undoped IrO_2 before and after iR correction 157

Figure 88. The Tafel plot of IrO_2:5 wt.% F before and after iR correction 158

Figure 89. The Tafel plot of IrO_2:10 wt.% F before and after iR correction 159

Figure 90. The Tafel plot of IrO_2:15 wt.% F before and after iR correction 160

Figure 91. The Tafel plot of IrO_2:20 wt.% F before and after iR correction 161

Figure 92. Koutecky - Levich plots in PEM based water electrolysis at 1.55 V, 1.65 V and 1.75 V (vs. NHE) in 1 N H_2SO_4 at 25°C for undoped IrO_2 164

Figure 93. Koutecky - Levich plots in PEM based water electrolysis at 1.55 V, 1.65 V and 1.75 V (vs. NHE) in 1 N H_2SO_4 at 25°C for IrO_2:5 wt.% F 165

Figure 94. Koutecky - Levich plots in PEM based water electrolysis at 1.55 V, 1.65 V and 1.75 V (vs. NHE) in 1 N H_2SO_4 at 25°C for IrO_2:10 wt.% F 166

Figure 95. Koutecky - Levich plots in PEM based water electrolysis at 1.55 V, 1.65 V and 1.75 V (vs. NHE) in 1 N H_2SO_4 at 25°C for IrO_2:15 wt.% F 167

Figure 96. Koutecky - Levich plots in PEM based water electrolysis at 1.55 V, 1.65 V and 1.75 V (vs. NHE) in 1 N H_2SO_4 at 25°C for IrO_2:20 wt.% F 168

Figure 97. Arrhenius plots for undoped IrO_2 over a temperature range of 25°C to 70°C in 1 N H_2SO_4 170

Figure 98. Arrhenius plots for IrO_2:5 wt.% F over a temperature range of 25°C to 70°C in 1 N H_2SO_4 171

Figure 99. Arrhenius plots for IrO_2:10 wt.% F over a temperature range of 25°C to 70°C in 1 N H_2SO_4 172

Figure 100. Arrhenius plots for IrO_2:15 wt.% F over a temperature range of 25°C to 70°C in 1 N H_2SO_4 173

Figure 101. Arrhenius plots for IrO_2:20 wt.% F over a temperature range of 25°C to 70°C in 1 N H_2SO_4 174

Figure 102. The variation of current vs. time for the IrO_2:F electrodes in 1 N H_2SO_4 under a constant potential of ~ 1.65 V at 40°C 176

Figure 103. Polarization curve of undoped and 10 wt.% F doped IrO_2 after the CA test 177

Figure 104. The Tafel plot of undoped IrO_2 powder after the CA test 178

Figure 105. The Tafel plot of IrO_2:10 wt.% F powder after the CA test 179

Figure 106. Polarization curve obtained in a single full cell PEM electrolyzer test for undoped IrO_2 and IrO_2:10 wt.% F powders at 50°C 181

Figure 107. Polarization curve obtained in a single full cell PEM electrolyzer test for undoped IrO_2 at 50°C and 80°C 182

Figure 108. XRD pattern of as prepared SnO_2:F after drying in the oven at 50°C and subsequent heat treatment at 300°C 184

Figure 109. XRD pattern of undoped and F doped $(Ir,Sn)O_2$ after heat treatment to 400°C 185

Figure 110. The TGA-DTA traces in air of $(Ir_{0.3}Sn_{0.7})O_2$ and $(Ir_{0.3}Sn_{0.7})O_2$:10 wt.% F showing weight loss with respect to temperature 186

Figure 111. The elemental x-ray mapping of Ir, Sn, O and F in $(Ir_{0.3}Sn_{0.7})O_2$:10 wt.% F 187

Figure 112. The bright field TEM image $(Ir_{0.3}Sn_{0.7})O_2$:10 wt.% F showing fine particles in the nanometer range 188

Figure 113. The XPS spectra of Ir $4f_{7/2}$ and $4f_{5/2}$ doublet of $(Ir,Sn)O_2$ and $(Ir,Sn)O_2$:F 190

Figure 114. The XPS spectra of Sn $3d_{5/2}$ and Sn $3d_{3/2}$ doublet of $(Ir,Sn)O_2$ and $(Ir,Sn)O_2$:F 191

Figure 115. The XPS spectra of O 1s of $(Ir,Sn)O_2$ and $(Ir,Sn)O_2$:F 192

Figure 116. EIS spectra of $(Ir,Sn)O_2$ obtained at OCP, 1.5 V, 1.6 V and 1.8 V in 1 N H_2SO_4 .. 195

Figure 117. EIS spectra of $(Ir,Sn)O_2$:10 wt.% F obtained at OCP, 1.5 V, 1.6 V and 1.8 V in 1 N H_2SO_4 196

Figure 118. EIS spectra of commercial IrO_2 obtained at OCP, 1.5 V and 1.6 V in 1 N H_2SO_4 . 197

Figure 119. The polarization curve of undoped and F doped $(Ir,Sn)O_2$ along with commercial IrO_2 in the presence of 1 N H_2SO_4 solution at 40°C with a scan rate of 1 mV/sec before and after iR correction 199

Figure 120. The Tafel plot of commercial IrO_2 before and after iR correction 200

Figure 121. The Tafel plot of $(Ir,Sn)O_2$ before and after iR correction 201

Figure 122. The Tafel plot of $(Ir,Sn)O_2$:10 wt.% F before and after iR correction 202

Figure 123. The variation of current vs. time for $(Ir,Sn)O_2$:F powders and commercial IrO_2 in the CA test performed in a 1 N H_2SO_4 solution at a constant potential of ~ 1.65 V ... 204

Figure 124. Polarization curve of $(Ir,Sn)O_2$:10 wt.% F powder after the CA test 206

Figure 125. The Tafel plot of $(Ir,Sn)O_2$:10 wt.% F powder after the CA test 207

Figure 126. XRD pattern of the as prepared Nb_2O_5:F 209

Figure 127. XRD pattern of undoped and F doped $(Ir,Nb)O_2$ 210

Figure 128. The TGA-DTA traces in air of $(Ir_{0.25}Nb_{0.75})O_2$:F showing weight loss corresponding to fluorine in the electro-catalyst 211

Figure 129. The elemental x-ray mapping of Ir, Nb, O and F in $(Ir_{0.25}Nb_{0.75})O_2$:10 wt.% F..... 212

Figure 130. The bright field TEM image $(Ir_{0.25}Nb_{0.75})O_2$:10 wt.% F shows the presence of fine nanoparticles 213

Figure 131. The XPS spectra of Ir $4f_{7/2}$ and Ir $4f_{5/2}$ doublet of $(Ir,Nb)O_2$ and $(Ir,Nb)O_2$:F 215

Figure 132. The XPS spectra of Nb $3d_{5/2}$ and Nb $3d_{3/2}$ doublet of $(Ir,Nb)O_2$ and $(Ir,Nb)O_2$:F .. 216

Figure 133. The XPS spectra of O 1s of $(Ir,Nb)O_2$ and $(Ir,Nb)O_2$:F 217

Figure 134. EIS spectra of $(Ir,Nb)O_2$ obtained at OCP, 1.5 V, 1.6 V and 1.8 V in 1 N H_2SO_4 . 220

Figure 135. EIS spectra of $(Ir,Nb)O_2$:10 wt.% F obtained at OCP, 1.5 V, 1.6 V and 1.8 V in 1 N H_2SO_4 221

Figure 136. The polarization curve of undoped and F doped $(Ir,Nb)O_2$ along with commercial IrO_2 in the presence of 1 N H_2SO_4 solution at 40°C with a scan rate of 1 mV/sec before and after iR correction 223

Figure 137. The Tafel plot of $(Ir,Nb)O_2$ before and after iR correction 224

Figure 138. The Tafel plot of $(Ir,Nb)O_2$:10 wt.% F before and after iR correction 225

Figure 139. The variation of current vs. time for $(Ir,Nb)O_2$:F powders and commercial IrO_2 in the CA test performed in a 1 N H_2SO_4 solution at a constant potential of ~ 1.65 V ... 226

Figure 140. Polarization curve of $(Ir,Nb)O_2$:10 wt.% F powder after the CA test 228

Figure 141. The Tafel plot of $(Ir,Nb)O_2$:10 wt.% F powder after the CA test 229

Figure 142. Polarization curve obtained in a single full cell PEM electrolyzer test for $(Ir,Nb)O_2$:F and $(Ir,Sn)O_2$:F powders at 50°C 230

Figure 143. Angle and top view of the elementary unit cell of the (110) rutile surface slab used: small - Ir, big - O, dark: F (for F1 configuration). Atoms denoted as 2 and 3 correspond to F2 and F3 configurations of fluorine distributions 239

Figure 144. Free energies of the intermediate reactions for pure IrO_2 240

Figure 145. Free energies of the intermediate reactions for F doped IrO_2 241

Figure 146. The unit cells for bulk (left) and (110) surface (right) calculations used for the atomic configuration of $Ir_{0.25}Sn_{0.75}O_{1.5}F_{0.5}$ 247

Figure 147. Total and partial density of states for IrO_2 250

Figure 148. Total density of states for IrO_2 and $(Ir,Sn)O_2$:F 251

Figure 149. Density of states at Fermi level for $(Ir,Sn)O_2$:F 252

Figure 150. Ir d-band partial density of states for IrO_2 and $(Ir,Sn)O_2$:F. The arrows denote positions of the d-band centers (ε_d) 254

Figure 151. Total and partial density of states for $(Ir_{0.25}Sn_{0.75})O_1F_1$ 256

Figure 152. Ru d-band partial density of states for RuO_2, $(Ru,Sn)O_2$ and $(Ru,Sn)O_2$:F. The arrows denote positions of the d-band centers (ε_d) 260

Figure 153. Total and partial density of states for $(Ru_{0.25}Sn_{0.75})O_{1.5}F_{0.5}$ 262

Figure 154. Total density of states for IrO_2, $(Ir_{0.25}Nb_{0.75})O_2$, and $(Ir_{0.25}Nb_{0.75})O_{1.25}F_{0.75}$ 266

Figure 155. Ir d-band projected DOS for IrO_2 (a), $(Ir_{0.25}Nb_{0.75})O_2$ (b), and $(Ir_{0.25}Nb_{0.75})O_{1.25}F_{0.75}$ (c). The arrows denote positions of the d-band centers (ε_d) 270

Figure 156. Total electronic density of states for $(Ir,Sn,Nb)O_2$ 277

Figure 157. Density of states at Fermi level for different compositions of $(Ir,Sn,Nb)O_2$ 278

Figure 158. Ir d-band partial density of states for $(Ir,Sn,Nb)O_2$. The arrows denote positions of the d-band centers (ε_d) 281

Figure 159. Total bulk density of electronic states for pure IrO_2 and $(Ir_{0.25}Sn_{0.375}Nb_{0.375})O_{2-x}F_x$ (x = 0, 0.5, 1, 1.5) 285

Figure 160. Total bulk density of states at Fermi level for IrO_2 and $(Ir,Sn,Nb)O_2$:F 287

Figure 161. Projected d-band density of states for IrO_2 and $(Ir,Sn,Nb)O_2$:F. The arrows denote positions of the d-band centers (ε_d) 289

Figure 162. Total and projected density of states for $(Ir_{0.25}Sn_{0.375}Nb_{0.375})O_2$ 291

Figure 163. Total and projected density of states for $(Ir_{0.25}Sn_{0.375}Nb_{0.375})O_1F_1$ 292

Figure 164. Cohesive energy of IrO_2 and $(Ir_{0.25}Sn_{0.375}Nb_{0.375})O_{2-x}F_x$ 294

Figure 165. A unit cell of Pt-Ru (1 1 1) surface slab. The arrows denote Pt and Ru atoms exchanges modeling the surface segregation 310

Figure 166. X-ray diffraction patterns of CSG-Pt(Ru)/C and CSG-Pt(Ru) obtained after thermal treatment in UHP Ar and UHP Ar - 1% O_2 atmosphere, respectively 315

Figure 167. HRTEM images along with SAD pattern of CSG-Pt(Ru)/C showing formation of nanocrystalline Pt(Ru) dispersed in the framework of amorphous C 316

Figure 168. TGA-DTA traces in air of CSG-Pt(Ru)/C and CSG-Pt(Ru) after final heat treatment in UHP Ar - 1% O_2 318

Figure 169. XRD pattern of CSG-Pt(Ru) obtained after heat treatment in UHP-Ar at 600°C ... 320

Figure 170. TEM and HRTEM images, along with SAD pattern of CSG-Pt(Ru) showing nanocrystalline Pt(Ru) alloy and lattice fringes of (111) plane of Pt(Ru) 321

Figure 171. The XPS spectra of Pt $4f_{7/2}$ and Pt $4f_{5/2}$ doublet for CSG-Pt(Ru) and JM-Pt(Ru) ... 322

Figure 172. The XPS spectra of Ru $3p_{3/2}$ for CSG-Pt(Ru) and JM-Pt(Ru) 323

Figure 173. The CO stripping voltammetry curve for CSG-Pt(Ru) in 0.5M H_2SO_4 325

Figure 174. The CO stripping voltammetry curve for JM-Pt(Ru) in 0.5M H_2SO_4 326

Figure 175. The polarization curve of CSG-Pt(Ru) and JM Pt(Ru) conducted at 40°C with a scan rate of 10 mV/sec 328

Figure 176. Polarization curve of DMFC single cell at various temperatures for the CSG-Pt(Ru) and JM-Pt(Ru) anode 330

Figure 177. Power density performance of DMFC single cell at various temperatures for the CSG-Pt(Ru) and JM-Pt(Ru) anode 331

Figure 178. Chronoamperometry plot of CSG-Pt(Ru) and JM-Pt(Ru) measured at 0.65 V vs. NHE 333

Figure 179. XRD patterns of Pt-Ru-Ni-Ti/C and Pt-Ru-Ni-Ti obtained after heat treatment in UHP-Ar at 500°C and sequential multiple treatments at 200°C in UHP-Ar-1% O_2, respectively 345

Figure 180. TGA-DTA traces in air of Pt-Ru-Ni-Ti/C and Pt-Ru-Ni-Ti after final heat treatment in UHP Ar - 1% O_2 347

Figure 181. XRD pattern of Pt-Ru-Ni-Ti obtained after heat treatment in UHP-Ar at 600°C ... 348

Figure 182. HRTEM images showing the nano-crystalline alloy and lattice fringes of the (111) plane of Pt-Ru-Ni-Ti 349

Figure 183. The XPS spectra of Pt $4f_{7/2}$ and Pt $4f_{5/2}$ doublet for Pt-Ru-Ni-Ti and JM catalyst.. 351

Figure 184. The XPS spectra of Ru $3p_{3/2}$ for Pt-Ru-Ni-Ti and JM catalyst 352

Figure 185. The XPS spectra of Ni $2p_{3/2}$ for Pt-Ru-Ni-Ti catalyst 353

Figure 186. The polarization curve of the quaternary Pt-Ru-Ni-Ti along with the JM catalyst conducted in 1 M CH_3OH and 0.5 M H_2SO_4 at 40°C with a scan rate of 10 mV/sec 355

Figure 187. Retention of current in the chronoamperometry plot over a period of 100 hours measured at 0.65 V vs. NHE 356

Figure 188. XRD pattern of Pt-Ru-Os-Ir based alloy obtained after drying in air at 120°C (a), further heat treatment in UHP-Ar at 450°C (b), and subsequent thermal treatments in UHP Ar-1% O_2 (c) 364

Figure 189. TGA and DSC traces after heat treatement in UHP Ar at 450°C and UHP Ar - 1% O_2 at 300°C 365

Figure 190. TEM bright field image of Pt-Ru-Os-Ir alloy showing nanoparticles of ~ 5 - 7 nm367

Figure 191. The polarization curves of Pt-Ru-Os-Ir alloy along with Pt-Ru tested at 40°C 369

Figure 192.The polarization curves of Pt-Ru-Os-Ir alloy along with Pt-Ru tested at 60°C 370

Figure 193. Electronic density of states for $MgNb_2O_6$ (a), and $MgTa_2O_6$ (b) 380

Figure 194. Electronic density of states for $ZnNb_2O_6$ (a), and $ZnTa_2O_6$ (b) 381

Figure 195. Electronic density of states for $MgNb_2O_6$ with Sc (a), B (b), and Al (c) 384

Figure 196. Electronic density of states for $ZnNb_2O_6$ with Sc (a), B (b), and Al (c) 386

Figure 197. Electronic density of states for $MgNb_2O_6$ with As (a), Cr (b), and W (c)..... 388

Figure 198. Electronic density of states for $ZnNb_2O_6$ with As (a), Cr (b), and W (c)..... 390

Figure 199. Electronic density of states for $MgNb_2O_6$ (a), and $ZnNb_2O_6$ (b) doped with F 391

Figure 200. Cohesive energy for all materials studied in eV/at..... 393

Figure 201. Variation of current vs. time in the chronoamperometry test performed on $(Zn_{0.9}Y_{0.1})Nb_2O_6$ in a 1 N H_2SO_4 solution at 1.75 V (vs. NHE)..... 396

Figure 202. Scanning Electron Microscope images of CVD derived VACNT (a), CVD derived VO_x thin film on Ni (b), and CVD deposited VO_x-VACNT heterostructures (c) . 408

Figure 203. EDX spectra of the CVD deposited thin film on Nickel (a) and CVD deposited-VACNT heterostructures (b)..... 409

Figure 204. Raman spectra of VACNTs (a) and Vanadium oxide coated on the CNTs (b) 411

Figure 205. HRTEM images of the vanadium oxide nanospheres coated on Multiwall CNTs . 412

Figure 206. XPS of CVD deposited VACNT-oxide nanosphere heterostructures..... 414

Figure 207. Cyclic voltammograms of the VO_x-VACNT (a), and VO_x thin film (b); Cyclic voltammograms of VO_x-VACNT and VOx thin film (c), Capacitance behavior of VO_x-VACNT and VO_x thin film (d), Areal capacitance of VO_x-VACNT (e), and cycling behavior of VO_x-VACNT and VO_x thin film. 417

Figure 208. Impedance behavior of thin film vanadium oxide (a) and vanadium oxide nanosphere-VACNT composite heterostructure (b)..... 422

Figure 209. XRD of VN prepared by HEMM taken as-prepared (a), after washing with DI water (b), and as-prepared milling time ranging from 5 to 180 minutes (c)..... 436

Figure 210. TEM image along with the SAD pattern of VN (a), and the HRTEM image of VN showing lattice fringes with a d spacing of ~0.24 nm 438

Figure 211. XPS data showing V 2p and O 1s peaks before cycling (a), and after cycling (b); and N 1s peaks before and after cycling (c) 440

Figure 212. Cyclic voltammogram of VN at a scan rate of 10 mV/s (a), and at different scan rates (b) 442

Figure 213. Gravimetric, Areal and Volumetric capacitence of VN as a function of scan rate . 445

Figure 214. Galvanostatic charge-discharge profile (a), and long term charge - discharge cyclability of HEMM synthesized VN 448

Figure 215. Specific capacity vs. cycle number of microcrystalline Sn cycled at a constant current of ~ 50 mA/g in the potential window 0.01 V - 1.2 V 457

Figure 216. Differential capacity vs. cell potential curves of microcrystalline Sn obtained after 1st cycle cycled at ~ 50 mA/g in the potential window 0.01 V - 1.2 V 458

Figure 217. SEM micrograph of pure Sn before (a), and after 10th cycle (b) 460

Figure 218. XRD patterns of C - 70 wt.% Sn generated after 5 minutes and 1 hour of milling. 461

Figure 219. Raman spectra of Sn/C mixture obtained after 1 hour of mechanical milling 463

Figure 220. Specific capacity and coulombic efficiency vs. cycle number of Sn/C obtained after 5 minutes of HEMM cycled at a constant current of ~ 50 mA/g 464

Figure 221. Specific capacity and coulombic efficiency vs. cycle number of Sn/C obtained after 1 hour of HEMM cycled at a constant current of ~ 50 mA/g 465

Figure 222. SEM micrograph of Sn/C mixture, obtained after 1 hour of HEMM before (a), and after 20 cycles (b) 466

Figure 223. Glancing angle XRD patterns of a-C/Si bi-layer thin film generated by rf magnetron sputtering on copper foil 474

Figure 224. SEM micrograph (a), and EDAX spectra (b) of a-C/Si thin film 475

Figure 225. Raman spectra of a-C/Si thin film show the presence of amorphous Si 476

Figure 226. Specific capacity and coulombic efficiency vs. cycle number of a-Si thin film composite cycled at a constant current of ~ 100 $\mu A/cm^2$ 478

Figure 227. Specific capacity and coulombic efficiency vs. cycle number of a-C/Si thin film composite cycled at a constant current of ~ 100 $\mu A/cm^2$ 479

Figure 228. Specific capacity and coulombic efficiency vs. cycle number of a-C/Si/C thin film composite cycled at a constant current of ~ 100 $\mu A/cm^2$ 480

Figure 229. Differential capacity vs. cell potential curves of a-C/Si thin film electrode obtained after 1st and 2nd cycle cycled at C / 2 rate 482

Figure 230. SEM micrograph of a-Si/C thin film anode (a), and a-Si film (b) after 75 cycles .. 484

ACKNOWLEDGEMENTS

To my grandparents

Dada & Baa

[Late Mr. Pramodrai M. Kadakia & Late Mrs. Kokilaben P. Kadakia]

Dada & Dadi

[Mr. Rameshchandra J. Shah & Mrs. Madhukanta R. Shah]

Firstly, I would like to thank my dissertation adviser, Dr. Prashant Kumta, who has mentored and supported me throughout my thesis work. I am thankful to him for being ingenious and having shown immense faith in me.

I am grateful to Dr. Ayyakkannu Manivannan for the fruitful discussions we have had, and for his help in performing X-ray Photoelectron Spectroscopy characterization. I would like to thank the rest of my Ph.D. thesis committee, Dr. Robert Enick and Dr. Di Gao, for their insightful comments. I would also like to thank all my lab members for their unceasing support. I am truly obliged to Dr. Moni Datta, Dr. Oleg Velikokhatnyi and Prashanth Jampani, for their valuable acumen and assistance with my research work in Proton Exchange Membrane based water electrolysis. I sincerely thank Dr. Abhijit Roy and Dr. Nicolaus Rock for their guidance during my initial stages in the lab.

In addition, I owe a lot of gratitude to my family and friends whose perpetual support and encouragement made my life in Pittsburgh replete with joy. Lastly, I am humbled and blessed by the unconditional love, warmth and affection shown by my grandparents, parents and brother Yash throughout my life.

1.0 INTRODUCTION

1.1 HYDROGEN

Hydrogen, composed of a single proton and electron, comprises 90% of all matter of the universe. Its extreme buoyancy allows hydrogen to disperse rapidly in case of accidental release and will ultimately end up escaping the earth's atmosphere or coming down as water when combined with the oxygen in the air [1]. Hydrogen has been considered as an attractive alternative to fossil fuels over the past decade and is considered by many a harbinger to the hydrogen economy. Furthermore, as the most lightweight fuel it has the potential to provide clean, reliable, and affordable energy supply to meet the growing global energy demand [2-4]. However a major impediment towards commercialization has been the ability to economically generate clean and pure hydrogen combined with cost effective strategies for storage and distribution [4-8].

Currently, most of the hydrogen is produced from fossil fuels like coal, natural gas and oil. The current technology for generating hydrogen is quite advanced but remains to be optimized for large scale production in order to increase energy efficiency, and reduce environmental impact and costs. The most economical and frequently used process for manufacture of hydrogen is catalytic steam reforming of natural gas, which is mainly composed of methane. Possible improvements of the process are mainly focused on recovery of thermal

energy, process integration, and gas purification [9, 10]. Another widely used method for hydrogen production is by coal gasification. These technologies are mature, but further improvements are still considerable and it takes into account innovative membranes for air separation, progress in gasifier configuration, hot gas purification systems, new solvents and membrane reactors for hydrogen separation.

Gasification and biomass conversion is an emerging technology for producing hydrogen via natural gas or heavy fuel oil. But, it is a high temperature process with substantial electricity inputs. Hydrogen can also be produced from water through thermochemical cycles, photoelectrochemically *i.e.* direct thermal or catalytic splitting of water; and photobiologically using sunlight and photosynthetic microorganisms. These processes have very low efficiencies and have not been explored commercially [1, 9, 10].

Water electrolysis or reverse fuel cell operation is the conversion of electric energy into hydrogen. In its present state, the process is significantly more expensive than hydrogen production from fossil fuels and covers only a small share of the world production. But, this process yields very high purity hydrogen and is a benign and environmental friendly process [3, 5, 8, 11, 12].

1.2 HYDROGEN PRODUCTION TECHNOLOGIES

The main requirement for hydrogen production comprises feedstock and energy. In today's world, the logical feed stocks for hydrogen production are hydrocarbon fuels (C_xH_y) and water (H_2O). However, extraction of hydrogen from either hydrocarbons or water requires energy. The

energy required for production of hydrogen, though will always be greater than the amount of energy released by hydrogen utilization. Hydrogen is currently being produced industrially by fossil fuels like natural gas, oil and coal.

Hydrogen production technologies such as steam reforming, partial oxidation of hydrocarbons, and gasification are mature and widely used. But, they need to be optimized for large-scale production in order to better efficiency, environmental impact, and, capital and operating costs. For these processes to be sustainable in the long time run, they need to be coupled with capture and storage of CO_2 which is the main by-product of these processes. Development of solutions for economical and cost-effective CO_2 capture is very essential to have an environmental friendly process. The cheapest and frequently used process is the catalytic steam reforming of natural gas. There is a lot of ongoing work on the improvements of this process focusing on thermal energy recovery, process integration and gas purification [9, 13]. The potential for further improvements is very much critically needed to take into consideration development of innovative membranes for air separation, modifications in gasifier configuration, and the hot gas purification systems amongst many more. There is also need for synthesizing new diluents, materials and solvents along with membrane reactors for hydrogen separation.

Other technologies such as coal gasification would be interesting if they are integrated into combined cycles with CO_2 capture and storage. Processes such as autothermal reforming and partial oxidation of hydrocarbons are used for heavier hydrocarbons. Other less explored process includes thermal or catalytic cracking of methane, which converts methane in hydrogen and carbon, without CO_2 production; and solar steam reforming, that in turn use concentrated solar energy as the heat source for reforming.

Hydrogen can also be produced from biomass using different biological processes and thermochemical processes *viz.,* gasification and pyrolysis. The thermochemical processes are similar to that used for coal gasification. The biomass comprises of agricultural and forest residues, industrial and urban wastes, and organic waste materials. A lot of improvement is needed in order to increase output, efficiency and reliability, along with decreasing costs. Photobiological hydrogen production uses sunlight and photosynthetic microorganisms for splitting water. These techniques are still at laboratory scale and the conversion efficiencies are way too low for commercial use.

Also, photoelectrochemical systems have been explored wherein the electric energy generation from solar light and its utilization to produce hydrogen from water are combined *via* an electrolyzer. It uses semiconductor devices introduced in a solution, which converts solar energy to chemical energy. It is a very promising approach to produce hydrogen, but considerable research needs to be done on developing materials and engineering the process in order for these systems to be used for large scale production.

All the above mentioned technologies are thus either energy intensive, or in their nascent stages. All the currently used commercial or large scale hydrogen production processes do not give us ultra high purity (UHP) hydrogen, with their primary dependence on scarce fossil fuel reserves and need to combat with reducing the pollutants generated in the processes. This high energy intensity of production and storage of hydrogen increases the net energy use, owing to investment in efforts to reduce the greenhouse gas emissions. High quality hydrogen can only be produced effectively by electrochemical conversion of water to hydrogen and oxygen. Electricity induced splitting of water offers no pollution or toxic by-products if the electricity is generated *via* renewable energy sources like photovoltaics, wind turbines, geothermal and hydropower. We

can thus envision this as a very plausible and ecologically sustainable option for energy production if the efficiency of water electrolysis can be improved [14-17].

1.3 WATER ELECTROLYSIS

A promising approach to produce hydrogen is by electricity induced splitting of water using alkaline, neutral or polymer electrolyte membrane (PEM) based water electrolysis [2, 11, 15, 16, 18]. This involves passing an electric current through the water to split it into hydrogen and oxygen. Electrolysis is less efficient than a direct chemical path but it offers virtually no pollution or toxic byproducts if the electric current is generated using renewable energy *viz.*, wind, solar, geothermal and hydropower [3, 8, 12, 15, 16, 19-23].

The high capital costs of current electrolyzers arise as a result of the use of expensive noble metal based electro-catalysts like IrO_2, RuO_2, Pt; use of relatively small systems of comparatively low efficiencies, combined with the added costs of customized power electronics, and labor intensive fabrication [2, 7, 9, 12, 22, 24, 25]. The approach nevertheless, is potentially very lucrative since it offers virtually no green house gas emission or toxic byproducts particularly, if the electric current is generated using renewable energy or nuclear energy sources. Consequently, it would provide a plausible option if the efficiency were increased by the generation of highly efficient non-noble metal/metal oxide based electro-catalysts or identification of electro-catalysts with significant reduction of the expensive noble metal fraction [2, 12, 15, 16, 24, 26-28].

Rutile type noble metal oxides, IrO_2 and RuO_2 are well known and are typically accepted as the archetypical standards for oxygen evolution reaction (OER) anode electrode catalysts in PEM based water electrolysis. However, the anodic over-potential and the cell resistance in electrolysis contribute to a majority of the losses witnessed in catalytic performance. In addition, the electro-catalyst based on IrO_2 and RuO_2 undergo electrochemical or mechanical degradation under extreme and highly corrosive electrochemical environments prevalent in the acid assisted water electrolysis which reduce the performance with time and moreover, diminish the service life of the electrode during OER [24, 29-31]. Therefore, the design, synthesis and processing of non-precious metal/metal oxide catalysts for OER electrodes exhibiting high activity and durability under the highly aggressive chemical environments of water electrolysis would be of paramount importance in significantly decreasing the overall capital costs.

For PEM electrolysis cells, non-precious metal catalysts for electrodes with high activity and durability would decrease overall capital costs. However, it is unlikely that a non-noble metal catalyst will be identified for PEM system, but ways to decrease noble metal loading need to be identified. Decreasing the noble metal loading as well as improving the catalytic activity and durability could be achieved using novel synthesis techniques to generate high surface area nanostructured electro-catalysts, or improved low cost support structure (diluents) for electro-catalyst [29, 30, 32-36]. Strategies involving less expensive, more durable materials as supports or diluents for expensive electro-catalyst that are easier to manufacture would immensely help to lower the costs.

The schematic layout of a water electrolysis cell is shown in **Figure 1** [37]. Hydrogen is produced by supplying water to the anode decomposing into oxygen, protons, and electrons. The protons are transported through the proton conductive membrane to the cathode. The electrons

exit the cell via the external circuit, which supplies the driving force (i.e. cell potential) for the reaction. At the cathode the electrons and protons re-combine to yield hydrogen gas. The volume of hydrogen gas produced is therefore twice the amount of oxygen gas.

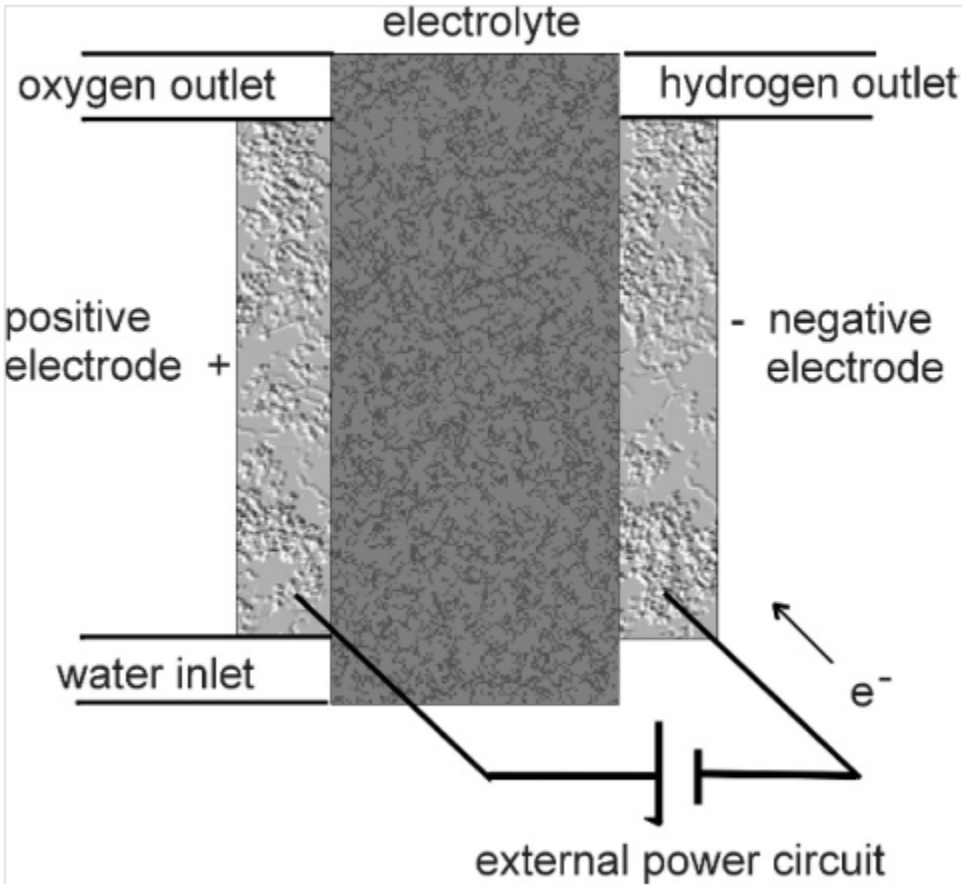

Figure 1. Schematic of a water electrolysis cell

2.0 BACKGROUND

2.1 TYPES OF ELECTROLYZERS

Three different types of electrolysis cells are proposed and they are classified into groups with respect to the electrolyte being used for the same. They are alkaline electrolysis cells, solid oxide electrolyzers and PEM based electrolysis. The overall electrolysis reaction is the sum of two electrochemical reactions (half-cell reactions) taking place at the electrodes. The anode is the electrode where oxidation of the reactants and/or intermediates occurs and cathode is where reduction reaction occurs.

2.1.1 Alkaline Electrolysis

Alkaline elctrolyzers is a mature technology wherein electrolysis reaction occurs in an alkaline solution of caustic potash solution at a concentration of 20 - 30 wt.% KOH between temperatures of 40°C and 90°C. The anode is typically made of nickel and the cathode of steel or stainless steel on which are coated the catalysts. The catalysts are often nickel based compounds with molybdenum on the cathode and mixed oxides of cobalt, nickel and/or lanthanum on the anode [3, 37-39]. The two electrodes are separated by a diaphragm which selectively allows the hydroxyl and water molecules to permeate through it, while restricting the mixing of the evolved

gases. The cell design can be of a tank type or a filter press type. The tank type uses monopolar electrodes fitted in a tank. This monopolar system offers a rugged system with a simple design and construction, but only at the expense of large power consumption. The filter press type uses hundreds of bipolar electrodes stacked together. The reactions taking place at each electrode are given below:

Anode (oxidation): $2OH^-_{(aq)} \rightarrow H_2O_{(l)} + 2e^- + 0.5O_{2\,(g)}$

Cathode (reduction): $2H_2O_{(l)} + 2e^- \rightarrow 2OH^-_{(aq)} + H_{2\,(g)}$

Overall Reaction: $H_2O_{(l)} \rightarrow H_{2\,(g)} + 0.5O_{2\,(g)}$

The major disadvantage of this system is that it uses a highly caustic electrolyte and is unable to produce hydrogen at high pressures. This results in addition of an external compressor, leading to added costs and complexity in the system. The alkaline electrolzer systems have a very low partial load range, limited current density and less efficiency (~ 30 - 35%) [40, 41]. The product gases cross-diffuse through the membrane causing a decrease in the efficiency, since the oxygen gets catalyzed back to water on the cathode side with the evolving hydrogen. The limiting maximum achievable current density is due to the massive ohmic losses across the electrolyte and the membrane. Gas purity is also compromised due to traces of electrolyte which need to be scrubbed. All these factors lead to a very bulky stack design configuration [3, 17, 39].

2.1.2 Solid Oxide Electrolysis

Solid oxide electrolyzer cells (SOEC) operate at high temperatures in the range of 700°C to 1000°C. At these temperatures, water in its vapor state *i.e.* steam is split into hydrogen and oxygen. The heat provides a lot of energy for this endothermic reaction which is favored with

increase in temperature, and hence the electrical energy needed for decomposition of water at such high temperatures is very less [17, 42]. The SOECs have a solid ionic conducting electrolyte, mostly yttria stabilized zirconia which has very good mechanical strength and oxygen ion conductivity at high temperatures. The cathode is usually based on nickel due to its high electrochemical activity. Ceramics with very high active surface are also employed in order to maximize transport of steam and gas. The anodes are usually mixed oxides possessing a perovskite structure such as strontium doped lanthanum manganite ($La_{0.6}Sr_{0.4}MnO_3$) [43, 44]. A tubular or a planar cell design can be employed for these systems. The planar cell design is usually selected as it offers higher power densities, although its sealing is very demanding [43]. The reactions taking place at each electrode are given below:

Anode (oxidation): $2O^{2-}{}_{(g)} \rightarrow O_{2\,(g)} + 4e^-$

Cathode (reduction): $2H_2O_{\,(g)} + 4e^- \rightarrow 2H_{2\,(g)} + 2O^{2-}{}_{(g)}$

Overall Reaction: $2H_2O_{\,(g)} \rightarrow 2H_{2\,(g)} + O_{2\,(g)}$

There are several issues affecting SOEC which include long start-up and shut-down time for the system, bulky system design along with sealing issues; thermal expansion and chemical instability due to the high temperatures used. There is a need for research and development of novel, facile and reduced cost, highly durable materials for SOECs. The durability and endurance of the electrodes is also very poor due to increase in electrical resistance and delamination of the oxygen electrode. Optimization of the material structure and detailed understanding of the electrochemistry and degradation mechanisms is required for large scale production of hydrogen by solid oxide electrolysis [42, 45].

2.1.3 PEM based Water Electrolysis

Polymer Electrolyte Membrane or Proton Exchange Membrane (PEM) based electrolyzer cells employ a solid polymer electrolyte, wherein a solid sulfonated polystyrene membrane (Nafion) is used as an electrolyte. This membrane has a very high protonic conductivity and low crossover rates. Since the electrolyte is a membrane, it is immobilized in the cell and will not lead to any leaching of the same [42, 46]. The PEM electrolyzer system has very compact stack design and can withstand very high pressures. High current densities can be achieved due to very less resistance of the thin polymer electrolyte membrane, and ultra high purity (UHP) hydrogen is produced due to low crossover rates. The high pressure operation helps in delivering the hydrogen at high pressure, thus reducing the energy requirement to compress and store the hydrogen. The widely used electrodes at the anode are iridium oxide (IrO_2) and/or ruthenium oxide (RuO_2) on a titanium support; and platinum on the cathode side [17, 47]. **Figure 2** shows the basic operation of a PEM electrolzer cell. The reactions taking place at each electrode are given below:

Anode (oxidation): $2H_2O_{(l)} \rightarrow O_{2\,(g)} + 4H^+_{(aq)} + 4e^-$

Cathode (reduction): $4H^+ + 4e^- \rightarrow 2H_{2\,(g)}$

Overall Reaction: $2H_2O_{(l)} \rightarrow 2H_{2\,(g)} + O_{2\,(g)}$

Due to the high voltage (> 1.5 V) and harsh acidic conditions in PEM based water electrolysis, the components have to be robust and highly corrosion resistant, especially at the oxygen evolution electrode. Carbon based materials cannot be used such as in PEM fuel cells since they undergo corrosion above 1 V. Hence, titanium and stainless steel supports are used at the anode as supports for the catalysts albeit with no electrochemical activity [47, 48]. The

electrolyte is also corrosive and this requires usage of expensive metal components in the cell design. The noble metal based electro-catalysts used at the electrodes are thus very expensive (Pt, IrO_2, RuO_2) and are still not very durable [39, 49]. More research is therefore required to synthesize cost effective catalysts which are more electrochemically active and robust in the acidic conditions to achieve the maximum power density. This method of hydrogen production can be envisioned for the creation of a novel hydrogen societyin the future, wherein hydrogen (energy carrier) is incorporated in an idealized energy cycle. Here, electricity from renewable energy sources would be the only input used to split water and the only output would be electric power.

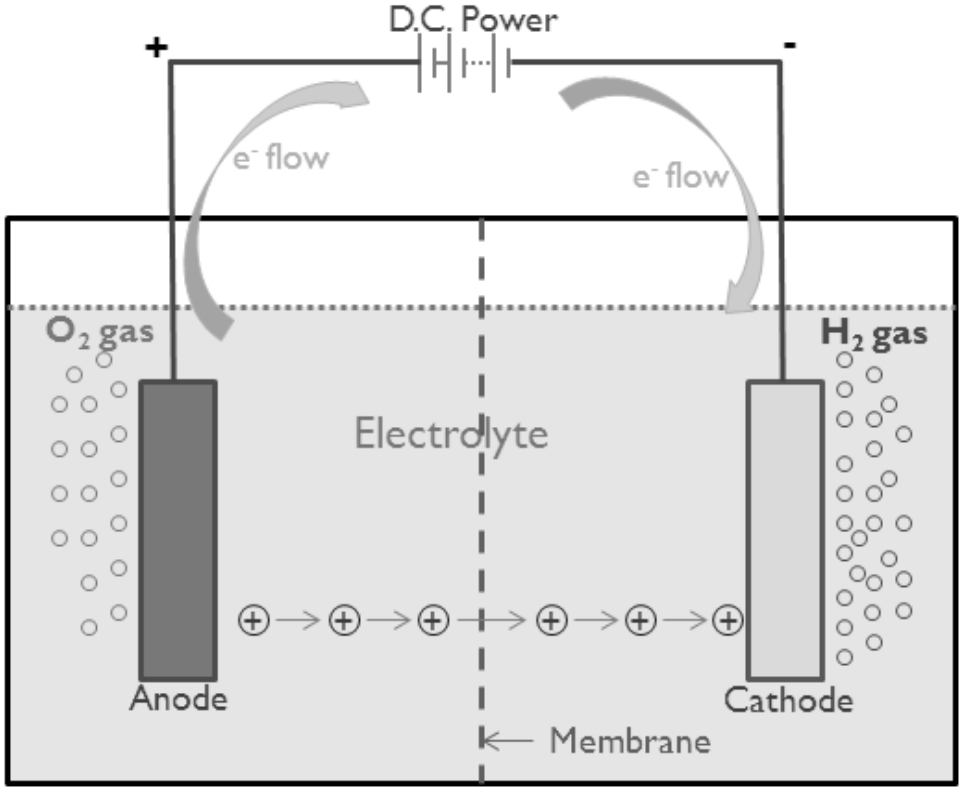

Figure 2. PEM electrolysis schematic diagram

2.2 FUNDAMENTALS

2.2.1 Thermodynamics and Kinetics

The energy required splitting one mole of water into hydrogen and oxygen corresponds to the enthalpy of formation of one mole of water. A part of this enthalpy of the reaction (ΔH_f) can be applied as thermal energy. The Gibbs free energy (ΔG_f) is the minimum amount of the enthalpy of the reaction that needs to be applied *via* electrical energy. From the electrochemists' point of view, the minimum reversible cell voltage needed to be applied can be expressed by the equation $V_r = \Delta G_f / nF$, where 'n' is the number of electrons per mole of product *i.e.* 2 in the case of water electrolysis, and F is the Faraday constant (96485 C/mol). At the standard conditions of temperature and pressure *i.e.* T = 25°C and P = 1 atm, $\Delta G_f \sim 237$ kJ/mol, $\Delta H_f \sim 285$ kJ/mol, and thus, $V_r \sim 1.23$ V. This potential corresponds to the standard reversible cell potential with respect to liquid water electrolysis [15, 42, 50].

The total energy required for splitting water can be supplied by a combination of electricity and heat. If heat cannot be incorporated in the system, the minimum cell voltage becomes related to the enthalpy of the reaction and this is defined as the thermo-neutral voltage. It can be expressed by the equation $V_{th} = \Delta H_f / nF$. At the standard conditions for temperature and pressure, $V_{th} \sim 1.48$ V. This demonstrates the reason higher temperatures are more advantageous for water electrolysis from a thermodynamic view point [38, 50].

The cell voltage of an operating electrolysis cell is higher than the thermodynamic ideal cell voltage. The total applied voltage or the real cell voltage can be described as the potential necessary to enhance the electron transfer. The real cell voltage is the sum of the ideal thermodynamic cell voltage (~1.23 V) along with the voltage drop caused due to ohmic resistance (iR) at a particular current density 'i'; the iR drop due to solution, electrode and membrane resistance; and the overpotentials at the cathode and the anode. The overpotentials at the cathode and anode are caused due to irreversible processes occurring at the electrode-electrolyte interface which is termed as the activation overpotential (kinetic limitation). This overpotential is dependent on the rate of exchange of electrons at the electrochemical interface under reversible conditions and on the reaction pathway or mechanism. The electro-catalysts used at the cathode and anode help increase the rate of the reaction at their respective electrodes.

The Tafel equation can be obtained from the Butler-Volmer equation when the reaction is driven infinitely in one specific direction *i.e.* either anodic or cathodic. The anodic Tafel equation is given below:

$\eta = (RT/\alpha F) \ln (i/i_0)$, where 'η' is the overpotential, 'R' is the universal gas constant, 'T' is the temperature (K), 'α' is the transfer co-efficient (0.5) and expresses the activation barrier of the electrochemical reaction, 'i' is the current density, and 'i_0' is the exchange current density. The Tafel slope from this equation is used to determine the reaction kinetics, and is very useful since the slopes are independent of the electrode surface area [51-53].

2.2.2 Reaction Mechanism

The calculated Tafel slope would give an indication of the reaction mechanism. In PEM based water electrolysis, water splitting occurs in the acidic media. Under the harsh acidic conditions, the interactions between hydrogen and the metal cathode is very weak. Thus, hydrogen evolution is much faster at the cathode as compared to oxygen evolution at the anode. The hydrogen evolution reaction is thus expectedly not considered to be the rate determining step [54-56]. The anodic reaction mechanism as reported in literature [53, 55] is given below, wherein the * represents an active site on the metal oxide surface:

$$2H_2O \rightarrow HO^{*} + H_2O + H^{+} + e^{-}$$

$$\rightarrow O^{*} + H_2O + 2H^{+} + 2e^{-}$$

$$\rightarrow HOO^{*} + 3H^{+} + 3e^{-}$$

$$\rightarrow O_2 + 4H^{+} + 4e^{-}$$

The Tafel slope would help determine the limiting step and thus confirm the number of electrons transferred in the course of electrolysis whilst using a particular electro-catalyst. The third reaction is thus the rate determining step of this mechanism and it has been proved theoretically and experimentally in literature [54, 55, 57-59].

3.0 GOALS AND OBJECTIVES

3.1 MOTIVATION

First row transition metal oxides such as AB_2O_4 type spinels (*E.g.* $NiCo_2O_4$, Co_3O_4), ABO_3 perovskites (*E.g.* $LaNiO_3$, $LaCoO_3$) or $A_{1-x}A'_xB_yB'_{1-y}O_3$ perovskite (*E.g.* $Ba_{0.5}Sr_{0.5}Co_{0.8}Fe_{0.2}O_{3-\delta}$) have been identified as cost effective alternatives in alkaline water electrolysis to IrO_2 as anodes in PEM electrolysis. However, although promising, the overall electrochemical response relative to state of the art IrO_2 electro-catalyst indicated the need for further work [2, 3, 27, 28]. Similarly, Nocera *et al.* [18, 26] reported phosphate based catalysts functioning at neutral pH.

In recent years however, it has been reported that PEM based water electrolysis systems offer several advantages over traditional alkaline and neutral pH based water electrolysis technologies. They include higher energy efficiency, greater production rates, increased product purity, use of much less corrosive electrolyte, and offering a more compact design thus rendering PEM electrolysis a simple, sustainable, and cost-effective technology for generating, compressing, and storing hydrogen [15, 16, 24, 31, 32, 37]. In addition, PEM electrolysis can be designed to electrochemically generate hydrogen at pressures of 200 psi or greater, thus eliminating the need for highly expensive mechanical compression which is required for conventional alkaline water electrolysis [16, 37]. Identification of non-precious metal catalysts or catalysts with substantially reduced noble metal contents exhibiting no reduction in

electrochemical activity compared to the noble metal oxide would hence constitute a major breakthrough in PEM based water electrolysis.

3.2 ELECTRO-CATALYST SYSTEMS

In PEM based water electrolysis, rutile type noble metal oxides, IrO_2 and RuO_2, have been identified and considered as gold standards for the oxygen electrode anode electro-catalyst [29-31, 33, 35, 36, 60-62]. Chen *et al.* [63, 64] examined potential oxide supports for oxygen electrode in PEM fuel cells: ebonex (primarily composed of Ti_4O_7), phase pure microcrystalline Ti_4O_7 and $Ti_{0.9}Nb_{0.1}O_2$. However, there is gradual loss of current associated with these supports due to the electrochemical instability of ebonex and Ti_4O_7 at oxygen evolution conditions above 1.6V in 1N H_2SO_4. In the search for electro-catalysts for PEM based water electrolysis, many less expensive and highly corrosion resistant metal oxides such as tin oxide (SnO_2), niobium oxide (Nb_2O_5), tantalum oxide (Ta_2O_5) or titanium oxide (TiO_2) have been explored as excellent alternative anode candidates to currently used expensive IrO_2 or RuO_2 electro-catalysts. Unfortunately, the above mentioned non-noble metal oxides show no catalytic activity for the oxygen evolution reaction in PEM based water electrolysis and furthermore, these systems also exhibit very poor electronic conductivity.

It has been reported that mixed oxides obtained by the addition of cheaper, economical oxides as supports such as SnO_2, Ta_2O_5, Nb_2O_5, TiO_2 with the noble metal oxide electro-catalyst, IrO_2 and/or RuO_2 (*E.g.* IrO_2 - SnO_2, RuO_2 - SnO_2, IrO_2 - Ta_2O_5, IrO_2 - SnO_2 - Nb_2O_5 *etc.*) [24, 29-32, 35, 36, 48, 57, 58, 60, 65-74] would reduce the cost of the noble metal loading by

maintaining the catalytic activity and electronic conductivity similar to the pure noble metal oxide, while also improving the overall corrosion characteristics of noble metal oxide electro-catalysts. However, such *mixed oxides* mixtures result in a decrease in active surface area and electrical conductivity with increase in the less economical non-conductive metal oxide content, and as a result no beneficial effect on the electrochemical performance is perceived with the addition of less expensive oxides beyond a threshold limit (*E.g.* above 50 at.%) [24, 29-32, 36, 48, 65-68, 74].

For instance, IrO_2 + Ta_2O_5 with the composition of 70 at.% IrO_2 has been identified as the best combination in binary oxide system in the presently commercial application owing to their good electroctalytic activities and high stability [30, 48, 68, 74]. However, the electrochemical properties IrO_2+Ta_2O_5 drastically degrade below 50 at.% Ta_2O_5. Therefore, the search for high performance alternative non-noble metal based electro-catalysts or electro-catalysts with significant reduction in noble metal content with comparable activity and durability as the pure noble metal oxides is thus a very pertinent and active area of research with potentially tremendous pay off.

Nb_2O_5 has also been identified as a promising candidate to substitute Ta_2O_5 since it presents similar properties and is cheaper than Ta_2O_5. However, only few studies have been performed based on IrO_2 + Nb_2O_5 as an anode for PEM based water electrolysis [71-73]. On the other hand, IrO_2 - SnO_2 mixtures have been extensively investigated with respect to oxygen evolution in acid environment due to the similarity between the two oxide structures [29, 32, 66]. In the case of IrO_2 + SnO_2 mixed electrodes synthesized by thermal decomposition of the corresponding metal salts on Ti plate, De Pauli *et al.* [29, 66] have reported a noticeable surface enrichment of IrO_2 accompanied by an increase of the surface charge of the mixed oxide in

comparison with the pure oxides and as a result a significant reduction of noble metal loadings has been reported. On the other hand, Marshall *et al.* [31, 32, 60] have reported a decrease in active surface area and electrical conductivity of $(Ir_xSn_{1-x})O_2$ solid solution with increase in SnO_2 content, and as a result no beneficial effect on electrochemical performance has been noticed with addition of SnO_2 to IrO_2 as an anode for PEM water electrolysis.

3.3 PROPOSED NOVEL STRATEGY

In order to develop a cost effective non-noble metal oxide as an electro-catalyst for PEM electrolysis, a two pronged prudent experimental and theoretical approach is required and reported herein to explore different OER electro-catalyst systems for PEM based water electrolysis. The catalyst systems should demonstrate excellent electronic conductivity, high electro-catalytic activity, high specific surface area, and excellent stability at pH ~ 0 and potential of ~ 1.5 V. A key aspect proposed is the generation of a solid solution of the parent noble metal oxide namely, the rutile structure containing varying amounts of the non-noble transition metal or Group IV oxide. By creation of such a solid solution, the inherent noble as well as chemically resistant structural characteristics of the parent, rutile noble metal oxide is maintained while also altering the electronic structure to mimic the parent noble metal oxide as evidenced by the calculation of the Fermi energy level and the corresponding shift in the d band center brought about by the solid solution and the doping of F, the lightweight anion but with remarkable ability to alter the electronic conductivity without compromising the chemical

stability and the electrochemical activity. Accordingly, work has been conducted in the following systems proposed as under.

3.3.1 Fluorine doped IrO_2

Work has been carried out to identify a novel dopant/alloying element for the noble metal oxide electro-catalyst (*E.g.* IrO_2 or RuO_2) in order to improve the catalytic activity compared to pure noble metal oxide electro-catalyst without compromising the corrosion stability of the electro-catalyst. Theoretical studies by *ab initio* calculations have shown fluorine to be a great candidate for a dopant in water electrolysis [55, 56]. Fluorine has been used as a dopant with IrO_2 as the anode electro-catalyst, denoted as IrO_2:F, with 0 to 30 wt.% F doping. IrO_2:F has been synthesized in the form of thin films and nanostructured electro-catalysts. Detailed kinetic studies have also been performed on the same for fundamental understanding of the electrochemical behavior. It shows the viability of F as a potential dopant and also has the potential to be a promising OER anode electro-catalyst that shows significant improvement of catalytic activity as compared to pure IrO_2 [34, 55].

3.3.2 Binary SnO_2 based electro-catalysts

High performance OER electro-catalysts have been synthesized based on highly corrosion resistant and electrically conductive F doped SnO_2. The F doped SnO_2 (SnO_2:F) with different F concentration has been extensively studied as transparent conducting oxide for solar cells, heat mirrors *etc* [75-77]. Due to the improved electronic conductivity of F doped SnO_2 with respect to

pure SnO_2 [78, 79], it would be an attractive alternative to other non-noble metal oxides for PEM based water electrolysis. It is well known that SnO_2:F is electrochemically inactive as an anode for PEM electrolysis IrO_2 or RuO_2 has been added in small amounts to SnO_2:F to synthesize a homogeneous solid solution. The electrochemical performance of the OER electrode consisting of a nanocrystalline solid solution of SnO_2:F and IrO_2 or RuO_2, denoted as $(Ir,Sn)O_2$:F or $(Ru,Sn)O_2$ respectively, was synthesized in the form of thin films and bulk nanomaterials of different compositions ranging from zero noble metal oxide incorporation to pure noble metal oxide.

Reduction in 70 - 80 at.% of the noble metal oxide is achieved when coupled with SnO_2:F. These reduced noble metal electro-catalysts show comparable electrochemical performance to pure IrO_2 / RuO_2. An important aspect is the generation of the nanocrystalline single phase solid solution of $(Ir,Sn)O_2$:F which expectedly displays a more favorable microstructure than the two phase mixtures (*E.g.* IrO_2 + SnO_2) with each particle representing the solid solution composition thereby acting as a catalyst unlike the local IrO_2 site alone serving as a catalyst for the two phase mixtures previously reported in the literature [29-32, 35, 67]. As a result, the stability of the catalysts is also not compromised, and it portends to be a potential electro-catalyst for PEM electrolysis with substantial reduction in overall costs [57, 58].

3.3.3 Binary Nb_2O_5 based electro-catalysts

This study demonstrates a novel anode electro-catalyst for PEM water electrolysis based on highly corrosion resistant niobium oxide. Nb_2O_5 is known for its applications in metallurgy for production of robust materials with extreme hardness, electrochromic coatings, and

nanocrystalline solar cells [80, 81]. Niobium oxide has previously been studied as a support along with IrO_2 and/or RuO_2 as a thin film on titanium substrate for water electrolysis [71-73, 82]. But, the electrochemical properties, catalytic activity and stability degrade when the noble metal oxide content is reduced below ~50 at.%. In this approach, F doped Nb_2O_5 was used in order to improve the electrical conductivity of iridium oxide. The single phase solid solution of $(Ir,Nb)O_2$:F has been synthesized in the nanopowder form by a two step sol-gel approach. This yields a favorable microstructure and results in ~ 75 at.% decrease in the IrO_2 content. The stability of the catalysts is superior to the commercially available IrO_2.

3.3.4 Ternary metal oxide electro-catalysts

A novel support has been identified for the electro-catalysts has been shown to not only decrease the precious metal loading without compromising the electrochemical activity of the noble metal oxide electro-catalyst, but also improves the corrosion stability for the OER. In this study, IrO_2 has been used as anode electro-catalyst due to its higher corrosion resistance in the PEM electrolysis condition compared to RuO_2, though it shows slightly lower electrochemical activity than RuO_2 [30, 83]. On the grounds of the very promising performances shown by both $(Ir,Sn)O_2$ and $(Ir,Nb)O_2$ as an anode electro-catalyst, investigation has been carried out on the synthesis and characterization of composite ternary Ir-Sn-Nb oxide systems.

In this direction, a single phase solid solution of IrO_2, SnO_2 and NbO_2 of compositions $(Ir_{1-2x}Sn_xNb_x)O_2$ with x ranging from 0 to 0.50, denoted as $(Ir,Sn,Nb)O_2$, has been synthesized by thermal decomposition of a mixture of metal salt precursors on Ti foil as a thin film OER catalyst for PEM electrolysis. For better understanding of the electrochemical activity, long term

stability of the (Ir,Sn,Nb)O_2 electro-catalyst has also been carried out to complement the present experimental study. Reduction in ~ 60 at.% IrO_2 gives similar electrochemical performance and much enhanced chemical robustness (durability) than pure IrO_2 [24]. This is due to the stronger Nb-O bonds as compared to the Ir-O bonds incorporated in the IrO_2 lattice structure.

As F helped in increasing the activity of the (Ir,Sn)O_2 and (Ir,Nb)O_2 electro-catalysts leading to much enhanced performance, the novel ternary oxide electro-catalyst has been doped with fluorine in order to improve the catalytic activity in order to further decrease the amount of IrO_2. Correspondingly, F doped (Sn,Nb)O_2 has been used as a support with the noble metal oxide as the catalyst for anode oxidation in PEM based water electrolysis [59]. This novel catalyst system of F doped Ir-Sn-Nb oxide, denoted as (Ir,Sn,Nb)O_2:F, helps increase the electro-catalytic activity and improve the durability of the electro-catalyst with further reduction in IrO_2 content.

4.0 EXPERIMENTAL DETAILS

4.1 THIN FILM ELECTRO-CATALYST PREPARATION

4.1.1 F doped IrO_2

Iridium tetrachloride [$IrCl_4$, 99.5%, Alfa Aesar] and ammonium fluoride [NH_4F, Alfa Aesar] were used as the sources for Ir oxide and F, respectively. Stock solution corresponding to $IrCl_4$ of desired compositions was dissolved in absolute ethanol inside an atmosphere controlled glove box (MBraun Unilab Work station) to prevent any undesired side reaction. On the other hand, NH_4F was dissolved in ethanol-deionised (DI) water mixture (5:1 volume ratio). The stock solutions $IrCl_4$ and NH_4F of desired compositions ($NH_4F/IrCl_4$: 0.04, 0.085, 0.14, 0.19 and 0.33) are then mixed together to synthesize IrO_2: x wt.% F electro-catalyst with x = 0, 5, 10, 15, 20 and 30, respectively. The resulting solution was then spin coated on pretreated titanium substrates (99.99%, 0.005 in thick, Alfa Aesar) of ~ 1 cm^2 areas (Specialty coating Systems Inc, Model P6712) with rotating speed of 500 rpm for 10 sec. Prior to coating, the Ti substrate was sand blasted and then etched in boiling HCl (30 wt.%) for 30 minutes in order to ensure maximum adhesion of the coating. The HCl treated Ti foil was washed with purified water by the Milli-Q system and dried at 130^{o}C before coating. The thin film precursors deposited on the pretreated titanium substrate were dried at 60°C for 2 hours. Following this, they were thermally treated to

400°C for 4 hours in air to decompose the precursors and, as a result IrO_2:F films of different compositions are generated on the Ti foils. The loading of the IrO_2:F deposited on the Ti foil is ~ 0.3 mg/cm^2 irrespective of the different compositions.

4.1.2 Binary F doped (Ir,Sn)O_2

Iridium tetrachloride [$IrCl_4$, 99.5%, Alfa Aesar], tin (II) chloride dihydrate [$SnCl_2$. $2H_2O$, 98%, Alfa Aesar] and ammonium fluoride [NH_4F, 98%, Alfa Aesar] were used as the sources for Ir, Sn and F, respectively. Stock solution corresponding to $IrCl_4$ and $SnCl_2.2H_2O$ of the desired compositions were dissolved in absolute ethanol inside an atmosphere controlled glove box and NH_4F was dissolved in ethanol-DI water mixture (5:1 volume ratio). The stock solutions $IrCl_4$, $SnCl_2.2H_2O$ and NH_4F of composition $(Ir_ySn_{1-y})O_2$: x wt.% F, where y ranges from 0 to 1 and x = 0, 5, 10 and 15 are then mixed together to synthesize (Ir,Sn)O_2:F electro-catalyst. The resulting solution was then spin coated on the pretreated titanium substrates (99.99%, 0.005 in thick, Alfa Aesar) of ~ 1 cm^2 areas (Specialty coating Systems Inc, Model P6712) with rotating speed of 500 rpm for 10 sec. Prior to coating, the Ti substrate was sand blasted and then etched in boiling HCl (30 wt.%) for 30 minutes in order to ensure maximum adhesion of the coating. The HCl treated Ti foil was washed with purified water by the Milli-Q system and dried at 130^{o}C before coating. The thin film precursors deposited on the pretreated titanium substrate were dried at 60°C for 2 hours. Following this drying, they were thermally treated at 400°C for 4 hours in air to decompose the precursors and, as a result gives the (Ir,Sn)O_2:F films of different compositions are generated on the Ti foils with the loading being ~ 0.3 mg/cm^2 irrespective of the different compositions.

4.1.3 Binary F doped $(Ru,Sn)O_2$

Ruthenium trichloride [$RuCl_3$, 99.9%, Alfa Aesar], tin (II) chloride dihydrate [$SnCl_2.\ 2H_2O$, 98%, Alfa Aesar] and ammonium fluoride [NH_4F, 98%, Alfa Aesar] were used as the sources for Ru, Sn and F, respectively. Stock solution corresponding to $RuCl_3$ and $SnCl_2.2H_2O$ of the desired compositions were dissolved in absolute ethanol inside an atmosphere controlled glove box and NH_4F was dissolved in ethanol-DI water mixture (5:1 volume ratio). The stock solutions $RuCl_3$, $SnCl_2.2H_2O$ and NH_4F of composition $(Ru_ySn_{1-y})O_2$: x wt.% F, where y ranges from 0 to 1 and x = 0, 5, 10 and 15 are then mixed together to synthesize $(Ru,Sn)O_2$:F electro-catalyst. The resulting solution was then spin coated on the pretreated titanium substrates (99.99%, 0.005 in thick, Alfa Aesar) of ~ 1 cm^2 areas (Specialty coating Systems Inc, Model P6712) with rotating speed of 500 rpm for 10 sec. Prior to coating, the Ti substrate was sand blasted and then etched in boiling HCl (30 wt.%) for 30 minutes in order to ensure maximum adhesion of the coating. The HCl treated Ti foil was washed with purified water by the Milli-Q system and dried at 130^{o}C before coating. The thin film precursors deposited on the pretreated titanium substrate were dried at 60°C for 2 hours. Following this drying, they were thermally treated at 400°C for 4 hours in air to decompose the precursors and, consequently generate $(Ru,Sn)O_2$:F film of different compositions are generated on the Ti foils. The loading of the $(Ru,Sn)O_2$:F deposited on the Ti foil is ~ 0.3 mg/cm^2 irrespective of the different compositions.

4.1.4 Ternary $(Ir,Sn,Nb)O_2$

Figure 3 shows the molar ratio of Ir:Sn:Nb compositions chosen to investigate as an anode electo-catalyst for PEM based water electrolysis. Iridium tetrachloride [$IrCl_4$, 99.5%, Alfa Aesar], tin (II) chloride dihydrate [$SnCl_2$. $2H_2O$, 98%, Alfa Aesar] and niobium chloride [$NbCl_5$, 99.95%, Alfa Aesar] were used as the sources for Ir, Sn and Nb, respectively. Stock solution corresponding to $IrCl_4$, $SnCl_2.2H_2O$ and $NbCl_5$ of desired compositions were dissolved in absolute ethanol inside the glove box to prevent any undesired side reaction. The stock solutions $IrCl_4$, $SnCl_2.2H_2O$ and $NbCl_5$ of composition $(Ir_{1-2x}Sn_xNb_x)O_2$, where x ranges from 0 to 1 are then mixed together to synthesize $(Ir,Sn,Nb)O_2$ electro-catalyst. The resulting solution was then spin coated on pretreated titanium substrates (99.99%, 0.005 in thick, Alfa Aesar) of ~ 1 cm^2 areas (Specialty coating Systems Inc, Model P6712) with rotating speed of 500 rpm for 10 sec. Prior to coating, Ti substrate was sand blasted and then etched in boiling HCl (30 wt.%) for 30 min in order to ensure a maximum adhesion of the coating. The HCl treated Ti foil was washed with purified water by the Milli-Q system and dried at 130^{o}C before coating. The thin film precursors deposited on the pretreated titanium substrate were dried at 60°C for 2 hours. Following this, they were thermally treated to 400°C for 4 hours in air to decompose the metal precursor and, as a result $(Ir,Sn,Nb)O_2$ film of different compositions is formed on the Ti foil. The loading of $(Ir,Sn,Nb)O_2$ deposited on the Ti foil is ~ 0.3 mg/cm^2 irrespective of compositions.

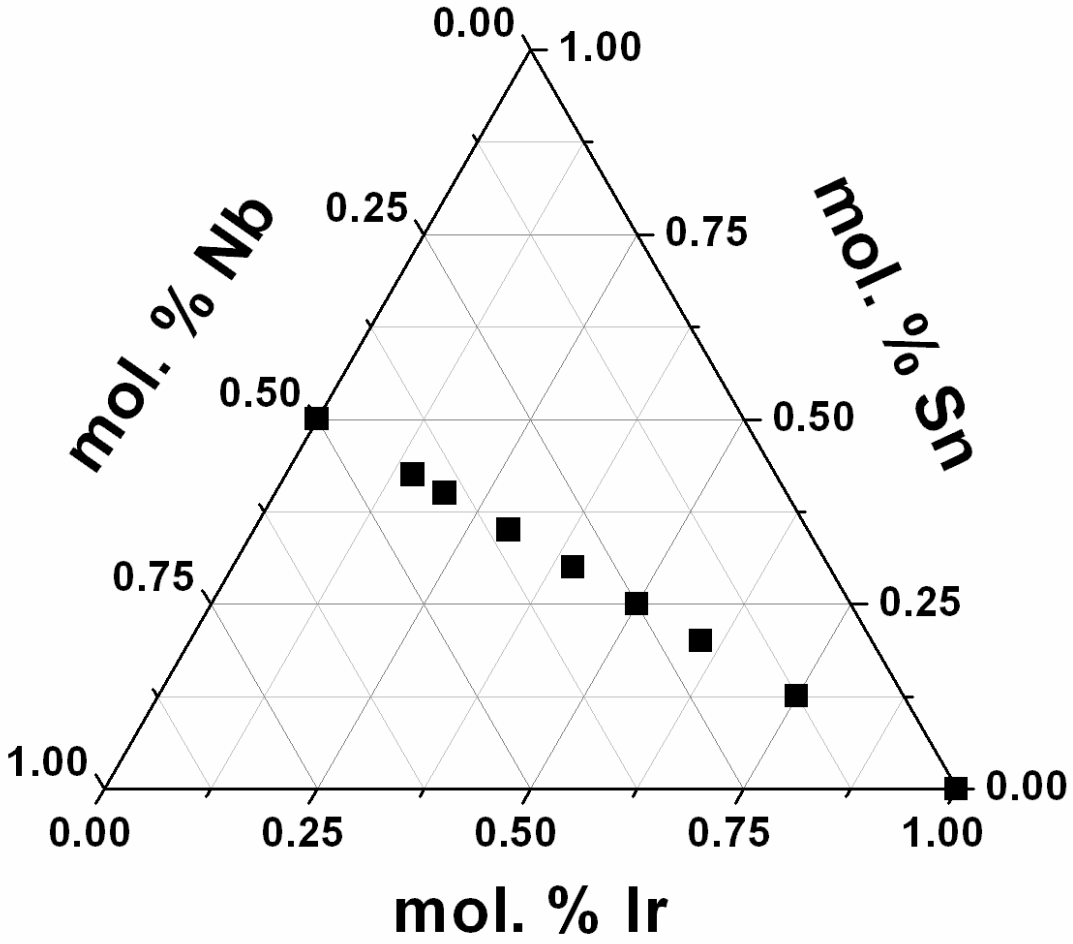

Figure 3. Molar ratio of (Ir,Sn,Nb)O_2 chosen to investigate as an anode electro-catalyst in PEM water electrolysis

4.1.5 Ternary F doped (Ir,Sn,Nb)O_2

Iridium tetrachloride [$IrCl_4$, 99.5%, Alfa Aesar], tin (II) chloride dihydrate [$SnCl_2$. $2H_2O$, 98%, Alfa Aesar], niobium chloride [$NbCl_5$, 99.95%, Alfa Aesar] and ammonium fluoride [NH_4F,

98%, Alfa Aesar] were used as the sources for Ir, Sn, Nb and F, respectively. Stock solution corresponding to $IrCl_4$, $SnCl_2.2H_2O$ and $NbCl_5$ of desired compositions were dissolved in absolute ethanol inside the glove box to prevent any undesired side reaction. NH_4F was dissolved in ethanol-DI water mixture (5:1 volume ratio). The stock solutions $IrCl_4$, $SnCl_2.2H_2O$, $NbCl_5$ and NH_4F of composition $(Ir_{0.3}Sn_{0.35}Nb_{0.35})O_2$: x wt.% F, where x = 0, 5, 10, 15 and 20 are then mixed together to synthesize (Ir,Sn,Nb)O_2:F electro-catalyst. The resulting solution was then spin coated on pretreated titanium substrates (99.99%, 0.005 in thick, Alfa Aesar) of ~ 1 cm^2 areas (Specialty coating Systems Inc, Model P6712) with rotating speed of 500 rpm for 10 sec. Prior to coating, Ti substrate was sand blasted and then etched in boiling HCl (30 wt.%) for 30 min in order to ensure a maximum adhesion of the coating. The HCl treated Ti foil was washed with purified water by the Milli-Q system and dried at 130ºC before coating. The thin film precursors deposited on the pretreated titanium substrate were dried at 60°C for 2 hours. Following this, they were thermally treated to 400°C for 4 hours in air to decompose the metal precursors and, as a result (Ir,Sn,Nb)O_2:F film of different compositions is generated on the Ti foil with the loading being ~ 0.3 mg/cm^2 irrespective of the different compositions.

4.2 NANOPARTICULATE CATALYST SYNTHESIS

4.2.1 F doped IrO_2

Iridium tetrachloride [$IrCl_4$, 99.5%, Alfa Aesar], and ammonium fluoride [NH_4F, 98%, Alfa Aesar] were used as the precursor sources for Ir and F, respectively. IrO_2:F was synthesized

using the modified Adams fusion method, first reported by Adams *et al.* [84] and used by other researchers as well [67, 85]. The precursors were taken in stoichiometric amounts and completely dissolved in D.I. water by the Milli-Q system [18.2 MΩ.cm deionized water; Milli-Q Academic, Millipore]. They were then mixed with excess of sodium nitrate [$NaNO_3$, 99%, Alfa Aesar] dissolved in D.I. water. The resulting mixture was homogenized by stirring vigorously for 2 hours and the water is then carefully evaporated at 60°C. The mixture is then introduced into a furnace wherein it is heated to 500°C at a ramp rate of 50 K/min, and then held at 500°C for 1 hour. The salt mixture is then washed multiple times with D.I. water in order to remove all the excess salt. The resulting powder is then dried in an oven at 60°C for 24 hours to form the IrO_2:x wt.% F electro-catalyst, where x ranges from 0 to 20.

4.2.2 Binary F doped (Ir,Sn)O_2

Iridium tetrachloride [$IrCl_4$, 99.5%, Alfa Aesar], tin (II) chloride hydrate [$SnCl_2$. xH_2O, 99.995%, Alfa Aesar] and ammonium fluoride [NH_4F, 98%, Alfa Aesar] were used as the precursor sources for Ir, Sn and F, respectively. For synthesizing SnO_2:F, a mixed-surfactant template route has been employed as reported previously in literature [86]. A mixed cationic surfactant Cetyl trimethylammonium bromide [CTAB, 95%, Aldrich] is used for preparing undoped and fluorine doped SnO_2. CTAB is dissolved completely in D.I. water by the Milli-Q system [18.2 MΩ.cm deionized water, Milli-Q Academic, Millipore] to which a solution of 6 wt.% ammonium hydroxide (Fisher Scientific) is added. After homogenizing this mixture, a solution of tin chloride hydrate dissolved in D.I. water is introduced that gave a white slurry. For preparing SnO_2:F, NH_4F dissolved in D.I. water is also introduced after the addition of

$SnCl_2.xH_2O$. The resulting solution is vigorously stirred for 4 hours. It is then aged at room temperature for 48 hours. The precipitate obtained after filtration is thoroughly washed with D.I. water. It is then dried in an oven at 50°C followed by heat treatment in air at 300°C which resulted into SnO_2:F. For the preparation of (Ir,Sn)O_2:F, $IrCl_4$ was dissolved in ethanol along with the appropriate amount of the as-prepared SnO_2 or SnO_2:F. The solution was then dried in an alumina crucible in an oven at 60°C for 3 hours. This crucible was then subjected to heat treatment in air at 400°C for 4 hours in order to form $(Ir_xSn_{1-x})O_2$: y wt.% F, where x ranges from 0.2 to 0.8 and y = 0 and 10.

4.2.3 Binary F doped (Ir,Nb)O_2

Iridium tetrachloride [$IrCl_4$, 99.5%, Alfa Aesar], niobium (V) chloride [$NbCl_5$, 99.95%, Alfa Aesar] and trifluoroacetic acid [CF_3COOH, 99%, Alfa Aesar] were used as the sources or precursors for Ir, Nb and F, respectively. For preparing undoped and fluorine doped niobium oxide, a procedure similar to the sol-gel method previously reported in literature is used [87]. $NbCl_5$ powder was dissolved in absolute ethanol (200 proof, Fisher Scientific) inside an atmosphere controlled glove box (MBraun Unilab Work station) to prevent any undesired side reaction which yielded a clear yellow solution. Preparation of 10 wt.% F doped Nb_2O_5 was carried out using trifluoroacetic acid dissolved in ethanol followed by mixing with $NbCl_5$ solution. This solution was then added to 0.3 M ammonium hydroxide solution. The mixture is then washed with D.I. water multiple times and a white precipitate is obtained. The precipitate is taken in a round bottom flask which is kept under ice. 6 wt.% hydrogen peroxide is then dispersed in to the precipitate and the mixture is stirred for *c.a.* 15 minutes in ice until a

transparent yellow sol is obtained. This sol is then allowed to gel in a sealed round bottom flask at 75°C for 24 hours. The gel is then dried at 75°C for 48 hours to form amorphous 10 wt.% F doped Nb_2O_5 or undoped Nb_2O_5. The preparation of F doped $(Ir,Nb)O_2$ was performed by dissolving $IrCl_4$ in ethanol along with the appropriate amount of the as-prepared Nb_2O_5 or Nb_2O_5:F. This solution was then dried in a crucible in an oven at 60°C for 3 hours and subsequent heat treatment in air at 400°C for 4 hours in order to form $(Ir_xNb_{1-x})O_2$: y wt.% F, where x ranges from 0.2 to 0.8 and y = 0 and 10.

4.3 PHYSICAL AND CHEMICAL CHARACTERIZATION

4.3.1 X-ray Characterization

In order to perform qualitative phase analysis, all the synthesized materials were characterized by X-ray diffraction (XRD) using Philips XPERT PRO system employing CuK_α (λ = 0.15406 nm) radiation with operating voltage and current at 45kV and 40mA, respectively. The XRD peak profile of the thin films of different compositions was analyzed using Pseudo-Voigt function to determine the Lorentzian and Gaussian contribution of the peak. The integral breadth of the Lorentzian contribution, determined from peak profile analysis using single line approximation method after eliminating the instrumental broadening and lattice strain contribution, is used in the Scherrer formula to calculate the effective crystallite size [88].

4.3.2 Specific surface area Determination

The specific surface area of the nanopowders synthesized as anode electro-catalysts for PEM water electrolysis was analyzed using the common nitrogen adsorption / desorption method pioneered by Brunauer-Emmett-Teller, commonly referred to as BET technique. Each sample was first vacuum degassed, weighed (Denver Instruments SI403), and then tested using a Micromeritics ASAP 2020. Multipoint BET surface areas are reported for all synthesized powders.

4.3.3 Thermogravimetric Analysis

In order to understand the phase formation and decomposition temperature, thermogravimetric and differential thermal analysis (TGA-DTA) has been conducted on the fluorine doped nanostructured powders using a TGA-DTA machine (Netzsch STA 409PC/4/H/Luxx TG-DTA). The TGA-DTA analysis was carried out employing a heating rate of 10°C/min from room temperature up to 700°C in air. A small quantity of the material was loaded into an alumina crucible and placed into the Netzsch STA 409PC/4/H/Luxx TG-DTA instrument. A protective ultra high purity (UHP) argon gas flow of 40 ml/min and a carrier gas flow *i.e.* air of 25 ml/min was used. The gas flows were allowed to stabilize for ~ 30 minutes before the materials are tested.

4.3.4 Microstructure Analysis

To investigate the microstructure of the thin film electrodes, scanning electron microscopy (SEM) and transmission electron microscopy (TEM) was conducted. Quantitative elemental analysis and distribution of elements (x-ray mapping) was investigated using the energy dispersive X-ray spectroscopy (EDX) analyzer integrated into the SEM machine. Philips XL-30FEG equipped with an EDX detector system comprised of an ultrathin beryllium window and Si(Li) detector operating at 20 kV was employed for the secondary electron (SE) image, elemental and x-ray mapping analyses.

JEOL 4000EX operating at 400 kV was employed for conducting TEM analysis to evaluate the particle size and the structure. High resolution transmission electron microscopy (HRTEM) analysis was conducted on the samples using JEOL JEM - 2100F to further investigate the morphology. For the thin films, the particles are obtained by mechanically abrading the powders from top of the several micron thick films synthesized by spin coating techniques. The TEM analysis samples are prepared by dispersing the catalyst in ~ 5 ml of ethanol and ultrasonicating for 10 minutes. A Formvar carbon coated 300 mesh Cu grid (Electron Microscopy Sciences) was placed on a piece of filter paper on which the ultrasonicated solution was pipetted.

4.3.5 X-ray Photoelectron Spectroscopy

X-ray photoelectron spectroscopy (XPS) was done on selected electro-catalysts in order to determine the electronic states of the elements that exist in the alloy. The catalysts analyzed by

XPS used a Physical Electronics (PHI) model 32-096 X-ray source control and a 22-040 power supply interfaced to a model 04-548 X-ray source with an Omni Focus III spherical capacitance analyzer (SCA). The system is routinely operated within the pressure range of 10^{-8} to 10^{-9} Torr (1.3×10^{-6} to 1.3×10^{-7} Pa). The system was calibrated in accordance with the manufacturer's procedures utilizing the photoemission lines E_b of Cu $2p_{3/2}$ (932.7 eV), E_b of Au $4f_{7/2}$ (84 eV) and E_b of Ag $3d_{5/2}$ (368.3 eV) for a magnesium anode. All the reported intensities are experimentally determined peak areas divided by the instrumental sensitivity factors. Charge correction was obtained by referencing the adventitious C 1s peak to 284.8 eV.

4.4 ELECTROCHEMICAL CHARACTERIZATION

4.4.1 Set-up

Electrochemical characterization was conducted on all the synthesized electro-catalysts using a five port jacketed reaction cell (Ace Glass Inc.) in which was assembled a 3-electrode test system as shown in **Figure 4**. The testing was executed using a VersaSTAT 3 (Princeton Applied Research). A solution of 1 N sulfuric acid was used as the electrolyte which also served as the fuel. The solution is kept at a constant temperature of 40°C using a Fisher Scientific 3006S Isotemp Refrigerator Circulator. The reference electrode was a XR 200 mercury/mercurous sulfate electrode [Hg/Hg_2SO_4, Radiometer Analytical] which has a potential of ~ +0.654 V with respect to the Standard Hydrogen Electrode (SHE / NHE). Platinum foil (Alfa Aesar, 0.25 mm thick, 99.95%) was used as the counter electrode.

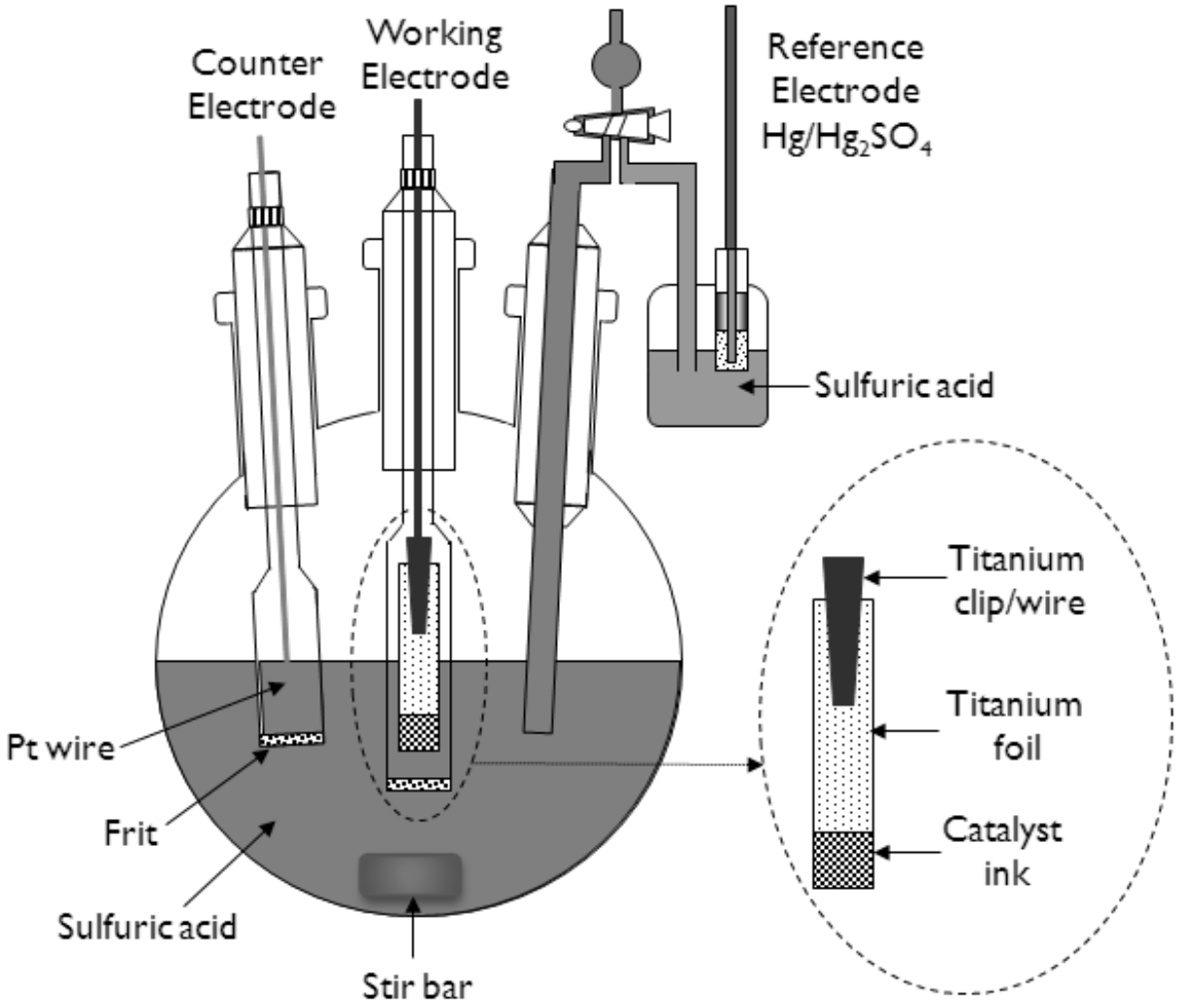

Figure 4. Three electrode cell set-up for electrochemical testing

The thin films of IrO_2:F, $(Ir,Sn)O_2$:F, $(Ru,Sn)O_2$:F, $(Ir,Sn,Nb)O_2$ and $(Ir,Sn,Nb)O_2$:F of different compositions coated on the Ti foil were used as the working electrode with an exposed surface area ~ 1 cm^2 with a total loading of ~ 0.3 mg/cm^2 for each system.

For the nanoparticulate electro-catalysts, the working electrodes were prepared by uniformly spreading the catalyst ink on porous titanium foil [50 % porosity, Accumet Materials

Co.] on an area of ~ 1 cm^2. The catalyst ink consisted of 85 wt.% catalyst and 15 wt.% Nafion 117 solution [5 wt.% solution in lower aliphatic alcohols, Sigma-Aldrich]. The total loading on the Ti foil for all the electro-catalyst compositions was ~ 0.3 mg/cm^2.

4.4.2 Polarization Testing

A current - voltage scan is conducted by cycling between 0 to 2 V (*vs.* NHE) at 10 mV/s for multiple cycles and the current response is measured. Once complete, polarization curves are recorded by stepping the voltage from open circuit potential (OCP) to 2V (*vs.* NHE) while measuring the current response. This difference between the two tests is that the polarization test contains information about the onset potential of the system which can prove valuable in understanding the viability of the anode electro-catalysts.

4.4.3 Electrochemical Impedance Spectroscopy (EIS)

Electrochemical Impedance Spectroscopy (EIS) has been used to determine the solution resistance, electrode resistance and the polarization resistance of the electro-catalyst using a suitable circuit model such as $R_s(R_eQ_1)(R_{ct}Q_{dl})$, where R_s is the solution resistance, R_e is the electrode resistance, R_{ct} is the polarization / charge transfer resistance, Q_1 is the constant phase element (CPE) and Q_{dl} includes both the double layer capacitance (C_{DL}) and pseudocapacitance (C_{PC}) [48, 52, 85]. The ohmic resistance (R_Ω) has been be used to perform the ohmic loss (iR_Ω) correction, whereas the polarization resistance (R_{ct}) has been used to understand the electrochemical activity of the electro-catalyst. The uncorrected polarization curve and the non-

linear Tafel plot encounter a large amount of ohmic / solution resistance (R_s) which is determined from the EIS plot at high frequencies. This helps us in preparing the linear Tafel plots and the iR corrected polarization curves. The plots after correcting for the ohmic loss help us in evaluating the inherent electro-catalytic property of the electrodes. The Tafel plot after iR correction is given by the following equation:

$$\eta = b \log i + a$$

Here 'η' is the overpotential, 'b' is the Tafel slope, 'i' is the current density and 'a' determines the exchange current density. The corresponding Tafel slope (b) is used to determine the reaction kinetics [51, 52]. Electrochemical impedance spectroscopy has been carried out in the frequency range of 100 mHz - 100 kHz using the electrochemical work station (VersaSTAT 3, Princeton Applied Research). Impedance data has been modeled by using the ZView software from Scribner Associates.

4.4.4 Kinetic Studies

Rotating disk electrode (RDE) experiments have been carried out on select electro-catalysts in order to obtain information about the kinetics and mechanism of the electrochemical reaction. It helps confirm the number of electrons getting transferred in the OER and calculate the apparent activation energy of the reaction. The RDE tests were performed in a three electrode system, using the same reference electrode and counter electrode as described before. A titanium disk insert [5 mm OD, 4 mm thick, mirror polish; Pine Research Instrumentation] was used for the working electrode. The catalyst ink was deposited on the Ti disk and dried in an ethanol saturated environment overnight. The disk was then heated to 130°C for 2 hours.

A multiple small potential step measurement has been used for all RDE measurements, first used by Chu *et al.* [89]. Potential steps of 5 mV are given starting from open circuit potential and current is recorded at every potential for 16 seconds. The last value of the current is taken into consideration for accurate analysis *i.e.* there is a decay time of 15 seconds in order to ensure that the electrode double layer charging current and the adsorption current is negligible [89]. The RDE experiments have been done by varying speeds from 500 rpm to 2000 rpm. The Koutecky - Levich plot, widely used for RDE studies [89-91], is represented by the following equations which involve the kinetic current (i_k) and Levich current (i_L), as given below:

$$i^{-1} = i_k^{-1} + i_L^{-1}$$

$$i_k = k\ n\ A\ F\ C$$

$$i_L = 0.62\ n\ F\ A\ D^{2/3}\ \omega^{1/2}\ \upsilon^{-1/6}\ C$$

Here, 'i' is the current (A), 'k' is the kinetic rate constant of the reaction (cm/s), 'n' is the electron transfer number, 'A' is the electrode area (0.19625 cm^2), 'F' is the Faraday constant (96485 As/mol), 'C' is the concentration of reactive species (1.3 x 10^{-6} mol/cm^3), 'D' is the diffusion coefficient (1.7 x 10^{-5} cm^2/s), 'ω' is the rotation rate (radians/s), and 'υ' is the viscosity (0.01 cm^2/s) [91-95]. The slope of the Koutecky - Levich plot *i.e.* i^{-1} *vs.* $\omega^{-1/2}$ helps determine the number of electrons (n) transferred in the reaction and the intercept gives the kinetic rate constant (k) of the reaction.

The influence of temperature on the OER has been studied for selected anode catalysts in order to calculate the apparent activation energy (E_a). In the RDE setup, a high rotation speed of 1500 rpm was used and multiple small potential step measurement as mentioned before was carried out in the temperature range of 25°C - 70°C. The Arrhenius relation is given below:

$$i = k_0 \exp(-E_a/RT)$$

Here, 'k_0' is the pre-exponential factor, 'E_a' is the apparent activation energy (J/mol), 'R' is the universal gas constant (8.314 J/mol K), and 'T' is the temperature (K). A plot of ln i *vs.* T^{-1} *i.e.* the Arrhenius plot would help in determination of the apparent energy of activation [96-99].

4.4.5 Chronoamperometry

In order to study the long term structural stability or chemical robustness of the synthesized electro-catalysts, chronoamperometry (CA) *i.e.* current signal as a function of time has been conducted for the anode catalysts. Testing of the electrodes was performed for 12 - 48 hours using 1 N H_2SO_4 as the electrolyte (fuel) at 40°C under a constant voltage of ~ 1.65 V (*vs*. NHE) without iR correction.

Elemental analysis of the media collected after the stability testing (CA) was performed by inductively coupled plasma optical emission spectroscopy (ICP-OES, iCAP 6500 duo Thermo Fisher) in order to determine the amount of iridium, ruthenium, tin and/or niobium leached in the solution. Standards for getting the calibration lines were procured from Sigma Aldrich. They were then diluted with the stock solution used for CA tests *i.e.* 1 N sulfuric acid.

4.4.6 Single full cell test Analysis

The catalyst ink for the anode and cathode consisted of 85 wt.% catalyst and 15 wt.% Nafion 117 solution (5 wt.% solution in lower aliphatic alcohols, Sigma-Aldrich). For the single cell testing, a membrane electrode assembly was fabricated by using a Nafion 115 membrane sandwiched between the two gas diffusion electrodes coated with the catalyst ink. The cathode catalyst used

for the single cell test was Platinum black (Sigma Aldrich) supported on a Teflon treated carbon paper (Electrochem Inc.). The anode materials were the best lectro-catalyst composition powders synthesized *i.e.* IrO_2:10 wt.% F, $(Ir_{0.3}Sn_{0.7})O_2$:10 wt.% F and $(Ir_{0.25}Nb_{0.75})O_2$:10 wt.% F which were also compared with pure IrO_2 (undoped). The backing layer used on the anode side was titanium felt (60% porosity, Electrochem Inc.). The Nafion 115 membrane was pretreated first with a 3 wt.% hydrogen peroxide solution to its boiling point in order to oxidize any organic impurities. Subsequently, it was boiled in D.I. water followed by immersion in a boiling 1 N sulfuric acid solution to eliminate any metallic impurities. Finally, it is treated multiple times in D.I water to remove any traces of remnant acid. This membrane is then stored in D.I. water to avoid dehydration. The membrane electrode assembly (MEA) was then fabricated by placing the two nafion impregnated electrodes (anode and cathode) on both sides of the pretreated nafion membrane. This assembly was then hot-pressed in a 25T hydraulic lamination hot press with dual temperature controller (MTI Corporation) at a temperature of 125°C. The pressure applied was approximately 40 atm for ~ 30 seconds to ensure good contact between the electrodes and the membrane. This 5 layer MEA is then used in the single cell testing.

The 5 layer MEA prepared was then sandwiched between two Teflon gaskets of 5 mils thickness. The area of the electrodes and the hole in the gaskets was a square area of 5 cm^2. This assembly is then placed in Proton's test cell and the tests were conducted at Proton OnSite (Wallingford, CT). All the samples were heat soaked by flowing 65°C water throughout the cell for 1 hour prior to testing. The polarization curve was taken at 50°C by ramping up the current, stepping in 1 minute intervals of 100 mA/cm^2. The polarization curve is then run back down at 1 minute intervals. The polarization curves were then run back up and down at 1 minute intervals until the forward and reverse scans basically overlaid each other.

5.0 RESULTS AND DISCUSSION

5.1 THIN FILMS

5.1.1 F doped IrO_2

5.1.1.1 Structural Analysis

Figure 5 shows the XRD patterns of thin film IrO_2:F with 10, 20 and 30 wt.% F synthesized by thermal decomposition of homogeneous mixture of $IrCl_4$ and NH_4F ethanol-DI water solution coated on Ti foil at 400°C for 4 hours. The XRD patterns of IrO_2:F of different compositions, shows a rutile type tetragonal structure similar to pure IrO_2, which suggests the formation of complete solid solution between IrO_2 and F without any undesirable phase formation (*E.g.* IrF_3). The lattice parameter (a ~ 0.4547 nm, c ~ 0.3136 nm) and molar volume of IrO_2:F (~ 19.53 ± 0.04 cm^3/mol) of different compositions, calculated using least square refinement techniques, is comparable with pure IrO_2 (~ 19.64 ± 0.04 cm^3/mol) [24] which suggest that F^- substitution for O^{-2} has no significant effect on the molar volume of IrO_2:F. This may be largely due to the fact that the ionic radius of O^{-2} (125pm) is comparable with F^{-1} (120pm). The effective crystallite size of IrO_2:F, calculated using the Scherrer formula from the integral breadth of the Lorentzian contribution determined from peak profile analysis using single line approximation method after

eliminating the instrumental broadening and lattice strain contribution [88], is in the range of ~ 4 - 6 nm irrespective of compositions indicating the nanocrystalline nature of the catalyst.

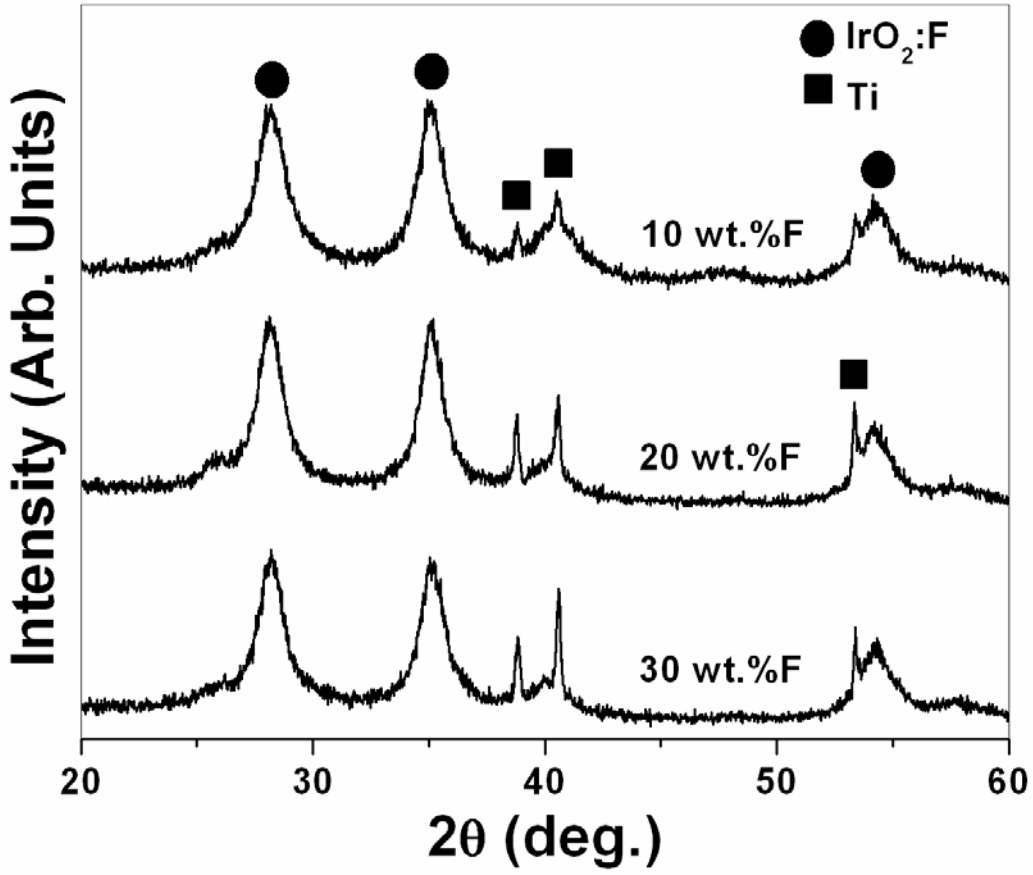

Figure 5. XRD patterns of thin film IrO2:F with 10, 20 and 30 wt.% F coated on Ti foil

The presence of elemental Ir and O in the IrO_2:F film of different compositions has also been confirmed using energy dispersive X-ray spectroscopy analysis (EDX) attached to the SEM. However, the presence of F could not be detected in the EDX analysis. Suitable spectroscopic techniques, such as wavelength dispersive x-ray florescence and Rutherford

backscattering, needs to be used for accurate determination of F in the F-doped IrO_2 [100]. It must be mentioned here that the real F content in IrO_2:F thin film will be different than the staring composition due to expected loss of F (high volatility) during thermal decomposition of the starting precursors at 400°C [100]. The SEM image along with EDX of the IrO_2:F film with 10 wt.% F, shown in **Figure 6**, indicates the presence of Ir and O, and the characteristic sintered "mud-crack" type morphology of IrO_2:F film coated on the Ti foil typically seen for chemically derived thin films.

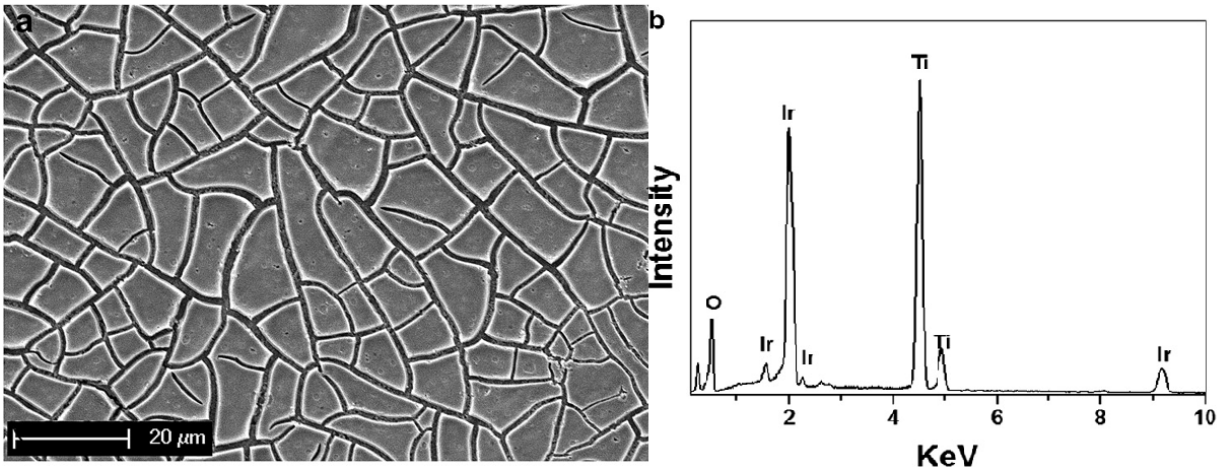

Figure 6. The SEM micrograph (a) along with EDAX (b) of IrO2:F film with 10wt.% F

5.1.1.2 Electrochemical Testing

The electrochemical activity of nanocrystalline thin film of IrO_2:F of different F compositions has been studied as a suitable oxygen evolution anode electro-catalyst for PEM based water electrolysis. The polarization curve of pure IrO_2 and IrO_2:F film of different F compositions, conducted in the presence of 1 N H_2SO_4 solution at 40^{o}C with a scan rate of 1 mV/sec, shown in

Figure 7, clearly indicates that the oxygen evolution reaction (water splitting) occurs at a potential of ~ 1.43 V *vs.* NHE irrespective of the varying F compositions. The polarization curve of IrO_2:F of different F compositions, shows that the electrochemical activity of IrO_2:F increases with increasing F content up to ~ 20 wt.% F.

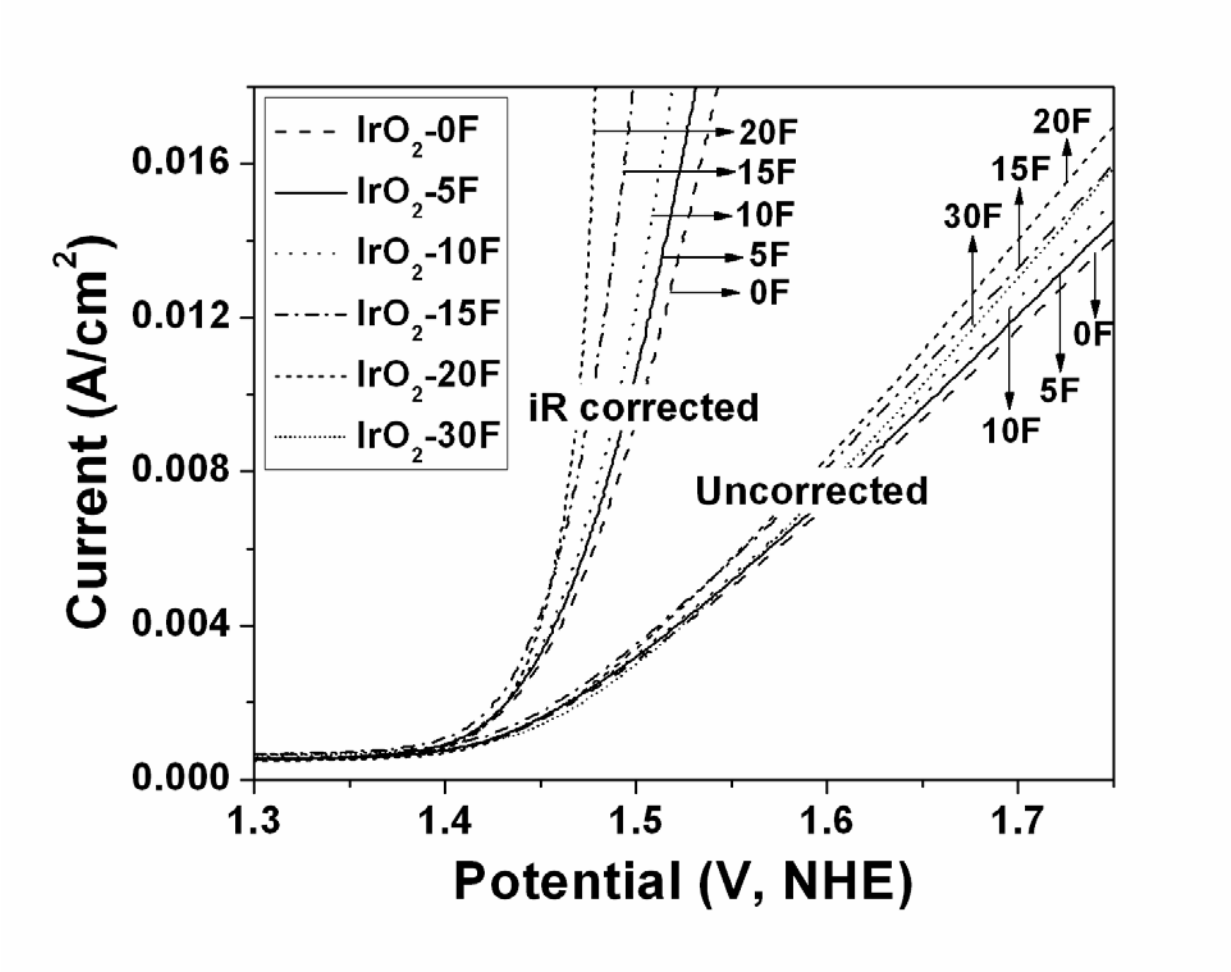

Figure 7. The polarization curve with iR correction of IrO_2:F films conducted in the presence of 1 N H_2SO_4 solution at 40°C with a scan rate of 1 mV/sec

It must be mentioned here that the present results also include the ohmic loss (iR loss) in the polarization curve which is known to arise mainly due to the solution resistance. In the present study, the solution resistance has been determined from electrochemical impedance spectroscopy to be approximately, ~ 16 Ωcm^2. The current density at ~ 1.65 V (*vs.* NHE) of IrO_2:F for different F compositions with a total loading ~ 0.3 mg/cm^2, plotted and shown in **Figure 8**, indicates that the current density of IrO_2:F increases up to 20 wt.% F beyond which there is a decrease in the current density suggesting a reduction in the electrochemical activity. The IrO_2:F with 20 wt.% F shows a current density of ~ 0.01116 ± 0.0001 A/cm^2 which is ~ 19 % higher to that of pure IrO_2 (~ 0.0094 A/cm^2) at ~ 1.65 V. On the other hand, it has been noticed that the current density decreases with increase in F content above 20 wt.% F.

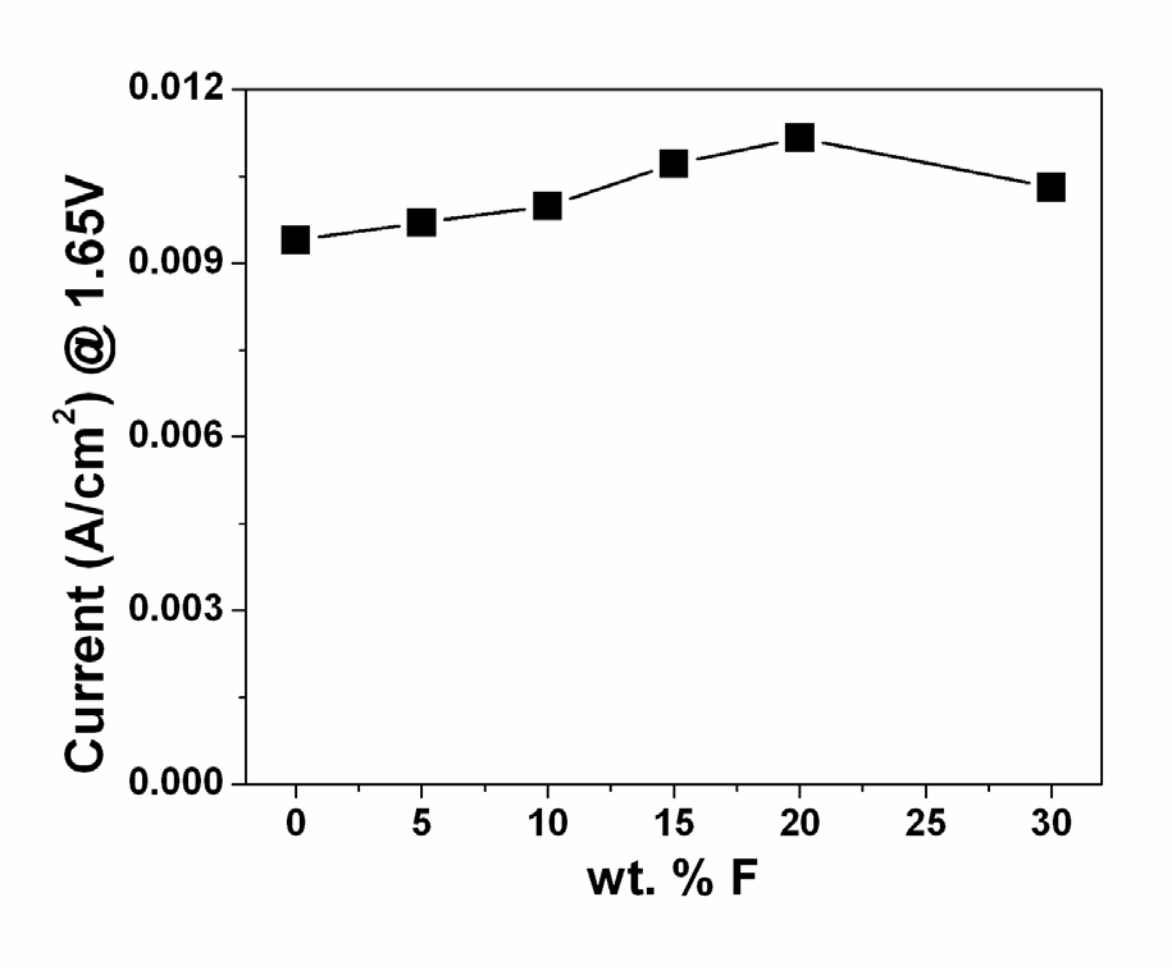

Figure 8. The variation of current density at ~ 1.65 V (*vs.* NHE) with F content of the doped IrO_2:F anode electro-catalyst

In order to study the corrosion and structural stability of anode electro-catalyst IrO_2:F in 1 N H_2SO_4, chronoamperometry (CA) test is conducted for 24 hours at 40^oC at a constant voltage of 1.65 V. The CA curves, obtained at a constant voltage of ~ 1.65 V, of IrO_2:F with 5, 10 and 20 wt.% F along with pure IrO_2, are shown in **Figure 9**. The IrO_2:F electrodes categorically show higher initial current with increase in F content due to their higher oxygen evolution activity as demonstrated in the polarization curves (**Figure 7**). The CA curve shows a marked decay of

current (10 % of the initial value) for all electrodes in the initial 1 hour which may arise either due to significant dissolution of the irregular coatings located at the edge of the mud cracks or diffusion controlled reaction [30]. A steady decay of current (13 % after 24 hours in comparison with the 1 hour value) has been noticed after 1 hour of initial period for IrO_2:F and pure IrO_2 which suggests that IrO_2:F (up to 20 wt.% F) has similar structural stability compared to pure IrO_2 [34].

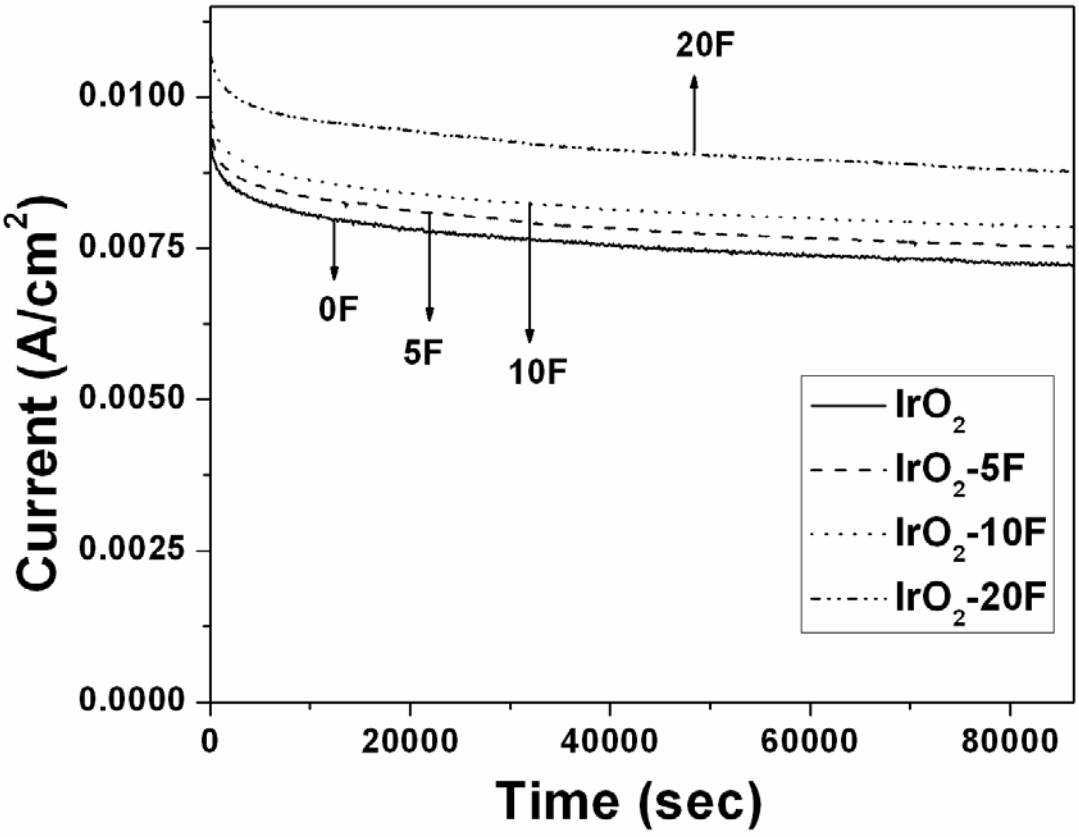

Figure 9. Variation of current *vs.* time in the accelerated life test of IrO_2:F performed in a 1 N H_2SO_4 solution under ~ 1.65 V at 40°C

However, the ICP results, conducted in the H_2SO_4 electrolyte solution collected after 24 hours of CA measurement, show no presence of Ir up to 20 wt.% F doping which suggests that the steady decay of current of IrO_2:F during CA measurement may arise due to loss of fuel rather than the dissolution of IrO_2 electro-catalyst. In the present experimental condition, it has been noticed that ~ 9 ml fuel has been lost after 24 hours of CA measurement for the F doped IrO_2 due to the high OER activity. The present study therefore successfully identifies IrO_2:F as a promising anode electro-catalyst with the ability to significantly improve the electro-catalytic performance and electrochemical stability. The IrO_2:F anode electro-catalysts can therefore be expected to exhibit significant reduction in capital cost of PEM based water electrolyzers due to the significant improvement in the electrochemical activity and stability.

5.1.2 Binary F doped $(Ir,Sn)O_2$

5.1.2.1 Structural Analysis

The XRD patterns, shown in **Figure 10**, of $(Ir,Sn)O_2$: x wt.% F thin film of optimal composition corresponding to 20 mol.% IrO_2 - 80 mol.% SnO_2 (x=0) deposited on the pretreated Ti foil. It shows peaks corresponding to single phase rutile type tetragonal structure suggesting the formation of a single phase homogeneous solid solution of IrO_2 and SnO_2 [$(Ir,Sn)O_2$] without indicating any undesirable phase separation (*E.g.* IrO_2 + SnO_2). The compositions we study will be denoted as $(Ir,Sn)O_2$:F henceforth.

The molar volume of $(Ir,Sn)O_2$, calculated using the least square refinement technique, is ~ 21.20 ± 0.05 cm^3/mol, which is in good agreement with the expected value determined by considering the change of molar volume of SnO_2 (21.66 cm^3/mol) and IrO_2 (19.22 cm^3/mol)

solid solution following the Vegard's law further confirming formation of the solid solution. The effective crystallite size of $(Ir,Sn)O_2$, calculated using the Scherrer formula from the integral breadth of the Lorentzian contribution determined from peak profile analysis employing the single line approximation method after eliminating the instrumental broadening and lattice strain contribution [88], is in the range of ~ 5 - 7 nm confirming the nanocrystalline nature of the Ir containing Sn oxide solid solution. In order to improve the electrical conductivity of the $(Ir,Sn)O_2$, fluorine has been introduced into the structure to substitute for oxygen at nominal compositions of 5, 10 and 15 wt.% F. The XRD patterns of the $(Ir_{0.2}Sn_{0.8})O_2$:F solid solution corresponding to the different compositions, shown in **Figure 10**, confirms the retention of the tetragonal structure similar to the parent $(Ir,Sn)O_2$. The calculated molar volume of $(Ir,Sn)O_2$:F (~ 21.20 ± 0.05 cm^3/mol) is comparable with undoped $(Ir,Sn)O_2$ which suggests that F^- doping on O^{-2} sites has no significant effect on the molar volume of $(Ir,Sn)O_2$:F. This may be due to the comparable ionic radius of O^{-2} (125 pm) with F^{-1} (120 pm). The calculated effective crystallite size of $(Ir,Sn)O_2$:F is also in the range of ~ 4 - 7 nm which is comparable with $(Ir,Sn)O_2$ suggesting that F^- doping has no significant effect on the refinement of crystallite size of $(Ir,Sn)O_2$.

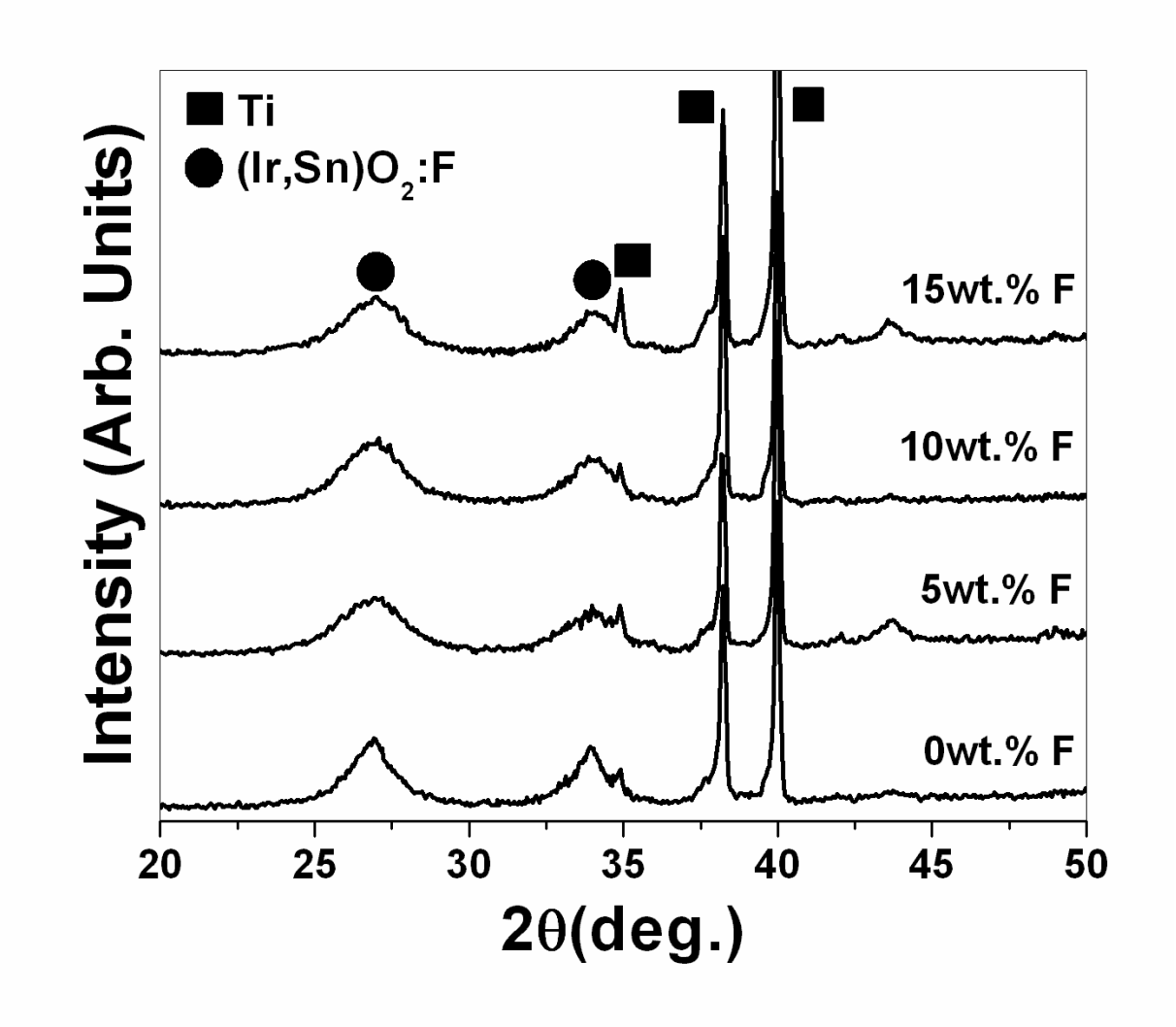

Figure 10. XRD patterns of $(Ir_{0.20}Sn_{0.80})O_2$:F of different compositions coated on Ti foil

The presence of elemental Ir, Sn and O in the (Ir,Sn)O2:F film of different compositions has been confirmed using energy dispersive X-ray spectroscopy analysis (EDX) configured to the SEM. However, the presence of F could not be detected in the EDX analysis as outlined in **Section 5.1.1.1**. The SEM image along with x-ray mapping and EDX of the $(Ir,Sn)O_2$:F film containing 10 wt.% F, shown in **Figure 11**, indicates the presence of the characteristic "mud-crack" type morphology of the representative composition of $(Ir,Sn)O_2$:F film coated on the Ti

foil. Elemental x-ray maps of Ir, Sn and O testify that Ir and Sn are homogeneously distributed within the (Ir,Sn)O_2:F particles without being segregated on any specific site. Quantitative elemental composition analysis of the (Ir,Sn)O_2:F films obtained by EDX further shows that the measured elemental compositions of Ir and Sn are close to the nominal composition. The bright field TEM image of (Ir,Sn)O_2:F particles collected from the representative film composition containing 10 wt.% F depicted in **Figure 12** confirms the nanometer sized (~ 10 - 15 nm) state of the fine particles.

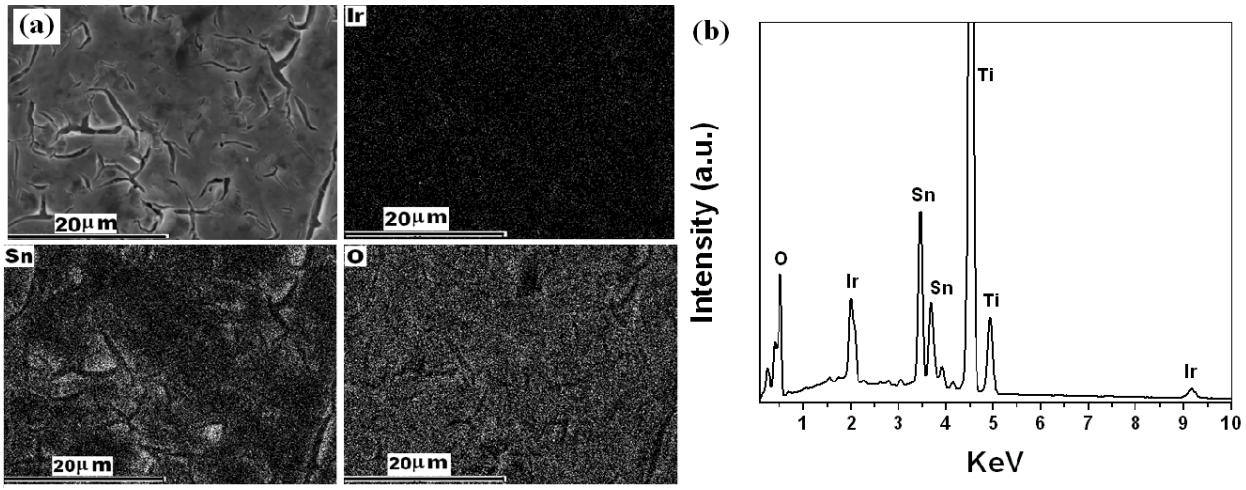

Figure 11. The SEM micrograph along with x-ray mapping of Ir, Sn and O (a), and EDAX (b) of $(Ir_{0.20}Sn_{0.80})O_2$:F film

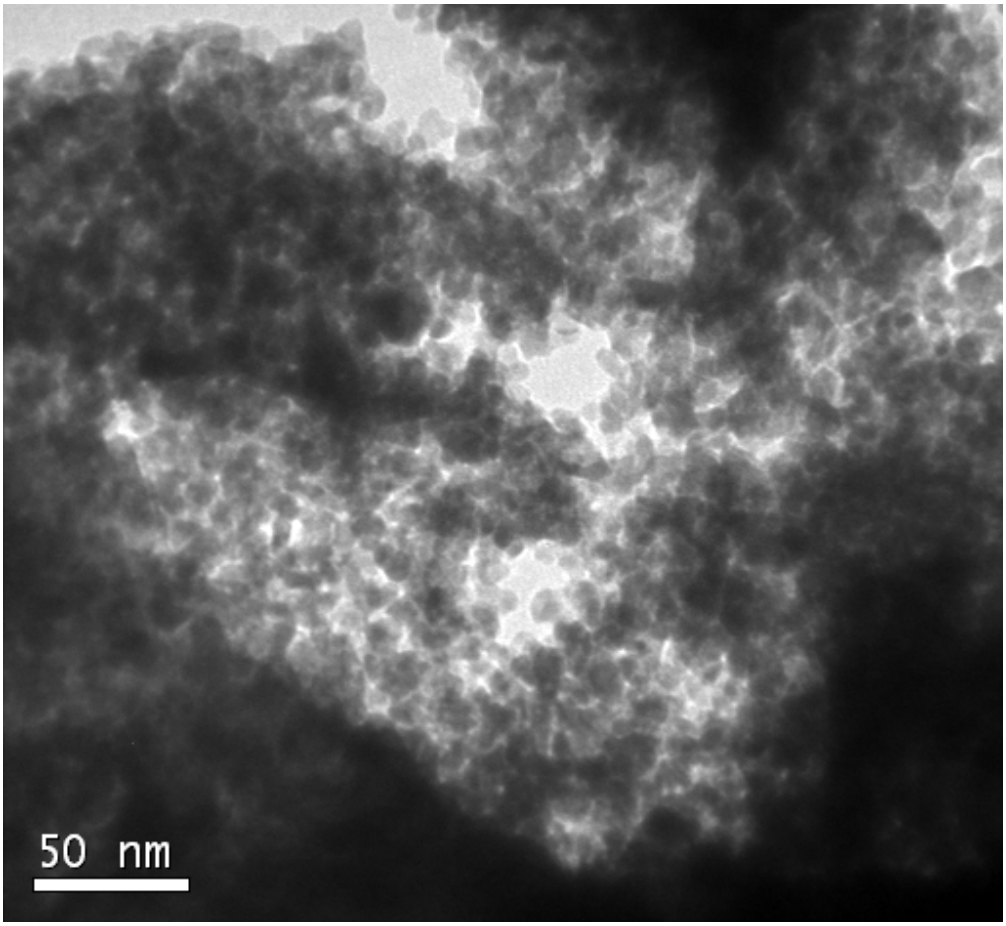

Figure 12. The bright field TEM image $(Ir_{0.2}Sn_{0.8})O_2$:10F film shows the presence of fine particles in the nanometer range (~ 10 - 15 nm)

5.1.2.2 Electrochemical Testing

In the present study, the linear polarization curve and non-linear Tafel plot are most often encountered due to ohmic resistance contribution which mainly arises due to solution resistance of the electrolyte (R_s), oxide film electrode resistance (R_e) and accumulation of oxygen bubble covering the electrode surface during water electrolysis at higher current density (R_{bub}) [51, 52]. In order to evaluate the inherent electrochemical property / electrode kinetics of the studied

electro-catalysts, the polarization curve of different samples, conducted in the presence of 1 N H_2SO_4 solution at 40^oC with a scan rate of 1 mV/sec, is therefore plotted after accounting for total ohmic loss (iR_Ω) correction. The value of R_s and R_e of different samples, tabulated in **Table 1**, is obtained from electrochemical impedance spectroscopy (EIS) measurement at different potential with respect to NHE at 40^oC. The impedance parameters are obtained by fitting the experimental data as shown in **Figure 13** using ZView software from Scribner Associtates utilizing the circuit model $R_s(R_eQ_1)(R_{ct}Q_{dl})$, where R_s is the solution resistance, R_e is the electrode resistance, R_{ct} is the charge transfer resistance, Q_1 is the constant phase element and Q_{dl} includes contributions from both the double layer capacitance and pseudocapacitance [48, 85].

Table 1. Impedance parameters and Tafel slope of IrO_2 and $(Ir,Sn)O_2$:F thin film

Composition	R_s (Ω cm^2)	R_e (Ω cm^2)	R_{ct} (Ω cm^2)	Tafel slope (b)
IrO_2	13.8	1	6	60
$(Ir_{0.8}Sn_{0.2})O_2$	12.1	2.7	15	76
$(Ir_{0.8}Sn_{0.2})O_2$:5F	13.1	1.8	10	70
$(Ir_{0.8}Sn_{0.2})O_2$:10F	13.3	1	6.7	62

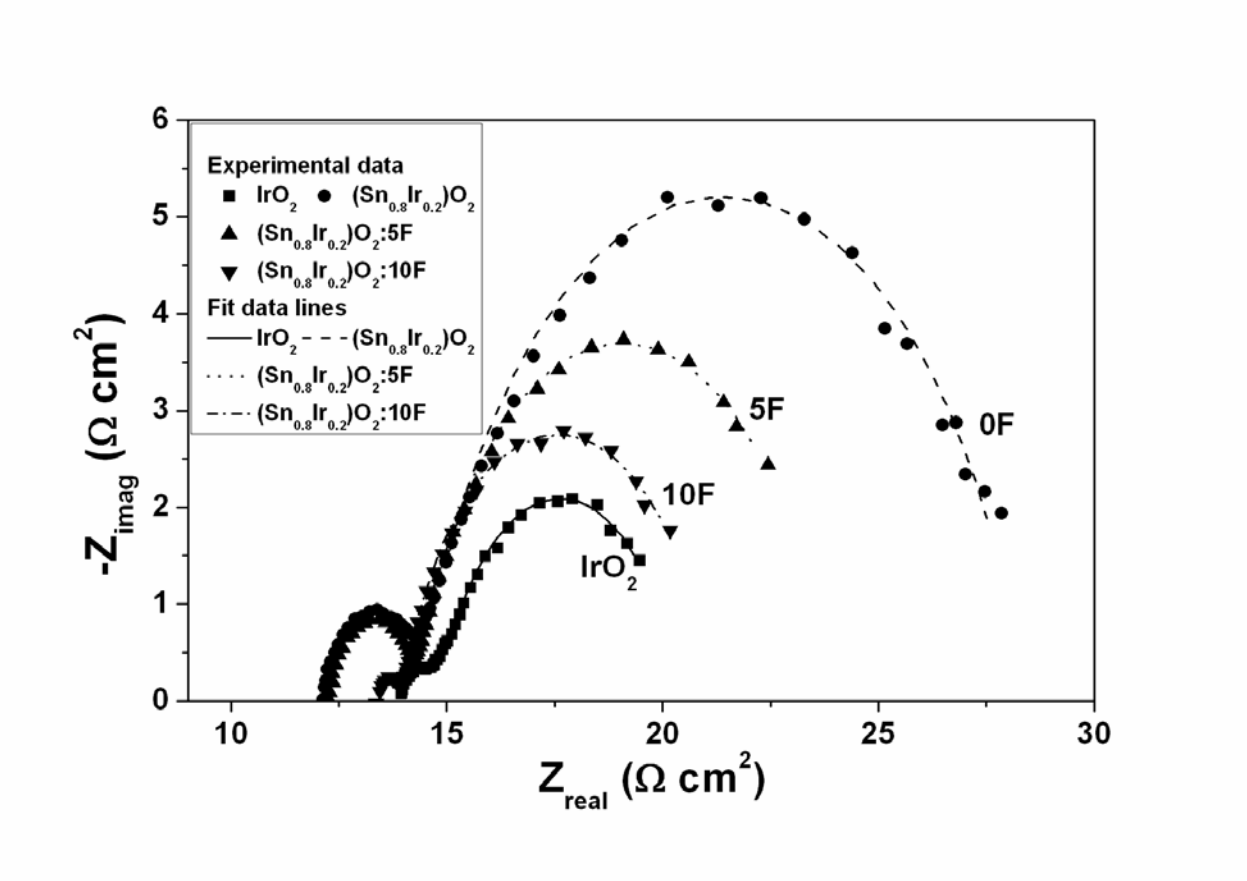

Figure 13. The EIS plot obtained at 1.6 V at 40°C in the presence of 1 N H_2SO_4 solution in the frequency range of 100 mHz - 100 kHz

As shown in **Table 1**, the value of R_e of (Ir,Sn)O_2:F decreases with increase of F content in the parent (Ir,Sn)O_2 lattice which may arise due to increase in electronic conductivity of (Ir,Sn)O_2:F with increase in F content. The (Ir,Sn)O_2:F with 10 wt.% F shows almost identical electrode resistance (R_e ~ 1 Ωcm^2) with pure IrO_2 which suggest that both possess identical electronic conductivity. It can also be noticed that the solution resistance and electrode resistance of IrO_2 and $(Ir_{0.2}Sn_{0.8})O_2$:F is unchanged with change of potential as seen in **Figure 14**, respectively. The low frequency EIS plot of pure IrO_2 and (Ir,Sn)O_2:F shows a well formed semicircle related to OER and also shows that the diameter of the low frequency semicircle,

which should be a measure of the polarization resistance (R_{ct}); and thereby the catalytic activity of the electrode, decreases with increase of F content. The above results suggest that the electrochemical activity of (Ir,Sn)O_2:F increases with increase in F content as the polarization resistance value becomes similar to that of pure IrO_2.

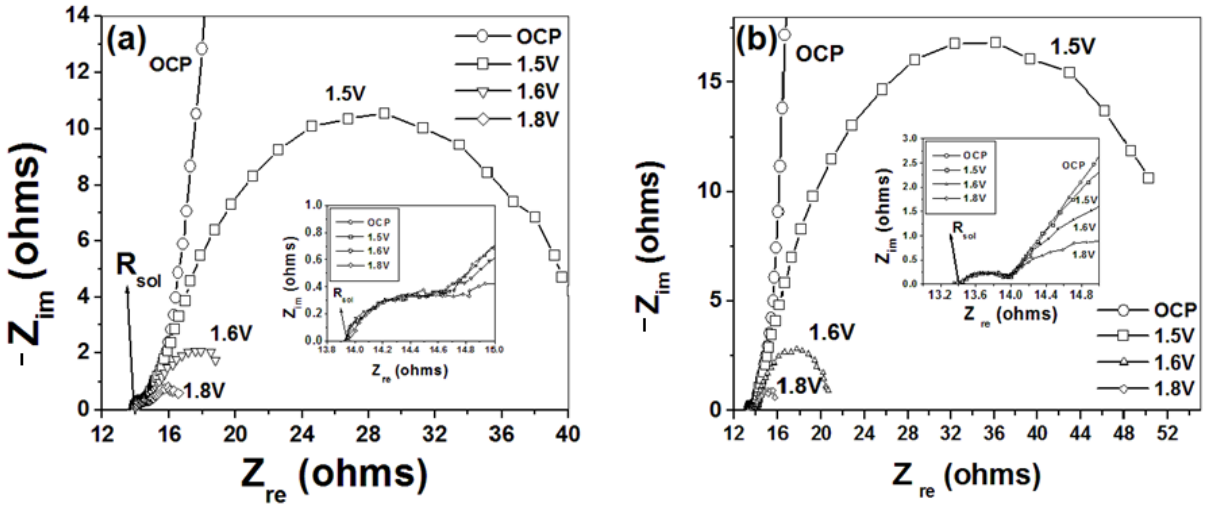

Figure 14. The EIS plot obtained at open circuit potential and different voltages for pure IrO_2 (a), and (Ir,Sn)O_2:10F (b) in the frequency range of 100 mHz - 100 kHz

The polarization curve of pure SnO_2:F and IrO_2 film, before and after ohmic resistance correction ($iR_\Omega = iR_{sol}+iR_e$) without considering the bubble resistance, conducted in the presence of 1 N H_2SO_4 solution at 40^{o}C with a scan rate of 1 mV/sec, is shown in **Figure 15**. Nanocrystalline pure IrO_2 clearly indicates the occurrence of the water splitting reaction at a potential of ~ 1.43V *vs.* NHE. The current density at ~ 1.55 V after iR_Ω correction (*vs.* NHE) is ~ 0.014 ± 0.001 A/cm^2 at 40^{o}C with a total loading ~ 0.3 mg/cm^2 of IrO_2. The Tafel slope of pure IrO_2, calculated from iR corrected Tafel plot, is ~ 60 mV/decade, which corresponds to the two electron pathway reaction assuming a transfer coefficient of ~ 0.5 [30, 48, 53, 101].

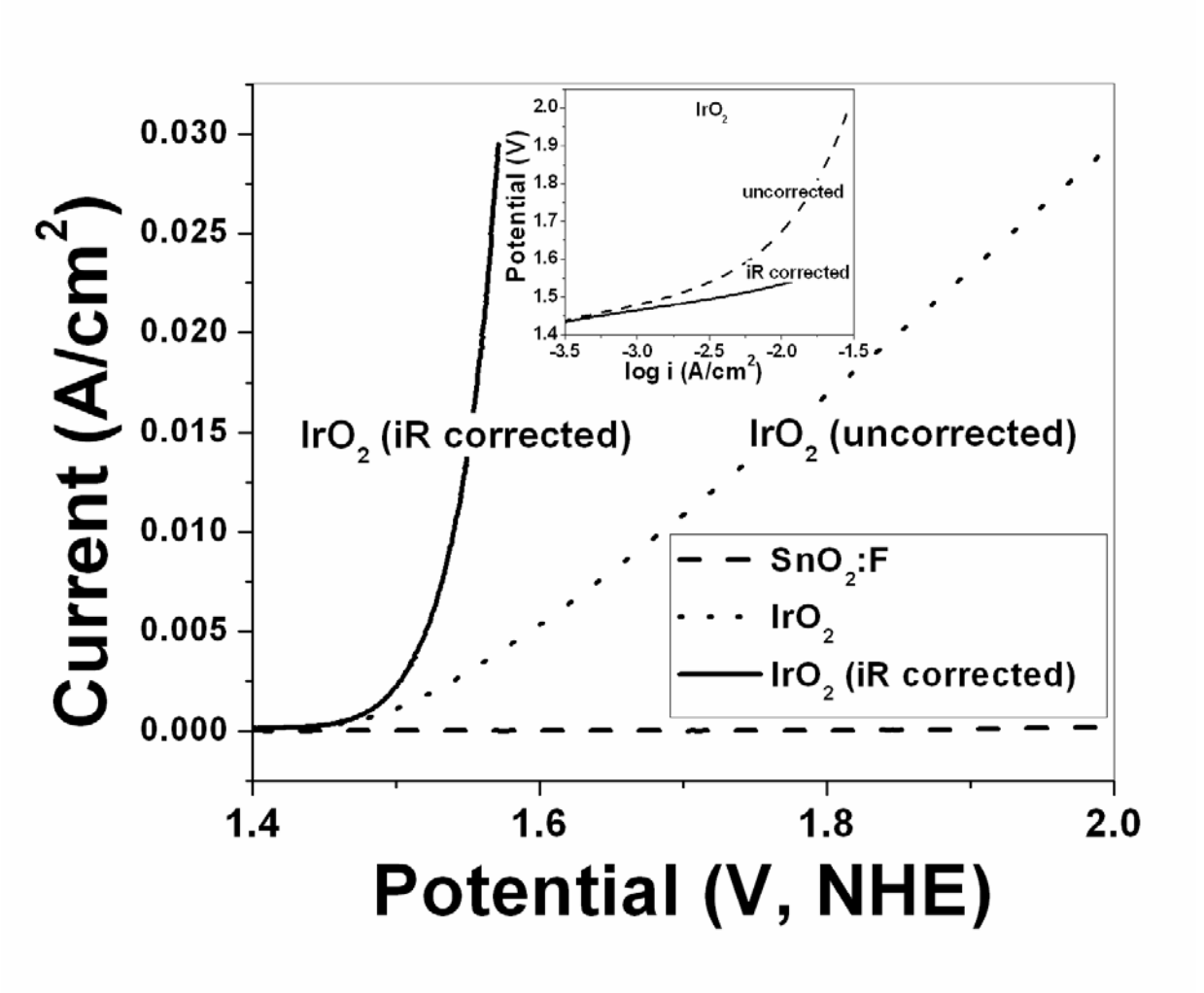

Figure 15. The polarization curve of pure IrO_2 and SnO_2:10F film before and after iR correction, and the inset shows the Tafel plot of pure IrO_2 before and after iR correction

The polarization curve for (Ir,Sn)O_2:F films before and after iR correction corresponding to the different compositions of F, plotted in **Figure 16**, also shows that water splitting (oxygen evolution reaction) occurs at the potential of ~1.43 V (*vs.* NHE) irrespective of the composition which is identical to that of pure IrO_2. Furthermore, the current density at ~ 1.55 V (*vs.* NHE) after iR correction for undoped (Ir,Sn)O_2 solid solution (0 F) with an identical total loading ~ 0.3

mg/cm^2 is ~ 0.0042 ± 0.0001 A/cm^2 at 40^{o}C which is almost three times lower than pure IrO_2. However, the current density of (Ir,Sn)O_2:F increases with increase in F content. In fact, (Ir,Sn)O_2:F containing 10 wt.% F shows a current density of ~ 0.014 ± 0.001 A/cm^2 at ~ 1.55 V (*vs.* NHE) which is comparable to that of pure IrO_2.

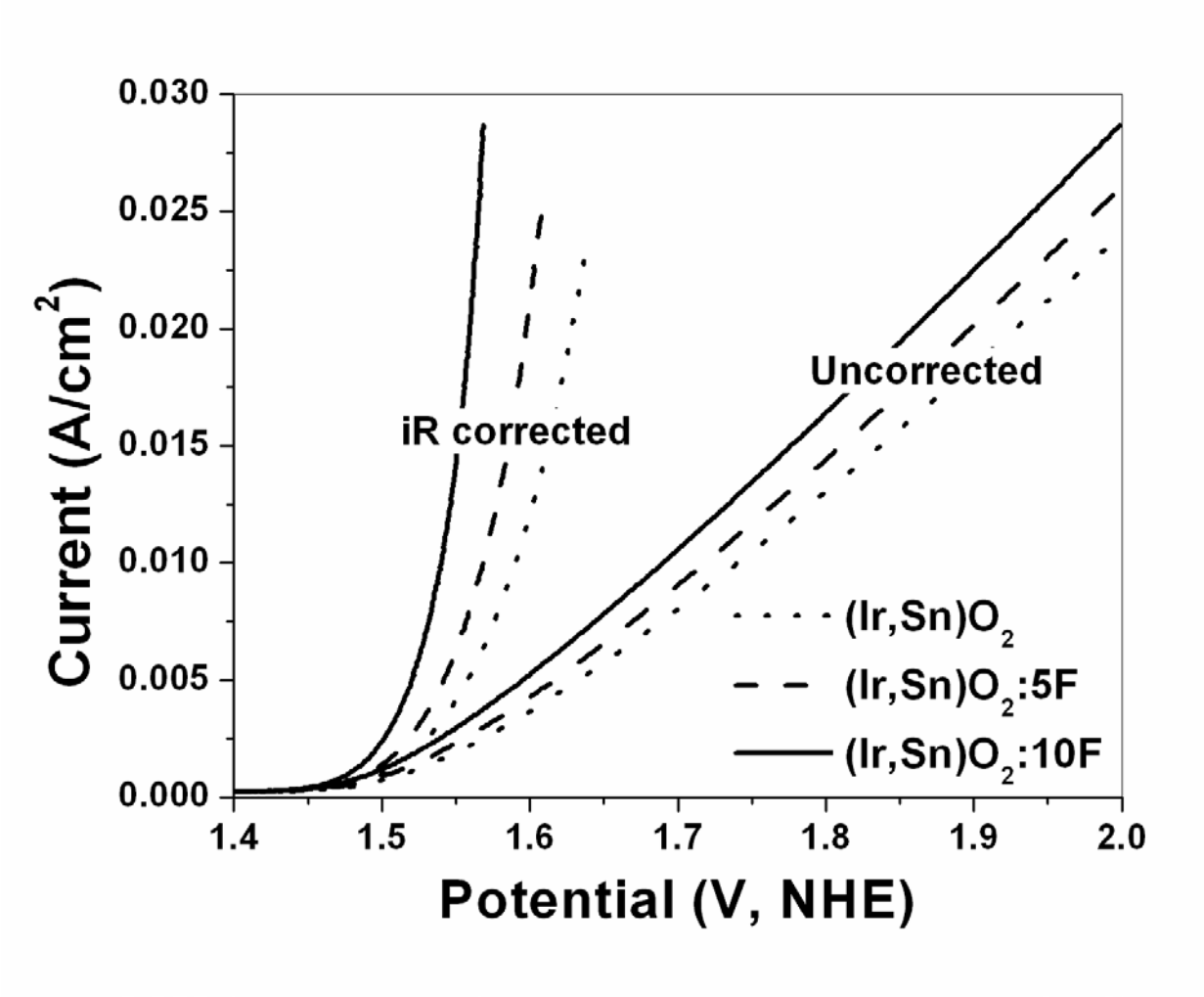

Figure 16. The polarization curve of (Ir,Sn)O_2:F film conducted in the presence of 1 N H_2SO_4 solution at 40°C with a scan rate of 1 mV/sec before and after iR correction.

On the other hand, it has also been observed that the current density decreases with increase in F content above 10 wt.% F as shown in **Figure 17**. The Tafel slope of (Ir,Sn)O_2:F with 0, 5, and 10 wt.% F (**Table 1**), calculated from the corresponding Tafel plots shown in **Figure 18**, is 76, 70 and 62 mV/decade respectively, which suggests that the electrochemical activity of (Ir,Sn)O_2:F increases with increase in F content and corresponding decrease of Tafel slope with increase in F. Moreover, the Tafel slope value of ($Ir_{0.2}Sn_{0.8}$)O_2:10F is similar to that of pure IrO_2 (inset of **Figure 15**). These results clearly suggest that (Ir,Sn)O_2:F with 10 wt.% F, exhibits similar electrochemical activity as that of pure IrO_2, and is indeed a promising candidate as anode electro-catalyst for PEM based water electrolysis.

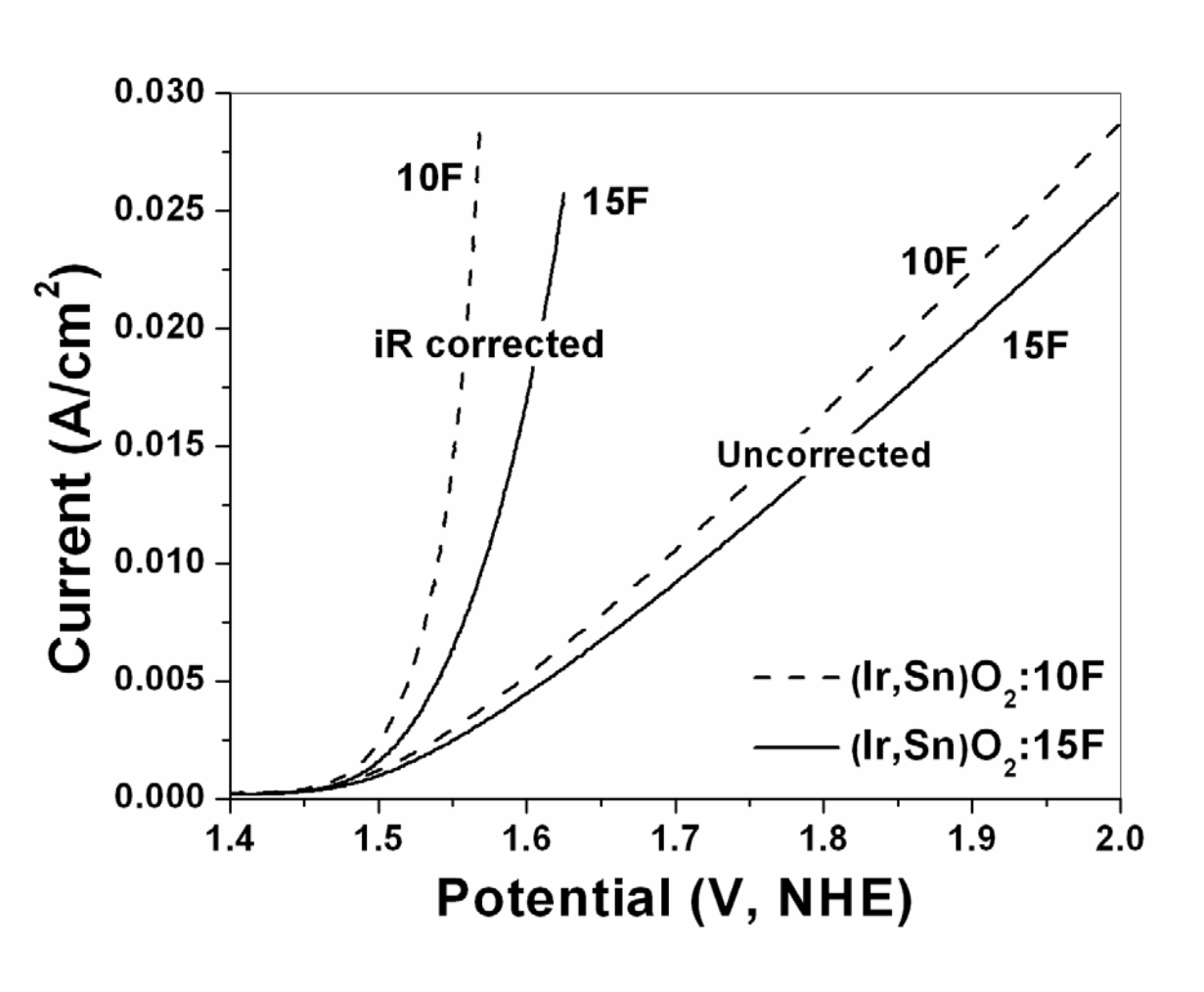

Figure 17. The polarization curve for high F doping of (Ir,Sn)O_2:F film conducted in the presence of 1 N H_2SO_4 solution at 40°C before and after iR correction

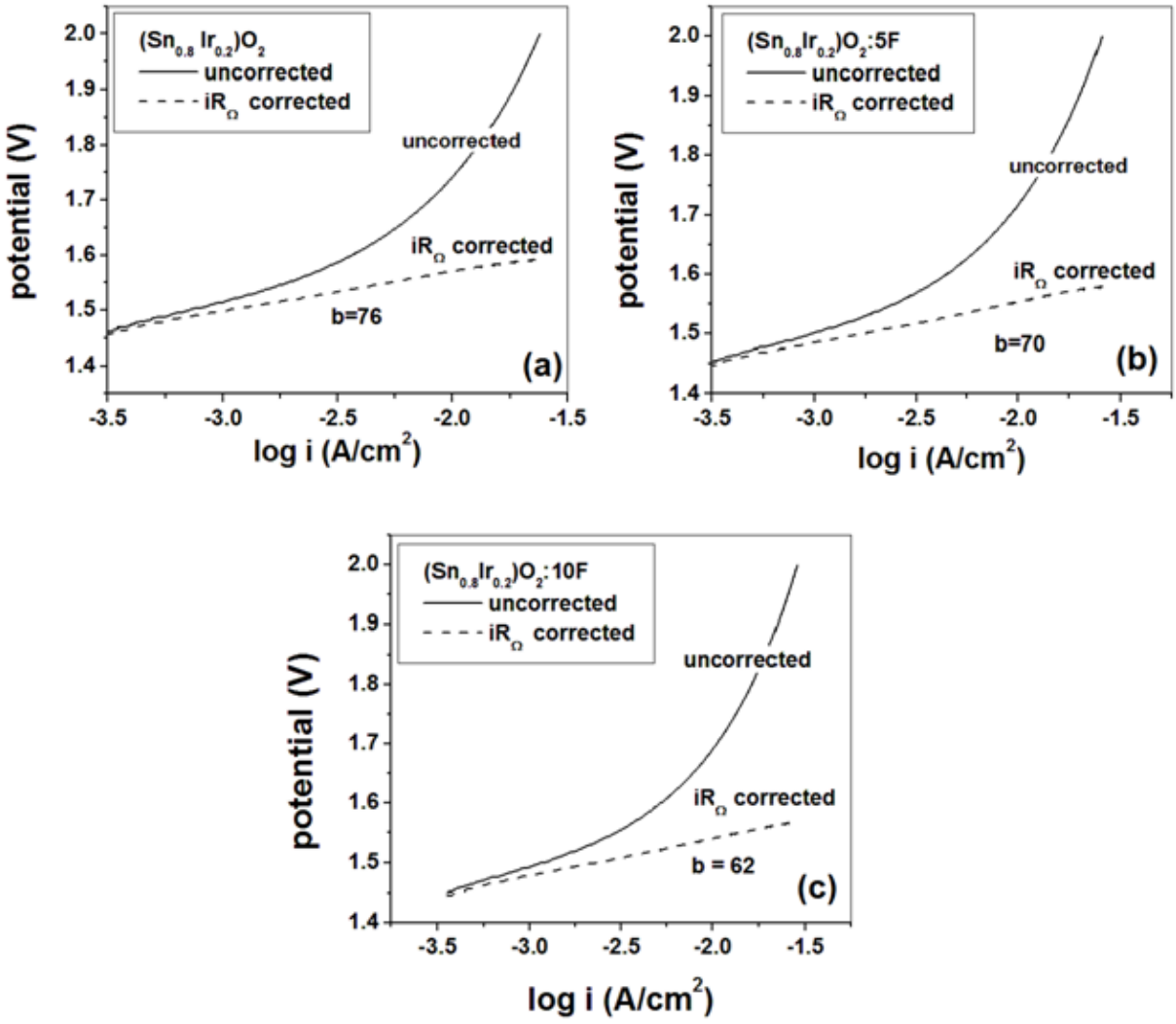

Figure 18. The Tafel plot of $(Ir_{0.2}Sn_{0.8})O_2$ (a), $(Ir_{0.2}Sn_{0.8})O_2$:5F (b), and $(Ir_{0.2}Sn_{0.8})O_2$:10F (c), before and after iR correction, showing the Tafel slope

Multiple small potential step voltammetry was performed for the rotating disk electrode studies in order to study the fundamental kinetics and calculate the apparent activation energy of the OER. The catalyst ink coated Ti disk insert was rotated at speeds varying from 500 rpm to 2000 rpm. **Figure 19** shows the Koutecky - Levich plot *i.e.* i^{-1} *vs.* $\omega^{-1/2}$ for the most optimum

electro-catalyst composition of $(Ir_{0.2}Sn_{0.8})O_2$:10 wt.% F. The current values at different rotation speeds have been plotted at three potentials of 1.55 V, 1.65 V and 1.75 V (*vs.* NHE) without iR correction. The potentials are not iR corrected since the tests have been conducted in-situ (*via* multiple small potential step voltammetry) from which the RDE results are reported directly. This dynamic testing process does not allow accounting for the iR drop from the solution resistance. These RDE plots at different potentials give parallel straight lines of similar nature; and the current increases with increase in voltage as expected, causing a decrease in the value of i^{-1}. This trend is thus consistent with the results obtained from the polarization curves (**Figure 16**). From the slope of the graphs, the number of electrons transferred (n) is determined as explained in **Section 4.4.4**. The average value of 'n' determined at the three voltages for the $(Ir_{0.2}Sn_{0.8})O_2$:10F electro-catalyst is ~ 1.81. The kinetic rate constant (k) of an electrochemical reaction not only varies with the applied potential, but is also dependent on many other factors *viz.*, temperature, electrode surface structure, composition of the catalyst, surface adsorption and reaction intermediates [95, 96, 102, 103]. The range of 'k' is in between 0.055 and 0.075 cm/s. The RDE tests and the Koutecky - Levich plot confirm the two electron pathway mechanism for the OER in PEM electrolysis for all our explored catalyst compositions. This further elucidates the high electrochemical activity and the close to ideal Tafel slope of the 10 wt.% F doped $(Ir,Sn)O_2$, portending it to be a preferred OER electro-catalyst composition for PEM electrolyzer cells.

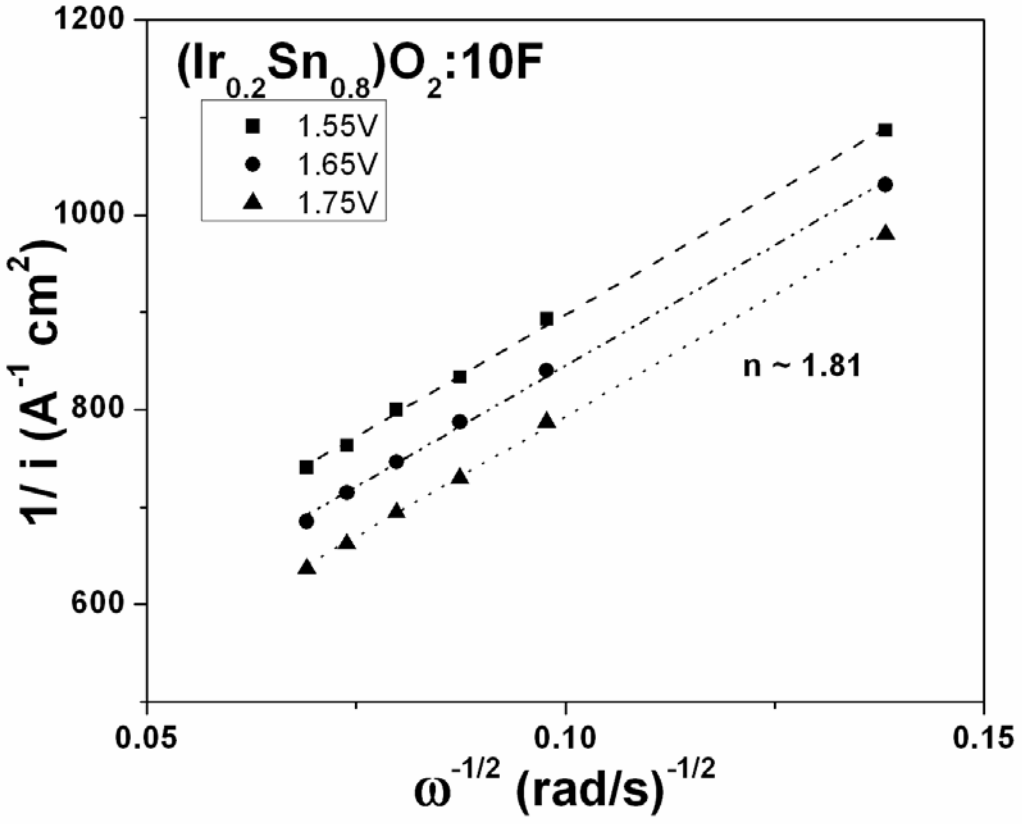

Figure 19. Koutecky - Levich plot in PEM based water electrolysis at 1.55 V, 1.65 V and 1.75 V (*vs.* NHE) in 1 N H_2SO_4 at 25°C for $(Ir_{0.2}Sn_{0.8})O_2$:10 wt.% F

The influence of temperature on the OER was studied in order to calculate apparent activation energy from the Arrhenius relationship as explained before in **Section 4.4.4**. The Arrhenius plots *i.e.* ln i *vs.* T^{-1} for $(Ir_{0.2}Sn_{0.8})O_2$:10 wt.% F is shown in **Figure 20**. The temperature was varied between 25 - 70°C and data points in these graphs have been plotted at three different potentials of 1.55 V, 1.65 V and 1.75 V (*vs.* NHE) as used before. The slope of these lines was averaged in order to calculate the E_a which is ~ 25.2 ± 1.5 kJ/mol. This E_a value is lesser and in the range of values reported for the OER by other researchers [97, 98, 104-107].

The E_a value for all the electrodes being similar to the powder catalysts (undoped and F doped IrO_2) as shown in **Section 5.2.2.2** suggests that the OER on the electrodes proceeds *via* the same reaction mechanism [97, 108]. The reaction mechanism has been previously reported by Nørskov *et al.* and in our earlier publication [53-55]. This four step reaction mechanism occurring during PEM based water electrolysis is described in **Section 2.2.2**.

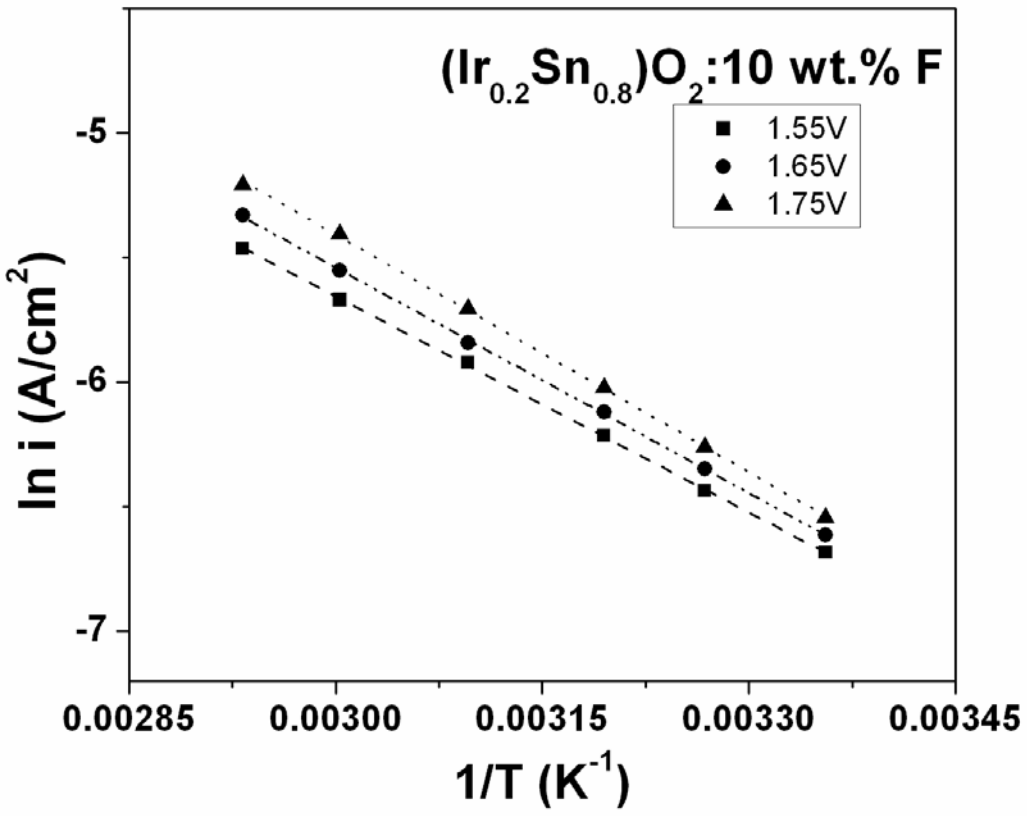

Figure 20. Arrhenius plot for $(Ir_{0.2}Sn_{0.8})O_2$:10 wt.% F at 1.55 V, 1.65 V and 1.75 V (*vs.* NHE) over a temperature range of 25°C to 70°C

In order to study the electrochemical stability of the anode electro-catalyst (Ir,Sn)O_2:F in 1N H_2SO_4, CA test is conducted for 12 hours at 40^oC at a constant voltage. The CA curves, obtained at a constant voltage of ~ 1.65 V (*vs.* NHE), of (Ir,Sn)O_2:10 wt.% F combined with that of pure IrO_2 are shown in **Figure 21**. The CA curve clearly shows a marked decay of current (13 % of the initial value) for both electrodes in the initial 30 minutes. A steady state of current ~ 0.006 A/cm^2 has also been achieved however after 1 hour of the initial period for (Ir,Sn)O_2:F and pure IrO_2 over the test run. This indicates similar structural stability of (Ir,Sn)O_2:F compared to IrO_2. The ICP results, conducted in the H_2SO_4 electrolyte solution collected after CA measurement, show no presence of Ir up to 10 wt.% F suggesting that the steady decrease of current during CA measurement may arise due to loss of fuel rather than dissolution of IrO_2 electro-catalyst [57].

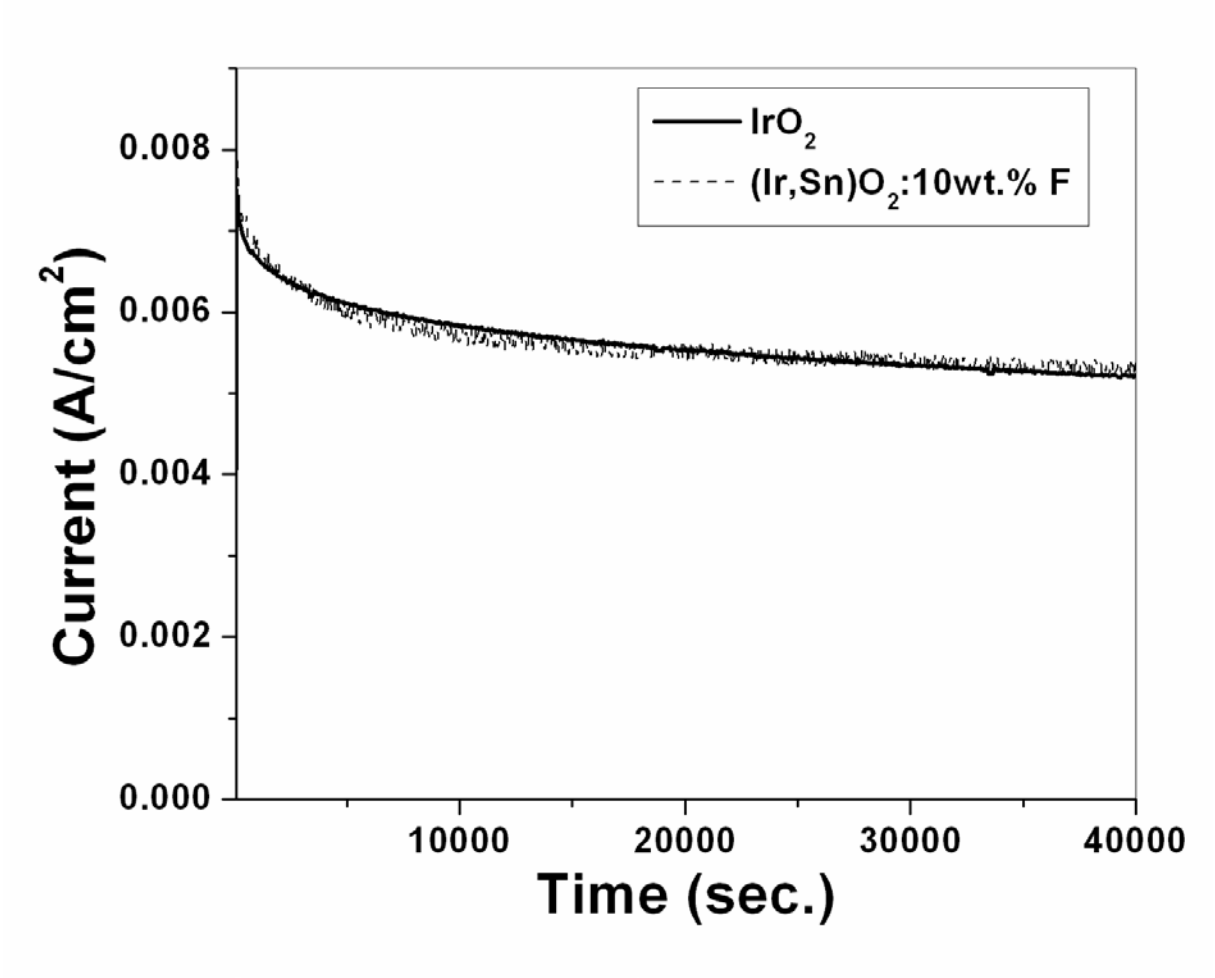

Figure 21. Variation of current *vs.* time in the accelerated life test of pure IrO_2 and $(Ir_{0.2}Sn_{0.8})O_2$:10F performed in a 1 N H_2SO_4 solution under ~ 1.65 V at 40°C

After the conclusion of the CA test, the IrO_2 and the $(Ir_{0.2}Sn_{0.8})O_2$:10 wt.% F thin film electrodes were subject to polarization testing as seen in **Figure 22** in order to determine the activity of the electrodes after long term structural stability tests. The Tafel plots from these polarization curves (post CA measurement) after iR correction are shown in **Figure 23** and **Figure 24**. A Tafel slope of ~ 77 mV/decade and ~ 82 mV/decade was obtained for pure IrO_2 thin film and $(Ir,Sn)O_2$:10 wt.% F respectively. This is slightly higher but still close and

comparable to the values obtained from the polarization tests conducted before CA (**Figure 15** and **Figure 18**). This test further demonstrates the robustness of the electro-catalysts.

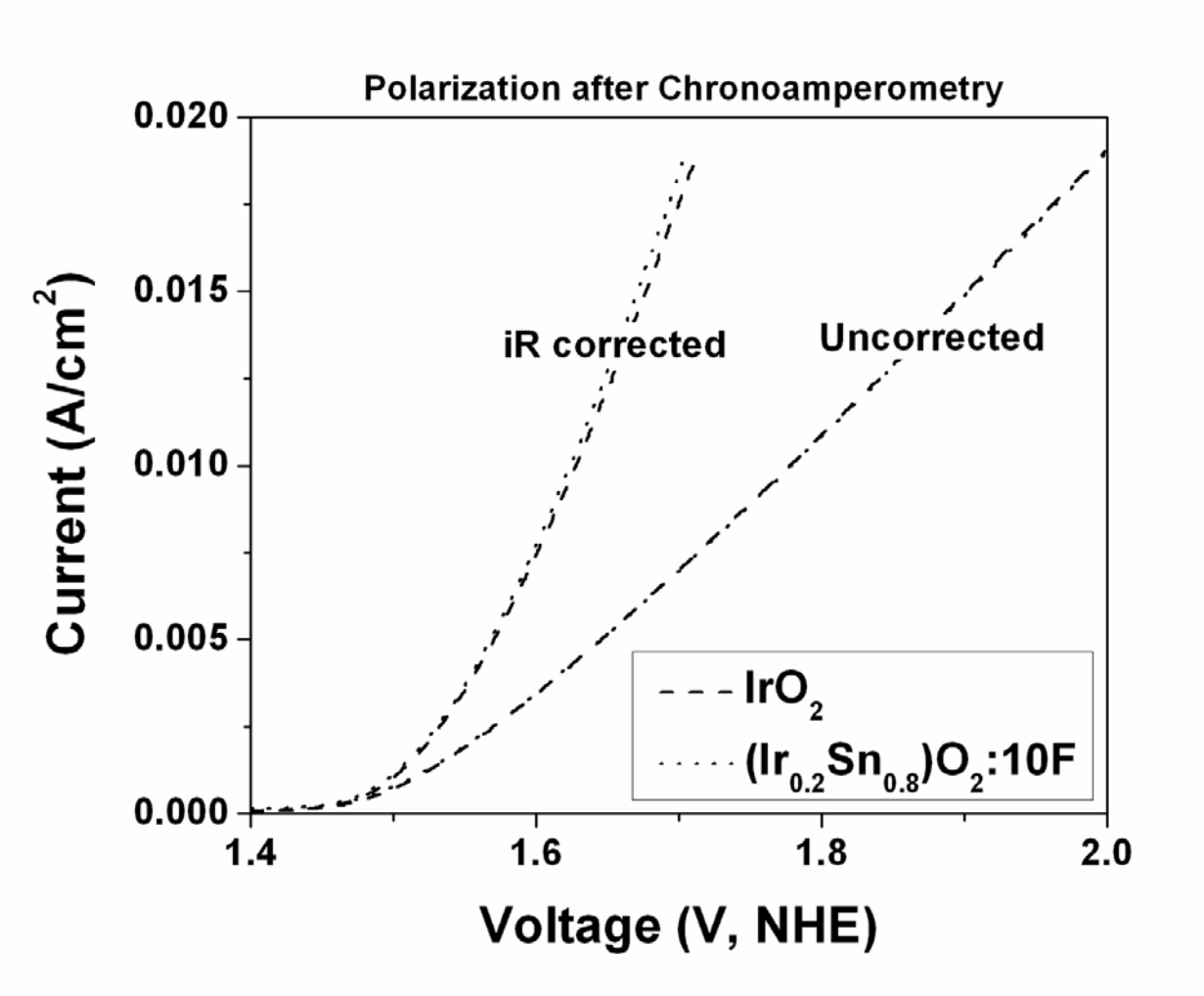

Figure 22. Polarization curve of IrO_2 and (Ir,Sn)O_2:10 wt.% F thin film after the CA test

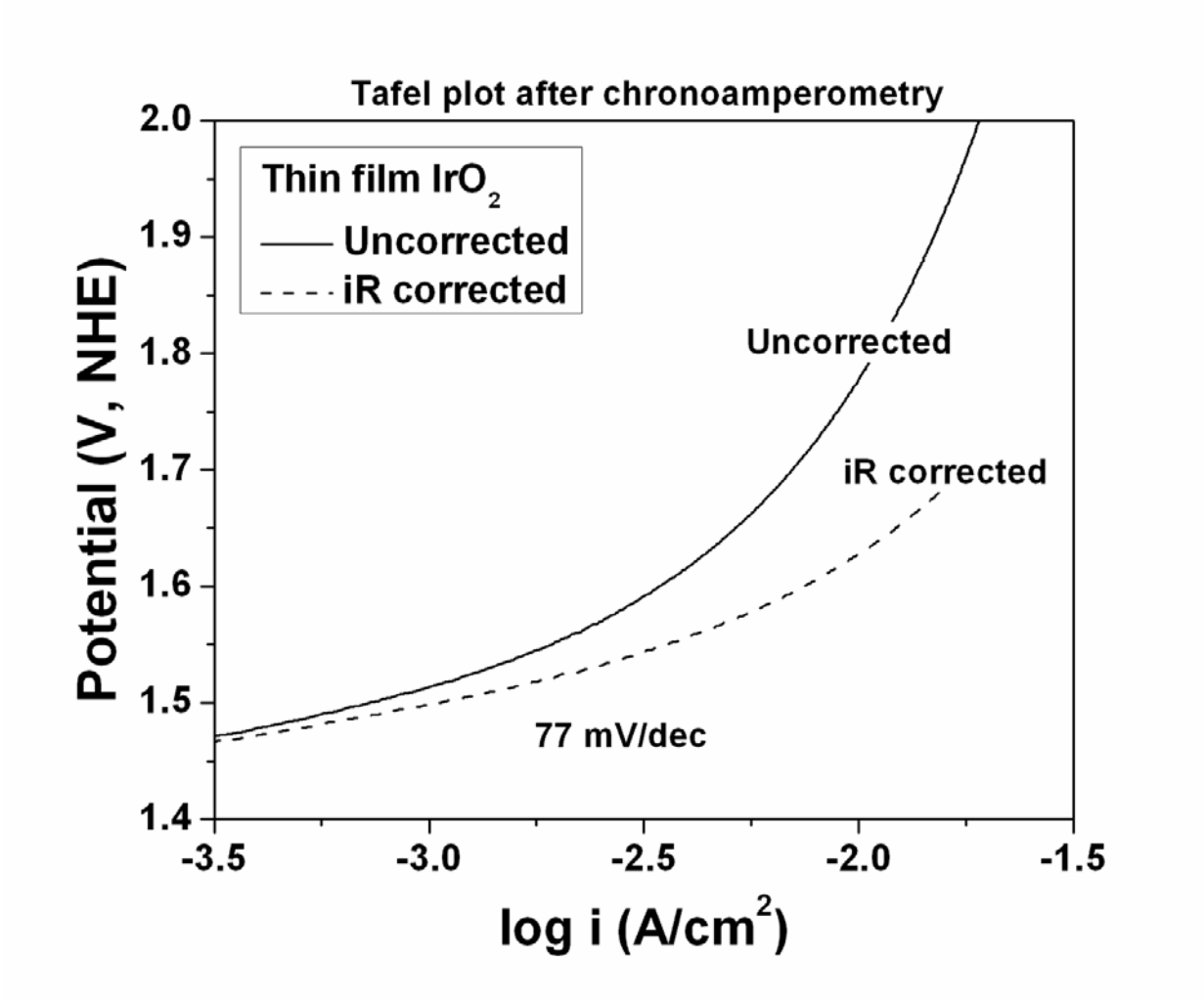

Figure 23. The Tafel plot of pure IrO_2 after the CA test

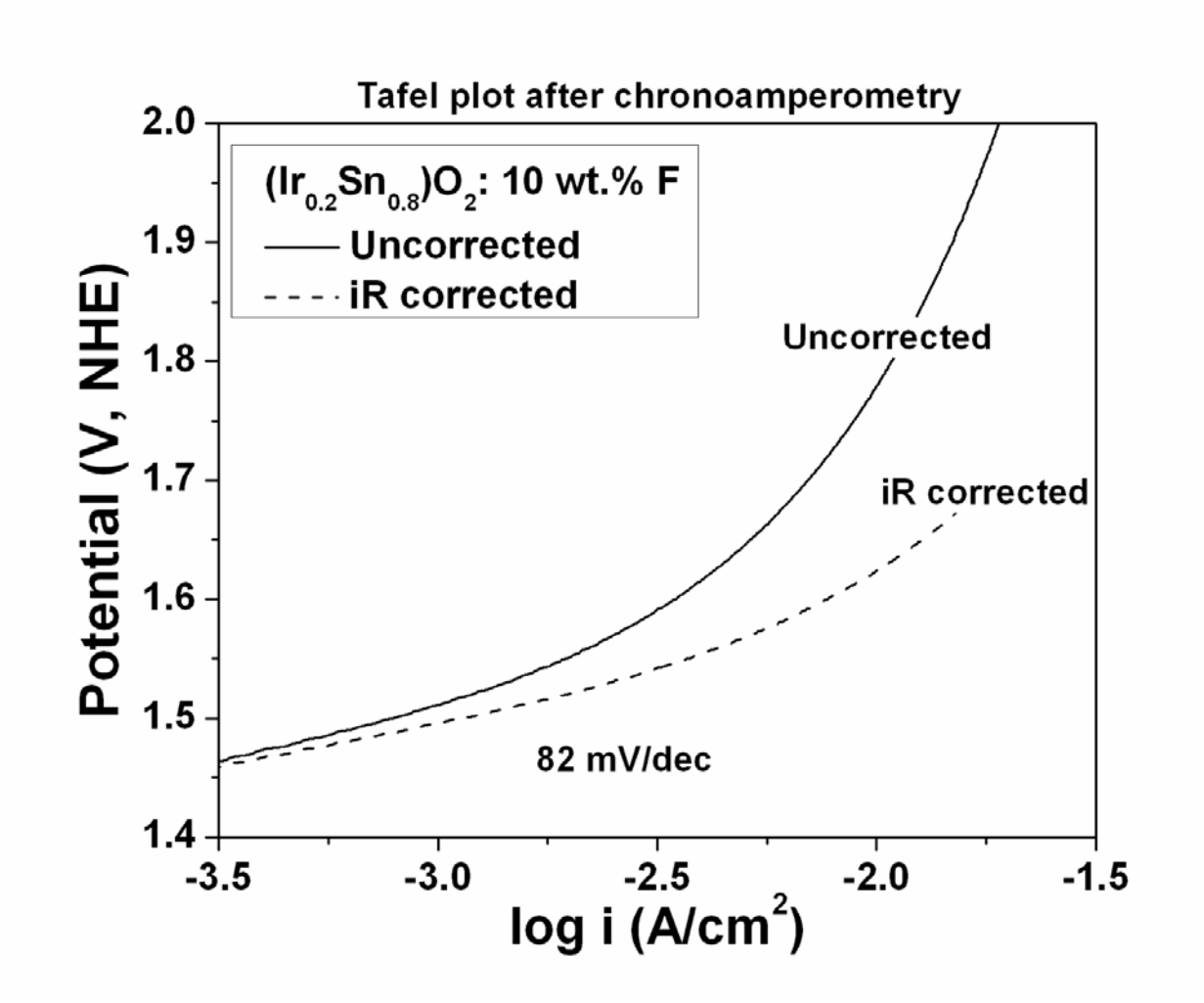

Figure 24. The Tafel plot of (Ir,Sn)O_2:10 wt.% F thin film after the CA test

The present experimental study thus successfully demonstrates that F doped ($Ir_{0.20}Sn_{0.80}$)O_2, synthesized as a thin film on Ti foil, shows an improve in electrochemical performance with the addition of F suggesting that this system is indeed a promising OER electro-catalyst for PEM based water electrolysis. Identification of such non-noble metal based catalysts or electro-catalysts with significant reduction of expensive noble metal contents (*E.g.* IrO_2, Pt) with comparable or higher electrochemical performance as the standard noble metal/oxide for PEM based water electrolysis would result in reduction in the overall capital

costs of PEM based water electrolyzers, and therefore, attainment of the targeted hydrogen production cost (< $ 3.0 / gge delivered) comparable to conventional liquid fuels.

5.1.3 Binary F doped $(Ru,Sn)O_2$

5.1.3.1 Structural Analysis

Figure 25 shows the XRD patterns of thin films of RuO_2 and SnO_2 synthesized by thermal decomposition of $RuCl_3$ and $SnCl_2.2H_2O$ ethanol solution, respectively, coated on Ti foil following heat treatment at 400°C for 4 hours. The XRD patterns of the RuO_2 and SnO_2 thin film show tetragonal structure as expected. The XRD patterns of the most optimized electro-catalyst composition having only 20 at.% RuO_2 *i.e.* $(Ru_{0.2}Sn_{0.8})O_2$:F with different F compositions (0, 5, 10, 15 wt.%), shown in **Figure 26**, also show the peaks corresponding to tetragonal structure which suggest the formation of complete solid solution without any undesirable phase separation (*E.g.* $SnO_2 + RuO_2$). Formation of metastable solid solution between RuO_2 and SnO_2 as well as in the other oxide systems such as RuO_2, SbO_2, and SnO_2 has been reported by other researchers [32, 109, 110]. However, it should be noted that $(Ru,Sn)O_2$:15 wt.% F shows an extra peak for SnO_2 which indicates that excess F substitution leads to phase separation. The calculated effective crystallite size for all of the $(Ru,Sn)O_2$:F films is in the range of ~ 5 - 10 nm which is comparable with $(Ru,Sn)O_2$ suggesting that F^- doping has no significant effect on the refinement of crystallite size of $(Ru,Sn)O_2$.

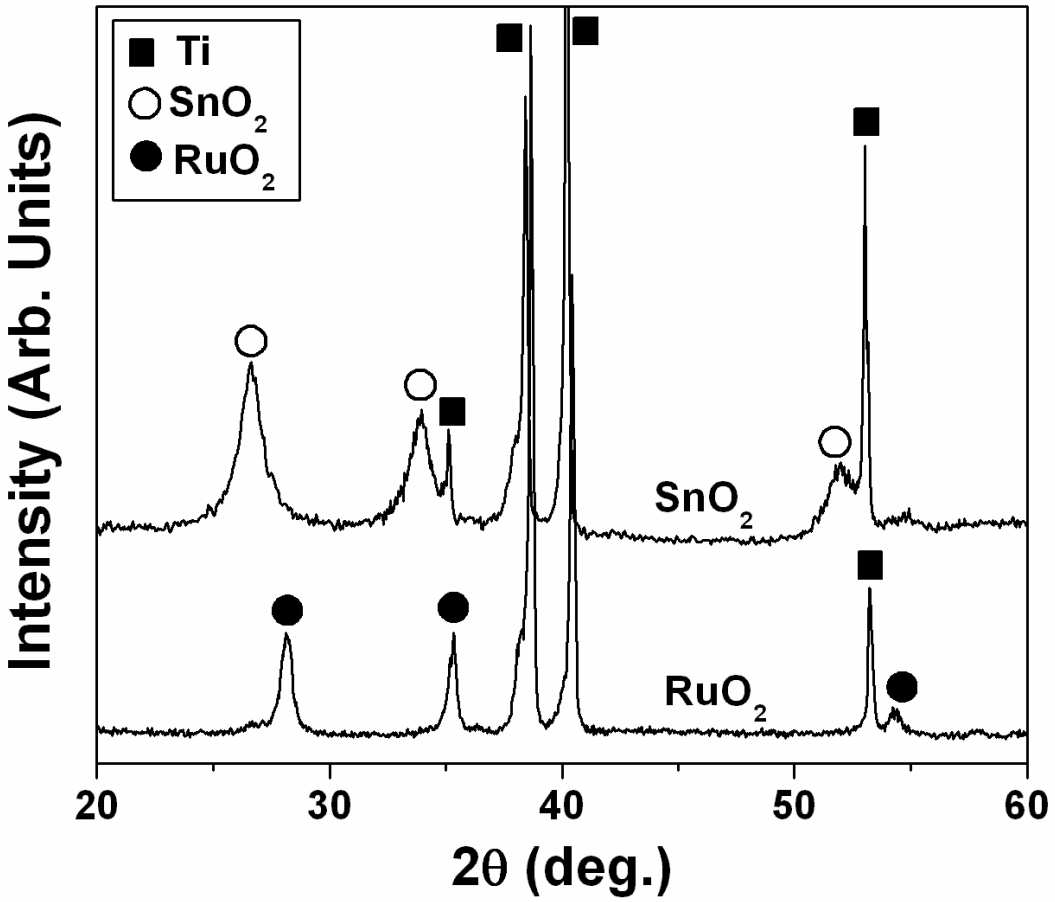

Figure 25. XRD patterns of thin film RuO_2 and SnO_2 coated on a Ti foil

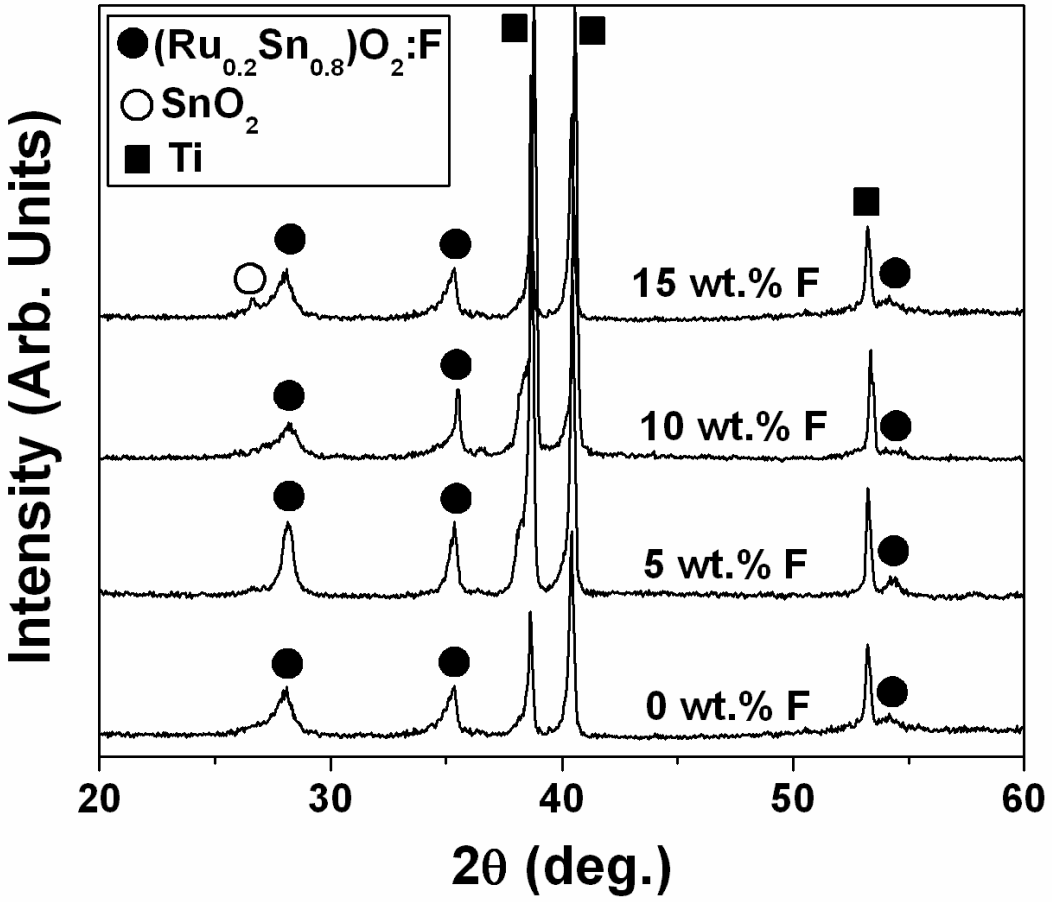

Figure 26. XRD patterns of thin film $(Ru_{0.2}Sn_{0.8})O_2$:F for different F compositions coated on Ti foil

The presence of The presence of elemental Ru, Sn and O in the (Ru,Sn)O_2:F film of different compositions has been confirmed using energy dispersive x-ray analysis (EDX) configured to the SEM, although as expected, the presence of F could not be detected. The SEM image along with elemental x-ray mapping, shown in **Figure 27**, is for a representative (Ru,Sn)O_2:F film containing 10 wt.% F. It indicates the presence of the characteristic "mud-crack" morphology of the (Ru,Sn)O_2:F film coated on Ti foil, and also validates the presence of

Ru, Sn and O which are homogeneously distributed within the $(Sn,Ru)O_2$:F particles (see the elemental dot maps in **Figure 27**) without being segregated on any specific site or on any particular region of the particle.

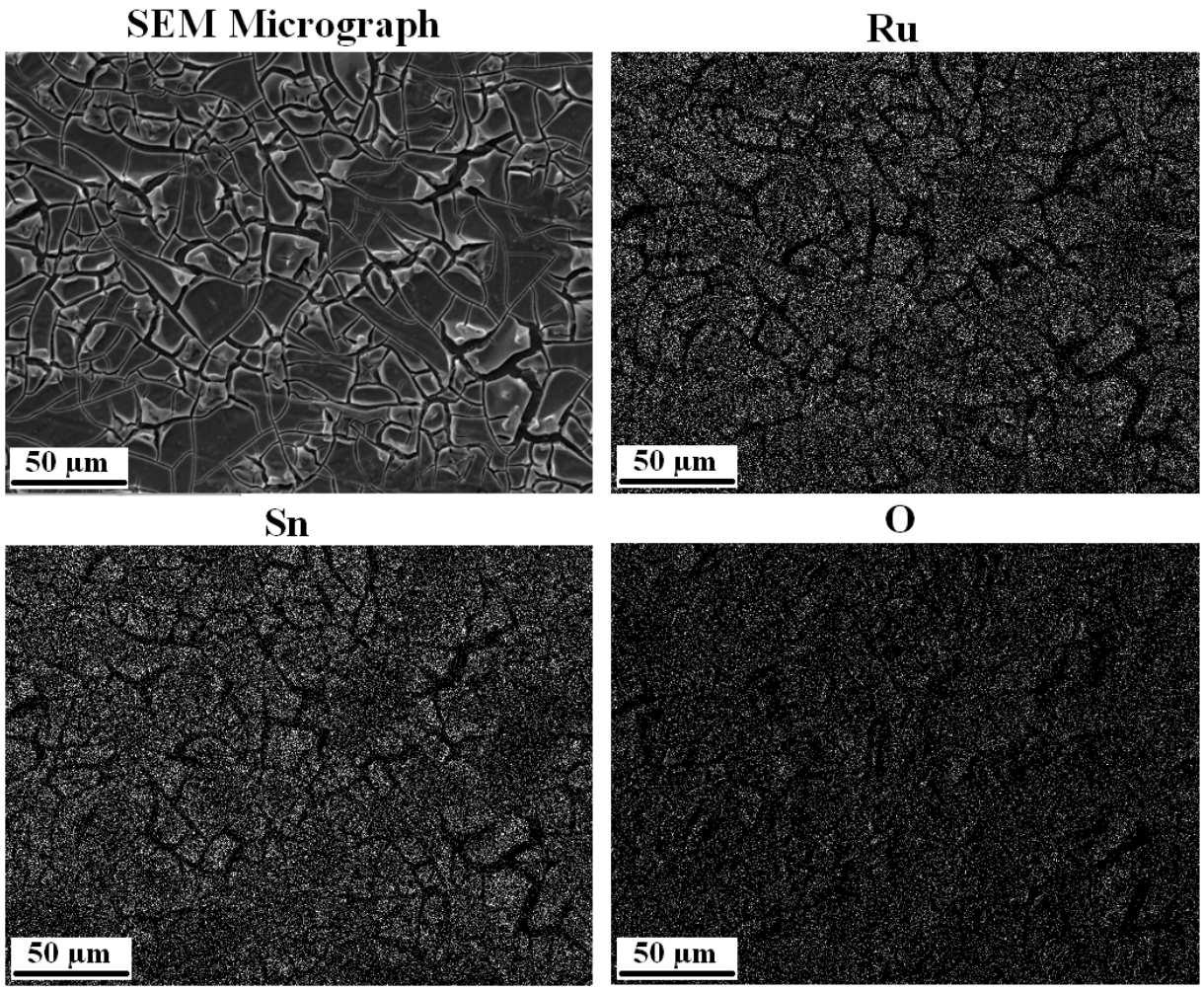

Figure 27. The SEM micrograph along with x-ray mapping of Ru, Sn and O

Figure 28 shows the quantitative analysis of the elemental composition of the representative $(Ru,Sn)O_2$:10F films obtained by EDX (a) and the TEM image (b). The EDX shows that the measured elemental composition of Sn and Ru which is 77.4 at.% and 22.6 at.%

respectively are expectedly close to the nominal composition. Elemental composition of the other electro-catalysts was also measured by EDX and was found to be similar to the nominal composition. The bright field TEM image of $(Ru,Sn)O_2$:F particles as seen in **Figure 28** (b), collected from the $(Ru,Sn)O_2$:10 wt.% F film confirms nanostructured fine particles of ~ 10 - 15 nm corresponding to the $(Ru,Sn)O_2$:F solid solution.

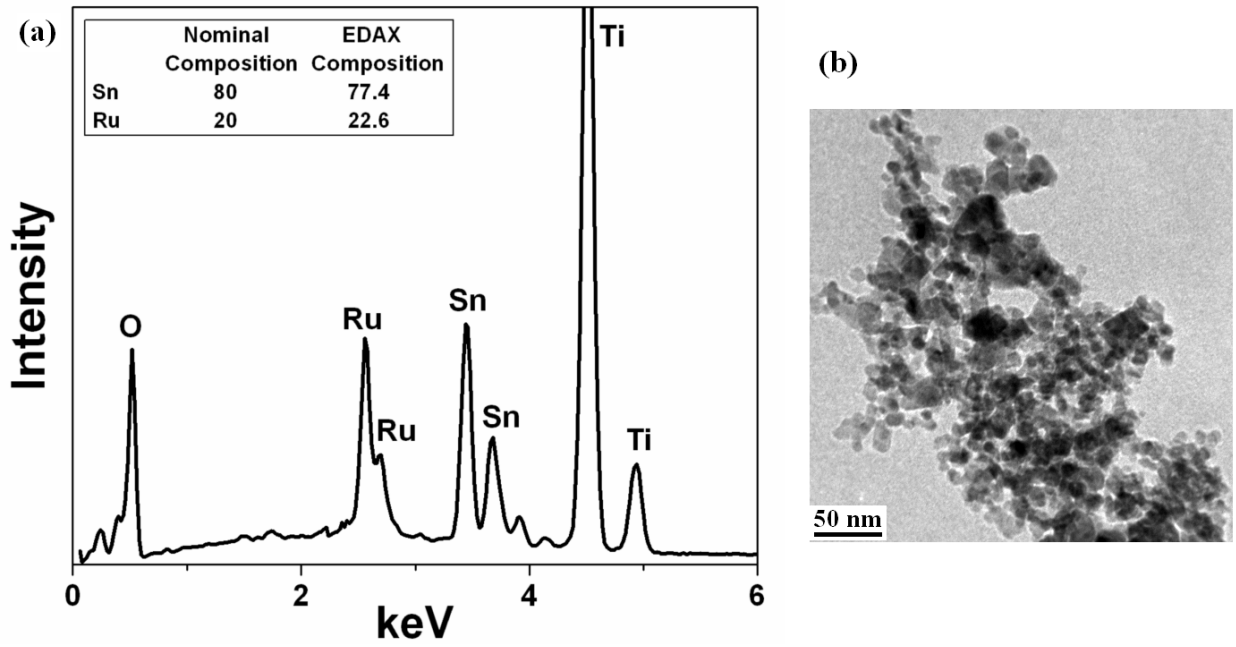

Figure 28. The EDX (a), and TEM imaging (b) of $(Ru,Sn)O_2$:10F thin film

5.1.3.2 Electrochemical Testing

The electrochemical activity of RuO_2 and $(Ru,Sn)O_2$:F thin films of different composition has been studied as an OER anode electro-catalyst for PEM based water electrolysis. It should be noted that the linear polarization curve and non-linear Tafel plots are typically most often encountered due to a large contribution of ohmic resistance (R_Ω) which mainly arises due to the

solution resistance of the electrolyte (solution resistance, R_s), the oxide film electrode resistance (R_e) and the accumulation of oxygen gas bubble covering the electrode surface during water electrolysis occurring at higher current densities (bubble resistance, R_{bub}) [83, 111]. These contributions were also observed in the present study. In order to evaluate the inherent electrochemical property or the electrode kinetics of the electro-catalyst studied herein, the polarization curve of different samples, conducted in the presence of 1 N H_2SO_4 solution at 40°C with a scan rate of 1mV/sec, is plotted after appropriately correcting for the total ohmic loss (iR_Ω). The total ohmic loss (iR_Ω) is the sum value of the solution resistance (R_s) and the electrode resistance (R_e). The value of R_s and R_e, respectively of the different samples, tabulated in **Table 2**, is obtained from electrochemical impedance spectroscopy (EIS) measurements conducted at different potentials with respect to NHE at 40^{o}C.

Table 2. Impedance parameters and Tafel slope of RuO_2 and $(Ru,Sn)O_2$:F

Composition	R_s (Ωcm^2)	R_e (Ωcm^2)	R_{ct} (Ωcm^2)	Tafel slope (b)
RuO_2	13.5	1.1	3.10	77
$(Ru_{0.2}Sn_{0.8})O_2$	12.3	3.2	4.96	76
$(Ru_{0.2}Sn_{0.8})O_2$:5F	10.6	2.0	4.65	67
$(Ru_{0.2}Sn_{0.8})O_2$:10F	12.3	1.5	4.17	65

Figure 29 shows the electrochemical impedance plot of RuO_2 and $(Sn,Ru)O_2$:F obtained at 1.6 V, the typical voltage selected for evaluating the optimal performance of the catalyst at

40°C in the presence of 1 N H_2SO_4 solution in the frequency range of 100 mHz - 100kHz. The impedance parameters (**Table 2**) is obtained by fitting the experimental data using the ZView software from Scribner Associates with a circuit model $R_s(R_eQ_1)(R_{ct}Q_{dl})$, where R_s is the solution resistance, R_e is the electrode resistance, R_{ct} is the charge transfer resistance, Q_1 is the constant phase element (CPE) and Q_{dl} includes contributions from both the double layer capacitance and pseudo-capacitance, respectively [65, 67]. R_s is the resistance encountered at high frequencies due to charge transfer in the solution. R_e is the resistance faced in the circuit due to electron transfer from the electrode to the current collector (*i.e.* our coated Ti foil substrate). It has been observed that the solution resistance (R_s) and the electrode resistance (R_e) of RuO_2 and $(Ru,Sn)O_2$:F for the different F containing compositions is unchanged with change in potential. As shown in **Table 2**, the value of the electrode resistance (R_e) of $(Ru,Sn)O_2$:F decreases with increase in F content in the parent $(Ru,Sn)O_2$ lattice which may arise due to the improved electronic conductivity of $(Ru,Sn)O_2$:F with increase in F. Consequently, $(Ru,Sn)O_2$:F with 10 wt.% F exhibits almost identical electrode resistance (R_e ~ 1.5 Ωcm^2) as pure RuO_2 (R_e ~ 1.1 Ωcm^2) suggesting the identical electronic conductivity of both systems. The low frequency EIS plot of pure RuO_2 and $(Ru,Sn)O_2$:F (**Figure 29**) shows a well formed semicircle related to OER and also indicates that the diameter of the low frequency semicircle typically a measure of the polarization resistance (R_{ct}) decreases with increase in F. The above results therefore clearly suggests that the electrochemical activity of $(Ru_{0.2}Sn_{0.8})O_2$:F increases with increase in F and moreover, the polarization resistance (R_{ct}) value of $(Ru_{0.2}Sn_{0.8})O_2$:10F is similar (~ 4.2 Ωcm^2) to that of pure RuO_2 (~ 3.1 Ωcm^2) which further indicates that both systems will likely exhibit almost equivalent electro-catalytic activity as detailed below.

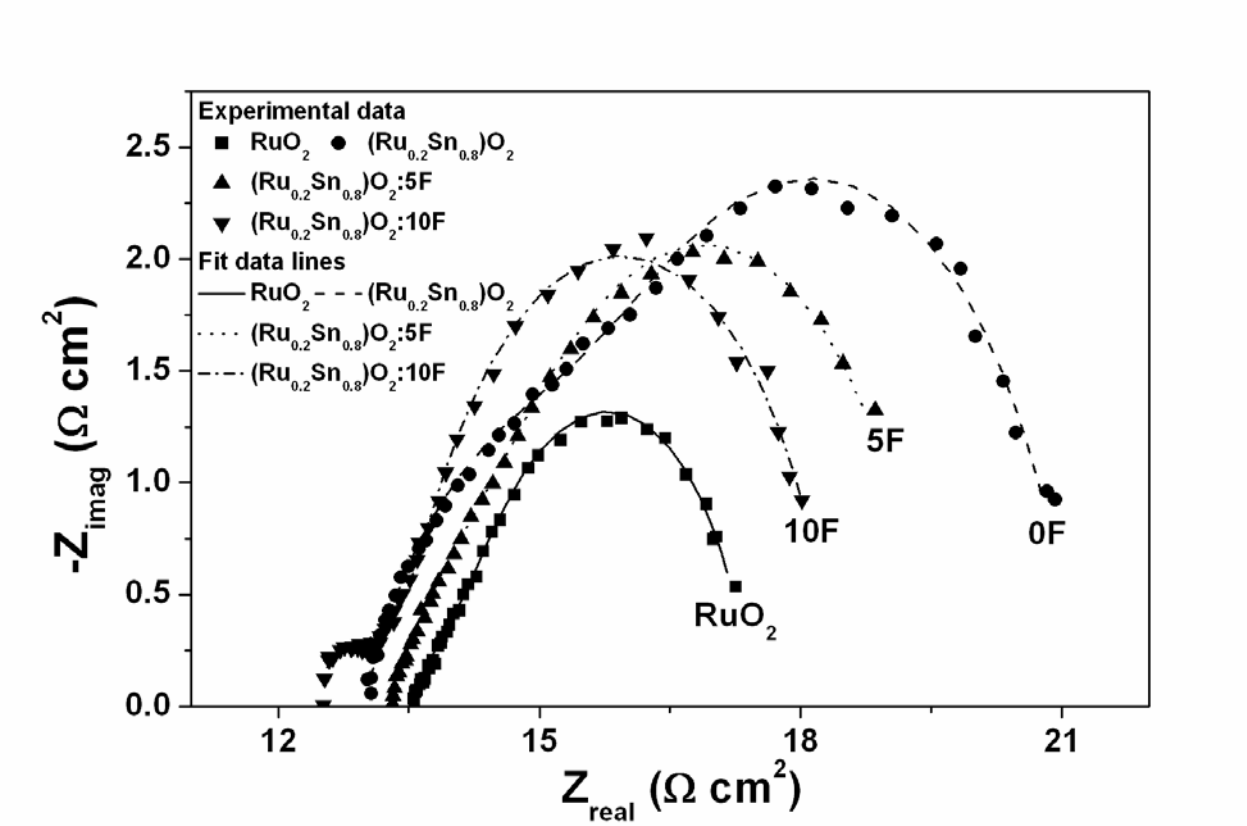

Figure 29. The EIS plot of (Ru,Sn)O_2:F and RuO_2 obtained at 1.6 V in the presence of 1 N H_2SO_4 solution in the frequency range of 100 mHz - 100 kHz

The polarization curve of pure SnO_2:F and RuO_2 film, before and after ohmic resistance correction ($iR_\Omega = iR_s + iR_e$) without considering the bubble resistance, conducted in the presence of 1 N H_2SO_4 solution at 40°C with a scan rate of 1 mV/sec, is shown in **Figure 30**. The polarization curve of SnO_2:F as expected shows no catalytic activity at all for water electrolysis. On the other hand, nano-crystalline, undoped and pure RuO_2 clearly indicates the occurrence of the water splitting or OER at a potential of ~ 1.42 V *vs.* NHE. The current density at ~ 1.55 V (*vs.* NHE), a voltage selected to evaluate the electrochemical activity for water electrolysis

obtained from iR_Ω corrected plot is ~ 0.0176 ± 0.001 A/cm^2 at 40^{o}C with a total loading ~ 0.3 mg/cm^2 of RuO_2. The polarization curve for the various (Ru,Sn)O_2:F film compositions containing different amounts of F before and after iR_Ω correction, plotted in **Figure 31** also shows that water splitting occurs at the potential of ~1.42 V (*vs.* NHE) irrespective of the composition which is identical to that of pure RuO_2. Furthermore, the current density at ~ 1.55 V (*vs.* NHE) obtained from iR_Ω corrected plot for undoped (Ru,Sn)O_2 solid solution (0 F) with an identical total loading of ~ 0.3 mg/cm^2 is ~ 0.009 ± 0.0001 A/cm^2 at 40°C which is almost 50 % of that of pure RuO_2. However, the current density of (Ru,Sn)O_2:F increases with increase in F content. In fact, (Ru,Sn)O_2:F containing 10 wt.% F has a current density at ~ 1.55 V (*vs.* NHE) of ~ 0.0175 ± 0.001 A/cm^2 which is comparable with that of pure RuO_2. However, the trend does not continue with increase in F content and it can be seen that the current density unfortunately decreases with continued increase in F content above 10 wt.% F as seen in **Figure 32**. (Ru,Sn)O_2:15 wt.% F has lesser catalytic activity, and this could potentially arise due to the phase separation of SnO_2 from (Ru,Sn)O_2:F as observed in the XRD pattern (**Figure 26**). **Figure 33** shows the variation of current density for all undoped compositions of binary (Ru,Sn)O_2 and F doped ($Ru_{0.2}Sn_{0.8}$)O_2 at a potential of ~ 1.75 V (*vs.* NHE) from all the polarization tests.

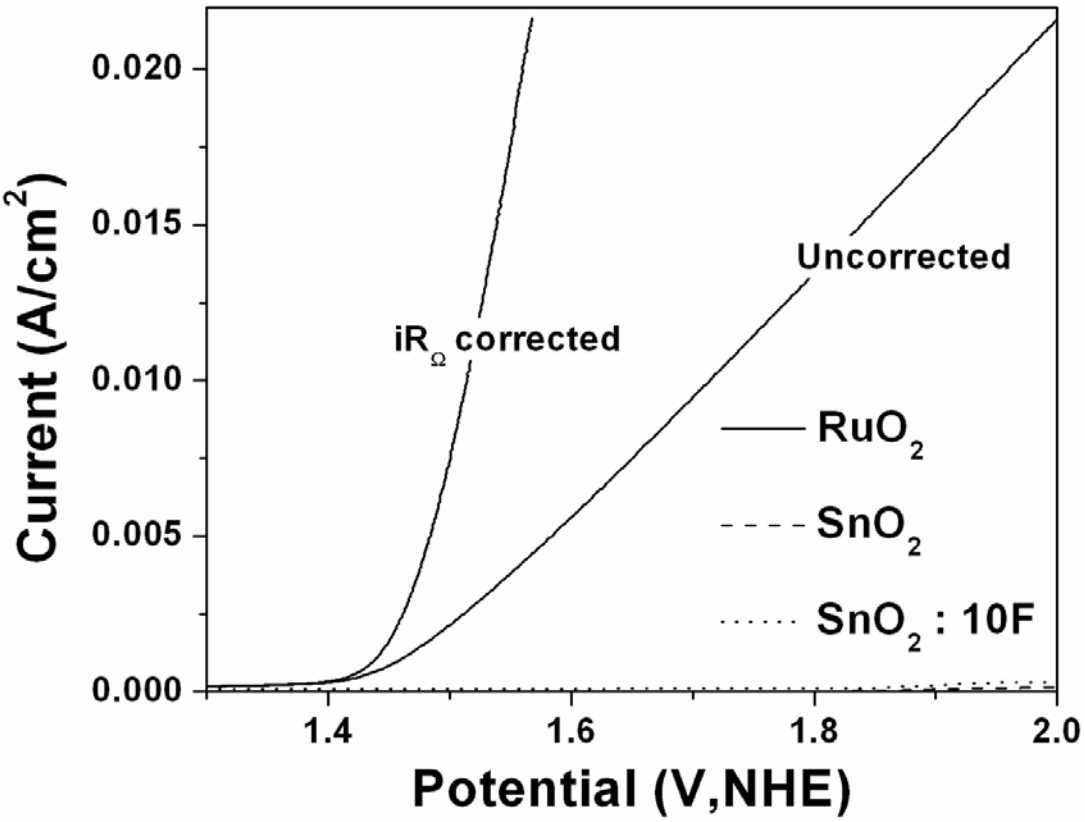

Figure 30. The polarization curve of pure RuO_2, SnO_2 and SnO_2:10F film conducted in the presence of 1 N H_2SO_4 solution at 40°C with a scan rate of 1mV/sec

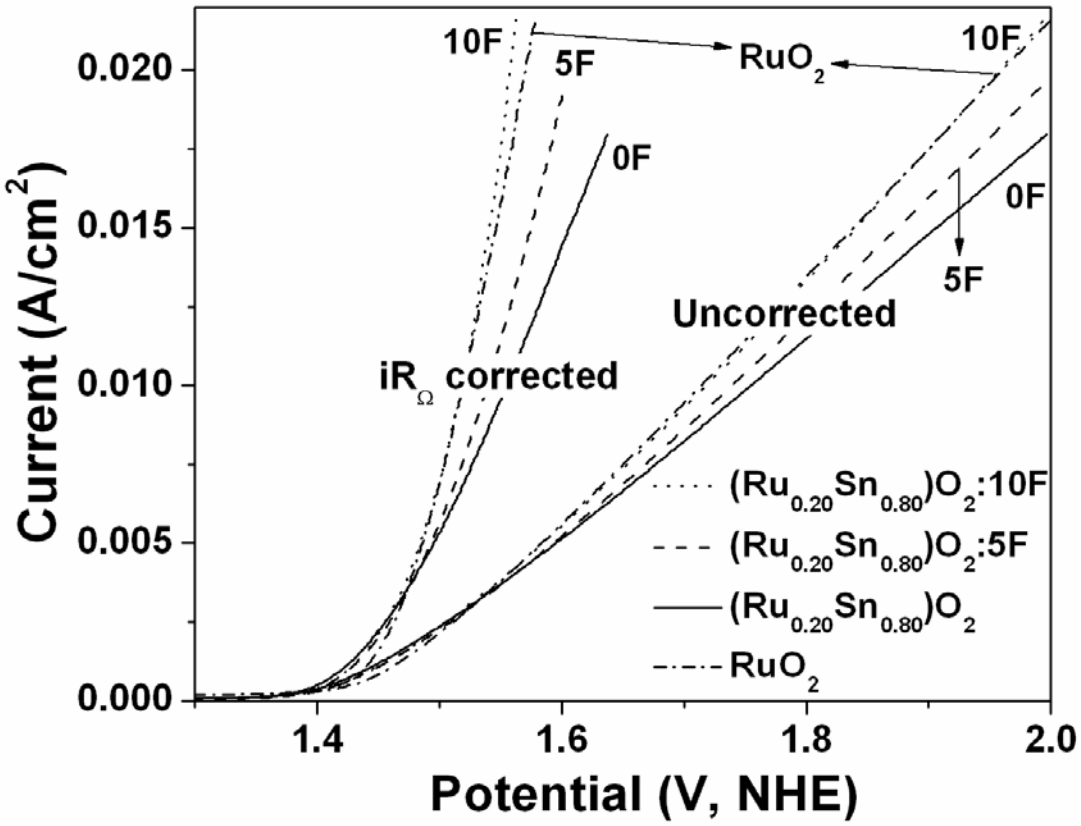

Figure 31. The polarization curve of $(Ru,Sn)O_2$:F film of different F compositions conducted in 1 N H_2SO_4 at 40°C with a scan rate of 1mV/sec before and after iR correction

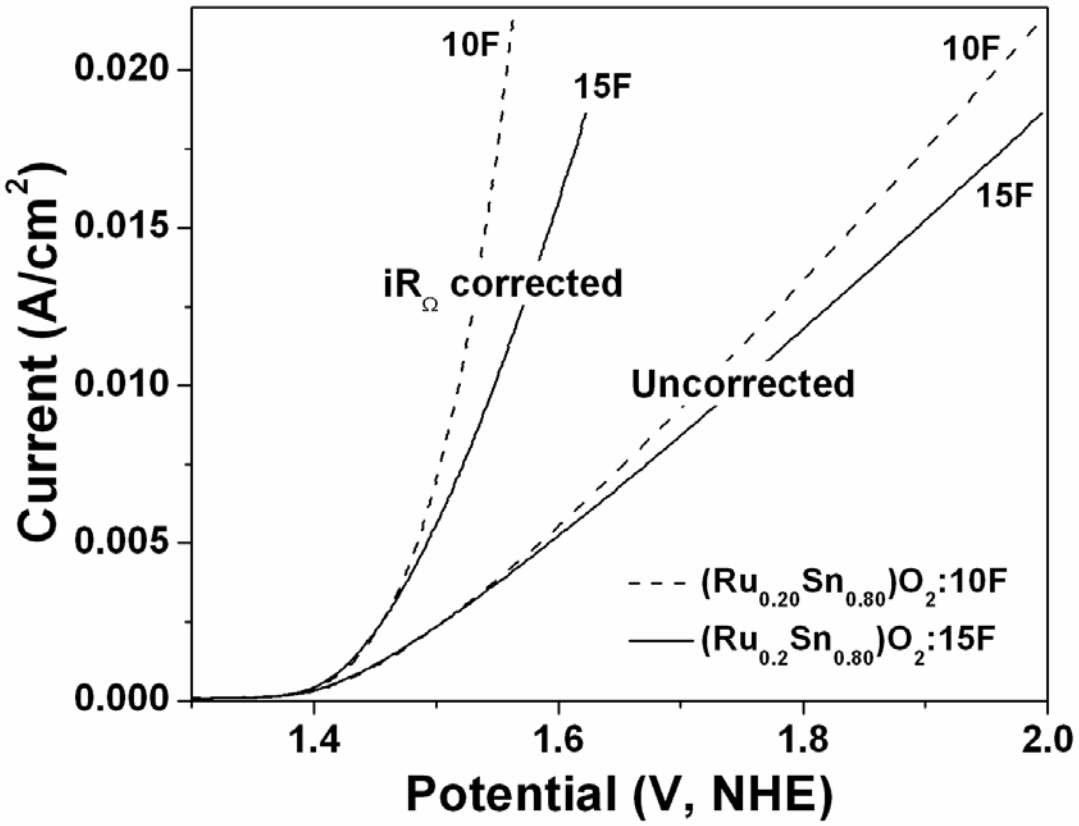

Figure 32. The polarization curve for high F doping of (Ru,Sn)O_2:F film conducted in 1 N H_2SO_4 solution at 40°C before and after iR correction with a scan rate of 1mV/sec

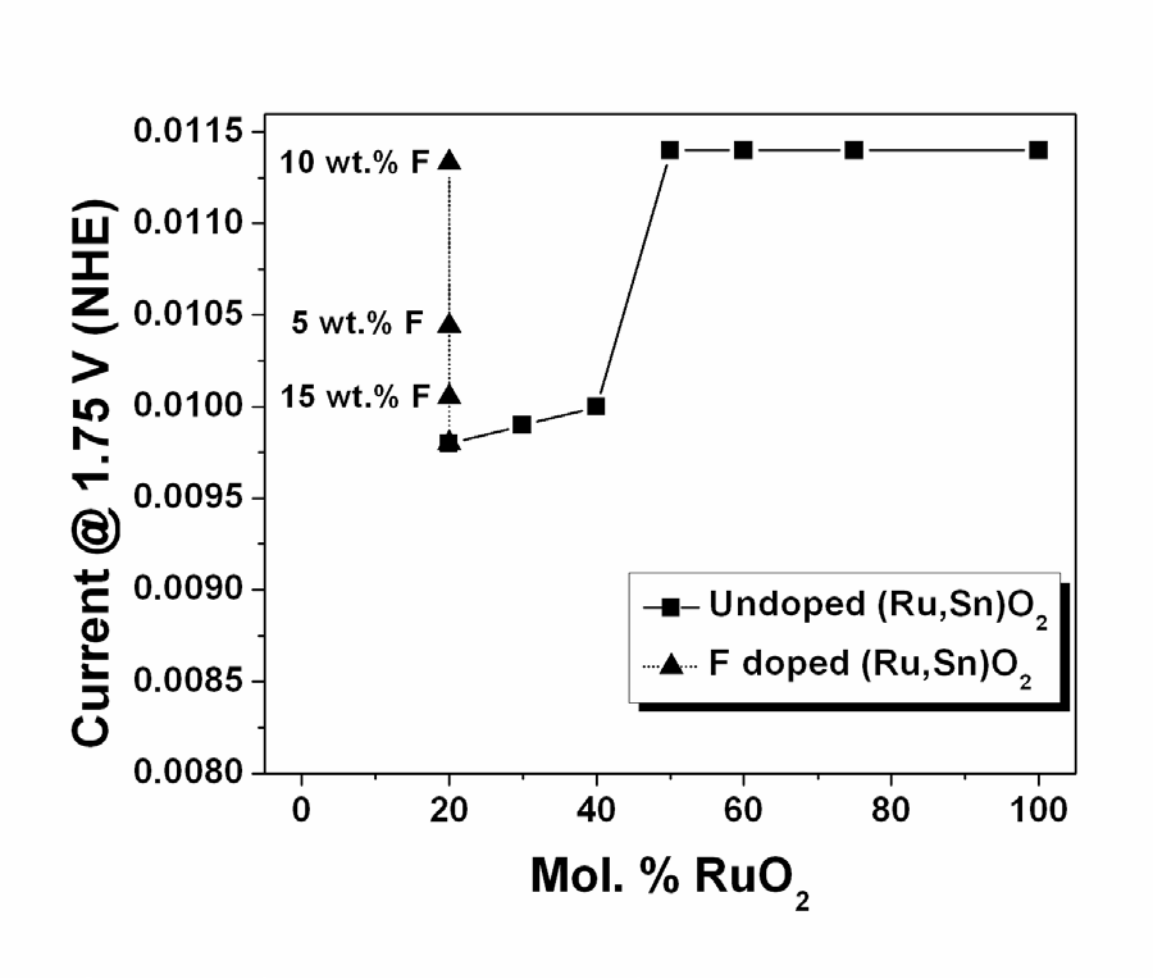

Figure 33. Variation of current density at ~ 1.75V (*vs.* NHE) with compositions of undoped and F doped (Ru,Sn)O_2 anode electro-catalyst

Figure 34, **Figure 35**, **Figure 36** and **Figure 37** shows the Tafel plots of pure RuO_2, (Ru,Sn)O_2, (Ru,Sn)O_2:5 wt.% F, and (Ru,Sn)O_2:10 wt.% F respectively. The Tafel slopes of RuO_2 and $(Ru_{0.2}Sn_{0.8})O_2$:F with 0, 5 and 10 wt.% F calculated from the corresponding iR_Ω corrected Tafel plots, are 77, 76, 67 and 65 mV/decade, respectively. This suggests that the electrochemical activity of (Ru,Sn)O_2:F increases with increase in F with the corresponding decrease in the Tafel slope for increasing F content reaching an optimal value for

$(Ru_{0.2}Sn_{0.8})O_2$:10F thus exhibiting comparable electrochemical activity to that of pure RuO_2. These results therefore clearly suggest that $(Ru,Sn)O_2$:F containing 10wt% F nominal composition is indeed a promising candidate as an OER anode electro-catalyst for PEM based water electrolysis. It should be noted that although the exact amount of F incorporated in the structure cannot be detected using EDAX analysis, it is nevertheless clear that with increasing amount of F there is significant increase in the electrochemical activity reaching an optimal value for the nominal composition of the oxide containing 10 wt.% F.

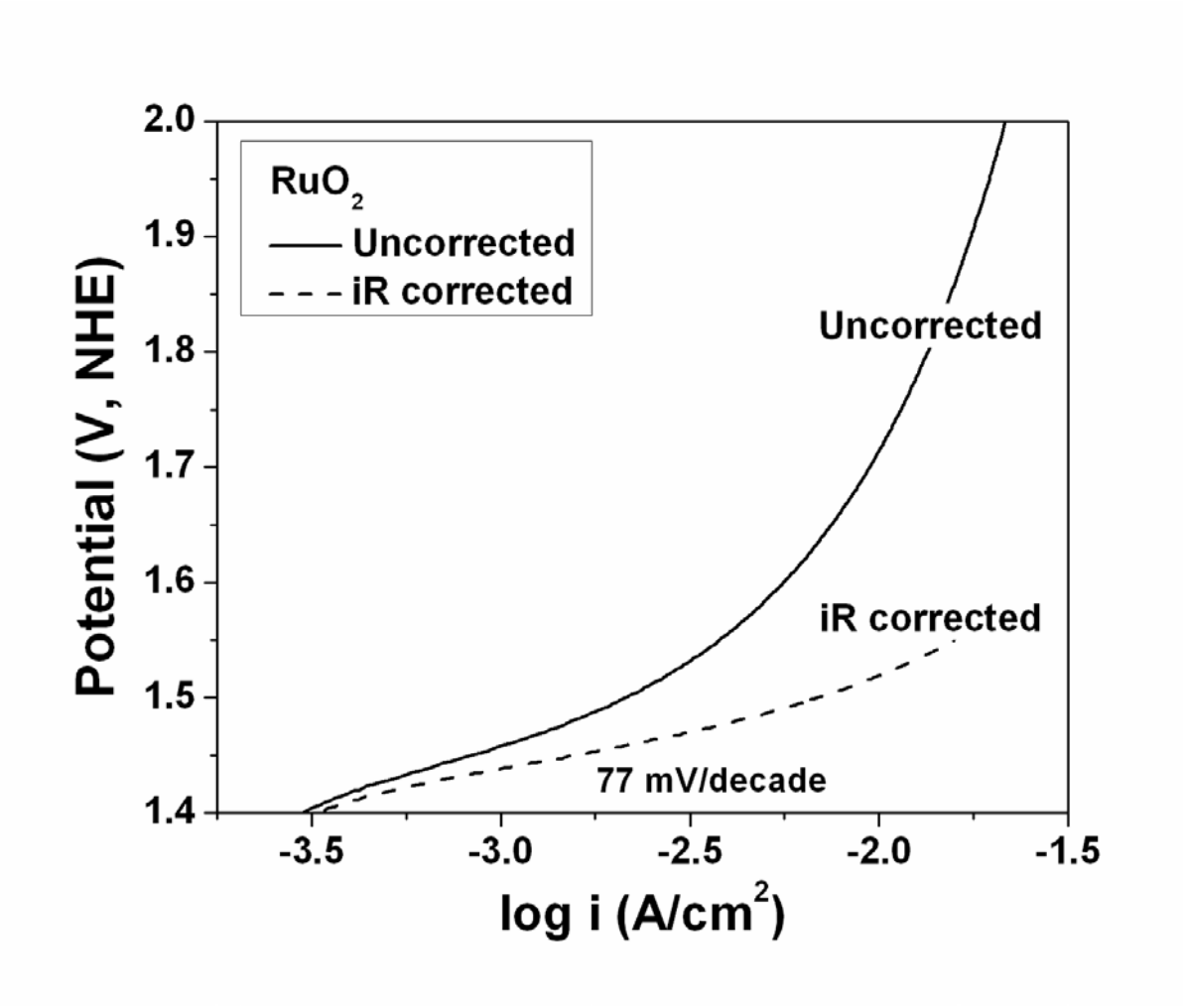

Figure 34. The Tafel plot of pure RuO_2 before and after iR correction

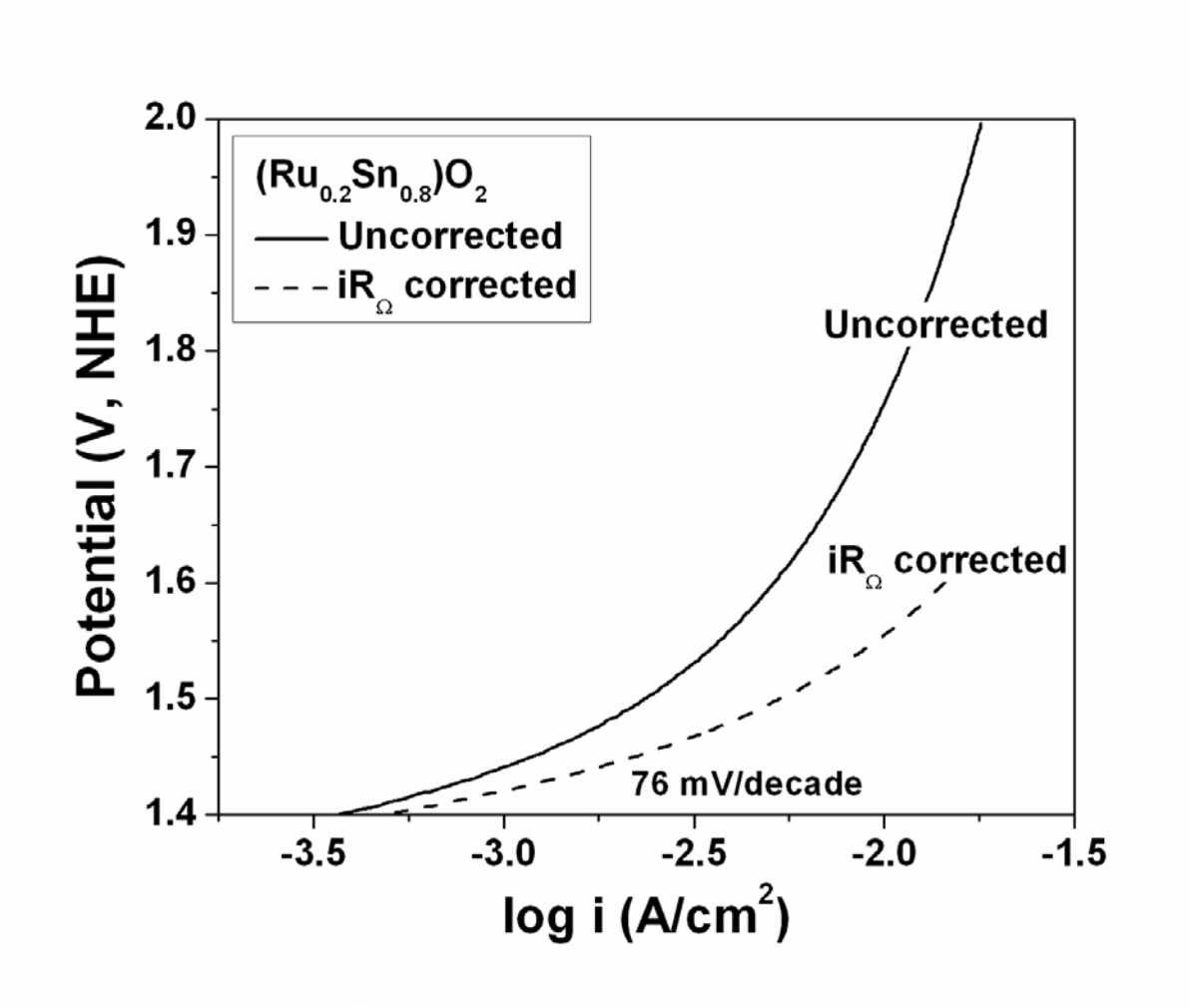

Figure 35. The Tafel plot of $(Ru_{0.2}Sn_{0.8})O_2$ before and after iR correction

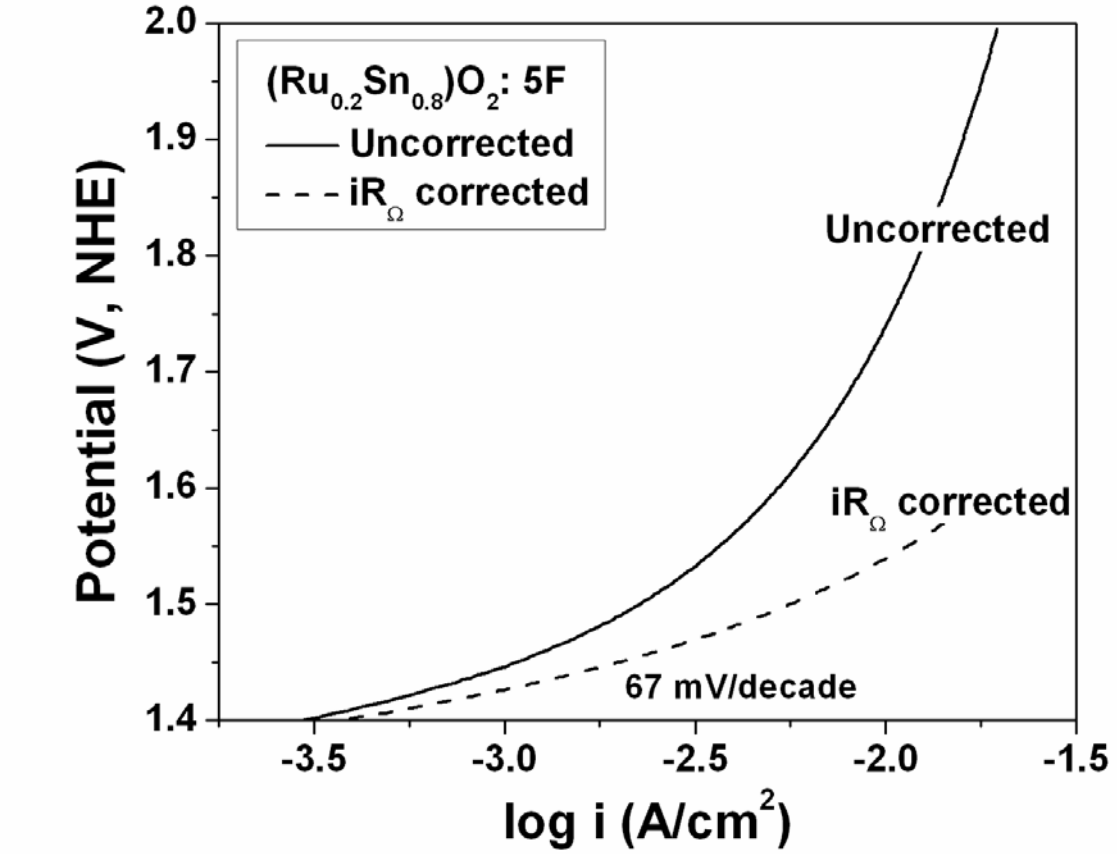

Figure 36. The Tafel plot of $(Ru_{0.2}Sn_{0.8})O_2$:5 wt.% F before and after iR correction

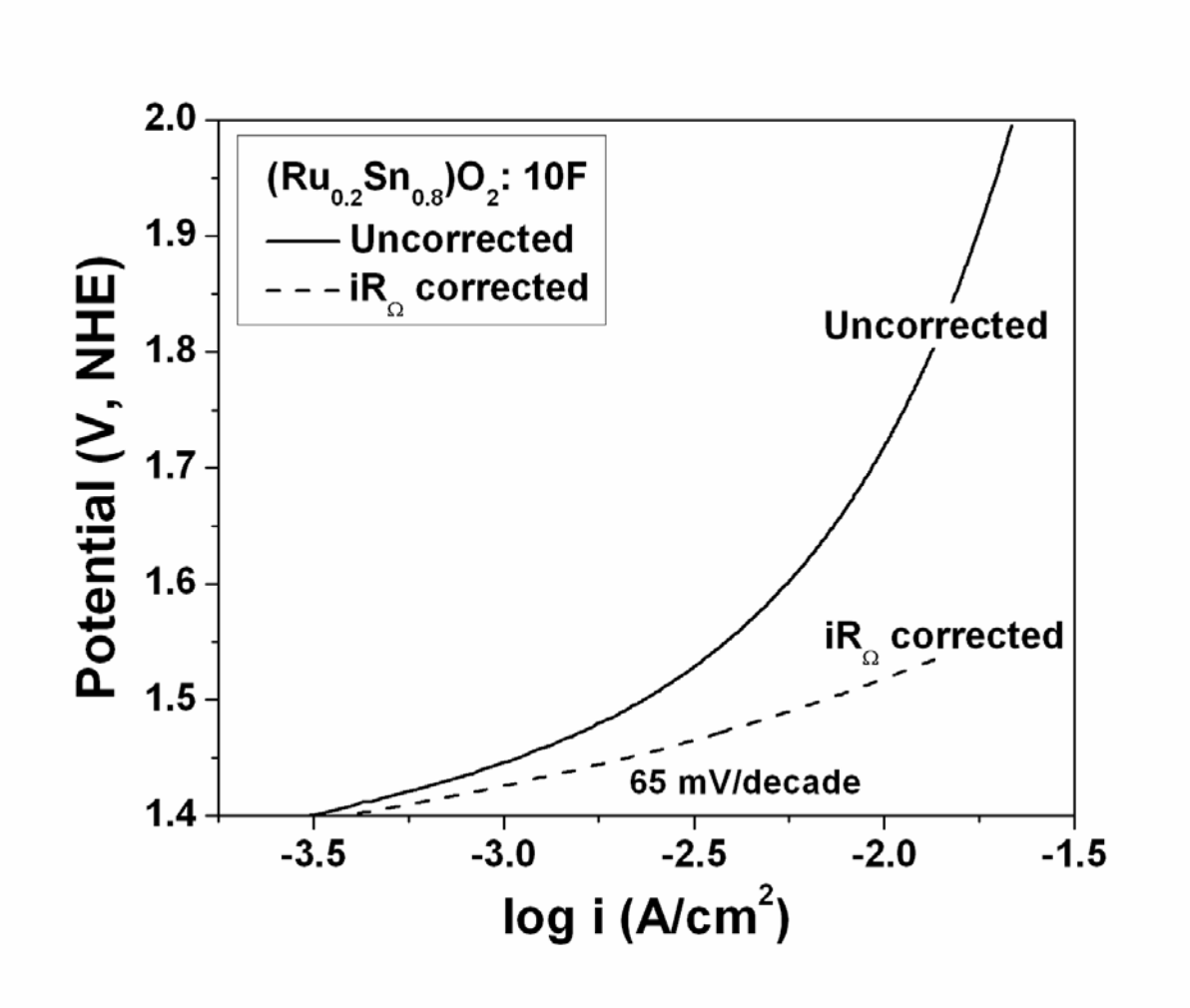

Figure 37. The Tafel plot of $(Ru_{0.2}Sn_{0.8})O_2$:10 wt.% F before and after iR correction

In order to study the electrochemical stability (durability) of the anode electro-catalyst (Ru,Sn)O_2:F in 1 N H_2SO_4 during OER, CA test is conducted for 12 hours at 40°C at a constant voltage of ~ 1.5 V (after iR_Ω correction), a standard accepted potential for estimating electrochemical activity. Hence, this was also selected as the potential for determining the current density for assessing the degradation or loss of activity of the catalyst as a function of time in CA studies. The CA curves, obtained at a ~ 1.5 V, for (Ru,Sn)O_2:F combined with that of pure RuO_2 are shown in **Figure 38**. The CA curve clearly shows a decrease in current (after iR_Ω

correction) with time which may be due to either dissolution of the irregular coating located at the edge of the mud cracks [30], diffusion controlled reaction or evaporation induced loss of electrolyte. A steady decrease in current has been noticed after 2 hours of the initial period for both (Ru,Sn)O_2:10 wt.% F and pure RuO_2 which suggests that ($Ru_{0.2}Sn_{0.8}$)O_2:10F has similar structural stability compared to pure RuO_2.

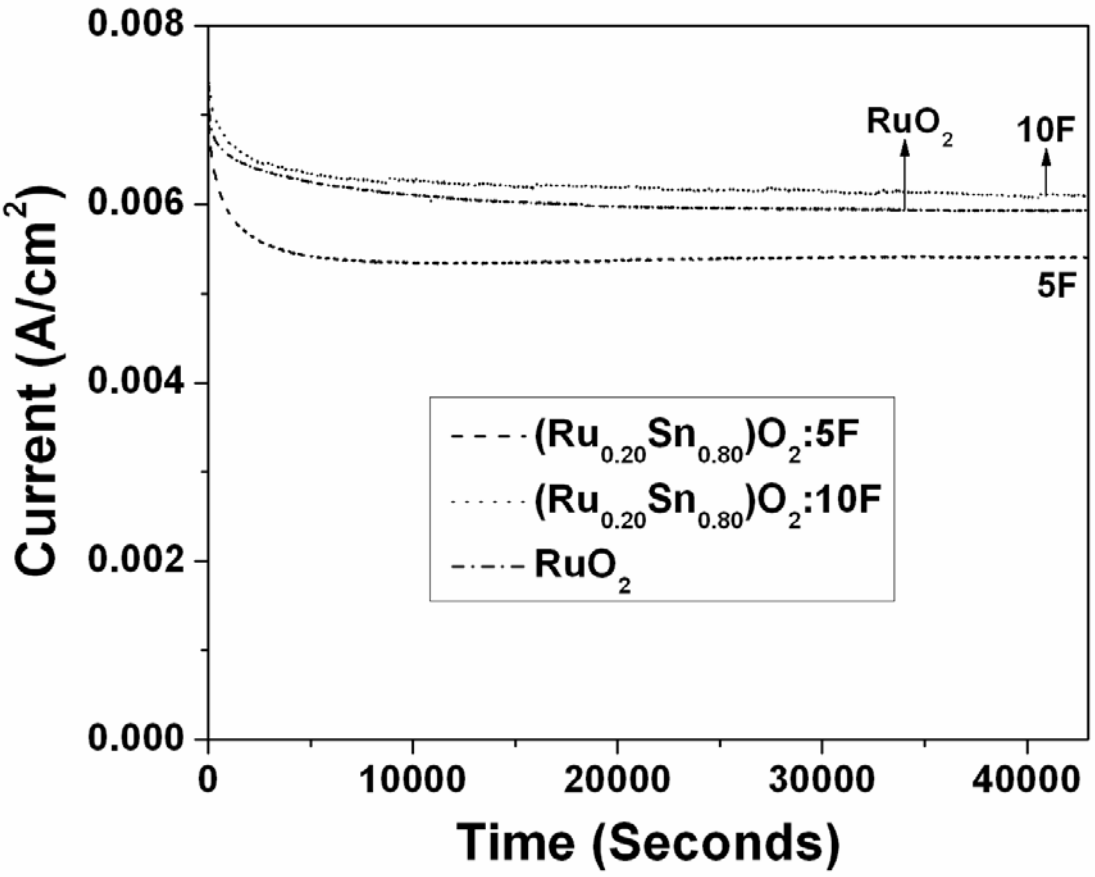

Figure 38. The variation of current *vs.* time in the durability test of pure RuO_2 and (Ru,Sn)O_2:F performed in a 1 N H_2SO_4 solution under ~ 1.5 V at 40°C

However, the ICP analysis conducted on the 1 N H_2SO_4 electrolyte solution collected after 12 hours of CA measurement, shows no presence of Ru up to 10 wt.% F which suggest that the steady decrease in current for RuO_2 and $(Ru_{0.2}Sn_{0.8})O_2$:10F during the CA measurement may arise due to loss of fuel rather than dissolution of the Ru from the electro-catalyst present on the surface of the electrode. However, it has been noticed from ICP analysis that Sn is leached in minute amounts in the solution. $(Ru_{0.2}Sn_{0.8})O_2$:F with 0, 5 and 10 wt.% F solutions after 12 hours of CA have 0.253 ppm, 0.227 ppm and 0.202 ppm of Sn respectively.

After the conclusion of the CA test, the RuO_2 and the $(Ru_{0.2}Sn_{0.8})O_2$:10 wt.% F thin film electrodes were subject to polarization testing as seen in **Figure 39** in order to determine the activity of the electrodes after long term structural stability tests. The Tafel plots from these polarization curves (post CA measurement) after iR correction are shown in **Figure 40** and **Figure 41**. A Tafel slope of ~ 92 mV/decade and ~ 94 mV/decade was obtained for pure RuO_2 thin film and $(Ru,Sn)O_2$:10 wt.% F respectively. This is slightly higher but still close and comparable to the values obtained from the polarization tests conducted before CA (**Figure 34** and **Figure 37**). This test further demonstrates the robustness of the electro-catalysts.

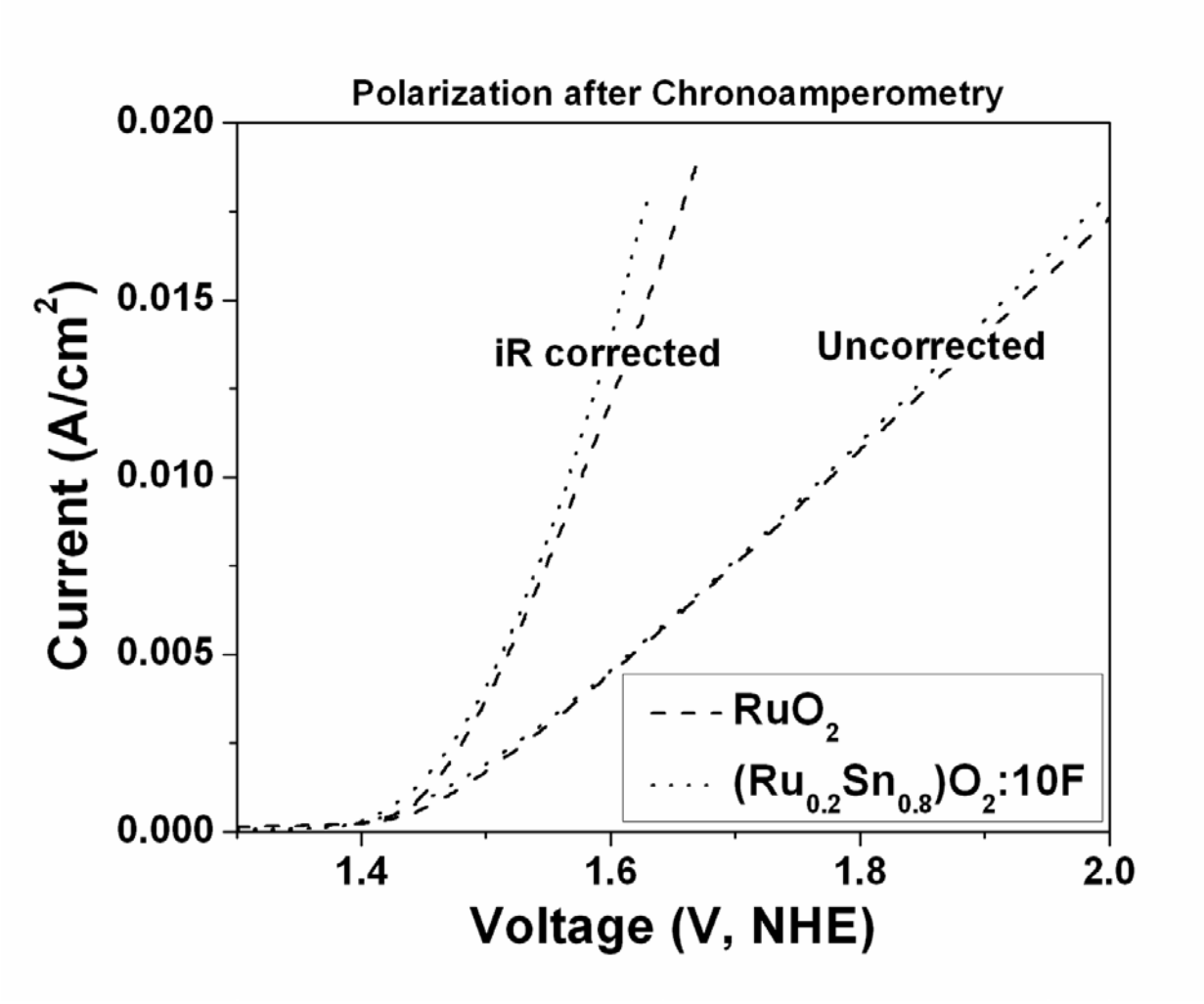

Figure 39. Polarization curve of RuO_2 and (Ru,Sn)O_2:10 wt.% F thin film after the CA test

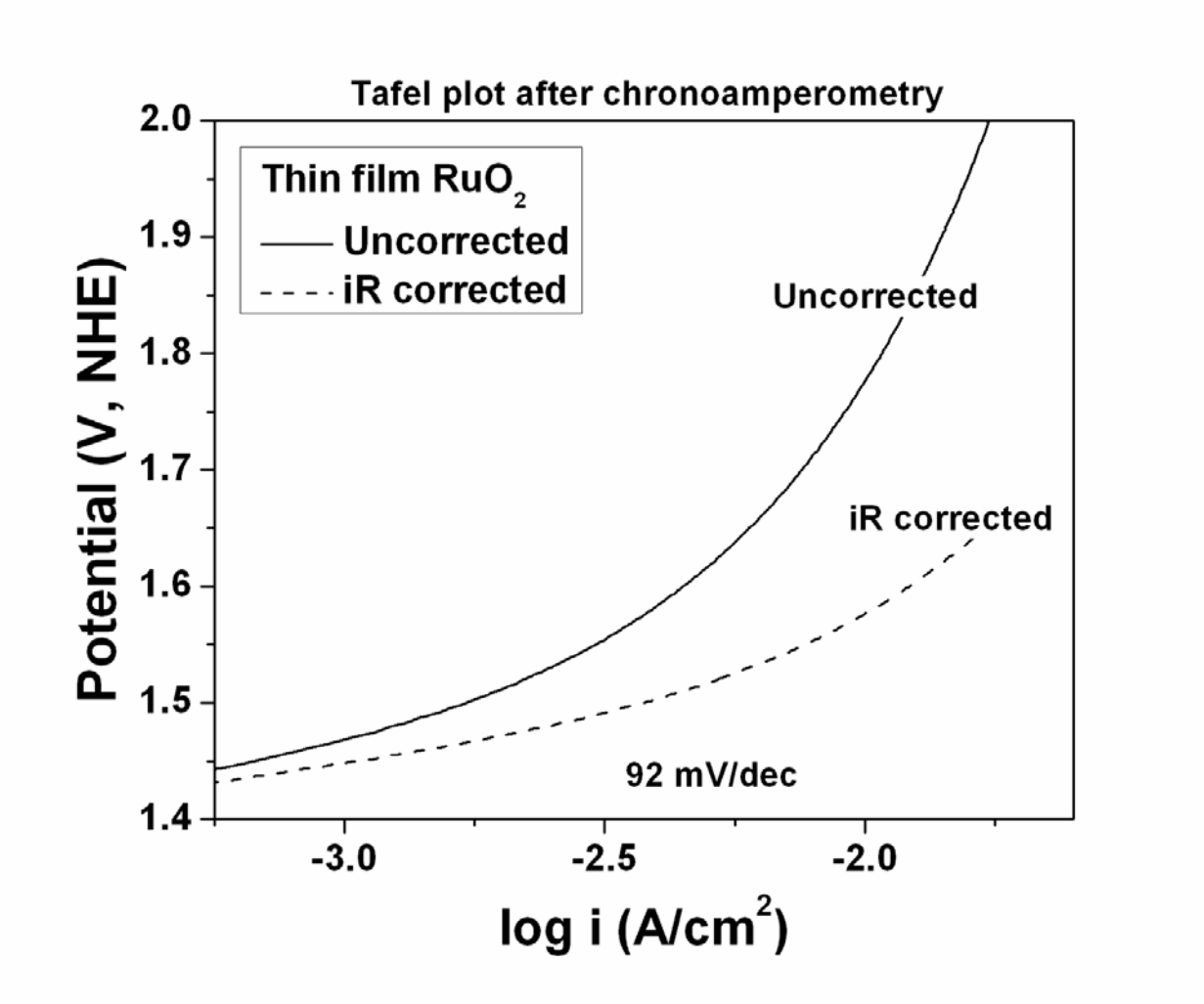

Figure 40. The Tafel plot of RuO_2 thin film after the CA test

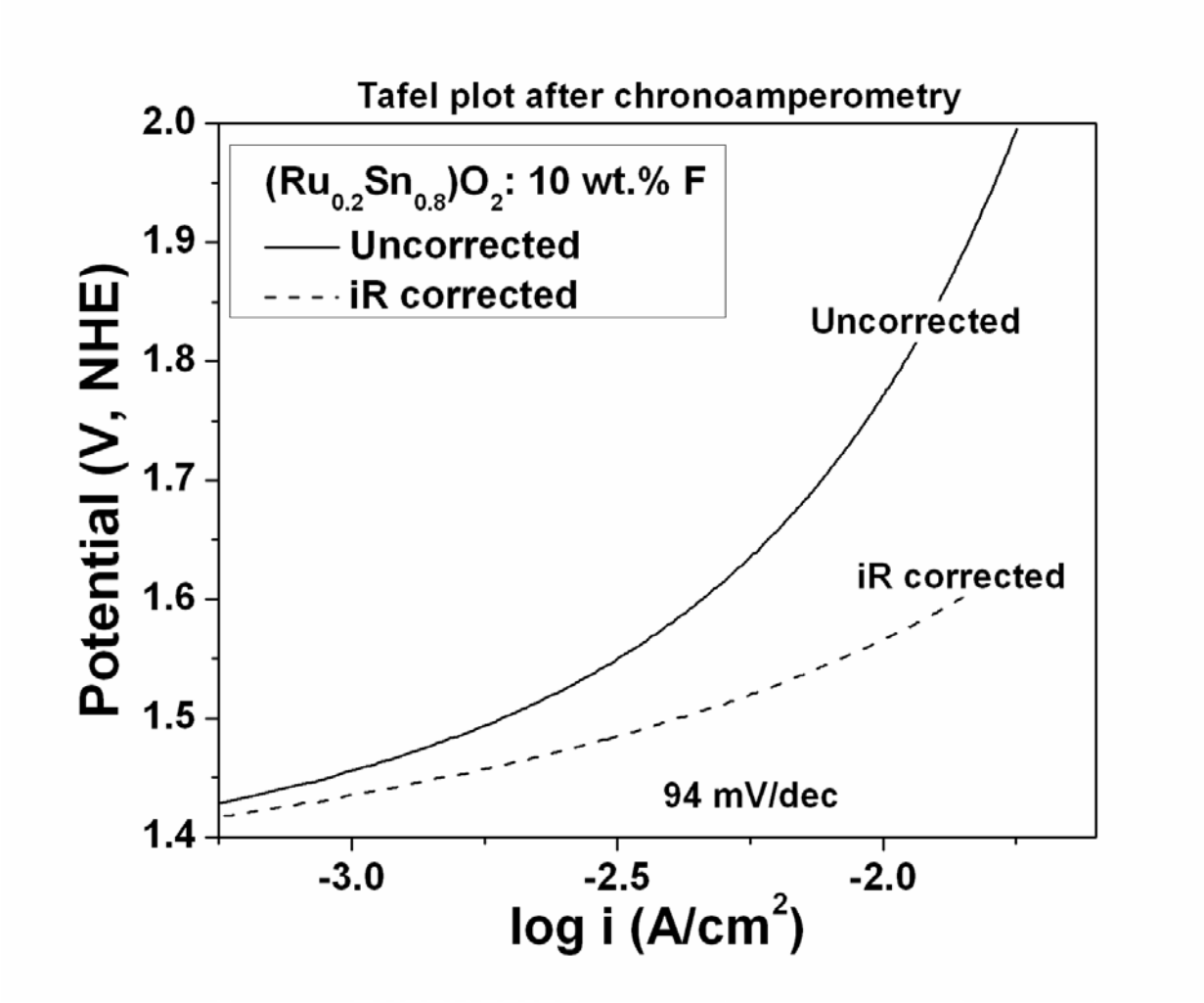

Figure 41. The Tafel plot of (Ru,Sn)O_2:10 wt.% F thin film after the CA test

This experimental study successfully demonstrates that F doped ($Ru_{0.20}Sn_{0.80}$)O_2 is a promising OER electro-catalyst for PEM based water electrolysis. The electrochemical performance including the current density, polarization resistance, Tafel slope and stability / durability at an optimal composition of 10 wt.% F matches that of pure RuO_2. As a result, we conclude that ($Ru_{0.20}Sn_{0.80}$)O_2:10 wt.% F is potentially a preferred oxygen evolution electro-catalyst composition for water electrolysis resulting in ~ 80 % reduction in the noble metal oxide

content. This system and the composition can thus be considered to portend a significant reduction in the overall capital cost of PEM based water electrolyzers.

5.1.4 Ternary (Ir,Sn,Nb)O_2

5.1.4.1 Structural Analysis

Figure 42 shows the XRD patterns of thin film pure IrO_2 and SnO_2 synthesized by thermal decomposition of $IrCl_4$ and $SnCl_2.2H_2O$ ethanol solution, respectively, coated on Ti foil at 400°C for 4 hours. It also shows the XRD patterns of representative composition $(Sn_{0.5}Nb_{0.5})O_2$ synthesized by thermal decomposition of homogeneous mixture $SnCl_2.2H_2O$ and $NbCl_5$ ethanol solution with Sn:Nb molar ratio 1:1 coated on Ti foil at 400°C for 4 hours. The XRD patterns of IrO_2 and SnO_2 show tetragonal structure as expected. The XRD pattern of $(Sn_{0.5}Nb_{0.5})O_2$ also shows tetragonal structure similar to tetragonal SnO_2 structure without any detectable peaks of orthorhombic or monoclinic Nb_2O_5 which suggest Nb_2O_5 forms a solid solution with SnO_2 [$(Sn,Nb)O_2$]. Formation of solid solution of Nb_2O_5 with SnO_2, synthesized by Pechni process, has also been reported in literature [60, 112].

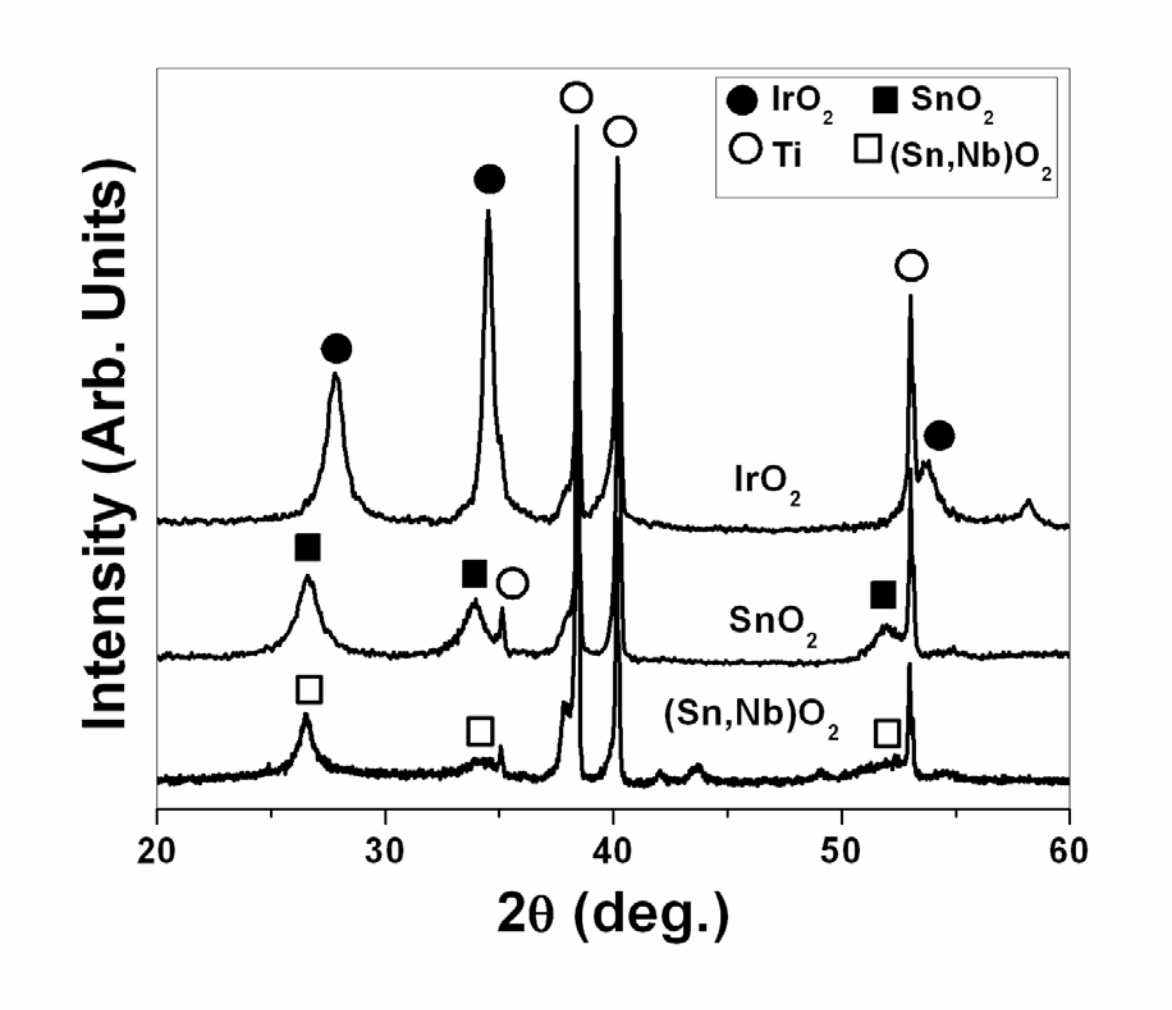

Figure 42. XRD patterns of thin film IrO_2, SnO_2 and $(Sn_{0.50}Nb_{0.50})O_2$ coated on Ti foil

The lattice parameter (nm) as well as molar volumes, calculated using least square refinement techniques, of thin film IrO_2, SnO_2 and $(Sn_{0.5}Nb_{0.5})O_2$ are shown in **Table 3**. The lattice parameter and the molar volume of $(Sn,Nb)O_2$ is very close to pure SnO_2 due to the ionic radius of Sn^{+4} (69 pm) being comparable with Nb^{+4} (68 pm) as well as the molar volume of SnO_2 (21.65 cm^3/mol) and NbO_2 (21.17 cm^3/mol) being close to each other in the bulk state. It also shows the effective crystallite sizes, calculated using Pseudo - Voigt function of single line approximation method, of thin film IrO_2, SnO_2 and $(Sn_{0.5}Nb_{0.5})O_2$. The thin film IrO_2, SnO_2 and

$(Sn_{0.5}Nb_{0.5})O_2$ are nanocrystalline in nature (below 20 nm). It must be mentioned here that the molar volume of nanocrystalline (~14 nm) IrO_2 is higher (~ 2 %) than the corresponding bulk state volume (~ 19.22 cm^3/mol) which suggests that IrO_2 exhibits lattice softening with refinement of crystallite size (CS) as also reported for other systems [113].

Table 3. Lattice parameter, molar volumes and crystallite size of $(Ir,Sn,Nb)O_2$ compositions

Composition	a=b (nm)	c (nm)	V_m (cm^3/mol)	CS (nm)
IrO_2	0.4537	0.3169	19.64	14
SnO_2	0.4736	0.3188	21.53	10
$(Sn_{0.5}Nb_{0.5})O_2$	0.4751	0.3149	21.40	8
$(Ir_{0.75}Sn_{0.125}Nb_{0.125})O_2$	0.4565	0.3414	19.74	8.5
$(Ir_{0.6}Sn_{0.2}Nb_{0.2})O_2$	0.4578	0.3416	19.83	8.4
$(Ir_{0.5}Sn_{0.25}Nb_{0.25})O_2$	0.4589	0.3139	19.90	9
$(Ir_{0.4}Sn_{0.3}Nb_{0.3})O_2$	0.4599	0.3132	19.96	9
$(Ir_{0.3}Sn_{0.35}Nb_{0.35})O_2$	0.4608	0.3131	20.02	3.7
$(Ir_{0.20}Sn_{0.40}Nb_{0.40})O_2$				3.3
$(Ir_{0.15}Sn_{0.425}Nb_{0.425})O_2$				3

On the other hand, the XRD patterns of ternary IrO_2-SnO_2-NbO_2 system of different compositions synthesized by thermal decomposition of homogeneous mixture of $IrCl_4$, $SnCl_2.2H_2O$ and $NbCl_5$ ethanol solution coated on Ti foil are shown in **Figure 43** and **Figure 44**. The XRD patterns of different compositions show the peaks corresponding to tetragonal structure which suggest the formation of complete solid solutions between IrO_2, SnO_2 and NbO_2 [$(Ir,Sn.Nb)O_2$]. Formation of metastable solid solution between IrO_2 and SnO_2 ($Ir_{1-x}Sn_xO_2$) as well as in the other systems such as IrO_2 - SbO_2 - SnO_2 and SnO_2 - IrO_2 - Ta_2O_5 has been reported by other researchers [32, 57, 60, 63, 65]. The lattice parameters and molar volume, calculated using least square refinement techniques, of $(Ir,Sn,Nb)O_2$ of different compositions are tabulated in **Table 3**.

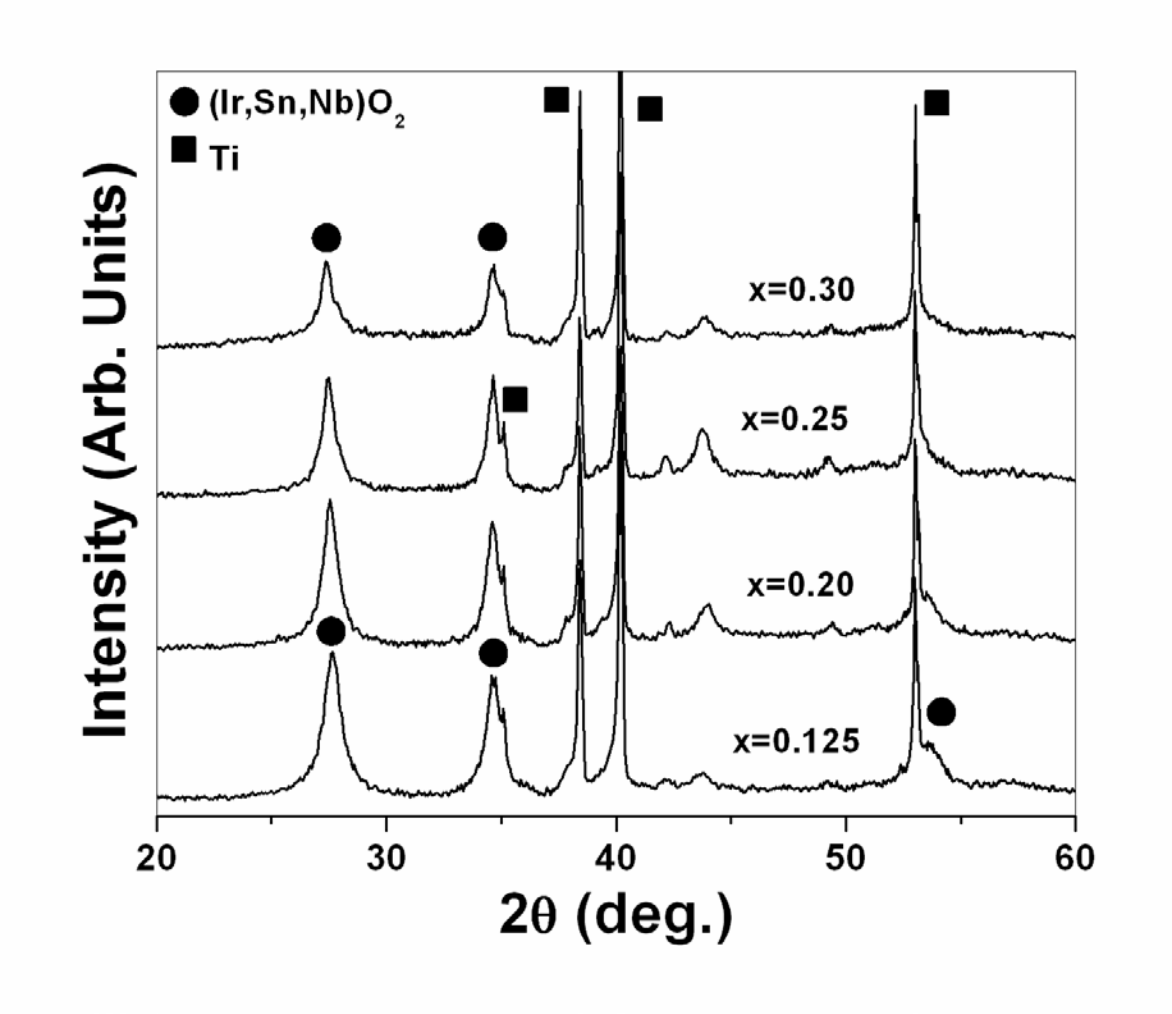

Figure 43. XRD patterns of $(Ir_{1-2x}Sn_xNb_x)O_2$ with x = 0.125, 0.20, 0.25, 0.30 coated on a Ti foil

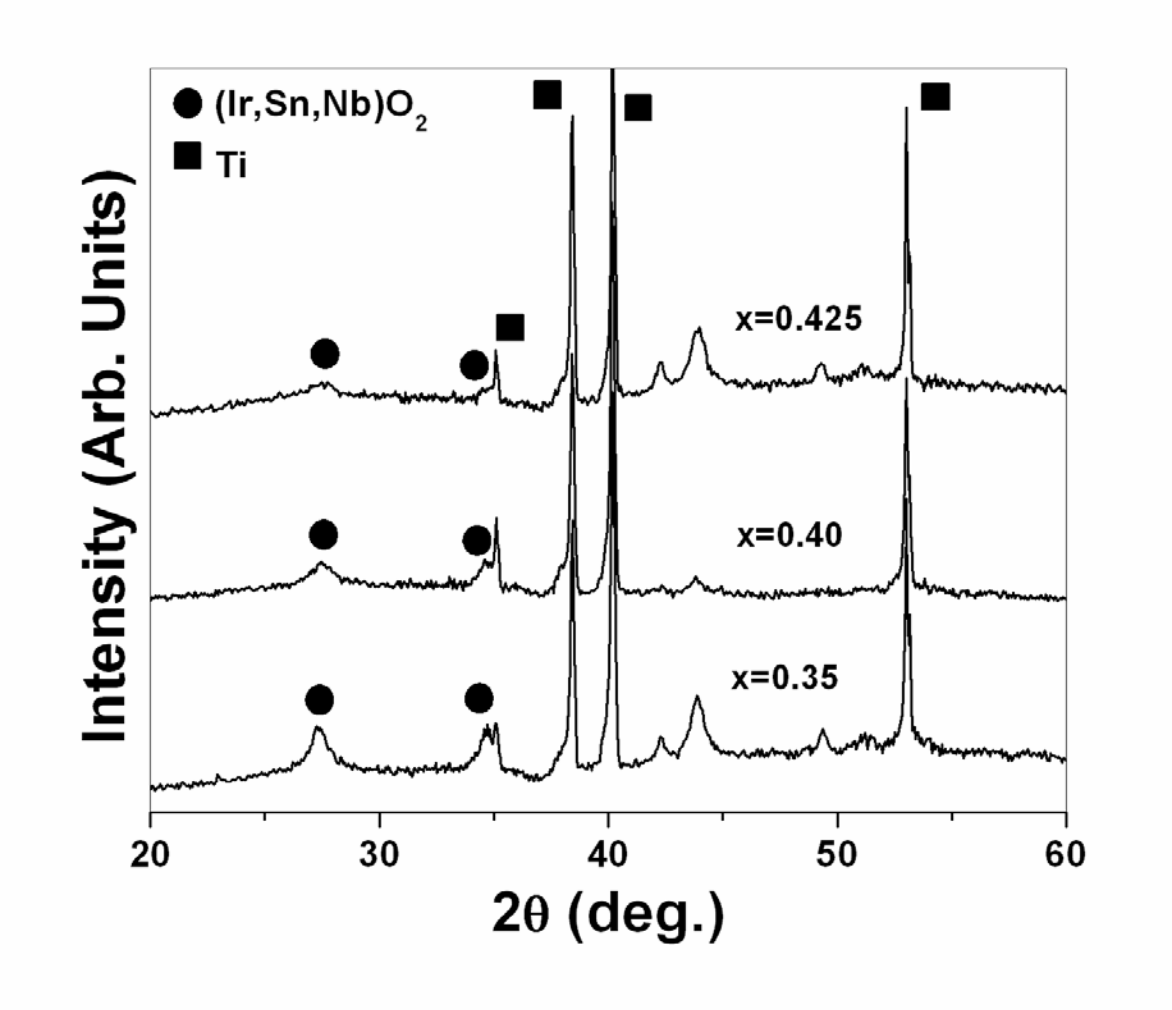

Figure 44. XRD patterns of $(Ir_{1-2x}Sn_xNb_x)O_2$ with x = 0.35, 0.40 and 0.425 coated on Ti foil

The lattice parameter and molar volume of $(Ir_{0.20}Sn_{0.40}Nb_{0.40})O_2$ (x = 0.40) and $(Ir_{0.15}Sn_{0.425}Nb_{0.425})O_2$ (x = 0.425) has not been reported because the XRD peak position not accurately detectable due to low intensity and large broadening of the XRD peaks (**Figure 44**). The crystallite size remains almost same (~ 8 - 9 nm) up to x = 0.30 (40 mol%. IrO_2), with a sudden decrease in crystallite size (~ 3 nm) observed at x = 0.35 (30 mol.% IrO_2). This result clearly suggests that $(Ir,Sn,Nb)O_2$ with higher percentage of $(Sn,Nb)O_2$ exhibit smaller crystallite size than IrO_2 rich composition. De Pauli *et al.* [29, 66] also suggested that high surface charge,

proportional to the active surface concentration, of SnO_2 rich IrO_2+SnO_2 system could arise due to increase in surface area with the addition of SnO_2.

The presence of elemental Ir, Sn and Nb in the (Ir,Sn,Nb)O_2 film of different compositions has been confirmed using energy dispersive X-ray spectroscopy analysis (EDX) attached to the SEM. The SEM image along with EDX of the $(Ir_{1-2x}Sn_xNb_x)O_2$ film of composition x = 0.40 $[(Ir_{0.2}Sn_{0.4}Nb_{0.4})O_2]$ and x = 0.125 $[(Ir_{0.75}Sn_{0.125}Nb_{0.125})O_2]$, shown in **Figure 45** and **Figure 46**, respectively; indicates the presence of "mud-cracked" morphology of (Ir,Sn,Nb)O_2 film coated on the pretreated Ti foil. However, it must be mentioned here that the coating morphology of the (Ir,Sn,Nb)O_2 electro-catalyst, synthesized by thermal decompositions of the homogeneous mixtures of the metal precursors on pretreated Ti foil, is affected by the composition. The coatings obtained with higher IrO_2 concentration (**Figure 46**) appear less cracked compared to lower IrO_2 containing composition (**Figure 45**). The high magnification SEM image of x = 0.125 shows the presence of fine particles in the nanometer range (~ 10 - 15 nm) which is comparable with the calculated crystallite size from the XRD pattern. Quantitative analysis of the elemental composition of (Ir,Sn,Nb)O_2 films obtained by EDX, as presented in **Figure 47** and **Table 4**, shows that the measured elemental contents are close to the nominal composition.

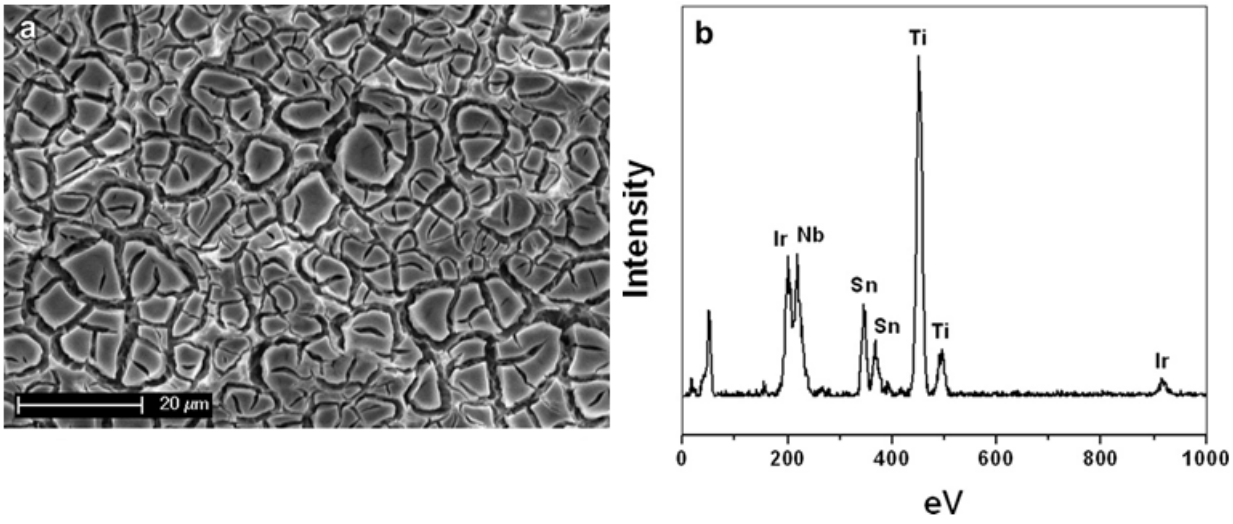

Figure 45. The SEM micrograph (a), and EDAX spectra (b) of $(Ir_{0.2}Sn_{0.4}Nb_{0.4})O_2$ film

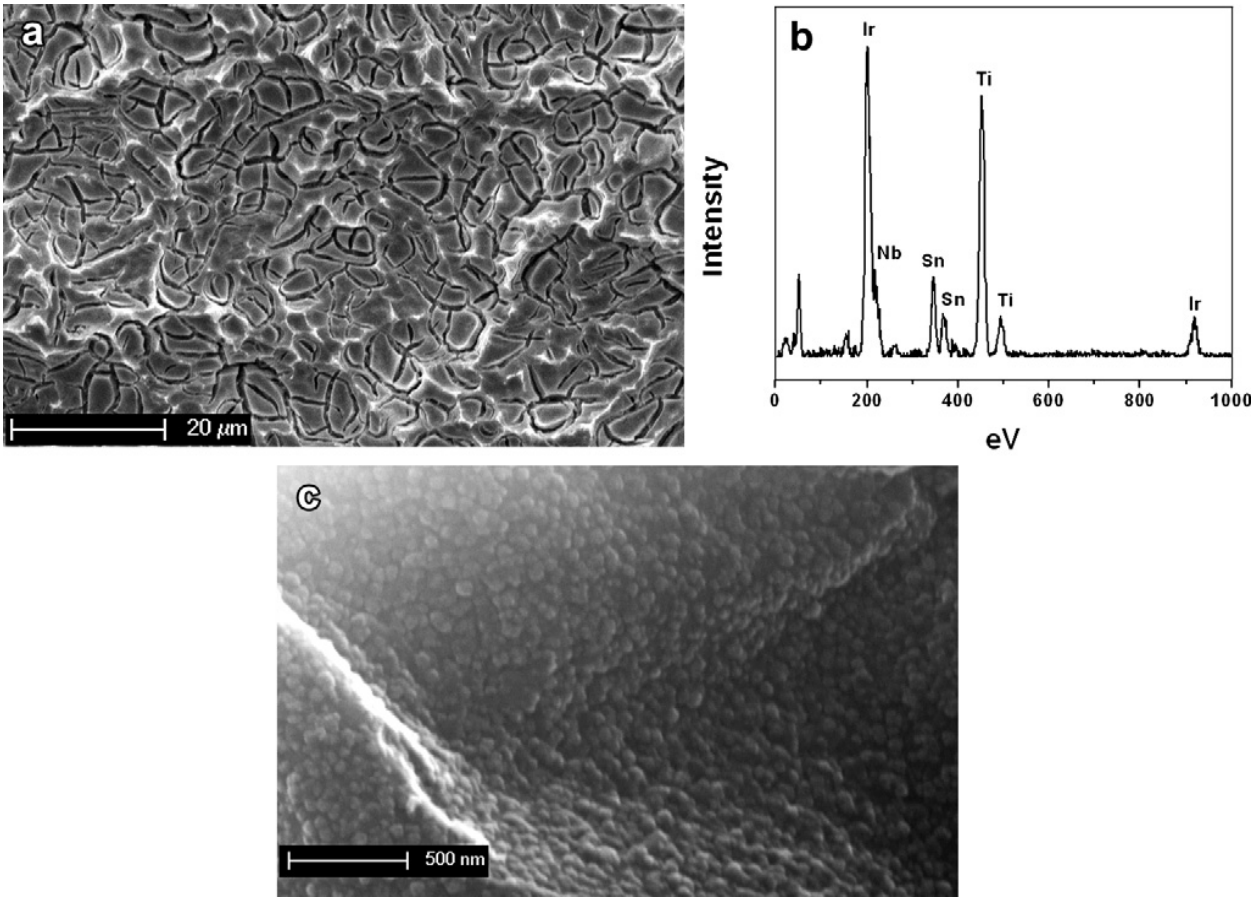

Figure 46. The SEM micrograph (a), EDAX (b), and high magnification SEM image (c) of $(Ir_{0.75}Sn_{0.125}Nb_{0.125})O_2$ film showing the presence of fine nano-particles.

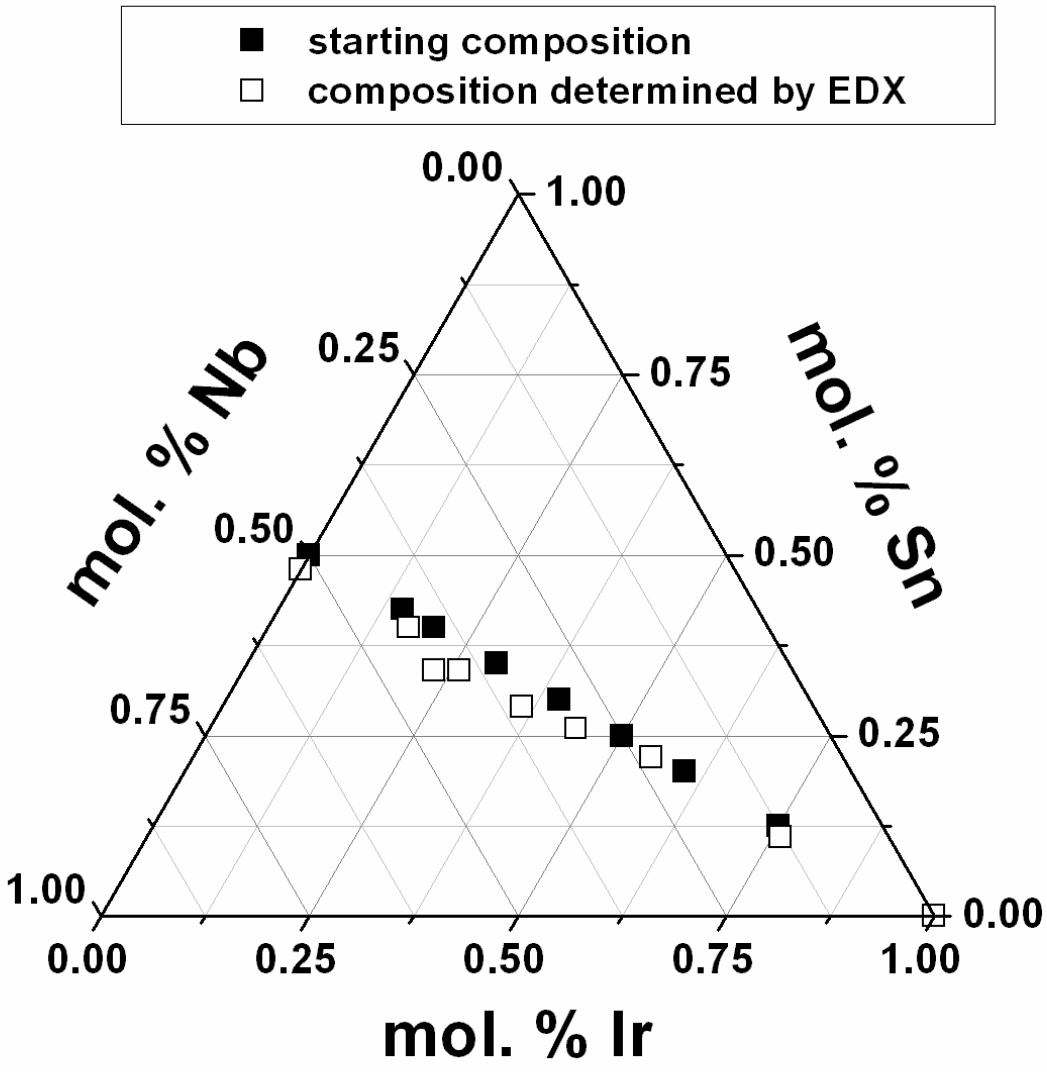

Figure 47. The nominal and EDAX determined molar ratio of (Ir,Sn,Nb)O_2 anode electro-catalyst for PEM based water electrolysis

Table 4. Starting compositions compared to compositions determined by EDX analysis for $(Ir,Sn,Nb)O_2$

Nominal Composition (at. %)			EDX composition (at. %)		
Ir	**Sn**	**Nb**	**Ir**	**Sn**	**Nb**
	50	50		48	52
75	12.5	12.5	76	11	13
60	20	20	55	22	23
50	25	25	44	26	30
40	30	30	36	29	35
30	35	35	26	34	40
20	40	40	23	34	43
15	42.5	42.5	17	40	43

In order to determine the valence state of Ir, Sn, Nb and O in the IrO_2 and SnO_2 as well as ternary $(Ir,Sn,Nb)O_2$ systems, the XPS studies of the thin film have been performed. The XPS spectra of Ir 4f peaks of pure IrO_2 and $(Ir,Sn,Nb)O_2$ thin film of different compositions are shown in **Figure 48**. The XPS spectra of Ir corresponding to pure IrO_2 and $(Ir,Sn,Nb)O_2$ shows the presence of Ir $4f_{5/2}$ and Ir $4f_{7/2}$ doublet. The binding energy of Ir $4f_{5/2}$ and Ir $4f_{7/2}$ of pure IrO_2

and (Ir,Nb,Sn)O_2 is ~ 65.0 eV and ~ 62.0 eV, respectively; and the O1s peak is centered at ~ 530 eV, as shown in **Figure 49** which is consistent with the values of bulk IrO_2. On the other hand, the XPS spectra of Sn corresponding to pure SnO_2 and (Ir,Sn,Nb)O_2 thin film of different compositions is shown in **Figure 50**. The XPS spectra of Sn 3d shows the peak separation of Sn $3d_{5/2}$ and Sn $3d_{3/2}$ for pure SnO_2 as well as (Ir,Sn,Nb)O_2 with a binding energy of ~ 487 eV and ~ 495 eV, respectively; and O1s line centered at ~ 530 eV (**Figure 49**) which is consistent with stoichiometric SnO_2. The XPS spectra of Nb in $(Ir_{1-2x}Sn_xNb_x)O_2$ thin film of compositions x = 0.30 to x = 0.425, shown in **Figure 51**, shows the peak separation of Nb $3d_{5/2}$ and Nb $3d_{3/2}$ with a binding energy of ~ 207 eV and ~ 210 eV, respectively; which corresponds to NbO_x.

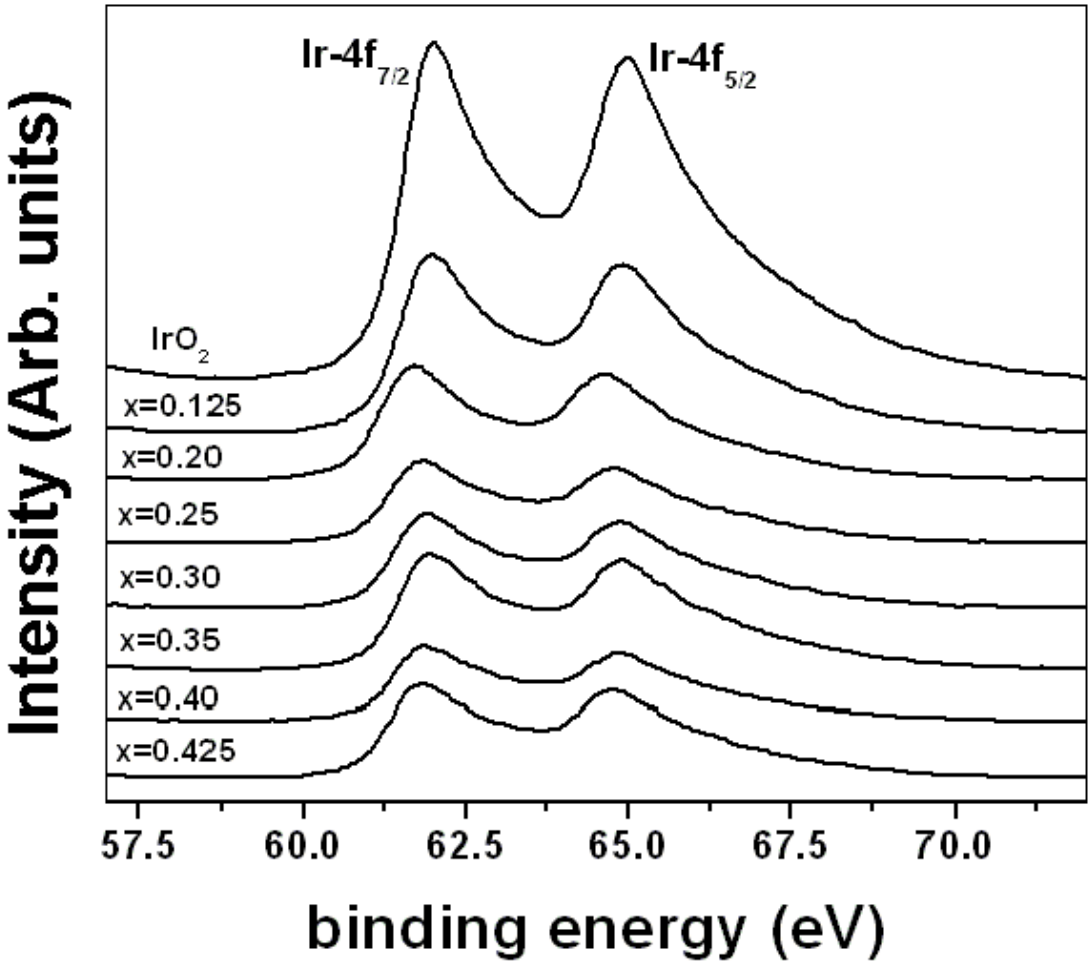

Figure 48. The XPS spectra of Ir $4f_{7/2}$ and $4f_{5/2}$ doublet of pure IrO_2 and $(Ir,Sn,Nb)O_2$ thin film

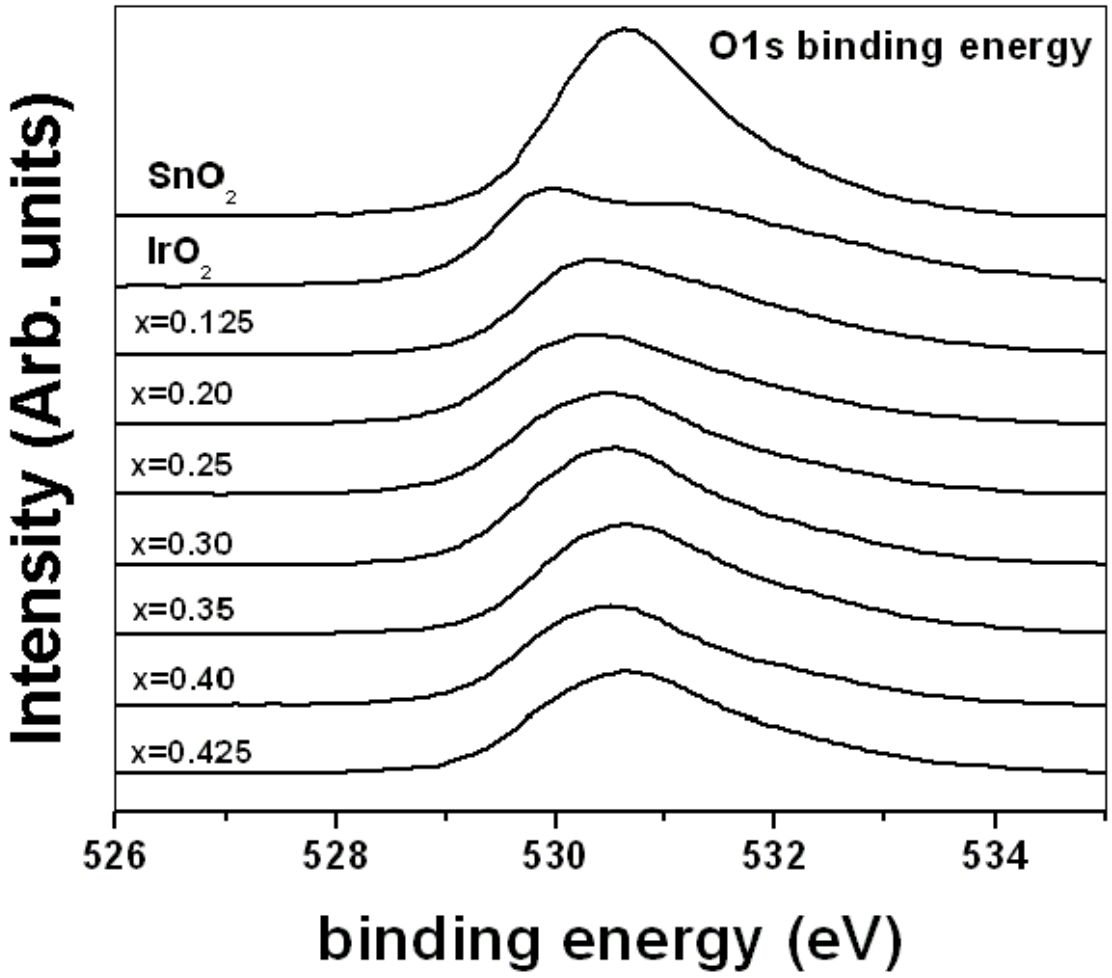

Figure 49. The XPS spectra of O1s of pure IrO_2, SnO_2 and $(Ir,Sn,Nb)O_2$ thin film

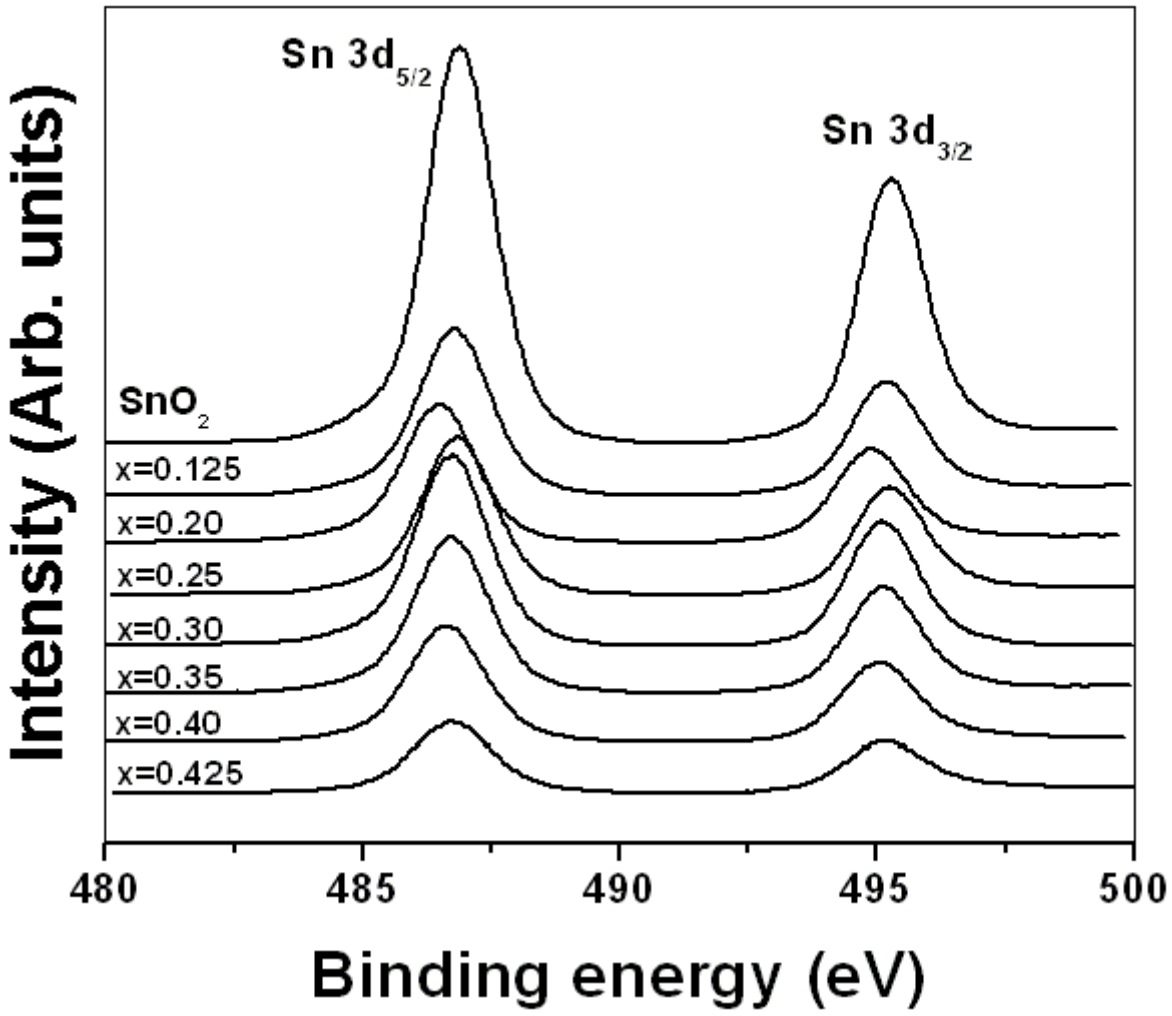

Figure 50. The XPS spectra of Sn $3d_{5/2}$ and Sn $3d_{3/2}$ doublet of pure SnO_2 and $(Ir,Sn,Nb)O_2$ thin film

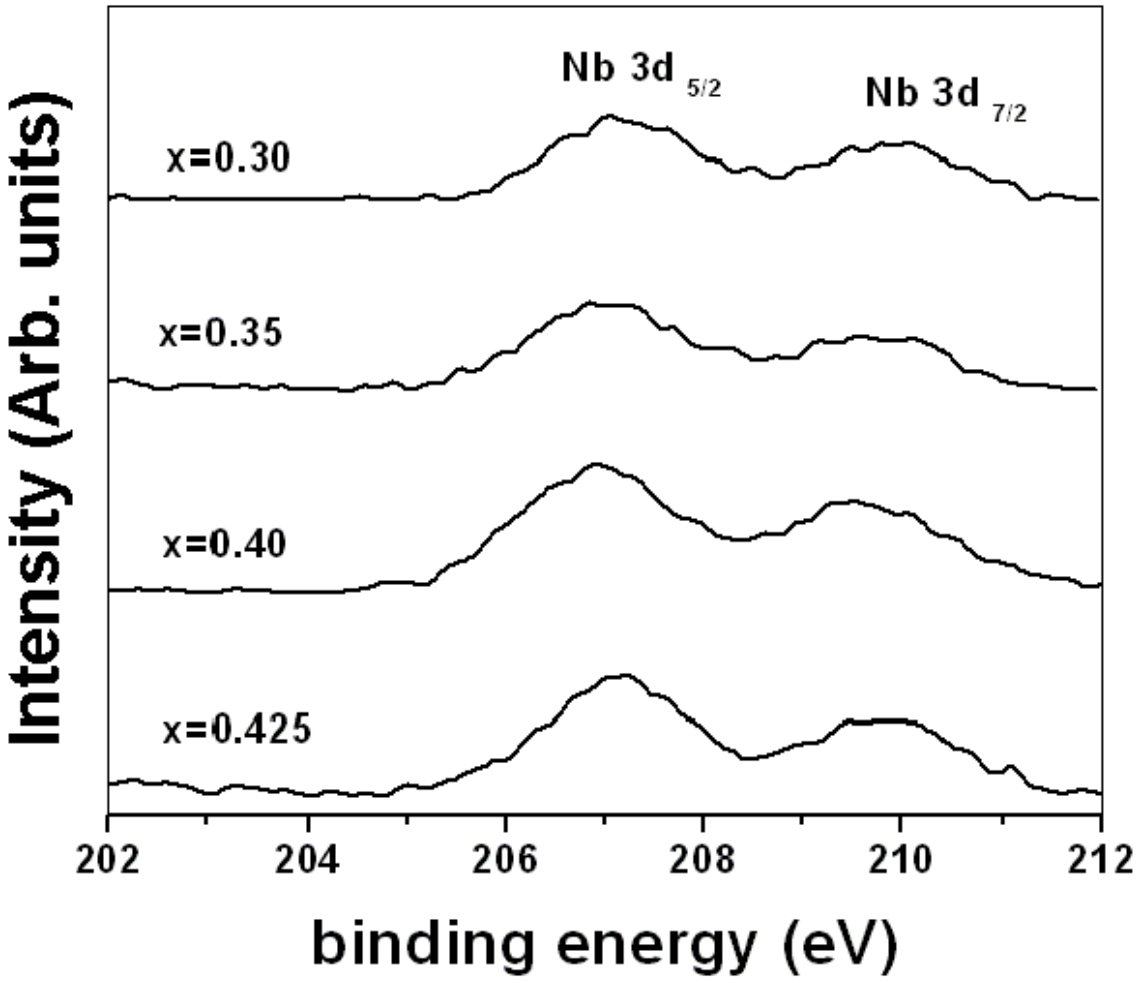

Figure 51. The XPS spectra of Nb $3d_{7/2}$ and Nb $3d_{5/2}$ doublet of $(Ir,Sn,Nb)O_2$ thin films

5.1.4.2 Electrochemical Testing

The electrochemical activity of thin film nanocrystalline IrO_2, $(Sn,Nb)O_2$ and $(Ir,Sn,Nb)O_2$ of different compositions has been studied as suitable oxygen reduction anode electro-catalyst for PEM based water electrolysis. The polarization curve of pure IrO_2 and $(Sn_{0.50}Nb_{0.50})O_2$ film, conducted in the presence of 1 N H_2SO_4 solution at 40°C with a scan rate of 1 mV/sec, is shown

in **Figure 52**. The polarization curve of IrO_2 clearly indicates that water splitting (oxygen evolution reaction) reaction occurring at a potential of ~ 1.43 V *vs.* NHE. The current density at ~ 1.65 V (*vs.* NHE), the typical voltage for determining the electrochemical activity is ~ 0.0094 A/cm^2 with a total loading ~ 0.3 mg/cm^2 of IrO_2. On the other hand, $(Sn,Nb)O_2$ shows no catalytic activity for water electrolysis as expected. In the present study, linear polarization curve and non-linear tafel plot are most often encountered due to large contribution of ohmic resistance (R_Ω) which mainly arises due to solution resistance of the electrolyte (solution resistance, R_s), oxide film electrode resistance (R_e) and accumulation of oxygen bubble covering the electrode surface during water electrolysis at higher current density (bubble resistance, R_{bub}) [51, 52]. **Figure 53** shows the polarization curve of selected $(Ir_{1-2x}Sn_xNb_x)O_2$ samples, before and after ohmic resistance correction ($iR_\Omega = iR_{sol} + iR_e$) without considering R_{bub}. It indicates that water splitting *i.e.* OER occurs at the potential of ~ 1.43 V (*vs.* NHE) irrespective of composition which is identical to that of pure IrO_2.

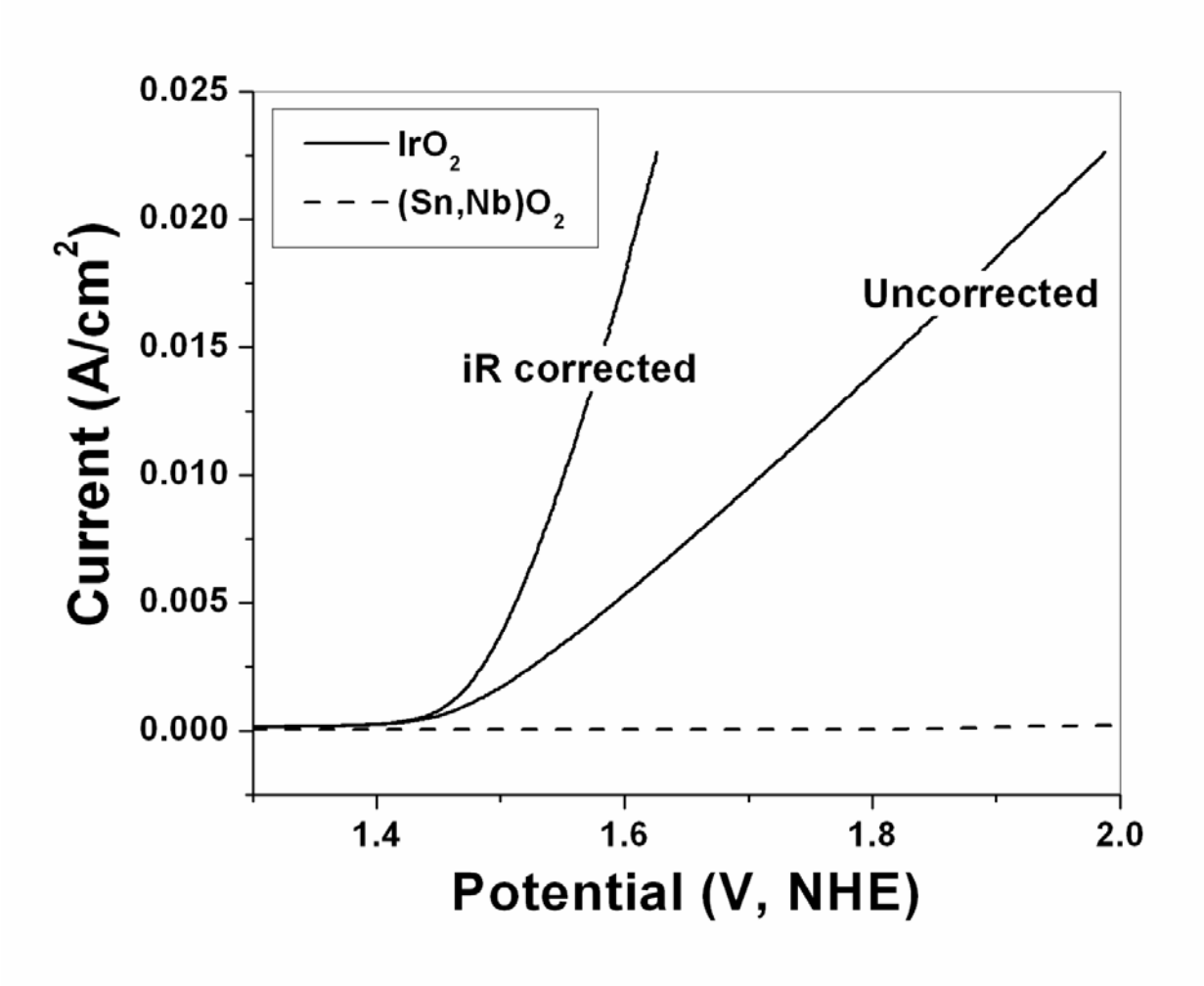

Figure 52. The polarization curve of pure IrO_2 and $(Sn_{0.50}Nb_{0.50})O_2$ film conducted in the presence of 1 N H_2SO_4 solution at 40°C

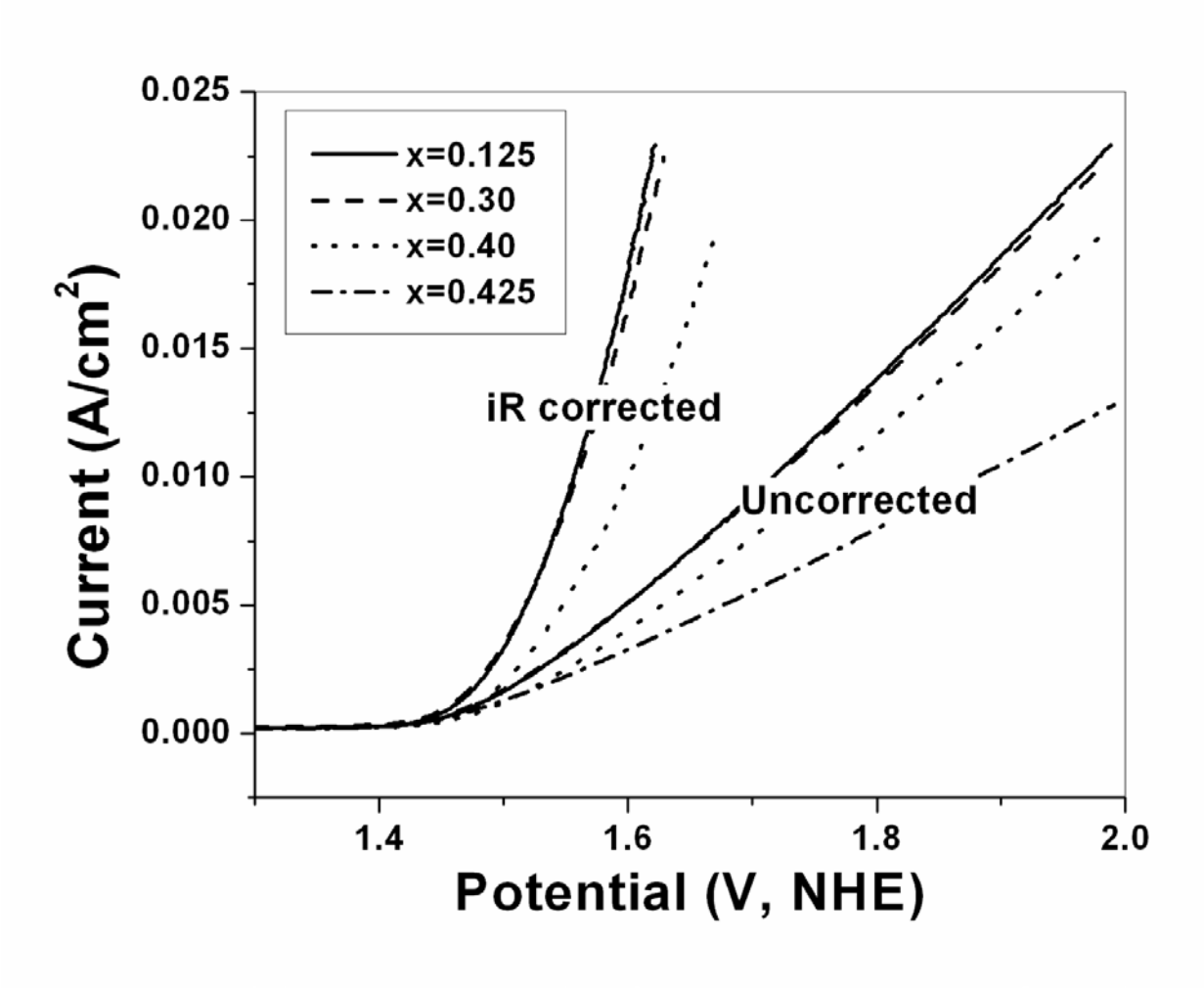

Figure 53. The polarization curve with iR correction of $(Ir_{1-2x}Sn_xNb_x)O_2$ films conducted in the presence of 1 N H_2SO_4 solution at 40°C

The current density at ~ 1.65V (*vs.* NHE) of (Ir,Sn,Nb)O_2 for the different compositions with a total loading ~ 0.3 mg/cm^2 is plotted in **Figure 54**. The current density of $(Ir_{1-2x}Sn_xNb_x)O_2$ up to x = 0.30 (*i.e.* 40 mol.% IrO_2) is ~ 0.0092 ± 0.0002 A/cm^2 which is similar to that of pure IrO_2. The above results clearly suggest that the capital cost *i.e.* the noble metal IrO_2 loading could be reduced by ~ 60 mol.% with the addition of (Sn,Nb)O_2 while still maintaining similar electrochemical activity as that of pure IrO_2. The electrochemical activity however decreases

with further reduction in IrO_2 below 40 mol.% (x = 0.3), which may be due to the lattice predominantly being $(Sn,Nb)O_2$ below 40 mol.% IrO_2; and as a result, the IrO_2 concentration at the surface is depleted with respect to $(Sn,Nb)O_2$. Nevertheless, it should be noted that the electrochemical activity of $(Ir_{0.20}Sn_{0.40}Nb_{0.40})O_2$ is only ~ 20 % lower than that of pure IrO_2 though the noble metal oxide loading is reduced by 80 mol.%.

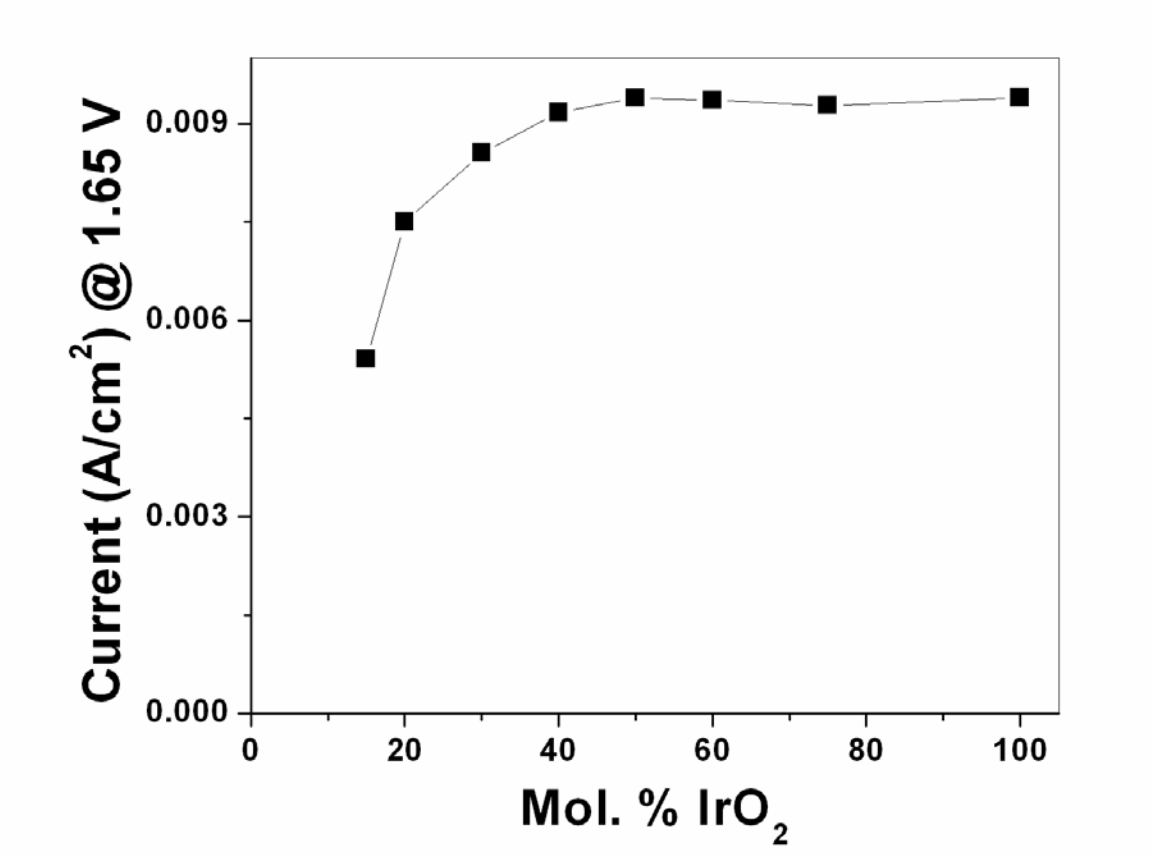

Figure 54. Variation of current density at ~ 1.65V (*vs.* NHE) for various compositions of $(Ir,Sn,Nb)O_2$ thin film electro-catalyst

In order to study the structural stability of anode electro-catalyst $(Ir,Sn,Nb)O_2$ in 1 N H_2SO_4, chronoamperometry (CA) is conducted for 48 hours at 40°C at a constant voltage of ~

1.65 V (*vs.* NHE) without iR correction for select samples. The CA curves, of (Ir,Sn,Nb)O_2 with a composition of ($Ir_{0.4}Sn_{0.3}Nb_{0.3}$)O_2 that displays similar electrochemical activity as pure IrO_2 is plotted along with pure IrO_2, in **Figure 55**. The CA curve shows a marked decay of current (~ 13 % of the initial value) for both electrodes in the initial period of 30 minutes during the oxygen evolution processes which may be due to significant dissolution of irregular coatings located at the edge of the mud cracks [30], or may be due to diffusion controlled reactions. A steady state of current ~ 0.006 A/cm^2 has been achieved after 1 hour of initial period for ($Ir_{0.4}Sn_{0.3}Nb_{0.3}$)O_2, whereas pure IrO_2 shows a continuous drop in current at a constant rate which may which may be due to the continuous loss of active IrO_2 catalyst from the surface.

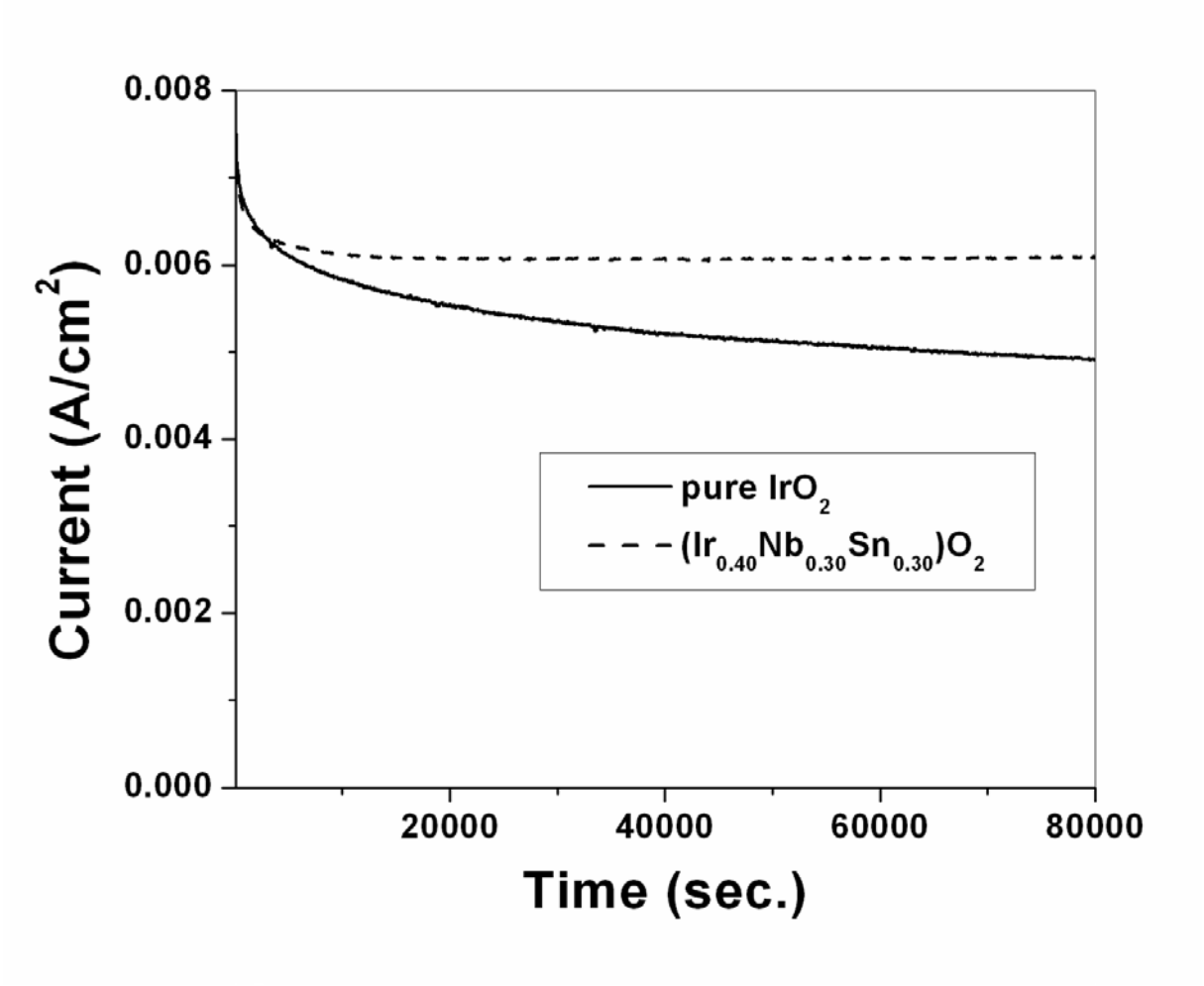

Figure 55. Variation of current *vs.* time in the accelerated life test of pure IrO_2 and $(Ir_{0.4}Sn_{0.3}Nb_{0.3})O_2$ performed in 1 N H_2SO_4 at 40°C at ~ 1.65 V

The ICP results, conducted in the H_2SO_4 electrolyte solution collected after CA measurement, show the presence of ~ 0.44 ppm of Sn, ~ 0.28 ppm of Nb and only ~ 0.14 ppm of Ir for $(Ir_{0.4}Sn_{0.3}Nb_{0.3})O_2$ whereas pure IrO_2 shows ~ 0.35 ppm of Ir which suggests that the incorporation of $(Sn,Nb)O_2$ improves the corrosion rate of IrO_2. The improved corrosion of $(Ir,Nb,Sn)O_2$ electrode compared to that of pure IrO_2 electrodes is primarily attributed to the formation of a solid solution of IrO_2-SnO_2-NbO_2. Since both SnO_2 and NbO_2 are chemically very

stable, the homogenous mixing of IrO_2 with SnO_2 and NbO_2 by forming a solid solution increases the overall chemical stability and decreases the rate of IrO_2 dissolution. This leads to a significant increase in the electrode service life under the operating conditions of PEM based water electrolysis.

After the conclusion of the CA test, the $(Ir_{0.4}Sn_{0.3}Nb_{0.3})O_2$ thin film electrode was subject to polarization testing as seen in **Figure 56** in order to determine the activity of the electrode after the long term structural stability test. The Tafel plot from these polarization curves after iR correction is shown in **Figure 57**. The Tafel slope after the CA test is ~ 84 mV/decade and is comparable to pure IrO_2 (~ 77 mV/decade) as seen in **Figure 23**. This test further demonstrates the robustness of the ternary electro-catalyst.

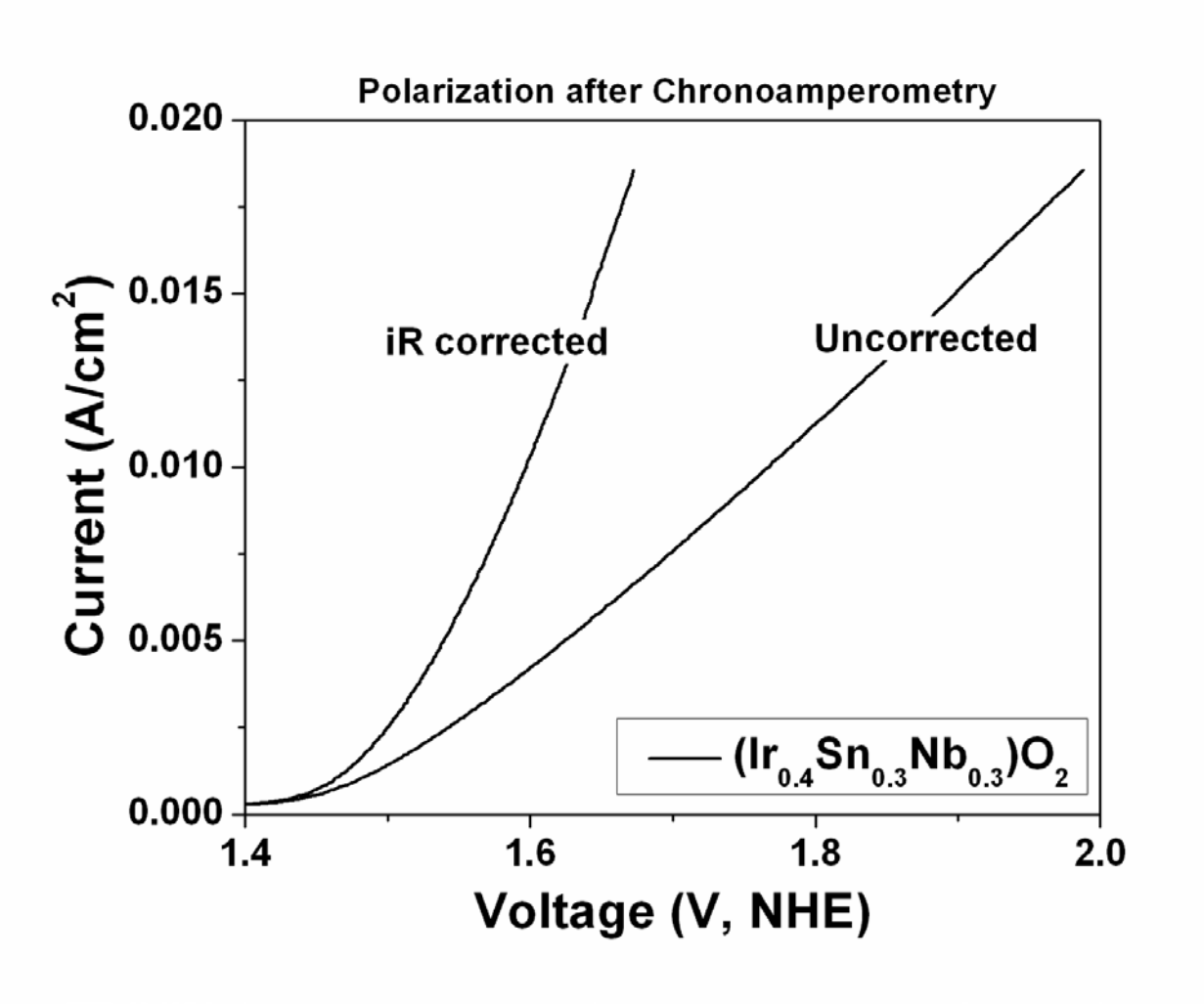

Figure 56. Polarization curve of (Ir,Sn,Nb)O_2 thin film after the CA test

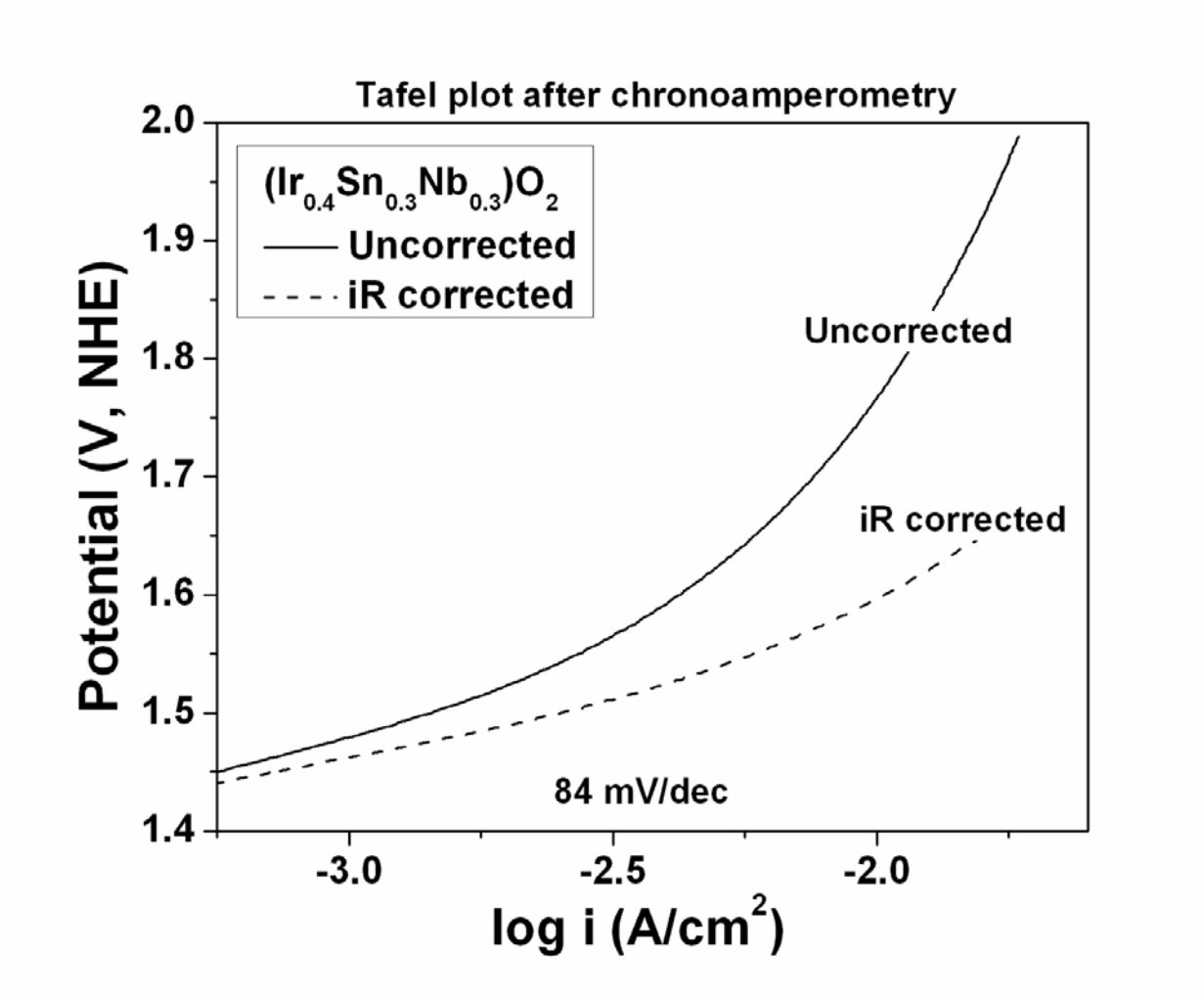

Figure 57. The Tafel plot of (Ir,Sn,Nb)O_2 thin film after the CA test

The present study therefore successfully identifies promising (Sn,Nb)O_2 supports or diluents for IrO_2 anode electro-catalyst with the ability to significantly reduce the noble metal oxide loading with enhanced durability / chemical stability, and without compromising the electro-catalytic performance. The (Ir,Sn,Nb)O_2 anode electro-catalysts are therefore expected to exhibit significant reduction in capital cost of PEM based water electrolyzers.

5.1.5 Ternary F doped (Ir,Sn,Nb)O_2

5.1.5.1 Structural Analysis

The x-ray diffraction (XRD) patterns of thin film (Ir,Sn,Nb)O_2:F synthesized by thermal decomposition of $IrCl_4$, $SnCl_2.2H_2O$, $NbCl_5$ and NH_4F solution coated on the Ti foil and heat treated at 400°C for 4 hours is shown in **Figure 58**. The XRD pattern of (Ir,Sn,Nb)O_2 exhibits a rutile type tetragonal structure similar to pure IrO_2 [24] suggesting the formation of complete solid solution between IrO_2, SnO_2 and NbO_2. No additional peaks are seen other than rutile IrO_2 which concludes there is no undesirable phase formation. Formation of solid solution of Nb_2O_5 with SnO_2, synthesized by the Pechni process, has also been reported [112]. The lattice parameter of (Sn,Nb)O_2 is comparable to pure SnO_2 since the ionic radius of Sn^{+4} (69 pm) is very close to that of Nb^{+4} (68 pm). Also, the molar volume of tin and niobium dioxides are ~ 21.65 and ~ 21.17 cm^3/mol respectively. In order to improve the electronic conductivity of (Ir,Sn,Nb)O_2, fluorine is incorporated in the structure to replace oxygen at nominal compositions of 5, 10, 15 and 20 wt.% F, as outlined in the **Section 4.1.5**. The XRD patterns showing the (Ir,Sn,Nb)O_2:F solid solution for up to 15 wt.% F compositions, confirms the retention of the tetragonal rutile structure similar to the parent (Ir,Sn,Nb)O_2 [24, 34, 57, 59]. The lattice parameter (a ~ 0.46 nm, c ~ 0.31 nm) and molar volume of (Ir,Sn,Nb)O_2:x wt.% F (~ 20 cm^3/mol), calculated using least square refinement technique, is similar to pure IrO_2 (~19.7 cm^3/mol). This clearly indicates no effect of F^- substitution for O^{2-} on the molar volume of (Ir,Sn,Nb)O_2:F. It should be noted that this might be due to the ionic radius of O^{2-} and F^- being similar (125 pm and 120 pm, respectively) [114]. The effective crystallite size of (Ir,Sn,Nb)O_2:F,

calculated using the Scherrer formula, is ~ 4 - 6 nm irrespective of the amount of fluorine doping. This elucidates the nanocrystallinity of all the synthesized electro-catalysts.

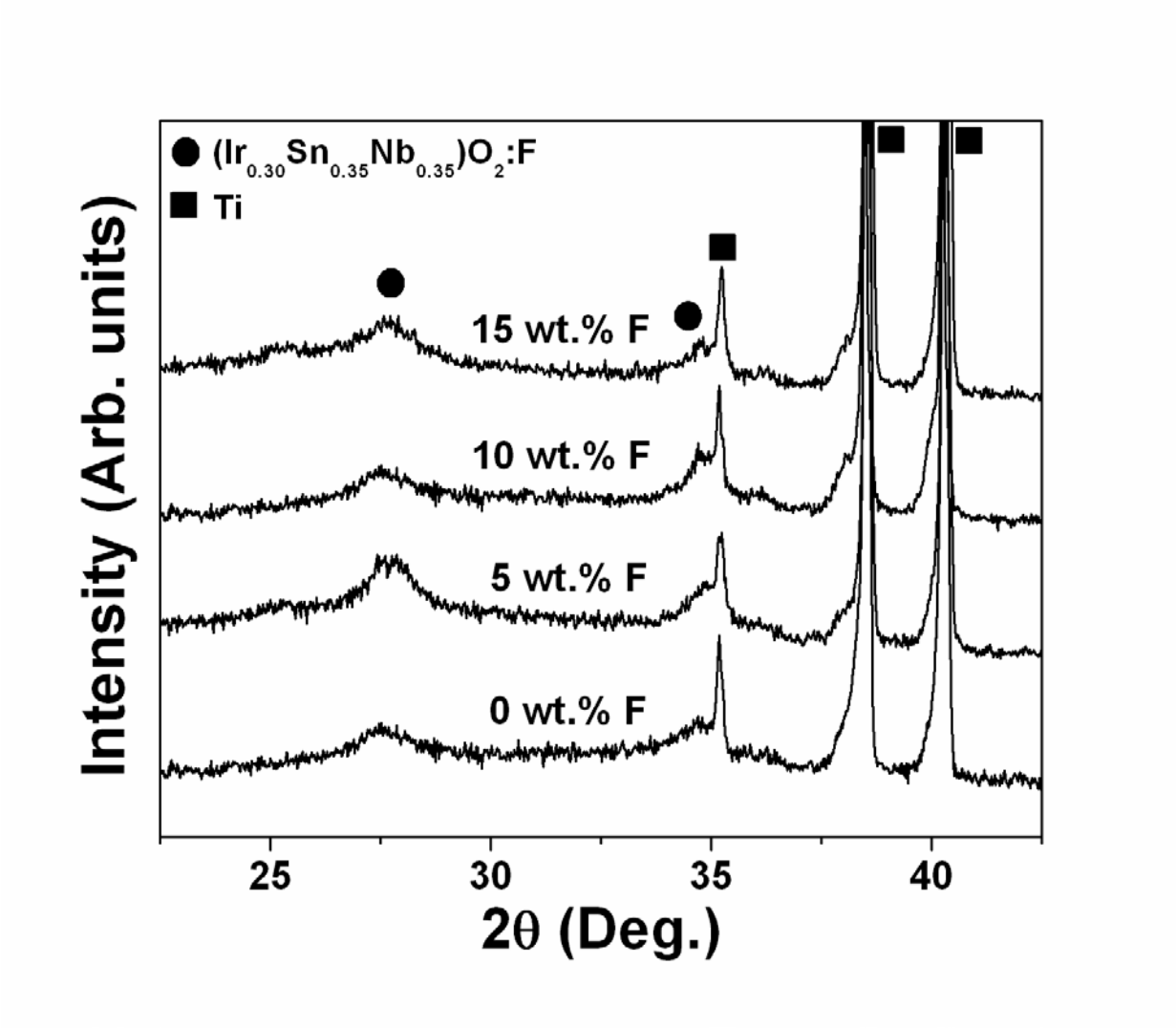

Figure 58. XRD patterns of thin film $(Ir_{0.30}Sn_{0.35}Nb_{0.35})O_2$:F of different compositions coated on Ti foil

Energy dispersive x-ray spectroscopy (EDX) confirms the presence of elemental Ir, Sn and Nb in the (Ir,Sn,Nb)O_2:x wt.% F thin film, where x ranges from 0 to 20. However, EDX

analysis could not detect the presence of F as expected (It has been outlined in **Section 5.1.1.1**). It should be noted that the final F content in the (Ir,Sn,Nb)O_2:F thin film might not be the same as the nominal composition we started with due to the expected loss of the highly volatile F species during heat treatment of the precursors in air at 400°C for 4 hours. The x-ray mapping and EDX of the representative ($Ir_{0.30}Sn_{0.35}Nb_{0.35}$)$O_2$:10 wt.% F film, is shown in **Figure 59** and **Figure 60**, respectively. **Figure 59** clearly indicates the presence of Ir, Sn, Nb and O, which are homogeneously distributed within the (Ir,Sn,Nb)O_2:F grains without being segregated on any specific site [59]. The SEM image shows a characteristic sintered "mud-crack" type morphology typically seen in chemically derived thin films. Quantitative composition analysis of the elements by EDX for all the (Ir,Sn,Nb)O_2:F films confirms that the final elemental composition is very similar to the starting / nominal composition of the films barring the presence of F. Although EDX could not categorically confirm the presence of F in this present study, the improved electrochemical performance serves as a testimony of the presence of fluorine in the lattice.

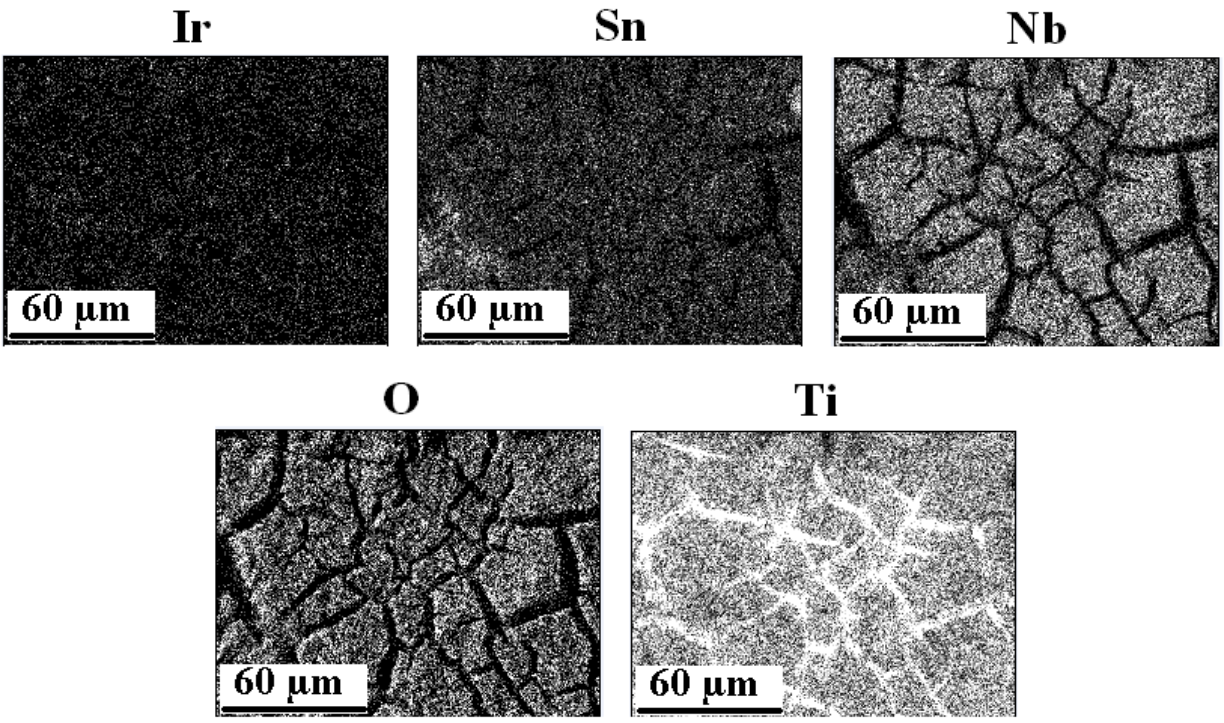

Figure 59. The x-ray mapping of Ir, Sn, Nb, O and Ti of the SEM micrograph of $(Ir_{0.30}Sn_{0.35}Nb_{0.35})O_2$:10 wt.% F film

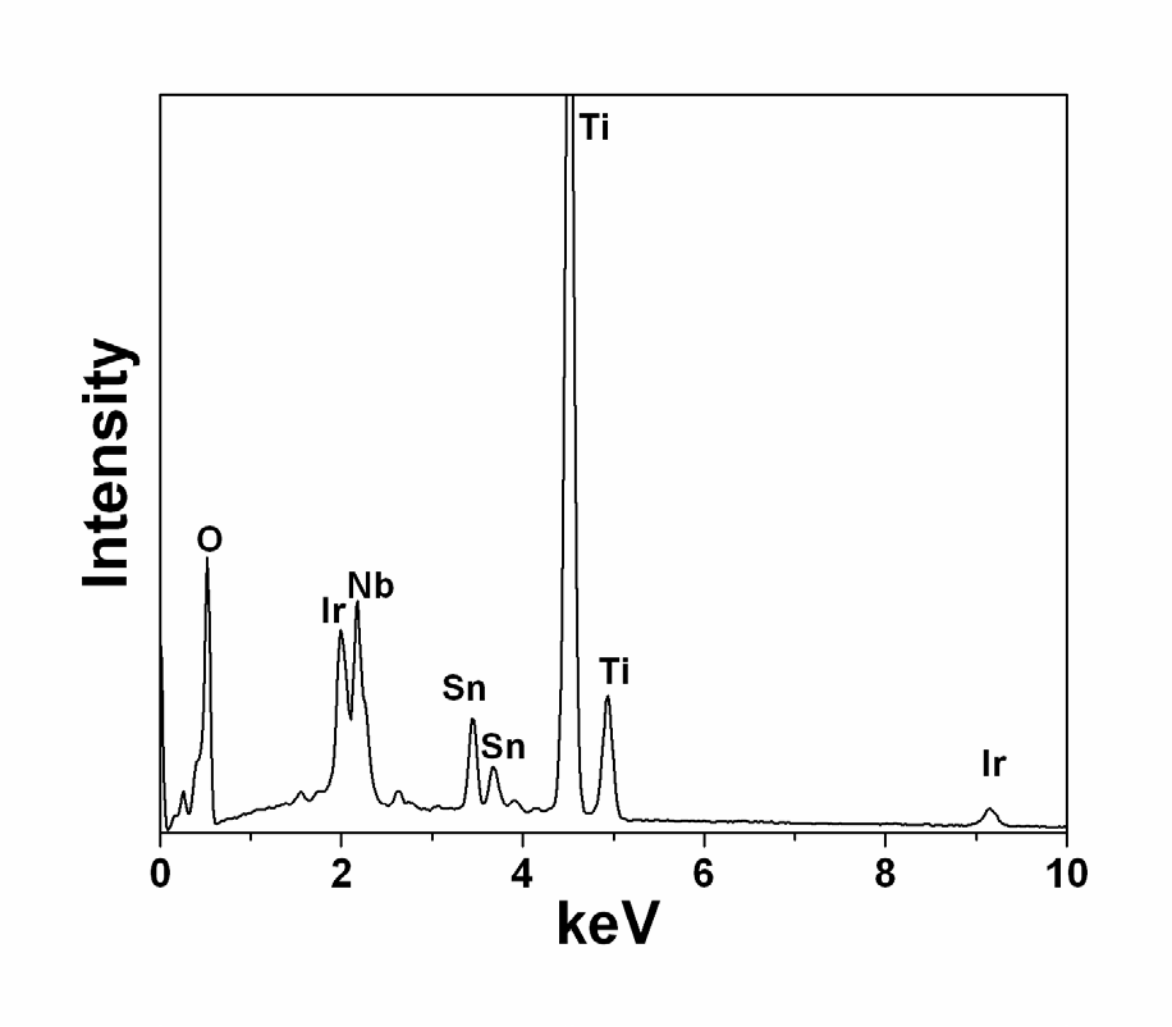

Figure 60. EDX of $(Ir_{0.30}Sn_{0.35}Nb_{0.35})O_2$:10 wt.% F coated on a Ti thin film

5.1.5.2 Electrochemical Testing

The electrochemical activity has been studied for the nanocrystalline thin film (Ir,Sn,Nb)O_2:F as a suitable anode electro-catalyst for the OER *via* PEM electrolysis. The linear polarization curve and non-linear Tafel plot are encountered due to ohmic resistance, which arises due to solution resistance (R_s) and electrode resistance (R_e) [51, 52]. The polarization curves of (Ir,Sn,Nb)O_2:F help us evaluate the electrode kinetics after we account for ohmic loss correction. Polarization

was done in presence of 1 N sulfuric acid at a scan rate of 1 mV/sec at 40°C. **Figure 61**, **Figure 62**, **Figure 63** and **Figure 64** shows the EIS plot of IrO_2, $(Ir,Sn,Nb)O_2$, $(Ir,Sn,Nb)O_2$:5 wt.% F, and $(Ir,Sn,Nb)O_2$:10 wt.% F, respectively obtained at open circuit potential (OCP), 1.5 V, 1.6 V and 1.8 V (*vs.* NHE) at 40°C in the frequency range of 100 mHz - 100 kHz. It is seen that R_s of IrO_2 and $(Ir,Sn,Nb)O_2$:F is unchanged at different voltages. From the EIS plot, the semicircle seen at low frequencies is due to OER which would be a measure of polarization resistance (R_{ct}). The R_{ct} values decrease with increase in F content, indicating increase in electrochemical activity of the electro-catalyst. **Table 5** shows R_s and R_{ct} at 1.6 V for different F doping along with the Tafel slope. These results suggest that the electrochemical activity of $(Ir_{0.30}Sn_{0.35}Nb_{0.35})O_2$:F increases with increase in F content up to 10 wt.% F.

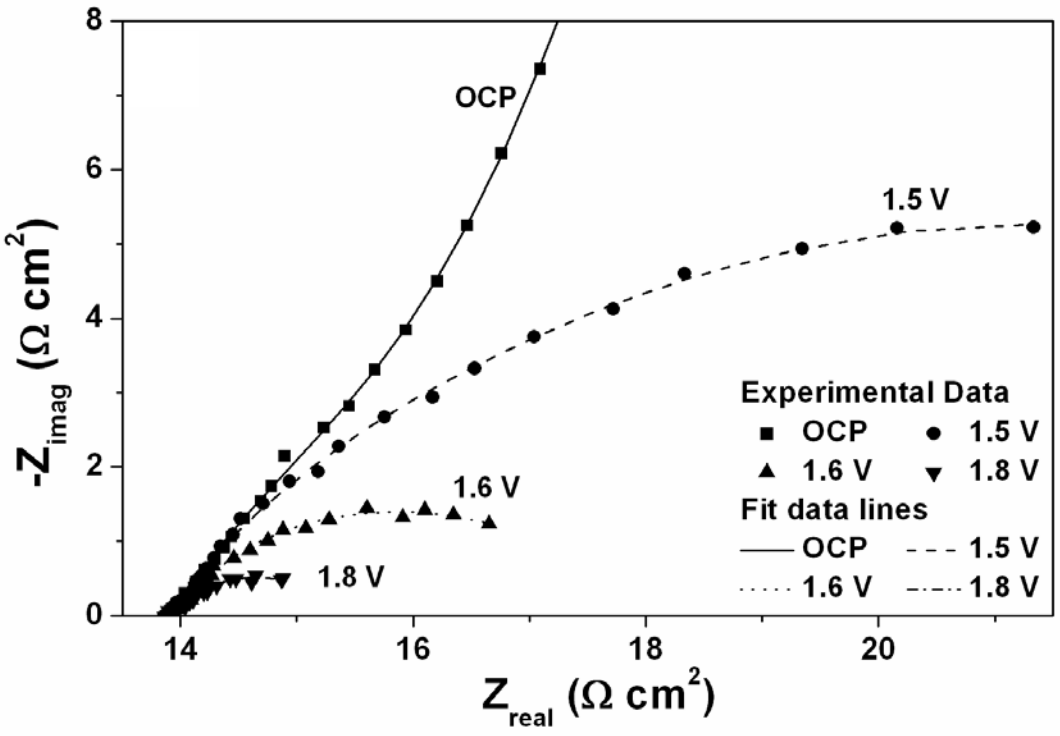

Figure 61. EIS spectra of pure IrO_2 obtained at OCP, 1.5 V, 1.6 V and 1.8 V in 1 N H_2SO_4

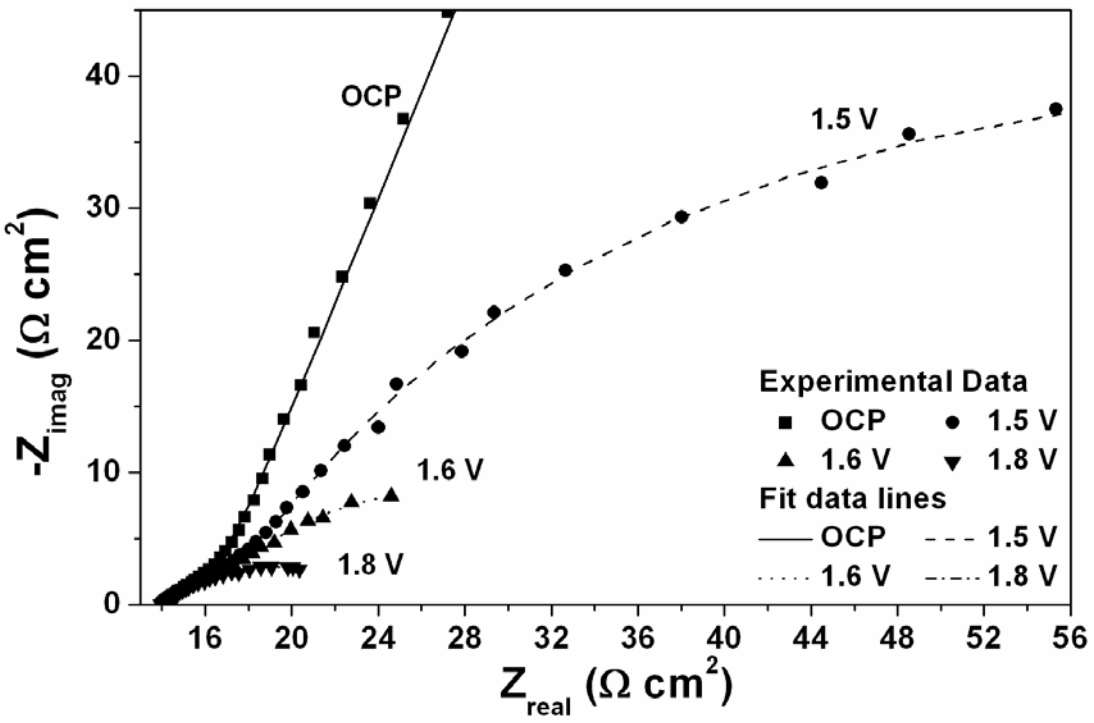

Figure 62. EIS spectra of (Ir,Sn,Nb)O_2 obtained at OCP, 1.5 V, 1.6 V and 1.8 V in 1 N H_2SO_4

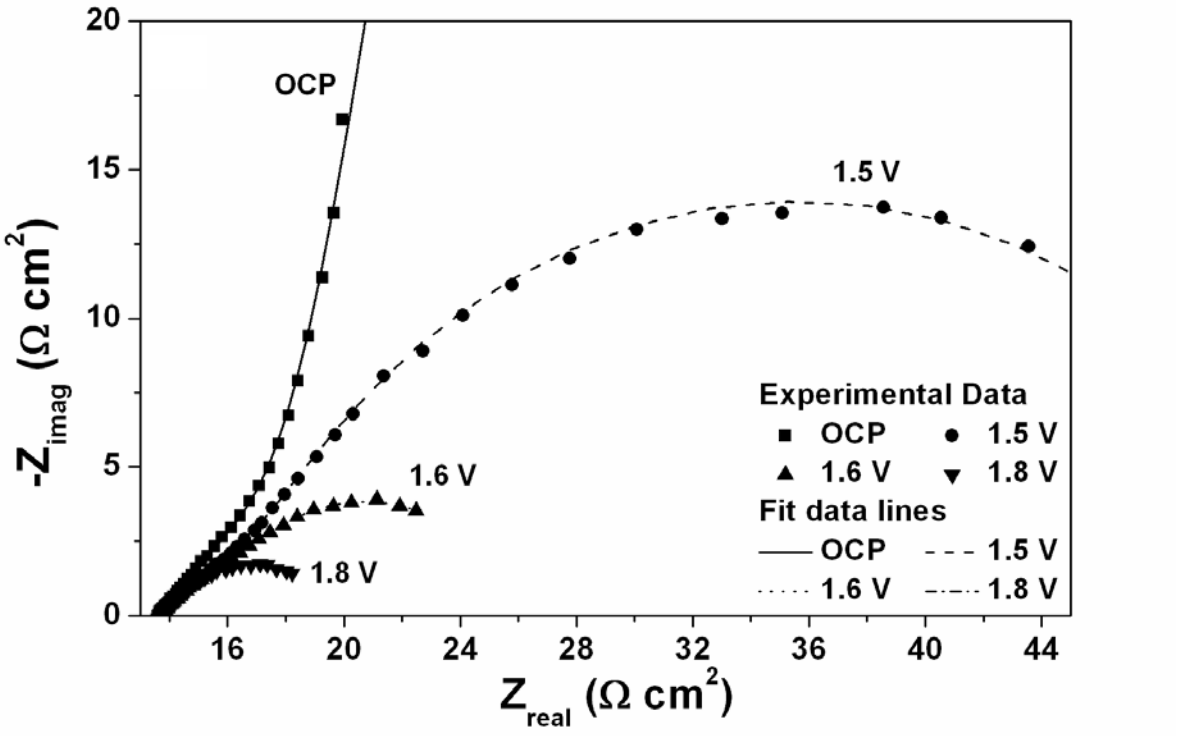

Figure 63. EIS spectra of (Ir,Sn,Nb)O_2:5 wt.% F obtained at OCP, 1.5 V, 1.6 V and 1.8 V in 1 N H_2SO_4

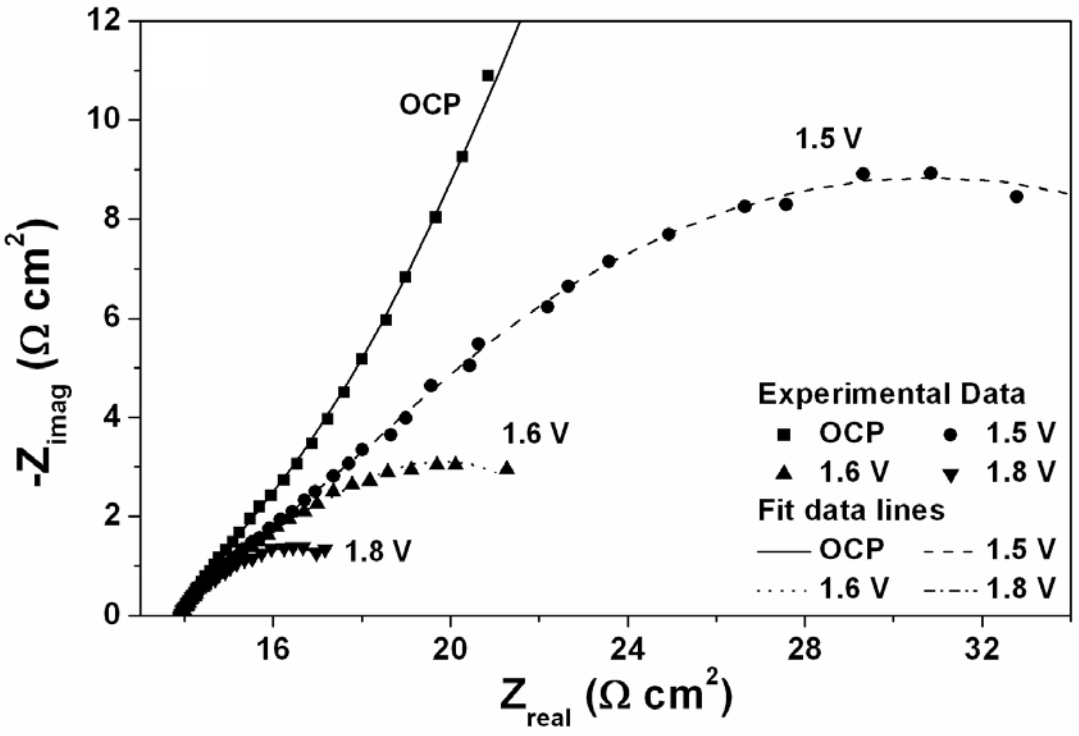

Figure 64. EIS spectra of (Ir,Sn,Nb)O_2:10 wt.% F obtained at OCP, 1.5 V, 1.6 V and 1.8 V in 1 N H_2SO_4

Table 5. Impedance parameters and Tafel slope of IrO_2 and $(Ir,Sn,Nb)O_2$:F thin film

Electro-catalyst composition	R_s (Ω cm^2)	R_{ct} (Ω cm^2)	Tafel slope (mV/dec)
IrO_2	13.84	6.48	71
$(Ir_{0.30}Sn_{0.35}Nb_{0.35})O_2$	14.02	23.75	98
$(Ir_{0.30}Sn_{0.35}Nb_{0.35})O_2$:5 wt.% F	13.69	11.99	85
$(Ir_{0.30}Sn_{0.35}Nb_{0.35})O_2$:10 wt.% F	13.87	9.98	77
$(Ir_{0.30}Sn_{0.35}Nb_{0.35})O_2$:15 wt.% F	13.48	15.18	102
$(Ir_{0.30}Sn_{0.35}Nb_{0.35})O_2$:20 wt.% F	13.55	16.73	106

Figure 65 shows the polarization curve of pure IrO_2 and $(Ir_{0.30}Sn_{0.35}Nb_{0.35})O_2$:F thin film with 0, 5 and 10 wt.% F, before and after ohmic resistance correction conducted at a scan rate of 1 mV/sec. Nanocrystalline pure IrO_2 clearly indicates that the onset of OER or water splitting occurs at a potential of ~ 1.43 V *vs.* NHE. The current density at ~ 1.55 V (*vs.* NHE), considered in the range of typically selected voltages for electrochemical activity for water electrolysis obtained from the iR corrected plot is ~ 0.012 A/cm^2 with a total loading ~ 0.3 mg/cm^2 of IrO_2. The Tafel slope of pure IrO_2, calculated from the iR corrected Tafel plot (over-potential η vs. log i) shown in **Figure 66**, is ~ 71 mV/decade, which corresponds to the well known two electron pathway reaction, assuming the transfer coefficient of ~ 0.5 [30, 48, 53, 101].

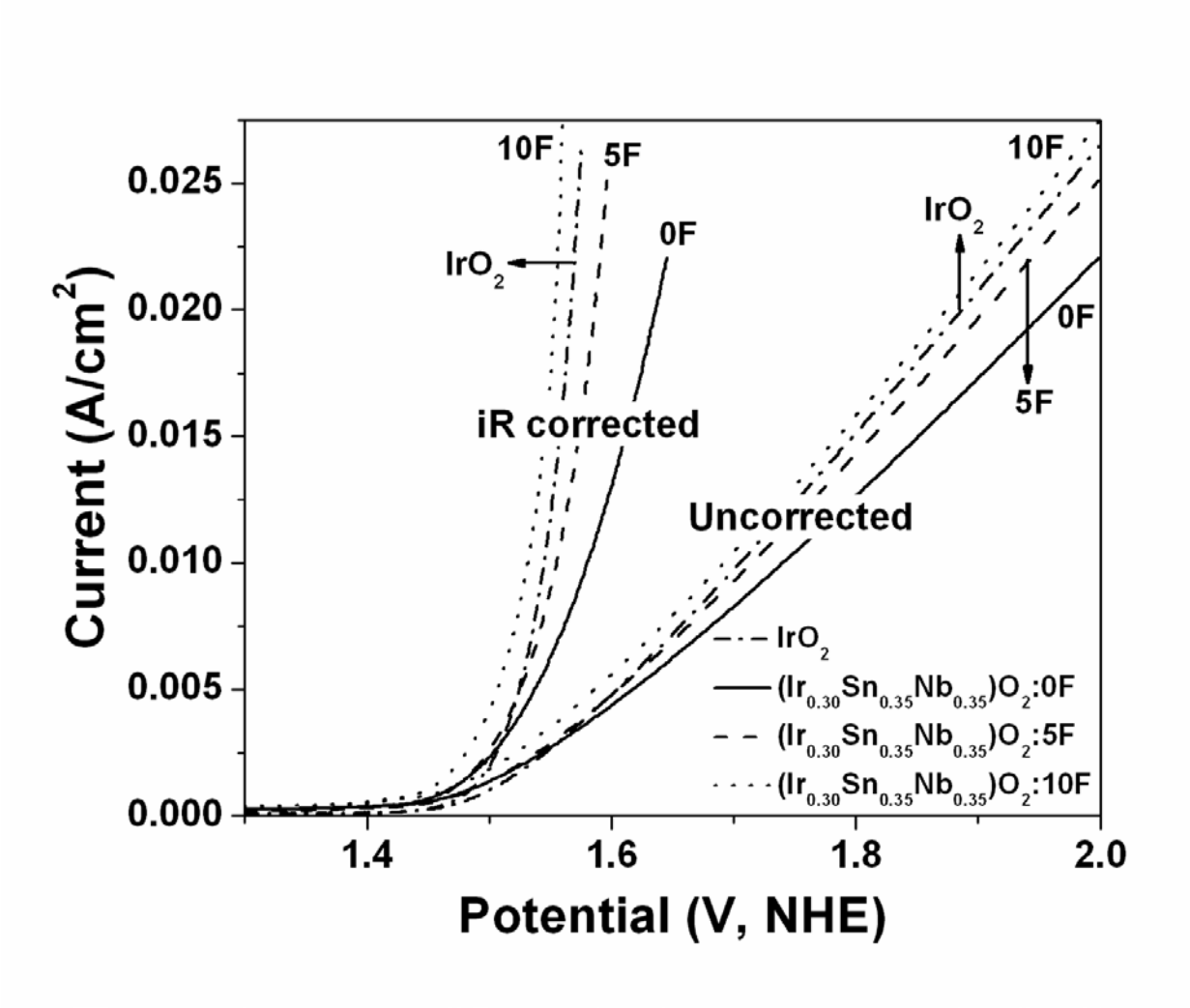

Figure 65. The polarization curve of pure IrO_2 and (Ir,Sn,Nb)O_2:F with 0, 5 and 10 wt.% F before and after iR correction conducted at a scan rate of 1 mV/sec

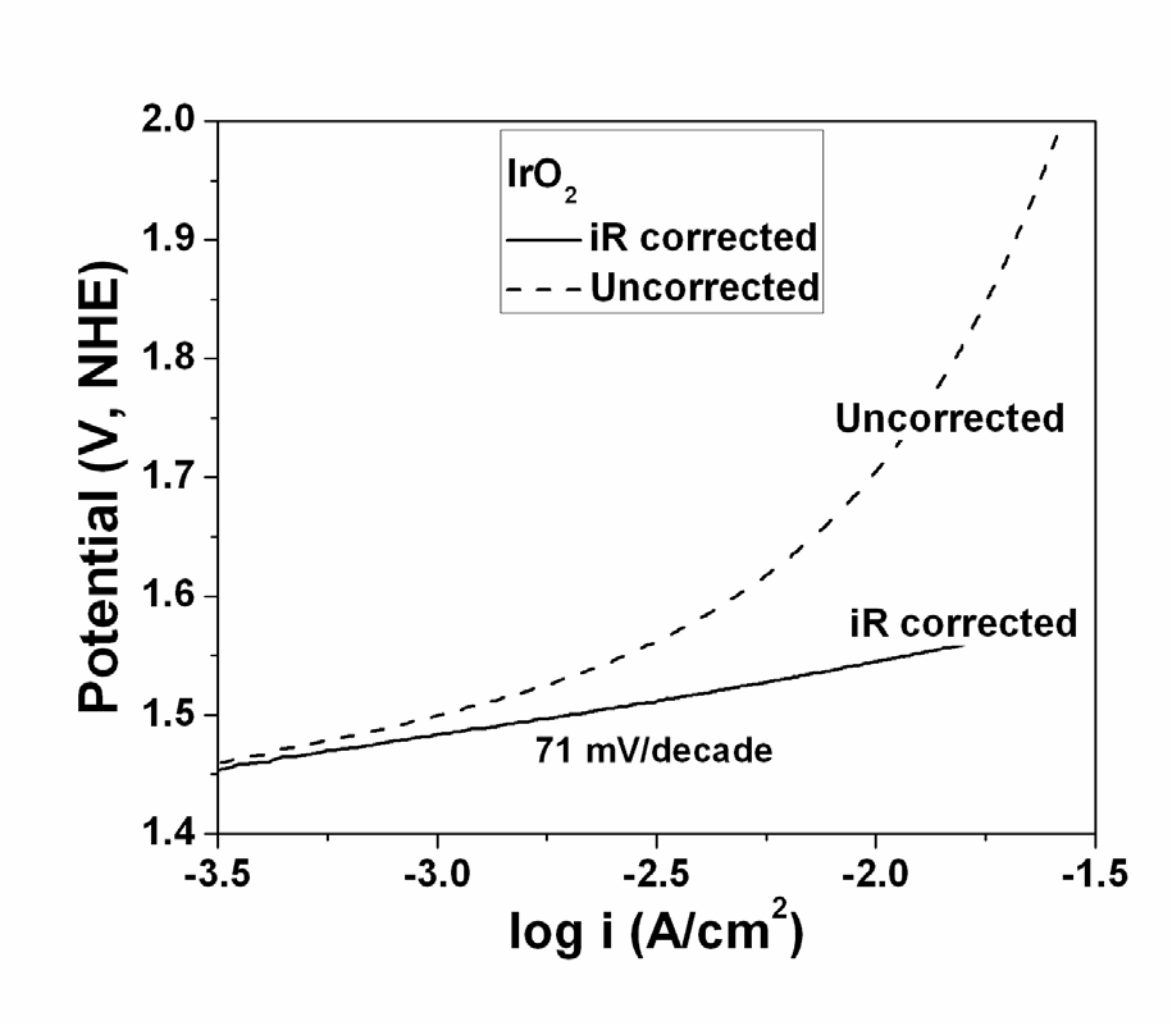

Figure 66. The Tafel plot of IrO_2 before and after iR correction

The polarization curve for the various (Ir,Sn,Nb)O_2:F films before and after iR correction corresponding to the different compositions of F, also shows OER occurring at a potential of ~ 1.43 V (*vs.* NHE) for all the compositions. Furthermore, the current density at ~ 1.55 V (*vs.* NHE) obtained from the iR corrected plot for undoped (Ir,Sn,Nb)O_2 solid solution (0 F) with an identical total loading of ~ 0.3 mg/cm^2 is ~ 0.0063 A/cm^2 which is almost half that of pure IrO_2 (**Figure 65**). Interestingly, the current density of (Ir,Sn,Nb)O_2:F increases with increasing F

content. In fact, (Ir,Sn,Nb)O_2:10 wt.% F shows a current density of ~ 0.016 A/cm^2 at ~ 1.55 V (*vs.* NHE) which is slightly more than that of pure IrO_2 for the same identical loading of ~ 0.3 mg/cm^2. But, we observe from **Figure 67** that the current density decreases with continued increase in F above 10 wt. % F. **Figure 68** shows the variation in current density of ($Ir_{0.30}Sn_{0.35}Nb_{0.35}$)$O_2$:F along with pure IrO_2 at ~ 1.75 V (*vs.* NHE) without iR correction. **Figure 69**, **Figure 70**, **Figure 71**, **Figure 72** and **Figure 73** shows the Tafel plots of (Ir,Sn,Nb)O_2, (Ir,Sn,Nb)O_2:5 wt.% F, (Ir,Sn,Nb)O_2:10 wt.% F, (Ir,Sn,Nb)O_2:15 wt.% F and (Ir,Sn,Nb)O_2:20 wt.% F respectively. The Tafel slope of (Ir,Sn,Nb)O_2:F with 0, 5, 10, 15 and 20 wt.% F, calculated from the corresponding iR corrected Tafel plots, are 98, 85, 77, 102 and 106 mV/decade. This clearly suggests that the electrochemical activity of (Ir,Sn,Nb)O_2:F increases with the corresponding decrease in the Tafel slope and increase in F content up to 10 wt.%. These results indicate that (Ir,Sn,Nb)O_2:10 wt.% F is the optimal composition exhibiting similar electrochemical activity as that of pure IrO_2.

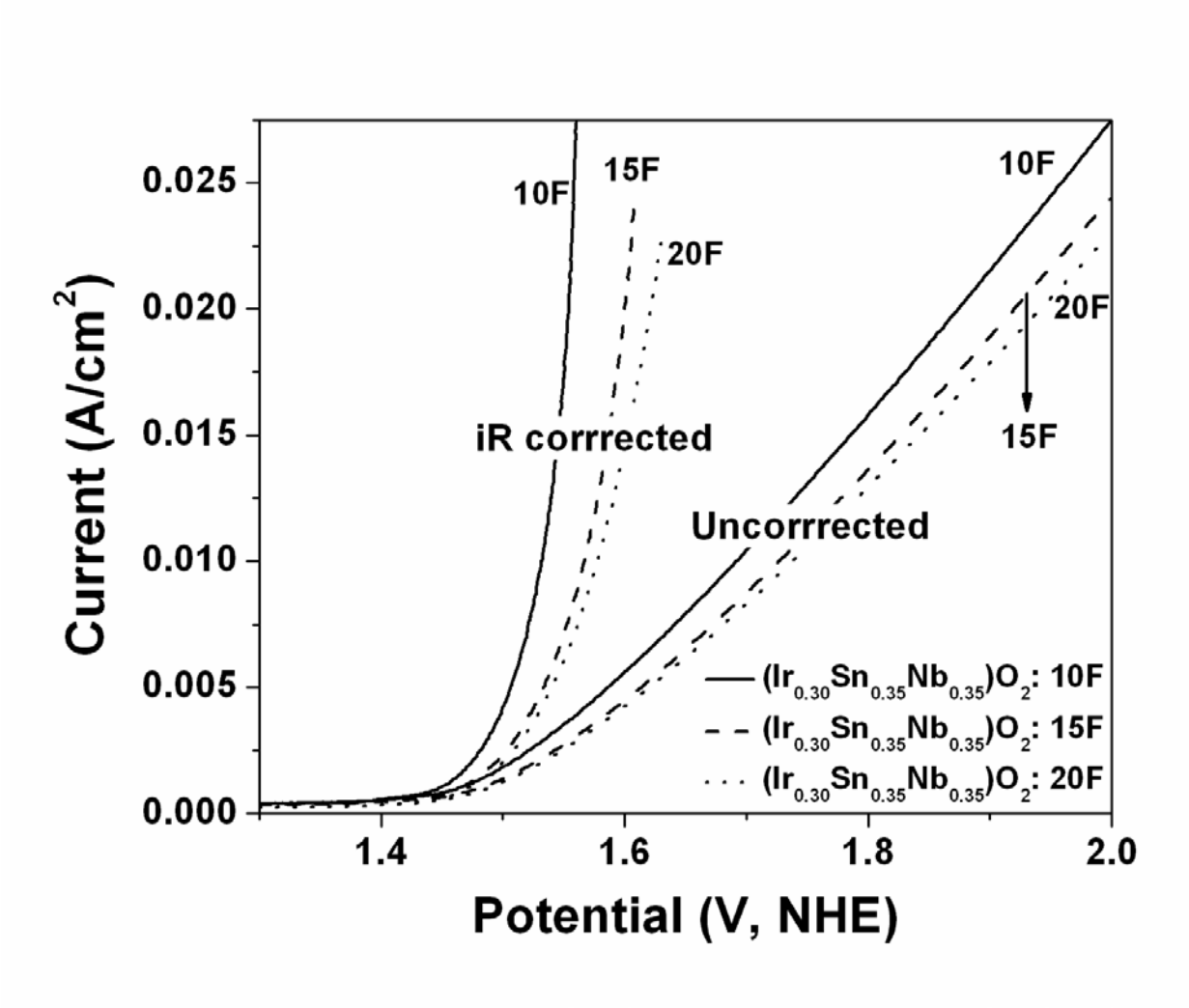

Figure 67. The polarization curve of (Ir,Sn,Nb)O_2:F with 10, 15 and 20 wt.% F before and after iR correction conducted at a scan rate of 1 mV/sec

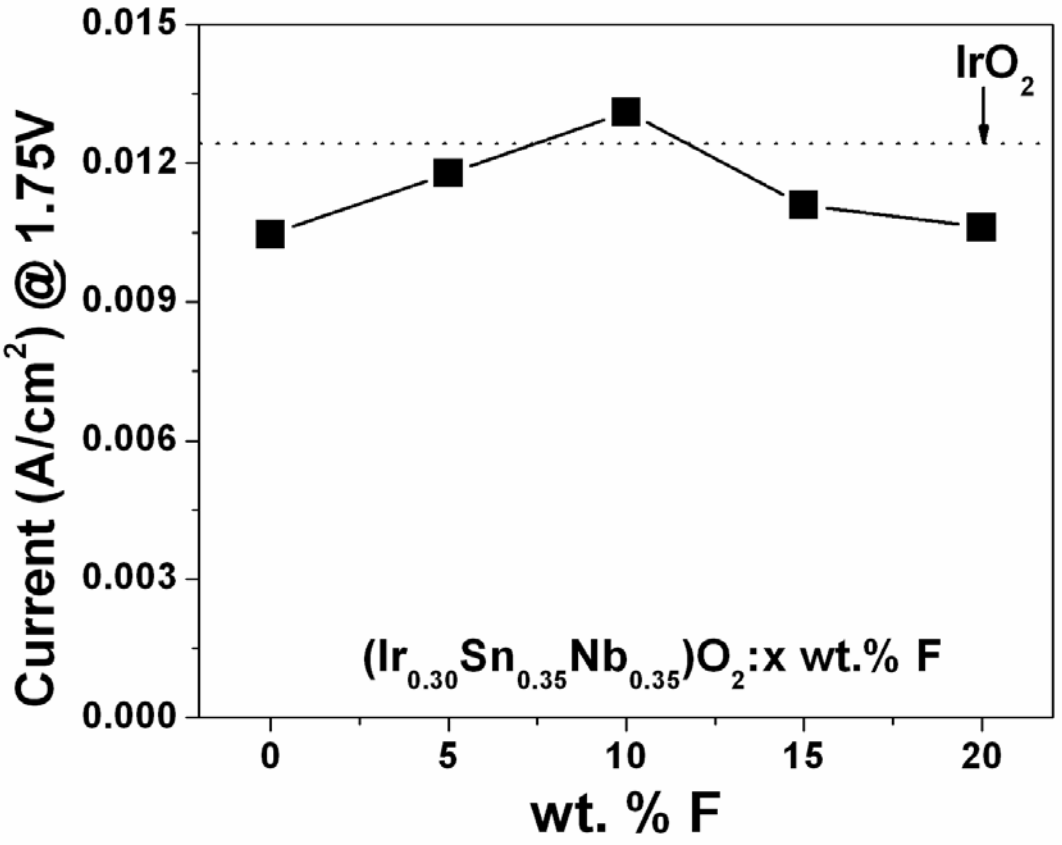

Figure 68. Variation of current density at ~ 1.75V (vs. NHE) for (Ir,Sn,Nb)O_2:F anode electro-catalyst

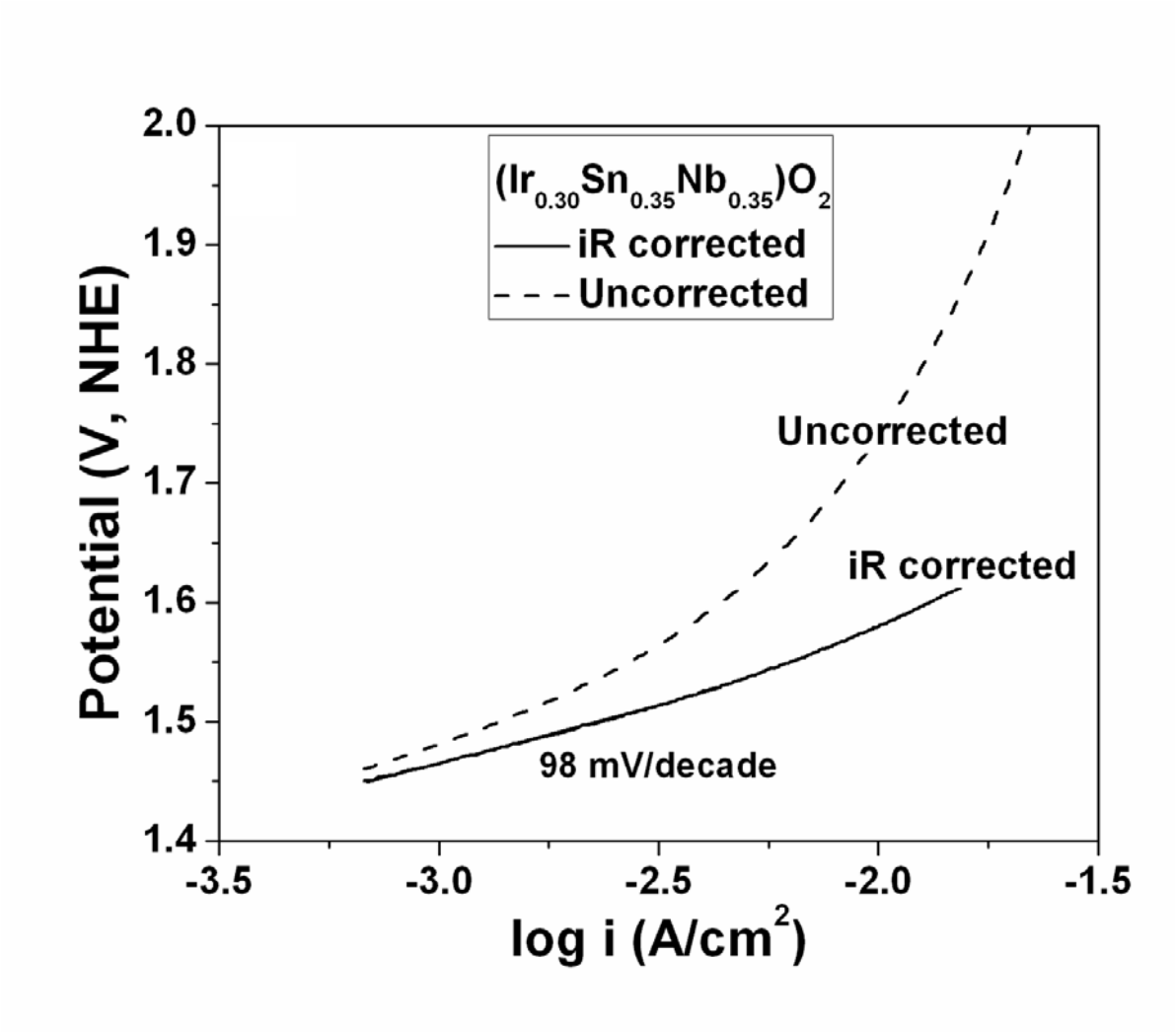

Figure 69. The Tafel plot of (Ir,Sn,Nb)O_2 before and after iR correction

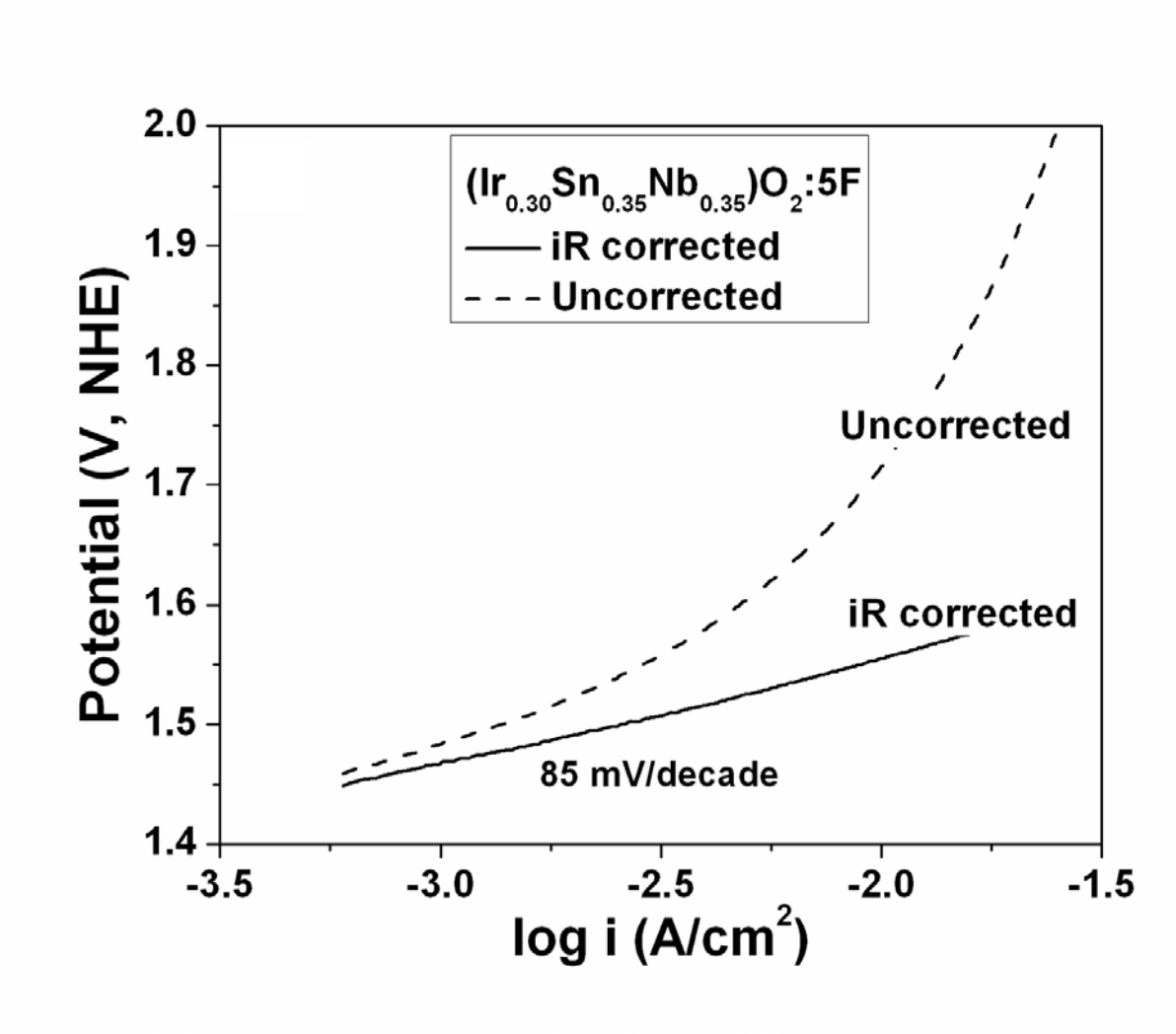

Figure 70. The Tafel plot of (Ir,Sn,Nb)O_2:5 wt.% F before and after iR correction

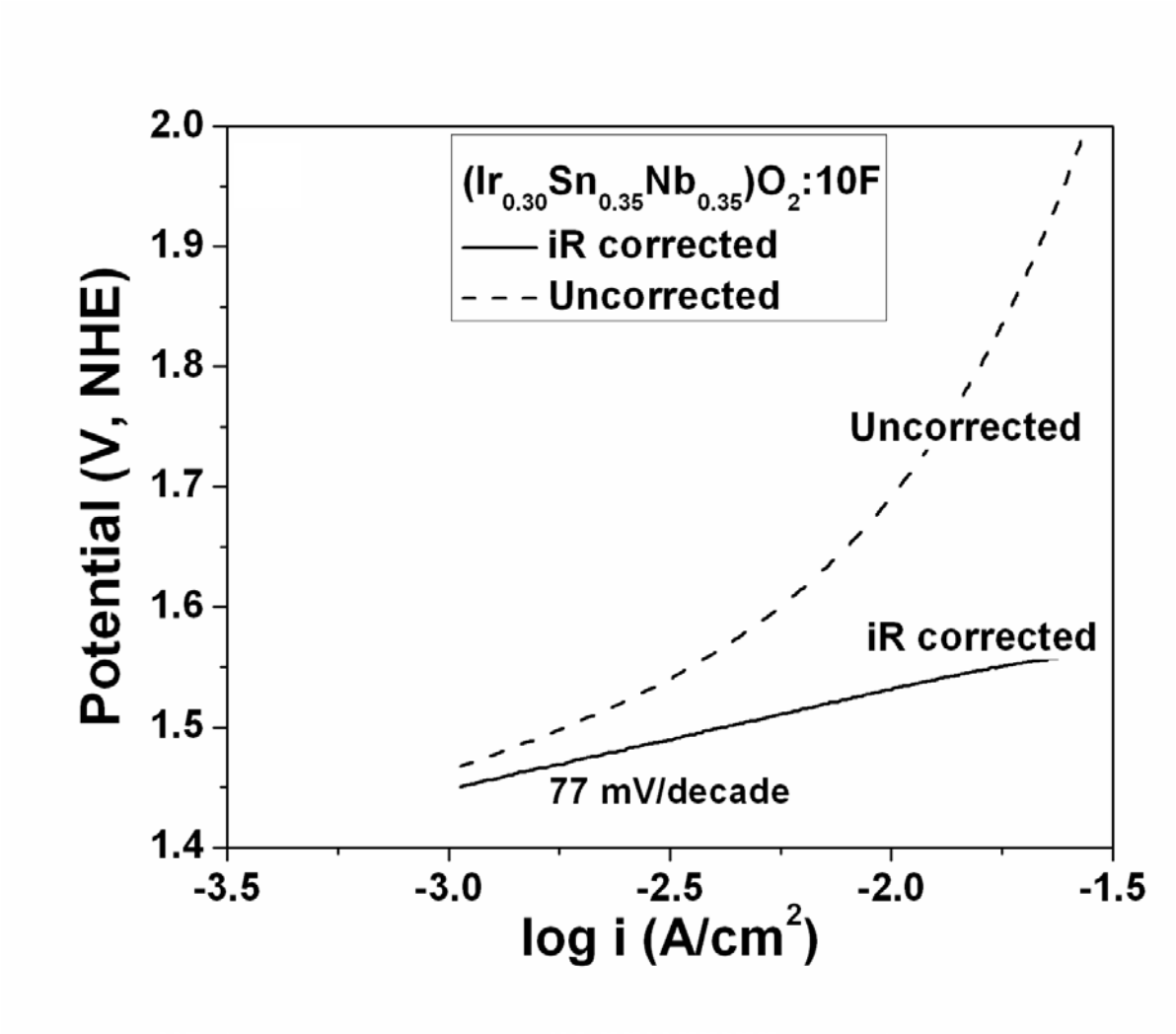

Figure 71. The Tafel plot of (Ir,Sn,Nb)O_2:10 wt.% F before and after iR correction

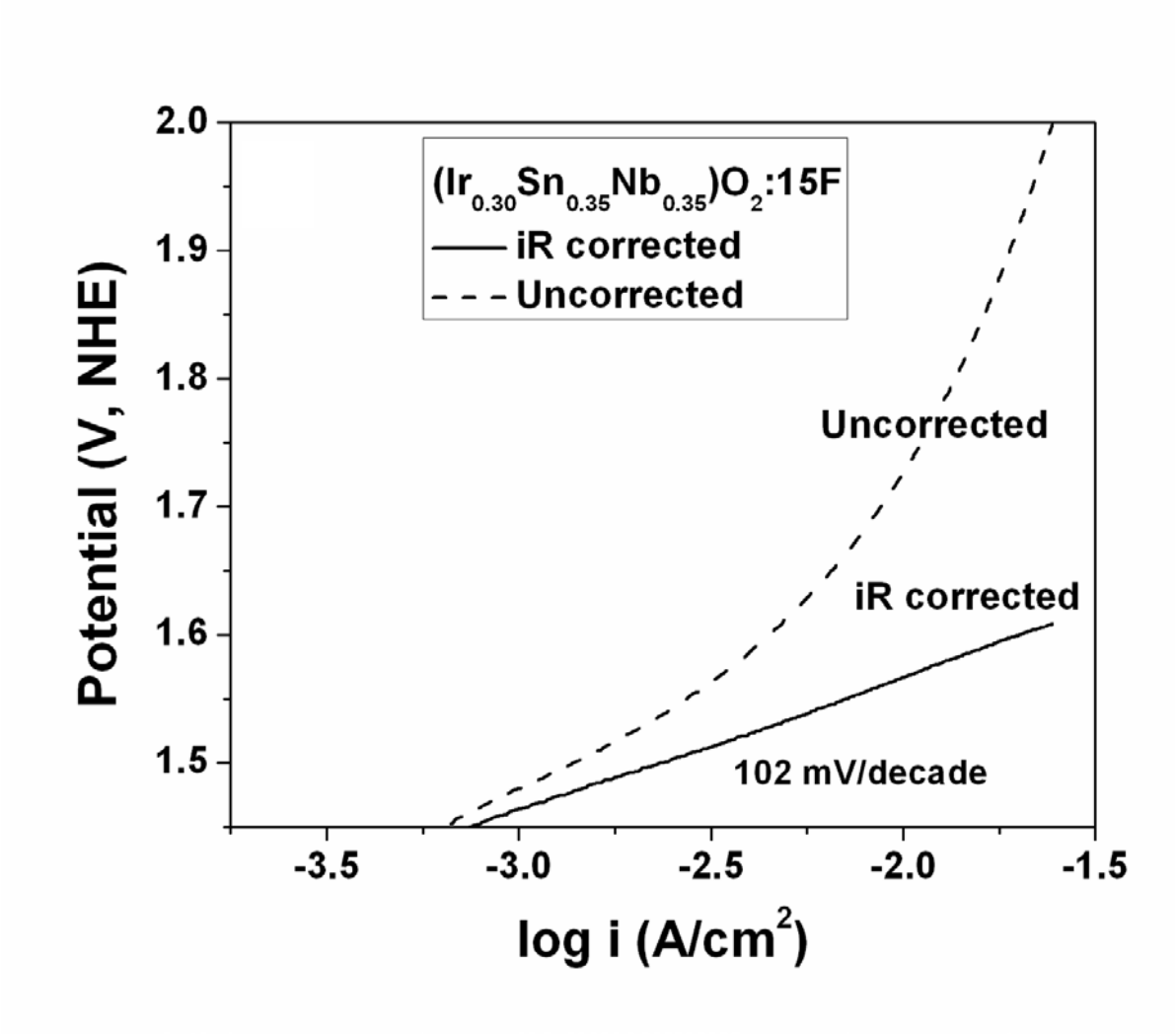

Figure 72. The Tafel plot of (Ir,Sn,Nb)O_2:15 wt.% F before and after iR correction

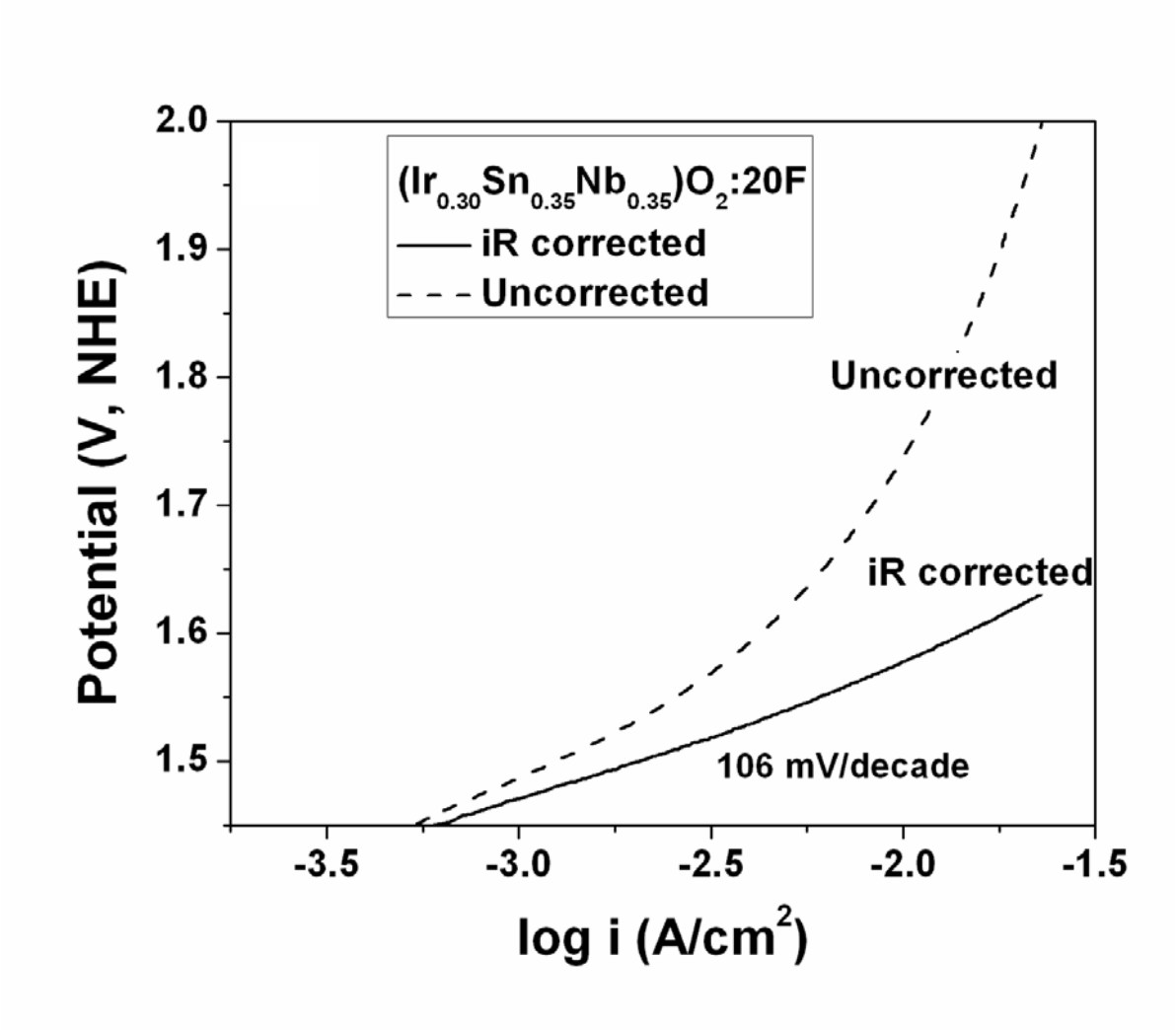

Figure 73. The Tafel plot of (Ir,Sn,Nb)O_2:20 wt.% F before and after iR correction

The durability of the anode electro-catalyst (Ir,Sn,Nb)O_2:F has been studied by choronoamperometry (CA) measurement *i.e.* current signal *vs.* time conducted at a constant potential for a duration of 24 hours. The CA curves of (Ir,Sn,Nb)O_2:F along with IrO_2, shown in **Figure 74**, are obtained at a constant voltage of ~ 1.65 V (*vs.* NHE without iR correction). The higher initial current for the (Ir,Sn,Nb)O_2:F electrodes is due to higher OER activity as demonstrated in **Figure 68**. There is a sharp drop in current for the initial small period of time (~

1 hour) for all the electrodes tested. This might be because of dissolution of the electro-catalyst material due to irregular coatings at the edge of the mud cracks [30]. A steady decay of current nevertheless, is seen after this initial period for (Ir,Sn,Nb)O_2:F up to 10 wt.% F which suggests that (Ir,Sn,Nb)O_2:F (up to 10 wt.% F) has similar long term durability as pure IrO_2. The steady decay of current for (Ir,Sn,Nb)O_2:F might be due to continuous exhaustion of fuel [34, 57]. As F content is increased over 10 wt. %, the stability seems to decrease compared to the undoped (Ir,Sn,Nb)O_2.

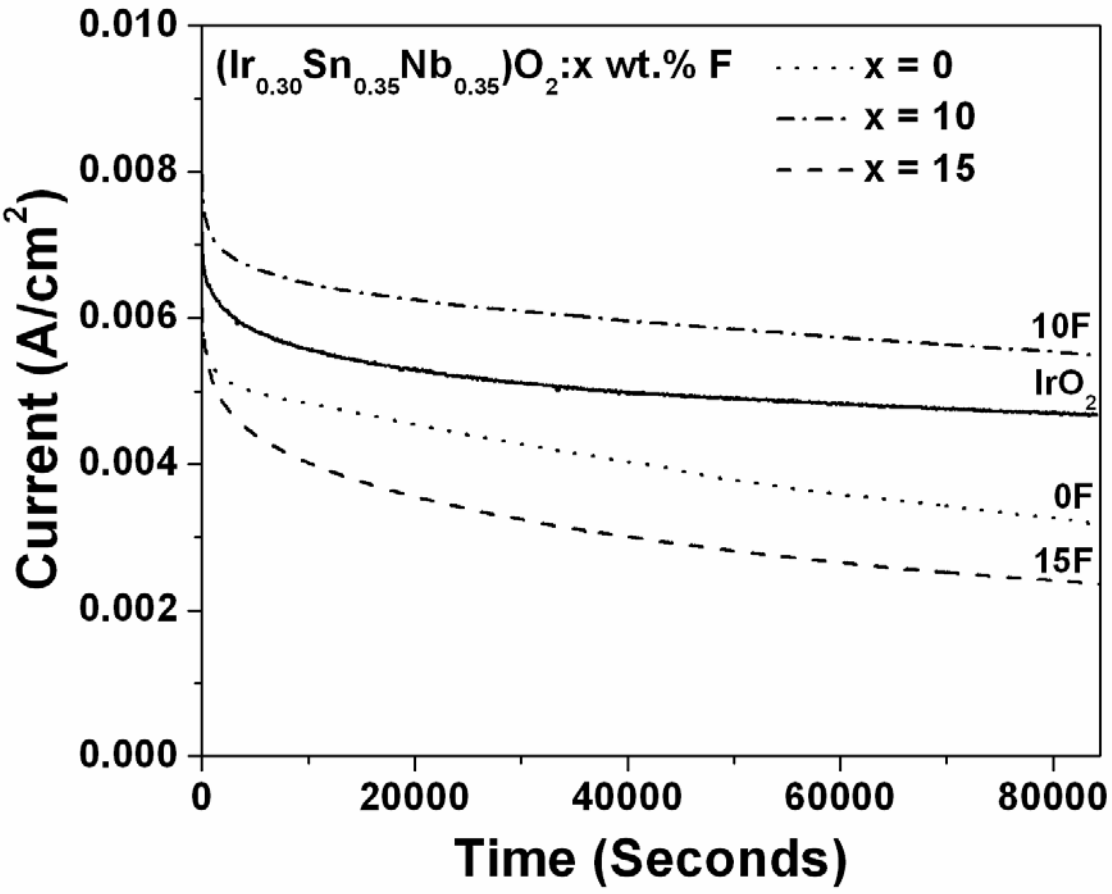

Figure 74. The variation of current *vs.* time measurement of pure IrO_2 and $(Ir_{0.30}Sn_{0.35}Nb_{0.35})O_2$:F performed in a 1 N H_2SO_4 solution under ~ 1.65 V at 40°C

ICP was conducted on the H_2SO_4 electrolyte solution collected after the CA curves have been recorded. Pure IrO_2 electro-catalyst also shows ~ 0.2 ppm Ir leached out into the solution and (Ir,Sn,Nb)O_2:10 wt.% F showed no Ir, ~ 0.15 ppm of Sn and ~ 0.15 ppm of Nb. However, the (Ir,Sn,Nb)O_2 electro-catalyst with 15 wt.% F dopant shows ~ 0.27 ppm of Ir, ~ 0.33 ppm of Sn and ~ 0.24 ppm of Nb in the solution after CA clearly reflecting a more unstable catalyst.

After the conclusion of the CA test, the (Ir,Sn,Nb)O_2:10 wt.% F thin film electrode was subject to polarization testing as seen in **Figure 75** in order to determine the activity of the electrodes after long term structural stability tests. The Tafel plot from the polarization curve (post CA measurement) after iR correction is shown in **Figure 76**. A Tafel slope of ~ 95 mV/decade is obtained for (Ir,Sn,Nb)O_2:10 wt.% F respectively. This is slightly higher but still close and comparable to the values obtained from the polarization test conducted before CA (**Figure 71**). This test further demonstrates the robustness of the electro-catalysts.

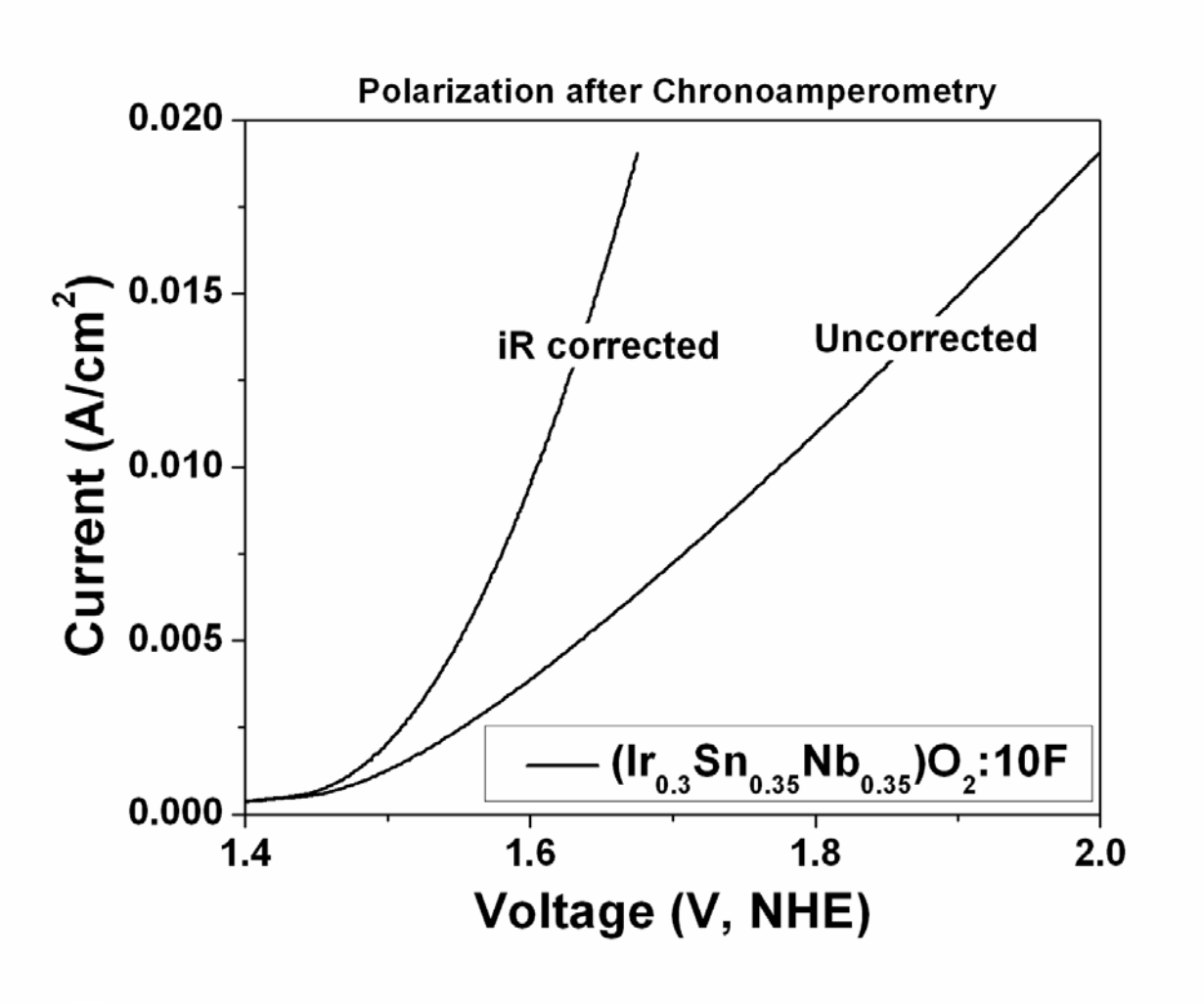

Figure 75. Polarization curve of (Ir,Sn,Nb)O_2:10 wt.% F thin film after the CA test

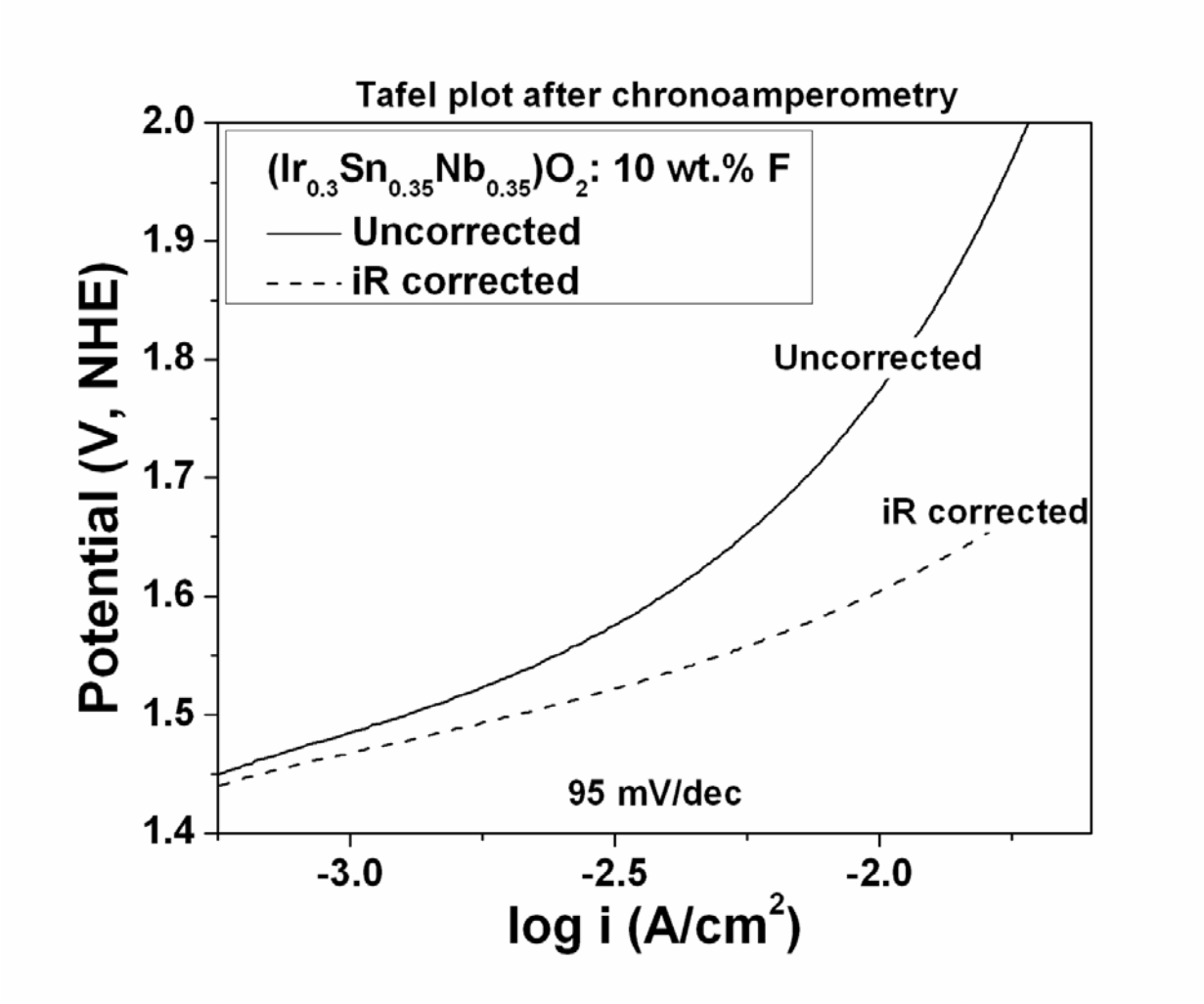

Figure 76. The Tafel plot of (Ir,Sn,Nb)O_2:10 wt.% F thin film after the CA test

The present study therefore successfully identifies ($Ir_{0.30}Sn_{0.35}Nb_{0.35}$)$O_2$:10 wt.% F as a promising anode electro-catalyst material that not only improves the catalytic activity but also the does not compromise the electrochemical stability. The excellent electrochemical activity and durability exhibited by ($Ir_{0.30}Sn_{0.35}Nb_{0.35}$)$O_2$:10 wt.% F renders it an excellent material for its use as an anode in PEM based electrolysis. We can thus expect the (Ir,Sn,Nb)O_2:F catalysts to exhibit significant reduction in the overall costs of PEM electrolyzers.

5.2 NANOSTRUCTURED POWDERS

5.2.1 F doped IrO_2

5.2.1.1 Structural Analysis

X-ray diffraction, specific surface area measurements and transmission electron microscopy characterization was done in order to study the structure of the electro-catalysts synthesized. The XRD patterns of the IrO_2:F powders after heat treatment to 500°C are shown in **Figure 77**. The XRD patterns show a rutile type tetragonal structure similar to pure IrO_2 for all the electro-catalysts. No additional peak (*E.g.* iridium fluoride) is observed which indicates formation of a complete solid solution between IrO_2 and F without any undesired phase separation as seen previously [34]. This might arise due to the fact that the ionic radius of O^{2-} (125 pm) is comparable to that of F^{1-} (120 pm) [114]. The relative broad peaks seen in the XRD patterns are due to the nanocrystalline nature of the synthesized catalysts. The effective crystallite size of IrO_2:F, calculated using the Scherrer formula from the integral breadth of the Lorentzian contribution determined from peak profile analysis using single line approximation method after eliminating the instrumental broadening and lattice strain contribution [88] is ~ 3 - 4 nm for different F compositions which is similar to that of pure undoped IrO_2 (~ 4 nm).

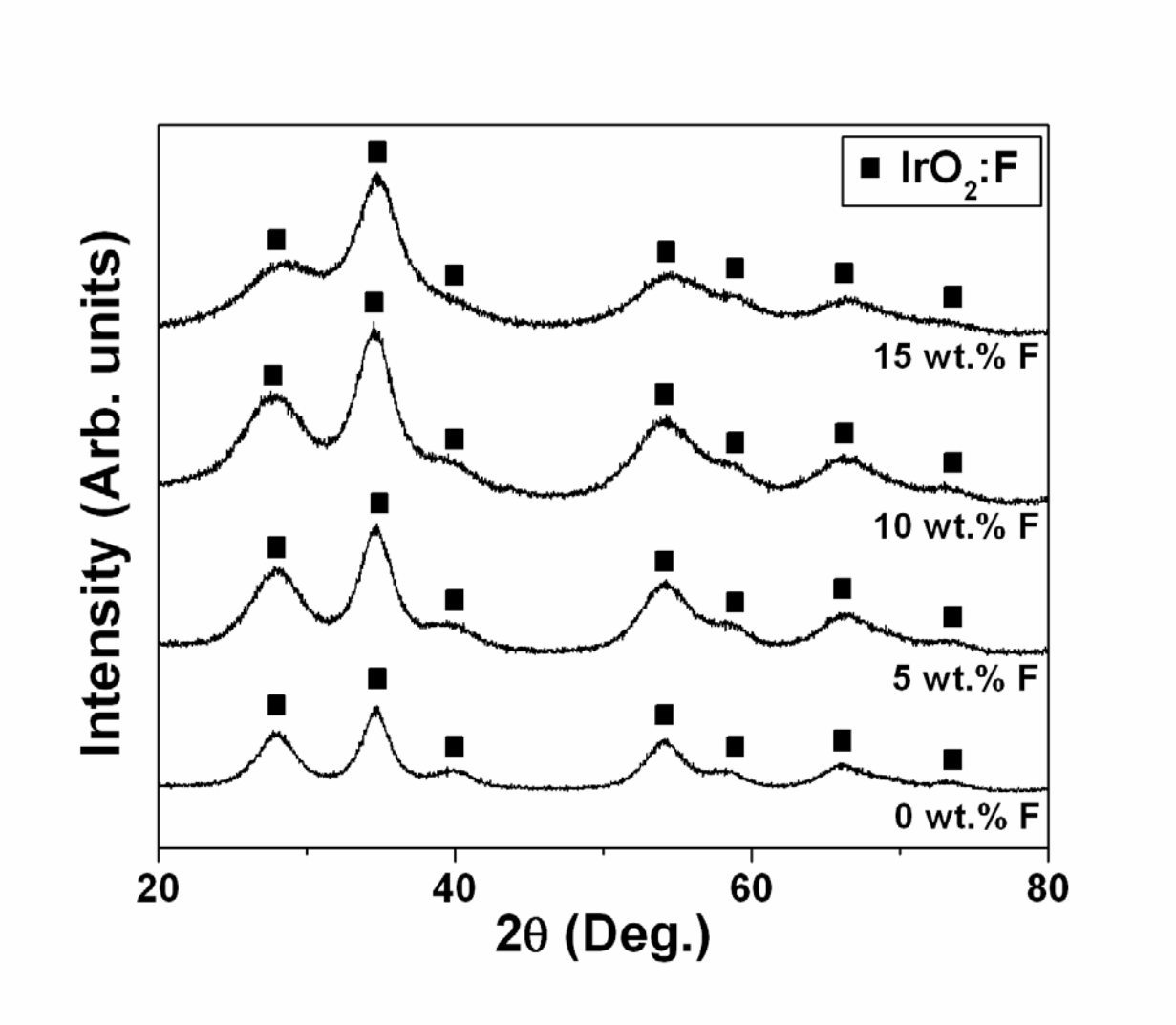

Figure 77. The XRD pattern of the nanostructured IrO_2:F of different compositions

The specific surface area (SSA) of IrO_2:F measured by the BET technique ranged from 100 - 200 m^2/g for varying F compositions. Pure IrO_2 had a SSA of ~ 191 m^2/g and IrO_2:x wt.% F had a SSA of ~ 184 m^2/g, 157 m^2/g, 129 m^2/g and 100 m^2/g for x = 5, 10, 15 and 20 respectively. These SSA values are much higher than that of commercial IrO_2 (~ 20 m^2/g). The decrease in the SSA of IrO_2:F with increasing F doping might be because of heat released due to the exothermic phenomenon of NH_4F burning, occurring during the synthesis of the catalyst

powders. This heat released might lead to agglomeration of IrO_2:F nanoparticles causing a decrease in the SSA [115]. A decrease in the specific surface area with incorporation of F for other materials and catalyst systems has been reported by other researchers too [115-118]. The bright field TEM image shown in **Figure 78**, of a representative electro-catalyst composition of IrO_2:10 wt.% F confirms the nanometer scale (~5 - 10 nm) of the particles. The HRTEM image, shown in **Figure 79**, confirms the nanostructured nature of the electro-catalysts, with the d spacing being ~0.312 nm ± 0.005 nm, that matches well with the d_{110} spacing of pure IrO_2 which is 0.318 nm [119].

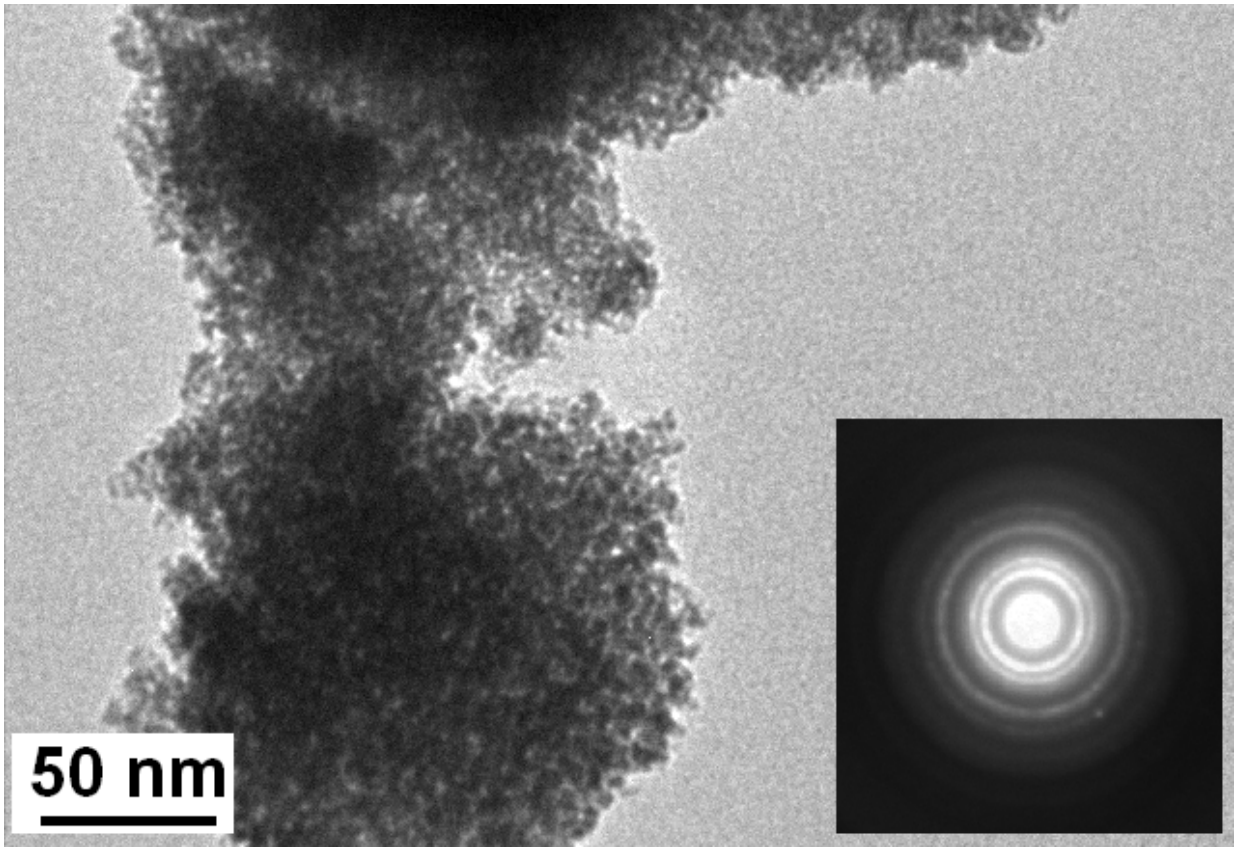

Figure 78. The bright field TEM image of nanostructured IrO_2:10 wt.% F electro-catalyst

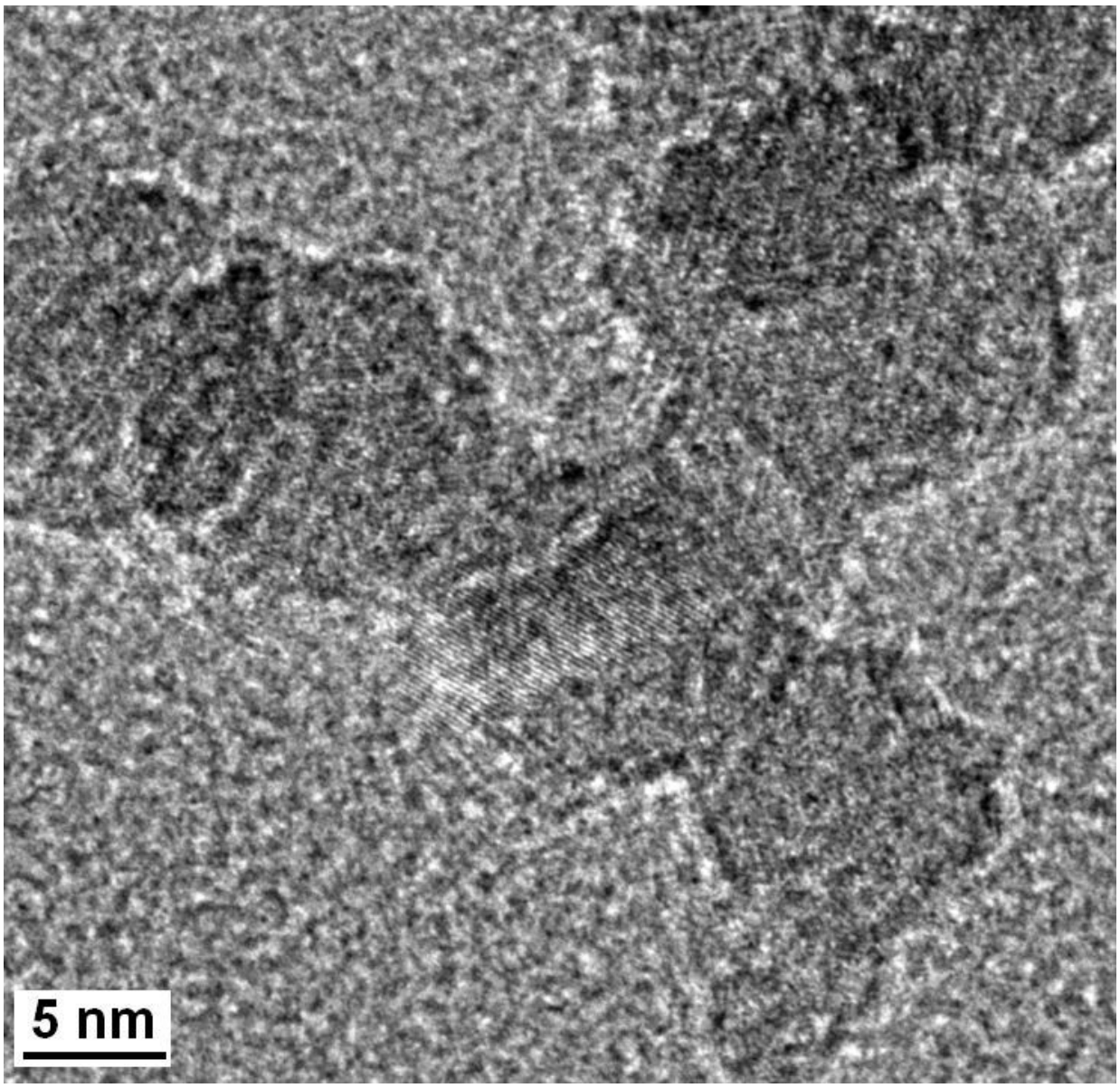

Figure 79. The HRTEM image of IrO_2:10 wt.% F confirming the nanoparticulate nature of the electro-catalyst

5.2.1.2 Electrochemical Testing

The electrochemical activity of nanostructured IrO_2:F with F doping ranging from 0 to 20 wt.% has been studied as an OER catalyst for use as an anode in PEM based water electrolysis. Polarization was conducted at a scan rate of 1 mV/sec in 1 N H_2SO_4 at 40°C. The uncorrected polarization curve and the non-linear Tafel plot encounters a large amount of ohmic/solution resistance (R_s) which is determined from the electrochemical impedance spectroscopy (EIS) plot at high frequencies [51, 52]. This helps us in preparing the linear Tafel plots and the iR corrected polarization curves. The plots after correcting for the ohmic loss help us in evaluating the inherent electro-catalytic property of the electrodes. **Figure 80** and **Figure 81** shows the EIS plots of undoped IrO_2 and IrO_2:5 wt.% F, respectively at open circuit potential (OCP), 1.5 V, 1.6 V and 1.7 V (*vs.* NHE). The EIS curves of IrO_2:10 wt.% F, IrO_2:15 wt.% F, and IrO_2:20 wt.% F are plotted in **Figure 82**, **Figure 83** and **Figure 84**, respectively at OCP, 1.5 V, 1.6 V and 1.7 V (*vs.* NHE). It is observed that the R_s values obtained at high frequencies for all IrO_2:F electrodes at various potentials is very similar (~ 16.1 ± 0.4 Ωcm^2). The EIS plots show a well formed semi-circular arc at low frequencies and its diameter gives the polarization resistance (R_{ct}). **Table 6** enlists the impedance parameters *i.e.* R_s and R_{ct} for all the synthesized electro-catalysts (IrO_2:F) at different potentials. It is observed that the R_{ct} value at all potentials decreases when F doping is increased from 0 to 10 wt.% F. R_{ct} is the resistance due to electron transfer at the electrochemical interface. A lower value of R_{ct} indicates there will be less resistance faced by the electrode during the OER and would result in enhanced catalytic performance and activity. It is also seen that the R_{ct} increases when F doping is raised to 15 and 20 wt.% F. As the R_{ct} increases, a decrease in the electrochemical activity is expected.

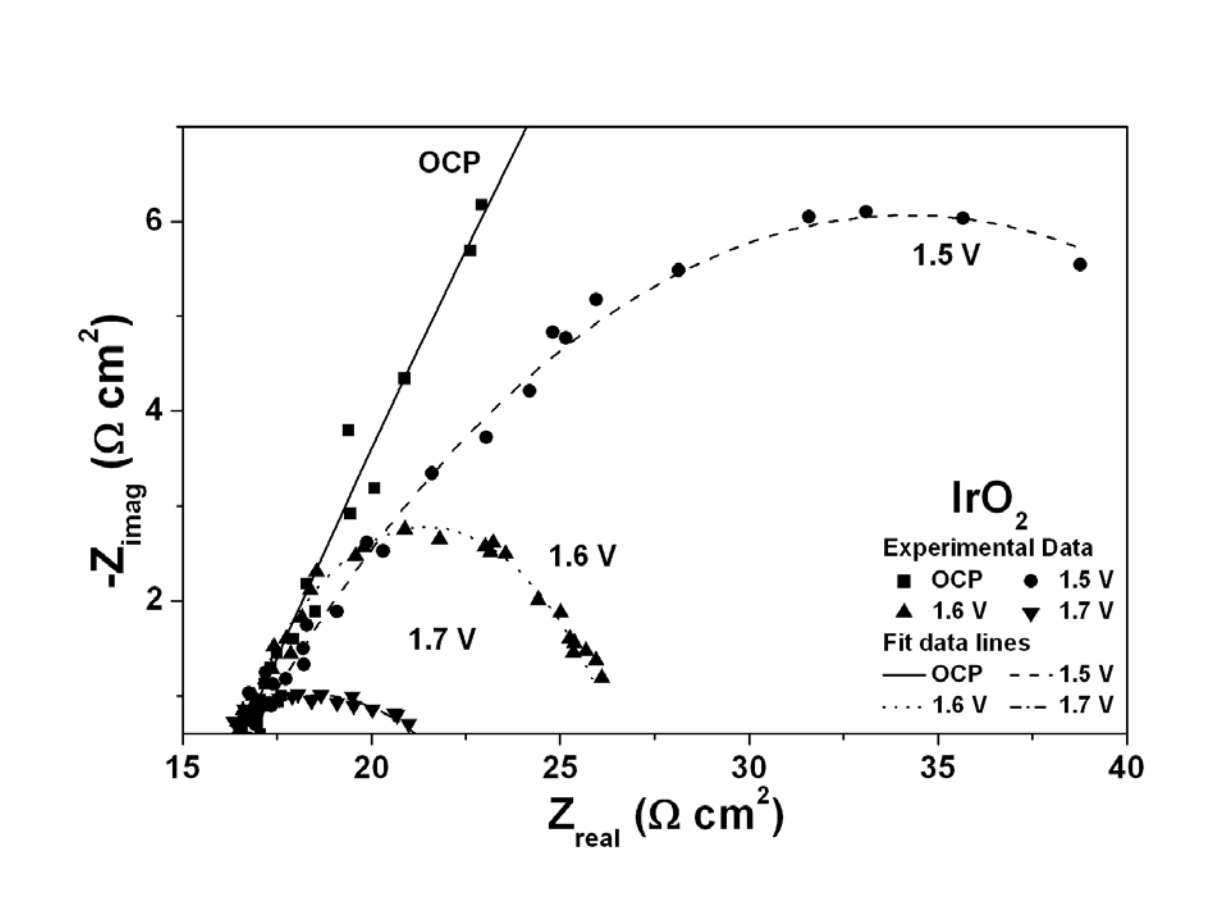

Figure 80. EIS spectra of undoped IrO_2 in a solution of 1 N H_2SO_4 at 40°C

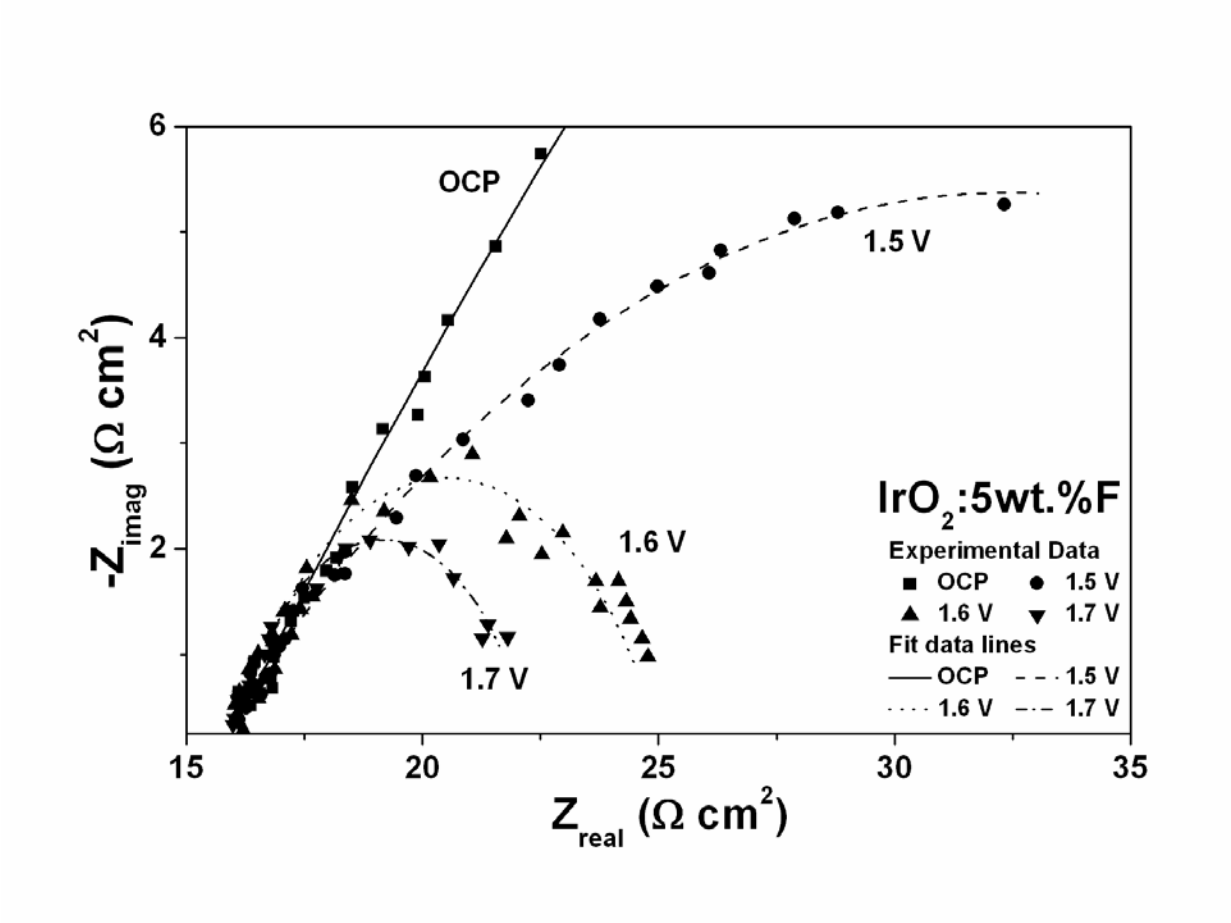

Figure 81. EIS spectra of IrO_2:5 wt.% F in a solution of 1 N H_2SO_4 at 40°C

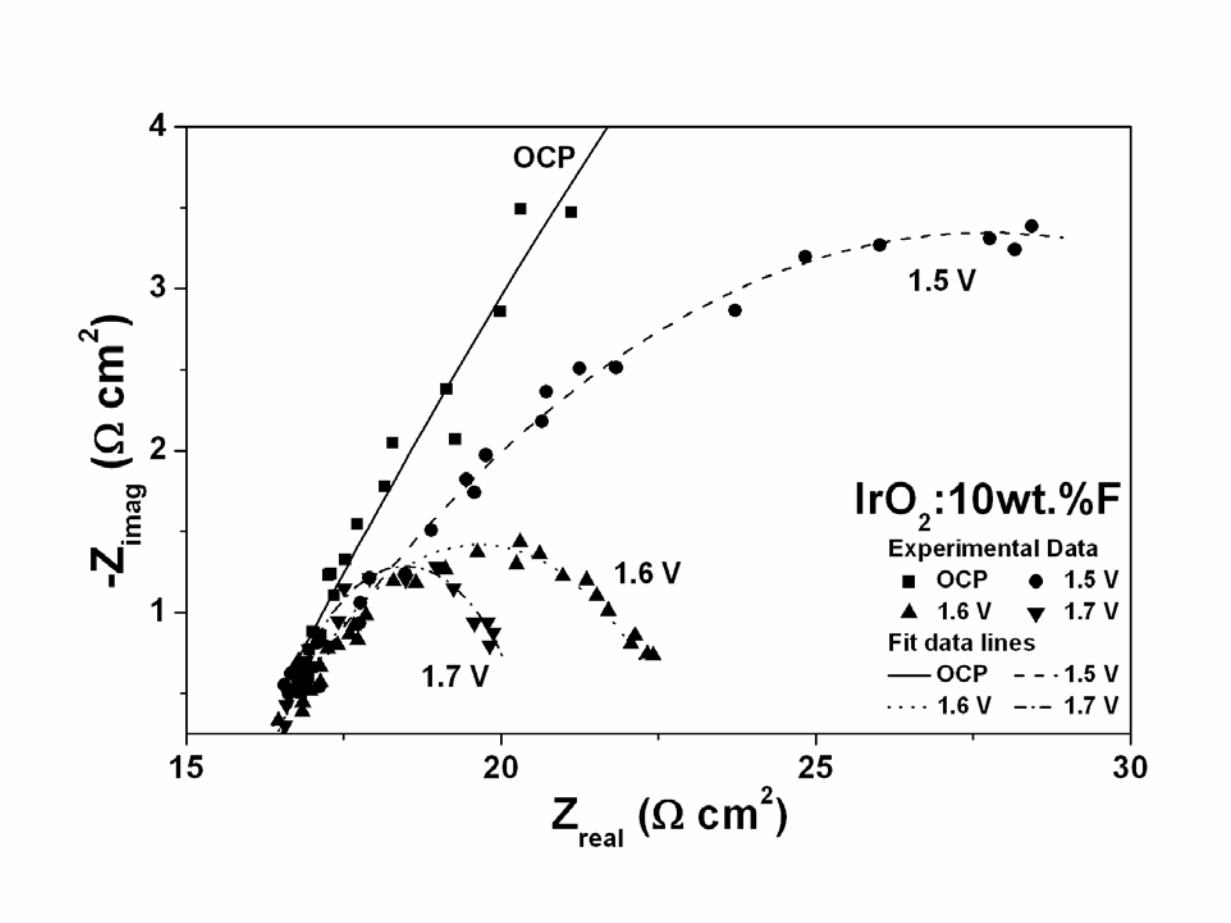

Figure 82. EIS spectra of IrO_2:10 wt.% F in a solution of 1 N H_2SO_4 at 40°C

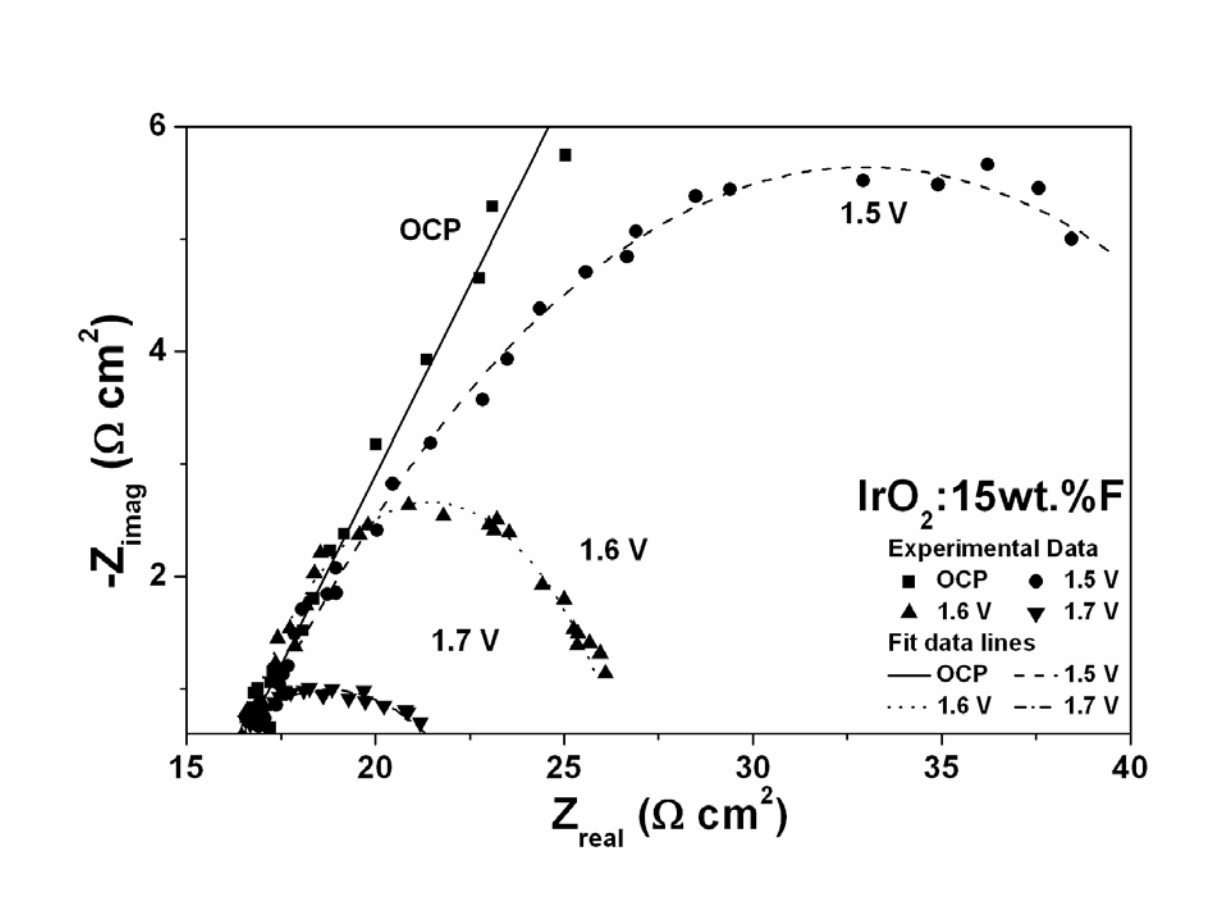

Figure 83. EIS spectra of IrO_2:15 wt.% F in a solution of 1 N H_2SO_4 at 40°C

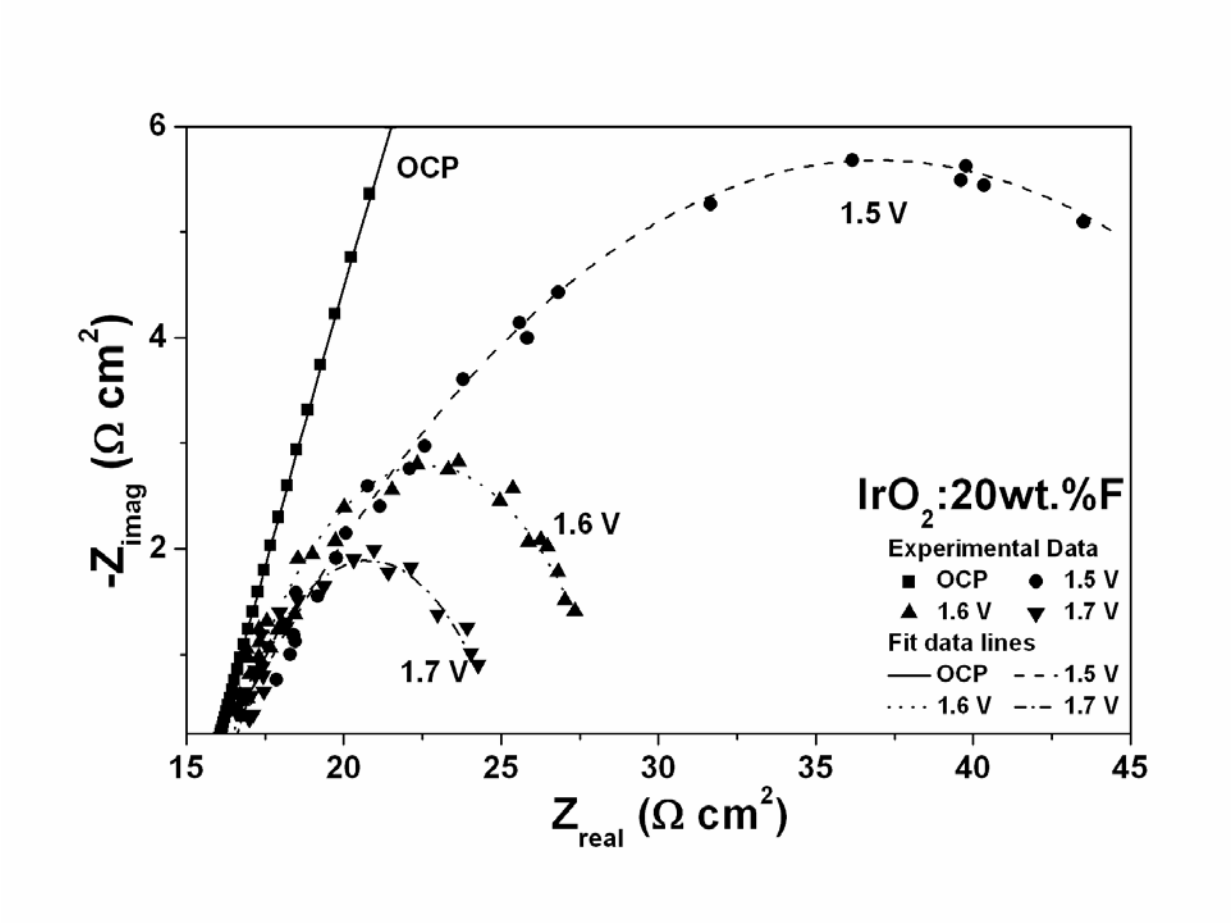

Figure 84. EIS spectra of IrO_2:20 wt.% F in a solution of 1 N H_2SO_4 at 40°C

Table 6. Impedance parameters of IrO_2:F powder catalyst

	F doping (wt.%)	OCP	1.5 V	1.6 V	1.7 V
R_s (Ω cm^2)	0	15.96	15.99	16.04	16.30
	5	16.08	15.95	15.87	16.01
	10	16.07	15.87	16.17	16.39
	15	15.71	15.96	15.94	16.46
	20	15.84	15.95	16.24	16.40
R_{ct} (Ω cm^2)	0	203.4	36.42	11.53	8.13
	5	154.2	32.39	9.29	5.65
	10	126.4	23.69	6.96	3.76
	15	175.5	33.99	11.03	8.04
	20	200.8	42.00	12.75	6.98

Figure 85 shows the polarization tests on nanocrystalline IrO_2, IrO_2:5 wt.% F and IrO_2:10 wt.% F. It is clearly seen that the onset of electrolysis or the OER starts at ~ 1.43 V (*vs.* NHE). The current density at ~ 1.48 V after iR correction (*vs.* NHE), which is in the standard range of accepted voltages for determining electro-catalytic activity in PEM electrolysis conditions, is ~ 0.0088 ± 0.0002 A/cm^2 for undoped IrO_2 with a total loading of ~ 0.3 mg/cm^2.

At the same voltage of ~ 1.48 V and a total loading of ~ 0.3 mg/cm^2; IrO_2:5 wt% F and IrO_2:10 wt.% F have a current density of ~ 0.0133 ± 0.0002 A/cm^2 and 0.030 ± 0.0002 A/cm^2, respectively. Fluorine doping of 10 wt.% thus shows an appreciable increase in the current density with respect to pure IrO_2 (*ca.* 3.3 times) implying a great increase in the electrochemical activity of the catalyst. As F doping is increased to 15 and 20 wt.%, it is observed *via* **Figure 86** that the onset of the OER remains similar and is ~ 1.43 V (*vs.* NHE) for the catalysts. But, the current obtained decreases for the same loading of ~ 0.3 mg/cm^2. The current density at ~ 1.48 V (*vs.* NHE) for 15 wt.% F and 20 wt.% F doped IrO_2 is ~ 0.0112 ± 0.0002 A/cm^2 and 0.010 ± 0.0002 A/cm^2, respectively. These results also agree very well with the EIS plots as an increase in R_{ct} is seen after increasing F doping above 10 wt.% (**Table 6**). This suggests that IrO_2:10 wt.% F is the most optimized electro-catalyst yielding very high electro-catalytic activity than pure IrO_2.

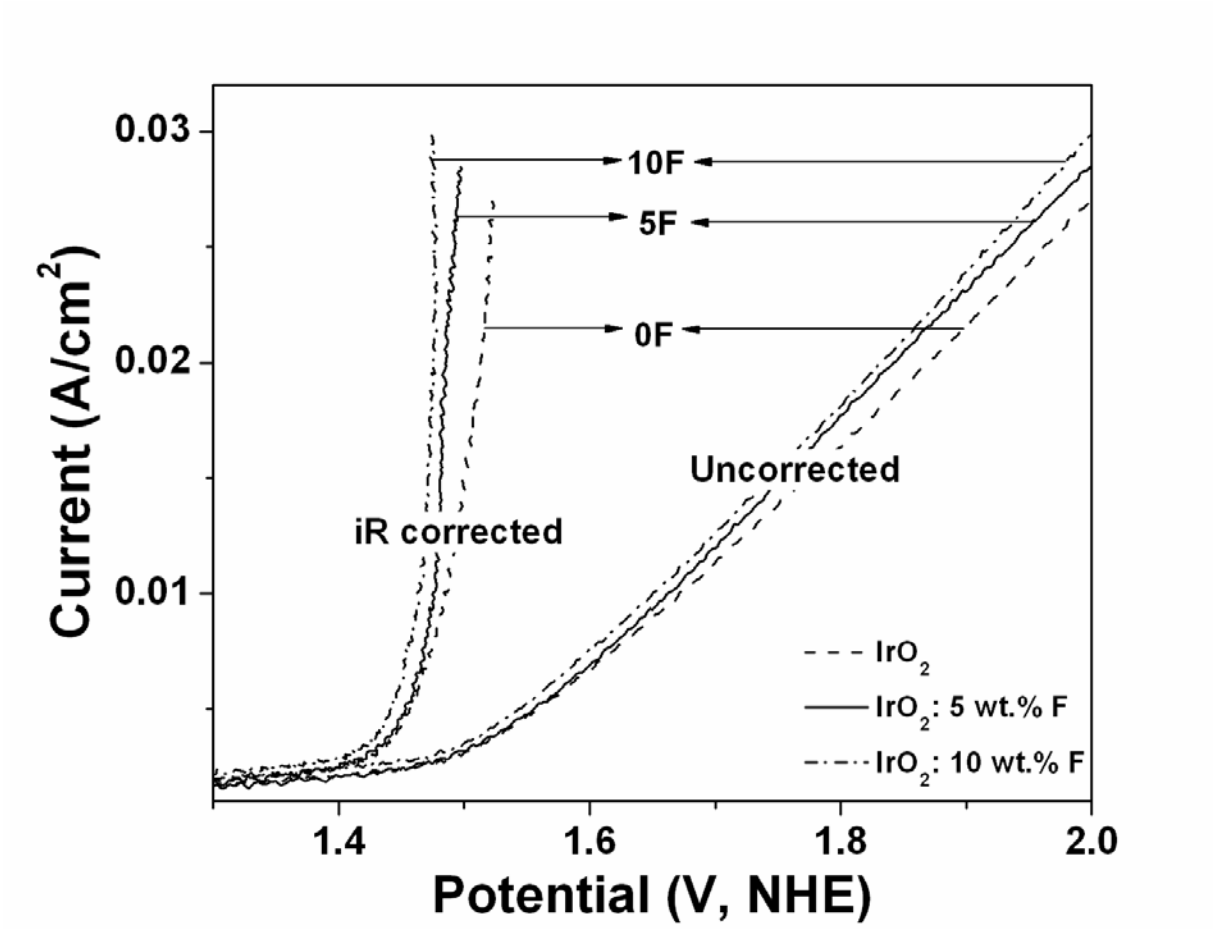

Figure 85. Polarization testing of undoped IrO_2, IrO_2:5 wt.% F and IrO_2:10 wt.% F conducted at a scan rate of 1 mV/sec in 1 N H_2SO_4 at 40°C

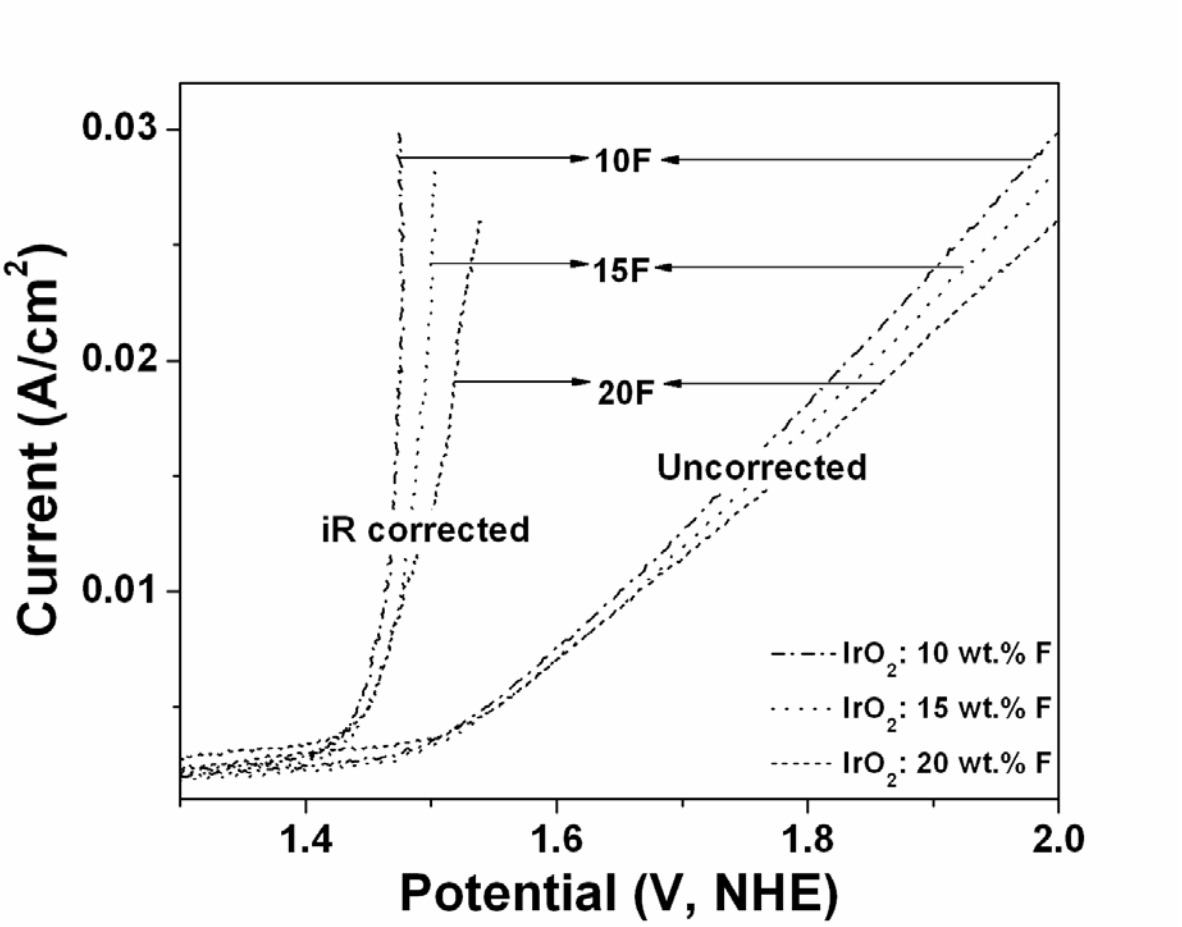

Figure 86. Polarization testing of IrO_2:10 wt.% F, IrO_2:15 wt.% F and IrO_2:20 wt.% F conducted at a scan rate of 1 mV/sec in 1 N H_2SO_4 at 40°C

Figure 87, **Figure 88**, **Figure 89**, **Figure 90** and **Figure 91** show the uncorrected and iR corrected Tafel plots for IrO_2:F with 0, 5, 10, 15 and 20 wt.% F, respectively and the Tafel slopes are calculated from these iR corrected Tafel plots. An ideal Tafel slope of ~ 62 mV/dec would correspond to the well known two electron pathway mechanism, assuming a transfer coefficient of 0.5 [30, 48, 53]. It is observed that undoped pure IrO_2 has a Tafel slope of ~ 93 mV/dec. It has been determined that with 5, 10, 15 and 20 wt.% F doping of IrO_2, the Tafel slope is ~ 77

mV/dec, 64 mV/dec, 85 mV/dec and 116 mV/dec, respectively. The Tafel slopes along with other RDE parameters have been reported in **Table 7**. This explains the increase in electrochemical activity or current density, which is favored by a decrease in the Tafel slope and corresponding increase in F content up to 10 wt.% as demonstrated in the polarization curves (**Figure 85** and **Figure 86**). These results further confirm that 10wt.% F doped IrO_2 is the most optimized composition resulting in enhanced catalytic activity with the least Tafel slope.

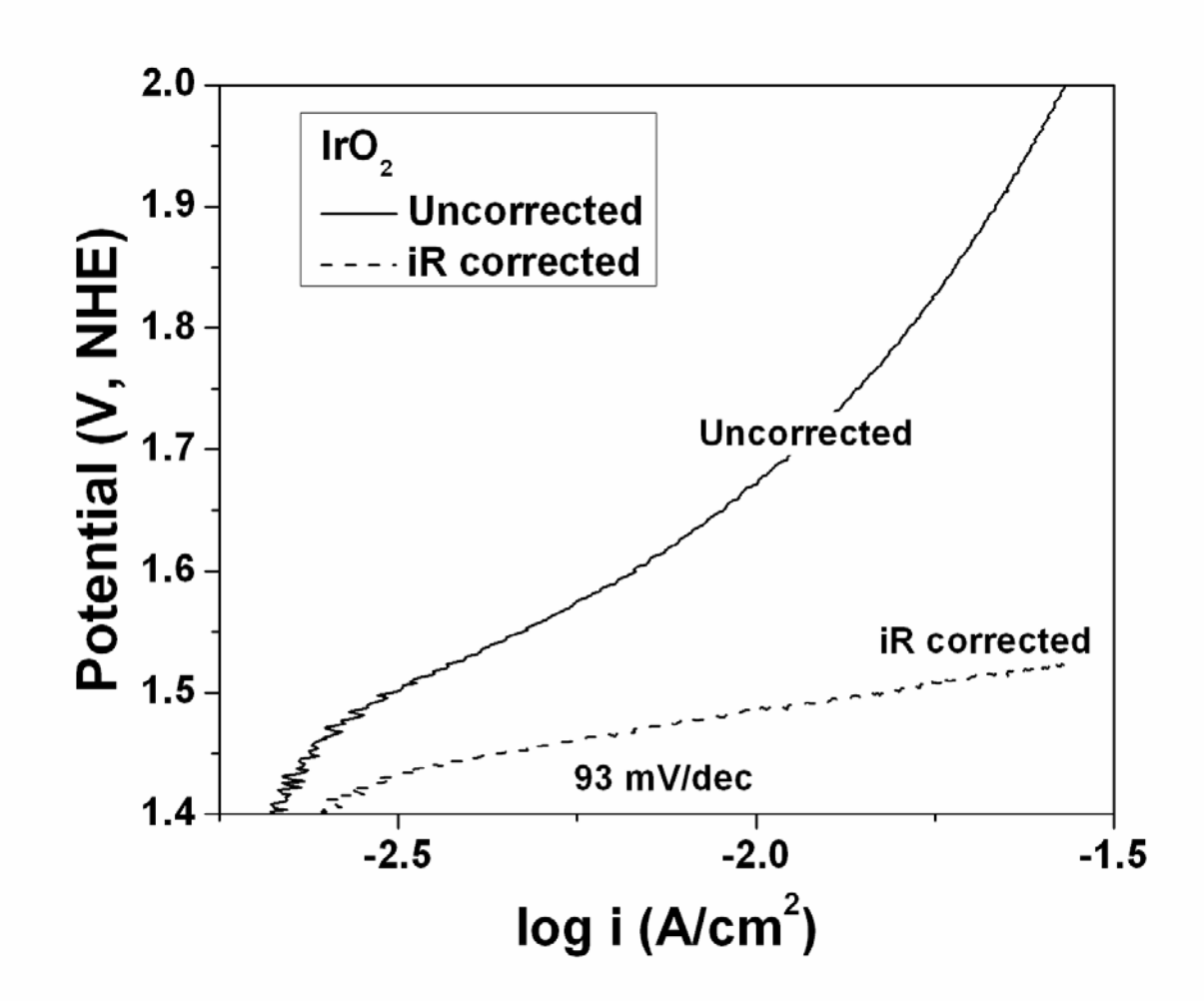

Figure 87. The Tafel plot of undoped IrO_2 before and after iR correction

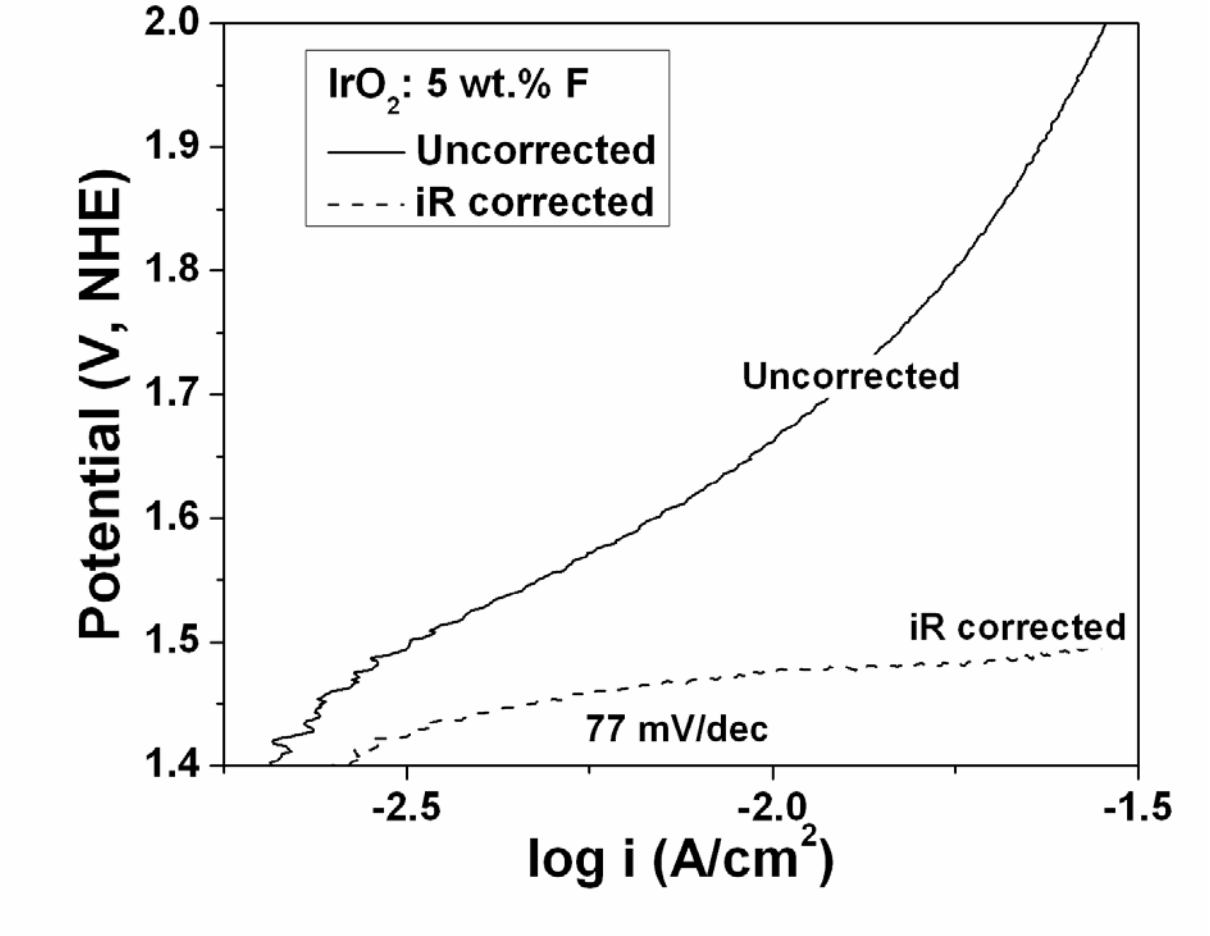

Figure 88. The Tafel plot of IrO_2:5 wt.% F before and after iR correction

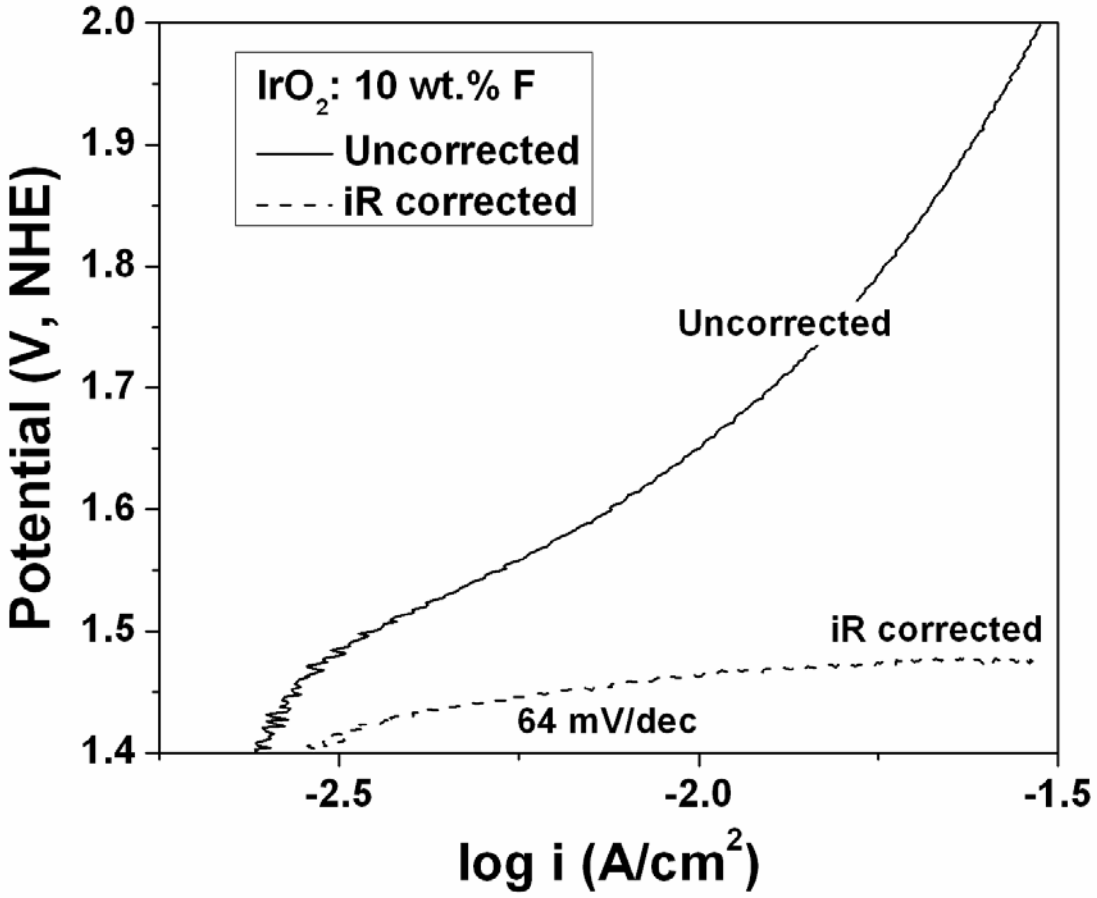

Figure 89. The Tafel plot of IrO_2:10 wt.% F before and after iR correction

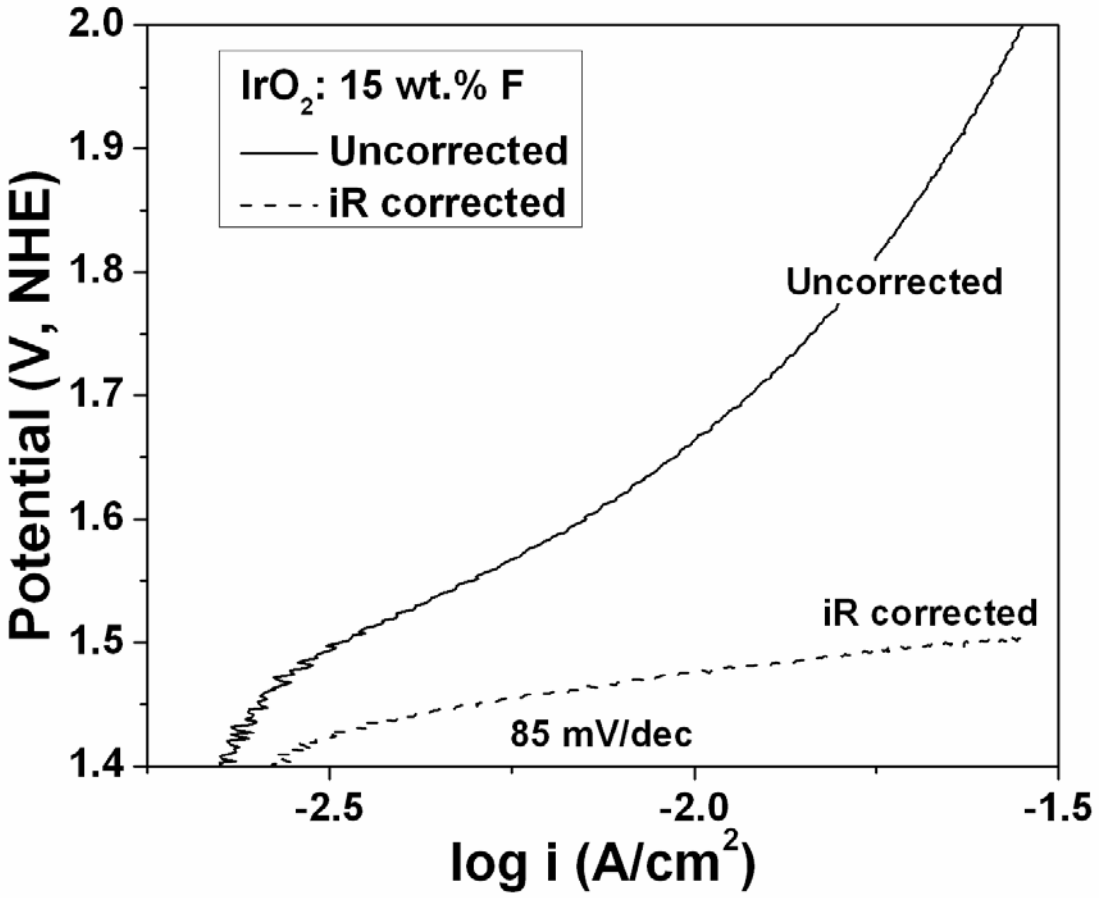

Figure 90. The Tafel plot of IrO_2:15 wt.% F before and after iR correction

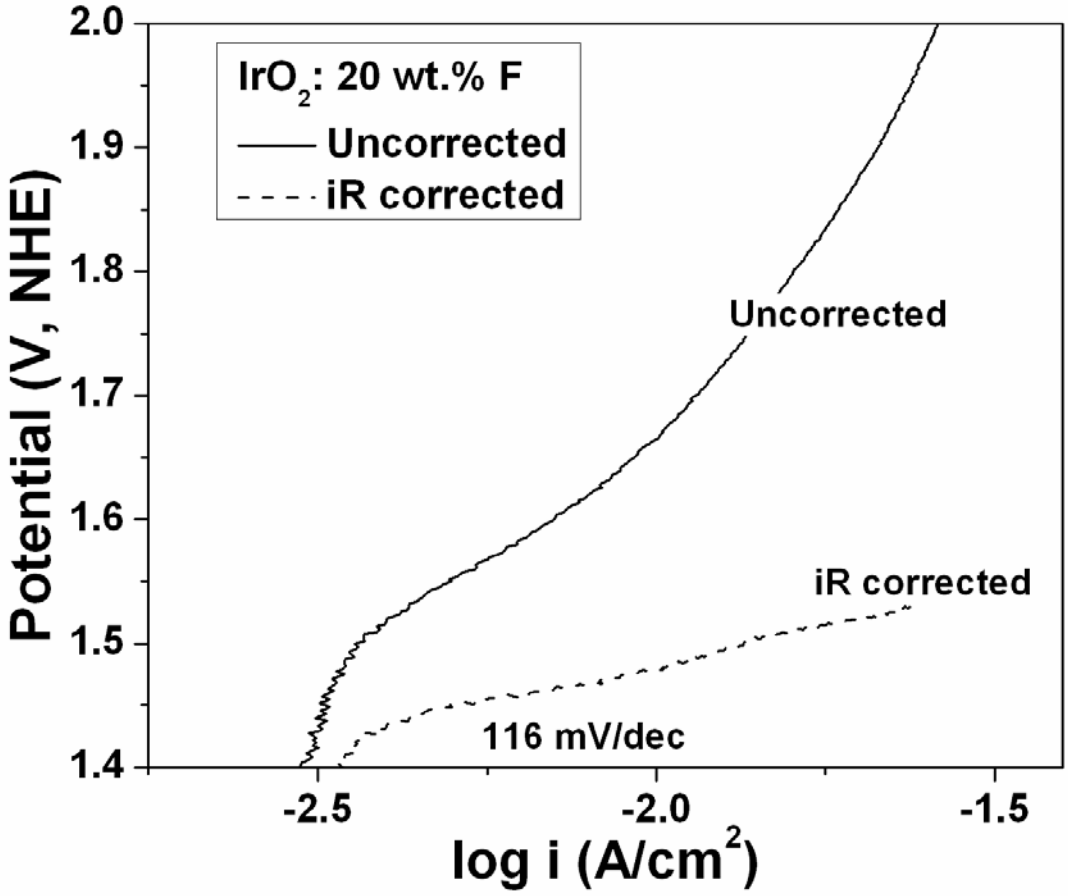

Figure 91. The Tafel plot of IrO_2:20 wt.% F before and after iR correction

Table 7. The Tafel slope, number of electrons transferred in the OER and the kinetic rate constant from the Koutecky - Levich plots for IrO_2:F

F doping (wt. %)	Tafel slope (mV/dec)	n	k (cm/s)		
			1.55 V	1.65 V	1.75 V
0	93	1.78	0.0618	0.0708	0.0826
5	77	1.86	0.0660	0.0763	0.0853
10	64	1.92	0.0656	0.0717	0.0823
15	85	1.82	0.0652	0.0743	0.0874
20	116	1.61	0.0679	0.0810	0.1010

Multiple small potential step voltammetry was performed for the rotating disk electrode studies in order to study the fundamental kinetics and calculate the apparent activation energy of the OER. The catalyst ink coated Ti disk insert was rotated at speeds varying from 500 rpm to 2000 rpm. **Figure 92** and **Figure 93** shows the Koutecky - Levich plot *i.e.* i^{-1} *vs.* $\omega^{-1/2}$ for undoped IrO_2 and IrO_2:5 wt.% F, respectively. **Figure 94**, **Figure 95** and **Figure 96** shows the Koutecky - Levich plot for IrO_2:10 wt.% F, IrO_2:15 wt.% F and IrO_2:20 wt.% F, respectively. The current values at different rotation speeds have been plotted at three potentials of 1.55 V, 1.65 V and 1.75 V (*vs.* NHE) without iR correction. The potentials are not iR corrected since the tests have been conducted in-situ (*via* multiple small potential step voltammetry) from which the RDE results are reported directly. This dynamic testing process does not allow accounting for the

iR drop from the solution resistance. These RDE plots at different potentials give parallel straight lines of similar nature; and the current increases with increase in voltage as expected, causing a decrease in the value of i^{-1}. At any given potential and rotation speed, it is observed that the current density increases categorically when the F doping is increased up to 10 wt.% and then decreases with 15 and 20 wt.% F doping. This trend is thus consistent with the results obtained from the polarization curves (**Figure 85** and **Figure 86**). From the slope of the graphs, the number of electrons transferred (n) is determined as explained in **Section 4.4.4**. The average value of 'n' determined at the three voltages for all IrO_2:F electro-catalysts along with the Tafel slope and kinetic rate constant (k) has been tabulated in **Table 7**. The kinetic rate constant of an electrochemical reaction not only varies with the applied potential, but is also dependent on many other factors *viz.*, temperature, electrode surface structure, composition of the catalyst, surface adsorption and reaction intermediates [95, 96, 102, 103]. The RDE tests and the Koutecky - Levich plot confirm the two electron pathway mechanism for the OER in PEM electrolysis for all our explored catalyst compositions. The 'n' value is closest to 2 for IrO_2:10 wt.% F doped electro-catalyst (**Figure 94**) corroborating the fact that it is the best composition amongst all the other F doped and undoped IrO_2 electro-catalyst. Increased F doping (above 10 wt.% F) leads to slight decrease in the 'n' value which is the number of electrons transferred during the OER. This is because the polarization resistance increases as observed in the impedance plots and reported in **Table 6**, impeding the electron transfer process in the electrochemical interface. This in turn also gives us lesser values of current density for the catalysts with higher F doping amounts as seen in the polarization curves (**Figure 86**). This further elucidates the high electrochemical activity and the close to ideal Tafel slope of the 10

wt.% F doped IrO_2, portending it to be a preferred OER electro-catalyst composition for PEM electrolyzer cells.

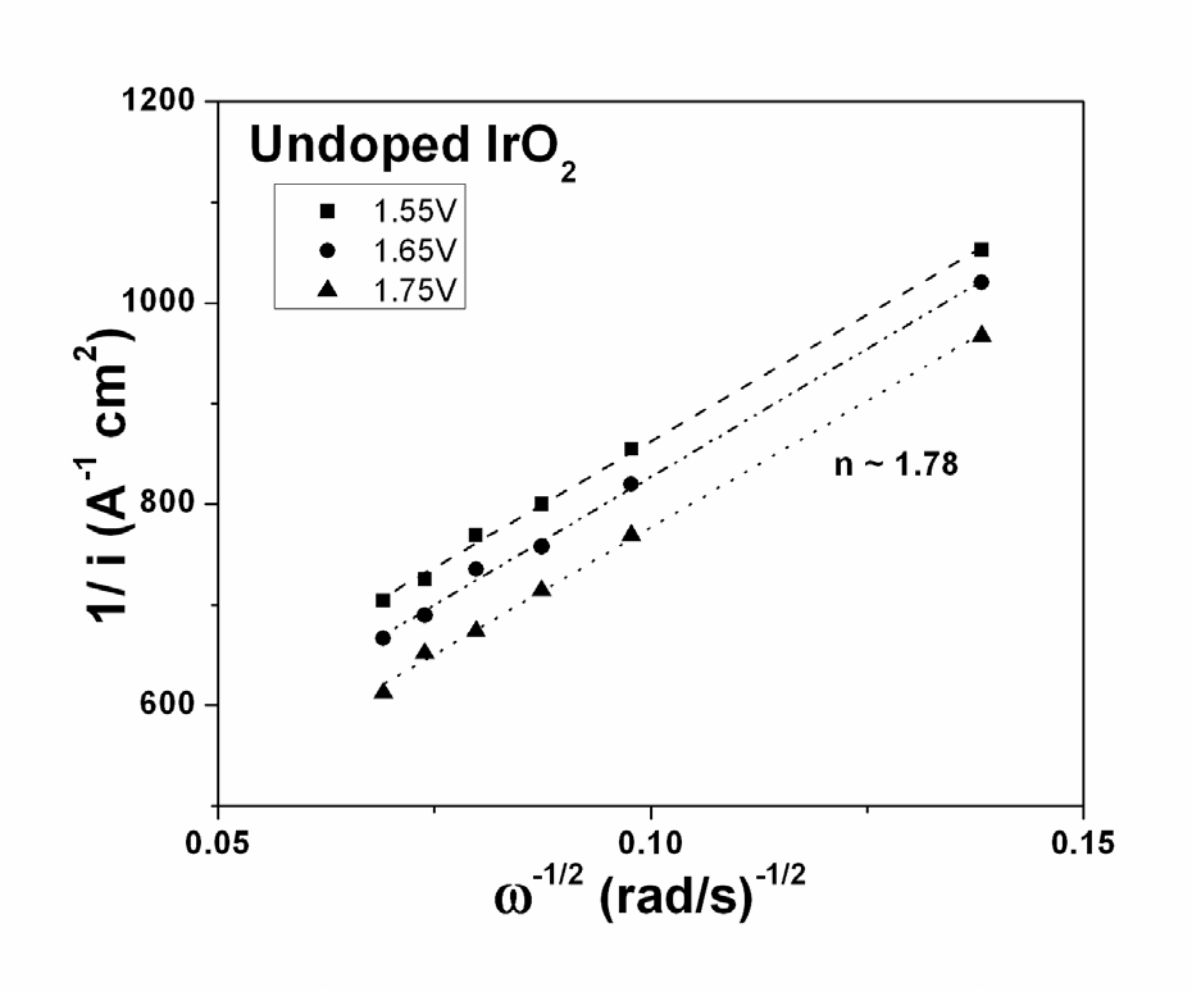

Figure 92. Koutecky - Levich plots in PEM based water electrolysis at 1.55 V, 1.65 V and 1.75 V (*vs.* NHE) in 1 N H_2SO_4 at 25°C for undoped IrO_2

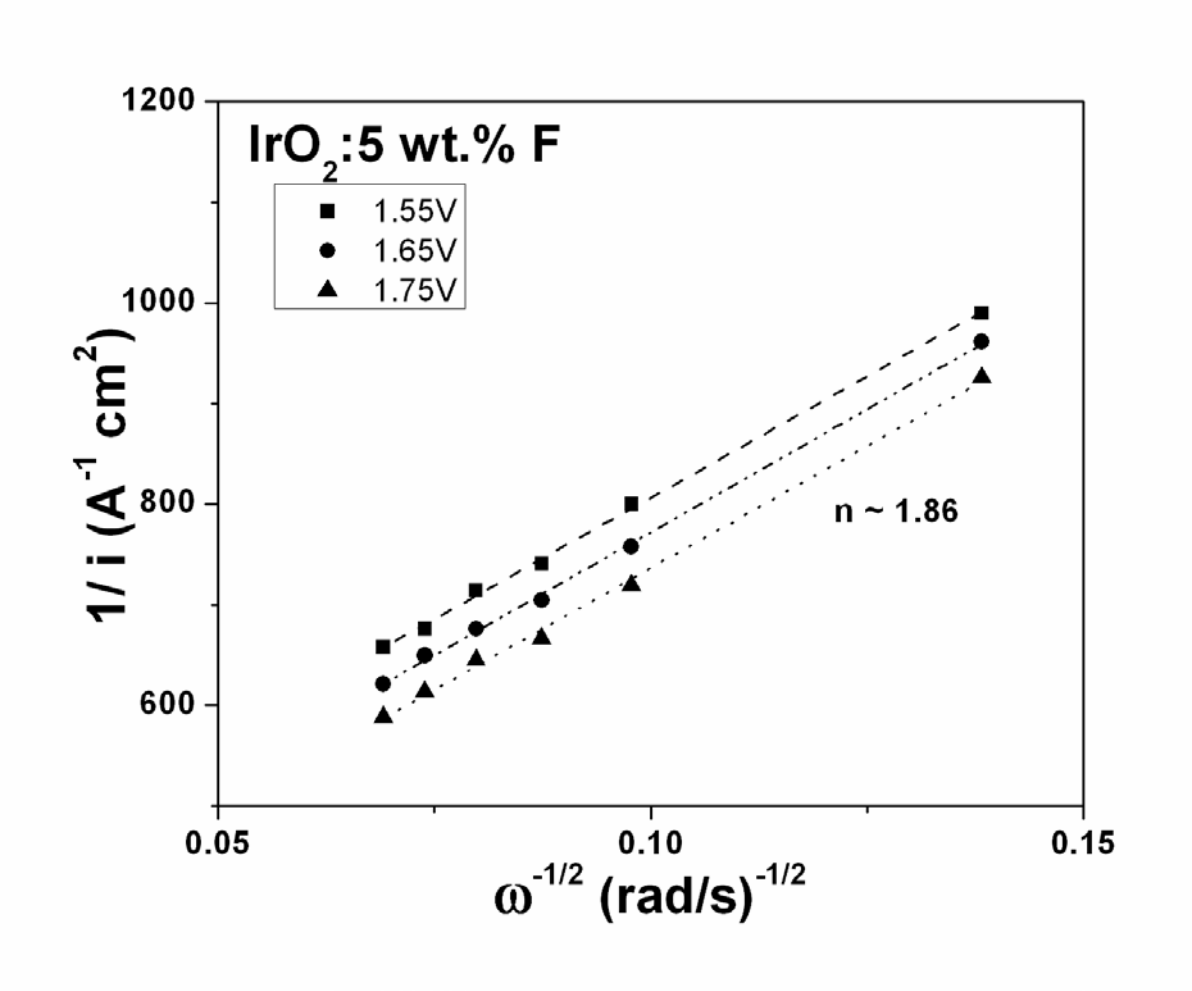

Figure 93. Koutecky - Levich plots in PEM based water electrolysis at 1.55 V, 1.65 V and 1.75 V (*vs.* NHE) in 1 N H_2SO_4 at 25°C for IrO_2:5 wt.% F

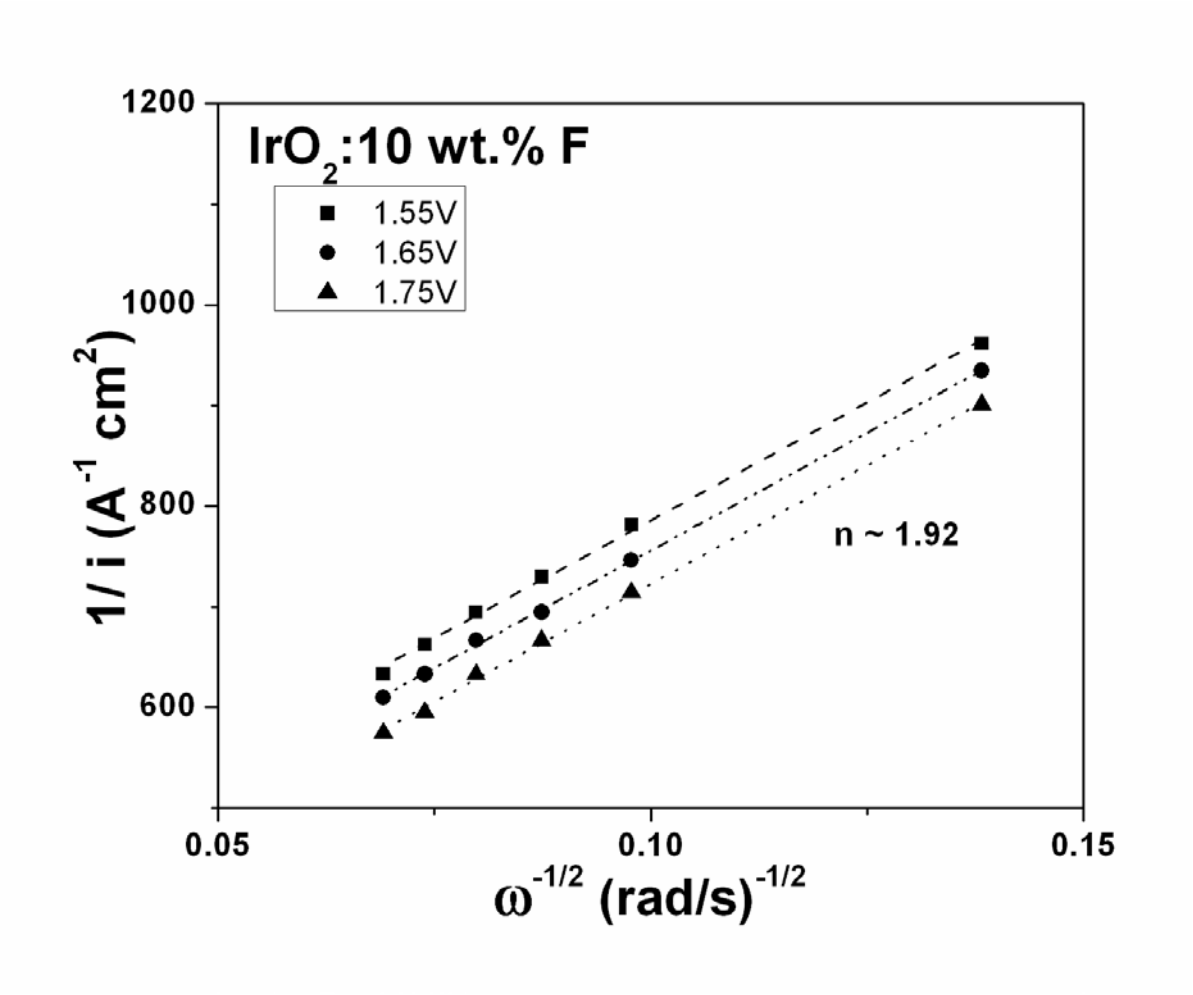

Figure 94. Koutecky - Levich plots in PEM based water electrolysis at 1.55 V, 1.65 V and 1.75 V (*vs.* NHE) in 1 N H_2SO_4 at 25°C for IrO_2:10 wt.% F

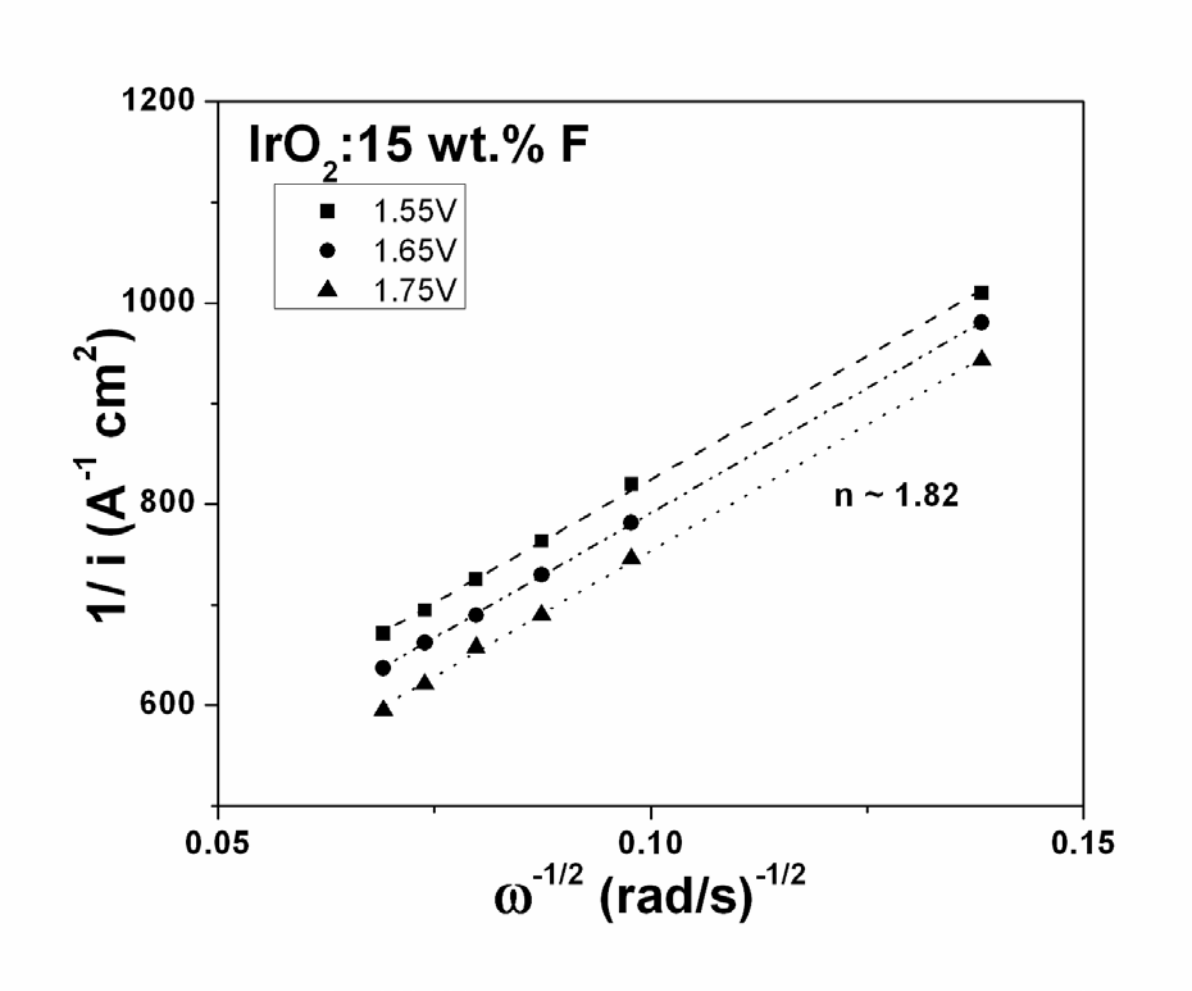

Figure 95. Koutecky - Levich plots in PEM based water electrolysis at 1.55 V, 1.65 V and 1.75 V (*vs.* NHE) in 1 N H_2SO_4 at 25°C for IrO_2:15 wt.% F

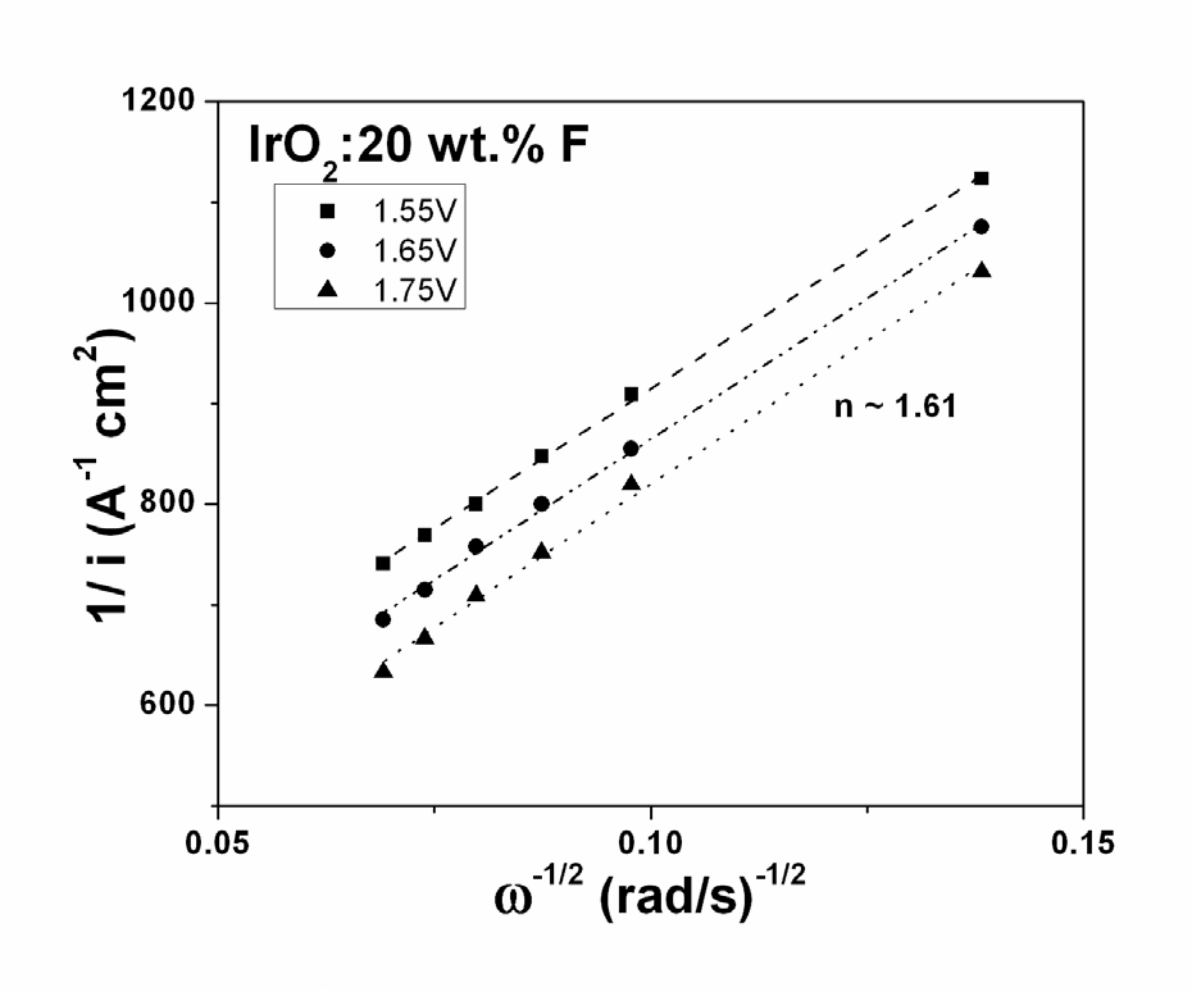

Figure 96. Koutecky - Levich plots in PEM based water electrolysis at 1.55 V, 1.65 V and 1.75 V (*vs.* NHE) in 1 N H_2SO_4 at 25°C for IrO_2:20 wt.% F

The influence of temperature on the OER was studied in order to calculate apparent activation energy from the Arrhenius relationship as explained previously in **Section 4.4.4**. The Arrhenius plots *i.e.* ln i *vs.* T^{-1} for IrO_2, IrO_2:5 wt.% F, IrO_2:10 wt.% F, IrO_2:15 wt.% F and IrO_2:20 wt.% F, are shown in **Figure 97**, **Figure 98**, **Figure 99**, **Figure 100**, and **Figure 101** respectively. The temperature was varied between 25 - 70°C and data points in these graphs have been plotted at three different potentials of 1.55 V, 1.65 V and 1.75 V (*vs.* NHE) as used before.

The slopes of these lines was averaged in order to calculate the E_a which is ~ 25.2 ± 1.5 kJ/mol for the IrO_2:F electro-catalysts. This E_a value is lesser and in the range and order of values reported for the OER by other researchers [97, 98, 104-107]. The E_a value for all the electrodes being similar suggests that the OER on all electrodes proceeds *via* the same reaction mechanism [97, 108]. The reaction mechanism has been previously reported by Nørskov *et al.* and in our earlier publication [53-55]. This four step reaction mechanism occurring during PEM based water electrolysis has been reported in **Section 2.2.2**.

Although there is no difference in the activation barrier owing to similar E_a values for all the synthesized powder catalysts, the inherent kinetics are most optimal for the IrO_2:10 wt.% F electro-catalyst possibly due to difference in the activity and number of catalytically active sites [108]. This has not only been confirmed from the polarization curves (**Figure 85** and **Figure 86**), but is also evident from the different 'n' values obtained from the Koutecky - Levich plots (**Table 7**). This is because of the difference in the anodic polarization and charge transfer properties as observed in the impedance and Tafel plots.

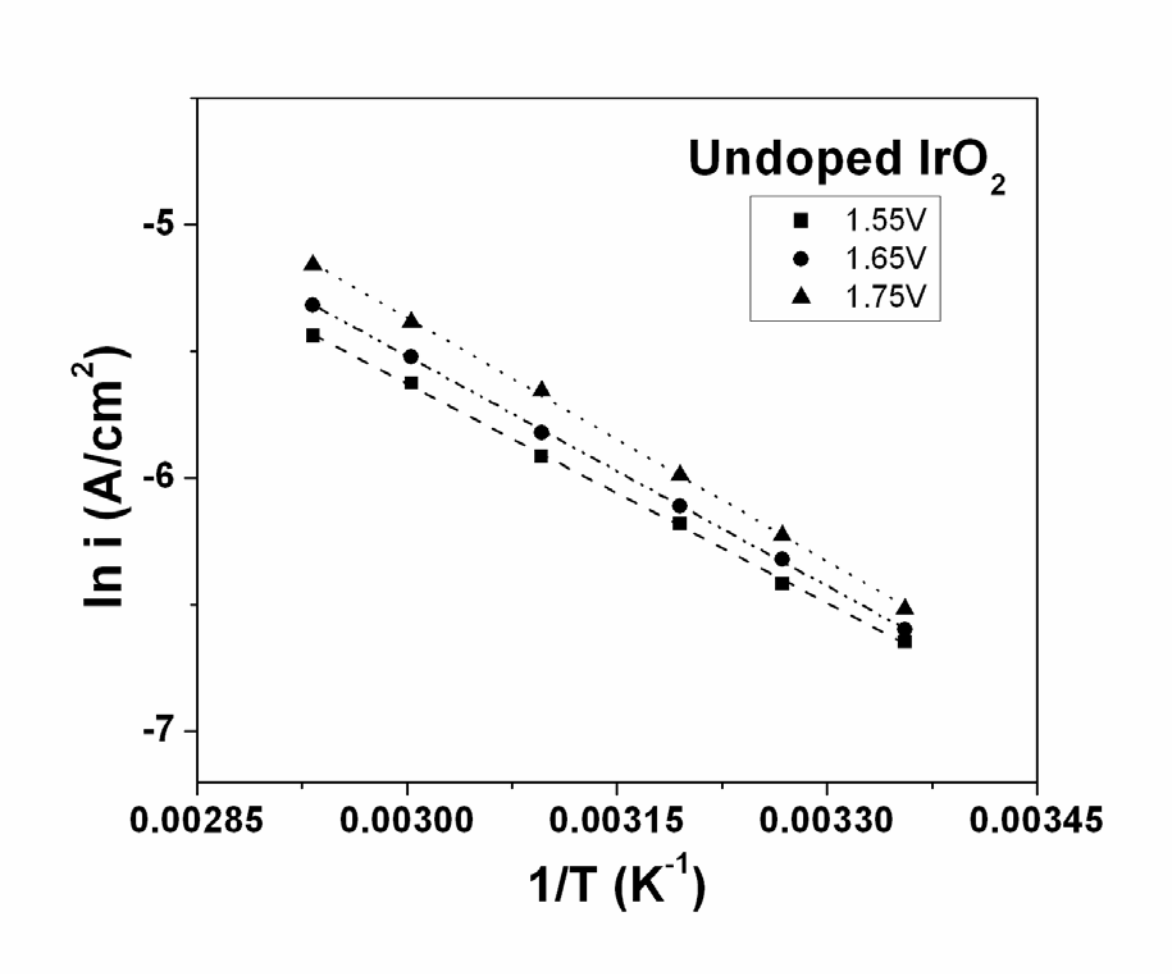

Figure 97. Arrhenius plots for undoped IrO_2 over a temperature range of 25°C to 70°C in 1 N H_2SO_4

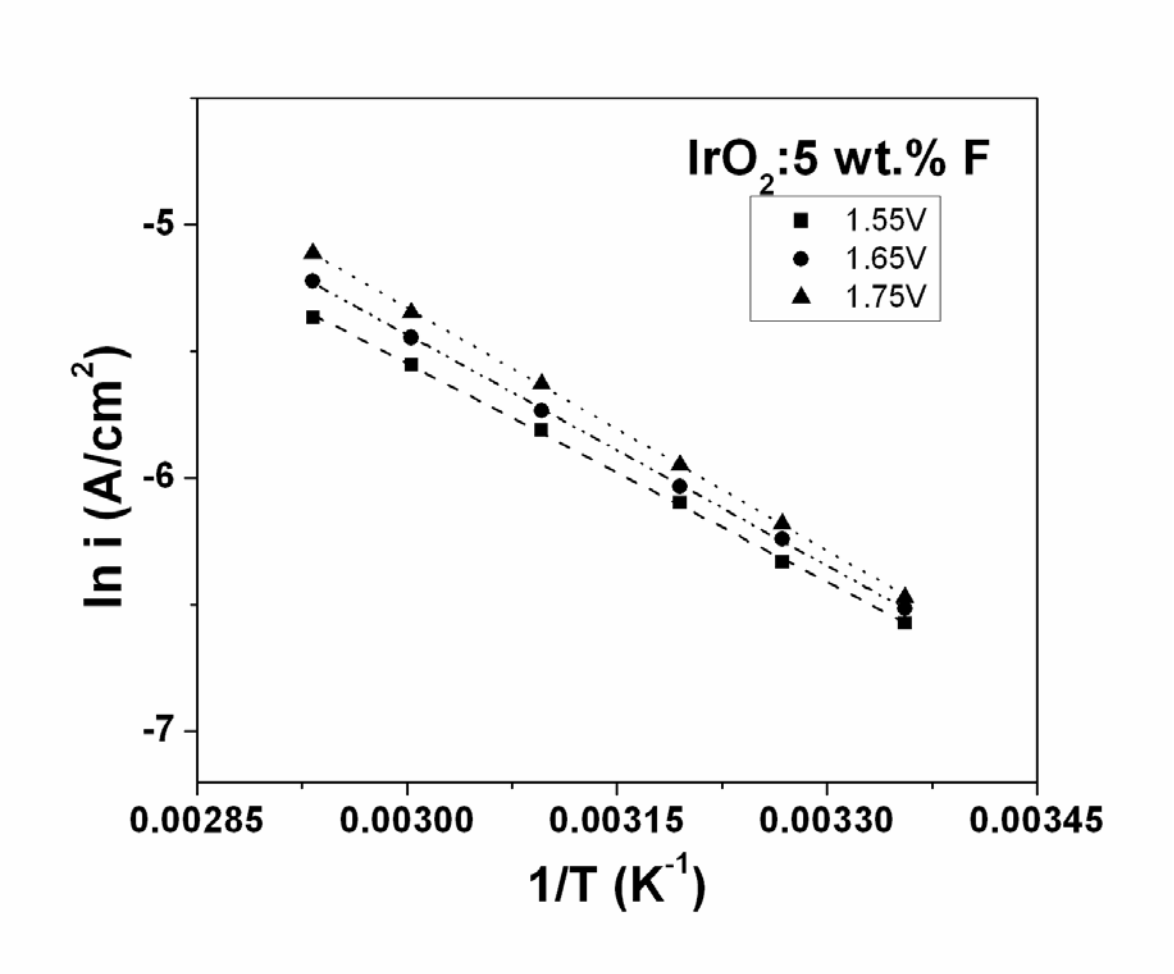

Figure 98. Arrhenius plots for IrO_2:5 wt.% F over a temperature range of 25°C to 70°C in 1 N H_2SO_4

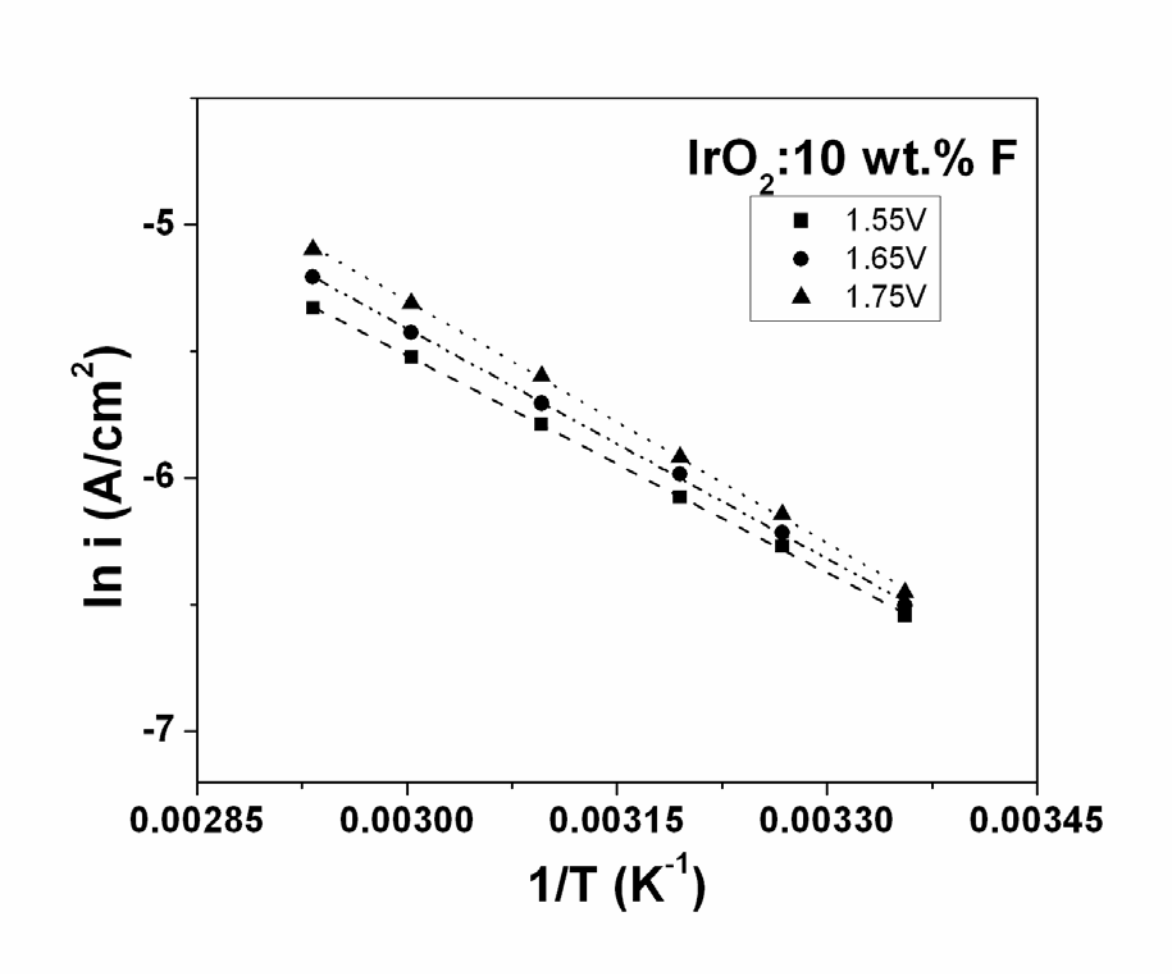

Figure 99. Arrhenius plots for IrO_2:10 wt.% F over a temperature range of 25°C to 70°C in 1 N H_2SO_4

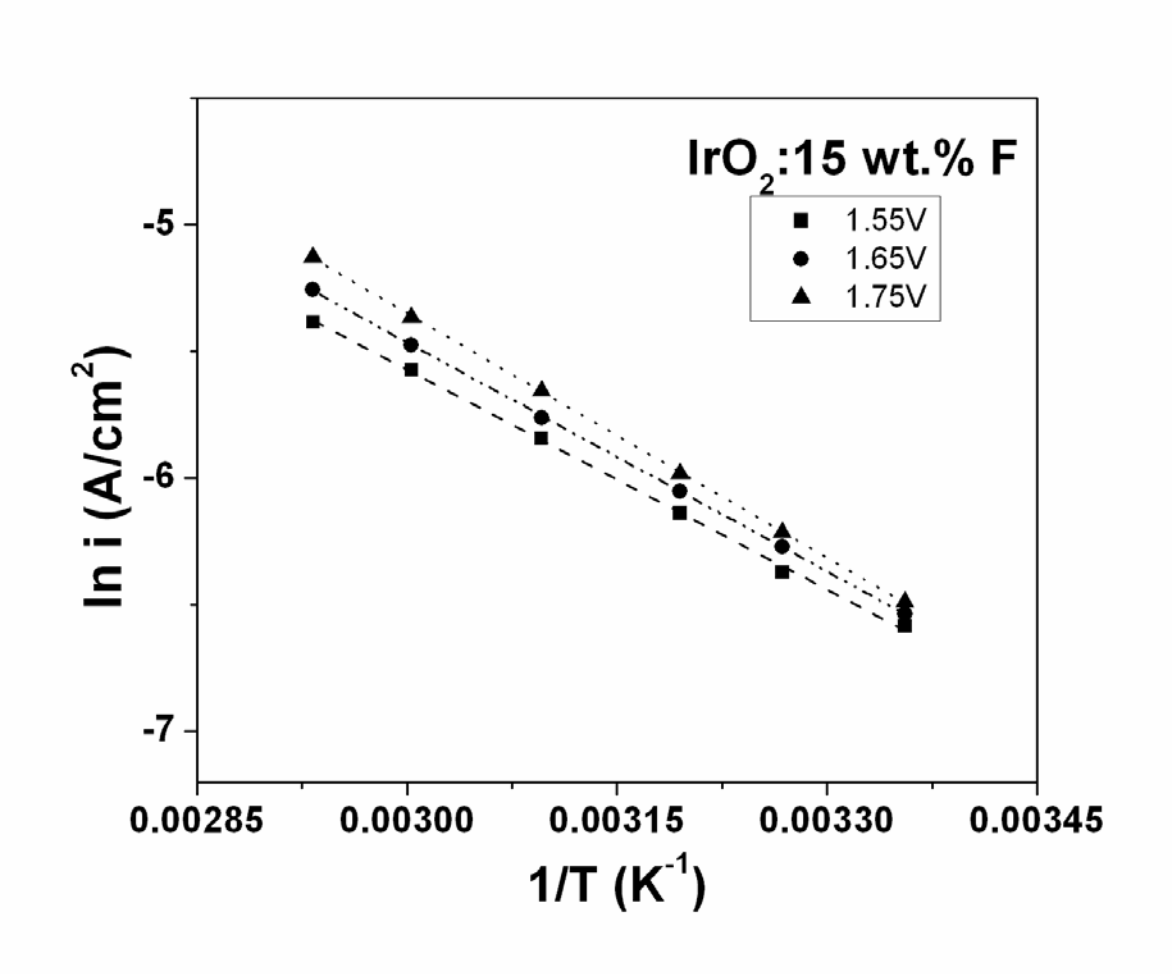

Figure 100. Arrhenius plots for IrO_2:15 wt.% F over a temperature range of 25°C to 70°C in 1 N H_2SO_4

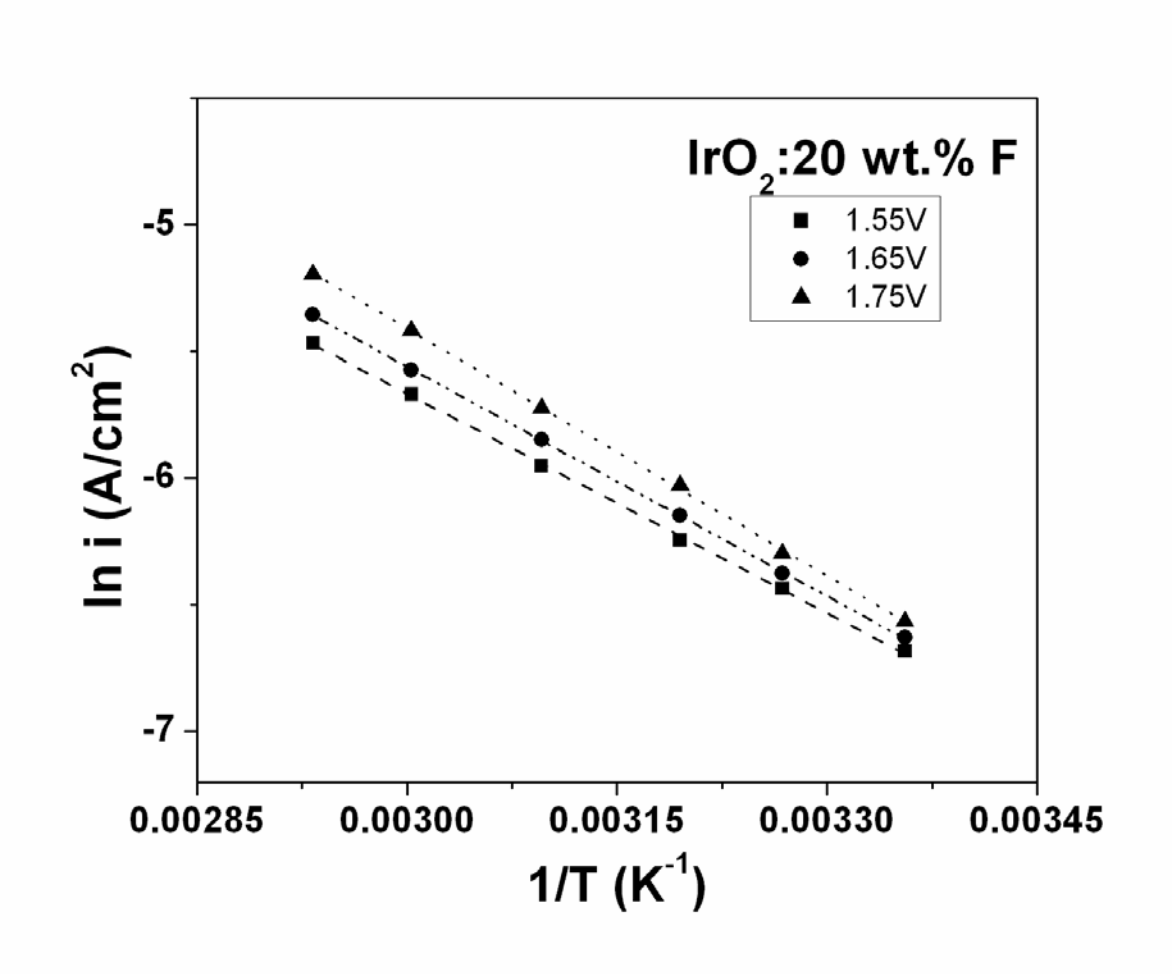

Figure 101. Arrhenius plots for IrO_2:20 wt.% F over a temperature range of 25°C to 70°C in 1 N H_2SO_4

The robustness and chemical stability of the synthesized electro-catalysts have been studied by chronoamperometry (CA) testing. **Figure 102** shows the CA curves for the IrO_2:F catalysts conducted at a constant voltage of ~ 1.65 V (*vs.* NHE) without iR correction for 12 hours. The IrO_2:10 wt.% F electrode shows higher current than the other electrodes since it inherently has higher catalytic activity. A steady decay of current may arise due to the dissolution of the catalyst material along the edges of the support [24, 30, 58], or due to

continuous exhaustion of the electrolyte/fuel (H_2SO_4) owing to the high electrochemical activity of the electro-catalysts [34, 59, 120]. It is evident in **Figure 102** by the slope of the different curves that the higher fluorine doped catalysts *i.e.* IrO_2 doped with 15 and 20 wt.% F degrade slightly faster than the undoped, 5 and 10 wt.% F doped IrO_2. The best powder electro-catalyst material reported herein (IrO_2:10 wt.% F), shows excellent durability and current retention, albeit exhibiting very high electrochemical activity. On an overall basis, the CA response shows an acceptable stability with respect to the drop in current observed and reported widely by researchers in other publications [57, 120, 121]. Inductively coupled plasma optical emission spectroscopy (ICP-OES) studies were conducted on the electrolyte media after the conclusion of the CA test (*i.e.* after 12 hours). No Ir was found to have leached out from any of the F doped or undoped IrO_2 catalysts, confirming that the drop in current is mainly because of the exhaustion of the fuel due to the high catalytic activity of the nanostructured powder electro-catalysts. The stability results complement and strengthen our earlier claims and findings; suggesting that IrO_2:10 wt.% F electro-catalyst is an optimized composition for use as an OER anode catalyst in PEM based water electrolysis.

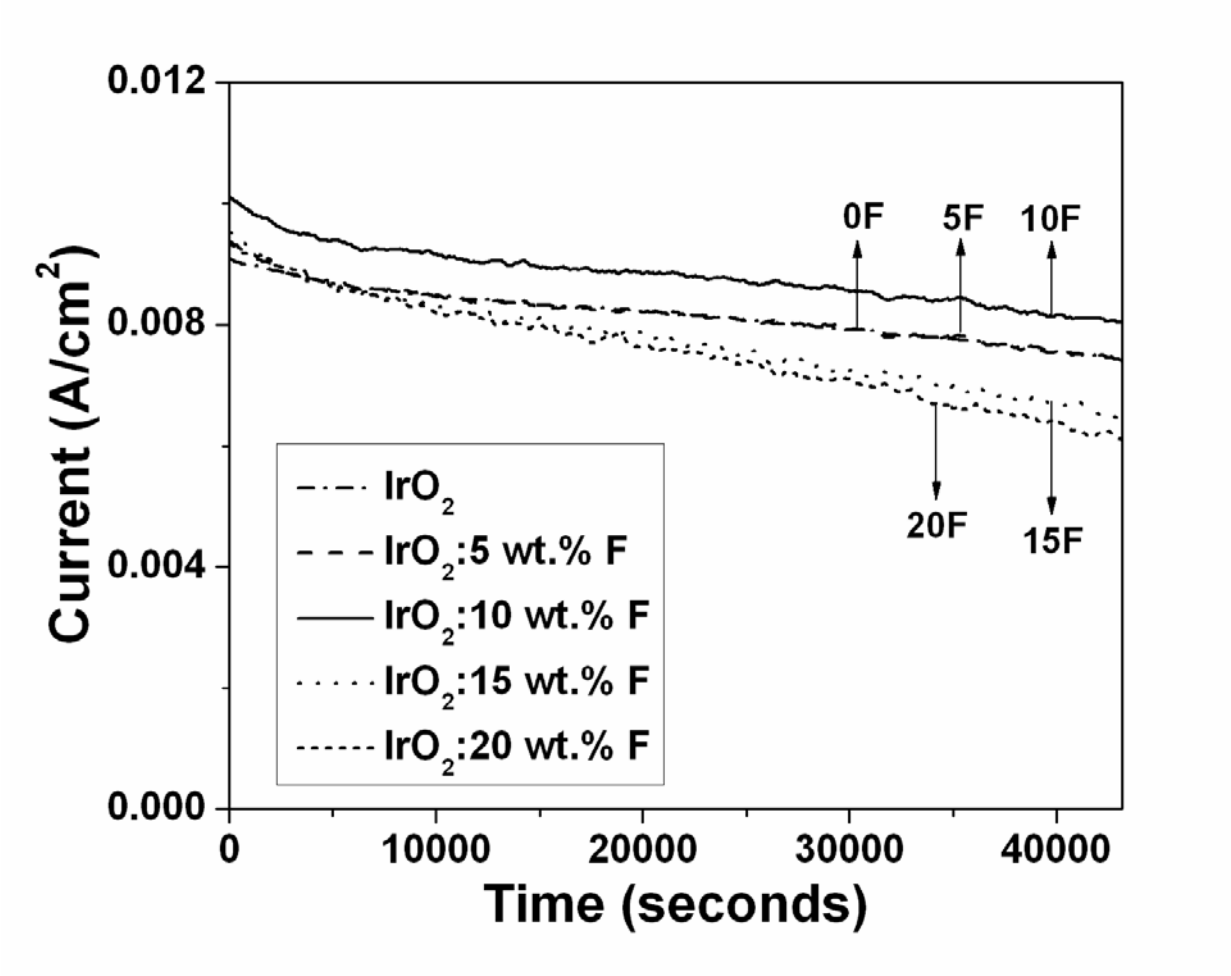

Figure 102. The variation of current *vs.* time for the IrO_2:F electrodes in 1 N H_2SO_4 under a constant potential of ~ 1.65 V at 40°C

After the conclusion of the CA test, the undoped and 10 wt.% F doped IrO_2 electrodes were subject to polarization testing as seen in **Figure 103** in order to determine the activity of the electrodes after long term structural stability tests. The Tafel plots from these polarization curves (post CA measurement) after iR correction are shown in **Figure 104** and **Figure 105**. A Tafel slope of ~ 112 mV/decade and ~ 90 mV/decade was obtained for undoped IrO_2 and IrO_2:10 wt.% F, respectively. This is slightly higher (~ 93 mV/decade for IrO_2 and ~ 64 mV/decade for IrO_2:10

wt.% F) but still close and comparable to the values obtained from the polarization tests conducted before CA (**Figure 87** and **Figure 89**). This test further demonstrates the robustness of the electro-catalysts.

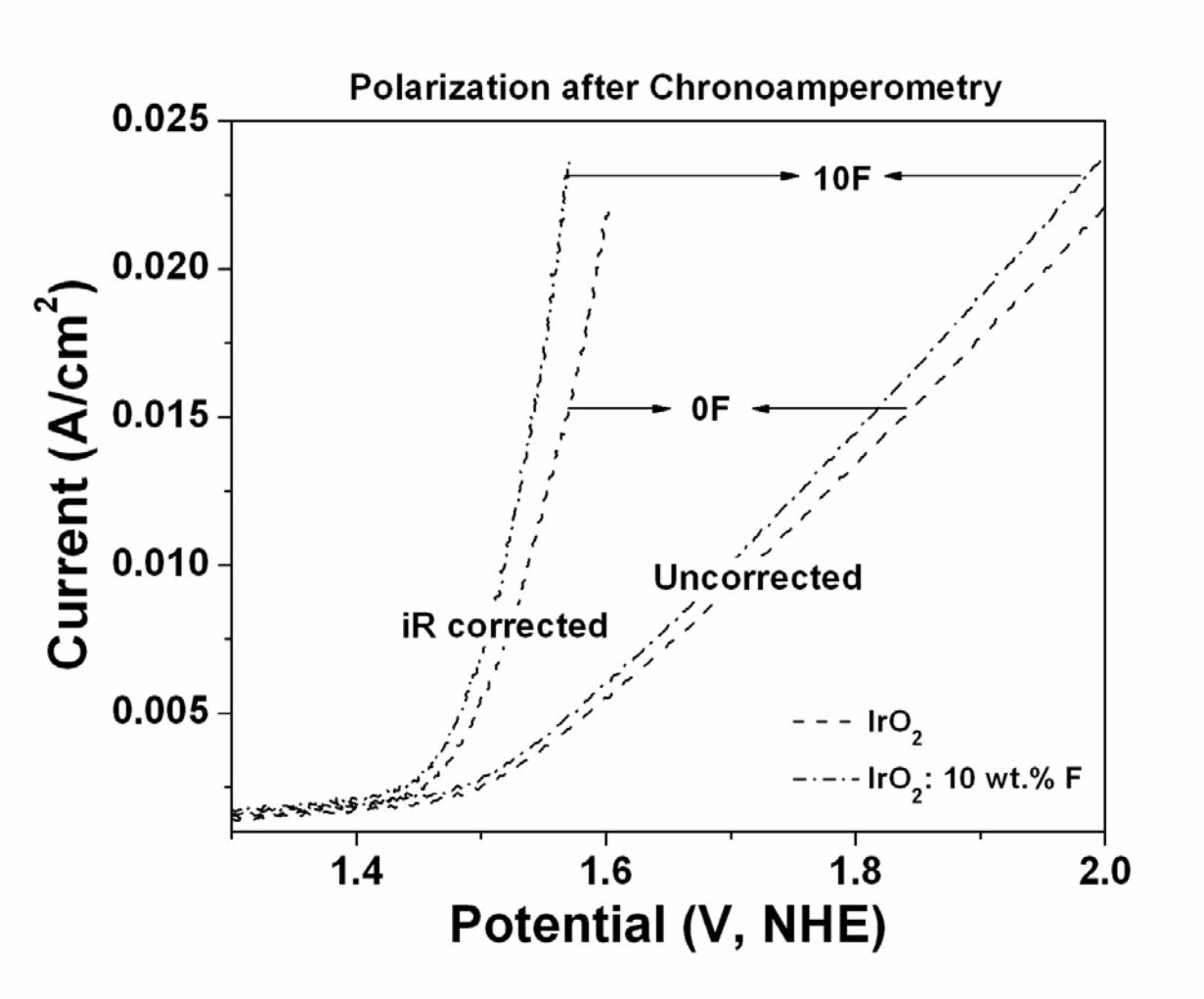

Figure 103. Polarization curve of undoped and 10 wt.% F doped IrO_2 after the CA test

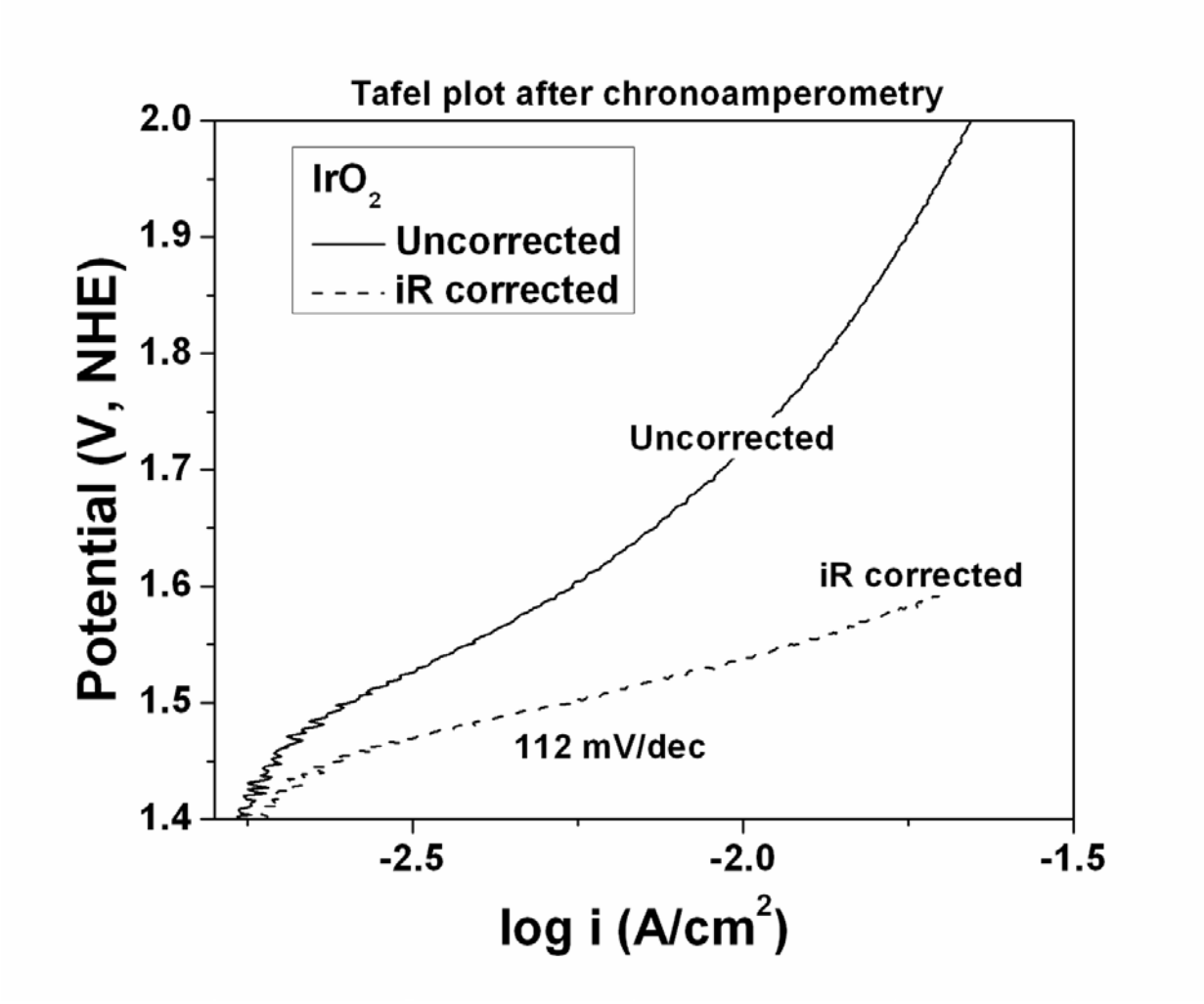

Figure 104. The Tafel plot of undoped IrO_2 powder after the CA test

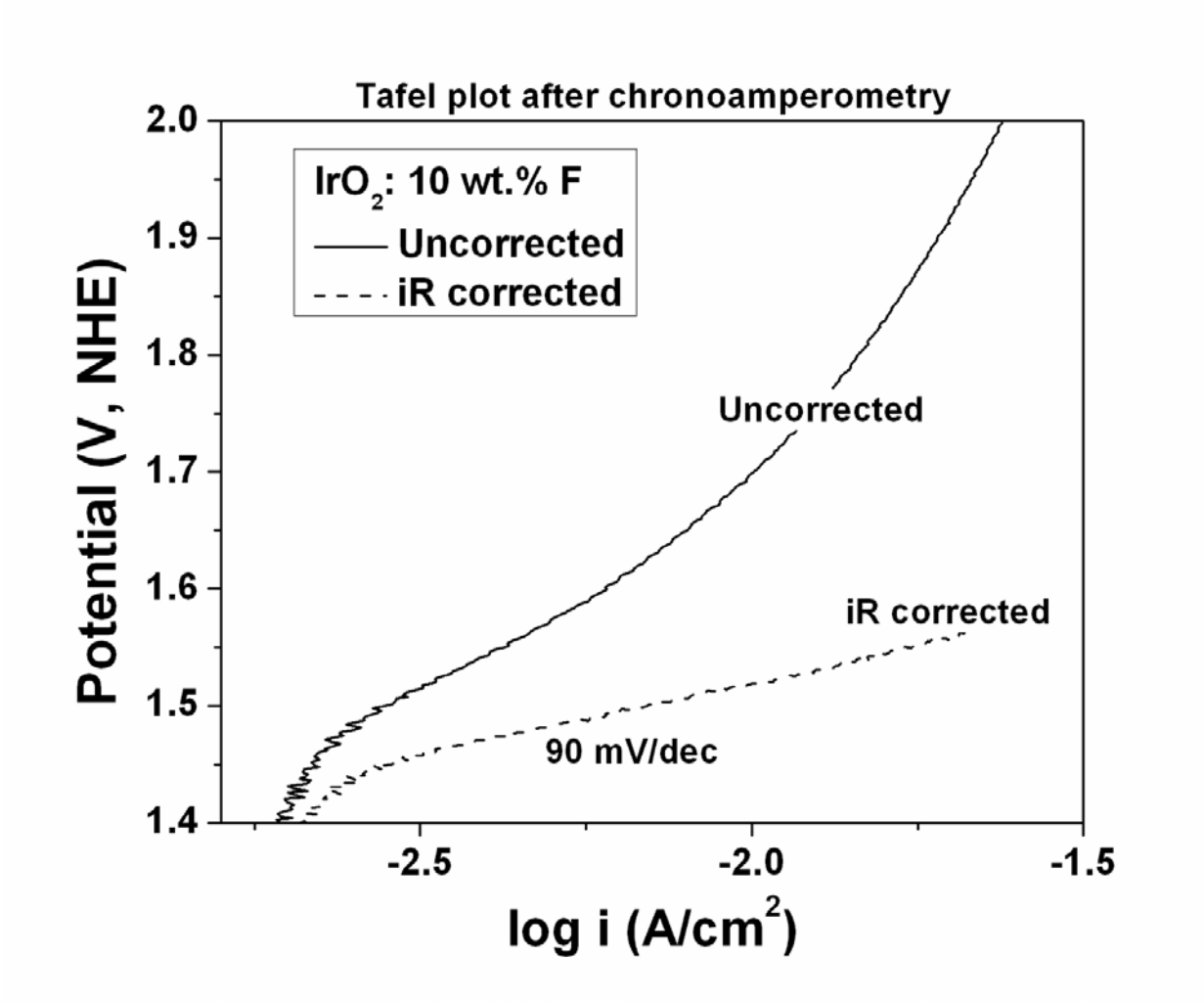

Figure 105. The Tafel plot of IrO_2:10 wt.% F powder after the CA test

Finally, the best electro-catalyst composition of IrO_2:10 wt.% F was tested at Proton OnSite in a single full cell set-up for PEM based water electrolysis. These results were compared with undoped pure IrO_2 which was also tested in the same conditions. The polarization curve, shown in **Figure 106**, was obtained by ramping up and down the current at 1 minute intervals until the forward and reverse scans overlaid each other. It is seen that the 10 wt.% F doped IrO_2 electro-catalyst exhibits much superior electro-catalytic activity than its undoped counterpart. The current density at ~ 2 V, a standard assessment voltage for single full PEM electrolyzer tests,

is ~ 1.1 A/cm^2 and ~ 0.5A/cm^2 for IrO_2:10 wt.% F and IrO_2, respectively. This implies an approximately 2.2 times rise in the current for the F doped electro-catalyst with respect to pure IrO_2. This is in good agreement with the polarization curves (**Figure 85**) and the increase in current observed. The polarization curves in the half cell and full cell set-up, along with the electrochemical impedance spectra, Tafel plots and the RDE graphs confirm that 10 wt.% F doping enhances the electrochemical activity of IrO_2 to a very great extent. A higher loading of pure IrO_2 (~ 3.4 mg) was done for the full cell PEM electrolyzer test at at 50°C and 80°C, and the results have been shown in **Figure 107**. The polarization curves show much more electrochemical activity as expected. The current density at ~ 2 V is ~ 0.8 A/cm^2 and ~ 1.75 A/cm^2, for the tests at 50°C and 80°C, respectively.

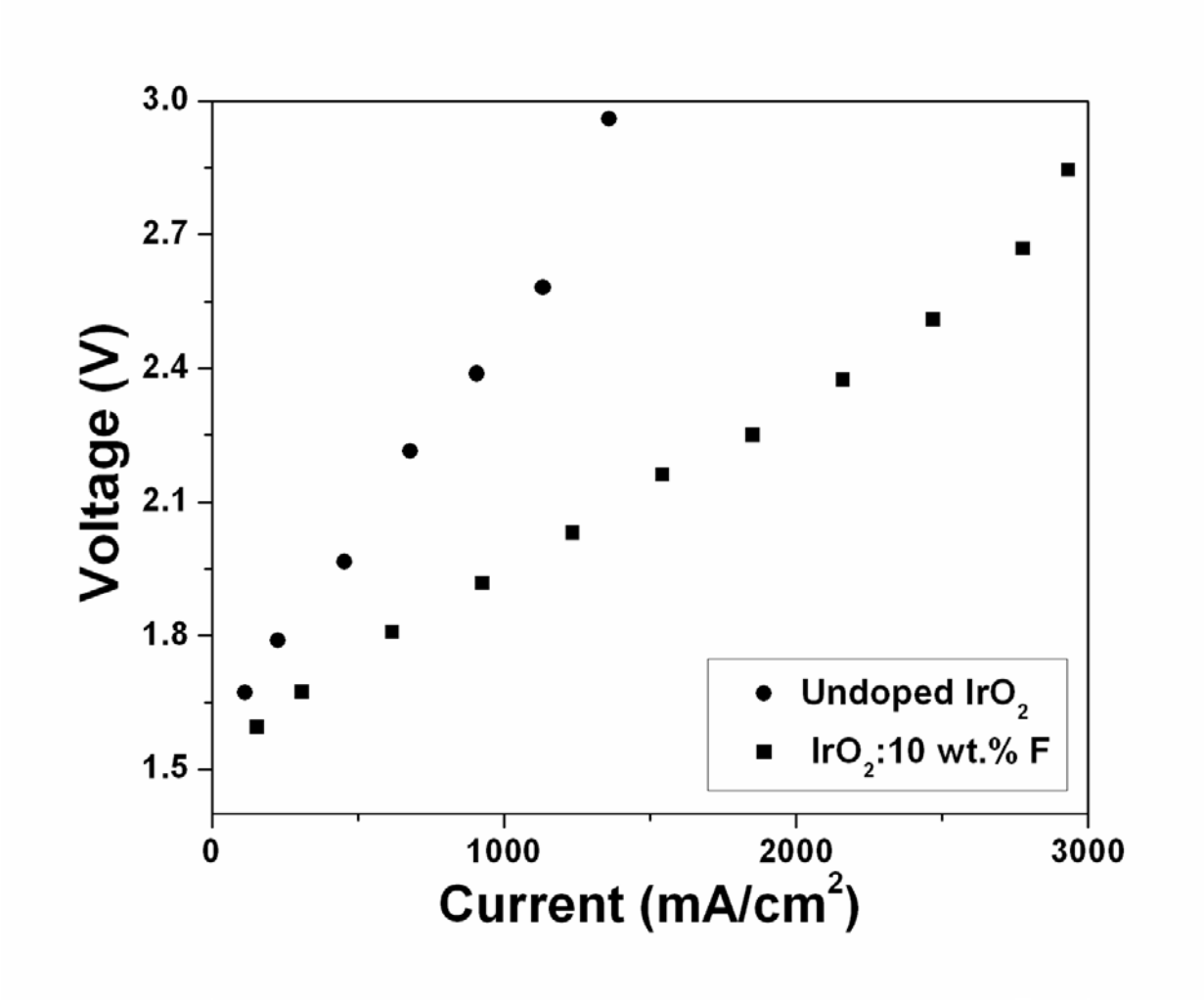

Figure 106. Polarization curve obtained in a single full cell PEM electrolyzer test for undoped IrO_2 and IrO_2:10 wt.% F powders at 50°C

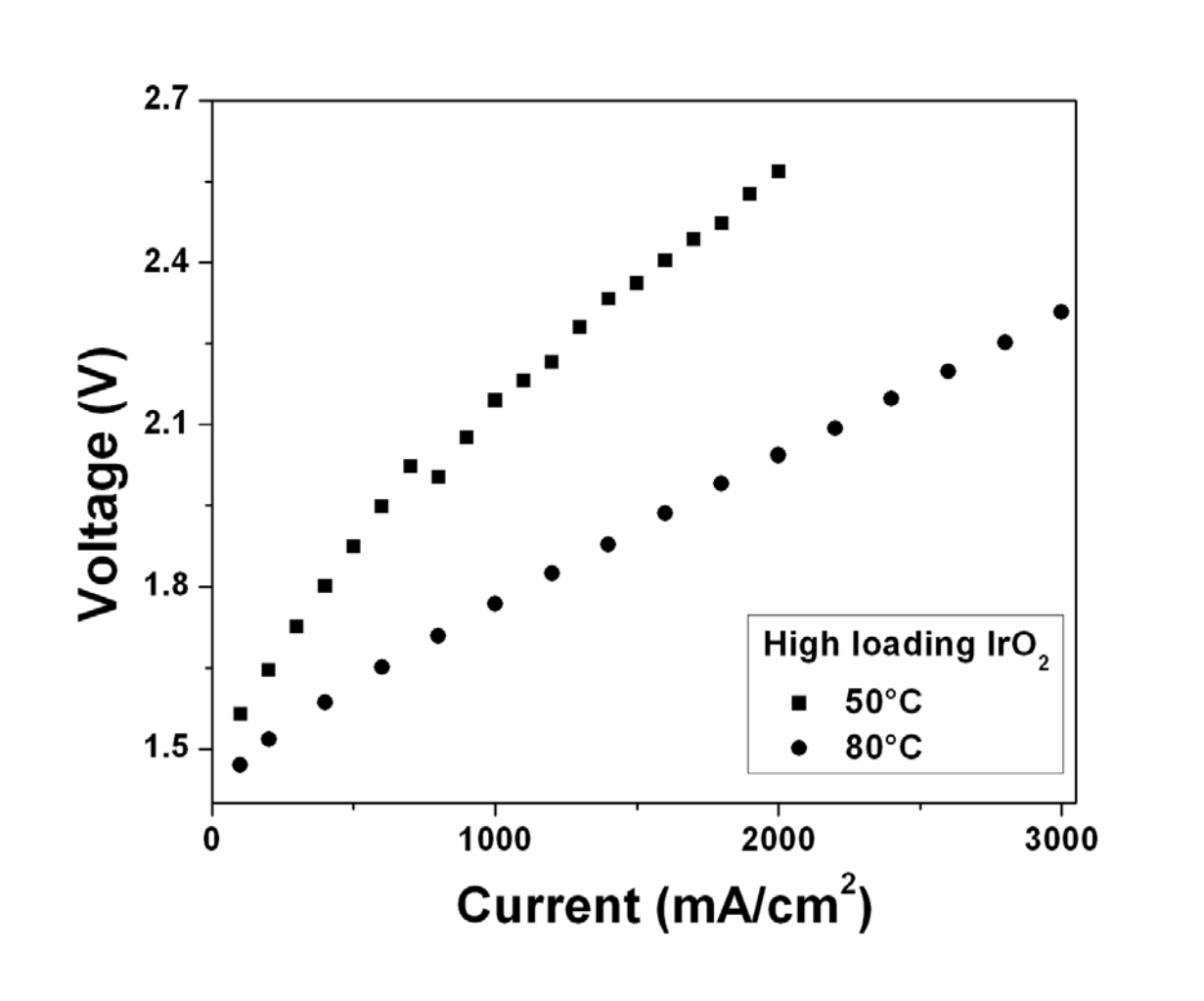

Figure 107. Polarization curve obtained in a single full cell PEM electrolyzer test for undoped IrO_2 at 50°C and 80°C

5.2.2 Binary F doped (Ir,Sn)O_2

5.2.2.1 Structural Analysis

Figure 108 shows the XRD pattern of the as-prepared SnO_2:F powder after oven drying at 50°C. The XRD pattern showed broad peaks corresponding to tin oxide which represents the

amorphous nature of the powder. We observe all crystalline phases of SnO_2 with possibly nanocrystalline peaks only after the powder is heat treated to 300°C. The specific surface area (SSA), measured by the BET technique, of 10 wt.% F doped SnO_2 powder is ~ 240 m^2/g while undoped SnO_2 has a SSA of ~ 160 m^2/g. **Figure 109** shows the XRD pattern of the electro-catalysts developed from mixed SnO_2:F and $IrCl_4$ solutions and heat treated to 400°C in air. They exhibit nanocrystalline peaks associated with single phase rutile type tetragonal IrO_2. The XRD pattern confirms the formation of a single phase homogeneous IrO_2 and SnO_2:F solid solution [(Ir,Sn)O_2:F], with no undesirable phase separation and/or mixed phase formation which is critical for better catalytic activity. The effective crystallite size of (Ir,Sn)O_2 and (Ir,Sn)O_2:F, calculated using the Scherrer formula from the integral breadth of the Lorentzian contribution determined from peak profile analysis using single line approximation method after eliminating the instrumental broadening and lattice strain contribution [88], is ~ 6.1 nm and ~ 5.5 nm respectively. ($Ir_{0.3}Sn_{0.7}$)O_2 and ($Ir_{0.3}Sn_{0.7}$)O_2:10wt.% F showed a SSA of ~ 47 m^2/g and ~ 56 m^2/g respectively as measured by the BET technique. The increase in surface area for the (Ir,Sn)O_2:F might be due to decrease in crystallite size. The TGA-DTA analysis of ($Ir_{0.3}Sn_{0.7}$)O_2:10F and ($Ir_{0.3}Sn_{0.7}$)O_2 carried out in air up to 700°C is shown in **Figure 110**. The undoped (Ir,Sn)O_2 shows no weight loss whereas its doped counterpart shows ~ 7 % weight loss. The weight loss thus would nearly correspond to the final amount of F (which is the volatile species) present in the ($Ir_{0.3}Sn_{0.7}$)O_2:10 wt.% F electro-catalyst.

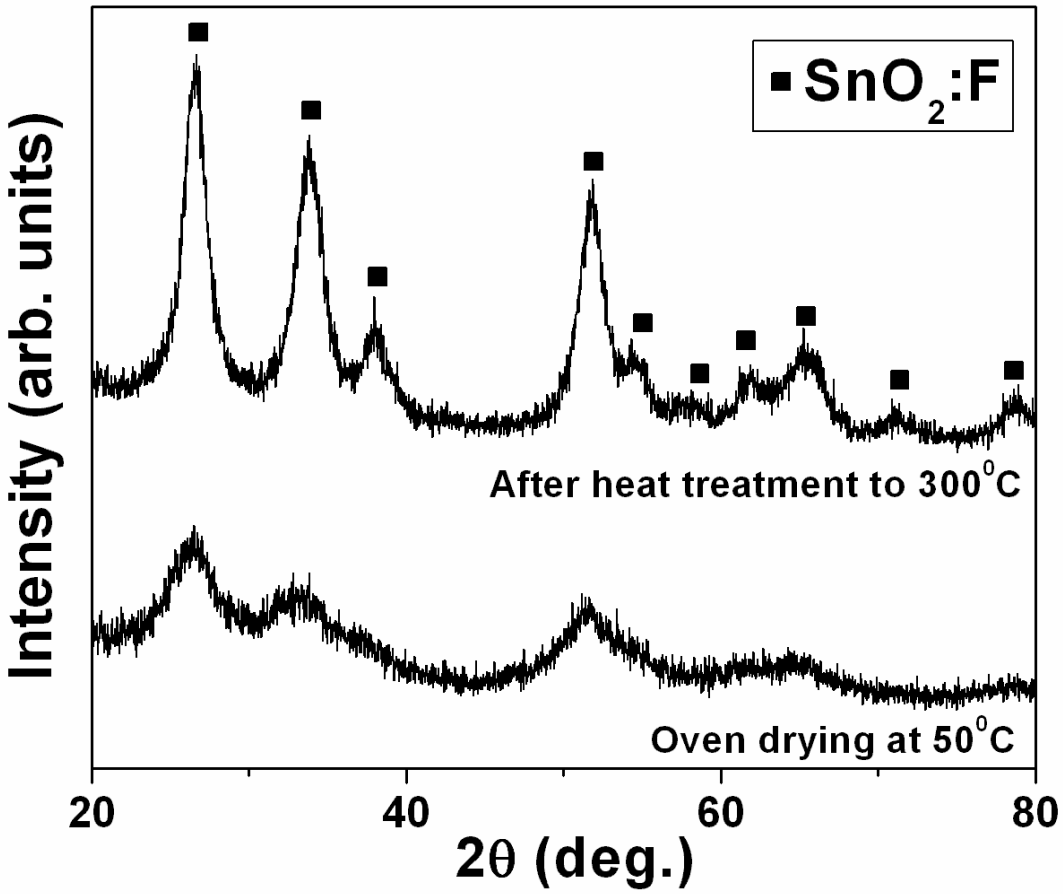

Figure 108. XRD pattern of as prepared SnO_2:F after drying in the oven at 50°C and subsequent heat treatment at 300°C

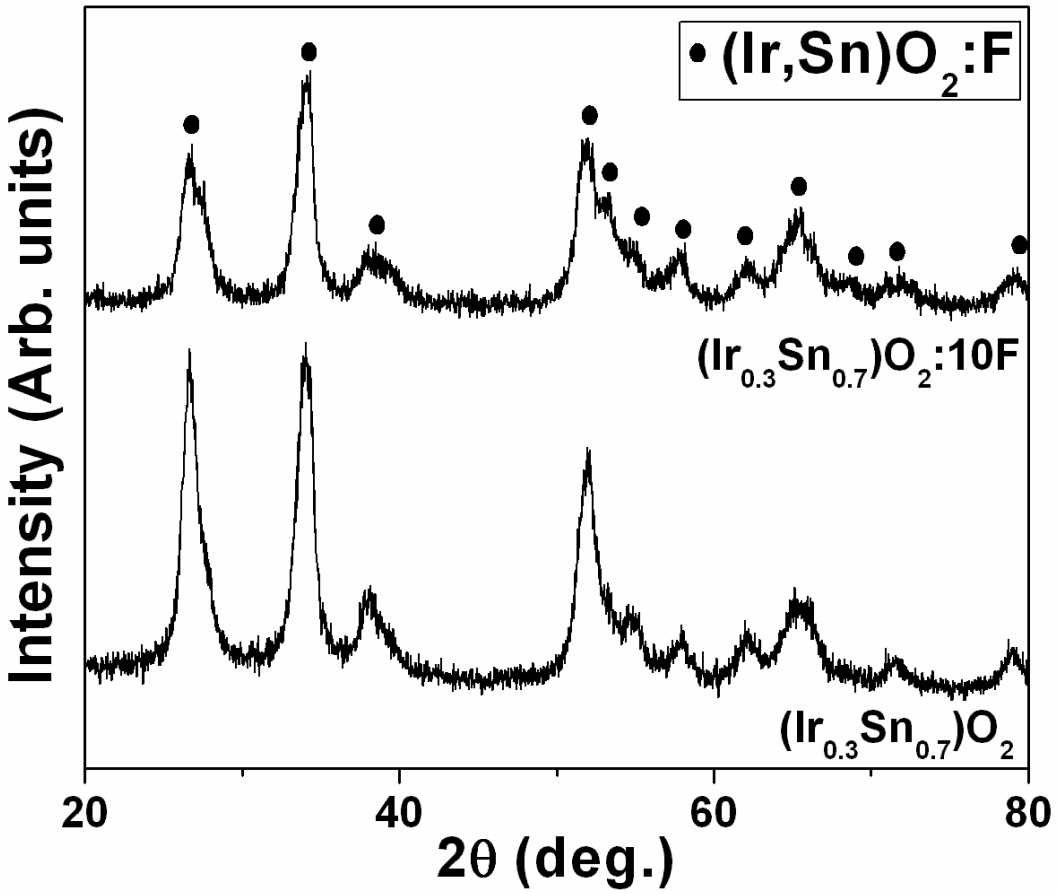

Figure 109. XRD pattern of undoped and F doped (Ir,Sn)O_2 after heat treatment to 400°C

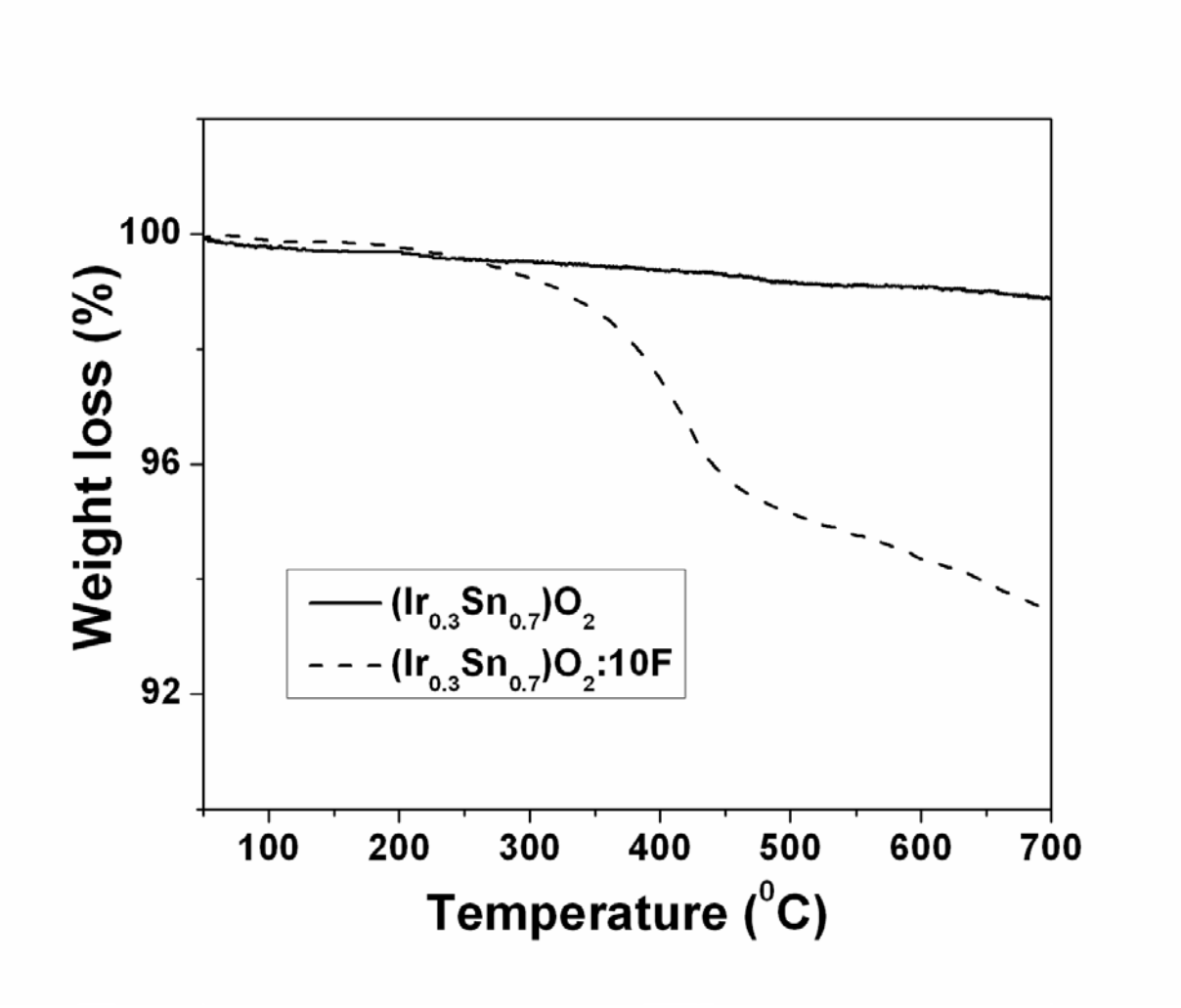

Figure 110. The TGA-DTA traces in air of $(Ir_{0.3}Sn_{0.7})O_2$ and $(Ir_{0.3}Sn_{0.7})O_2$:10 wt.% F showing weight loss with respect to temperature

The presence of elemental Ir and Sn in the (Ir,Sn)O_2:F powder has been confirmed using EDX attached to the SEM. **Figure 111** shows the elemental x-ray mapping *i.e.* the distribution of Ir, Sn, O and F in the powder. Elemental x-ray maps confirm that all the elements *viz.* Ir, Sn, O and F are homogeneously distributed within the (Ir,Sn)O_2:F particles without segregation on any specific site. Quantitative elemental composition analysis of the powders obtained by EDX further shows that the measured elemental compositions of Ir and Sn are close to the nominal

composition. The bright field TEM image of the $(Ir_{0.3}Sn_{0.7})O_2$:10 wt.% F powder shown in **Figure 112** reveals that the electro-catalyst size is in the range of ~ 5 – 10 nm nanometer.

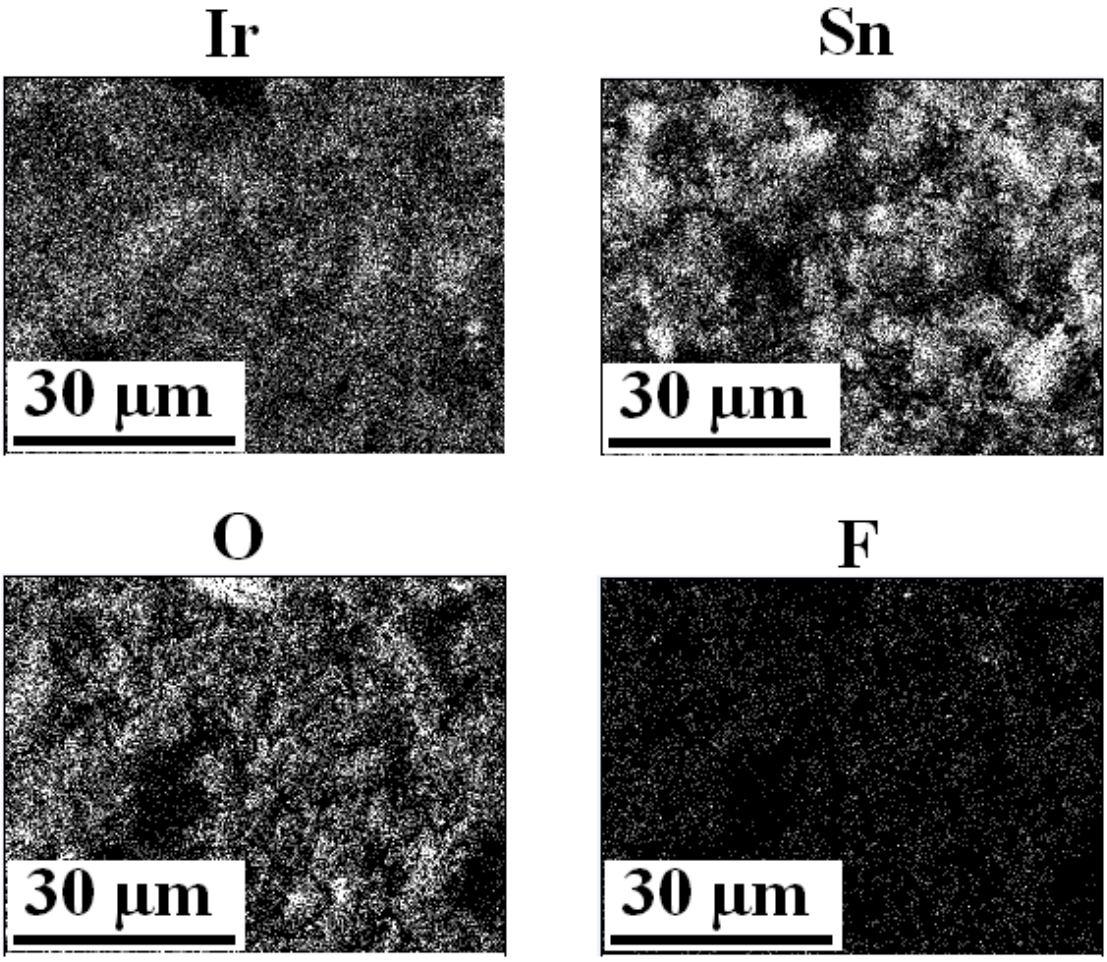

Figure 111. The elemental x-ray mapping of Ir, Sn, O and F in $(Ir_{0.3}Sn_{0.7})O_2$:10 wt.% F

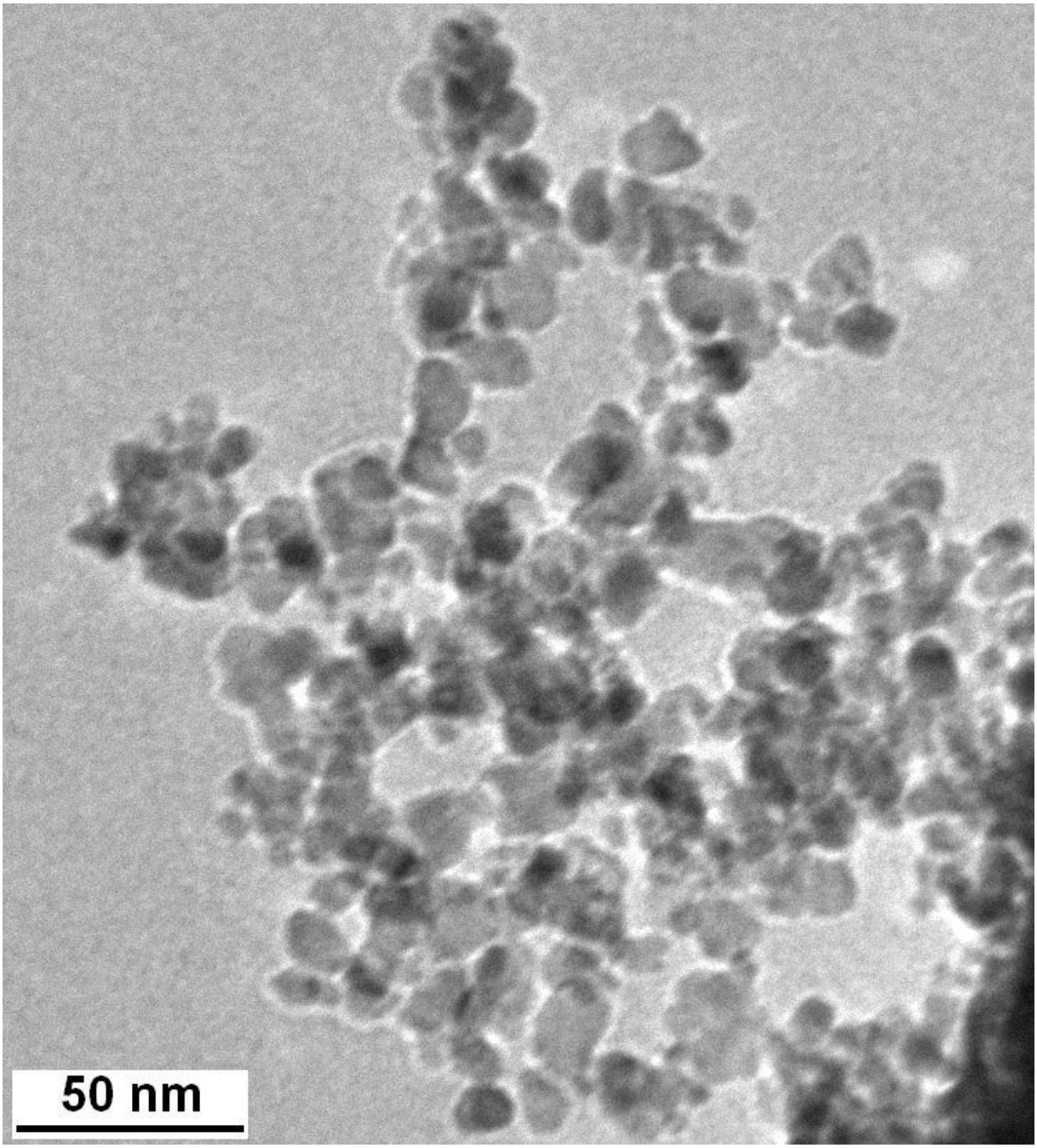

Figure 112. The bright field TEM image $(Ir_{0.3}Sn_{0.7})O_2$:10 wt.% F showing fine particles in the nanometer range

XPS has been carried out for $(Ir_{0.3}Sn_{0.7})O_2$ and $(Ir_{0.3}Sn_{0.7})O_2$:10F in order to determine the valence state of the elements. The XPS spectra of Ir, Sn and O1s are shown in **Figure 113**, **Figure 114** and **Figure 115**, respectively. The XPS spectra of Ir in $(Ir,Sn)O_2$ shows the presence of Ir $4f_{5/2}$ and Ir $4f_{7/2}$ doublet of binding energy ~ 61.6 eV and ~ 64.5 eV respectively, with the O1s peak being centered at ~ 530.7 eV. These values are associated with that of bulk IrO_2. The XPS spectra of Sn in $(Ir_{0.3}Sn_{0.7})O_2$ shows the Sn $3d_{5/2}$ and Sn $3d_{3/2}$ doublet with a binding energy of ~ 486.9 eV and ~ 495.3 eV respectively, which is consistent with the SnO_2. It is known that XPS is not adequate in determining the F content in F doped SnO_2. However, the binding energy of Ir 4f, Sn 3d and O1s core level increases by ~ 0.4 - 0.6 eV for $(Ir,Sn)O_2$:10F. This clearly indicates that there is stronger binding due to the higher electronegative F present in the lattice. Although the exact amount of fluorine could not be ascertained by XPS [57, 122], a weight loss of ~ 7 wt.% as seen in the TGA-DTA (**Figure 110**) confirms the presence of F in the electro-catalyst. The incorporation of F has a positive impact on the electrochemical activity of $(Ir,Sn)O_2$:F which is described later.

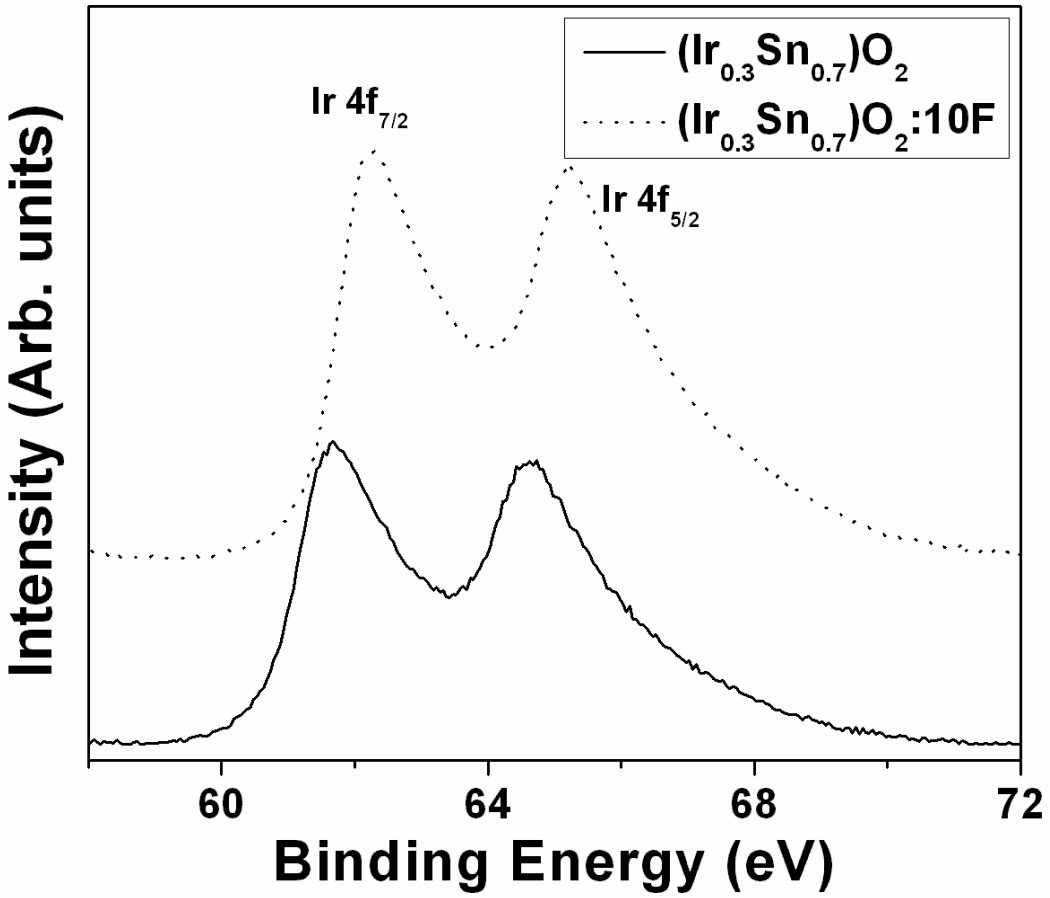

Figure 113. The XPS spectra of Ir $4f_{7/2}$ and $4f_{5/2}$ doublet of $(Ir,Sn)O_2$ and $(Ir,Sn)O_2$:F

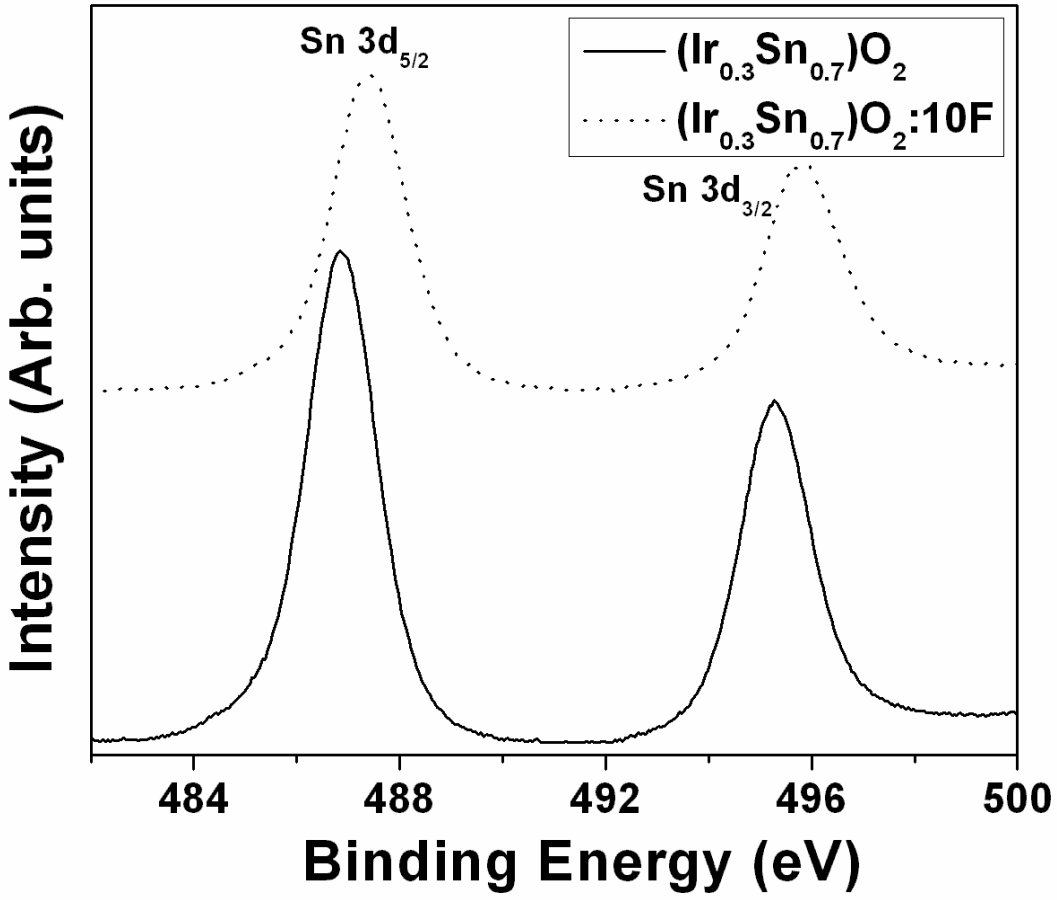

Figure 114. The XPS spectra of Sn $3d_{5/2}$ and Sn $3d_{3/2}$ doublet of $(Ir,Sn)O_2$ and $(Ir,Sn)O_2$:F

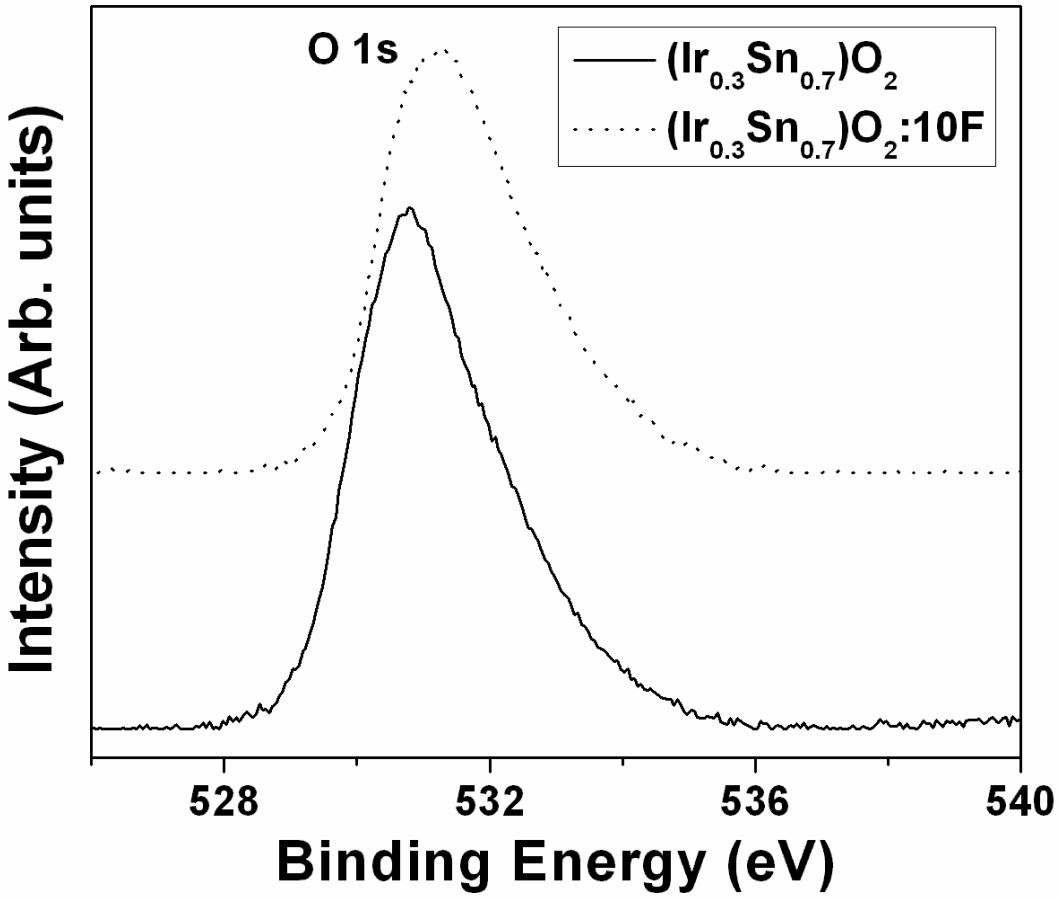

Figure 115. The XPS spectra of O 1s of (Ir,Sn)O_2 and (Ir,Sn)O_2:F

5.2.2.2 Electrochemical Testing

The electrochemical activity of commercial IrO_2 (Alfa Aesar), (Ir,Sn)O_2 and (Ir,Sn)O_2:F has been studied as an OER anode electro-catalyst for PEM electrolysis. The linear polarization curve and non-linear Tafel plot are encountered due to large contribution of R_Ω which mainly arises due to the R_s and R_e [51, 52]. In order to accurately know the electrode kinetics of the

electro-catalyst, the polarization curve, is plotted after appropriately correcting for the total ohmic loss (iR_Ω). The value of R_s, R_e, and R_{ct} for the catalysts, tabulated in **Table 8**, is obtained from EIS measurements conducted at different potentials (*vs*. NHE) in 1 N H_2SO_4 at 40^{o}C. **Figure 116, Figure 117** and **Figure 118** shows the EIS of $(Ir,Sn)O_2$, $(Ir,Sn)O_2$:10F and commercial IrO_2 obtained at open circuit potential (OCP), 1.5 V, 1.6 V and 1.8 V (*vs*. NHE) in the frequency range of 100 mHz - 100 kHz. It is seen that R_s for the electro-catalysts is similar and in the range of ~ 16 - 17 Ωcm^2 at various potentials. As seen in **Table 8**, R_e for $(Ir,Sn)O_2$:F is less compared to undoped $(Ir,Sn)O_2$ which may arise due to the improved electronic conductivity of $(Ir,Sn)O_2$:F. The low frequency EIS plot shows a semicircular arc related to OER whose diameter gives the polarization resistance (R_{ct}). F doped $(Ir,Sn)O_2$ has similar or even lesser R_{ct} values than commercial IrO_2 and undoped $(Ir,Sn)O_2$, which explains the increase in catalytic activity of the electrode with incorporation of F.

Table 8. Impedance parameters of nanoparticulate $(Ir,Sn)O_2$:F and commercial IrO_2

Voltage	Electro-catalyst	R_s (Ωcm^2)	R_e (Ωcm^2)	R_{ct} (Ωcm^2)
Open Circuit	$(Ir,Sn)O_2$:0F	16.96	7.69	2639
	$(Ir,Sn)O_2$:10F	16.38	3.42	1327
	IrO_2 (Alfa)	16.42	4.03	3577
1.5V	$(Ir,Sn)O_2$:0F	16.89	5.12	251.0
	$(Ir,Sn)O_2$:10F	17.16	3.87	198.8
	IrO_2 (Alfa)	16.31	3.36	44.89
1.6V	$(Ir,Sn)O_2$:0F	16.08	4.73	86.09
	$(Ir,Sn)O_2$:10F	16.81	2.16	29.2
	IrO_2 (Alfa)	16.38	2.57	14.76
1.8V	$(Ir,Sn)O_2$:0F	16.32	1.91	43.23
	$(Ir,Sn)O_2$:10F	16.67	1.23	13.82

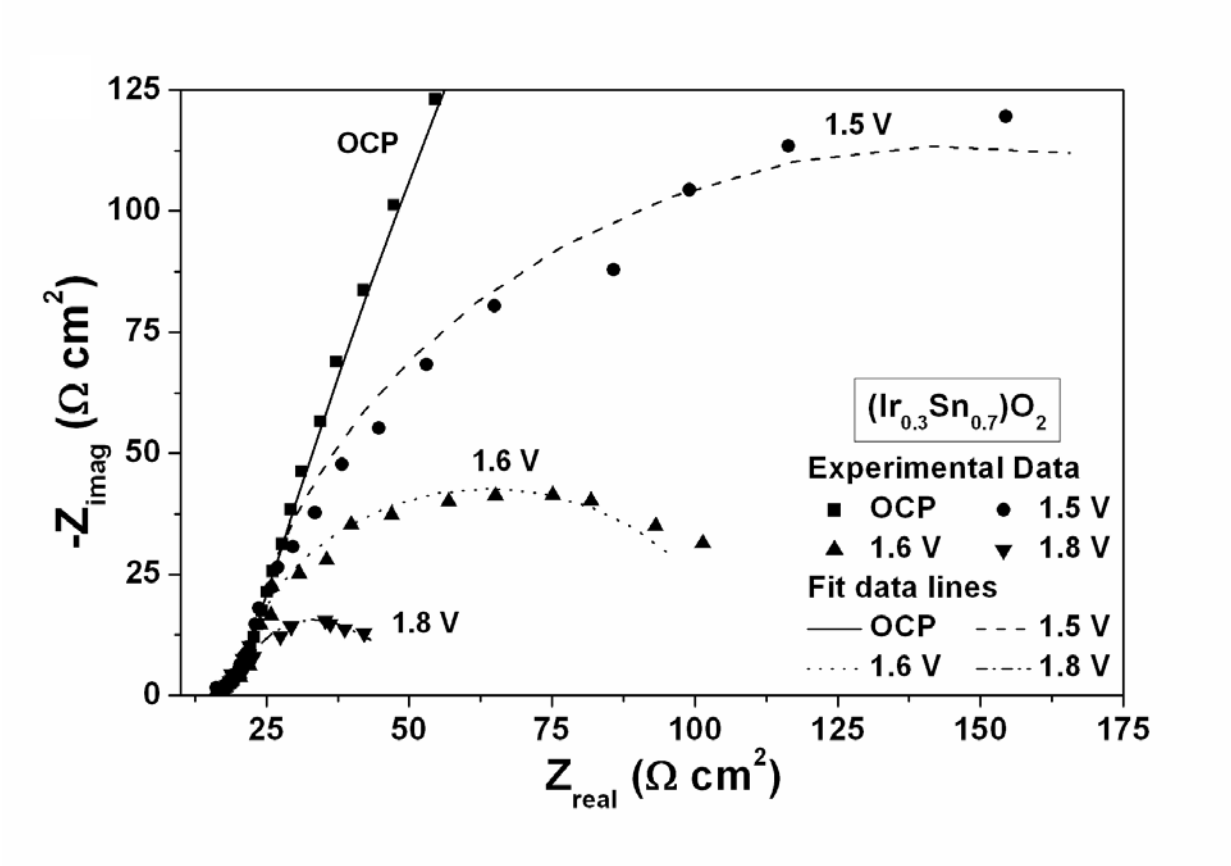

Figure 116. EIS spectra of $(Ir,Sn)O_2$ obtained at OCP, 1.5 V, 1.6 V and 1.8 V in 1 N H_2SO_4

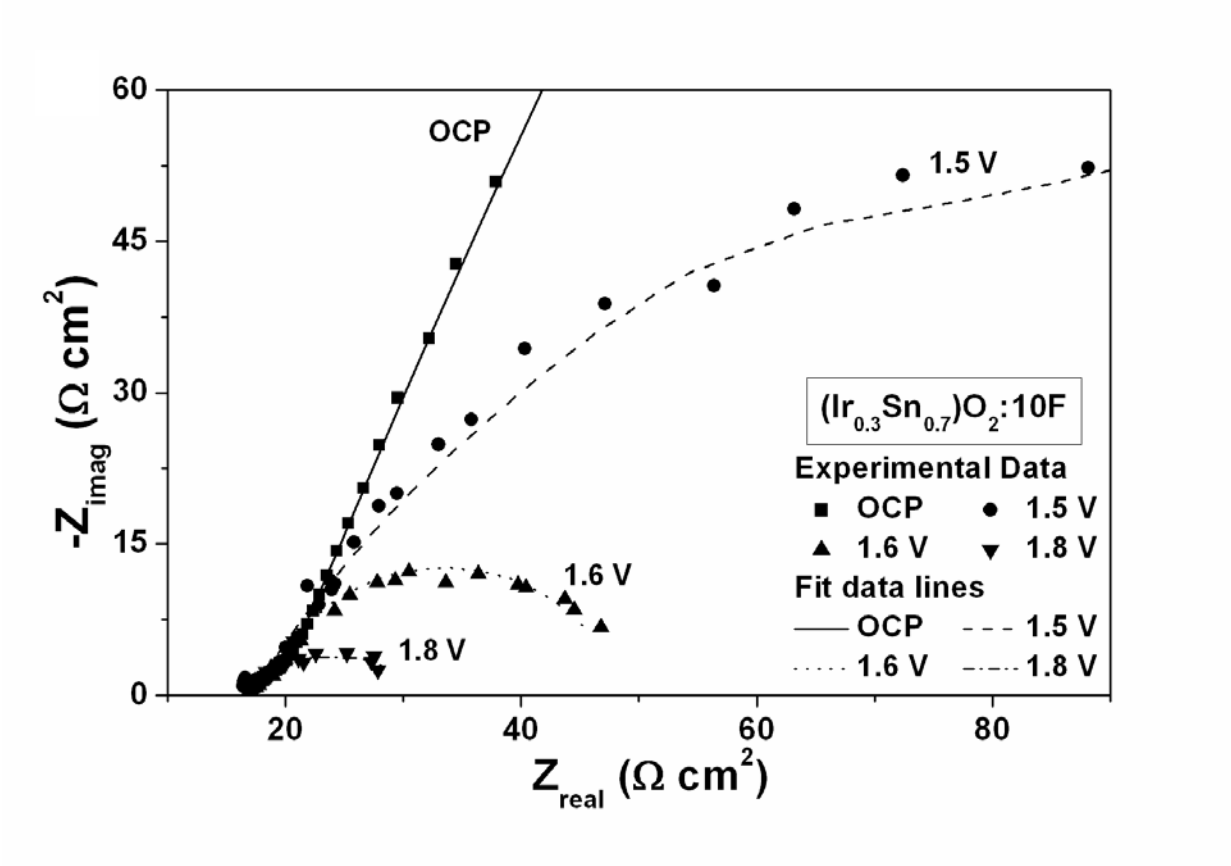

Figure 117. EIS spectra of (Ir,Sn)O_2:10 wt.% F obtained at OCP, 1.5 V, 1.6 V and 1.8 V in 1 N H_2SO_4

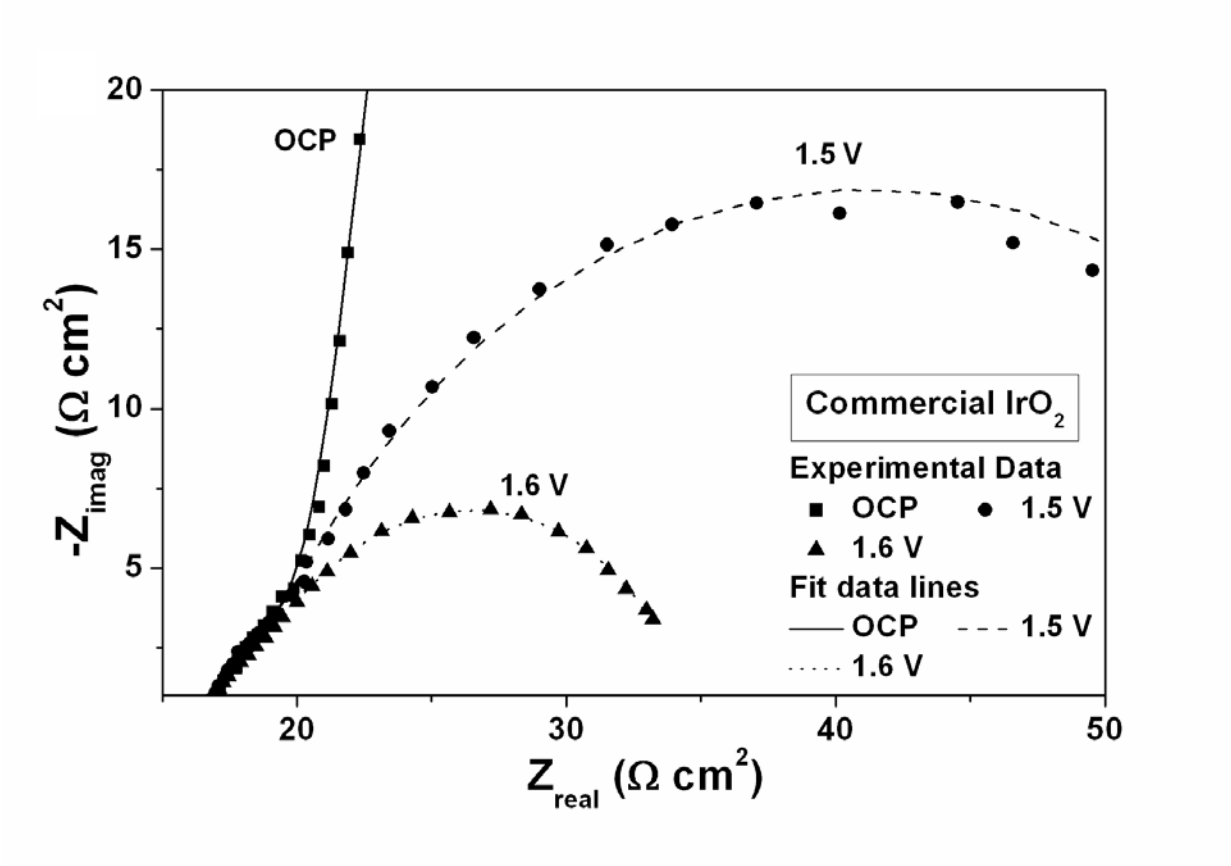

Figure 118. EIS spectra of commercial IrO_2 obtained at OCP, 1.5 V and 1.6 V in 1 N H_2SO_4

The polarization curve of commercial IrO_2 (Alfa Aesar), $(Ir,Sn)O_2$ and $(Ir,Sn)O_2$:F, before and after ohmic resistance correction ($iR_\Omega = iR_s + iR_e$) has been performed in 1 N H_2SO_4 solution at 40°C with a scan rate of 1 mV/sec as shown in **Figure 119**. The water splitting reaction (OER) occurs at a potential of ~ 1.43 V *vs*. NHE. The current density of IrO_2 at ~ 1.5 V (*vs*. NHE) after iR_Ω correction, a typical voltage selected to check for electrochemical activity for water electrolysis, is ~ 0.0125 ± 0.0002 A/cm^2 for a total loading ~ 0.3 mg/cm^2 of IrO_2. The current density at ~ 1.5 V (*vs*. NHE) obtained from the iR_Ω corrected curve for undoped $(Ir_{0.3}Sn_{0.7})O_2$ with the same IrO_2 loading (~ 0.3 mg/cm^2) is ~ 0.0032 ± 0.0002 A/cm^2 which is *ca.* 74% lower than commercial IrO_2. However, there is an increase in current density for

$(Ir_{0.3}Sn_{0.7})O_2$:10 wt.% F. The F doped electro-catalyst shows a current density of ~ 0.013 ± 0.0002 A/cm^2 at ~ 1.5 V (*vs.* NHE) which is slightly better than commercial IrO_2.

The Tafel slope of commercial pure IrO_2 is ~ 83 mV/decade and is calculated from the Tafel plot as shown in **Figure 120**. It is slightly higher than a two electron pathway reaction (Tafel slope ~ 62 mV/dec) assuming a transfer coefficient of ~ 0.5 [48, 53, 101]. The Tafel slope of $(Ir,Sn)O_2$ and $(Ir,Sn)O_2$:10F, calculated from their corresponding Tafel plots as shown in **Figure 121** and **Figure 122**, are ~ 108 mV/decade and ~ 70 mV/decade, respectively. This observation clearly suggests that the catalytic or electrochemical activity of $(Ir,Sn)O_2$:F increases with increase in F content with a decrease in the Tafel slope. An optimal value for $(Ir_{0.3}Sn_{0.7})O_2$:10 wt.% F is reached that exhibits comparable electrochemical activity as commercial IrO_2. These results indicate that $(Ir_{0.3}Sn_{0.7})O_2$:10 wt.% F is a promising candidate as an OER anode electro-catalyst especially with reduced noble metal content for PEM based water electrolysis.

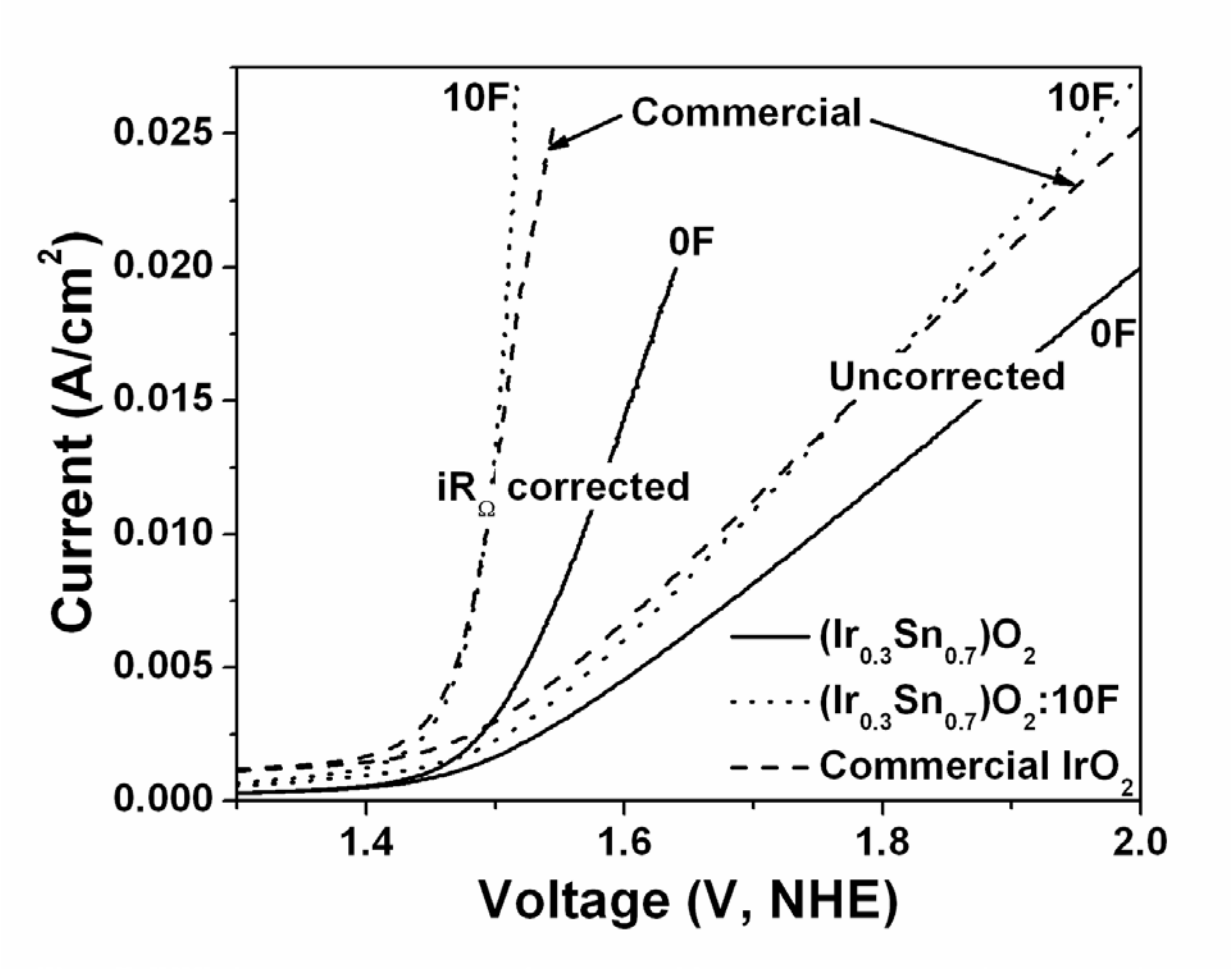

Figure 119. The polarization curve of undoped and F doped (Ir,Sn)O_2 along with commercial IrO_2 in the presence of 1 N H_2SO_4 solution at 40°C with a scan rate of 1 mV/sec before and after iR correction

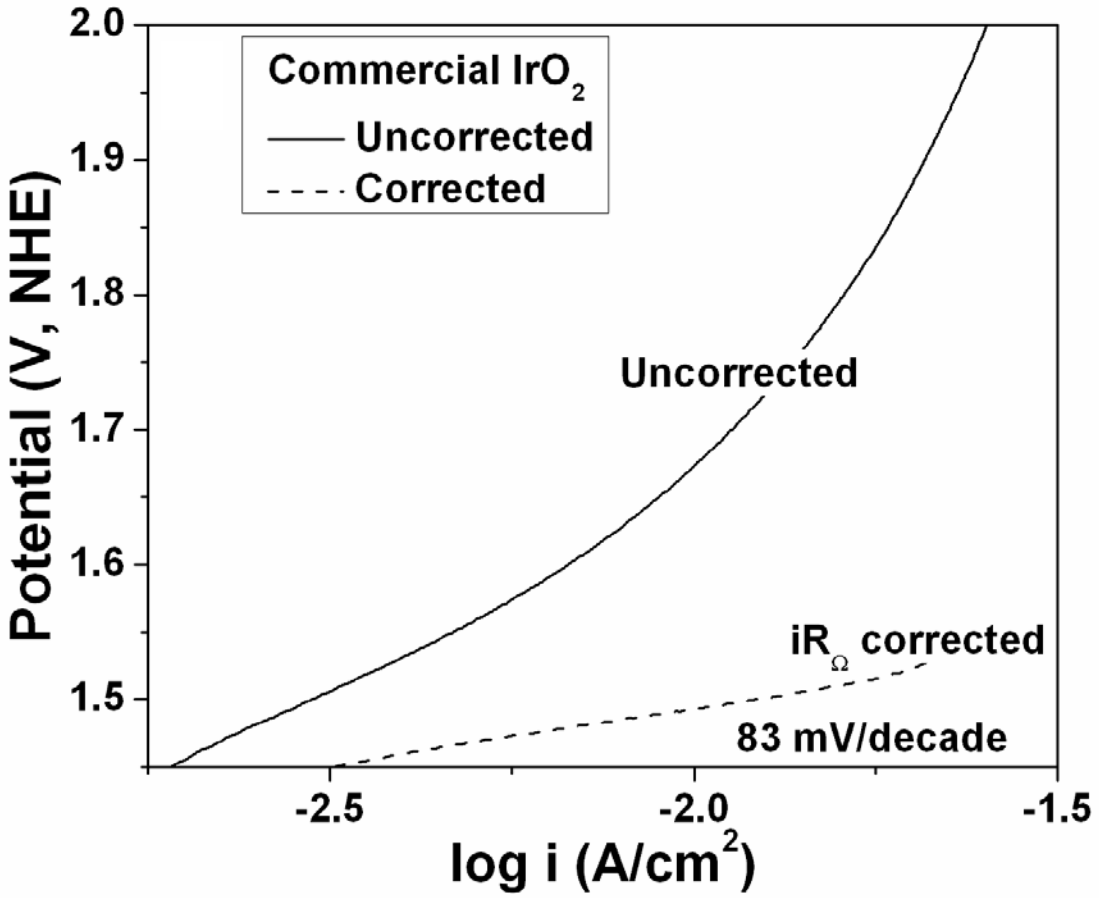

Figure 120. The Tafel plot of commercial IrO_2 before and after iR correction

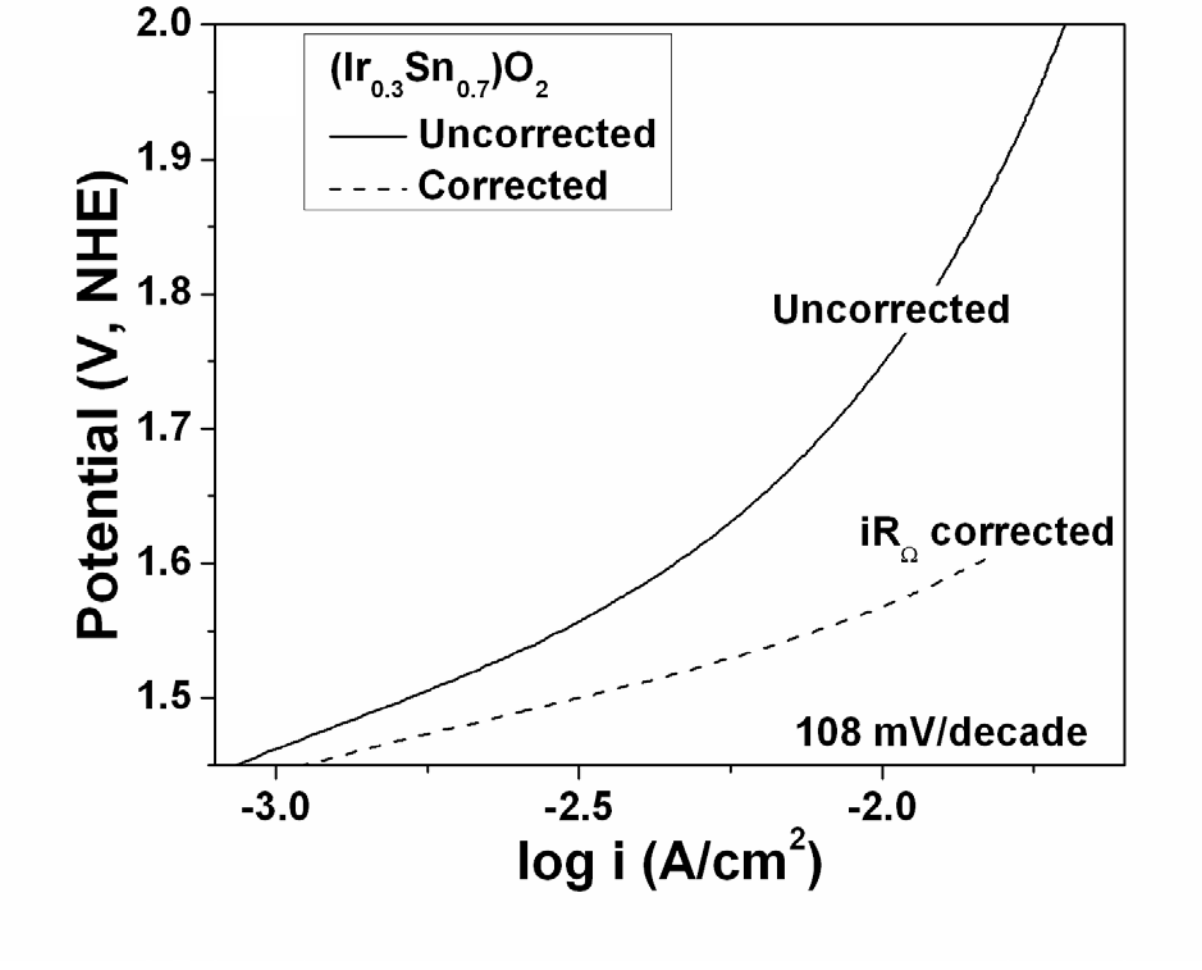

Figure 121. The Tafel plot of $(Ir,Sn)O_2$ before and after iR correction

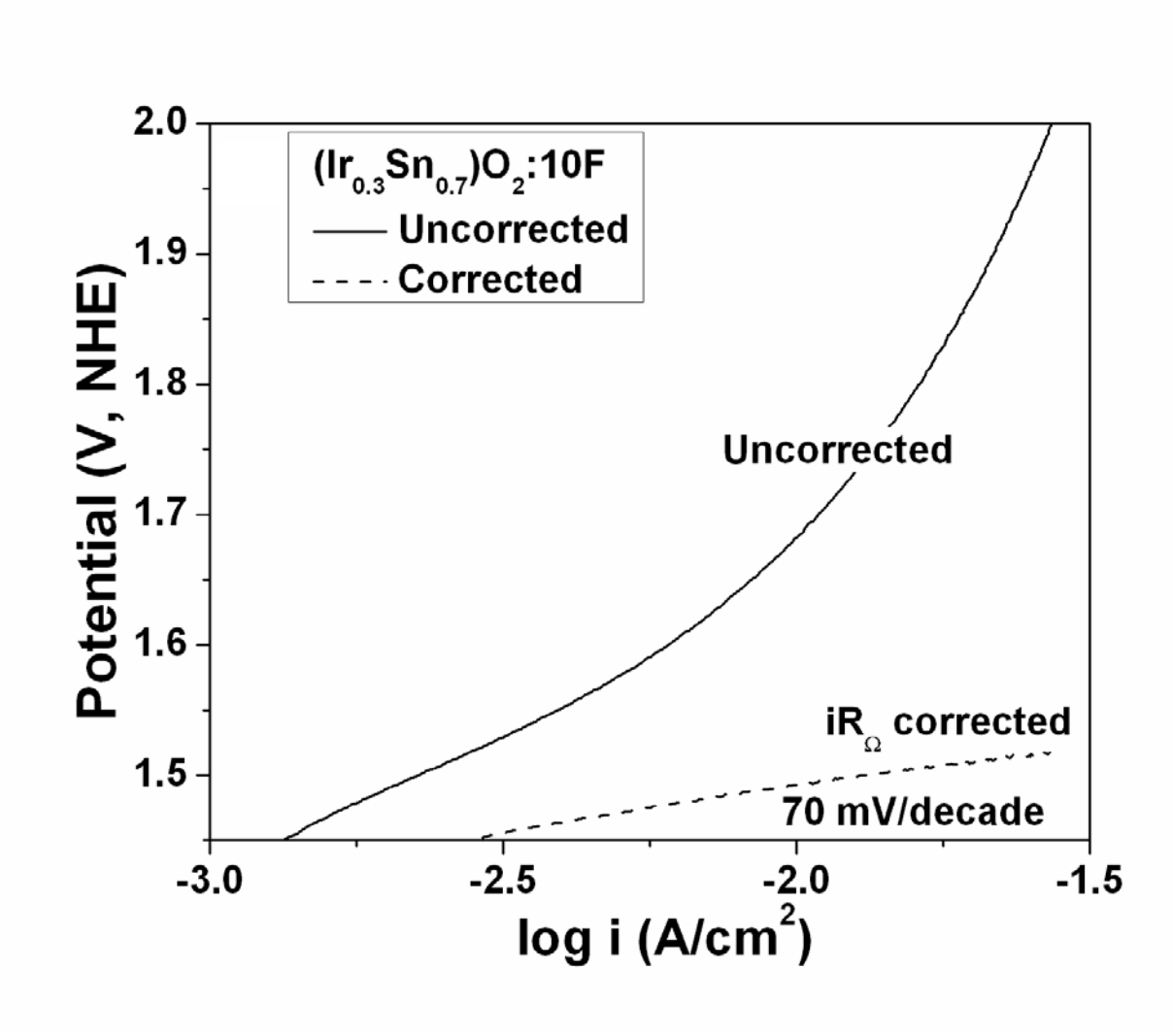

Figure 122. The Tafel plot of (Ir,Sn)O_2:10 wt.% F before and after iR correction

In order to study the stability of these anode electro-catalysts, chronoamperometry (CA) is conducted for 12 hours at a constant voltage of ~1.65 V (*vs.* NHE), for assessing the loss in the electrochemical activity of the catalyst. The CA curves for $(Ir_{0.3}Sn_{0.7})O_2$, $(Ir_{0.3}Sn_{0.7})O_2$:10wt.% F and commercial IrO_2 are compared in **Figure 123**. The undoped (Ir,Sn)O_2 has less initial current than the (Ir,Sn)O_2:10F and commercial IrO_2 because it inherently gives less current at a particular voltage (**Figure 119**). The decay of current for the catalysts can be attributed to

dissolution of electro-catalyst coating at the edge of the porous titanium support [30] and due to diffusion controlled reactions or by induced loss of electrolyte due to constant exhaustion of fuel [34, 57]. Commercial IrO_2 undergoes a lot of degradation and exhibits a steep decrease in current over time showing its instability whereas a steady decay of current is observed for the $(Ir,Sn)O_2$:F catalysts. This suggests that the chemical stability / durability of the reduced noble metal oxide catalysts is enhanced due to SnO_2 and F doped SnO_2 support, thus making them more robust than commercially pure IrO_2 which is regarded as a gold standard OER electro-catalyst for PEM electrolyzers.

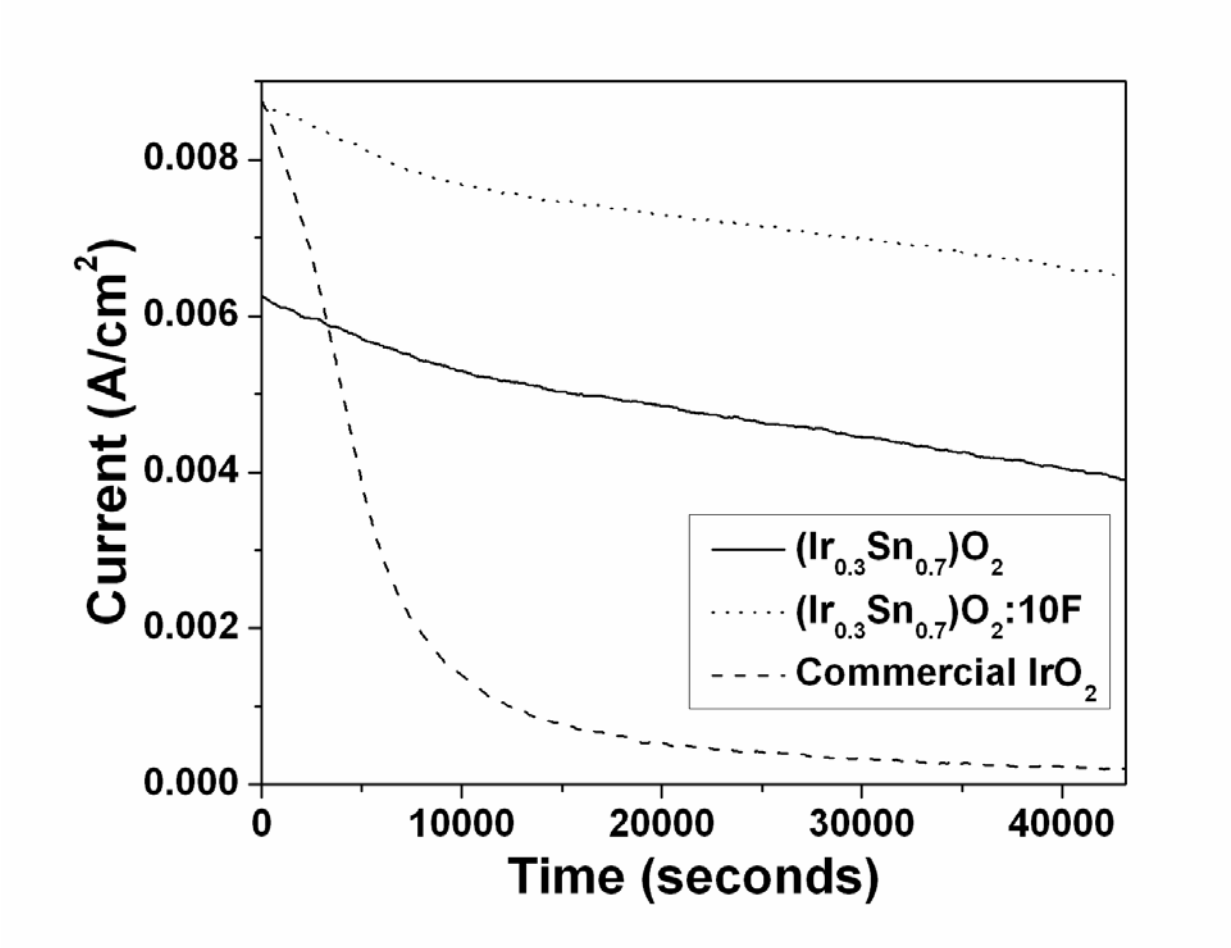

Figure 123. The variation of current *vs.* time for (Ir,Sn)O_2:F powders and commercial IrO_2 in the CA test performed in a 1 N H_2SO_4 solution at a constant potential of ~ 1.65 V

The ICP results conducted on the 1 N H_2SO_4 electrolyte solution after the CA measurement *i.e.* 12 hours shows the absence of Ir for the (Ir,Sn)O_2:F electro-catalysts whereas, commercial IrO_2 shows ~ 0.35 ppm of Ir leached out in the solution. $(Ir_{0.3}Sn_{0.7})O_2$ has ~ 0.16 ppm of Sn and $(Ir_{0.3}Sn_{0.7})O_2$:10 wt.% F has ~ 0.12 ppm of Sn present in the electrolyte solution after CA. This suggests that the steady decrease in current for the electro-catalysts may arise due to slight dissolution of the electro-catalyst from the surface.

After the conclusion of the CA test, the $(Ir_{0.3}Sn_{0.7})O_2$:10 wt.% F electrode was subject to polarization testing as seen in **Figure 124** in order to determine the activity of the electrodes after long term structural stability tests. The Tafel plot from the polarization curve (post CA measurement) after iR correction is shown in **Figure 125**. A Tafel slope of ~ 121 mV/decade was obtained for $(Ir,Sn)O_2$:10 wt.% F which is comparable to that of undoped IrO_2 after CA (~ 112 mV/decade) as seen in **Figure 104**. The present study therefore identifies $(Ir,Sn)O_2$:F as a promising anode electro-catalyst with the ability to significantly reduce the noble metal oxide loading with increased electro-catalytic performance as well as chemical and structural stability.

A single full cell test was done at Proton OnSite for the $(Ir_{0.3}Sn_{0.7})O_2$:10 wt.% F catalyst which has been shown and compared in **Section 5.2.3.2** along with the reduced noble metal $(Ir,Nb)O_2$:F catalyst powder.

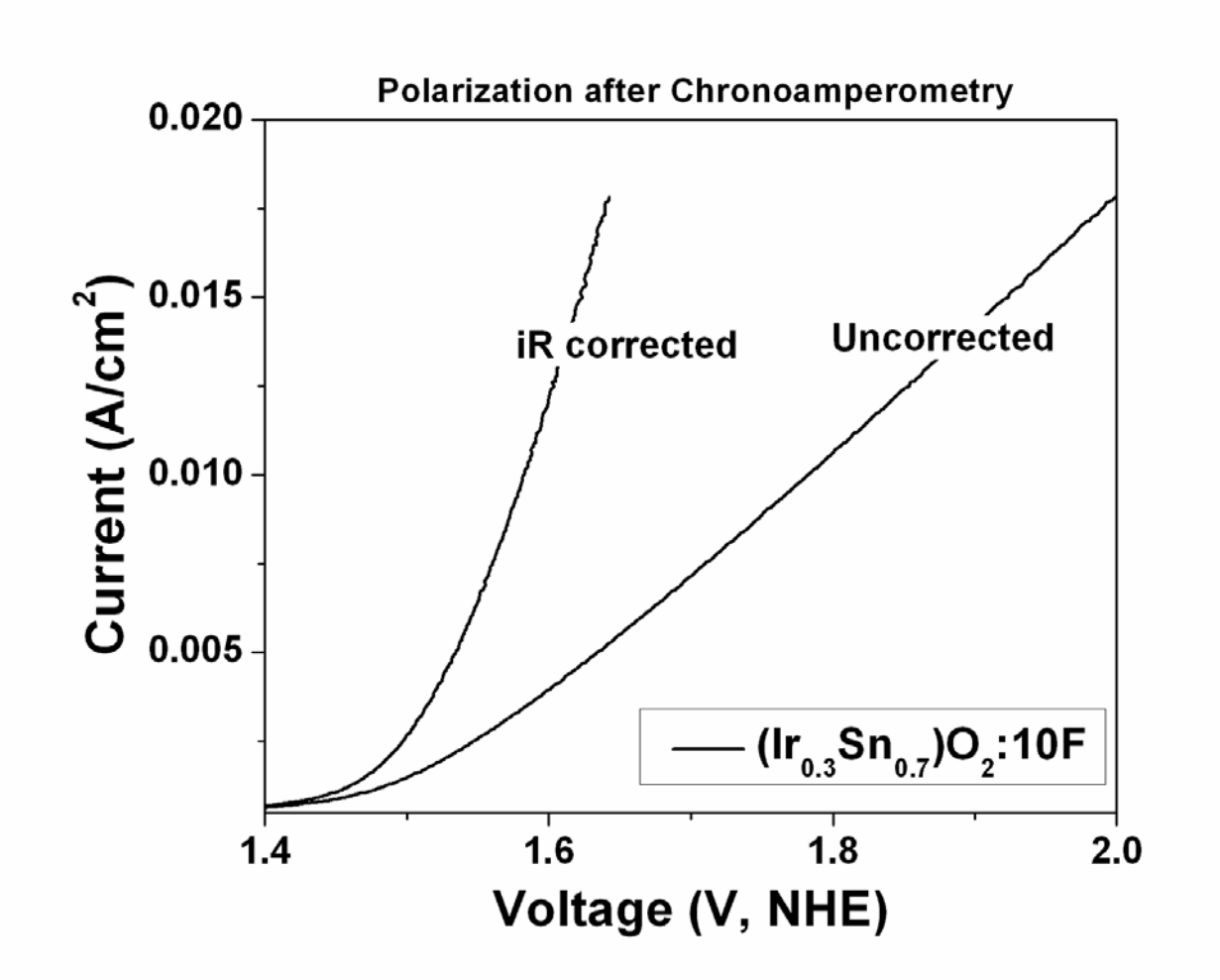

Figure 124. Polarization curve of (Ir,Sn)O_2:10 wt.% F powder after the CA test

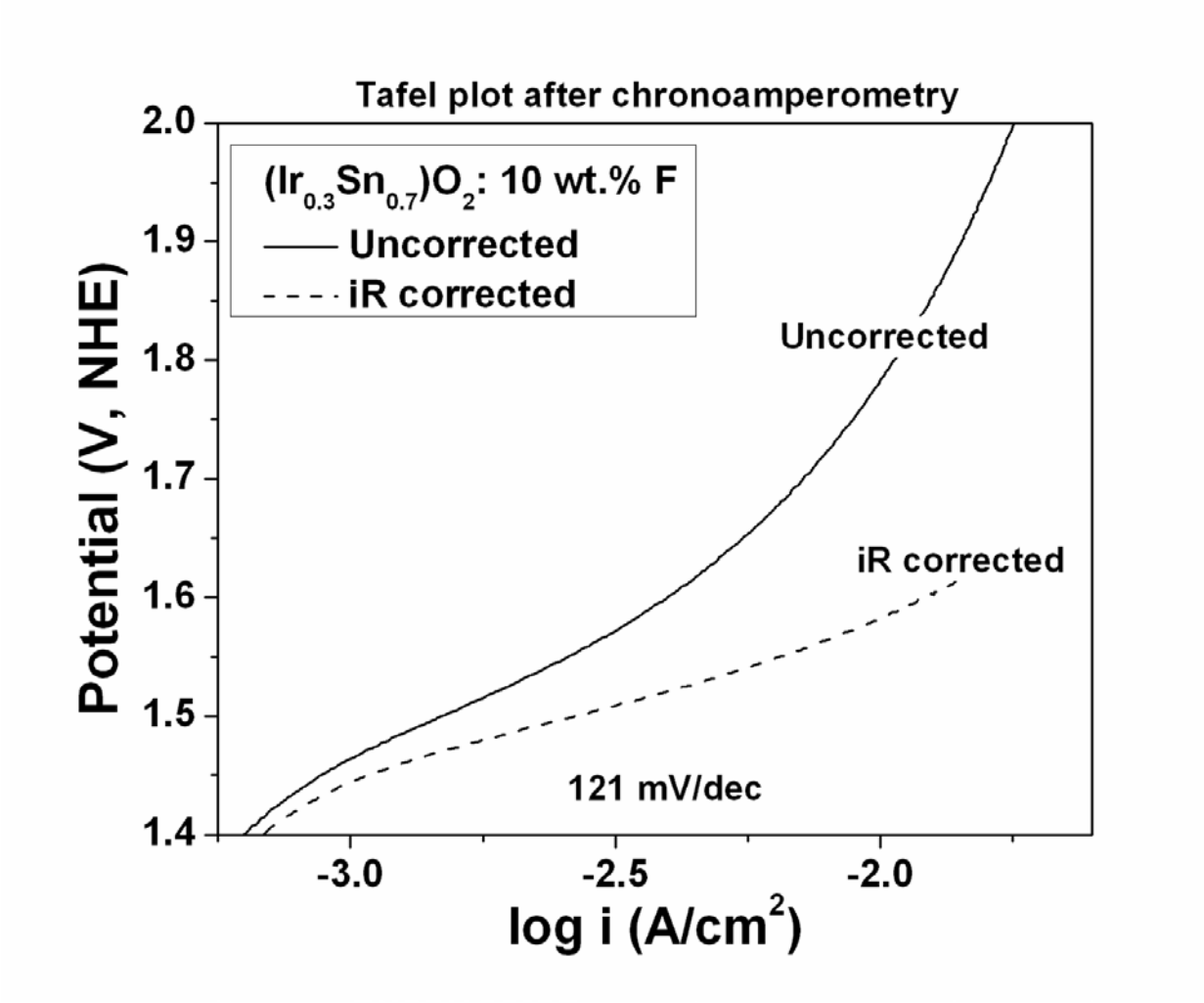

Figure 125. The Tafel plot of (Ir,Sn)O_2:10 wt.% F powder after the CA test

5.2.3 Binary F doped (Ir,Nb)O_2

5.2.3.1 Structural Analysis

The XRD pattern of the as-prepared Nb_2O_5: 10 wt.% F powder after drying in air at 75°C shown in **Figure 126** exhibits peaks corresponding to niobium oxide. The relatively broad nature of the peaks indicates the amorphous nature of the powder. According to the BET analysis, the

specific surface area of 10 wt.% F doped Nb_2O_5 powder is ~ 389 m^2/g while the specific surface area of undoped Nb_2O_5 is ~ 257 m^2/g. The solutions of Nb_2O_5:F and $IrCl_4$ were mixed and heat treated to 400°C in air. **Figure 127** reveals the XRD pattern of the electro-catalysts are nanocrystalline and contain crystalline phases mainly associated with tetragonal IrO_2. It is clear that all the peaks correspond to single phase rutile type tetragonal IrO_2 structure suggesting the formation of a homogeneous IrO_2 and Nb_2O_5:F solid solution, [(Ir,Nb)O_2:F] with no undesirable phase separation (*E.g.* IrO_2 + Nb_2O_5) and / or mixed phase formation which is critical for achieving the high catalytic activity. The effective crystallite size of (Ir,Nb)O_2 and (Ir,Nb)O_2:F, calculated using the Scherrer formula from the integral breadth of the Lorentzian contribution determined from peak profile analysis using single line approximation method after eliminating the instrumental broadening and lattice strain contribution [123], is ~ 5.4 nm and ~ 4.9 nm respectively. The TGA-DTA traces of undoped and 10 wt.% F doped (Ir,Nb)O_2 is shown in **Figure 128**. A weight loss of ~ 4 - 5 % is observed for the F doped electro-catalyst and confirms the removal of the volatile species *i.e.* fluorine from the catalyst. The TGA-DTA of undoped (Ir,Nb)O_2 shows almost no weight loss when subject to thermogravimetric analysis in air. The weight loss thus would nearly correspond to the final amount of F present in the ($Ir_{0.25}Nb_{0.75}$)O_2 :10 wt.% F electro-catalyst. ($Ir_{0.25}Nb_{0.75}$)O_2 and ($Ir_{0.25}Nb_{0.75}$)O_2:10 wt.% F have a specific surface area, measured by the BET technique, of ~ 77 m^2/g and ~ 99 m^2/g respectively. The increase in surface area for the (Ir,Nb)O_2:F is attributed to decrease in crystallite size.

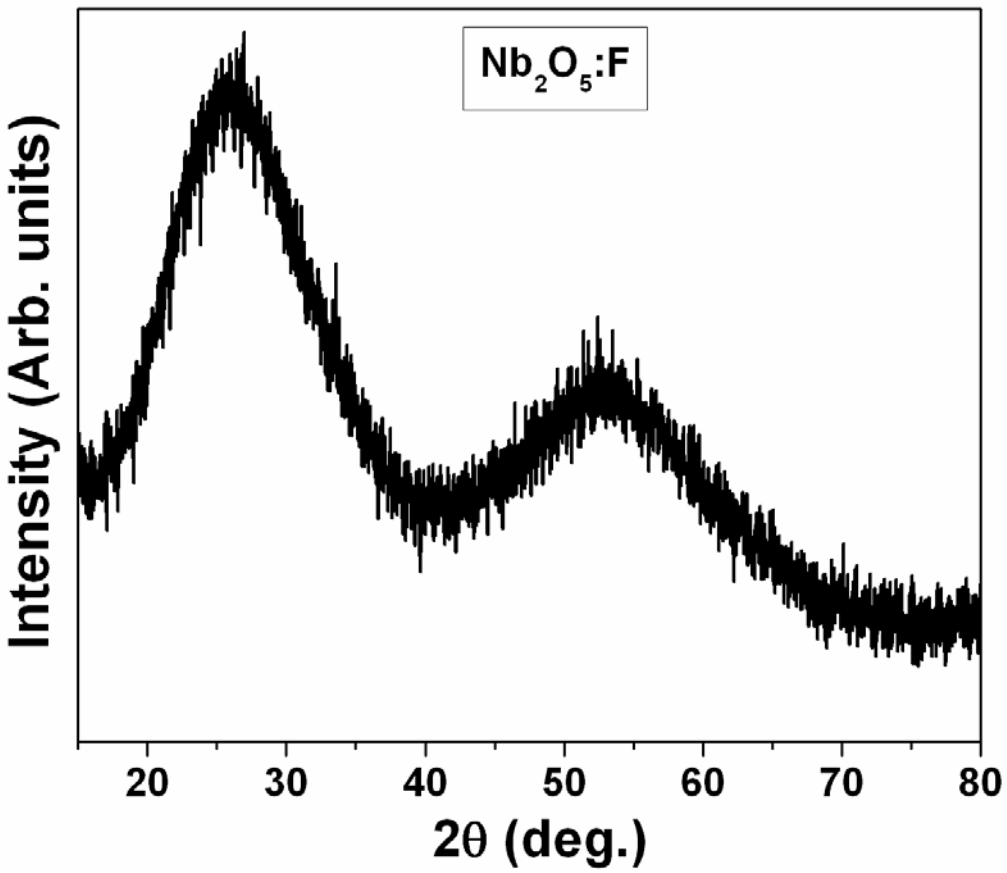

Figure 126. XRD pattern of the as prepared Nb_2O_5:F

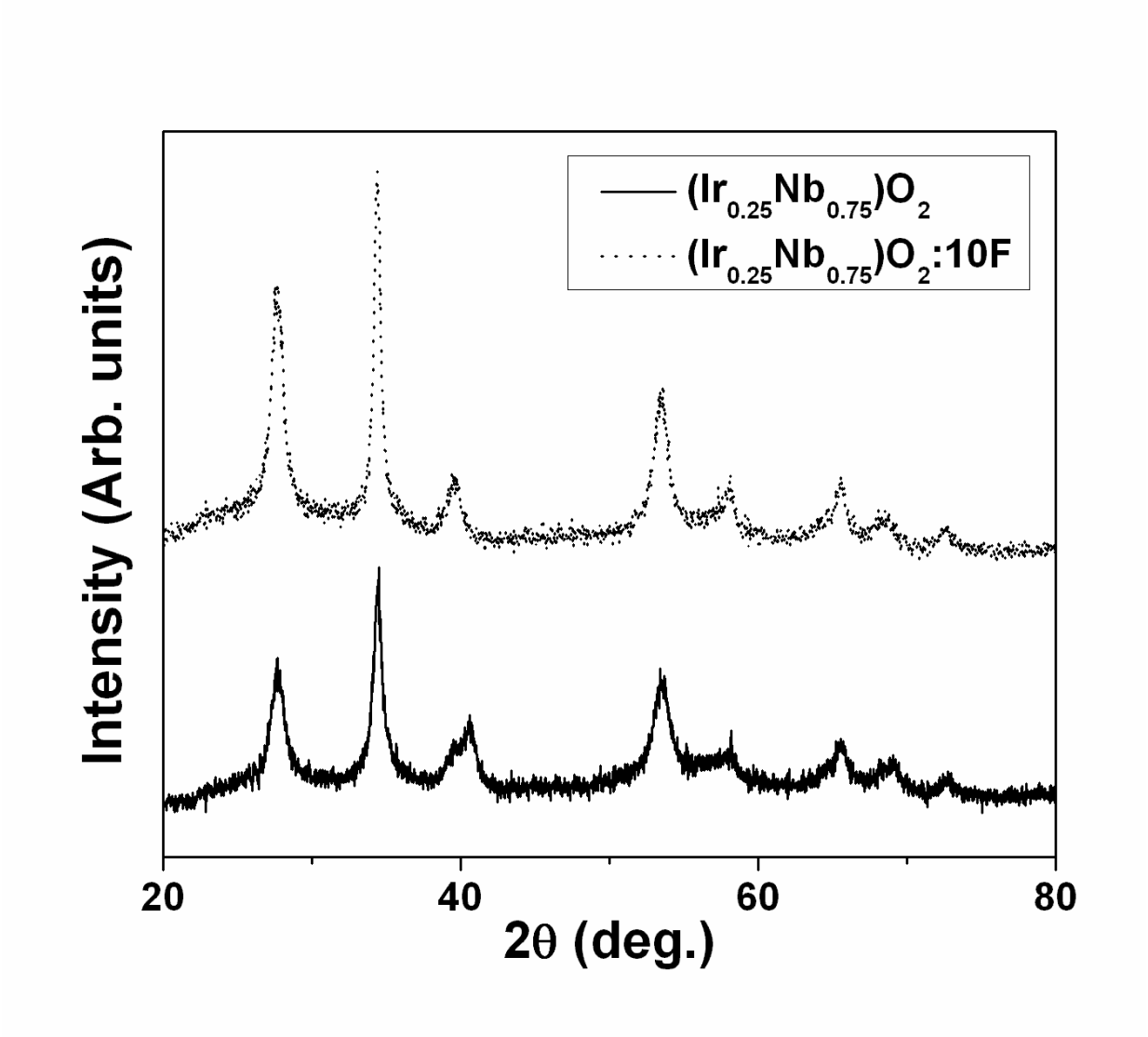

Figure 127. XRD pattern of undoped and F doped (Ir,Nb)O_2

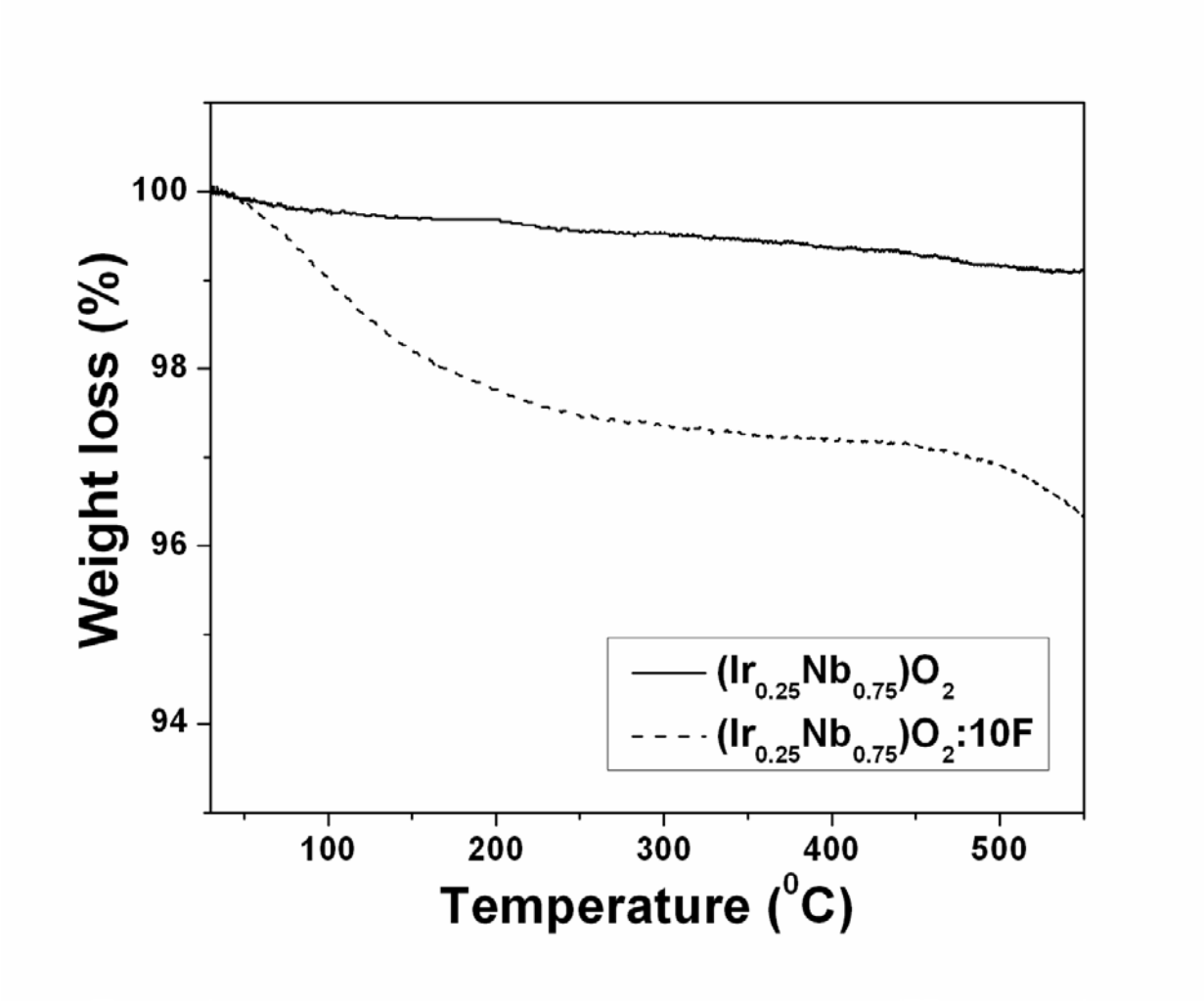

Figure 128. The TGA-DTA traces in air of $(Ir_{0.25}Nb_{0.75})O_2$:F showing weight loss corresponding to fluorine in the electro-catalyst

The presence of elemental Ir, Nb and O in $(Ir,Nb)O_2$:F representative sample has been confirmed using energy dispersive X-ray spectroscopy (EDX) attached to the SEM. The elemental x-ray mapping in **Figure 129** shows the distribution of Ir, Nb, O and F in $(Ir,Nb)O_2$:F. It confirms that all the elements *viz.* Ir, Nb, O and F are homogeneously distributed within the $(Ir,Nb)O_2$:F particles without segregation or separation at any specific site. Quantitative elemental composition analysis of the powders obtained by EDX further confirmed that the

measured elemental compositions of Ir and Nb are close to the nominal composition. The bright field TEM image of $(Ir_{0.25}Nb_{0.75})O_2$:10 wt.% F shown in **Figure 130** corroborates the nanometer sized fine particles in the range of ~ 4 - 8 nm. This corroborates well with the crystallite size calculated using the Scherrer formula from the x-ray diffraction patterns.

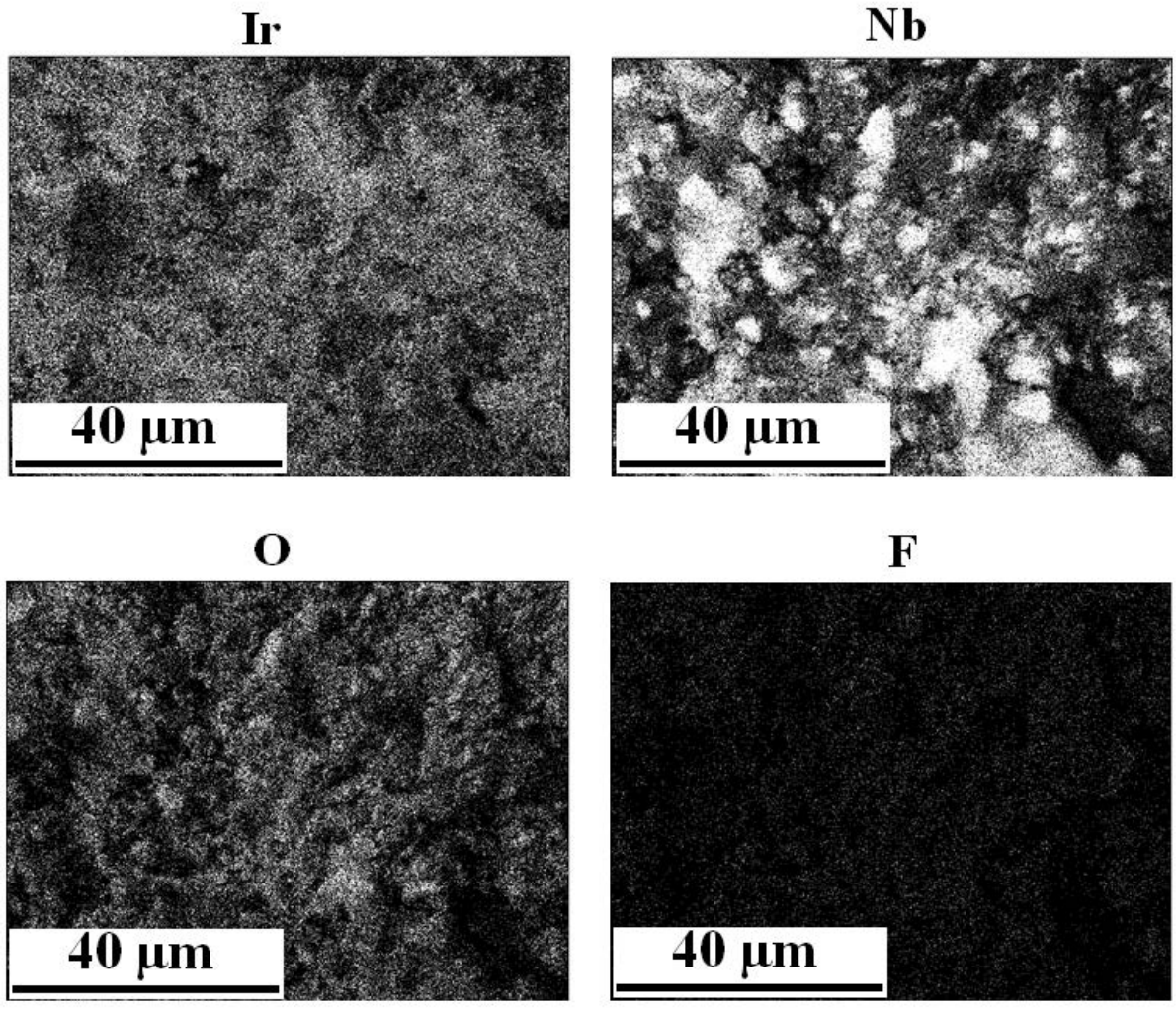

Figure 129. The elemental x-ray mapping of Ir, Nb, O and F in $(Ir_{0.25}Nb_{0.75})O_2$:10 wt.% F

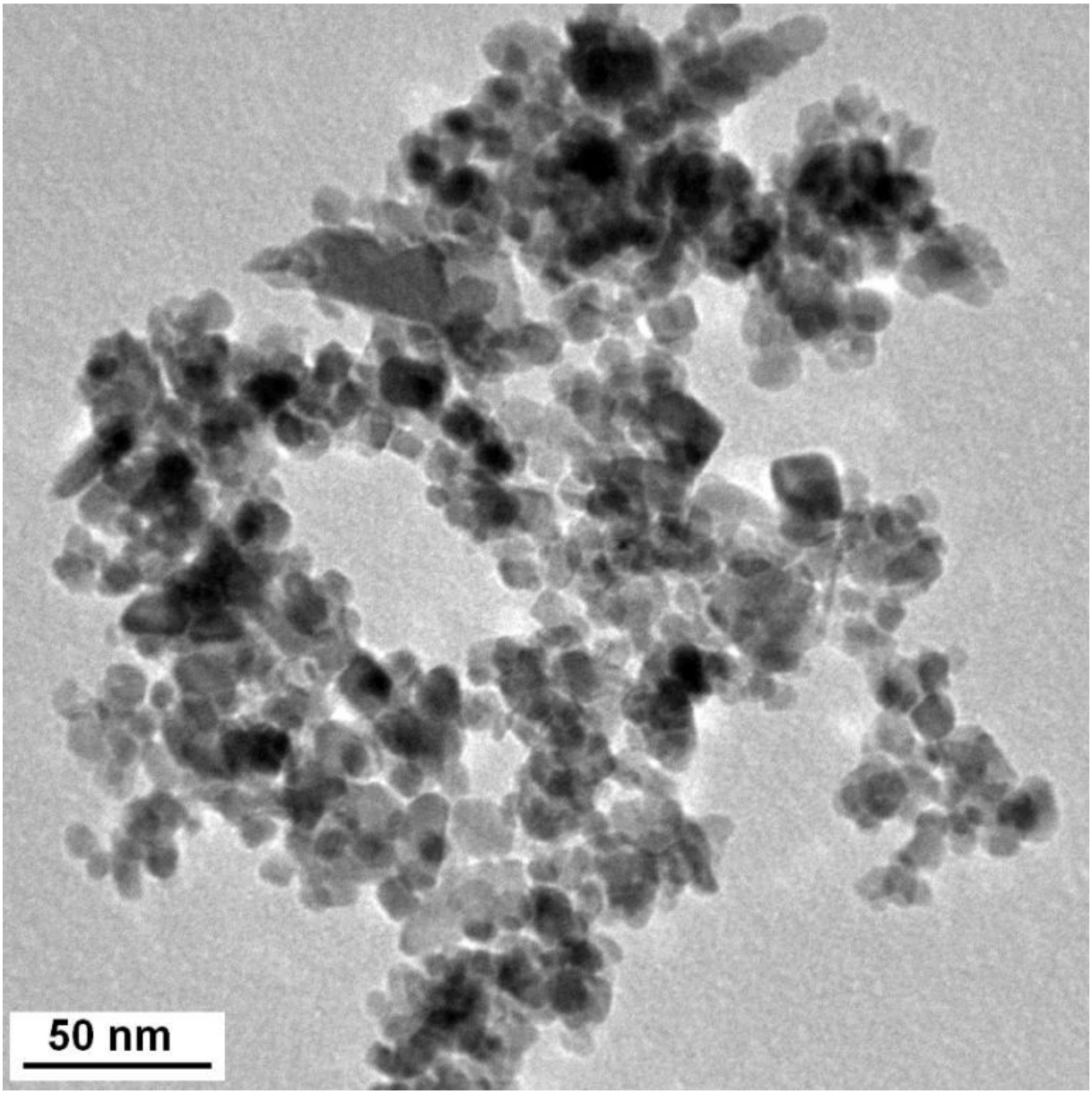

Figure 130. The bright field TEM image ($Ir_{0.25}Nb_{0.75}$)O_2:10 wt.% F shows the presence of fine nanoparticles

In order to determine the surface composition and chemical oxidation states, x-ray photoelectron spectroscopy (XPS) was carried out on the catalysts. The XPS spectra of Ir 4f, Nb 3d and O 1s of (Ir,Nb)O_2 and (Ir,Nb)O_2:F are shown in **Figure 131**, **Figure 132** and **Figure 133**,

respectively. The XPS spectra of Ir of $(Ir_{0.25}Nb_{0.75})O_2$ shows the presence of Ir $4f_{7/2}$ and Ir $4f_{5/2}$ doublet with binding energy ~ 61.6 eV and ~ 64.5 eV respectively, and the O 1s peak is centered at ~ 530.5 eV which is consistent with the values of bulk IrO_2. Also, the XPS spectra of Nb shows peak separation of Nb $3d_{5/2}$ and Nb $3d_{3/2}$ with a binding energy of ~ 207.5 eV and ~ 210.3 eV respectively (with the O1s line centered at ~530.5 eV), which is consistent with the values of stoichiometric NbO_x. But, XPS did not show any specific peak for fluorine. As reported previously, unequivocal confirmation of F could not be made by XRD and XPS measurements [57, 100, 124]. But, it is observed that the binding energy of Ir 4f, Nb 3d and O1s core level increases by ~ 0.4 - 0.6 eV for $(Ir_{0.25}Nb_{0.75})O_2$:10 wt.% F. This is an indirect indication of the stronger binding due to higher electro-negativity of F, suggesting its incorporation in the lattice. Although the exact amount and the nominal composition could not be conclusively stated [122], a weight loss of ~ 5 wt.% observed in the TGA-DTA (**Figure 128**) is caused due to F since the undoped electro-catalyst shows no weight loss in the TGA-DTA. Nevertheless, F incorporation clearly has a great impact on the electrochemical activity of $(Ir,Nb)O_2$:F solid solution as seen in the electrochemical results which is most likely attributed to the improved electronic conductivity and durability.

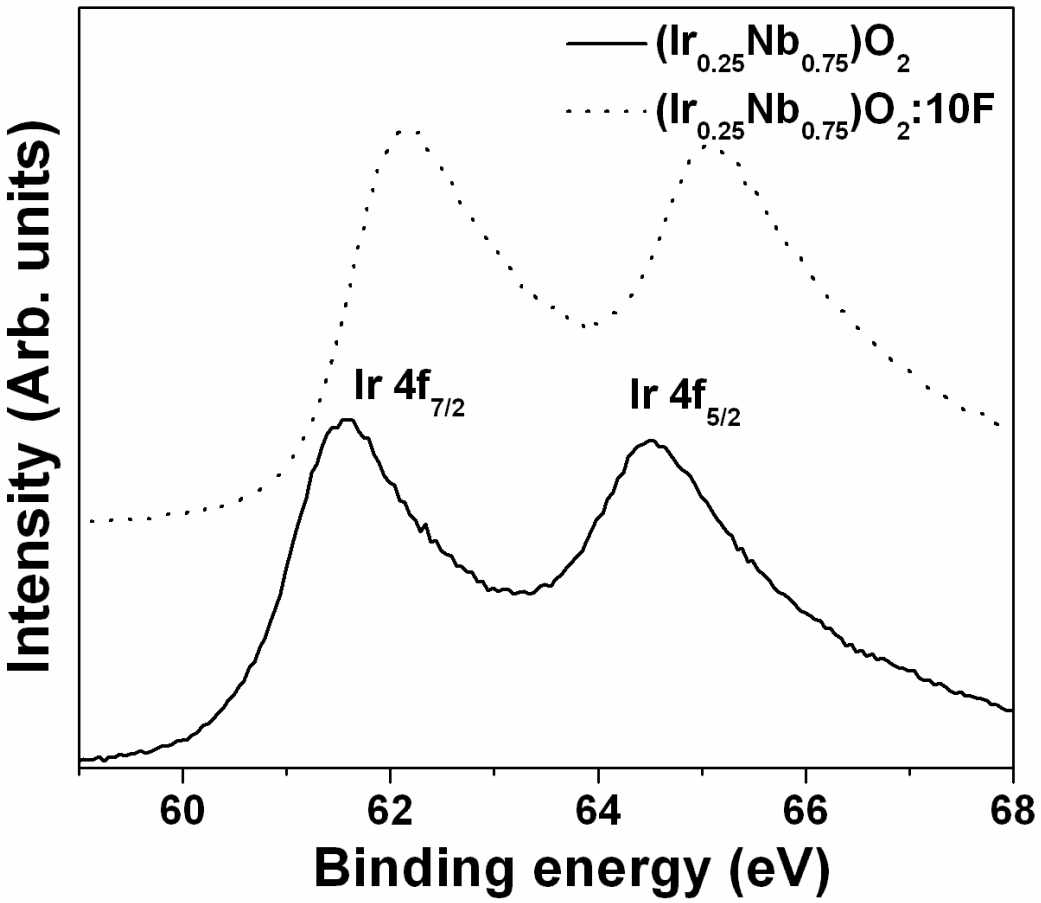

Figure 131. The XPS spectra of Ir $4f_{7/2}$ and Ir $4f_{5/2}$ doublet of (Ir,Nb)O_2 and (Ir,Nb)O_2:F

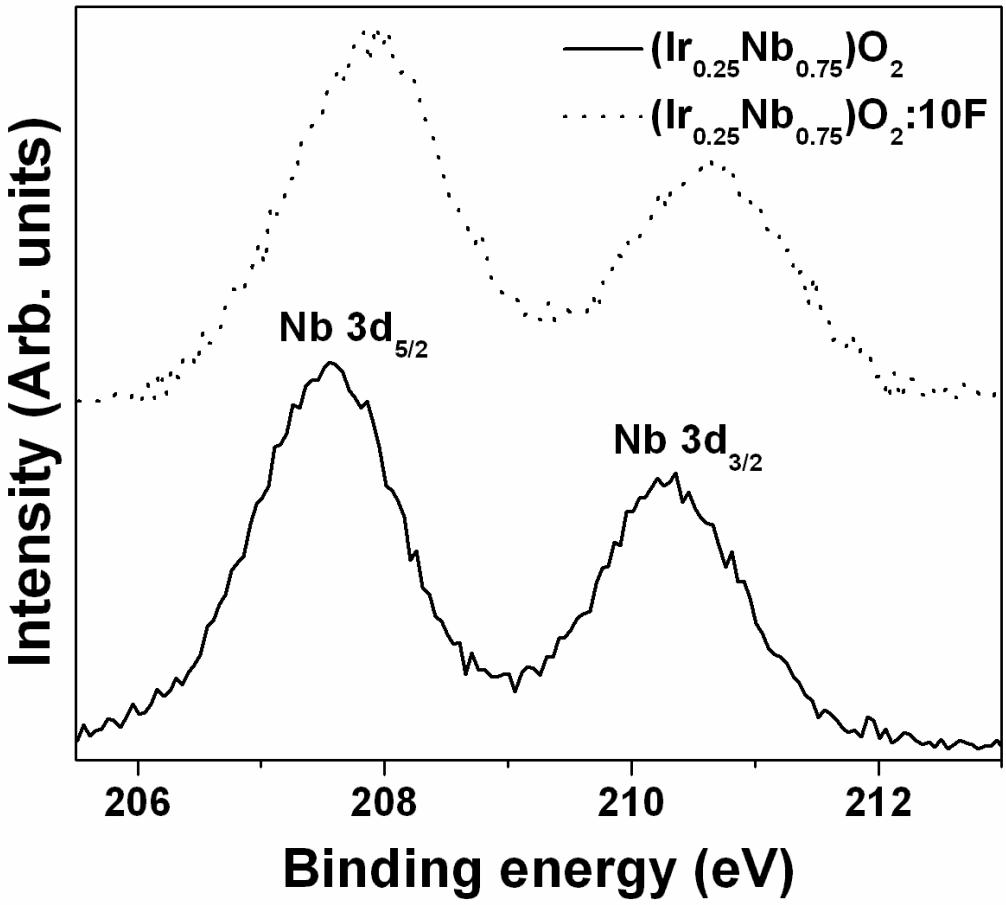

Figure 132. The XPS spectra of Nb $3d_{5/2}$ and Nb $3d_{3/2}$ doublet of $(Ir,Nb)O_2$ and $(Ir,Nb)O_2$:F

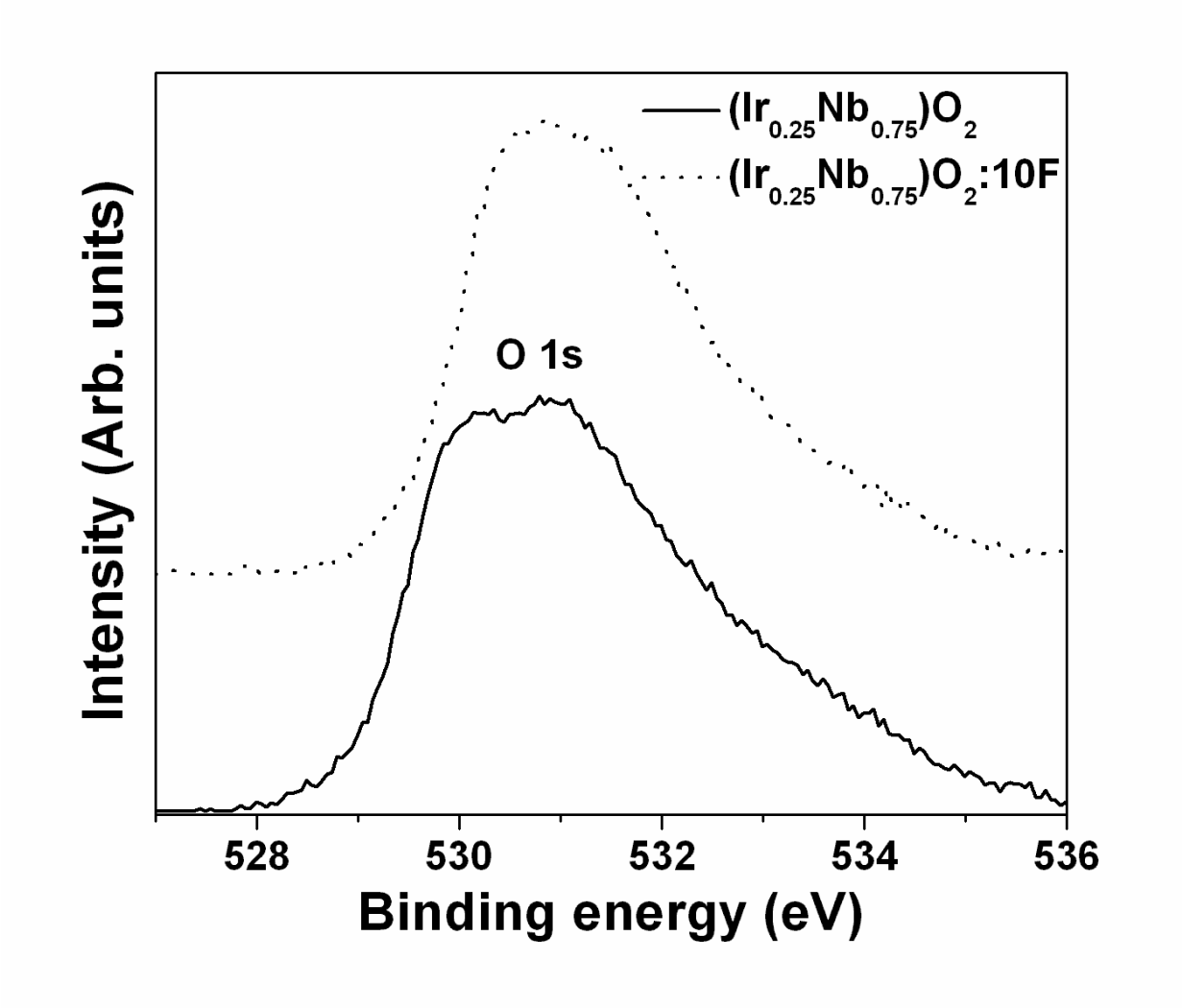

Figure 133. The XPS spectra of O 1s of (Ir,Nb)O_2 and (Ir,Nb)O_2:F

5.2.3.2 Electrochemical Testing

The electrochemical activity of commercially available IrO_2 (Alfa Aesar), (Ir,Nb)O_2 and (Ir,Nb)O_2:F has been examined as an OER anode electro-catalyst for PEM based water electrolysis. The linear polarization curve and non-linear Tafel plot are most often encountered due to large contribution of ohmic resistance (R_Ω) which is mainly due to R_s, R_e and bubble

resistance (R_{bub}) [51, 52]. The polarization curve of the electro-catalysts, is conducted in the presence of 1 N H_2SO_4 solution at 40^oC with a scan rate of 1 mV/sec in order to evaluate the inherent electrochemical property and electrode kinetics of the electro-catalyst studied herein. The value of R_s, R_e and R_{ct} is obtained from EIS measurements conducted at different potentials and are presented in **Table 9**.

Figure 134 and **Figure 135** show the electrochemical impedance spectroscopy (EIS) plot of (Ir,Nb)O_2 and (Ir,Nb)O_2:10F respectively, measured at open circuit potential (OCP), 1.5 V, 1.6 V and 1.8 V in the frequency range of 100 mHz - 100 kHz. The EIS polt for commercial IrO_2 has been plotted and shown in **Figure 118** (**Section 5.2.2.2**). The impedance parameters (**Table 9**) are calculated by fitting the experimental data using the ZView software from Scribner Associates with a circuit model $R_s(R_eQ_1)(R_{ct}Q_{dl})$. It should be noted that R_s for the undoped and doped electro-catalysts is unchanged with change in potential (~ 16.8 Ωcm^2). R_e is due to the resistance encountered due to electron transfer from the electrode to the current collector. The value of R_e for (Ir,Nb)O_2:F is less than the undoped (Ir,Nb)O_2 and is comparable to commercial IrO_2 which may arise due to the improved electronic conductivity of (Ir,Nb)O_2:F. A well formed semicircular arc is observed at low frequencies in the EIS plots. The diameter of this arc is typically a measure of the polarization / charge transfer resistance (R_{ct}). (Ir,Nb)O_2:F has similar or even lower R_{ct} values compared to commercial IrO_2 and (Ir,Nb)O_2, which explains the increase in catalytic activity of the electrode with incorporation of F.

Table 9. Impedance parameters of nanoparticulate $(Ir,Nb)O_2$:F and commercial IrO_2

Voltage	Electro-catalyst	R_s (Ωcm^2)	R_e (Ωcm^2)	R_{ct} (Ωcm^2)
Open Circuit	$(Ir,Nb)O_2$:0F	16.90	3.12	2958
	$(Ir,Nb)O_2$:10F	16.85	2.67	2445
	IrO_2 (Alfa)	16.42	4.03	3577
1.5V	$(Ir,Nb)O_2$:0F	16.69	6.11	77.56
	$(Ir,Nb)O_2$:10F	16.70	5.00	47.20
	IrO_2 (Alfa)	16.31	3.36	44.89
1.6V	$(Ir,Nb)O_2$:0F	16.71	4.71	17.90
	$(Ir,Nb)O_2$:10F	16.79	4.00	10.39
	IrO_2 (Alfa)	16.38	2.57	14.76
1.8V	$(Ir,Nb)O_2$:0F	16.78	2.75	6.81
	$(Ir,Nb)O_2$:10F	16.88	1.23	5.91

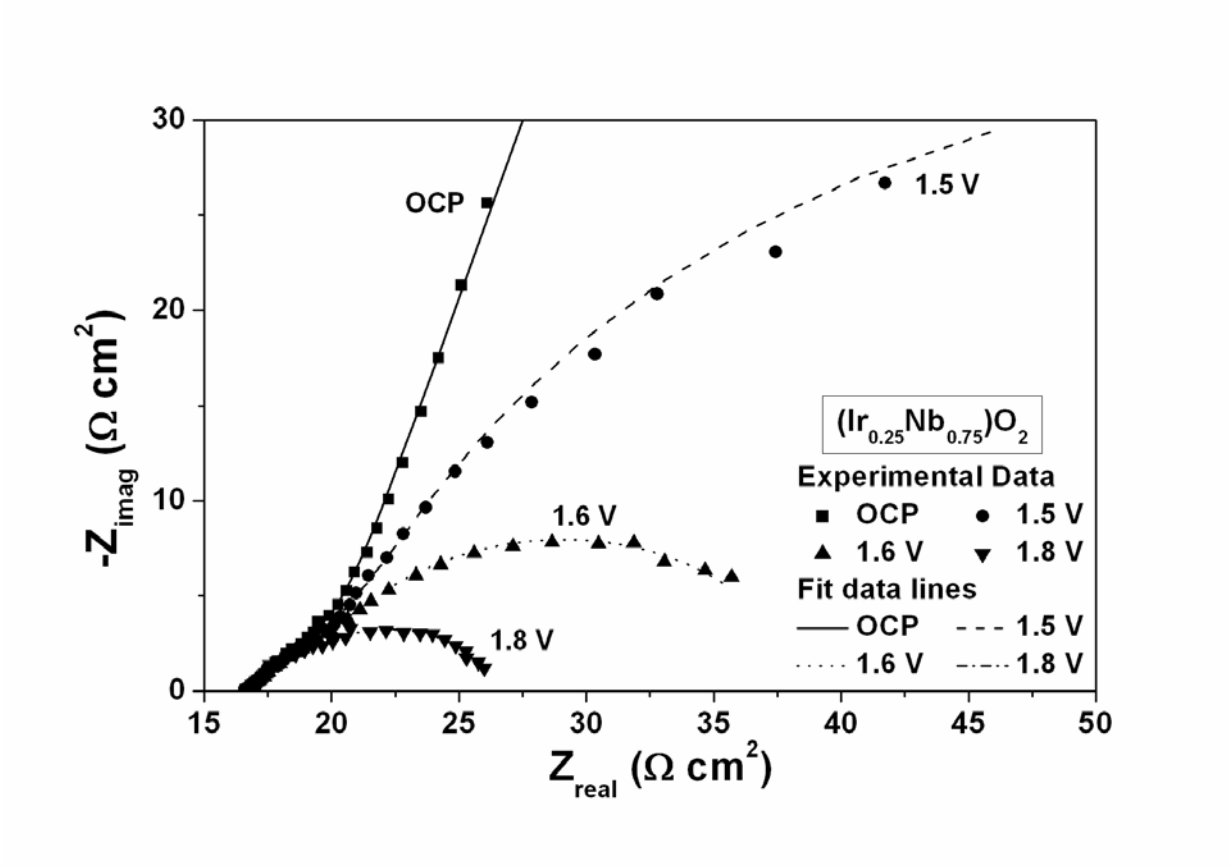

Figure 134. EIS spectra of (Ir,Nb)O_2 obtained at OCP, 1.5 V, 1.6 V and 1.8 V in 1 N H_2SO_4

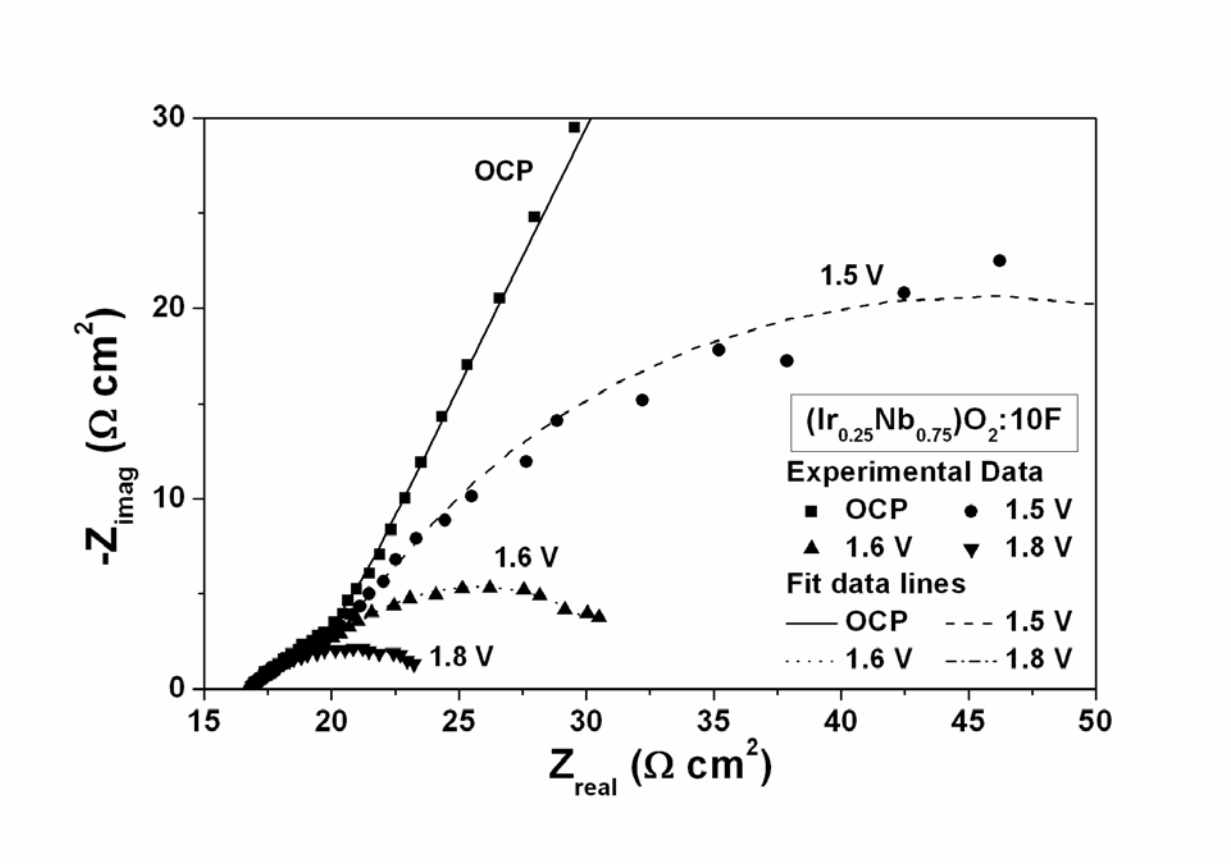

Figure 135. EIS spectra of (Ir,Nb)O_2:10 wt.% F obtained at OCP, 1.5 V, 1.6 V and 1.8 V in 1 N H_2SO_4

The polarization curve of commercial IrO_2 (Alfa Aesar), (Ir,Nb)O_2 and (Ir,Nb)O_2:F, before and after ohmic resistance correction ($iR_\Omega = iR_s + iR_e$) without considering R_{bub}, is shown in **Figure 136**. The water splitting reaction (OER) for commercial IrO_2 occurs at a potential of ~ 1.43V *vs.* NHE. The current density of IrO_2 at ~ 1.5V (*vs.* NHE), which is in the typical range of voltages selected to verify the electrochemical activity for water electrolysis, obtained from the iR_Ω corrected plot is ~ 0.0125 ± 0.0002 A/cm^2 for ~ 0.3 mg/cm^2 loading of IrO_2. The Tafel plot of commercial IrO_2 has been shown earlier in **Figure 120** (**Section 5.2.2.2**), which has a Tafel slope of ~ 83 mV/decade, which is slightly higher than what corresponds to a two electron

pathway reaction (Tafel slope ~ 62 mV/dec) assuming the transfer coefficient to be ~ 0.5 [48, 53, 57, 58]. The polarization curve for the (Ir,Nb)O_2 and (Ir,Nb)O_2:F before and after iR_Ω correction also shows OER occurring at a potential of ~ 1.43 V (*vs.* NHE) which is identical to that of pure IrO_2. But, the current density at ~ 1.5 V (*vs.* NHE) for undoped $(Ir_{0.25}Nb_{0.75})O_2$ with an identical IrO_2 loading of ~ 0.3 mg/cm^2 is ~ 0.008 ± 0.0002 A/cm^2 at 40^{o}C which is ~ 36 % lower than commercial IrO_2. However, the current density of $(Ir_{0.25}Nb_{0.75})O_2$:10 wt.% F increases. In fact, (Ir,Nb)O_2:F shows a current density of ~ 0.0133 ± 0.0002 A/cm^2 at ~ 1.5 V (*vs.* NHE) after iR_Ω correction which is slightly better than commercial IrO_2. The Tafel slope of (Ir,Nb)O_2 and (Ir,Nb)O_2:10F, calculated from the corresponding iR_Ω corrected Tafel plots, shown in **Figure 137** and **Figure 138**, is ~132 and ~78 mV/decade, respectively. This suggests that the electrochemical activity of (Ir,Nb)O_2:F increases with increase in F and corresponding decrease in the Tafel slope. It reaches an optimal value for (Ir,Nb)O_2:10 wt.% F exhibiting very similar electro-catalytic activity to that of commercial IrO_2 (~ 83 mV/decade). These results clearly suggest that $(Ir_{0.25}Nb_{0.75})O_2$:10 wt.% F is a promising candidate as an OER anode electro-catalyst for PEM based water electrolysis.

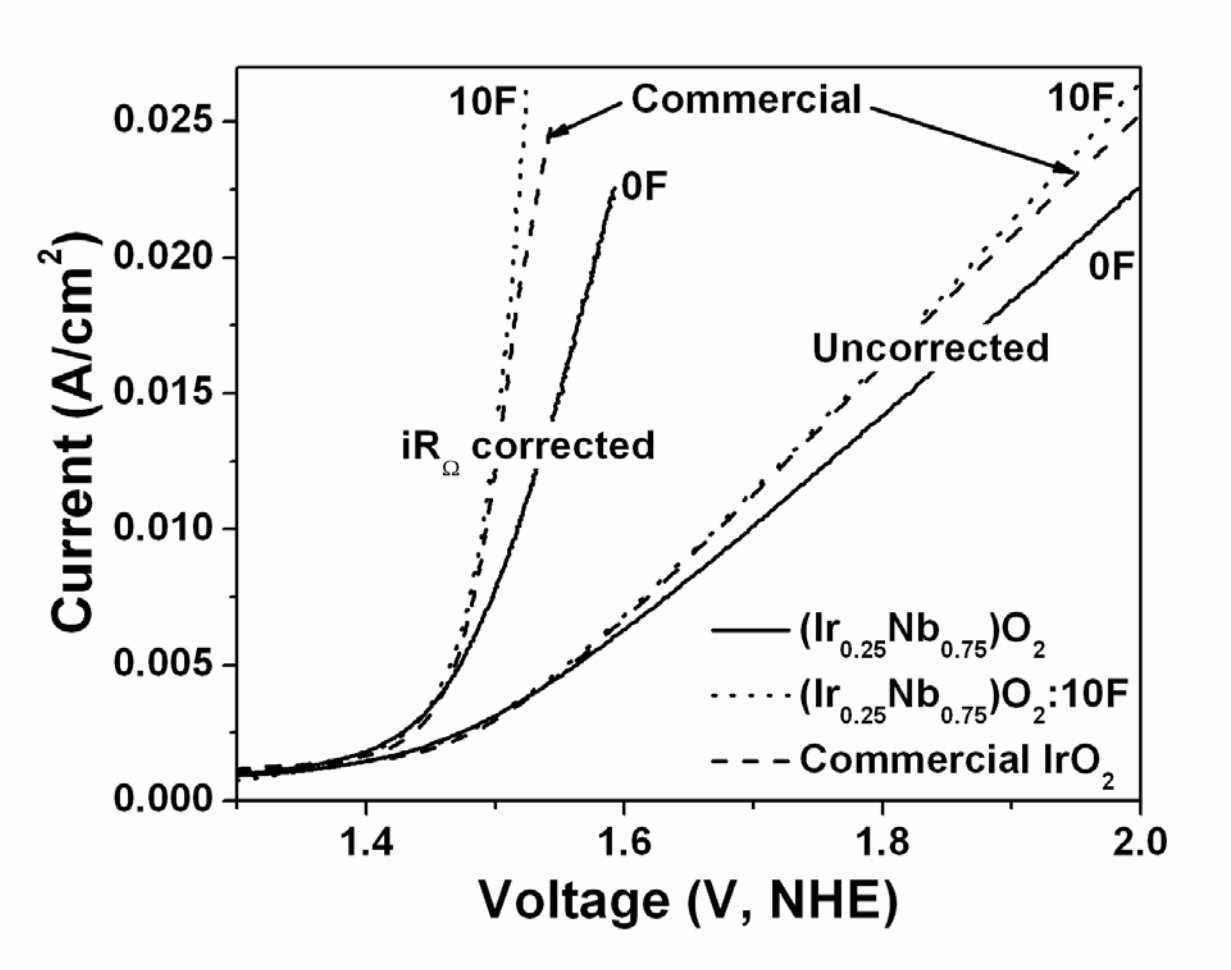

Figure 136. The polarization curve of undoped and F doped (Ir,Nb)O_2 along with commercial IrO_2 in the presence of 1 N H_2SO_4 solution at 40°C with a scan rate of 1 mV/sec before and after iR correction

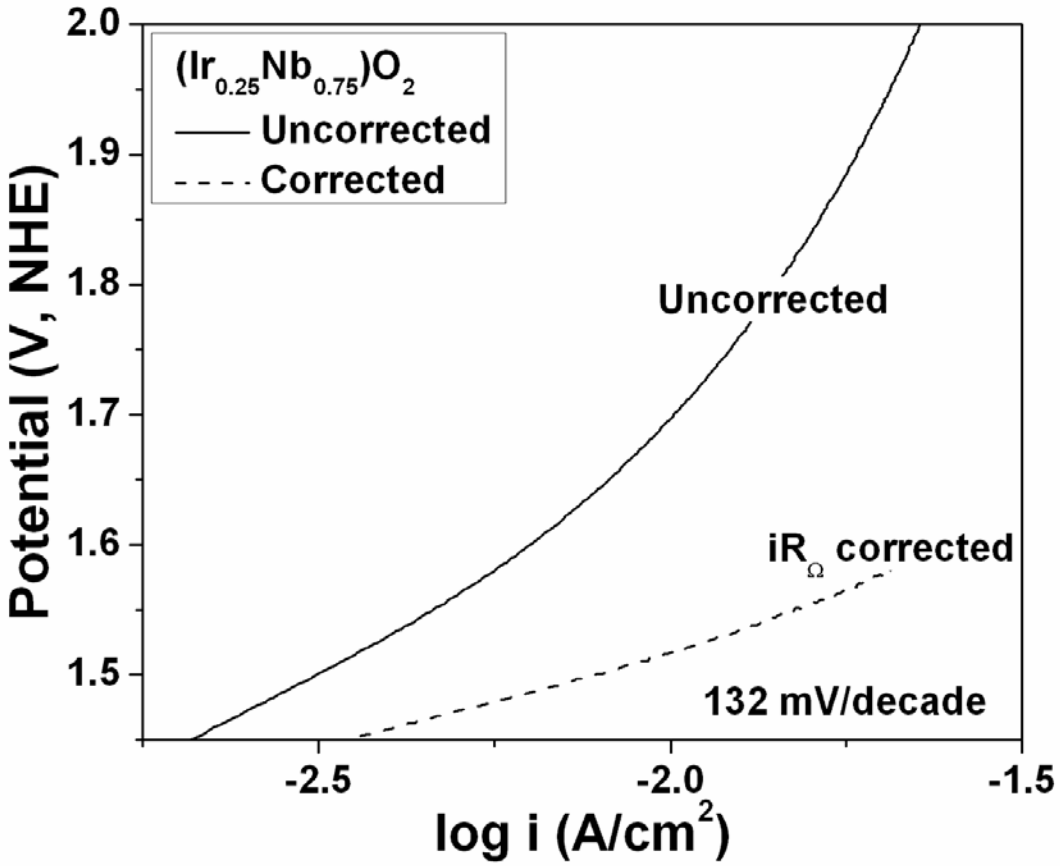

Figure 137. The Tafel plot of $(Ir,Nb)O_2$ before and after iR correction

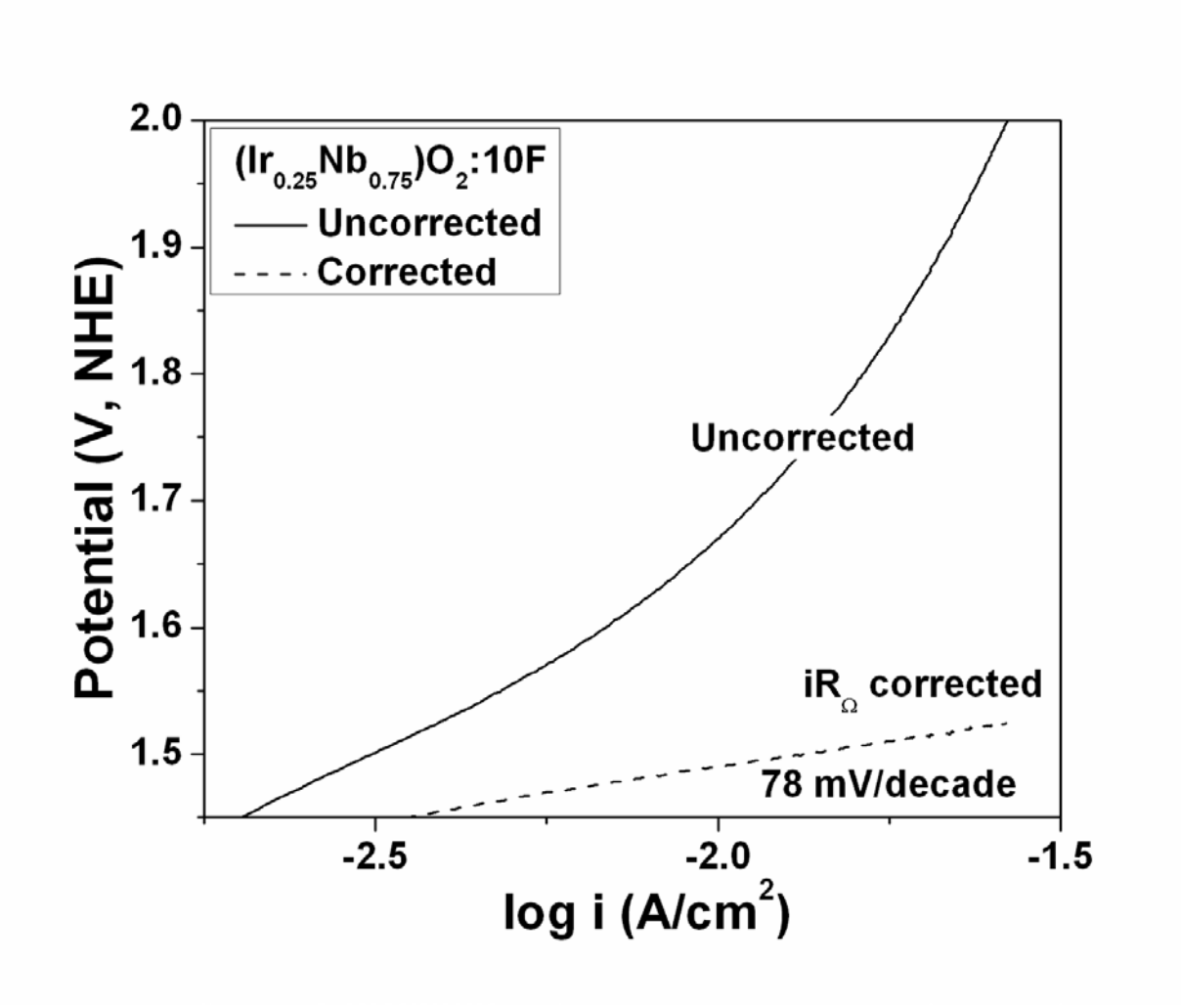

Figure 138. The Tafel plot of (Ir,Nb)O_2:10 wt.% F before and after iR correction

In order to examine the stability, chronoamperometry (CA) *i.e.* current measurement *vs.* time is conducted for 12 hours at a constant voltage of ~ 1.65 V (*vs.* NHE, without iR_Ω correction), to determine the degradation or loss of activity in CA studies. The CA curves of $(Ir_{0.25}Nb_{0.75})O_2$, $(Ir_{0.25}Nb_{0.75})O_2$:10 wt.% F and commercial IrO_2 are shown in **Figure 139**. The undoped $(Ir_{0.25}Nb_{0.75})O_2$ shows lesser initial current density because it inherently gives lesser catalytic activity than the doped catalyst and commercial IrO_2 (**Figure 136**). The decay of

current for the catalysts can be attributed to dissolution of coating at the edge of the porous titanium support [30], and by the induced loss of electrolyte [34, 57]. But, commercial IrO_2 undergoes a lot of degradation and gives a steep decrease in current over time showing its instability whereas a steady decay of current is observed for the $(Ir,Nb)O_2$:F electro-catalysts. This clearly suggests that Nb_2O_5:F support enhances the stability of IrO_2 to a very great extent.

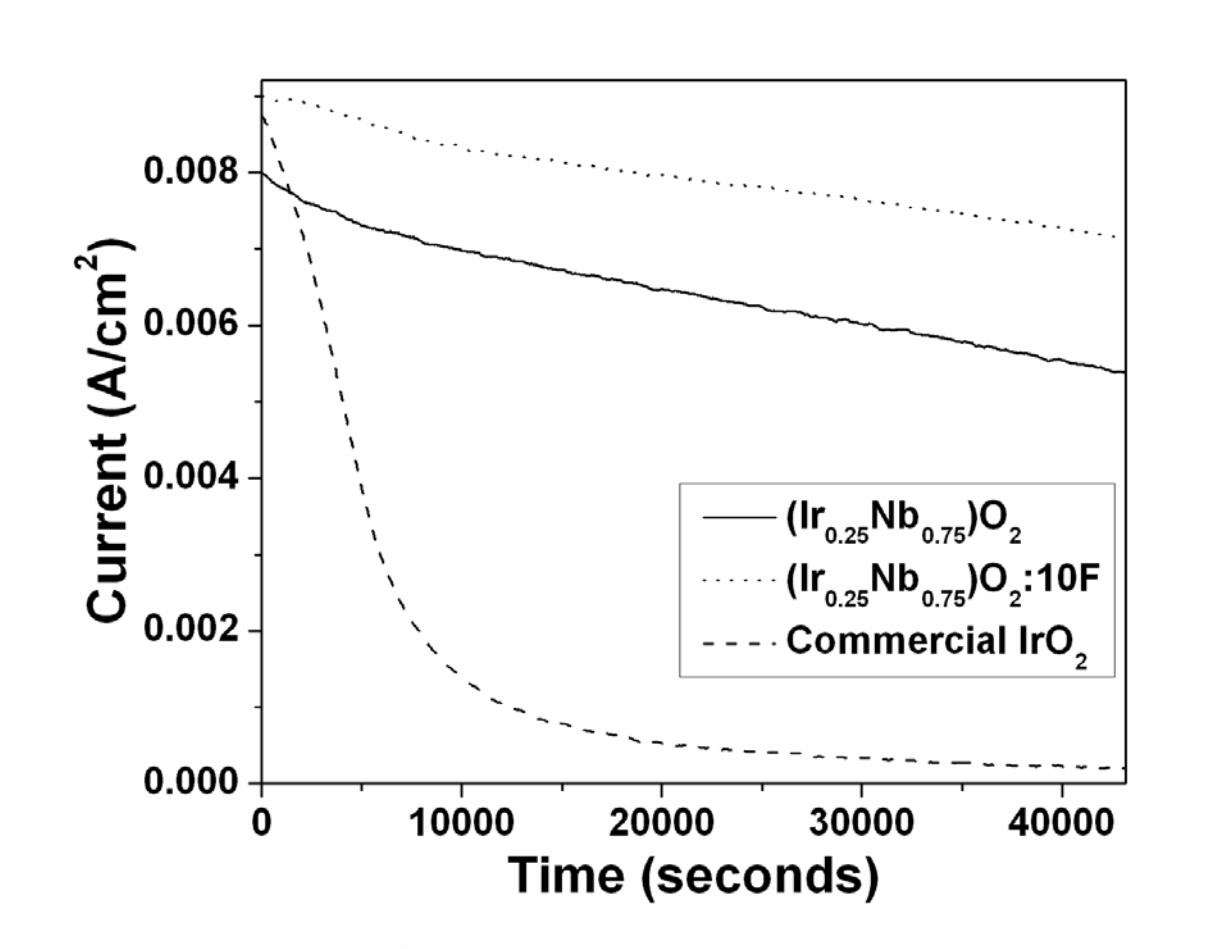

Figure 139. The variation of current *vs.* time for $(Ir,Nb)O_2$:F powders and commercial IrO_2 in the CA test performed in a 1 N H_2SO_4 solution at a constant potential of ~ 1.65 V

The ICP results conducted on the 1 N H_2SO_4 electrolyte solution after the CA measurement shows no presence of Ir and Nb for undoped and doped (Ir,Nb)O_2. However, commercial IrO_2 shows ~ 0.35 ppm of Ir leached out in the solution. This indicates that the decrease in current for the electro-catalysts may arise due to dissolution of the electro-catalyst from the surface.

After the conclusion of the CA test, the $(Ir_{0.25}Nb_{0.75})O_2$:10 wt.% F electrode was subject to polarization testing as seen in **Figure 140** in order to determine the activity of the electrodes after long term structural stability tests. The Tafel plot from the polarization curve (post CA measurement) after iR correction is shown in **Figure 141**. A Tafel slope of ~ 117 mV/decade was obtained for (Ir,Nb)O_2:10 wt.% F which is comparable to that of undoped IrO_2 after CA (~ 112 mV/decade) as seen in **Figure 104**. This test further demonstrates the robustness of the (Ir,Nb)O_2:F electro-catalyst.

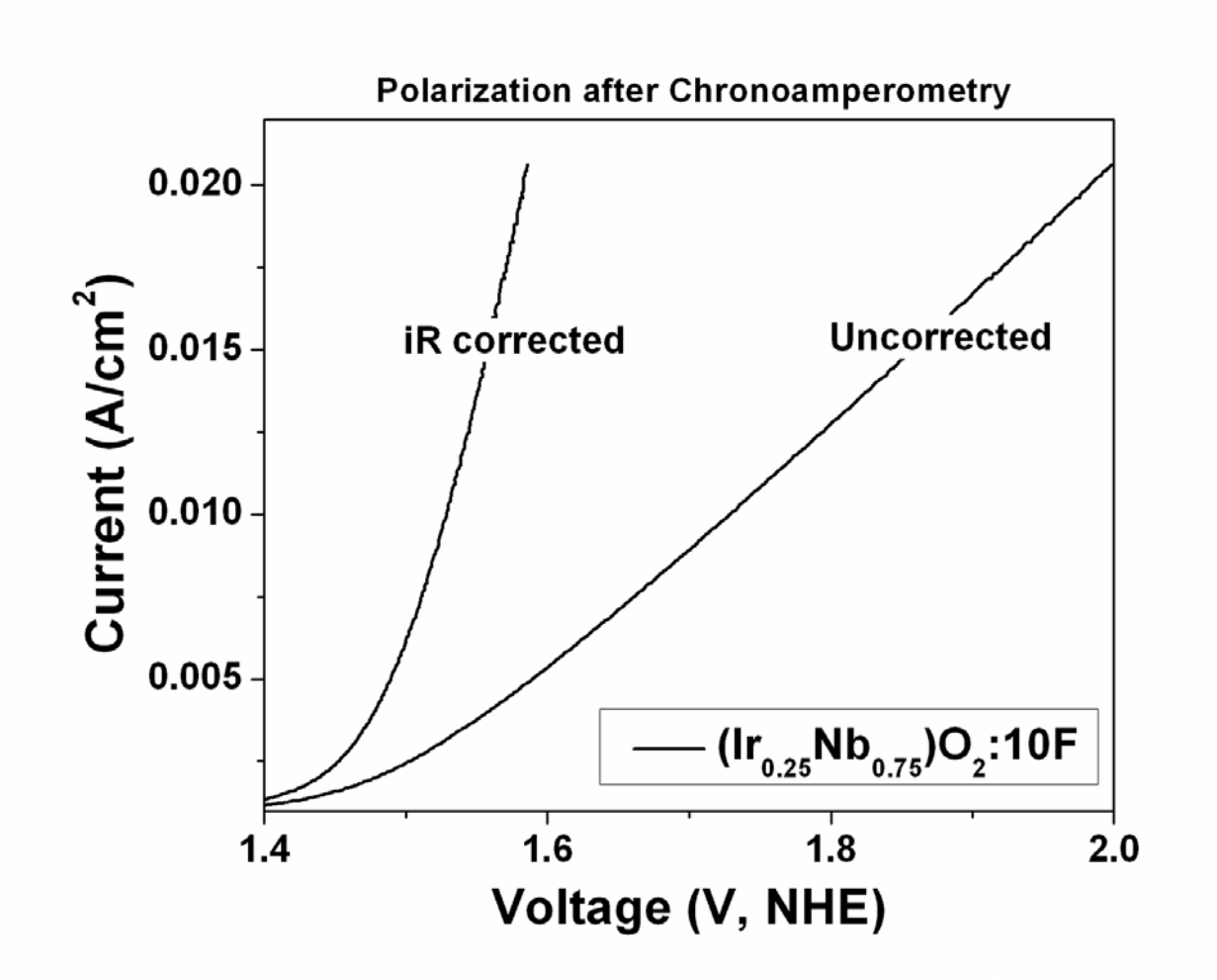

Figure 140. Polarization curve of (Ir,Nb)O_2:10 wt.% F powder after the CA test

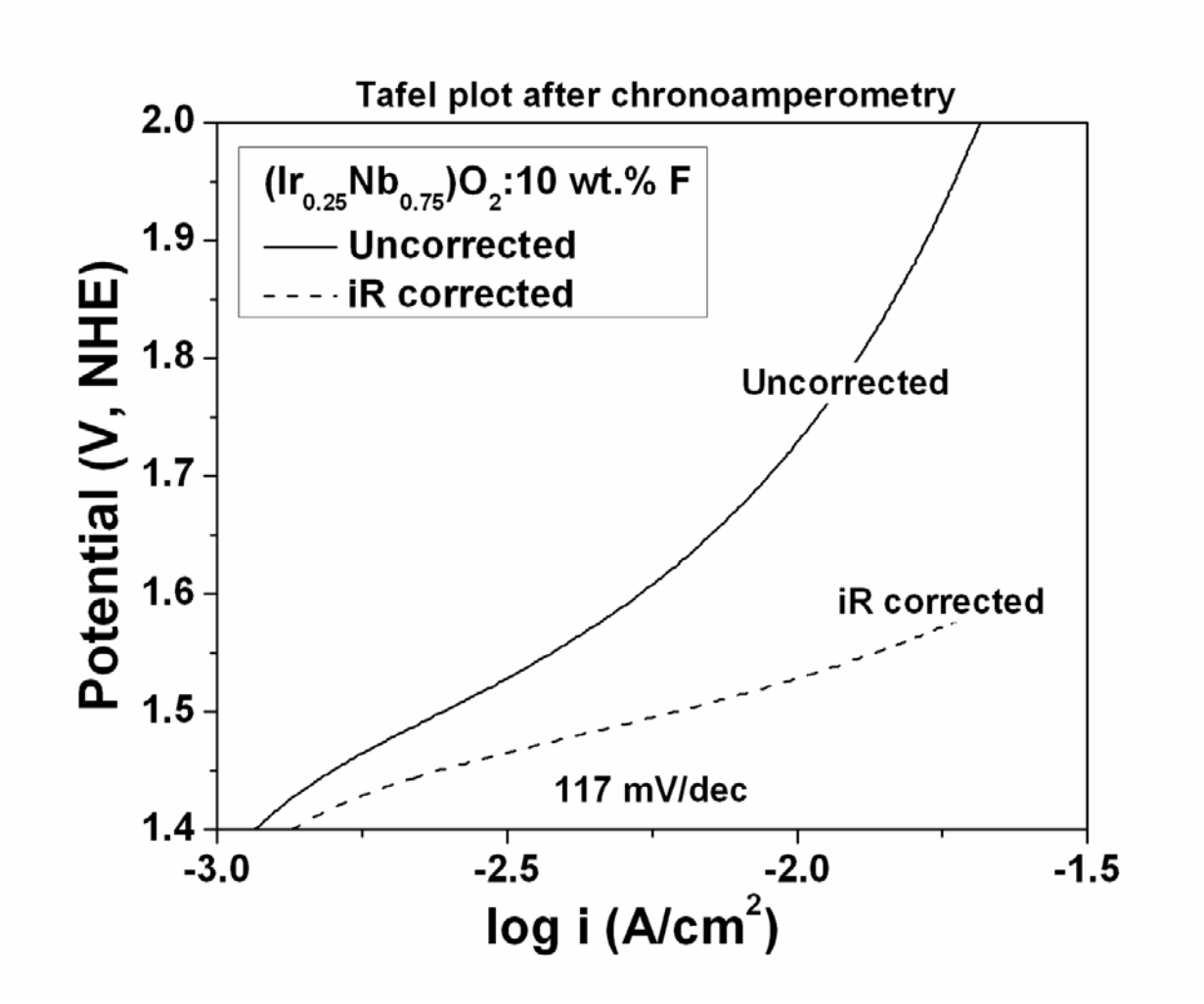

Figure 141. The Tafel plot of (Ir,Nb)O_2:10 wt.% F powder after the CA test

The best and optimized binary electro-catalyst compositions of ($Ir_{0.25}Nb_{0.75}$)O_2:10 wt.% F were studied and tested along with ($Ir_{0.3}Sn_{0.7}$)O_2:10 wt.% F at Proton OnSite in a single full cell set-up for PEM based water electrolysis. The polarization curve, shown in **Figure 142**, was obtained by ramping up and down the current at 1 minute intervals until the forward and reverse scans overlaid each other. It is seen that the (Ir,Nb)O_2:F exhibits much superior electro-catalytic activity than (Ir,Sn)O_2:F. The current density at ~ 2 V, a standard assessment voltage for single full PEM electrolyzer tests, is ~ 0.6 A/cm^2 and ~ 0.25A/cm^2 for ($Ir_{0.25}Nb_{0.75}$)O_2:10 wt.% F and

$(Ir_{0.3}Sn_{0.7})O_2$:10 wt.% F, respectively. Pure (undoped) IrO_2 shows a current of ~ 0.5 A/cm^2 at ~ 2 V as shown in **Section 5.2.1.2**. This implies that the reduced noble metal $(Ir,Nb)O_2$ catalyst is similar and comparable to pure IrO_2 and much better than $(Ir,Sn)O_2$:F. This might be due to the fact that no metal ions leach out in the stability test (chronoamperometry) for the binary $(Ir,Nb)O_2$:F catalyst as opposed to $(Ir,Sn)O_2$:F, where Sn leaches out to some extent (~ 0.12 ppm).

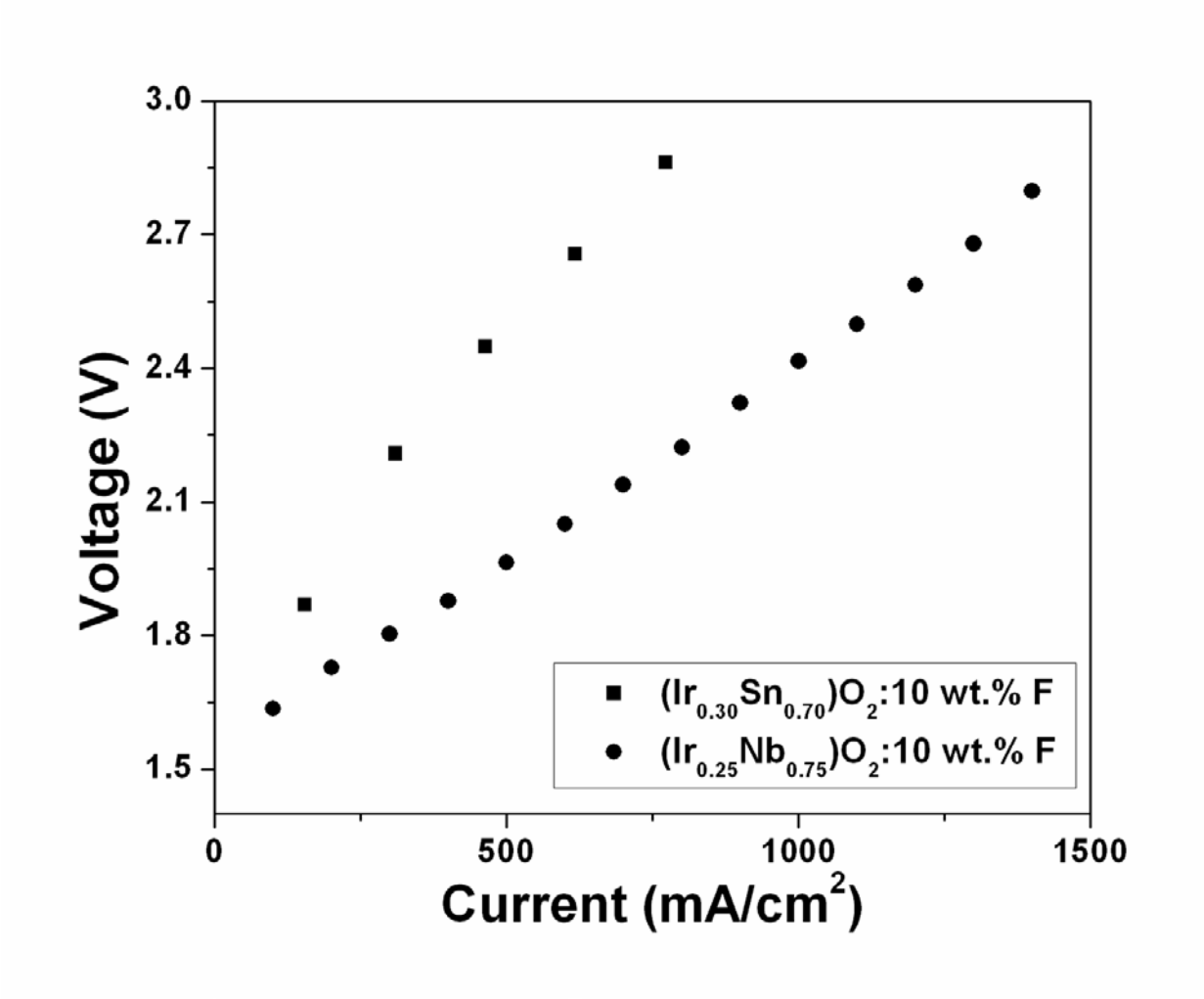

Figure 142. Polarization curve obtained in a single full cell PEM electrolyzer test for $(Ir,Nb)O_2$:F and $(Ir,Sn)O_2$:F powders at 50°C

In the present work, it is evident that the overall performance of $(Ir_{0.25}Nb_{0.75})O_2$:10 wt.% F catalyst is better than $(Ir_{0.3}Sn_{0.7})O_2$:F, and much superior to the commercially used pure IrO_2. This present study thus helps identify (Ir,Nb)O_2:F as a promising OER electro-catalyst with reduced noble metal oxide loading and increased catalytic performance, and chemical and structural stability.

6.0 FIRST PRINCIPLES CALCULATIONS

The Proton Exchange Membrane (PEM) water electrolysis cell consists primarily of a proton exchange membrane on which the anode and cathode are bonded. In a typical system, noble metal (*E.g.* Pt) or noble metal oxides (*E.g.* IrO_2) are utilized as catalysts for the anode with Pt being the catalyst for the cathode, respectively. Hydrogen is produced by supplying water to the anode decomposing into oxygen, protons, and electrons. At the cathode the electrons and protons re-combine to yield hydrogen gas. This is represented by the following equations:

Anode (oxidation): $2\ H_2O_{\ (l)} \rightarrow O_{2\ (g)} + 4\ H^+ + 4\ e^-$

Cathode (reduction): $4\ H^+ + 4\ e^- \rightarrow 2H_{2\ (g)}$

Overall Reaction: $2H_2O_{\ (l)} \rightarrow 2\ H_{2\ (g)} + O_{2\ (g)}$

The above reactions are primarily catalytically driven requiring the use of electro-catalysts as mentioned and discussed below. In order to develop electro-catalysts with high electrochemical activities, selectivity and stability, the fundamental dynamics of all the elementary processes occurring at the catalytically active sites must be understood. Modifications in the electronic structure of the system may strongly affect the thermodynamically stable intermediate states of the electrolytic process and hence, drastically change the overall catalytic activity of the material itself.

In the present day, using modern theoretical approaches *viz.*, Density Functional Theory (DFT), tremendous progress has been achieved in fundamental understanding of water splitting mechanisms in general and anodic oxygen evolution reactions in particular. Substantial effort in search of a single universal parameter describing catalytic activity of the given material has been made by Nørskov *et al.* [53, 54, 125, 126]. One of a very popular concept suggested by them was a position of the noble metal electronic d-band center serving as a simple descriptor for determining the catalytic activity of the surface. This descriptor has been defined as a gravity center of the d-band center of the noble metal ε_d usually located in the vicinity of the Fermi level. An optimal position of the d-band center thus provides an optimal interaction between the catalytic surface and the various species participating in the catalytic reactions predominantly occurring at the surface thus leading to an expected optimal catalytic activity [125, 126]. Later, they showed that transition metal as well as rutile oxide surfaces obey linear relations between O^* binding energy and the binding energy of other species relevant to the oxidation of water (OH^* and HOO^*) [53, 54]. Based in such relations they proposed a more reliable descriptor of the catalytic activity – the binding energy of O to the surface (ΔE_O). A volcano plot reflecting a dependence of the catalytic activity *vs.* ΔE_O demonstrated possible room for improving the electro-catalyst. Modifying electronic structure of the catalytic surface in such a way that binding energies of the intermediate species become more optimal in term of a position on the volcano plot may improve the catalytic activity to some extent.

All the first principle calculations reported herein have been done by *Dr. Oleg I. Velikokhatnyi*, a research faculty at University of Pittsburgh (*Dr. Kumta's Lab*). The theoretical studies complement the experimental results and help in the fundamental understanding of the catalytic activity and durability of the catalysts.

6.1 F DOPED IRIDIUM OXIDE

The present study is an attempt to reveal and analyze the reasons underlying the high electro-catalytic activity of fluorine doped IrO_2 synthesized by us [34]. Such a phenomenon needs to be analyzed and understood however; since this knowledge may prove to be vital in the design and development of novel electro-catalysts with excellent catalytic performance for PEM based electrolyzers.

It has been observed (**Figure 7**, **Figure 85** and **Figure 86**) that the onset potential is the same for all compositions of the IrO_2:F. The difference is in the slopes of the lines which points to the fact that the kinetics of the OER rather than thermodynamics is dependent on the F content. However, as a first approximation for determining just qualitative trend but not the precise value of the catalytic activity as a function of the F concentration, only the thermodynamic aspects of the problem have been considered. Various kinetic barriers such as effects of the electric field and surface charges as well as proton transfer barriers although quite important, would not probably significantly change the qualitative trends derived from the pure thermodynamic considerations. Only experimental in situ spectroscopy of surface intermediates combined with atomic-level analysis and a reliable theoretical computational framework will ultimately be able to resolve kinetic activation barriers, elementary steps, and nature of the active site of the OER on metal oxide surfaces [127].

6.1.1 Computational Methodology

In PEM based water electrolysis, the water splitting process in an acidic media where the corresponding anodic reaction mechanism similar to [53] could be sequentially written as follows:

$$2H_2O \rightarrow HO^* + H_2O + H^+ + e^-$$

$$\rightarrow O^* + H_2O + 2H^+ + 2e^-$$

$$\rightarrow HOO^* + 3H^+ + 3e^-$$

$$\rightarrow O_2 + 4H^+ + 4e^-$$

The * represents an active site on the metal oxide surface. Under acidic conditions due to the weak interactions between hydrogen and the metal cathode, hydrogen evolution is much faster on the cathode rather than oxygen evolution on the anode and hence cannot be considered to be the primary rate determining step of the overall catalytic activity [54].

Free energies ΔG of all the four anodic intermediate reactions described above determine electric potentials at which a certain specific reactions would occur. Thus a systematic analysis of all calculated free energies may elucidate the rate determining / limiting step of the electrolysis reaction which can serve as a measure of the electro-catalytic activity of the specific material that is under investigation. In order to obtain the free energies of all the intermediate reactions we will use an approach suggested and described in detail by Rossmeisl *et al.* [53, 54] and successfully applied for calculation of the catalytic activities of metals and metal oxides for water splitting. The general trend for the calculated over-potentials, such as $TiO_2 > IrO_2 > RuO_2$ appeared to be consistent with experimental observations although the absolute values are

slightly overestimated. Detailed analysis of the results may help understand role of fluorine in contributing to the improvement of the observed catalytic activity of IrO_2.

For the calculations, the reference potential was set to be that of the standard hydrogen electrode, in order to relate the chemical potential (the free energy per H) for ($H^+ + e^-$) to that of ½ H_2 in the gas phase. At pH 0 in the electrolyte and 1 bar of H_2 in the gas phase at 25°C, the reaction free energy of ½ $H_2 \rightarrow H^+ + e^-$ is zero at zero electrode potential. At standard conditions, the free energy ΔG_0 of the reaction $^*AH \rightarrow A + H^+ + e^-$, can be calculated as the free energy of the reaction $^*AH \rightarrow A + ½ H_2$.

ΔG_0 is represented as the following: $\Delta G_0 = \Delta E + \Delta ZPE - T\Delta S$. The reaction energy ΔE is calculated using density functional theory (DFT). The zero point energy correction (ΔZPE), and change in entropy (ΔS) is calculated using DFT calculations of the vibrational frequencies taken from Kandoi *et al.* [128] and from the standard tables for gas phase molecules [129]. For the adsorbed O, OH and OOH species, the corrections are 0.05 eV, 0.35 eV and 0.4 eV, respectively. H_2O and H_2 in the gas phase are used as references states. Also, the entropy for gas phase water is calculated at 0.035 bars since this is the equilibrium pressure in contact with liquid water at 298 K. The free energy of gas phase water at these conditions is equal to the free energy of liquid water. ΔG_0 of the total reaction is fixed at the experimental value of 2.46 eV to avoid the calculation of the O_2 bond energy which is difficult to calculate accurately with DFT.

All the DFT calculations have been conducted using the generalized gradient approximation (GGA) for the exchange-correlation energy functional in a form suggested by Perdew and Wang [130]. The projector augmented wave (PAW) method and a plane wave basis set, as implemented in the Vienna Ab initio Simulation Package (VASP) has been used [131-133]. The atomic positions and the cell parameters, including the cell volume, are optimized by

minimizing the forces and stresses *via* the Hellmann - Feynman theorem. Standard PAW potentials were employed for the elemental constituents of all pure and doped compounds. For all the materials considered the plane wave cutoff energy of 520 eV has been chosen to maintain a high accuracy of the total energy calculations. The lattice parameters and internal positions of atoms were fully optimized during the double relaxation procedure employed, and consequently, the minima of the total energies with respect to the lattice parameters and internal ionic positions have been correspondingly determined. This geometry optimization was obtained by minimizing the Hellman - Feynman forces *via* a conjugate gradient method, so that the net forces applied on every ion in the lattice is maintained close to zero. The total electronic energies were converged within 10^{-5} eV/unit cell resulting in the residual force components on each atom to be lower than 0.01 eV/Å/atom, thus allowing for the accurate determination of the internal structural parameters. Bader charges were calculated by integrating electron densities within zero flux surfaces around nuclei and are converged to within 0.1 e compared to a grid 1.5 times denser along each lattice vector [134].

A surface covered with oxygen is chosen in contrast to the OH^* covered surface, since such a surface is less active and less stable than the O^* covered surface [53]. Thus, the rutile type (110) preferred surface covered with oxygen has been chosen for calculation of the free energies for undoped IrO_2 and with fluorine atoms located at the surface. The 2 x 2 surface unit cell for a symmetric 7 layer slab ~ 10.3 Å thick separated between its images perpendicular to the surface direction by vacuum space of ~ 20 Å, to prevent interaction between the slab and its adjacent images. All intermediate species such as O^*, OH^*, and OOH^* have been attached to the coordinated unsaturated sites on both sides of the slab. Three middle layers were fixed with the lattice parameter corresponding to the bulk IrO_2, while all other layers of the slab together with

the intermediate species were fully relaxed. Hence, all the numerical data obtained from such a model should be divided by two. **Figure 143** shows a unit cell chosen for the calculations in the present study. Three different atomic distributions of F as a replacement of oxygen in the unit cell have been considered to analyze the difference between the electronic structures of pure and doped IrO_2 compounds as well as to assess the role and contribution of F on the catalytic activity. The first F atomic distribution consists of only one F atom located in place of oxygen and denoted with a number 1 in **Figure 143**. The second distribution is characterized by the introduction of an additional F atom marked with the number 2. And finally, the third arrangement of the F atoms in the unit cell consists of three F atoms positioned at all three places marked with the numbers 1, 2, and 3. Furthermore, in the text we will refer to these three F-configurations as F1, F2, and F3, respectively. Such unit cells covered by adsorbed oxygen monolayer together with intermediate species at the surface were used for calculations of the free energies of all the four elementary reactions.

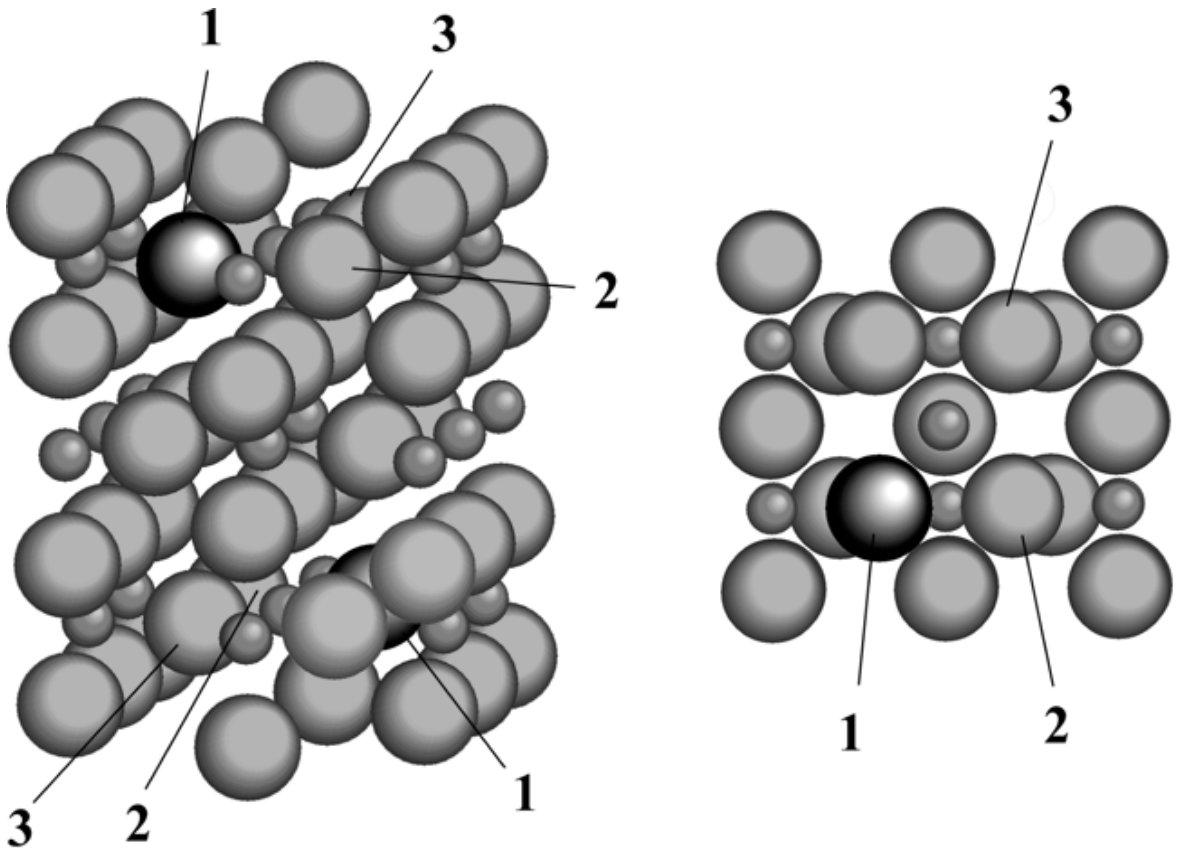

Figure 143. Angle and top view of the elementary unit cell of the (110) rutile surface slab used: small - Ir, big - O, dark: F (for F1 configuration). Atoms denoted as 2 and 3 correspond to F2 and F3 configurations of fluorine distributions

6.1.2 Theoretical Discussion

The resulting free energies for all the four intermediate reaction steps for pure IrO_2 are presented in **Figure 144**. One can see that the third step of the stairs for undoped IrO_2 has a largest value of 1.51 eV and corresponds to the formation of HOO^* at the surface. This step can be considered as truly rate limiting because an applied potential not less than 1.51 V is required to render all the

four reactions to be exothermic and to force the overall water-splitting process to proceed on the surface. These results agree quite well with the literature [53] wherein the authors also confirmed the third step as rate limiting, although with higher overpotential (~ 0.56 V). The overpotential obtained in the present study is lower (~ 0.28 V) and is more close to the experimentally obtained value (~ 1.43 V). The seemingly large difference between the experimentally observed and calculated results can be attributed to a difference between the models of the surface slabs used in these two studies.

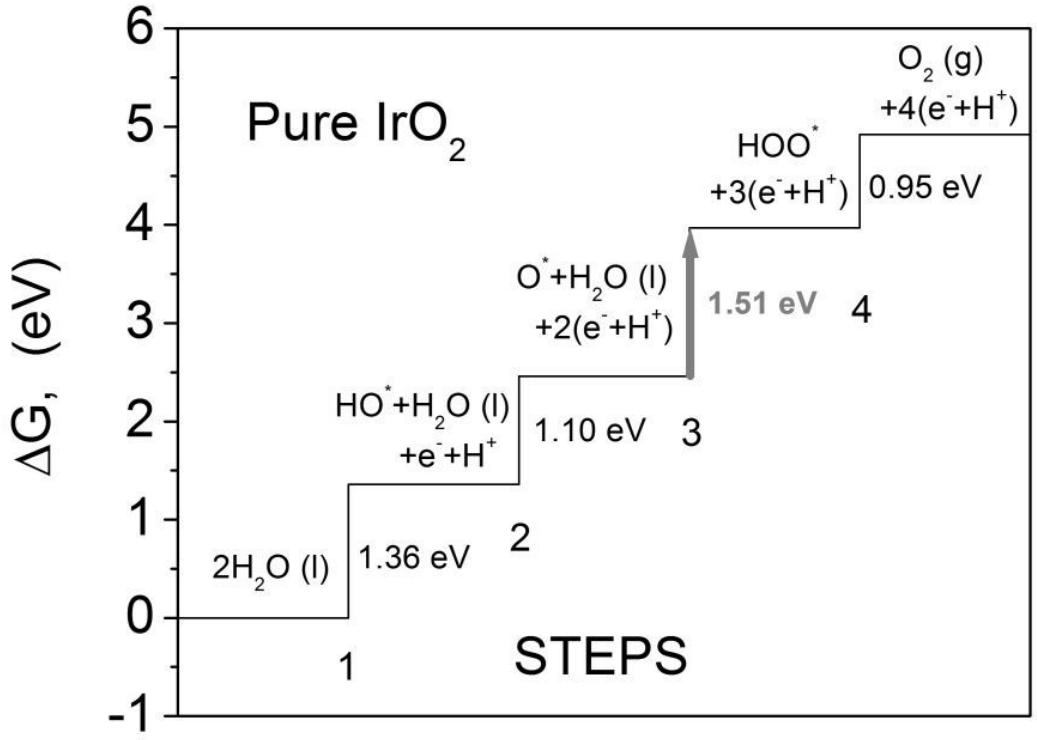

Figure 144. Free energies of the intermediate reactions for pure IrO_2

Quite similar energetics to pure IrO_2 are observed for F doped IrO_2 with different F distributions shown in **Figure 145**. For all the three cases again the formation of HOO^* is the largest step as that calculated for pure IrO_2 although with lower values than that calculated for the undoped oxide. One can see that the corresponding values of the HOO^* formation for all F configurations are less than that of pure IrO_2 and decrease with gradual F content increments in the material. Corresponding overpotentials for F1, F2, and F3 configurations are 0.21, 0.15, and 0.11 V, respectively. This rather noticeable decrease in the overpotential for F doped IrO_2 in comparison with pure IrO_2 (~ 0.28 V) indicates an increase in the catalytic activity in the presence of fluorine in the oxide matrix, which correlates well with the experimental data.

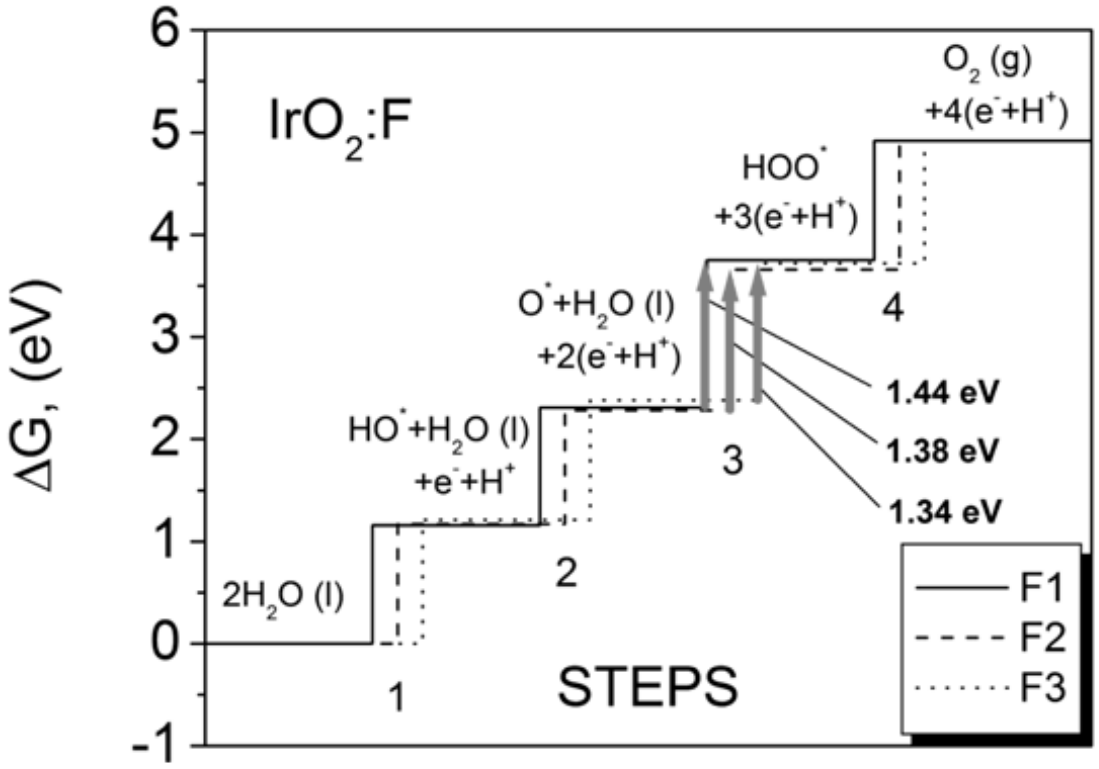

Figure 145. Free energies of the intermediate reactions for F doped IrO_2

Such a decrease in the energy difference for the third elementary step in the case of F doped IrO_2 is due to a stronger interaction between the adsorbed oxygen O^* and the surface. As a result, there is a decrease in the total energy of the system in comparison with undoped IrO_2, making it more feasible for the species to adsorb at the surface, consequently rendering the system more electrochemically active. Such an enhancement in adsorption could be understood from consideration of the effective ionic charges by means of the Bader charge analysis conducted in the present study. Using this technique [134], the total electronic charges of the constituent ions of the intermediates and adjacent ions on the pure and F doped IrO_2 surfaces are calculated. **Table 10** summarizes the effective electronic charges for the terminating oxygen atoms $^*O$ in all intermediates as well as for F ion adjacent to these $^*O$ atoms in case of F1 doped surface and charges for O ions located at the same site as F but in the pure IrO_2. One can see that F charges are systematically smaller than those of substituted oxygen ones. This charge reduction leads to decrease of the partial electrostatic repulsion between F doped surface and the intermediates. The electrostatic energy is directly proportional to the product of the charges, so that we can roughly estimate contribution of such repulsion to the total energy of the system. The next line in **Table 10**, $q(^*O)q(O)/q(^*O)q(F)$, contains products of the corresponding charges for pure and doped surfaces. One can see that in case of F doping such products are lower than that for pure IrO_2 due to a smaller effective F ion charge. Since the electrostatic repulsion generally contributes towards destabilization of the interatomic interactions, one can conclude that F doping decreases the repulsive component of the total energy making the system more stable with stronger binding between F doped surface and all intermediate species.

Table 10. Bader charges of the terminated oxygen ions *O adsorbed to the pure and F doped surfaces for *OH, *O and *OOH

	*OH		*O		*OOH	
	IrO_2	F1	IrO_2	F1	IrO_2	F1
*O--	-1.35	-1.36	-0.62	-0.64	-0.42	-0.39
O / F	-0.76	-0.60	-0.75	-0.61	-0.79	-0.59
q(*O)q(O) / q(*O)q(F)	1.03	0.82	0.465	0.39	0.33	0.23
Δ	-0.21		-0.075		-0.10	

But, making the binding stronger does not necessarily lead to lowering the rate limiting step or ΔG. The relative difference between ΔG_{OOH} and ΔG_O for F doped surface must be lower than that for undoped material. In **Table 10**, the last line contains differences between corresponding charge products for F doped and pure surfaces. Such a difference could be considered as a qualitative measure of change in the electrostatic repulsive contribution into the free energy ΔG of the system in each intermediate step. The change of the charge product for *O contributing to lowering ΔG_O is smaller than the same quantity contributing to ΔG_{OOH} (- 0.075 *vs.* - 0.10) resulting in the overall decrease of the relative difference ΔG_{OOH} - ΔG_O. Thus, decreasing the free energy for splitting of the second water molecule with the formation of the HOO^{*} intermediate on the surface lowers the energy for the rate limiting step and correspondingly enhances the overall catalytic activity of the material.

For qualitative estimation of the structural and electrochemical stability of the F-doped IrO_2, the binding energy of F^* atom at the surface layer as well as the cohesive energy E_{coh} of the material has been calculated. Since the reaction $F_{2\,(g)} + 2\,H^+ + 2\,e^- \rightarrow 2\,HF_{(aq)}$ occurs at 3.05 V [135], considering $F_{2\,(g)}$ and $H_{2\,(g)}$ as reference states it seems plausible to determine whether F would be more stable on the surface or in the acidic form by means of comparison of the binding energy of F^* at the mentioned standard potential (3.05 V). In other words, if the binding energy of F^* is greater than - 3.05 eV, it would mean that F remains on the surface and does not dissolve into the acidic solution. The following relation for F^* binding energy has been used:

$$E_{bind}(F^*) = E(F^*) - [\,E(^*) + \tfrac{1}{2}\,E(F_2)\,]$$

Here, $E(F^*)$ and $E(^*)$ are the corresponding total energies of the slabs with fluorine atom and without it. $E(F_2)$ is the calculated energy for the isolated F_2 molecule. The corresponding calculation of E_{bind} (F^*) gives the value of - 3.96 eV, which is noticeable larger than the surface stability limit of - 3.05 eV. This result is confirmed by the chronoamperometry experiments conducted for a series of IrO_2:F with different F content in 1 N H_2SO_4 as shown in **Figure 9** and **Figure 102**. The calculations of the cohesive energies of the bulk materials with different F concentrations demonstrated slight decrease of E_{coh} with increase in the F content. It originates from lower Ir - F bond energies than Ir - O due to the reduced charge of F ions (bond lengths for Ir - O and Ir - F are 2.12 Å and 2.37 Å, respectively).

6.2 F DOPED IRIDIUM - TIN OXIDE

6.2.1 Computational Methodology

In this study, the thin film of $(Ir,Sn)O_2$ doped with F has been considered to exhibit the rutile structure with a tetragonal unit cell and space group P42/mnm following experimental validation. The rutile structure of $(Ir,Sn)O_2$:F thin film electrode has been confirmed experimentally from XRD analysis (**Figure 10** and **Figure 109**). This unit cell has been chosen as the basis for construction of the different super cells corresponding to the specific Ir, Sn and F concentrations of the oxide solid solution. To facilitate convenient calculations, the basic composition has been chosen as 25 at.% IrO_2 - 75 at. %SnO_2 . Such 25/75 composition although slightly different from the experimental ratio allows selection of smaller representative super-cells for all the calculation of bulk and surface electronic structures employed in the present study. Thus, $(Ir_{0.25}Sn_{0.75})O_2$ compound doped with different amounts of F has been considered for theoretical evaluation of the electronic conductivity, structural and electrochemical stability and catalytic activity.

For bulk calculations, the super cell has been chosen as the double rutile unit cell with four metals and eight oxygen atoms in the unit cell. Fluorine doping was simulated by replacing corresponding number of oxygen atoms with F according to the general formula unit as $(Ir_{0.25}Sn_{0.75})O_{2-x}F_x$, where x = 0, 0.5, 1.0, 1.5 corresponding to 0, 5.6, 11.0, and 16.4 wt.% F, respectively. For calculation of the (1 1 0) surface electronic properties of the materials, a two - dimensional slab repeated in (1 -1 0) direction with 36 atom unit cell and a vacuum distance ~ 12 Å between adjacent images of the slab was selected.

For calculating the total energies, electronic structure and density of electronic states the Vienna Ab-initio Simulation Package (VASP) was used within the projector-augmented wave (PAW) method [131-133] and the generalized gradient approximation (GGA) for the exchange-correlation energy functional in a form suggested by Perdew and Wang [130]. This program calculates the electronic structure and *via* the Hellmann - Feynman theorem, the inter-atomic forces are determined from first-principles. Standard PAW potentials were employed for the elemental constituents and the Ir, Sn, O and F potentials thus contained nine, four, six and seven valence electrons, respectively.

For all the materials considered, the plane wave cutoff energy of 520 eV has been chosen to maintain a high accuracy of the total energy calculations. The lattice parameters and internal positions of atoms were fully optimized employing the double relaxation procedure, and consequently, the minima of the total energies with respect to the lattice parameters and internal ionic positions have been determined. This geometry optimization was obtained by minimizing the Hellman - Feynman forces *via* a conjugate gradient method, so that the net forces applied on every ion in the lattice are close to zero. The total electronic energies were converged within 10 - 5 eV/un.cell resulting in the residual force components on each atom to be lower than 0.01 eV/Å/atom, thus allowing for an accurate determination of the internal structural parameters for the oxide. The Monkhorst - Pack scheme was used to sample the Brillouin Zone (BZ) and generate the ***k*** point grid for the solids and the different isolated atoms used in the present study. A choice of the appropriate number of ***k*** points in the irreducible part of the BZ was based on convergence of the total energy to 0.1 meV/atom.

It should also be noted that for Ir-Sn-O-F compositions, the corresponding atomic distributions are ambiguous and can be represented by different spatial configurations. To

eliminate this uncertainty several atomic configurations for each given composition have been constructed and only those configurations corresponding to minimal total energies have been selected for further numerical investigations of these specific compositions of the binary oxides. The elementary unit cells for bulk and surface calculations for $Ir_{0.25}Sn_{0.75}O_{1.5}F_{0.5}$ is presented in **Figure 146**.

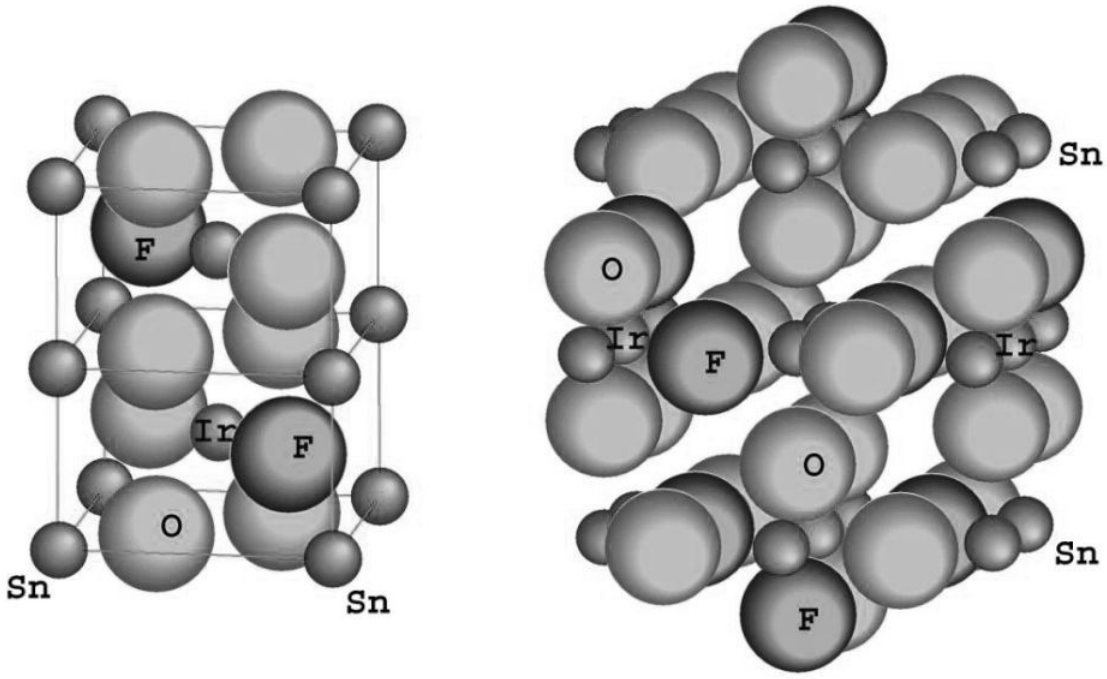

Figure 146. The unit cells for bulk (left) and (110) surface (right) calculations used for the atomic configuration of $Ir_{0.25}Sn_{0.75}O_{1.5}F_{0.5}$

6.2.2 Theoretical Discussion

The experimental results indicate that formation of single phase rutile type solid solution of F doped $(Sn_{0.80}Ir_{0.20})O_2$ with reduced Ir content and incorporation of F has a tremendous impact on the electrochemical activity (**Figure 16** and **Figure 119**) as well as the stability (**Figure 21** and **Figure 123**). The remarkable electrochemical activity of $(Ir,Sn)O_2$:F with 10 wt.% F is expected to depend on the electronic structure as well as electronic conductivity of the electrode since no significant change in structural parameters of molar volume and crystallite size with addition of different amount of F is observed. Improvement in electronic conductivity of F doped SnO_2 is well known and it has also been reported that 10 wt.% F exhibits the lowest resistivity [76, 77]. From a theoretical perspective, the effect of composition on the electronic structure in general, and the electronic conductivity with increase in F concentration in the oxide can thus be considered as one of the factors contributing to the improved electrochemical performance.

There are various published theoretical studies on pure IrO_2 and the electronic structure of the oxide is widely presented in the literature [78, 79, 136]. Furthermore, considering that IrO_2 is the gold standard for OER catalysts, a comparison of the IrO_2 electronic structure with that of $(Ir,Sn)O_2$:F oxides would certainly help provide insight into the role of fluorine in the context of the improved electrochemical performance observed. A systematic computational study was conducted to investigate the electronic properties of the solid solution of $(Ir_{0.25}Sn_{0.75})O_2$ doped with different F amounts. The total energy, electronic and optimized crystal structures, together with the total and projected densities of electronic states has been calculated using the first principles approach within the density functional theory. An effect of the introduction of F into

$(Ir,Sn)O_2$ on the electronic conductivity and the structural stability as well as the Ir d-band center position with increase in F concentration in the oxide is also discussed.

The total and projected densities of electronic states calculated for pure IrO_2 are shown in **Figure 147**. The main energy band structure of IrO_2 consists of two bands. The low energy band between - 19.2 eV and - 17.5 eV is composed of the 2s states of oxygen and the wide valence band around Fermi level consists of hybridized O 2p - Ir 5d states with two prominent peaks; correspond to the O 2p and Ir 5d states, thus contributing to the well known metallic conductivity of IrO_2. Incorporation of Sn into the IrO_2 matrix is however likely to augment the electronic properties of the compound and hence, the electronic structure of the bulk as well as the electronic structure of the most stable (1 1 0) surface have been calculated for $(Ir_{0.25}Sn_{0.75})O_{2-x}F_x$ with x = 0, 0.5, 1, and 1.5. The total electronic densities of states for all these compositions are correspondingly shown in **Figure 148**. It is seen that all of the compounds demonstrate metallic behavior although to different extents. Since in general, metallic conductivity is proportional to the density of states at Fermi level $n(E_F)$, it provides an opportunity to qualitatively evaluate the correlation between F concentration and the electronic conductivity of the oxide. **Figure 149** depicts the dependence of $n(E_F)$ *vs.* composition for $(Ir,Sn)O_2$:F. For comparison, the value of $n(E_F)$ are normalized to electrons per one $(Ir,Sn)O_2$:F formula unit. The graph clearly shows the reduction in conductivity of pure IrO_2 to $(Ir_{0.25}Sn_{0.75})O_2$ with IrO_2 introduction into the SnO_2 lattice representing a decrease in Ir-content of 0.25 atoms per formula unit. However, the incorporation of fluorine improves the conductivity drastically to an optimal value almost matching that of pure IrO_2 rendered at a F content of ~ 10 - 11 wt.% in the oxide.

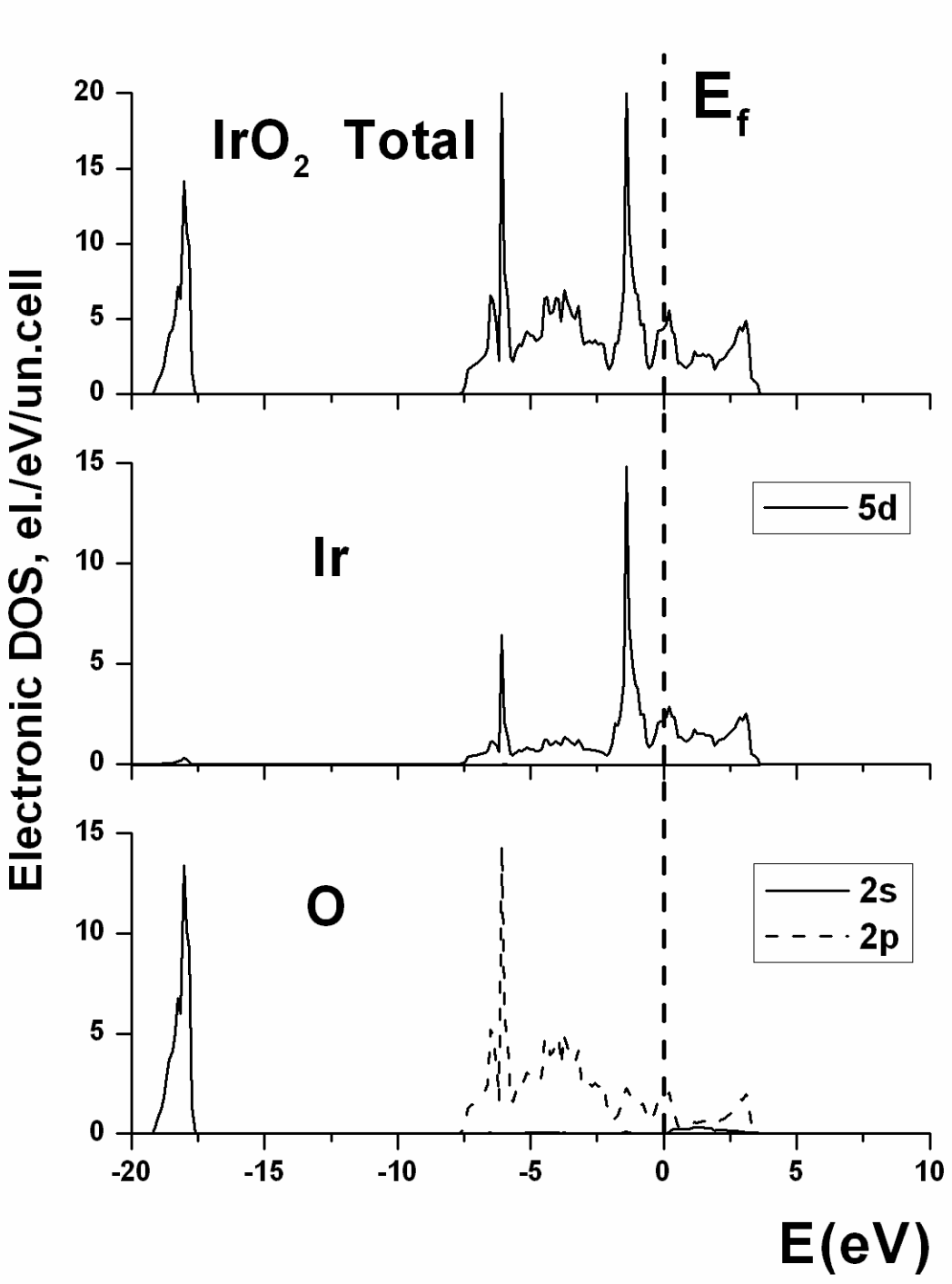

Figure 147. Total and partial density of states for IrO_2

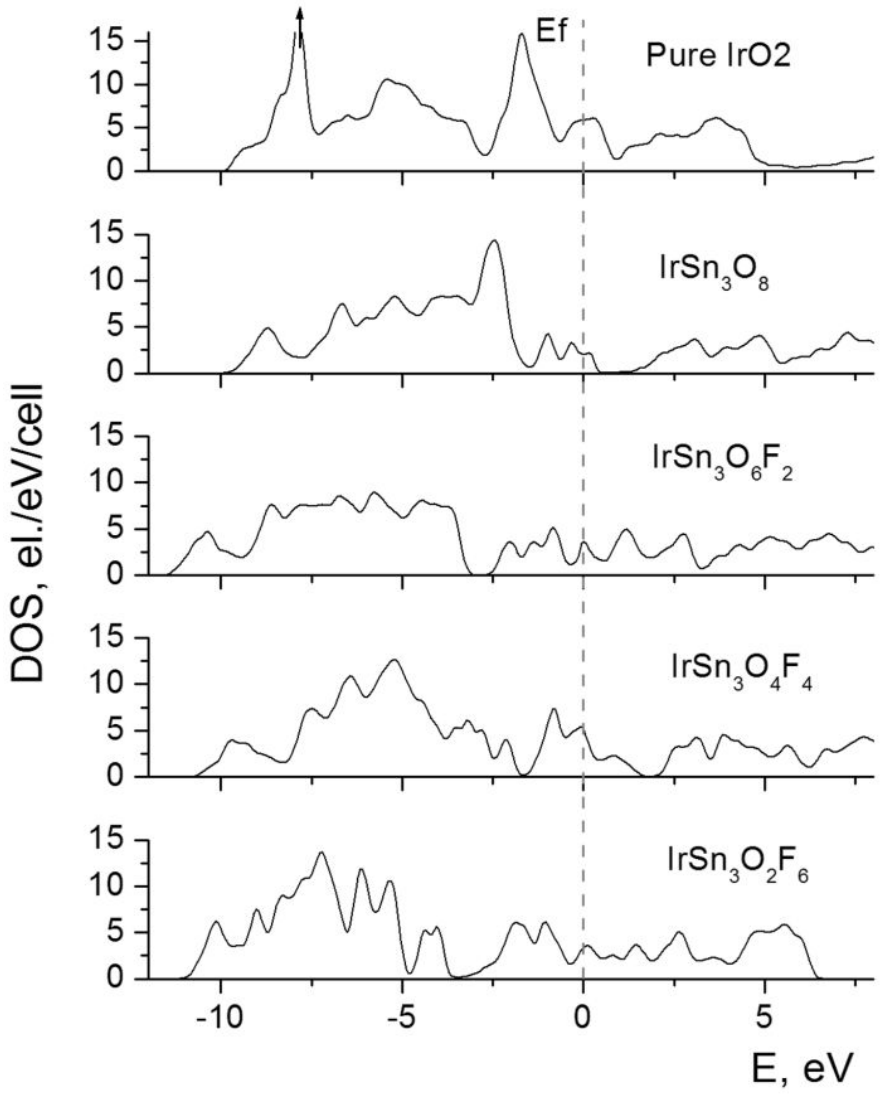

Figure 148. Total density of states for IrO_2 and $(Ir,Sn)O_2$:F

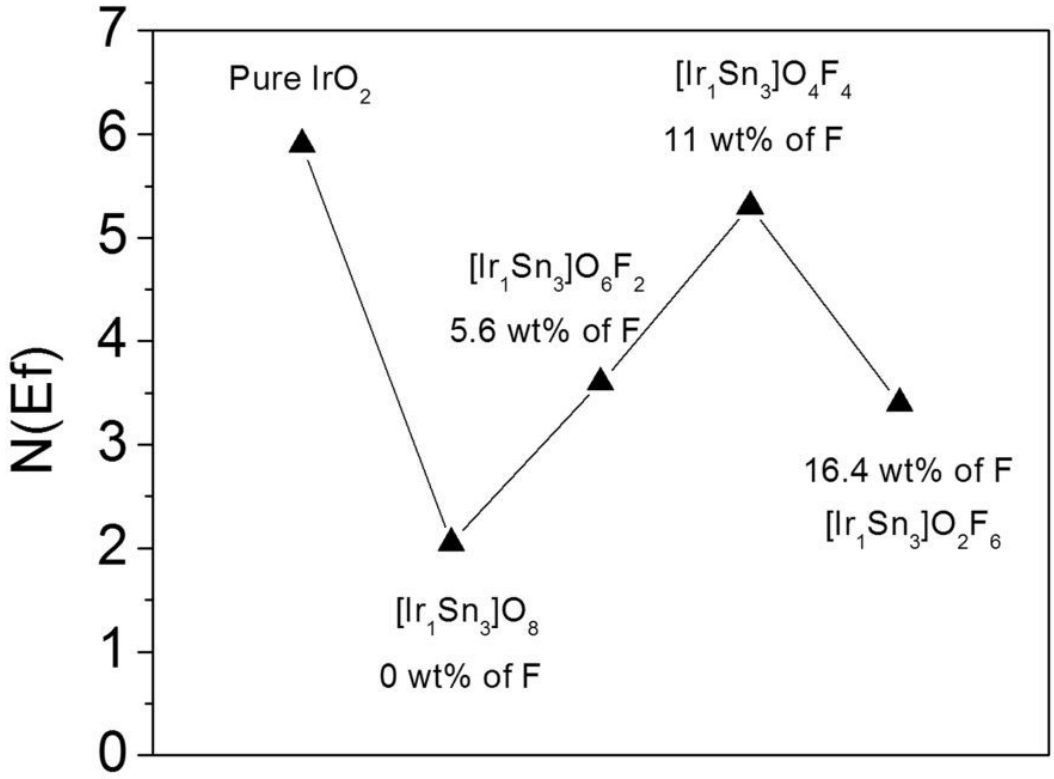

Figure 149. Density of states at Fermi level for (Ir,Sn)O_2:F

In recent years, a wide spread concept has been proposed by Nørskov *et al.* [125, 126] has been used effectively to define the catalytic activity of the surface. This descriptor has been defined as a gravity center of the d-band center of the noble metal ε_d usually located in the vicinity of the Fermi level. An optimal position of the d-band center thus provides an optimum highly favorable interaction between the catalytic surface and the various species participating in the catalytic reactions predominantly occurring on the surface leading to an expected maximum catalytic activity. Thus, such an interaction should be considered "just appropriate" implying leading to a moderate effect allowing the reagents and products to both adsorb at the surface and

also desorb most efficiently. Hence, an adjustment of the d-band center position with respect to the Fermi level may likely play a critical role contributing to the design of novel highly active and electrochemically stable electro-catalysts discussed herein.

In the present study the electronic structure of the stable (1 1 0) surfaces for all the $(Ir,Sn)O_2$ has been calculated and the positions of the corresponding Ir d-band centers have been obtained as a first moment of $n_d(E)$: $\varepsilon_d = \int n_d(E)E\mathrm{d}E / \int n_d(E)\mathrm{d}E$. **Figure 150** shows the partial Ir d-band densities of states together with the corresponding centers of these zones marked with vertical arrows on the graphs. One can see that the d-center for pure IrO_2 is located at ~ 1.33 eV below the Fermi level. This position was considered as a reference point for comparison of the catalytic activities of the other oxides considered in this study. Introduction of substantial amount of Sn (namely, 75 at %) to the oxide results in hybridization between Sn 5s, 5p and Ir 5d states leading to a shift of the Ir d-band center up to the position at - 0.75 eV below the Fermi level indicating that in general, an overall chemisorption reaction of the different species reacting at the surface is noticeably stronger for this composition rather than for pure IrO_2.

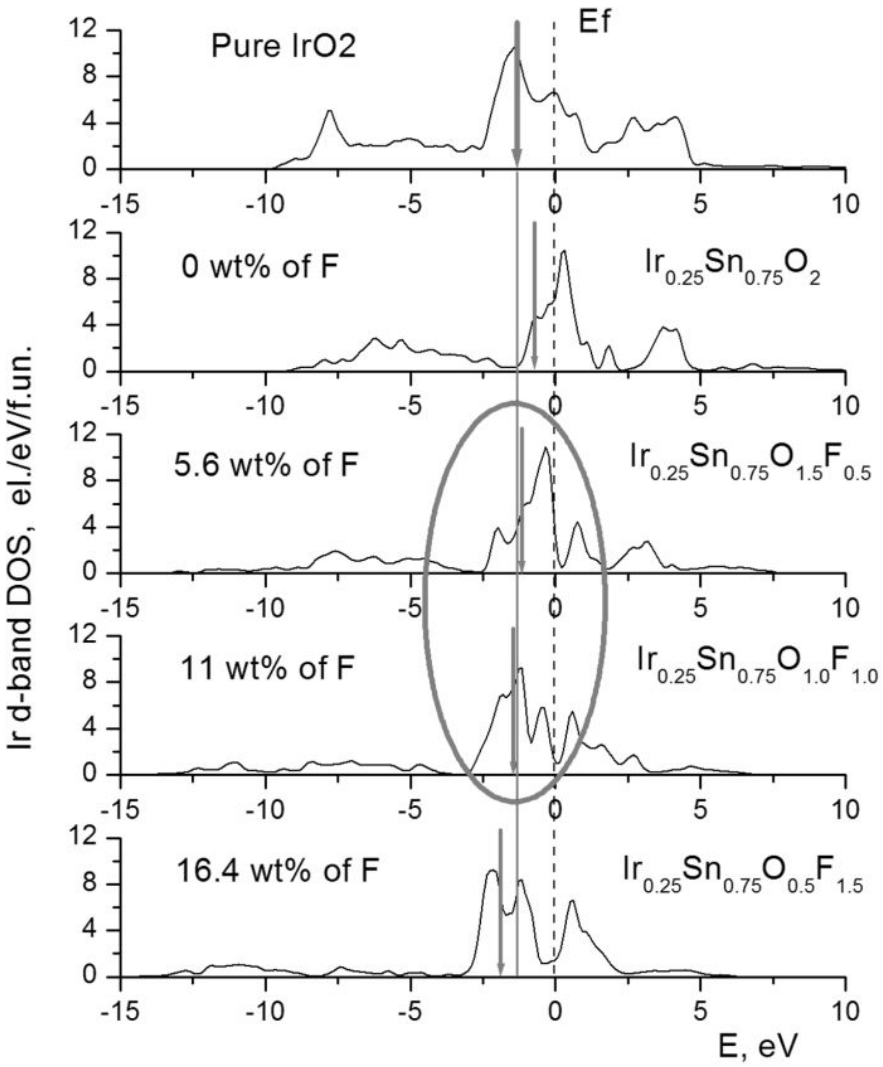

Figure 150. Ir d-band partial density of states for IrO_2 and $(Ir,Sn)O_2$:F. The arrows denote positions of the d-band centers (ε_d)

Assuming pure IrO_2 the gold standard OER catalyst demonstrates optimal catalytic activity corresponding to ε_d = - 1.33 eV one can therefore suggest that a significant drop in the activity observed experimentally for the undoped $(Ir,Sn)O_2$ (**Figure 16** and **Figure 119**) could be

most likely explained by the positive shift of the Ir d-band center deviating the catalytic activity from its optimal value. Such a behavior of the d-band center could be attributed to the complex hybridization of the electronic Ir d states and corresponding s and p states of Sn and O during the solid solution formation of the two binary oxides. Further consideration of the effects of fluorine doping in the formation of the electronic structure in general, can be explained in terms of this shift of the d-band center.

Figure 151 shows the total and partial density of states for $(Ir_{0.25}Sn_{0.75})O_{1.0}F_{1.0}$. Introduction of fluorine manifests in an appearance of the F 2p band mostly below - 5 eV with negligible amount of other states in the entire energy domain. Increase in F content results in more pronounced 2p states leading to a stronger hybridization effect between F 2p and Ir 5d states. As a result, the Ir d-band center location moves from - 0.75 eV for the non-fluorine composition downward towards the position corresponding to pure IrO_2 (- 1.33 eV) with increase in the F content. Thus, it is observed from **Figure 150** that at 5.6, 11 and 16.4 wt% of F, the d-band center passes accordingly through - 1.23 eV, - 1.41 eV and - 1.87 eV positions, respectively; indicating significant improvement in the overall catalytic activity with increase in the F concentration. The optimal F concentration at which the d-center of $(Ir,Sn)O_2$:F returns back to the position corresponding to pure IrO_2 can therefore be expected to be around 9 - 10 wt.% F which is in excellent agreement with our experimental results.

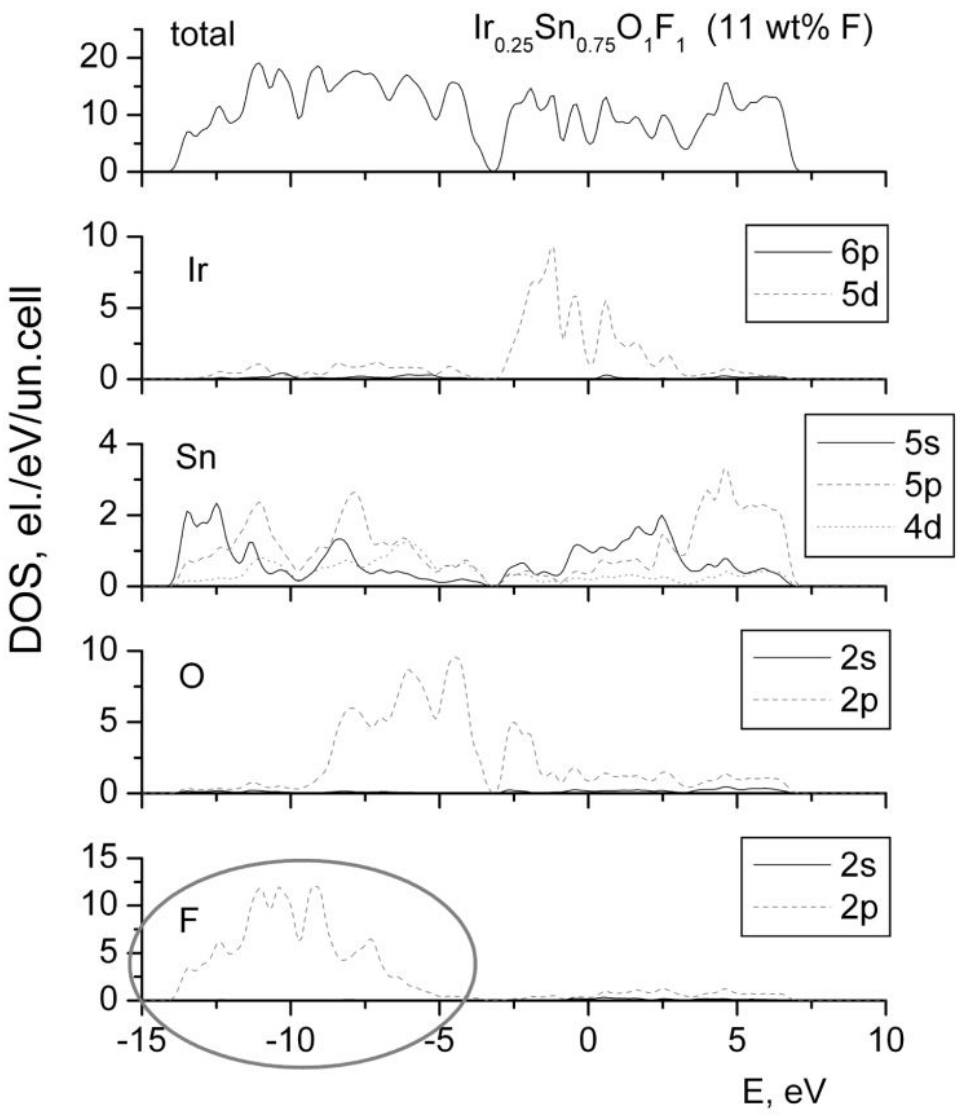

Figure 151. Total and partial density of states for $(Ir_{0.25}Sn_{0.75})O_1F_1$

Thus, with incorporation of F it can be seen that with the increase in F content, the d-band center shifts downward on the energy scale returning back to the position corresponding to pure IrO_2 at ~ 10 wt.% F rendering the system essentially mimicking the electronic and electro-catalytic properties of pure IrO_2. A combination of the improved metallic electronic conductivity

and the d-band center position being optimal conceivably renders this oxide demonstrating high catalytic activity experimentally observed comparable to pure IrO_2. The addition of a relatively small amount of Ir into the SnO_2 matrix thus drastically modifies the overall electronic structure of the resulting oxide introducing highly prominent 5d band of Ir modified by the 2p band of F.

6.3 F DOPED RUTHENIUM - TIN OXIDE

6.3.1 Computational Methodology

In order to obtain deeper insight into the intrinsic properties of the undoped $(Ru,Sn)O_2$ and F doped solid solutions, a continuous string of first principles studies have been conducted using Density Functional Theory methodology implemented in the Vienna Ab-initio Simulation Package (VASP) [131-133]. The projector augmented wave (PAW) method with the generalized gradient approximation (GGA) [130] for conducting the exchange - correlation corrections has been used for calculation of the total energies, electronic structures and optimized lattice parameters of the different model materials with chemical compositions similar to those compounds studied experimentally and described above in the present work. All the atoms were allowed to relax with the residual force components on each atom to be lower than ~ 0.01 eV/Å/atom, thus resulting in the accurate determination of the atomic positions; and total energy of the whole system. The Monkhorst - Pack scheme was used to sample the Brillouin Zone (BZ) and generate the ***k*** point grid for the solids and the different isolated atoms used in the present

study. A choice of the appropriate number of ***k*** points in the irreducible part of the BZ was based on convergence of the total energy to be 0.1 meV/atom. Standard PAW potentials were employed for the elemental constituents of all pure and doped compounds in the study.

As a model system, a 12 atom supercell containing two rutile type unit cells has been constructed to represent the following compositions of the materials considered: RuO_2, $(Sn_{0.25}Ru_{0.75})O_2$, $(Sn_{0.5}Ru_{0.5})O_2$, $(Sn_{0.75}\ Ru_{0.25})O_2$, $(Sn_{0.75}\ Ru_{0.25})O_{1.5}F_{0.5}$ and $(Sn_{0.75}\ Ru_{0.25})O_{1.0}F_{1.0}$. The last two compositions correspond to 6.4 and 12.7 wt.% F respectively. It should also be noted that for the Ru-Sn-O-F compositions, the corresponding atomic distributions are ambiguous and can be represented by different spatial configurations. To eliminate this uncertainty several atomic configurations for each given composition has been constructed and only those configurations corresponding to minimal total energies has been selected for further electronic structure analysis of these specific compositions of the binary oxides.

6.3.2 Theoretical Discussion

Theoretical studies help provide a fundamental understanding of the excellent electrochemical activity demonstrated by the $(Ru,Sn)O_2$:F electro-catalyts (**Figure 31** and **Figure 32**). A well known concept proposed by Nørskov *et al.* [125, 126] that a gravity center of the d-band of the noble metal ε_d may serve as a simple descriptor for determining the catalytic activity of the surface. Such a d-band center is usually located in the vicinity of the Fermi level and an optimal position of the d-band center would provide an optimal interaction between the catalytic surface and the various species participating in the catalytic reactions predominantly occurring on the surface. Thus, an adjustment of the d-band center position with respect to the Fermi level may

likely play a critical role in contributing to the design of novel highly active and electrochemically stable (Ru,Sn)O_2:F electro-catalysts.

For these purposes, the electronic structures of all the Ru based oxides has been calculated and the positions of the corresponding Ru d-band centers have been obtained as a first moment of $nd(E)$: $\varepsilon d = \int nd(E)E\mathrm{d}E / \int nd(E)\mathrm{d}E$. **Figure 152** shows the partial Ru d-band densities of states together with the corresponding centers of these zones marked with vertical arrows on the graphs. One can see that the d-band center for pure RuO_2 is located at ~ - 0.39 eV below the Fermi level. This position will be considered as a reference point for comparison of the catalytic activities of the other compounds; and correspondingly simulated in this theoretical study. Gradual introduction of increased amount of Sn (up to 75 at.%) to the oxide results in hybridization between the Sn 5s, 5p and Ru 4d-states leading to a shift of the Ru d-band center up to the position at - 0.22 eV below the Fermi level. This indicates an overall chemisorption reaction of different species reacting at the surface becoming noticeably stronger with increase of Sn concentration rather than for pure RuO_2.

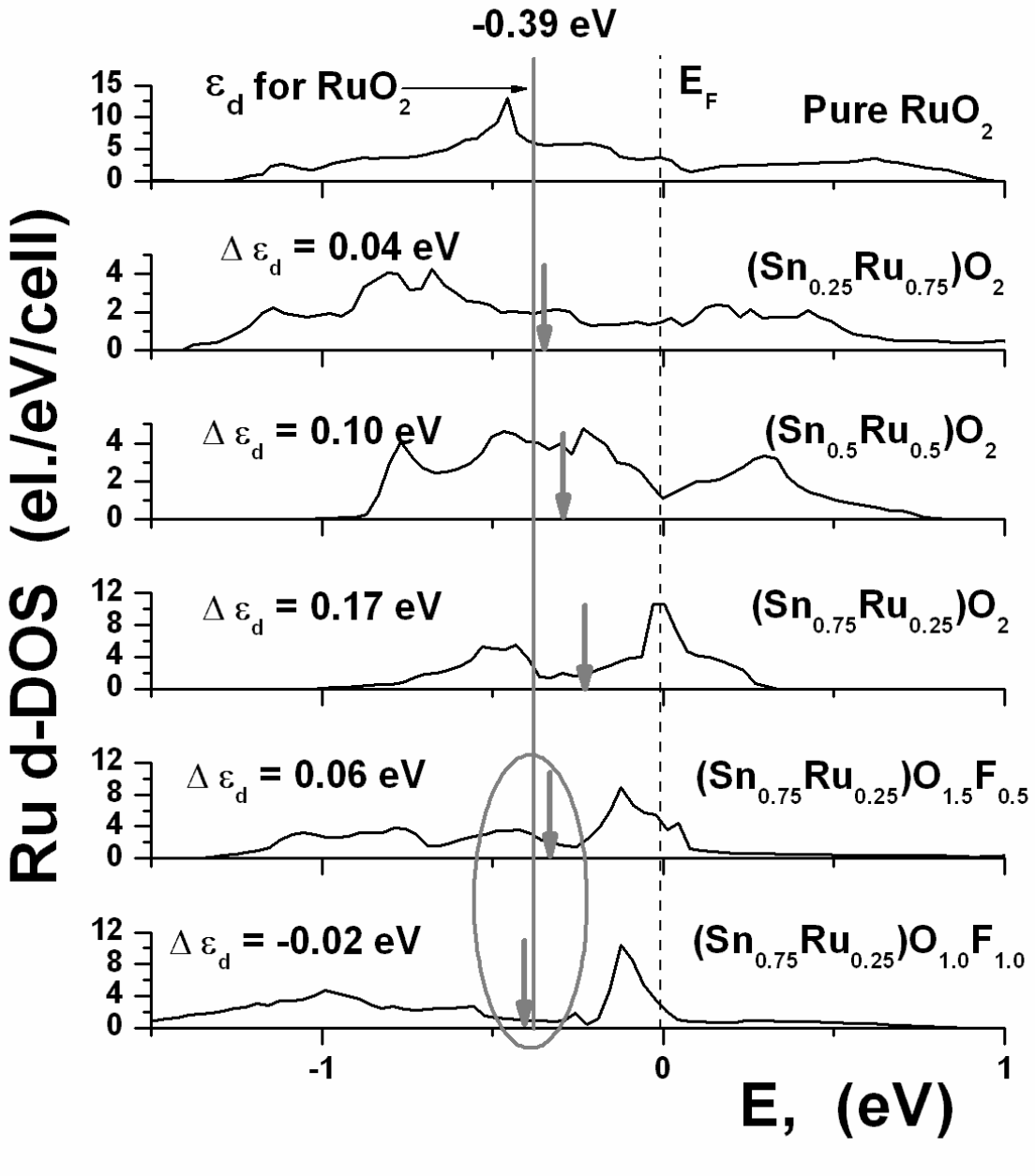

Figure 152. Ru d-band partial density of states for RuO_2, $(Ru,Sn)O_2$ and $(Ru,Sn)O_2$:F. The arrows denote positions of the d-band centers (ε_d)

Assuming that pure RuO_2 demonstrates an optimal catalytic activity corresponding to ε_d = - 0.39 eV, one can suggest a significant drop in the electrochemical activity observed

experimentally for $(Ru_{0.2}Sn_{0.8})O_2$ composition (**Figure 31**) could be most likely explained by a positive shift of the Ru d-band center deviating the catalytic activity from its optimal value. Such a behavior of the d-band center could be attributed to complex hybridization of the electronic Ru d-states and corresponding s and p states of Sn and O during formation of the binary oxide solid solution.

The effects of F doping on the catalytic activity of the materials can be considered from the electronic structure point of view and correspondingly, the d-band center shifting, in particular. Thus, it can be seen from **Figure 152** that for 6.4 wt.% F and 12.7 wt.% F, there is a gradual movement of the d band center resulting in ε_d almost matching that of pure RuO_2. **Figure 153** shows the total and partial density of states for $(Ru_{0.25}Sn_{0.75})O_{1.5}F_{0.5}$ composition. Introduction of fluorine manifests in an appearance of F 2p band mostly below - 5 eV with negligible amount of other states in a whole energy region. The higher the F content, the more pronounced these 2p states are and stronger is the effect of hybridization between F 2p and Ru 4d states. As a result, the Ru d-band center starts moving from - 0.22 eV for the undoped composition downward towards the position corresponding to pure RuO_2 (- 0.39 eV) with increase in the F content. It is seen that at 6.4 and 12.7 wt.% F, the d-band center passes - 0.33 eV and - 0.41 eV respectively, indicating an improvement in the catalytic activity with increase in F concentration. The optimal F concentration at which the d-center returns back to the position corresponding to pure RuO_2 is thus expected to be ~ 9 - 10 wt.% F which is in excellent agreement with the experimentally observed results (**Figure 33**).

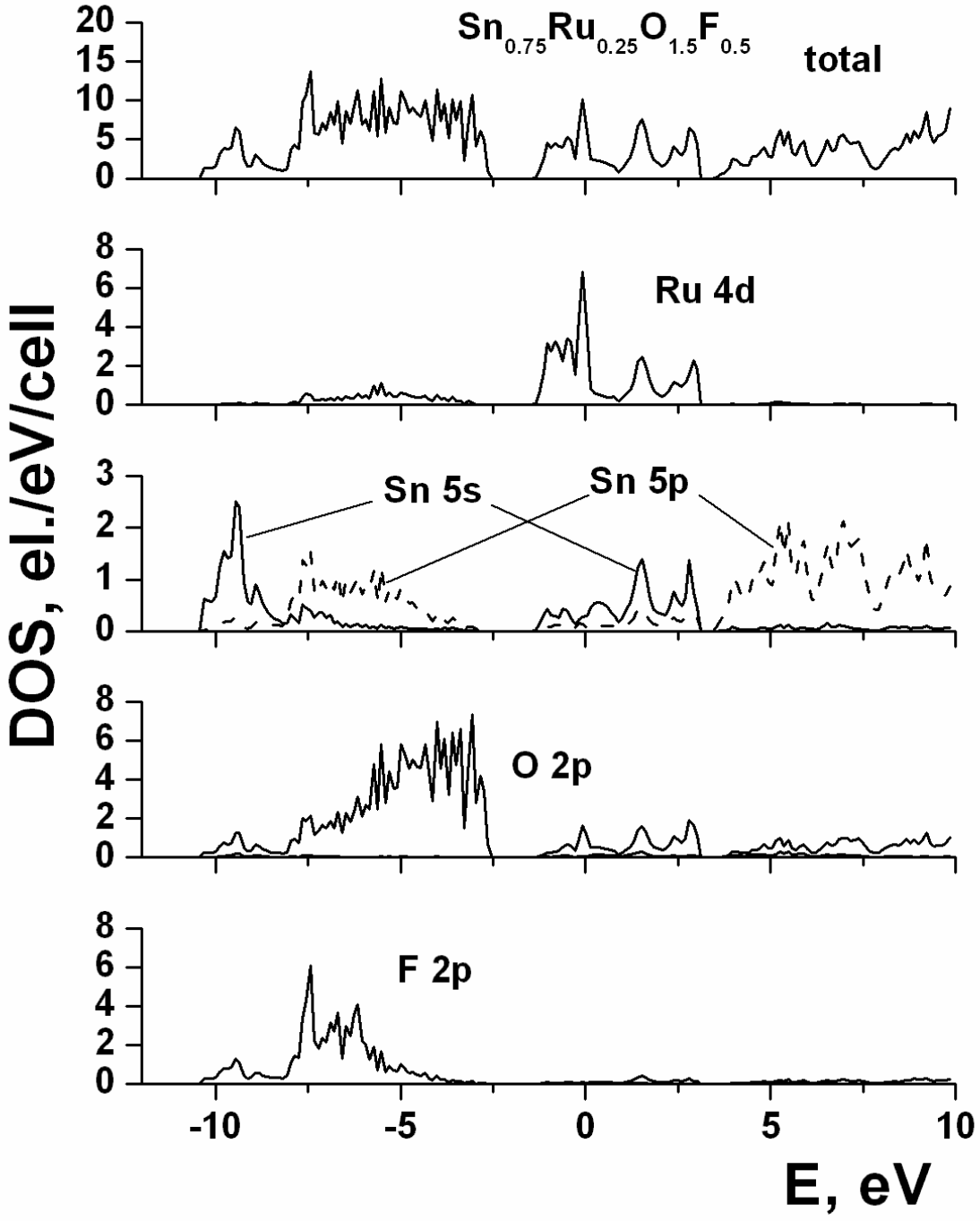

Figure 153. Total and partial density of states for $(Ru_{0.25}Sn_{0.75})O_{1.5}F_{0.5}$

Thus, the present theoretical study of the electronic structure peculiarities of the $(Ru,Sn)O_2$:F has demonstrated strong correlation between the d-band center position and the observed catalytic activity of the considered materials with the optimal composition corresponding to $(Ru_{0.25}Sn_{0.75})O_2$ doped with ~ 10 wt.% F rendering this material to demonstrate high electro-catalytic activity comparable to pure RuO_2.

6.4 F DOPED IRIDIUM - NIOBIUM OXIDE

6.4.1 Computational Methodology

The catalytic activity of virtually any electro-catalyst is expected to depend on the electronic structure as well as electronic conductivity, while the long term stability of the electrode is assumed to qualitatively depend on the cohesive energy of the system. The effect of compositions on the electronic and catalytic properties as well as on the structural stability of the material has been understood from the theoretical considerations. To obtain deeper insight into the intrinsic properties of undoped $(Ir_{0.25}Nb_{0.75})O_2$ as well as doped with ~ 9.4 wt.% F corresponding to the formula unit $(Ir_{0.25}Nb_{0.75})O_{1.25}F_{0.75}$, a series of ab-initio calculations of the electronic structure, equilibrium lattice parameters and cohesive energies of the above mentioned materials have been conducted using density functional theory (DFT) methodology implemented in the Vienna Ab-initio Simulation Package (VASP) [131-133]. The projector augmented wave (PAW) method with the generalized gradient approximation (GGA) for the exchange-correlation

energy functional in a form suggested by Perdew and Wang [130] has been applied in present study. The lattice parameters and internal positions of atoms were fully optimized employing the double relaxation procedure, where all atoms were allowed to relax with the residual force components on each atom to be lower than 0.01 eV/Å/atom, thus allowing for the accurate determination of the internal atomic positions and hence, the total energy of the whole system. The Monkhorst - Pack scheme was used to sample the Brillouin Zone (BZ) and generate the ***k*** point grid for the solids and the different isolated atoms used in the present study. A choice of the appropriate number of ***k*** points in the irreducible part of the BZ was based on convergence of the total energy to be 0.1 meV/atom. Standard PAW potentials were employed for the elemental constituents of all pure and doped compounds in the study.

As a model system, a 12 atom supercell containing two rutile type unit cells has been constructed to represent $(Ir_{0.25}Nb_{0.75})O_2$ and $(Ir_{0.25}Nb_{0.75})O_{1.25}F_{0.75}$ compositions. It should be noted that for $(Ir_{0.25}Nb_{0.75})O_{1.25}F_{0.75}$ composition, the corresponding atomic distributions are ambiguous and can be represented by different spatial configurations. There are 5 atoms of O and 3 atoms of F distributed randomly over 8 available oxygen sites in 12 atom super cell used for the calculations. To eliminate this uncertainty, several atomic configurations for this specific composition have been considered and a configuration corresponding to minimal total energy has been selected for further electronic structure and cohesive energy analysis. For calculation of the (1 1 0) surface electronic properties of the materials a two dimensional slab containing four oxygen and three metal layers repeated in (1 -1 0) direction with ~ 7 Å of thickness and a vacuum distance of ~ 14 Å between adjacent images of the slab was selected.

6.4.2 Theoretical Discussion

The main origins of enhanced electro-catalytic activity and the long-term structural stability of fluorine doped $Ir_{0.25}Nb_{0.75}O_2$ as seen in **Figure 136** and **Figure 139**, respectively can be understood from the electronic structure point of view. The total densities of electronic states calculated for pure IrO_2 as well as for undoped and F doped $Ir_{0.25}Nb_{0.75}O_2$ are shown in **Figure 154**. The band structure of IrO_2 consists of two main bands. One of them belongs to the oxygen 2s states located at around - 18 eV. Another band is the wide valence band around Fermi level and consisted of hybridized O 2p - Ir 5d states and provides a metallic type of electronic conductivity characteristic of IrO_2. Introduction of Nb and F into IrO_2 matrix changes the electronic structures of the compounds significantly with all major projected electronic states denoted with corresponding orbital numbers. However, all the materials remain metallic although with different electronic conductivity.

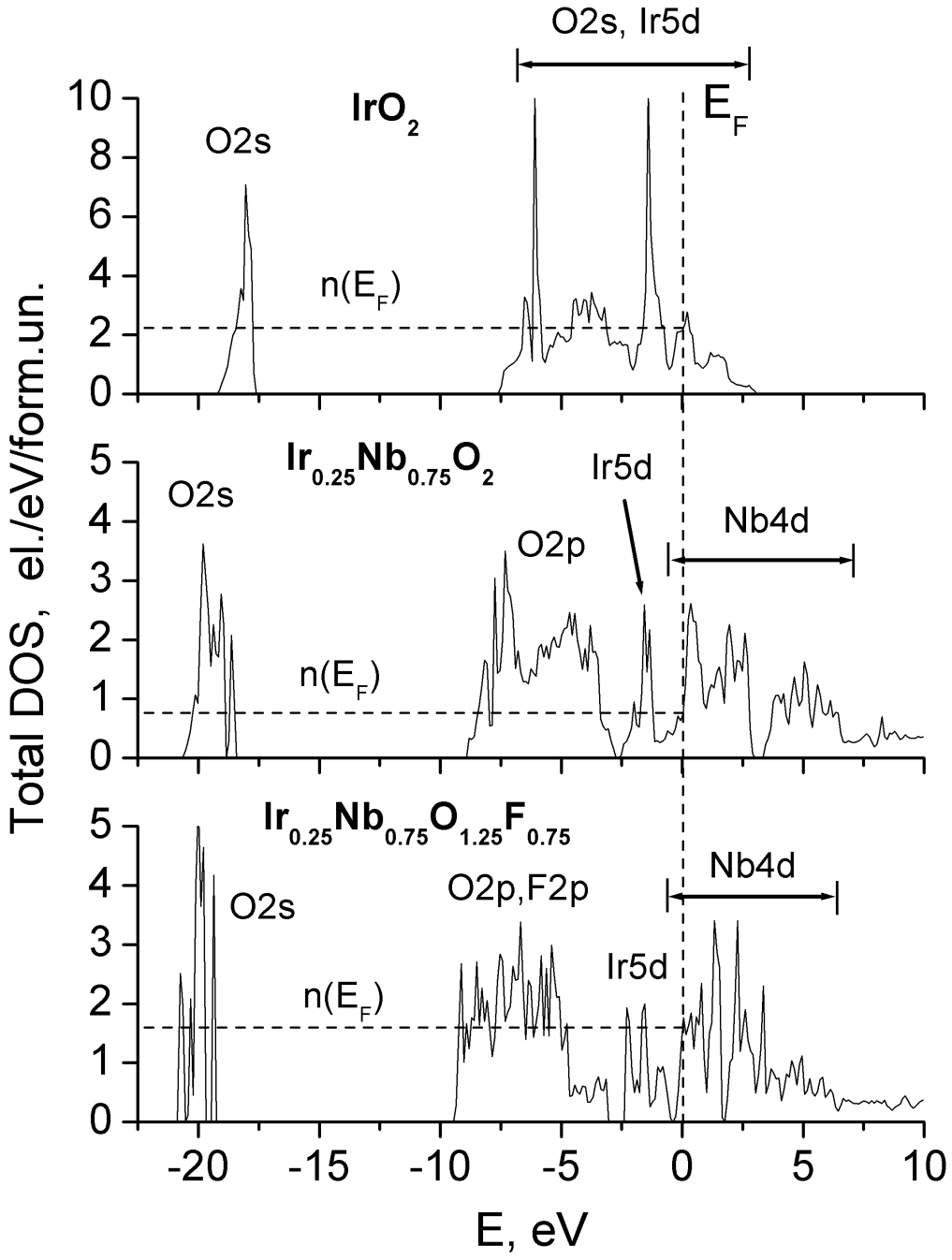

Figure 154. Total density of states for IrO_2, $(Ir_{0.25}Nb_{0.75})O_2$, and $(Ir_{0.25}Nb_{0.75})O_{1.25}F_{0.75}$

Since generally speaking, metallic conductivity is direct proportional to the density of states at Fermi level $n(E_F)$, a qualitative evaluation of the correlation between chemical compositions of the materials and their electronic conductivity becomes feasible and straightforward. **Table 11** collects the values of $n(E_F)$ corresponding to pure IrO_2, undoped and F doped $(Ir,Nb)O_2$. One can see that the $n(E_F)$ for pure IrO_2 is the highest among all the three compounds and can serve as a benchmark for the electronic conductivity of the other two materials. As expected, an introduction of a substantial amount of niobium oxide into IrO_2 results in a drastic decrease of the electronic conductivity, since Nb_2O_5 is a very poor electric conductor with a wide band gap of 3.9 eV [137]. Introduction of fluorine significantly improves the overall conductivity though not up to the value demonstrated for pure IrO_2. The role of fluorine doping into SnO_2 and $(Ir,Sn,Nb)O_2$ solid solutions has been discussed previously by us indicating significant improvement in the electronic conductivity of the compounds with an introduction of ~ 10 wt.% F due to an increase of the charge carrier concentration in the system [24, 56, 59]. Thus, such an increase in the conductivity of $Ir_{0.25}Nb_{0.75}O_2$:10 wt.% F may noticeably contribute to the high electro-catalytic activity of the compound.

Table 11. Calculated values of density of electronic states at Fermi level n(E_F), positions of the Ir d-band center ε_d, and the cohesive energy - E_{coh} for the catalysts.

	n(E_F) [el./eV/f.un.]	**ε_d (eV)**	**- E_{coh} [eV/f.un.]**
IrO_2	2.15	- 1.33	15.86
$Ir_{0.25}Nb_{0.75}O_2$	0.76	- 0.95	20.20
$Ir_{0.25}Nb_{0.75}O_{1.25}F_{0.75}$	1.62	- 1.41	18.81

Another aspect in the computational part of the present study relates to the qualitative evaluation of the electro-catalytic activity utilizing an inspiring concept proposed by Nørskov *et al.* [125, 126] regarding the existence of a simple descriptor for determining the catalytic activity of the surface. This descriptor has been defined as a gravity center of the noble metal d-band ε_d usually located in the vicinity of the Fermi level. An optimal position of ε_d thus provides an optimal highly favorable interaction between the catalytic surface and the various species participating in the elementary catalytic reactions during water electrolysis process. An appropriate control of the d-band center position with respect to the Fermi level may crucially contribute to the design of novel highly active and electrochemically stable electro-catalysts.

Since (1 1 0) is the most stable and hence, preferred surface for water electrolysis to occur, the corresponding electronic structure (1 1 0) surface calculations have been conducted to define Ir d-band center position and thus, to qualitatively evaluate the electro-catalytic activity of pure and F doped $Ir_{0.25}Nb_{0.75}O_2$ as compared to that of pure IrO_2 which is the gold standard OER

catalyst. Also, positions of corresponding Ir d-band centers have been obtained as a first moments of $n_d(E)$: $\varepsilon_d = \int n_d(E)E\mathrm{d}E / \int n_d(E)\mathrm{d}E$.

Figure 155 shows partial Ir d-band densities of states together with corresponding ε_d centers marked with vertical arrows on the plots. As mentioned above, ε_d for pure IrO_2 is - 1.33 eV below Fermi level that may serve as a reference point for the optimal position of the d-band center corresponding to the optimal catalytic activity of the compound [**Figure 155** (a)]. In case of $Ir_{0.25}Nb_{0.75}O_2$ [**Figure 155** (b)], an introduction of Nb leads to the noticeable shift of Ir d-band center up towards the Fermi level. It happens due to partial Ir 5d - Nb 4d hybridization, where Nb 4d electronic states locate above the Ir 5d states on the energy scale resulting in the position of ε_d at - 0.95 eV. This d-band shift explains the degradation of the overall catalytic activity (**Figure 136**). However, it is also observed that doping of $Ir_{0.25}Nb_{0.75}O_2$ compound by 10 wt.% F leads to an improvement in the catalytic activity as compared to fluorine free $Ir_{0.25}Nb_{0.75}O_2$.

Such an improvement could be expected from the Ir d-band center calculations of the model system $Ir_{0.25}Nb_{0.75}O_{1.25}F_{0.75}$ shown in **Figure 155** (c). It is seen that in presence of fluorine, ε_d moves back to almost the same (actually, slightly lower) position as that for pure IrO_2. This downward shift occurs because of the presence of lower energy fluorine 2p states located below Ir 5d electrons (not shown in the Figure). Thus, due to F 2p - Ir 5d hybridization, the Ir 5d band becomes wider as compared to the corresponding Ir 5d states in $Ir_{0.25}Nb_{0.75}O_2$; resulting in the movement of Ir d-band center lower on the energy scale. **Table 11** collects ε_d values calculated for all the three compositions.

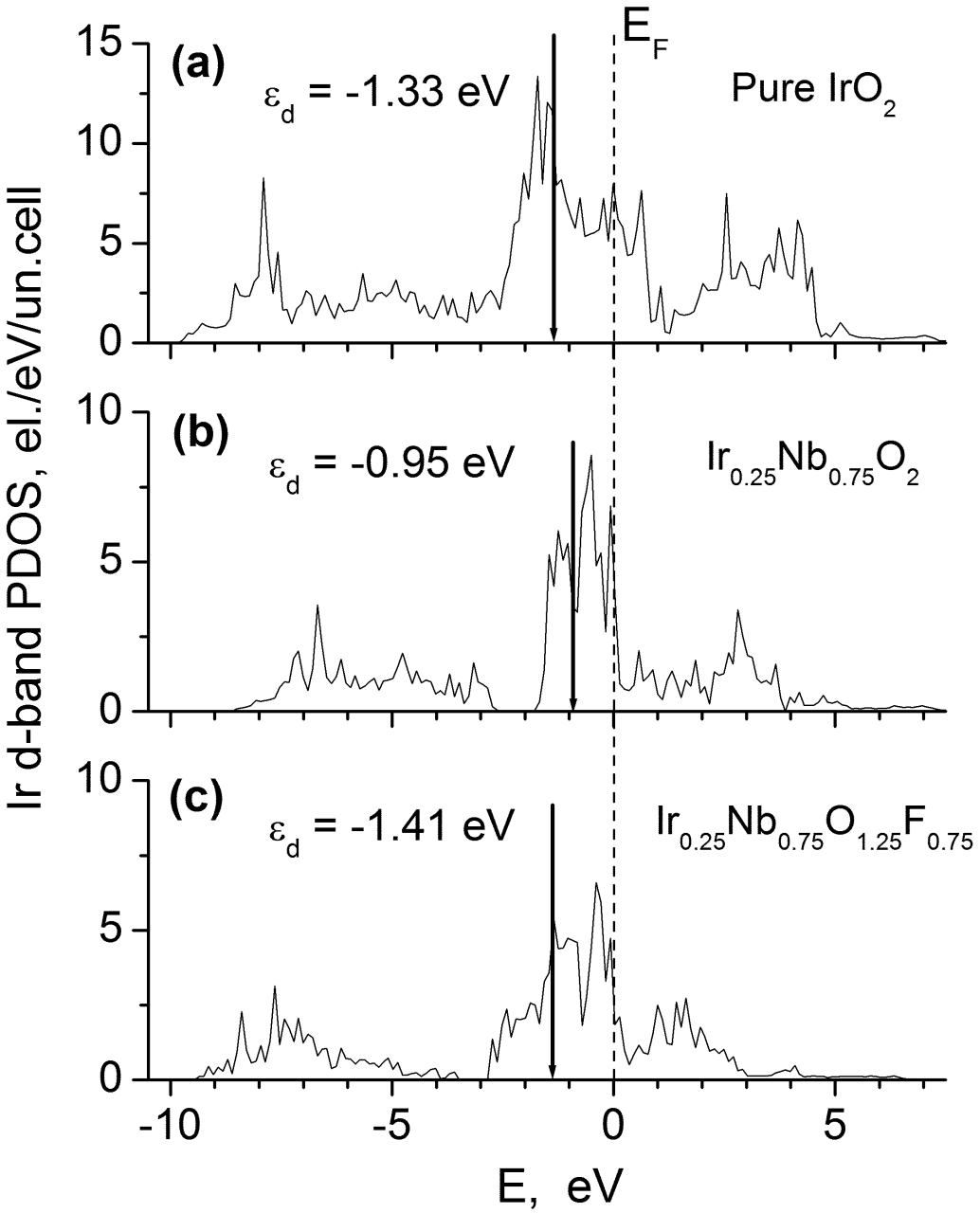

Figure 155. Ir d-band projected DOS for IrO_2 (a), $(Ir_{0.25}Nb_{0.75})O_2$ (b), and $(Ir_{0.25}Nb_{0.75})O_{1.25}F_{0.75}$ (c). The arrows denote positions of the d-band centers (ε_d)

The last aspect to be highlighted in the present study is the cohesive energy E_{coh}. In general, E_{coh} can be considered as a qualitative indicator of the structural and chemical stability of the system, thus the higher E_{coh} (the more negative value), the more stable and durable material is expected to be during long term electro-catalytic processes. It is observed (**Table 11**) that an introduction of Nb into IrO_2 oxide significantly improves the overall stability of $Ir_{0.25}Nb_{0.75}O_2$ due to presence of much stronger Nb - O bonds in comparison to Ir - O ones (calculated E_{coh} for pure NbO_2 is - 18.251 eV/f.un. *vs.* - 15.859 eV/f.un. for IrO_2). However, further F doping of $Ir_{0.25}Nb_{0.75}O_2$ compound results in relatively lower cohesive energy that occurs mainly due to lower ionic charge of F^- *vs.* O^{2-} and thus, significantly weakens the electrostatic component of Ir - F and Nb - F bonds than those of Ir - O and Nb - O ionic bonds. Nevertheless, even relatively less stable $Ir_{0.25}Nb_{0.75}O_2$:F compound is noticeably more stable than pure IrO_2, which is clearly indicated and confirmed by the chronoamperometry measurements shown in **Figure 139**.

6.5 IRIDIUM - TIN - NIOBIUM OXIDE

6.5.1 Computational Methodology

In this study, the thin film of $(Ir,Sn,Nb)O_2$ synthesized by thermal decomposition of chloride precursors on Ti substrate has been considered to exhibit the rutile structure with a tetragonal unit cell and space group P42/mnm following experimental validation. The rutile structure of

$(Ir,Sn,Nb)O_2$ thin film electrode has been confirmed experimentally from XRD analysis which has been presented in the results section (**Figure 43** and **Figure 44**). This unit cell has been chosen as the basis for construction of the different super cells corresponding to the specific Ir, Sn and Nb concentrations of the oxide solid solution. In particular, for IrO_2 and $(Sn_{0.5}Nb_{0.5})O_2$ the super cell has been chosen as the regular rutile unit cell with two metal and four oxygen atoms in the primitive unit cell. On the other hand, $(Ir_{1-2x}Sn_xNb_x)O_2$ with x = 0.125, 0.25 and 0.375 compositions were made to fit a fourfold super cell (1 x 1 x 4) comprising 8 metal and 16 oxygen atoms in the cell unit. For calculation of the (110) surface electronic properties of the materials, a two-dimensional slab repeated in (1 -1 0) direction with a vacuum distance ~ 15 Å between adjacent images of the slab was selected.

For calculating the total energies, electronic structure and density of electronic states the Vienna Ab-initio Simulation Package (VASP) was used within the projector-augmented wave (PAW) method [131-133] and the generalized gradient approximation (GGA) for the exchange correlation energy functional in a form suggested by Perdew and Wang [130]. This program calculates the electronic structure and *via* the Hellmann - Feynman theorem, the inter-atomic forces are determined from first principles. Standard PAW potentials were employed for the elemental constituents and the Ir, Sn, Nb, and O potentials thus contained nine, four, eleven and six valence electrons, respectively.

For all the materials considered the plane wave cutoff energy of 520 eV has been chosen to maintain a high accuracy of the total energy calculations. The lattice parameters and internal positions of atoms were fully optimized employing the double relaxation procedure, and consequently, the minima of the total energies with respect to the lattice parameters and internal ionic positions have been determined. This geometry optimization was obtained by minimizing

the Hellman - Feynman forces *via* a conjugate gradient method, so that the net forces applied on every ion in the lattice are close to zero. The total electronic energies were converged within 10 - 5 eV/un.cell resulting in the residual force components on each atom to be lower than 0.01 eV/Å/atom, thus allowing for the accurate determination of the internal structural parameters. The Monkhorst-Pack scheme was used to sample the Brillouin Zone (BZ) and generate the ***k*** point grid for the solids and the different isolated atoms used in the present study. A choice of the appropriate number of ***k*** points in the irreducible part of the BZ was based on convergence of the total energy to 0.1 meV/atom.

It should also be noted that for the ternary (Ir,Sn,Nb)O_2 compositions, the corresponding atomic distributions are ambiguous and can be represented by different spatial configurations. To eliminate this uncertainty several atomic configurations for each given composition have been constructed and only those configurations corresponding to minimal total energies have been selected for further numerical investigations of these specific compositions of the ternary oxides.

6.5.2 Theoretical Discussion

The computational component of the present study is an attempt to systematically investigate the electronic properties of the different solid solutions between IrO_2, SnO_2 and NbO_2. The compositions of the solid solutions chosen to model the compounds are pure IrO_2, $(Sn_{0.5}Nb_{0.5})O_2$, $(Ir_{0.75}Sn_{0.125}Nb_{0.125})O_2$, $(Ir_{0.50}Sn_{0.25}Nb_{0.25})O_2$ and $(Ir_{0.25}Sn_{0.375}Nb_{0.375})O_2$. The total energy, electronic and optimized crystal structures, total and projected densities of electronic states together with the cohesive energies for the different compositions of (Ir,Sn,Nb)O_2 have been calculated using the first principle approach within the density functional theory. An effect of

introduction of tin and niobium dioxides into IrO_2 on the electronic conductivity and structural stability of the compounds as well as a position of Ir d-band center with decrease of Ir-concentration in the material is discussed.

Although there are various published theoretical studies dedicated to pure IrO_2, and the electronic structure of the oxide [78, 79, 136], it is justifiably logical to describe the electronic structure of IrO_2 in the context of the present study. In addition, pure IrO2 corresponds to 0 at.% of tin and niobium oxides and thus represents a starting point for the current study employing a full range of Sn and Nb concentrations. **Table 12** summarizes the structural parameters calculated and experimentally obtained in the present study. It is seen that the calculated structural parameters are in a good agreement with experimental data (**Table 3**). Slight overestimations of calculated lattice parameters and molar volumes are expected for GGA approximation utilized in this study.

Table 12. Lattice parameters, cohesive energy and density of electronic states at Fermi level for IrO_2, SnO_2 and $(Ir,Sn,Nb)O_2$

Composition	a=b (nm)	c (nm)	V_m (cm^3/mol)	E_{coh} (eV/f.u.)	$n(E_f)$ el./eV/f.u.
IrO_2	0.4511	0.3235	19.82	-15.859	2.15
SnO_2	0.4772	0.3216	22.13	-15.237	0
$(Ir_{0.75}Sn_{0.125}Nb_{0.12.5})\ O_2$	0.4633	0.3182	20.57	-16.964	1.97
$(Ir_{0.50}Sn_{0.25}Nb_{0.25})O_2$	0.4722	0.3147	21.13	-17.315	1.23
$(Ir_{0.25}Sn_{0.375}Nb_{0.375})\ O_2$	0.4746	0.3203	21.72	-17.560	0.90
$(Sn_{0.5}Nb_{0.5})O_2$	0.4782	0.3206	22.07	-16.594	0.92

The total and projected densities of electronic states calculated for pure IrO_2 are shown in **Figure 147**. The main energy band structure of IrO_2 consists of two bands. The low energy band between - 19.2 eV and -17.5 eV is composed of the 2s states of oxygen and the wide valence band around Fermi level consists of hybridized O 2p - Ir 5d states with two prominent peaks corresponding to these O 2p and Ir 5d states and providing a metallic type of electronic conductivity characteristic of IrO_2. Introduction of Sn and Nb into IrO_2 matrix is supposed to change the electronic properties of the compound and thus, the electronic structure of bulk as well as the electronic structure of the most stable (1 1 0) surface has been calculated for the

ternary compositions of $(Ir_{1-2x}Sn_xNb_x)O_2$ with x = 0, 0.125, 0.25, 0.375 and 0.5 in the computational study. Total electronic densities of states for all these compositions are shown in **Figure 156**. It is observed that all the materials demonstrate metallic behavior, although to different extents. Since in general, the metallic conductivity is proportional to the density of states at Fermi level $n(E_F)$, it provides an opportunity to qualitatively evaluate the correlation between the residual amount of Ir in the ternary compounds and the electronic conductivity of the materials. **Figure 157** shows the variation of $n(E_F)$ with respect to various compositions of $(Ir,Sn,Nb)O_2$. For comparison, the values of $n(E_F)$ are normalized to electrons per one $(Ir_{1-2x}Sn_xNb_x)O_2$ formula unit. The graph shows that the conductivity decreases with decrease of Ir content up to 0.25 atoms per formula unit (x = 0.375) and then the conductivity value is maintained almost the same as zero content of Ir. Poor electronic conductivity is customarily expected to impair the overall catalytic activity of the material. However, reduction in the conductivity with decrease of IrO_2 concentration up to 50 mol.% most likely is not sufficient to significantly deteriorate the catalytic properties of the material as confirmed by the experimental results shown in **Figure 54**.

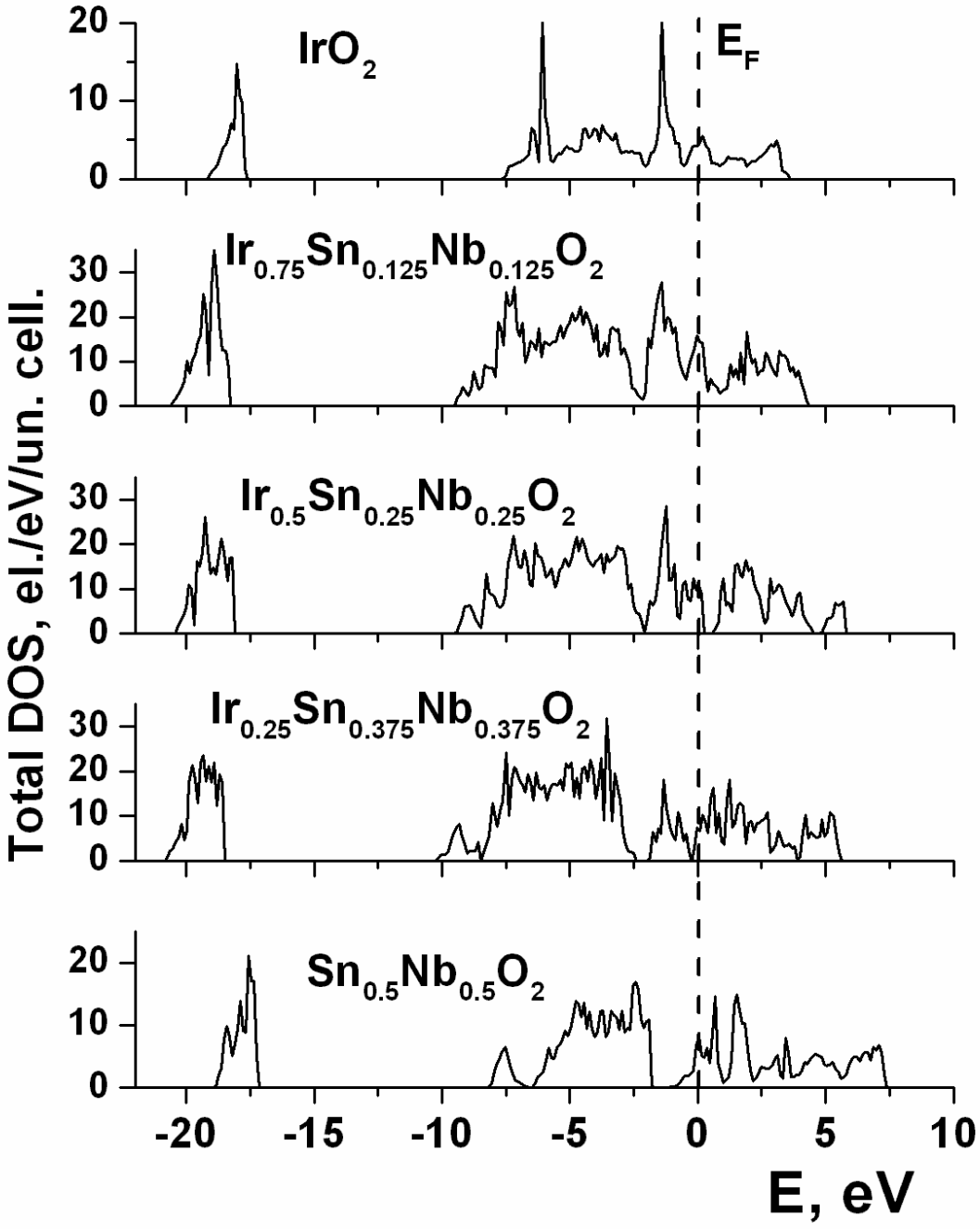

Figure 156. Total electronic density of states for (Ir,Sn,Nb)O_2

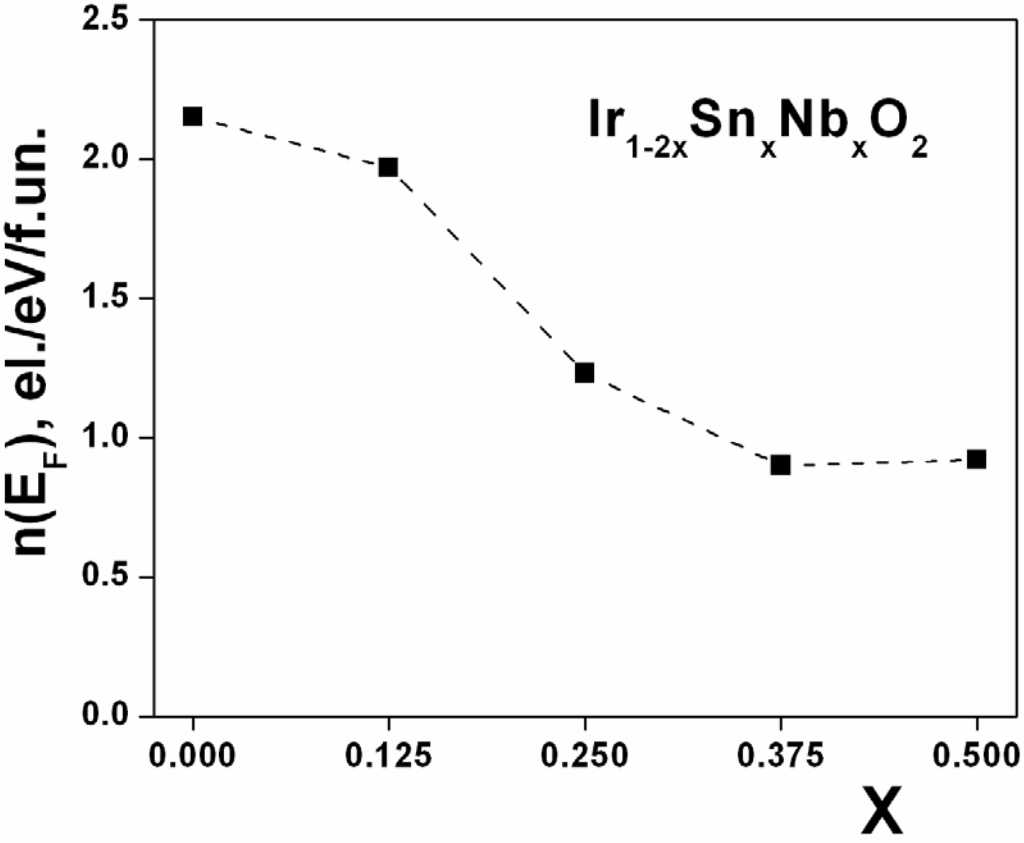

Figure 157. Density of states at Fermi level for different compositions of (Ir,Sn,Nb)O_2

In recent years, another aspect considered in the computational part relates to a wide spread concept proposed by Nørskov *et al.* [125, 126], that the catalytic activity of the surface could be qualitatively characterized by the simple descriptor obtained from the electronic structure of the material. This descriptor has been defined as a gravity center of d-band of the noble metal ε_d usually located in the vicinity of the Fermi level. An optimal position of the d-band center provides an optimal interaction between the catalytic surface and the various species participating in the catalytic reactions predominantly occurring at the surface. Since, such an interaction should be “just - right” implying resulting in a moderate effect allowing reagents and

products to adsorb at the surface and leave most efficiently. Thus, an adjustment of the d-band center position with respect to the Fermi level may play a critical role in designing novel catalyst materials.

Calculations have been done for the electronic structure of the stable (1 1 0) surfaces for all the mentioned (Ir,Sn,Nb)O_2 and the positions of corresponding d-band centers have been obtained as a first moment of $n_d(E)$: $\varepsilon_d = \int n_d(E)EdE / \int n_d(E)dE$, where $n_d(E)$ is a sum of projected densities of d-electrons of Ir, Sn and Nb.

Figure 158 shows partial Ir d-band densities of states together with corresponding centers of these zones marked with vertical arrows on the graphs. One can see that d-centers for Ir compositions from 100 at.% up to 50 at.% of IrO_2 locate virtually at the same position with respect to the Fermi level (- 1.31 eV to - 1.33 eV). However, further decrease in the Ir content causes a noticeable shift of the Ir d-band center upward and for 25 at.% IrO_2, ε_d reaches its position at - 0.49 eV indicating that an overall chemisorption reaction of different species reacting at the surface is noticeably stronger at this composition rather than at higher Ir content. Assuming that pure IrO_2 demonstrates an optimal catalytic activity corresponding to ε_d = - 1.33 eV, a significant drop in the activity is expected for IrO_2 content below 40 mol. % as seen experimentally in **Figure 53** which could be most likely due to a positive shift of the Ir d-band center deviating the catalytic activity from its optimal value. Such a behavior of the d-band center could be attributed to complex hybridization of electronic Ir d-states and corresponding d, s and p states of Sn, Nb and O during formation of the solid solution ternary oxide.

Another important aspect to be highlighted in the present study is the cohesive energy E_{coh} calculated for all the materials considered and collected in **Table 12**. It clearly shows that with a decrease in Ir concentration in the compound, there is an increase in the E_{coh} values (*i.e.*

more negative values). This would result in an overall improved structural and chemically stable (Ir,Sn,Nb)O_2. Such an improvement may be due to presence of much stronger Nb - O bonds in comparison with Ir - O ones since the calculated E_{coh} for pure NbO_2 is - 18.251 eV/f.un. *vs.* - 15.859 eV/f.un. for IrO_2. An increase in the cohesive energy of the iridium oxide doped with tin and niobium yields a robust and chemically stable ternary oxide (**Figure 55**) in comparison to the original pure IrO_2.

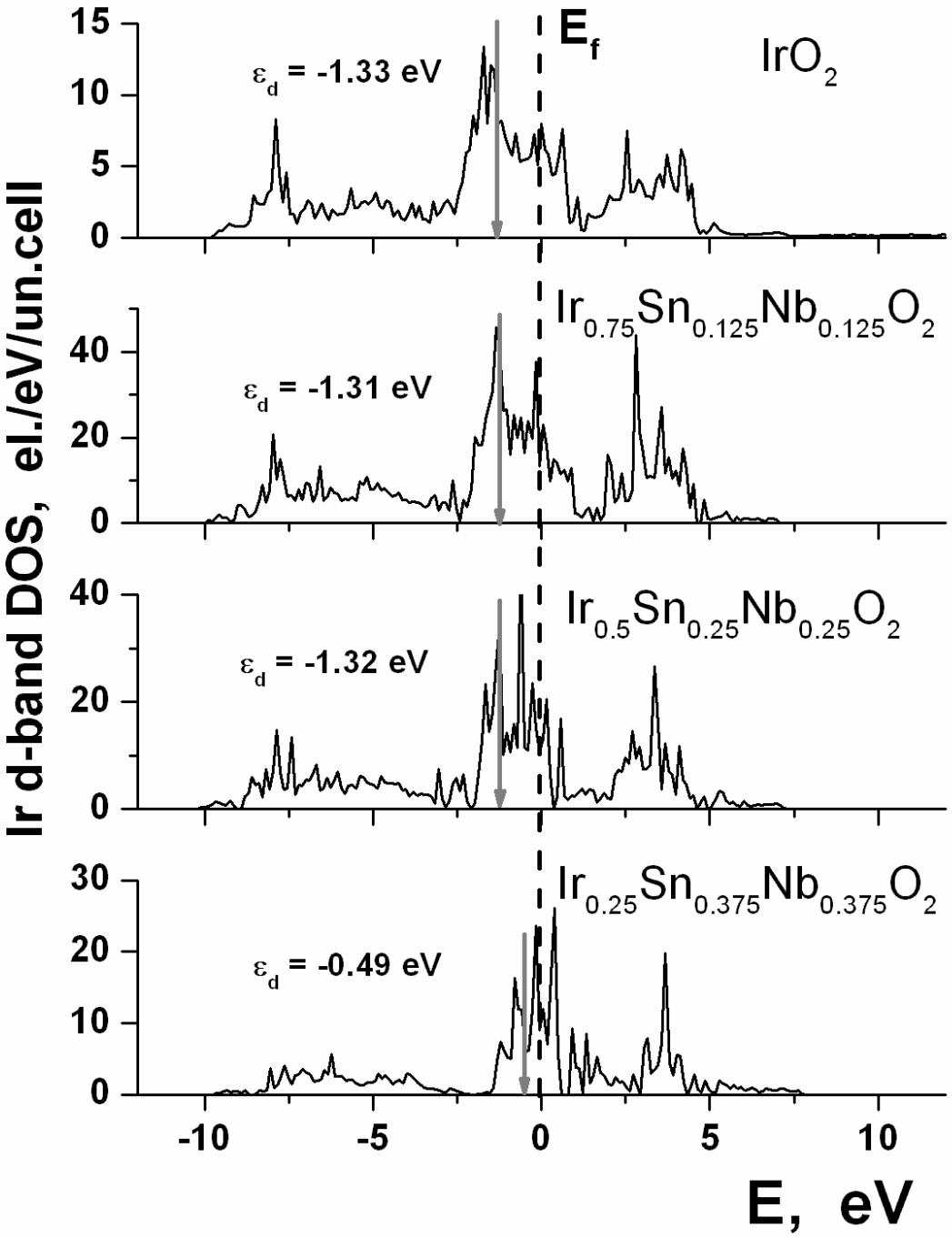

Figure 158. Ir d-band partial density of states for (Ir,Sn,Nb)O_2. The arrows denote positions of the d-band centers (ε_d)

6.6 F DOPED IRIDIUM - TIN - NIOBIUM OXIDE

6.6.1 Computational Methodology

The electrochemical activity of the (Ir,Sn,Nb)O_2:F electro-catalyst is expected to depend on the electronic structure and the electronic conductivity; and the cohesive energy of the system will qualitatively tell us more about the structural stability of the electrode materials. Theoretical calculations will help understand the effect of different (Ir,Sn,Nb)O_2:F compositions on the electronic conductivity, long term stability and the catalytic activity of the material. In the present study, the electronic properties of the solid solution between IrO_2, SnO_2 and NbO_2 with and without the incorporation of different amounts of F have been investigated to mimic the (Ir,Sn,Nb)O_2:F materials system. First principles approach has been used to calculate the total energy, electronic and optimized crystal structures; total and projected densities of electronic states along with the cohesive energies for pure IrO_2 and different compositions of (Ir,Sn,Nb)O_2:F using the density functional theory. Tin oxide, niobium dioxide and fluorine have been introduced with IrO_2 to study the electronic conductivity and structural stability of the compounds along with the electronic structure peculiarities related to the chemical compositions of the materials considered in the present study.

The bulk and (1 1 0) surface of (Ir,Sn,Nb)O_2 doped with different amount of F has been considered to exhibit rutile structure with a tetragonal unit cell and space group $P4_2/mnm$ following experimental validation. Based on this primitive rutile type unit cell there has been chosen a fourfold 2 x 2 x 1 super-cell with different atomic configurations corresponding to the specific Ir, Sn, Nb and F compositions of the oxide solid solutions. To facilitate convenient

calculations, the basic composition has been chosen as 25 at.% IrO_2 - 37.5 at.% SnO_2 - 37.5 at.% NbO_2 instead of 30/35/35 ratio used in the experiment. Such 25/37.5/37.5 composition, although slightly different from the experimental ratio, allows us to select smaller representative super-cells for all the calculation of bulk and surface electronic structures. Thus, the compositions of the solid solutions chosen to model the compounds considered in the experimental study are pure IrO_2 and $(Ir_{0.25}Sn_{0.375}Nb_{0.375})O_{2-x}F_x$, where x = 0, 0.5, 1.0 and 1.5 corresponding to 0, 4.5, 9.0 and 13.5 wt.% F, respectively. A two-dimensional slab repeated in (1 -1 0) direction with 36 atom unit cell and a vacuum distance ~ 12 Å between adjacent images of the slab was selected for calculating (1 1 0) surface electronic properties.

The Vienna Ab-initio Simulation Package (VASP) was used within the projector-augmented wave (PAW) method [131-133] and the generalized gradient approximation (GGA) for the exchange-correlation energy functional in a form suggested by Perdew and Wang [130] for calculating the total energies, electronic structure, and density of electronic states. It should be noted that for all the $(Ir,Sn,Nb)O_2$:F compositions, the corresponding atomic distributions are ambiguous and can be represented by different spatial configurations. Several atomic configurations have been constructed for each composition and only those configurations having the lowest total energies are considered for our calculations.

6.6.2 Theoretical Discussion

Figure 159 shows the total densities of electronic states calculated for pure IrO_2 and all solid solutions considered in the study. The IrO_2 band structure consists of two main bands. The 2s states of oxygen are in the low energy band between - 17.5 eV and - 19.2 eV. Around the Fermi

level, there is a wide valence band which has hybridized O 2p and Ir 5d states. O 2p and Ir 5d states have 2 prominent peaks that provide the metallic type of electronic conductivity to IrO_2. Tin, niobium and fluorine have been introduced into the IrO_2 matrix which noticeably changes the electronic structures of the compounds along with all major projected electronic states denoted with corresponding orbital numbers. It is observed (**Figure 159**) that all the materials remain metallic, although to different extent.

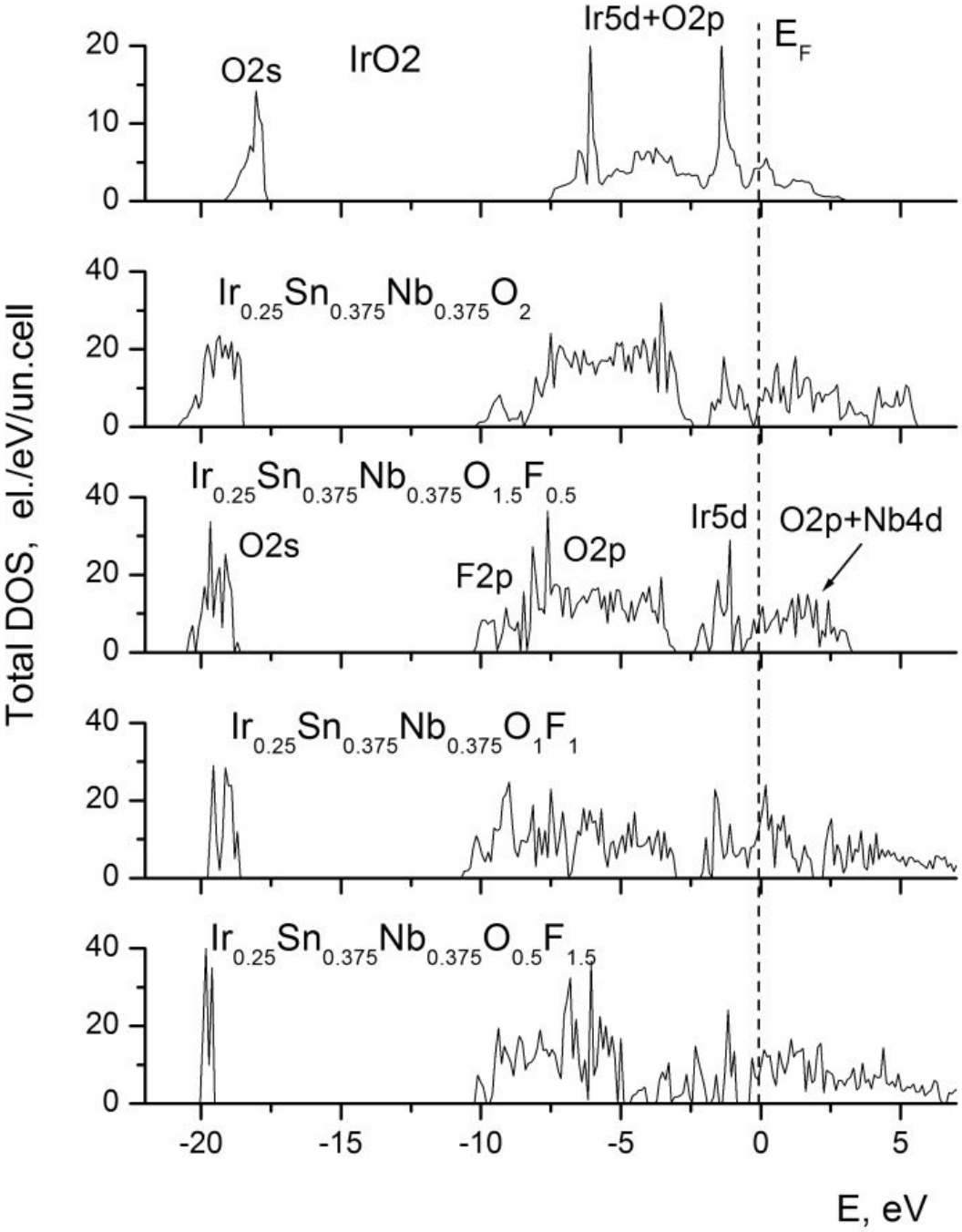

Figure 159. Total bulk density of electronic states for pure IrO_2 and $(Ir_{0.25}Sn_{0.375}Nb_{0.375})O_{2-x}F_x$ (x = 0, 0.5, 1, 1.5)

It is well known that the metallic conductivity of a material is proportional to the density of states at Fermi level $n(E_F)$. This would provide an opportunity for understanding and evaluating the correlation between chemical compositions of materials and their electronic conductivity. **Figure 160** shows the dependence of $n(E_F)$ *vs.* composition of $(Ir_{0.25}Sn_{0.375}Nb_{0.375})O_{2-x}F_x$. It is to be noted that the values of $n(E_F)$ have been normalized to electrons per one $(Ir_{0.25}Sn_{0.375}Nb_{0.375})O_{2-x}F_x$ formula unit for comparison. The value of $n(E_F)$ for pure IrO_2 is marked with a dash horizontal line as a benchmark of the electronic conductivity. It clearly shows that there is a drastic decrease in conductivity for 25 at.% IrO_2. Such a drop in the electronic conductivity is expected due to presence of substantial amount of SnO_2 known to be a very poor conductor with a high band gap of 3.6 eV [138]. Introduction of fluorine improves the overall conductivity reaching an optimal value at ~ 9 - 10 wt.% F. It agrees well with different theoretical studies and experimental validation for F doped tin oxide; wherein significant improvement in the electronic conductivity of SnO_2 is observed with introduction of ~ 10 wt.% F due to an increase of the charge carriers concentration in the system [24, 76, 139, 140]. Since a necessary condition for excellent catalytic activity of the system is high electronic conductivity, the dependence shown in **Figure 160** may shed light to some extent on the intrinsic reasons of high electro-catalytic activity of the $(Ir_{0.3}Sn_{0.35}Nb_{0.35})O_2$:10 wt.% F solid solution (**Figure 65**).

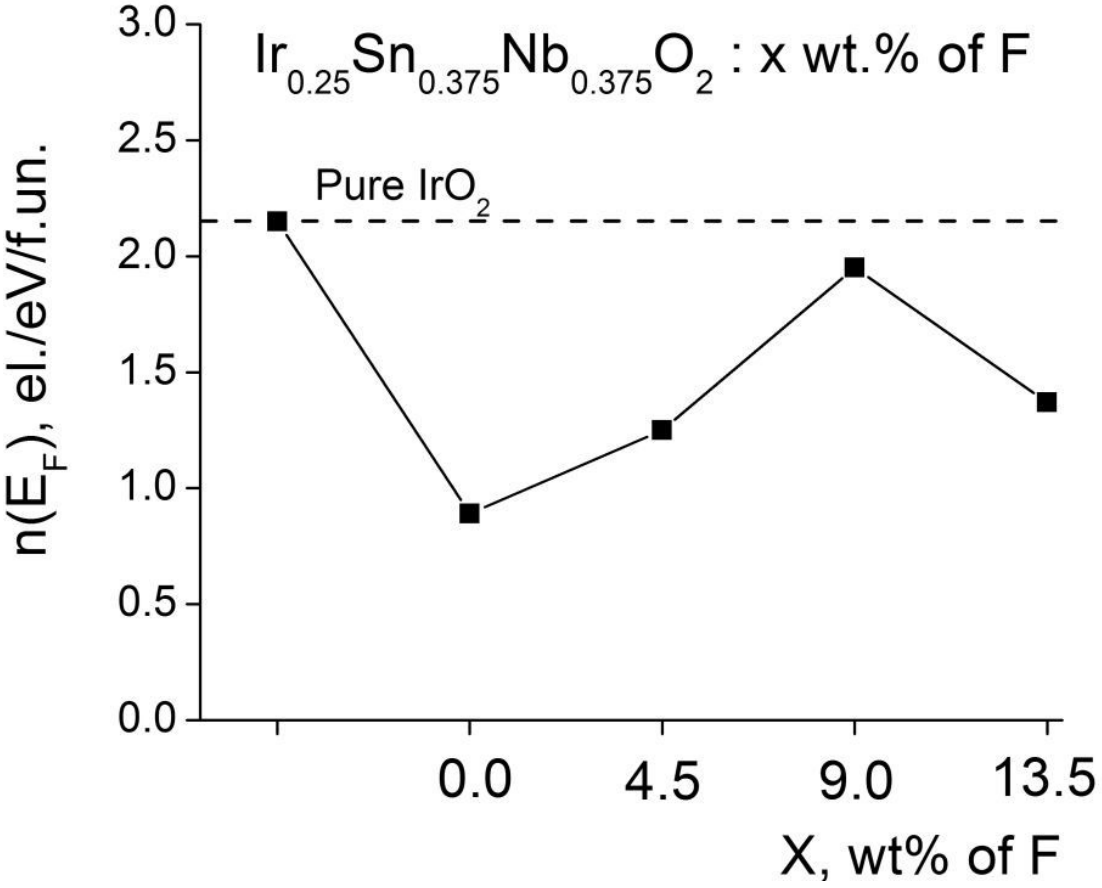

Figure 160. Total bulk density of states at Fermi level for IrO_2 and $(Ir,Sn,Nb)O_2$:F

Another aspect considered in the computational part of the present study relates to a wide spread concept proposed by Nørskov *et al.* [125, 126], that the catalytic activity of the surface could be qualitatively characterized by the simple descriptor obtained from the electronic structure of the material. Such a descriptor is determined as a position of a gravity center of d-band of the metal ε_d located usually in the vicinity of the Fermi level. The optimal position of the d-band center would provide, in turn, the optimal interaction between the surface and various species during catalytic water splitting on the surface leading to a maximum possible catalytic activity of the particular material. Hence, if an appropriate adjustment to the d-band center

position with respect to the Fermi level is done, it will very likely be critical in contribution to the design of novel highly active and electrochemically stable electro-catalysts discussed herein.

Calculations have been done for the electronic structure of the stable (1 1 0) surfaces for all the mentioned (Ir,Sn,Nb)O_2 and the positions of corresponding d-bands centers have been obtained as a first moment of $n_d(E)$: $\varepsilon_d = \int n_d(E)EdE / \int n_d(E)dE$, where $n_d(E)$ is a sum of projected densities of d-electrons of Ir, Sn and Nb. **Figure 161** shows the projected sums of Ir, Sn and Nb d-band densities of states with their corresponding centers. It is seen that the d-center for pure IrO_2 is located at ~ 1.33 eV below the Fermi level. This position was considered as a reference point for comparison of the catalytic activities of the other oxides in the present study. Substantial reduction of Ir content (up to 25 at.%) along with an introduction of Sn and Nb electronic states leads to a shift of the d-band center up to the position at - 0.09 eV below the Fermi level. This clearly indicates that an overall chemisorption reaction of various species at the surface is stronger for $(Ir_{0.25}Sn_{0.375}Nb_{0.375})O_2$ rather than for pure IrO_2.

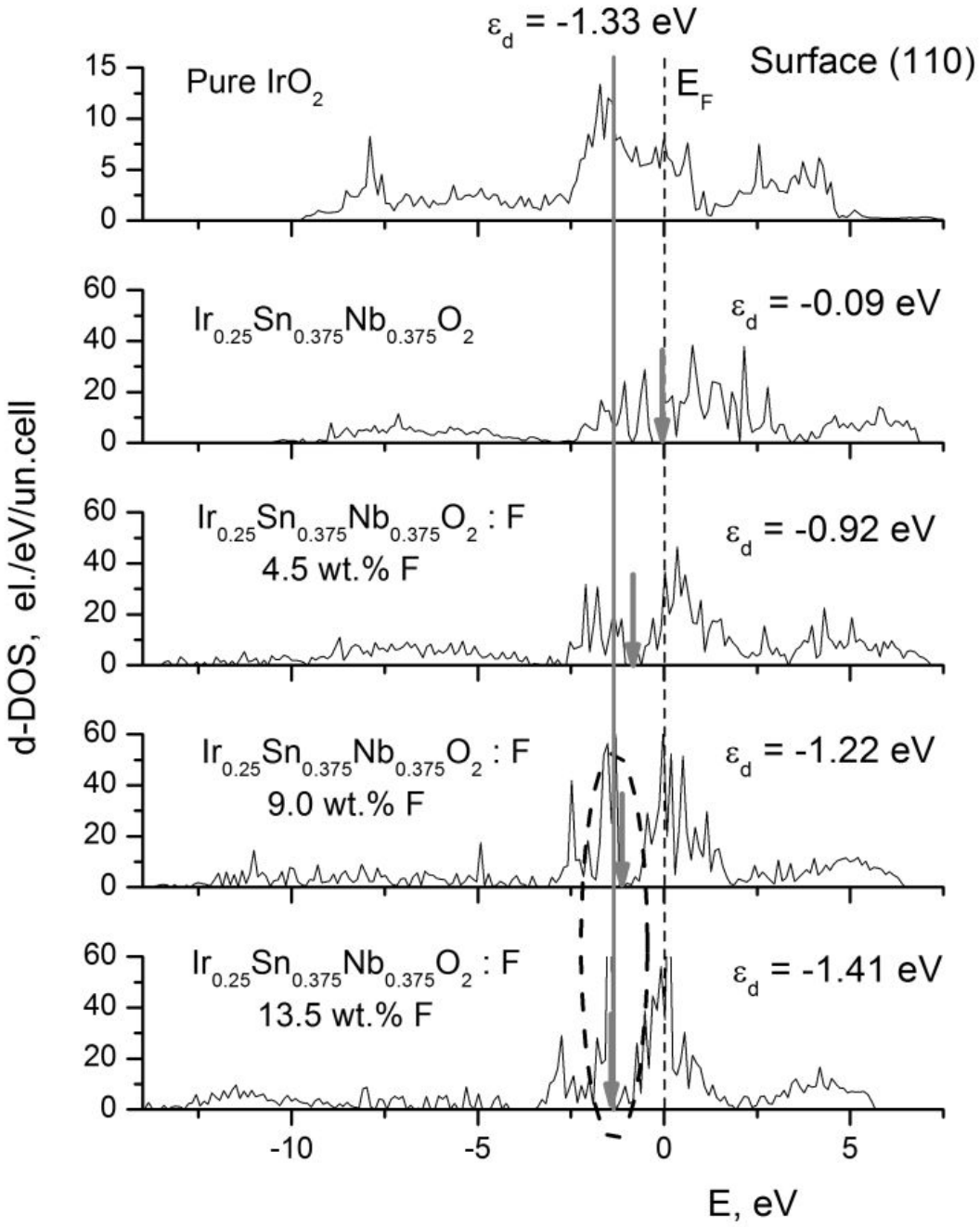

Figure 161. Projected d-band density of states for IrO_2 and (Ir,Sn,Nb)O_2:F. The arrows denote positions of the d-band centers (ε_d)

Assuming pure IrO_2 as the gold standard OER catalyst, it demonstrates optimal activity as a catalyst at ε_d = -1.33 eV. It can therefore be suggested that the decrease in electrochemical activity seen in $(Ir_{0.30}Sn_{0.35}Nb_{0.35})O_2$ electrode (**Figure 65**) might be due to the d-band center being at a more positive value and reducing the catalytic activity with respect to IrO_2. This shift in the d-band center could be attributed to an introduction of the additional Sn and Nb electronic states contributing to the total d-band of the system during formation of $(Ir,Sn,Nb)O_2$ solid solution. Further consideration of the effect of fluorine doping on the overall catalytic activity of the materials is conducted in terms of a change of the electronic structure of the compounds in general, and a shift in the position of the d-band center in particular.

Figure 162 and **Figure 163** shows the total and projected DOS of $(Ir_{0.25}Sn_{0.375}Nb_{0.375})O_2$ and $(Ir_{0.25}Sn_{0.375}Nb_{0.375})O_1F_1$, respectively. Introduction of F manifests in an appearance of the F 2p band around - 10 eV with negligible amount of other states in the entire energy domain. Increase in F content results in more pronounced 2p states leading to a stronger hybridization effect between F 2p, Ir 5d and Nb 4d states. As a result, the overall d-band center location moves from - 0.09 eV for the non-fluorine (undoped) composition downward towards the position corresponding to pure IrO_2 (- 1.33 eV) with increase in F content. It can therefore be perceived from **Figure 161** that at 4.5, 9.0 and 13.5 wt.% F, the d-band center passes accordingly through - 0.92 eV, - 1.22 eV and -1.41 eV positions, respectively; indicating significant improvement in the overall catalytic activity with increase in F concentration. The optimal F concentration at which the d-center of $(Ir,Sn,Nb)O_2$:F returns back to the position corresponding to pure IrO_2 can therefore be expected to be around 10 - 12 wt.% F which is in excellent agreement with the experimental results (**Figure 65** and **Figure 67**).

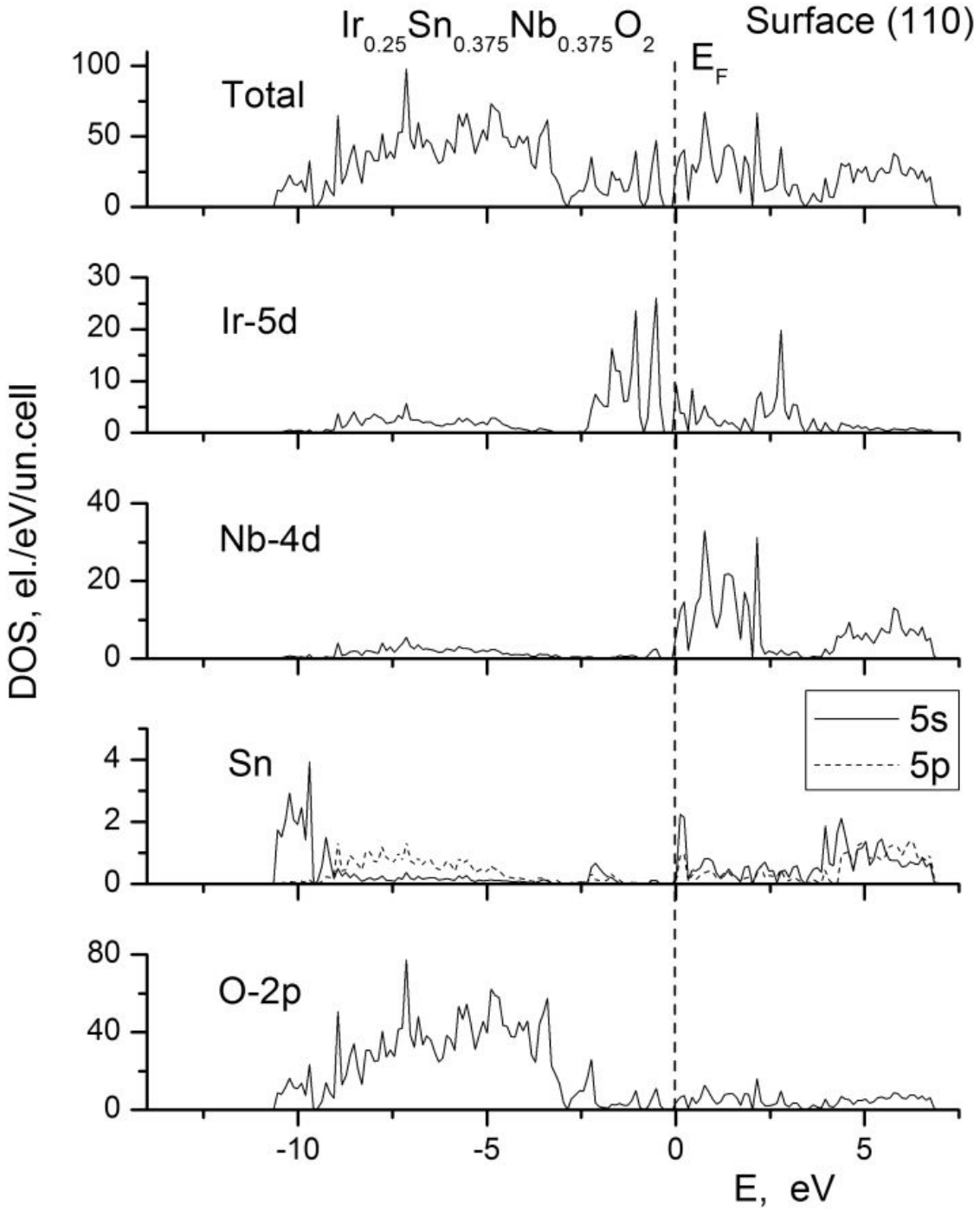

Figure 162. Total and projected density of states for $(Ir_{0.25}Sn_{0.375}Nb_{0.375})O_2$

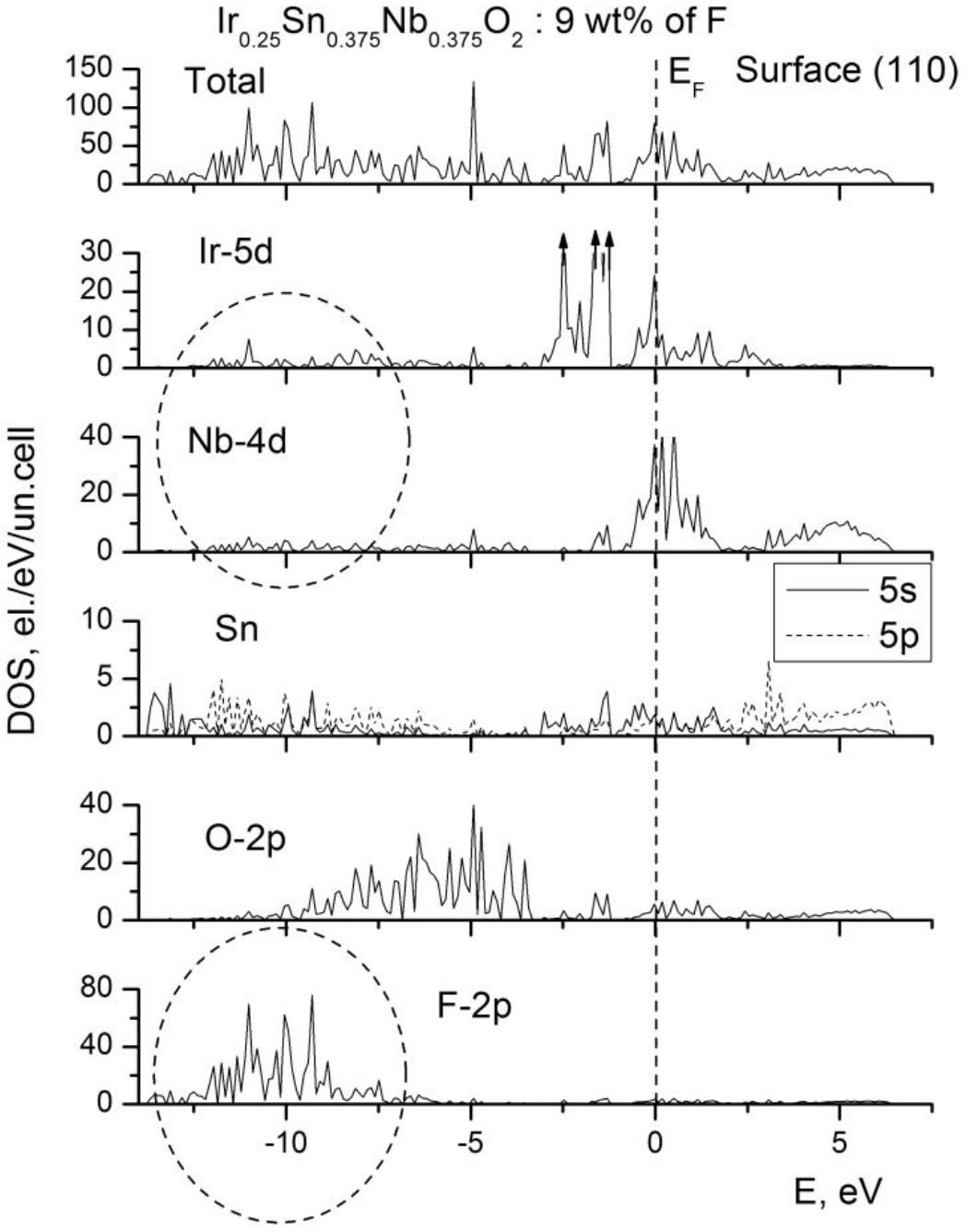

Figure 163. Total and projected density of states for $(Ir_{0.25}Sn_{0.375}Nb_{0.375})O_1F_1$

Hence, it is seen that with increase in F content, the d-band center shifts downward on the energy scale returning back to the position corresponding to pure IrO_2 at ~ 10 wt.% F rendering the system essentially mimicking the electronic and electro-catalytic properties of pure IrO_2. A combination of the improved metallic electronic conductivity and the d-band center position being optimal conceivably renders (Ir,Sn,Nb)O_2:F demonstrating high catalytic activity comparable to pure IrO_2. Additionally, for this composition it should be noted that the electronic structural change results in the entire oxide (not only Ir cations) becoming catalytically active mimicking the catalytic behavior of pure IrO_2.

Figure 164 shows the calculation of cohesive energy (E_{coh}) for the materials considered in this study. It is observed that reducing Ir concentration and simultaneous increase of Sn and Nb content in the catalyst material leads to a more negative value of E_{coh}. This can be attributed to the formation of Nb - O bonds which are more strong than Ir - O (calculated E_{coh} for pure NbO_2 is - 18.251 eV/f.un. *vs.* - 15.859 eV/f.un. for IrO_2). However, introduction of F leads to a gradual decrease in the cohesive energy (absolute value) due to weaker metal - F^- bonds in comparison with corresponding metal - O^{2-} ones (the lower negative charge of F^- leads to the weaker electrostatic metal - fluorine interaction). Nevertheless, such a negative effect of F doping does not significantly affect the overall stability of the material. As seen in **Figure 164**, E_{coh} of the F doped (Ir,Sn,Nb)O_2 becomes equal to that of pure IrO_2 approximately at ~ 7 wt.% F. Further increase in F content results in the material displaying less stability compared to pure IrO_2. Although the optimal composition of the oxide with ~ 10 wt.% F demonstrates slightly lower E_{coh} than the reference IrO_2, one can state that the overall stability of the material (qualitatively determined by the cohesive energy) is of the same order as pure IrO_2. This

conclusion also agrees well with the experimental results (**Figure 74**) obtained from the chronoamperometry curves.

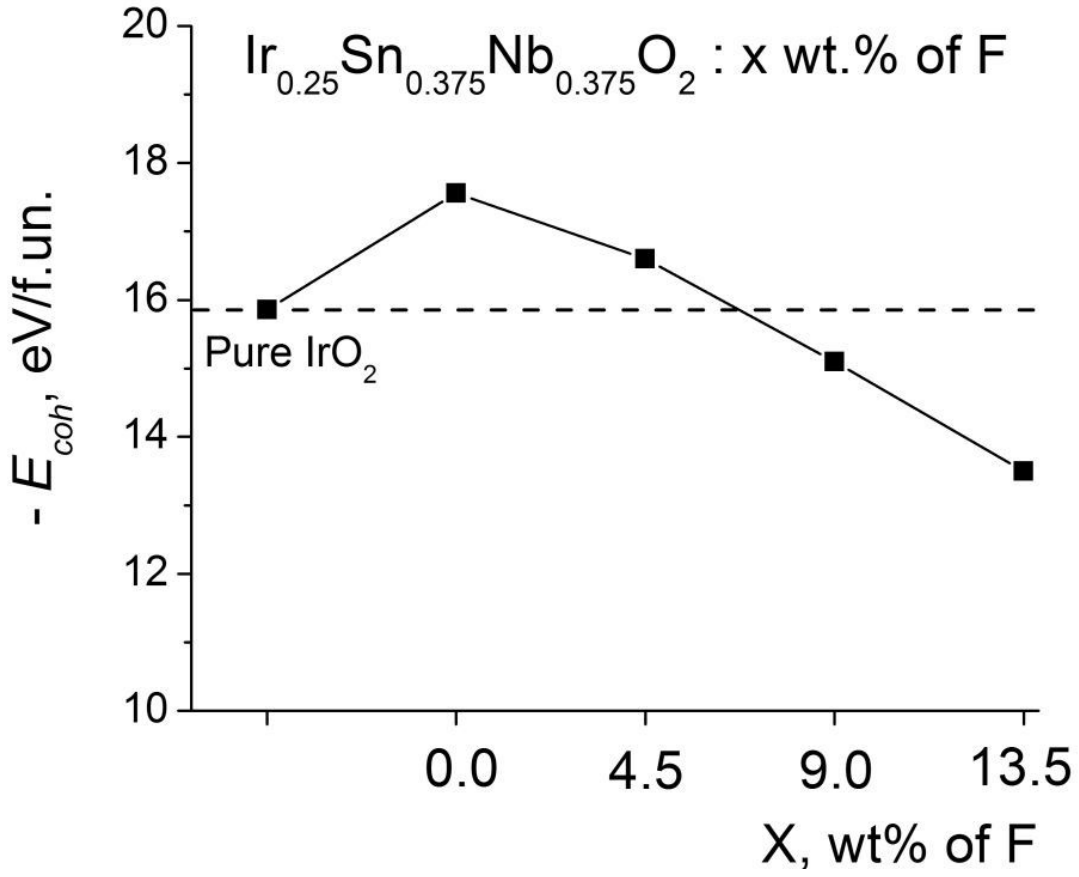

Figure 164. Cohesive energy of IrO_2 and $(Ir_{0.25}Sn_{0.375}Nb_{0.375})O_{2-x}F_x$

7.0 SUMMARY

Nanostructured robust mixed metal oxides with reduced noble metal content have been synthesized, characterized and developed for use as anode electro-catalysts in proton exchange membrane (PEM) based water electrolysis. The catalysts were developed in the form of thin films and nanostructured high specific surface area powders for the oxygen evolution reaction (OER). The experimental work in the thesis was primarily targeted towards accomplishment of better efficiency, durability and lower cost catalyst materials.

Electro-catalysts with significant decrease in the noble metal loading along with improved catalytic response using novel synthesis techniques were obtained. Strategies involved synthesizing less expensive and more durable high surface area nanostructured materials as supports or diluents for the expensive electro-catalyst, which would ultimately help in immensely lowering the overall costs. The electro-catalysts mentioned in the thesis thus portend to be potentially preferred for use as an anode OER material in PEM electrolyzers.

Different catalyst systems were chosen systematically in order to achieve excellent electrochemical activity without compromising the stability of the catalysts. Fluorine was used as the dopant not only with pure IrO_2, but also with the binary and ternary metal oxides which boosted the overall performance and electro-catalytic activity of the catalysts. Tin oxide and/or niobium oxide were chosen as supports with pure IrO_2 and RuO_2 in order to decrease the cost

due to the noble metal oxides. A reduction of up to ~ 80 at.% in the noble metal oxide content has been achieved for various electro-catalyst systems. The electro-catalysts in nano-crystalline form of 2D and 3D architectures with different morphology, microstructure and composition were prepared. Systematic structural and electrochemical characterization was carried out throughout the thesis to understand the relation between the catalyst structure and the electrochemical behavior.

7.1 THIN FILM CATALYSTS

The thin films have been synthesized by homogenizing the precursor solutions and heat treatment to 400°C. The synthesis technique resulted in formation of a complete solid solution for all the different catalyst systems. No phase separation or any extra peak was observed for the supports or dopant used in our studies. Detailed characterization and electrochemical studies were conducted to confirm the catalysts' potential as an OER anode for PEM electrolyzers.

The study of F doped IrO_2 which has been discussed in **Section 5.1.1** shows the viability of fluorine as a great dopant. It not only helps achieve greater electrochemical activity, but also does not comprise the stability of the resultant IrO_2:F electro-catalyst. These results gave the motivation for doping F in the various binary and ternary catalyst systems.

Consequently, F doped SnO_2 was used as a support with IrO_2 and RuO_2. SnO_2:F imparted stability to the overall structure and helped achieve comparable current density as the pure noble metal oxide counterpart even after reducing the expensive metal oxide content by ~ 80 at.%. Detailed results involving Tafel slope and Electrochemical Impedance Spectroscopy (EIS) have

been discussed in **Section 5.1.2** and **Section 5.1.3** for the binary thin film structures of $(Ir,Sn)O_2$:F and $(Ru,Sn)O_2$:F, respectively. Rotating disk electrode (RDE) studies were also conducted on the most optimized composition of $(Ir_{0.2}Sn_{0.8})O_2$:10 wt.% F to confirm the reaction mechanism and get the number of electrons getting transferred in the reaction.

Since niobium oxide is known to have greater cohesive energy than IrO_2 and SnO_2, a novel rutile structure of $(Ir,Sn,Nb)O_2$ was developed. The ternary compositions were all single phase confirming the formation of complete solid solution. They were characterized extensively *via* x-ray diffraction (XRD) and x-ray photoelectron spectroscopy (XPS). The $(Ir,Sn,Nb)O_2$ catalyst helped achieve similar electrochemical activity after decreasing IrO_2 by ~ 60 at.%. But, due to the incorporation of niobium oxide in the lattice, a much stable structure is achieved in comparison with pure IrO_2, the accepted gold standard anode in PEM based water electrolysis. This enabled the ternary catalyst materials to exhibit excellent resistance to corrosion and enhance chemical stability as discussed in **Section 5.1.4**. Fluorine doping to the ternary electro-catalysts has been discussed in **Section 5.1.5** which further decreased the noble metal oxide content without compromising the catalysts durability.

7.2 NANOPARTICULATE CATALYSTS

The electro-catalytic materials based on IrO_2:F, $(Ir,Sn)O_2$:F and $(Ir,Nb)O_2$:F in 3D architectures of nanoparticles were synthesized to achieve the compositional homogeneity at atomic and nanometer length scale. Synthesis of the nanostructured high surface area electro-catalyst architectures with manipulation of particle morphology and size was carried out to promote

cooperative, sequential reaction steps along different catalytic domains of the nanoscale structure.

F doped IrO_2 nanoparticles were synthesized by the modified Adams fusion approach giving us enormously high specific surface area catalysts. This resulted in enhance electro-chemical activity with no loss in stability. Detailed RDE experiments and kinetic studies, along with the long term structural stability tests and EIS studies were conducted as discussed in **Section 5.2.1**. The kinetic parameters obtained were most superior for IrO_2:10 wt.% F which was corroborated by other electrochemical tests like polarization, EIS and chronoamperometry (CA).

Nanoparticulate robust fluorine doped SnO_2 was used as a support with IrO_2. SnO_2:F was synthesized *via* a surfactant based approach to achieve high specific surface area supports. A single solid solution of IrO_2 with SnO_2:F resulted in reducing the IrO_2 content by ~ 70 at.% without compromising the electrochemical activity as compared to pure IrO_2. Enhanced corrosion resistance of the (Ir,Sn)O_2:F materials has been obtained and is discussed in **Section 5.2.2**. Significant characterization in the form of transmission electron microscopy (TEM), XRD and XPS was also carried out to complement the electrochemical results.

High surface area fluorine doped niobium oxides were developed as supports by a facile low temperature sol-gel technique. The electro-catalyst system of (Ir,Nb)O_2:F exhibited similar electrochemical activity as commercially used IrO_2 with reduction in noble metal by ~ 75 at.%. But, these binary electro-catalyst systems showed way better durability than the commercial IrO_2. Detailed structural characterization along with the electrochemical testing including extended time CA plots have been discussed in **Section 5.2.3**.

Identification of such non-noble metal based catalysts systems or electro-catalysts with significant reduction of expensive noble metal contents, yielding comparable or higher

electrochemical performance than the gold standards for PEM based water electrolysis; would result in reduction in the overall capital costs of PEM based water electrolyzers. This would thus help in the attainment of the targeted hydrogen production cost (< $ 3.0 / gallon gasoline equivalent delivered) comparable to conventional liquid fuels.

APPENDIX A

DIRECT METHANOL FUEL CELLS

Direct Methanol Fuel Cells (DMFC) offer efficient continuous energy and power with reduced greenhouse emissions. Commercialization of low cost DMFC has been thwarted by catalyst activity, stability, and loading constraints. Efforts are on-going to achieving ultra low loadings of high performance platinum group metal (PGM) electro-catalyst while also identifying non platinum group catalysts to improve performance and durability. Identification of such a catalyst remains an enigma with continuous on-going efforts. Herein, we report for the first time a novel complexed sol-gel (CSG) approach to synthesize nanocrystalline high specific surface area (HSA) binary and quaternary electro-catalyst exhibiting three fold higher electrochemically active surface area (ECSA) and ultra high electrochemical performance compared to commercially available Johnson Matthey Pt-Ru black catalyst, the currently accepted gold standard. Further, in identical single full cell DMFC configuration tests for methanol oxidation, current and power densities ~ 40 % higher than that displayed by the Johnson Matthey catalyst is achieved.

A.1 BINARY PLATINUM - RUTHENIUM CATALYST

A.1.1 Introduction

Cost and durability present two of the most significant challenges affecting the widespread commercialization of fuel cells for diverse applications encompassing stationary power, transportation power, portable power, auxiliary power units, and material handling equipment . The cost of fuel cell powered systems need to be reduced (*E.g.* projected target $ 30 / kW at 2017 for transportation fuel cell) in order to be considered competitive with conventional technologies [141-143]. Of the different fuel cell types, proton exchange membrane fuel cell (PEMFC), utilizing hydrogen as the fuel operating at low temperature (< 120^{o}C), has been considered for applications that require faster start-up times, and frequent starts and stops such as automotive applications, material handling equipment and auxiliary backup power [141-144].

On the other hand, methanol powered direct methanol fuel cell (DMFC) are well suited for portable power applications in consumer electronic devices wherein the power requirements are low. A significant fraction of the cost for PEMFC and DMFC arises due to the prohibitively expensive platinum group-metal (PGM) catalysts that are currently used in the anode and cathode to accelerate the electrochemical reactions [144-147]. For widespread commercialization of PEMFC and DMFCs, there is a critical need for continued advancements to minimize PGM loading or the development of equally performing non-PGM catalysts alternatives to reduce the cost [144-148]. The durability of catalysts is also an issue under conditions of load-cycling in harsh corrosive environment, and the mitigation of catalyst dissolution/degradation during operation of low-temperature and high-temperature fuel cells will certainly drives higher

performance leading to lower cost [145-149]. Moreover, while addressing cost and durability, fuel cell performance and efficiency must also meet or exceed that of competing technologies (*E.g.* battery) to allow for market penetration and the inherent environmental benefits of the technology.

A.1.2 Ultra active highly durable Pt-Ru electro-catalyst

In this vein, design and synthesis of effective electro-catalysts with improved electrochemical activity, improved durability / stability, reduced precious metal loading to ultra-low level and increased tolerance to air, fuel and system-derived impurities is of paramount importance. To meet the performance and efficiency, durability and cost requirements for fuel cells, significant research has been conducted over the years focusing largely on identifying new materials, and developing novel design and fabrication methods for catalysts and supports [145, 147, 148, 150-153]. The platinum catalyst is extremely sensitive to CO poisoning, making it necessary to employ an additional reactor, which adds cost, to reduce CO in the fuel gas if the hydrogen is derived from an alcohol or hydrocarbon fuel for PEMFC [144, 146, 148-150, 152]. Carbon monoxide generated as a by-product during methanol oxidation reaction (MOR) at low temperatures during DMFC operation inevitably leads to poisoning of the platinum catalyst surface which reduces the catalytic activity of platinum drastically causing it to become inactive by itself.

It is widely accepted that platinum / ruthenium catalysts are favorable for improving the CO tolerance of Pt catalysts [144-146, 150, 154-156]. It has also been reported that the electro-catalytic activity of a Pt-Ru catalyst with a Ru-decorated Pt surface in MOR is twice higher for

optimized Ru coverage as compared to Johnson Matthey Pt-Ru black alloy [JM-Pt(Ru)] catalysts [145, 150, 157]. Contrary to the Ru-decorated Pt, the structure of Pt-decorated Ru is more attractive for improving mass activity due to the low Pt content in the catalysts [145, 158, 159]. Kaplan *et al.* [159] showed that a Ru core-Pt shell catalyst performed much better (up to 36 %) at high temperatures than a JM-Pt(Ru) alloy catalyst, but displayed only a moderate improvement in the chronoamperometry (stability) test. It has been reported that well alloyed Pt-Ru catalysts have lower rates of Ru dissolution and, therefore, exhibit better service life [160, 161]. The previous studies therefore clearly demonstrate that design and synthesis of robust electro-catalysts exhibiting high electrochemically active surface area (ESCA) may represent a suitable microstructure which is expected to improve the electro-catalytic activity, reduce cost by ultra-low PGM loading and decrease the rate of dissolution of catalyst [144, 146, 148-151, 153-161].

In this context, a novel complex sol-gel process (CSG) has been developed to synthesize unsupported nanocrystalline Pt-Ru based binary, ternary and quaternary solid solution having high ESCA with excellent electrochemical activity and durable microstructure for the methanol oxidation reaction. In this complex sol-gel process, a homogeneous amorphous gel has been prepared by the complexation reaction between the acetylacetonate complexes of the respective noble metals using tetramethyl ammonium hydroxide (TMAH) as the complexing agent [162-164].

A.2 EXPERIMENTAL DETAILS

A.2.1 Electro-catalyst Preparation

Phase pure and high surface area Pt-Ru based catalysts were synthesized using the complexed sol-gel synthesis method. Platinum (II) acetylacetonate [Pt-acac: $Pt(C_5H_7O_2)_2$, Alfa Aesar] and Ruthenium(III) acetylacetonate [Ru-acac, $Ru(C_5H_7O_2)_3$, Alfa Aesar] were used as the sources for Pt and Ru respectively. Pt-acac and Ru-acac of the composition Pt-50 at.% Ru were dissolved at 50°C in 100 ml of acetone. Tetramethylammonium hydroxide [TMAH, $(CH_3)_4NOH$, 25% in methanol, Alfa Aesar], set at TMAH : (Pt + Ru) = 1.75 : 1, was then added to the solution to serve both as a high molecular weight organic complexing as well as a hydrolyzing agent. Pt-acac and Ru-acac tend to phase separate during drying and evaporation of the solvent. Thus, the addition of the high molecular weight organic reagent, tetramethylammonium hydroxide (TMAH), and its intended dual role to complex and induce hydrolysis of the starting noble metal precursors was found to be beneficial in yielding homogeneous amorphous gels containing Pt and Ru. After stirring for some time, the solvent was evaporated until the solution became viscous, transforming into a thixotropic gel. The viscous gel was dried in air at 120°C for 12 hours. The dried powder was then heat treated in ultra-high purity (UHP) argon at 500°C in order to decompose the amorphous gel structure. The powders were then heat treated multiple times in UHP Ar - 1% O_2 gas mixture at a lower temperature of 200°C than that reported earlier [162-164] based on the results of the thermo-gravimetric and differential thermal analysis (TGA-DTA). The heat treatments in UHP Ar - 1% O_2 helped in removing the carbon in a controlled manner making sure that there is no oxidation of the alloy.

A.2.2 Physical and Chemical Characterization

In order to perform qualitative phase analysis, the Pt-Ru alloy were characterized by X-ray diffraction (XRD) using Philips XPERT PRO system employing CuK_α (λ = 0.15406 nm) radiation with operating voltage and current at 45 kV and 40 mA, respectively. The XRD peak profile of Pt-Ru alloy was analyzed using the Pseudo-Voigt function to determine the Lorentzian and Gaussian contribution of the peaks. In order to understand the phase formation and decomposition temperature, thermogravimetric and differential thermal analysis (TGA-DTA) has been conducted on the as-prepared precursors as well as thermally treated powders using a TGA-DTA machine (Netzsch STA 409PC/4/H/Luxx TG-DTA). The TGA-DTA analysis has been carried out employing a heating rate of 10°C/min from room temperature up to 500°C in air.

To investigate the microstructure of CSG-Pt(Ru), transmission electron microscopy (TEM) and high resolution transmission electron microscopy (HRTEM) was conducted. JEOL 4000EX operating at 400 kV was employed for conducting TEM analysis to evaluate the particle size and the structure of particles. High resolution transmission electron microscopy (HR-TEM) analysis was conducted on the sample using JEOL JEM-2100F to investigate the particle size and morphology. The specific surface area of the catalysts was analyzed using the common nitrogen adsorption / desorption method pioneered by Brunauer-Emmett-Teller, commonly referred to as BET technique. Each sample was first vacuum degassed, weighed (Denver Instruments SI403), and then tested using a Micromeritics ASAP 2020. Multipoint BET surface areas are reported for all synthesized powders.

X-ray photoelectron spectroscopy (XPS) was used to investigate the valence states of Pt and Ru ions. All the catalysts were analyzed by XPS using a Physical Electronics (PHI) model

32-096 X-ray source control and a 22-040 power supply interfaced to a model 04-548 X-ray source with an Omni Focus III spherical capacitance analyzer (SCA). The system is routinely operated within the pressure range of 10-8 to 10^{-9} Torr (1.3×10^{-6} to 1.3×10^{-7} Pa). The system was calibrated in accordance with the manufacturer's procedures utilizing the photoemission lines E_b of Cu 2p3/2 - 932.7 eV, E_b of Au 4f7/2 - 84 eV and E_b of Ag 3d5/2 - 368.3 for a magnesium anode. All the reported intensities are experimentally determined peak areas divided by the instrumental sensitivity factors. Charge correction was obtained by referencing the adventitious C 1s peak to 284.8 eV.

A.2.3 Membrane Electrode Assembly Preparation

The catalyst ink was prepared for use in various characterization tests *viz.* cyclic voltammetry, polarization, chronoamperometry and single cell testing. The catalyst ink consisted of 85 wt.% catalyst and 15 wt.% Nafion 117 solution [5 wt.% solution in lower aliphatic alcohols, Sigma-Aldrich]. For the single cell testing, a membrane electrode assembly (MEA) was fabricated by using a Nafion 115 membrane and sandwiching it between the two gas diffusion electrodes coated with the catalyst ink. Cathode used for the single cell testing was Platinum black (Sigma Aldrich). The Nafion 115 membrane was pretreated first with a 3 wt.% hydrogen peroxide solution to its boiling point in order to oxidize any organic impurities. Then, it was boiled in D.I. water followed by immersion in a boiling 0.5M sulfuric acid solution to get rid of metallic impurities. Finally, it is treated multiple times in D.I water to remove any traces of acid left behind. This membrane is then stored in D.I. water to avoid dehydration. The MEA was then fabricated by placing the two nafion impregnated electrodes (anode and cathode) on both sides of

the wet pretreated nafion membrane. This assembly was then hot-pressed in a 25 T Hydraulic lamination hot press with dual temperature controller (MTI Corporation) at a temperature of 125°C. Pressure applied was ~ 40 atm for about 30 seconds to get good contact between the electrodes and the membrane. This MEA is then used in the single cell testing.

A.2.4 Electrochemical Characterization

Electrochemical testing was conducted on the sample using a five port jacketed reaction cell (Ace Glass Inc.) in which was assembled a 3-electrode test system. The testing was done using a VersaSTAT 3 (Princeton Applied Research). A solution of 1 M methanol and 0.5 M sulfuric acid was used as the electrolyte which also served as the fuel. The solution is kept at a constant temperature of 40°C using a Fisher Scientific 3006S Isotemp Refrigerator Circulator. The working electrodes were prepared by uniformly spreading the catalyst ink on teflonized carbon papers in an area of ~ 1 cm^2. The platinum loading on the electrodes was ~ 0.2 mg/cm^2. The reference electrode was a XR 200 mercury/mercurous sulfate electrode [Hg/Hg_2SO_4, Radiometer Analytical] that has a potential of ~ +0.654 V with respect to the Standard Hydrogen Electrode (SHE/NHE). Platinum foil (Alfa Aesar, 0.25 mm thick, 99.95%) was used as the counter electrode. The polarization curve is obtained at a scan rate of 10 mV/sec.

In order to have complete chemisorption of CO on the Pt sites, UHP nitrogen - 1% CO gas mixture was passed in a solution of 0.5 M sulfuric acid for 30 minutes at 0.0V *vs.* NHE. Nitrogen is then passed for 40 minutes to remove CO traces from the electrolyte solution. CO stripping voltammetry was done in the same 3-electrode test system using a VersaSTAT 3 (Princeton Applied Research). The working electrodes were prepared by uniformly coating the

catalyst ink to give us a catalyst loading of ~ 0.2 mg/cm^2. The temperature at which CO stripping was conducted was 25°C. CO was adsorbed by flowing UHP N_2 - 1% CO in the cell assembly at a constant voltage of 0 V (*vs.* NHE) for 30 minutes. The potential was kept at the same value of 0 V and the gas flow was switched to UHP N_2 for 40 minutes in order to get rid of the residual CO in the solution. After this, the potential was scanned back and forth twice from 0 to 1.2 V *vs.* NHE at a scan rate of 10 mV/s.

In order to study the long term structural stability or chemical robustness of the synthesized electro-catalysts, chronoamperometry (CA) *i.e.* current signal as a function of time has been conducted for the catalysts in the same 3 electrode test system. Testing of the electrodes was performed for 2 hours using 1 M CH_3OH and 0.5 M H_2SO_4 as the electrolyte (fuel) at 40°C under a constant voltage of ~ 0.65 V *vs*. NHE.

Elemental analysis of the media collected after the stability testing (chronoamperometry) was performed by inductively coupled plasma optical emission spectroscopy (ICP-OES, iCAP 6500 duo Thermo Fisher) in order to determine the amount of platinum and ruthenium leached in the solution. Standards for getting the calibration lines were procured from Sigma Aldrich [platinum standard for ICP and ruthenium ICP/DCP standard solution]. They were then diluted with the stock solution used for electrochemical testing and chronoamperometry (*i.e.* 1 M methanol and 0.5 M sulfuric acid).

A.2.5 Single cell Testing

The three layer membrane electrode assembly (MEA) prepared was sandwiched between two Teflon gaskets with high precision thickness which are capable of applying torque equally to

the gaskets. This five layer assembly is then placed in between two fuel cell grade isotropic graphite blocks (ElectroChem Inc.) having a serpentine flow pattern and an active area of 1 cm^2. There are two gold plated copper plates attached on the outer side which serve as current collector plates. These plates have a silicone rubber heater which helps in providing highest watt density and maintaining uniform cell temperature using the highly thermally conductive graphite blocks. 1 M methanol is used as the fuel and UHP Oxygen is used as the oxidant for the single cell test. Current - voltage curves were measured galvanostatically by using an automatic electronic load from Electrochem Incorporation at temperatures of 40°C, 60°C and 80°C.

A.2.6 Theoretical study

Since Pt-Ru exists in fcc disordered configuration we represented this solid solution as an intermetallic alloy with $L1_0$ tetragonal crystal structure and c/a ~ 1. Such an approximation is reasonable since we are interested in calculations of relative energy differences between various atomic configurations rather than absolute values of the structures.

To model Pt segregation five layer slabs of (1 1 1) and (1 0 0) surfaces have been selected for the calculation of total energies of different atomic distributions and Pt-compositions on first two top layers one of which is an immediate subsurface layer and another representing the surface layer. **Figure 165** demonstrates a unit cell of the (1 1 1) slab with two Pt and two Ru atoms on each layer.

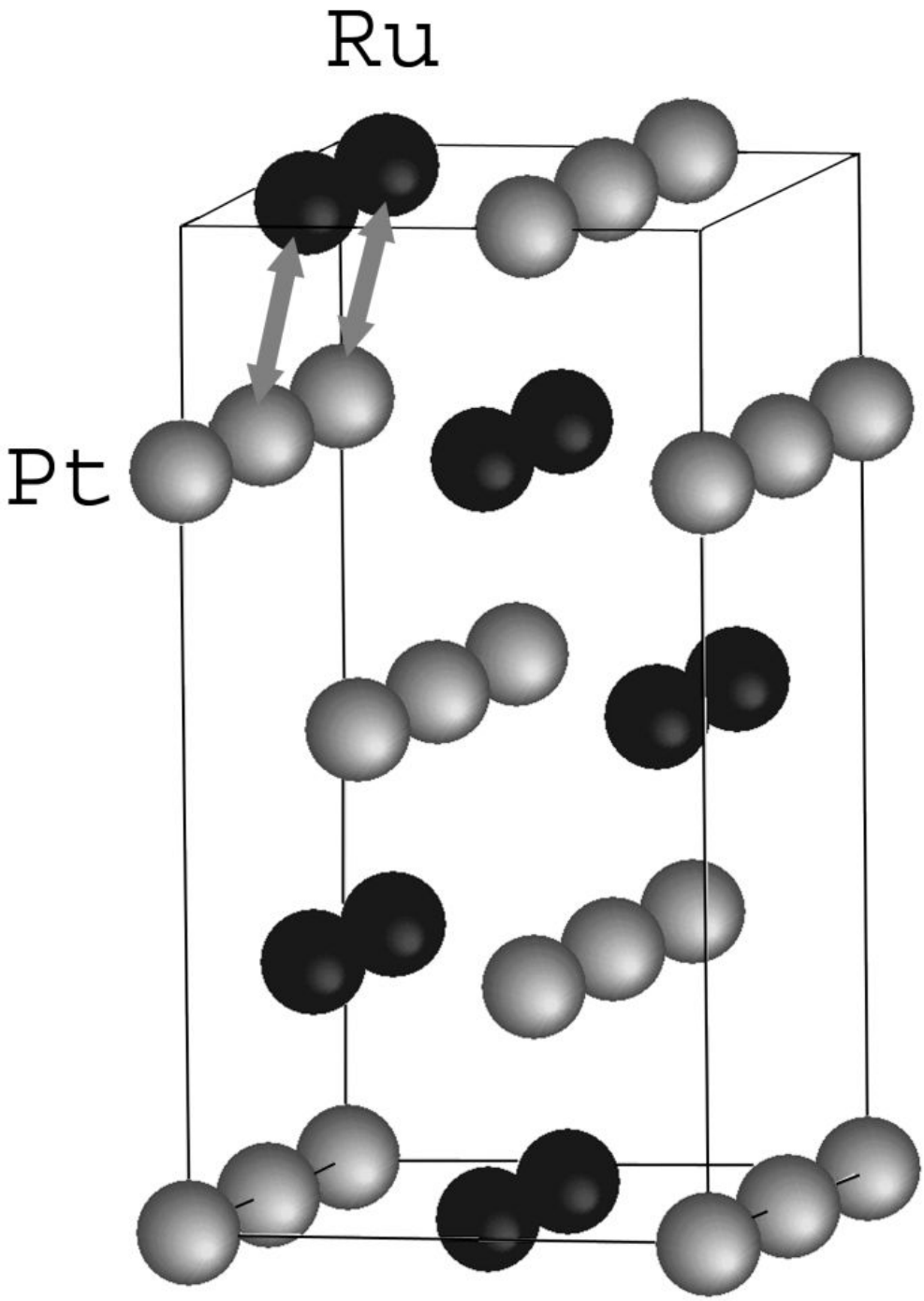

Figure 165. A unit cell of Pt-Ru (1 1 1) surface slab. The arrows denote Pt and Ru atoms exchanges modeling the surface segregation

Segregation of Pt to the surface layer can be represented by exchange of corresponding Pt and Ru atoms between those two top layers. Since, a periodic unit cell of the slab has been chosen in such a manner that each layer has two Pt and two Ru atoms, the first exchange of Pt and Ru atoms between two top layers provides 75 at.% Pt - 25 at.% Ru at the surface, while the second exchange of the atoms leads to the complete occupation of the surface layer by Pt atoms and the subsurface layer by Ru atoms.

The energy differential between an original non-segregated atomic distribution and these two partially segregated and fully segregated configurations gives segregation energy of Pt to the surface. Negative value is an indicative of the propensity to segregate, while positive value would represent either Ru segregation or no segregation.

For the calculations, the five layer slab has been separated from its image perpendicular to the surface direction by a vacuum layer equal to the thickness of this five layer slab which is about 9Å. In this study the Vienna ab-initio Simulation Package (VASP) , within the projector augmented-wave (PAW) method in the general gradient approximation (GGA) [131-133] for conducting the exchange-correlation corrections has been used for calculation of the total energies, electronic structures and optimized lattice parameters of different atomic configurations and crystallographic orientations of Pt-Ru model system. Two bottom layers have been fixed with the interlayer distance corresponding to the calculated optimized bulk lattice parameters, while the top three layers were allowed to relax with the residual force components on each atom to be lower than ~ 0.01 eV/Å/atom, thus resulting in the accurate determination of the atomic positions and hence, the total energy of the whole system.

As mentioned earlier, an experimental (1 1 1) inter-planar spacing (d_{111}) of disordered fcc-PtRu is ~ 0.223 nm. Our calculation gives the corresponding spacing of 0.2247 nm, which is

in excellent agreement with the experimental data supporting our initial assumptions. In addition to the different segregation energies, (1 1 1) and (1 0 0) surface energies for pure Pt, Ru and Pt-Ru alloy within fcc and $L1_0$ configurations were also calculated. The results are summarized in **Table 13**.

Table 13. Segregation energies of Pt and Ru to (1 1 1) surface and Pt only to (1 0 0) surface for two corresponding Pt and Ru atoms exchange steps. Surface energies for pure Pt, Ru and Pt-Ru are also presented for (1 1 1) and (1 0 0) crystallographic orientations

Surface		**(111) Pt / Ru**		**(100) Pt**	
E_{segr}		**50-75**	**75-100**	**50-75**	**75-100**
(eV/at)		-0.95 /+0.87	-0.70 / +0.55	-1.22	-0.97
E_{segr} (eV/at) average		-0.82/+0.71		-1.08	
E_{surf} (J/m^2)	Pt-Ru	1.88		2.15	
	Pt^{fcc}	1.54		1.83	
	Ru^{fcc}	1.95		2.24	

One can see, that movement of the first Pt atom from the subsurface layer to the surface gives an energy difference of - 0.95 eV, while the same action for Ru atom results in a positive change of the total energy equal to + 0.87 eV. The second exchange between the corresponding Pt and Ru atoms lead to similar results of - 0.70 eV and + 0.55 eV for Pt and Ru segregation energies, respectively. Negative values for Pt and positive values of segregation energies for Ru point out to the fact that Pt demonstrates a strong propensity for segregation to the surface which is observed experimentally. Similar results have been obtained for Pt segregation to (1 0 0) surface wherein the energies also demonstrate negative values.

An additional argument towards understanding of the Pt segregation might be obtained from the surface energy calculations for pure Pt, Ru and Pt-Ru alloy within fcc and $L1_0$ crystal structures with the cubic lattice parameter corresponding to the bulk Pt-Ru system that are collected in **Table 13**. One can observe that Pt and Ru surfaces demonstrate the lowest and the highest energy values respectively with Pt-Ru surface energy in between, which additionally justifies the Pt segregation. This trend is also observed for (100) crystallographic orientation, which is expected. Thus, our theoretical consideration of Pt segregation indeed has demonstrated the propensity of Pt to segregate to the surface.

A.3 RESULTS AND DISCUSSION

Figure 166 shows the XRD pattern of the heat treated powder obtained after thermal treatment of the gel powder. It confirms the formation of nanocrystalline Pt-Ru solid solution. The high

resolution TEM bright field image along with SAD pattern of thermally treated powder, shown in **Figure 167**, has confirmed the formation of nanocrystalline Pt(Ru) based alloy of particle size ~ 3 - 5 nm dispersed in the framework of non-conducting amorphous carbon which will be denoted as CSG-Pt(Ru)/C. The non-conducting porous amorphous carbon, formed due to decomposition of acetylacetonate complexes of Pt-Ru during pyrolysis, is expected to act as a nucleation site to nucleate nanocrystalline Pt(Ru) alloy on the surface of the carbon. The amorphous carbon also acts as a grain growth inhibitor for Pt(Ru) alloy for significant grain growth at high temperatures. Removal of the amorphous carbon is an important step to synthesize high surface area unsupported binary Pt(Ru) solid solution catalyst without significant grain growth and oxidation of the catalyst. In the present work, the thermal treatment process to remove the amorphous carbon has been optimized to synthesize phase pure high CO tolerant Pt(Ru) solid solution electro-catalysts, denoted as CSG-Pt(Ru), having very high ESCA and ultra-high catalytic activity.

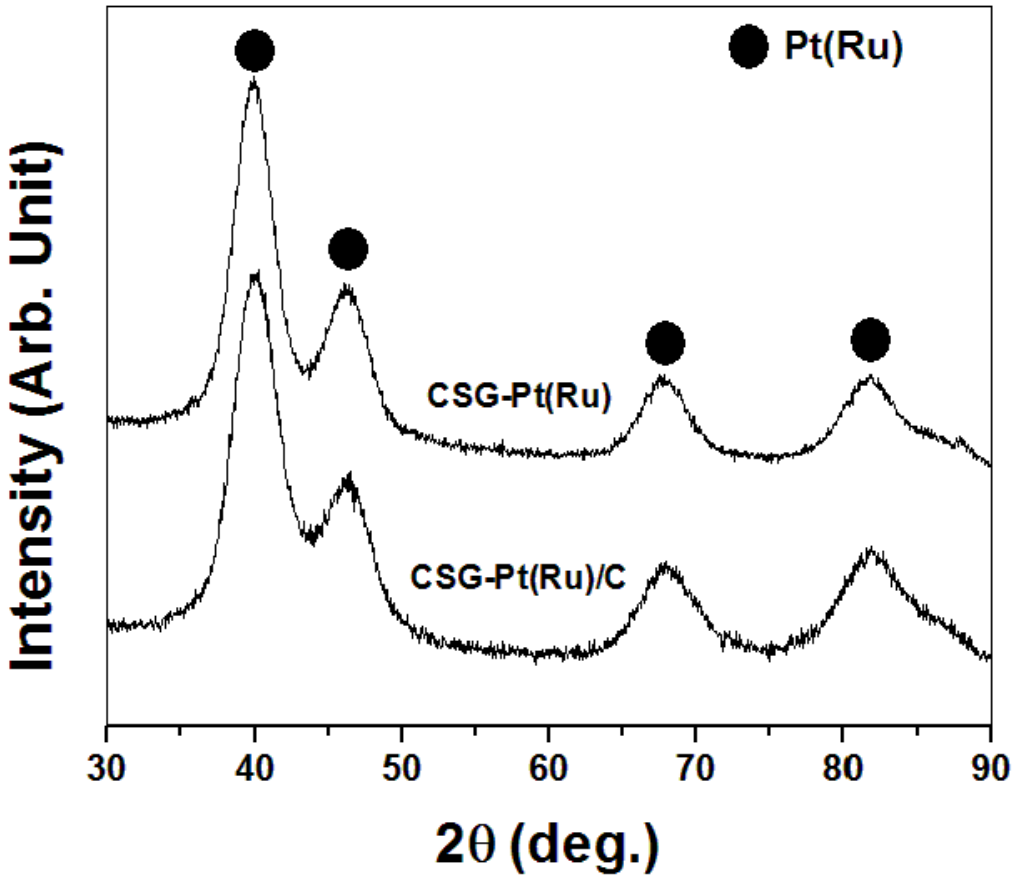

Figure 166. X-ray diffraction patterns of CSG-Pt(Ru)/C and CSG-Pt(Ru) obtained after thermal treatment in UHP Ar and UHP Ar - 1% O_2 atmosphere, respectively

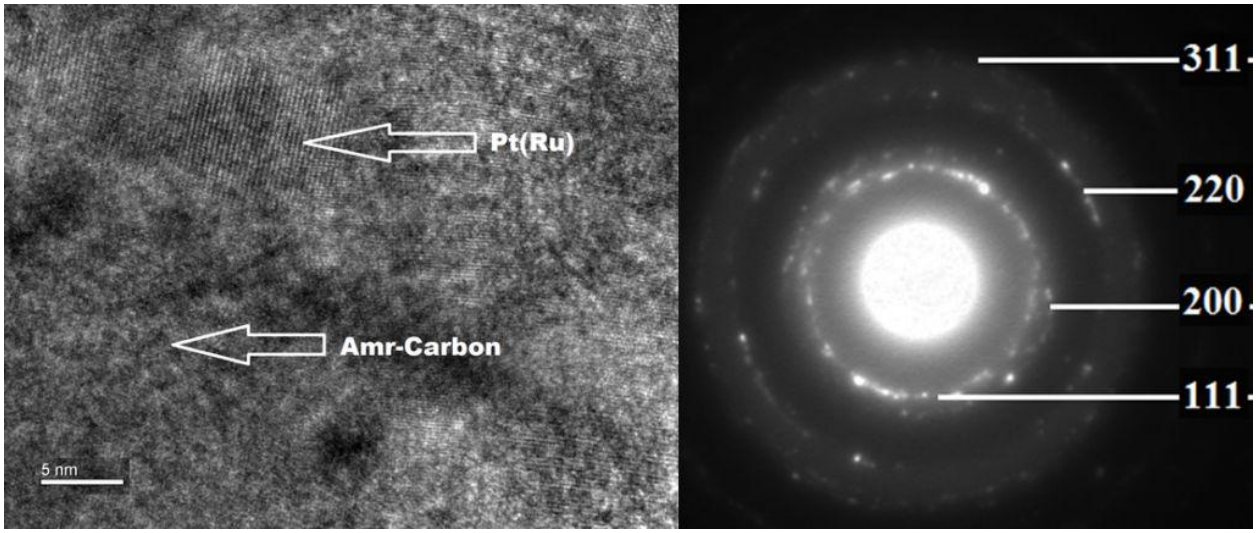

Figure 167. HRTEM images along with SAD pattern of CSG-Pt(Ru)/C showing formation of nanocrystalline Pt(Ru) dispersed in the framework of amorphous C

In order to remove the non-conducting amorphous carbon without inducing any significant grain growth of Pt(Ru) alloy, thus forming a phase pure nanocrystalline Pt(Ru) alloy, CSG-Pt(Ru)/C was subjected to multiple heat treatments in UHP Ar - 1% O_2 gas at very low optimized temperature of ~ 200°C for controlled removal of carbon to form a single phase CSG-Pt(Ru) alloy. Also, it should be noted that a lower heat treatment temperature in presence of 1% oxygen would ensure minimum or no significant oxidation of the resulting alloy.

The dried gel powder after heat treatment in UHP Ar at 500°C for 4 hours gave us nanocrystalline CSG-Pt(Ru)/C. But, a large amount of non-conducting amorphous carbon is present which was confirmed by the TGA-DTA analysis. CSG-Pt(Ru)/C has a very low specific surface area of *ca.* 10 m^2/g due to the presence of the non-conducting carbon. The TGA-DTA trace as shown in **Figure 168** shows an enormous weight loss from ~ 225°C - 300°C. This can be attributed to the oxidation and elimination of the carbon from CSG-Pt(Ru)/C. The low

temperature oxidation of carbon might be due to some catalytic activity of noble metals Pt and Ru in the powder. In order to remove this non-conducting carbon and form phase pure nanocrystalline Pt-Ru solid solution, multiple heat treatments in UHP Ar - 1% O_2 gas at ~ 200°C were done. The 1% O_2 present in the gas helped in controlled removal of carbon finally yielding a single phase nanocrystalline Pt(Ru) alloy. A lower temperature of ~ 200°C was selected because the TGA-DTA trace showed elimination of carbon started at ~ 225°C. Since the TGA-DTA is a dynamic process, we surmise that carbon removal starts at a lower temperature. Also, a lower heat treatment temperature in presence of 1% O_2 would ensure minimum or no significant oxidation of the resulting alloy. After the final heat treatment, we observe that there is little weight loss in the TGA-DTA which may be attributed to minimal carbon and/or moisture in the sample. The DTA trace also does not show any significant exothermic reaction confirming the removal of carbon. These results clearly show that there is no significant weight loss or significant exothermic reaction in the TGA/DTA.

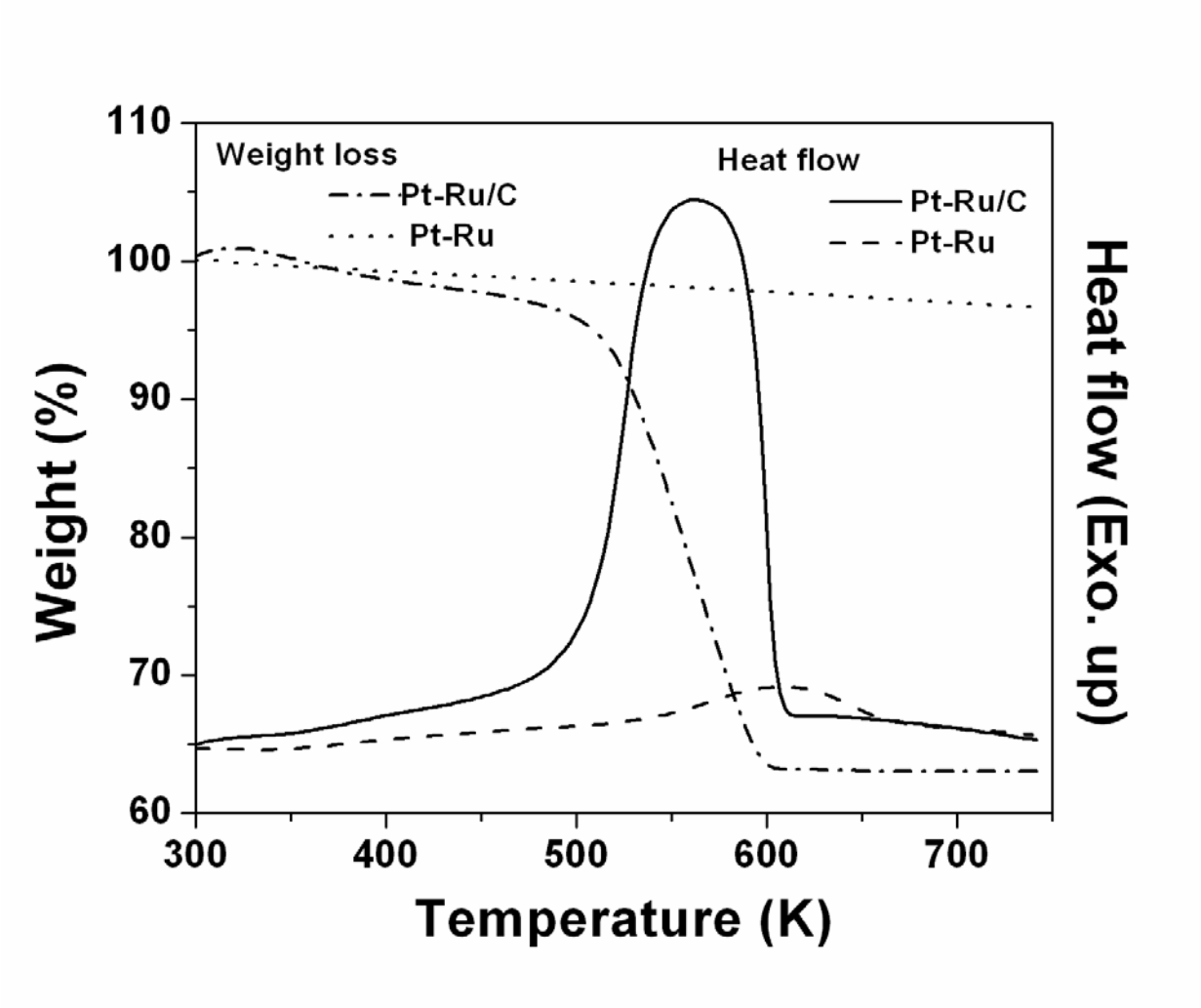

Figure 168. TGA-DTA traces in air of CSG-Pt(Ru)/C and CSG-Pt(Ru) after final heat treatment in UHP Ar - 1% O_2

The XRD patterns of the CSG-Pt(Ru) catalyst, (**Figure 166**) shows the presence of only fcc-Pt(Ru) peaks without any detectable hcp-Ru or RuO_2 peaks, and the calculated (111) interplaner spacing (d_{111}) of fcc-Pt(Ru) is ~ 0.223 nm which suggests the formation of solid solution of Ru in Pt [165, 166]. Heat treatment of CSG-Pt(Ru) electro-catalyst was further done in UHP - Ar atmosphere to 600°C to check if any amorphous RuO_2 is present in the CSG-Pt(Ru) catalyst. Its XRD pattern as seen in **Figure 169** shows only crystalline fcc Pt(Ru) peaks with no

additional peak of hcp-Ru or RuO_2, confirming single phase solid solution formation in the CSG-Pt(Ru) catalyst. The narrow crystalline peaks observed are due to heat treatment of the fully synthesized electro-catalyst [CSG-Pt(Ru)] in UHP-Ar at higher temperatures of ~ 600°C.

The TEM bright field image and high resolution transmission electron microscopy (HRTEM) image along with selected area diffraction (SAD) pattern of CSG-Pt(Ru) is shown in **Figure 170**. It confirms the formation of nanosized Pt(Ru) particles with a particle size of ~ 3 - 5 nm which is similar to CSG-Pt(Ru)/C suggesting no significant grain growth of Pt(Ru) during carbon removal processes. The HRTEM image of CSG-Pt(Ru) shows lattice fringes with a spacing of ~ 0.225 ± 0 004 nm which corresponds to the (111) interplaner spacing of face centered cubic Pt(Ru) [165, 166]. The spacing observed between the lattice fringes of (111) plane of Pt(Ru) in the HRTEM image is in good agreement with the calculated d_{111} value (~ 0.223 nm) from XRD patterns.

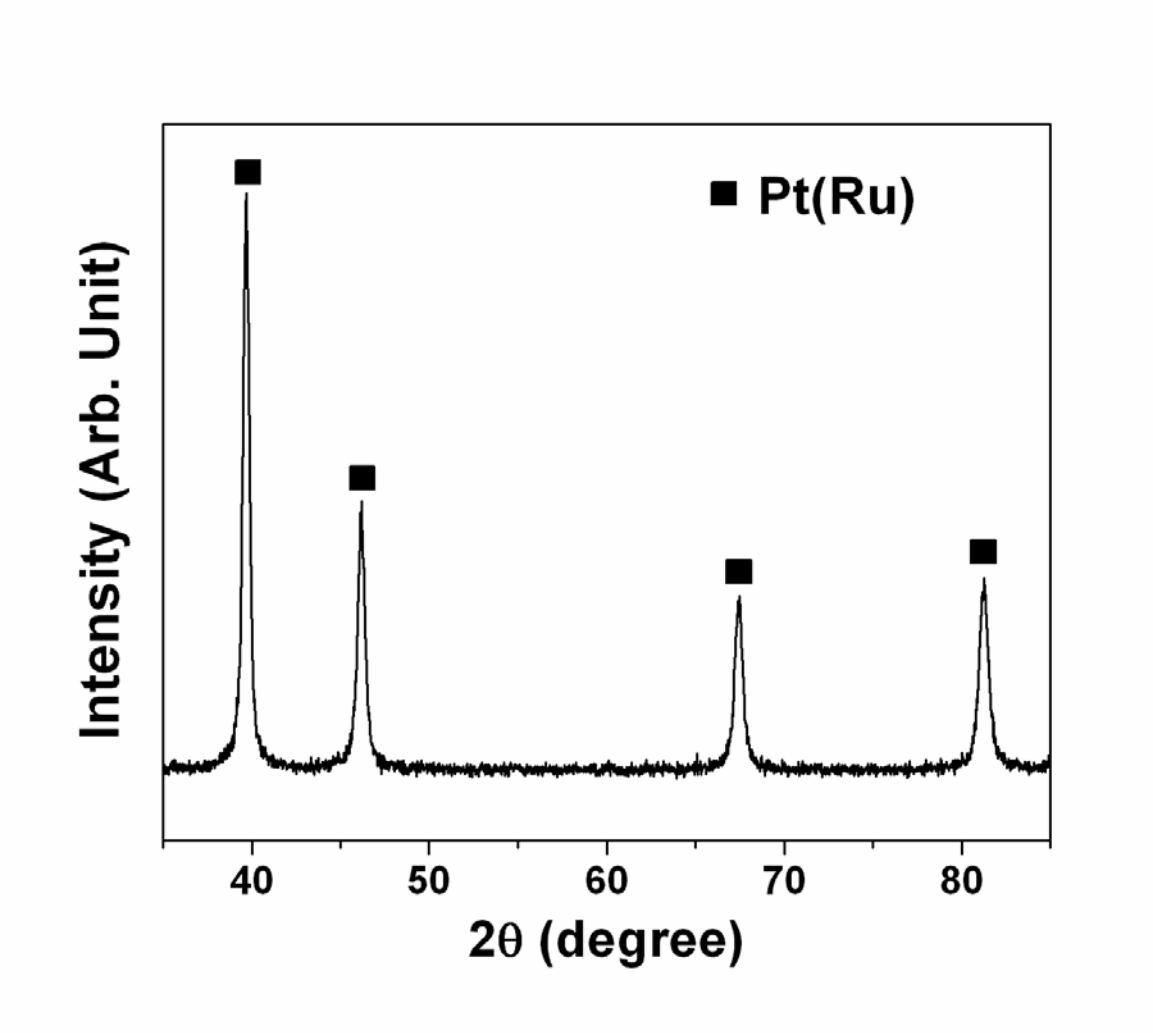

Figure 169. XRD pattern of CSG-Pt(Ru) obtained after heat treatment in UHP-Ar at 600°C

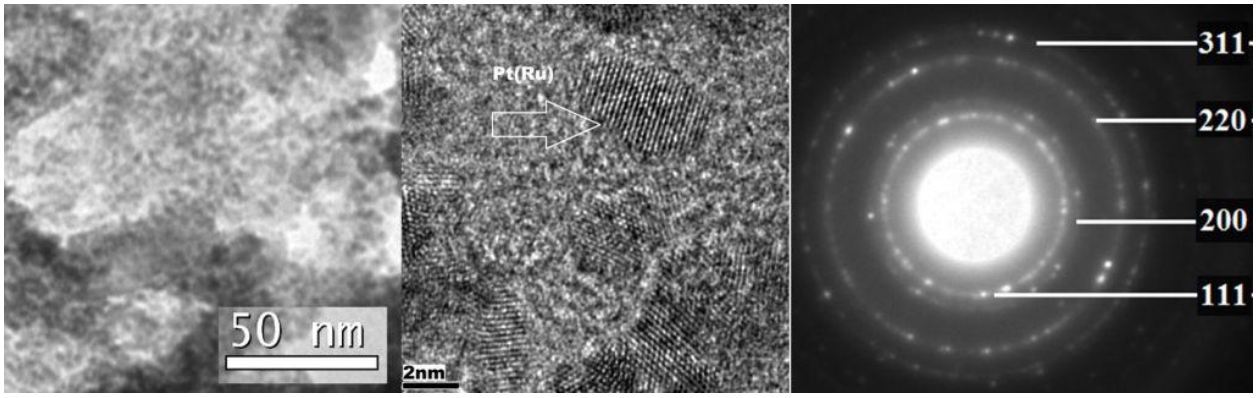

Figure 170. TEM and HRTEM images, along with SAD pattern of CSG-Pt(Ru) showing nanocrystalline Pt(Ru) alloy and lattice fringes of (111) plane of Pt(Ru)

In order to determine the surface composition and chemical oxidation states of platinum and ruthenium, x-ray photoelectron spectroscopy (XPS) techniques has been carried out for both CSG-Pt(Ru) and JM-Pt(Ru). The Pt 4f doublet peaks for the CSG-Pt(Ru), is observed at ~ 71.8 eV and ~ 75.1 eV, corresponding to Pt $4f_{7/2}$ and Pt $4f_{5/2}$ binding energy, respectively, in oxidation state of zero as shown in **Figure 171**. The shift of Pt $4f_{7/2}$ and Pt $4f_{5/2}$ of CSG-Pt(Ru) catalyst to slightly higher binding energy in comparison to JM-Pt(Ru) catalyst might be due to better alloying effect of Ru with Pt, which is expected to help in making the CO adsorption weaker [167, 168], and as a result a better electrochemical active catalyst. A shift in the binding energy might also be because of the final state relaxation due to the nanoparticulate size effect and Pt-Ru interaction as reported in other publications [169, 170]. In case of ruthenium, the Ru $3d_{3/2}$ spectrum overlaps the C 1s spectrum which prevents the accurate determination of the oxidation states of ruthenium. However, the Ru $3p_{3/2}$ spectrum, shown in **Figure 172**, is observed at ~ 462.5 eV and ~ 462 eV for CSG-Pt(Ru) and the JM-Pt(Ru) catalyst, respectively. The surface ratio of Pt/Ru, determined by the XPS, is 1.57 for the CSG-Pt(Ru) corresponding to the

composition of Pt - 39at.% Ru and 1.44 for the JM-Pt(Ru) corresponding to the composition of Pt - 41at.% Ru. This indicates that the surface composition of CSG prepared Pt(Ru) is quite similar in comparison to JM-Pt(Ru) catalyst. The electrochemically active Pt enrichment at the surface of nanocrystalline Pt(Ru) catalyst is expected due to lower cohesive energy of Pt (5.84 eV/atom) than Ru (6.74 eV/atom).

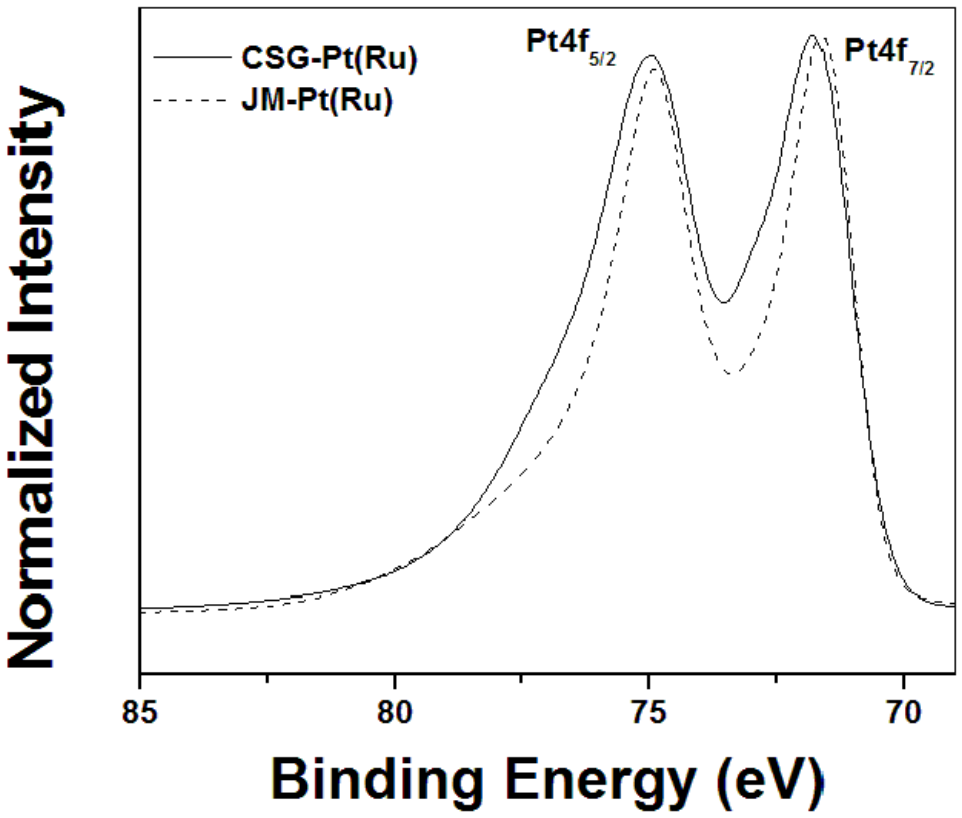

Figure 171. The XPS spectra of Pt $4f_{7/2}$ and Pt $4f_{5/2}$ doublet for CSG-Pt(Ru) and JM-Pt(Ru)

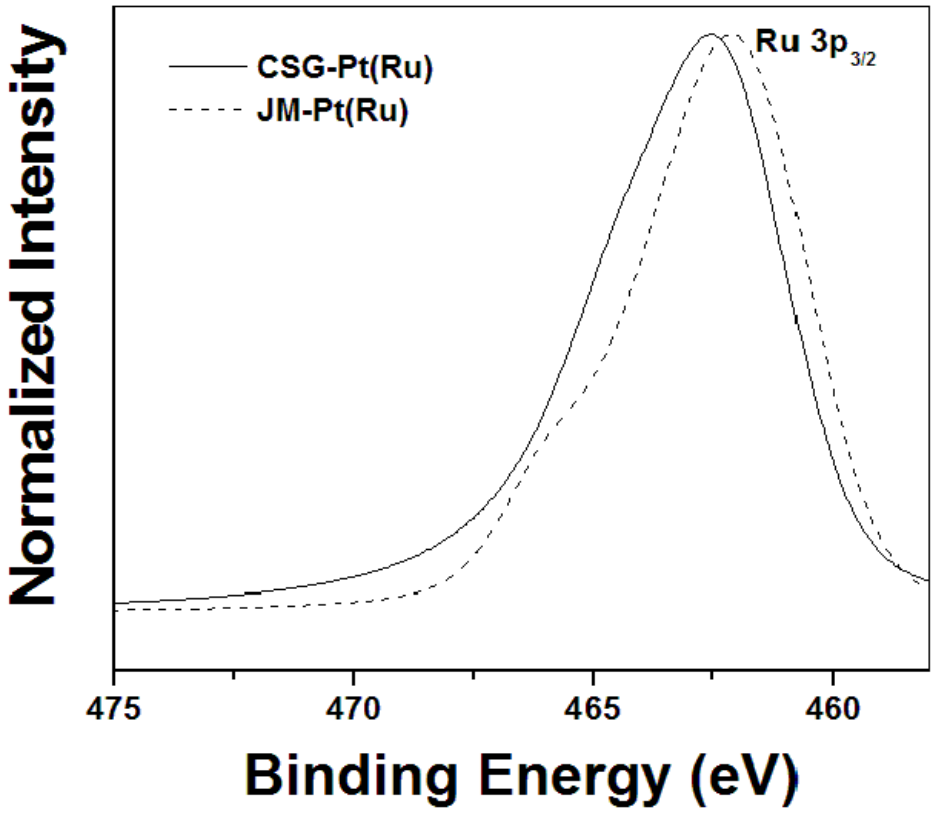

Figure 172. The XPS spectra of Ru 3p3/2 for CSG-Pt(Ru) and JM-Pt(Ru)

The theoretical study based on Density Functional Theory (DFT), described in the methods section, also indicates the propensity of Pt for segregation to the surface of Pt-Ru alloy. The energy difference between an original non-segregated atomic distribution and segregated configurations gives negative segregation energy for Pt and positive values of segregation energies for Ru collected in **Table 13**. The negative values for Pt segregation energy point out at the fact that Pt demonstrates a propensity for segregation to the surface which is observed experimentally and correlates well with other previously reported theoretical studies [63, 166, 168]. Similar results have been obtained for Pt segregation to both (1 1 1) and (1 0 0) surfaces

although to different extents. An additional argument towards understanding of the Pt segregation might be obtained from the surface energy calculations for pure Pt, Ru and Pt-Ru alloy within fcc and $L1_0$ crystal structures with the cubic lattice parameter corresponding to the bulk Pt-Ru system and also collected in **Table 13**. One can observe that Pt and Ru surfaces demonstrate the lowest and the highest energy values respectively with Pt-Ru surface energy in between, which additionally justifies the Pt segregation. This trend is also observed for (100) crystallographic orientation, which is expected. Thus, our theoretical study of segregation demonstrates the propensity of Pt to segregate to the surface in agreement with experiments.

The specific surface area, measured by BET techniques, of the CSG-Pt(Ru) catalyst is ~ 217 m^2/g which is ~ 3 times higher than the commercially available JM-Pt(Ru) catalyst (specific surface area ~75 m^2/g). In order to determine the electrochemically active surface area (ECSA), which has great influence on the electrochemical activity of the Pt(Ru) electro-catalyst, CO stripping voltammetry has been performed on both the CSG-Pt(Ru) and JM-Pt(Ru) catalyst. The CO stripping voltammetry curves of the CSG-Pt(Ru) catalyst and the JM-Pt(Ru) catalyst, shown in **Figure 173** and **Figure 174**, respectively, shows the anodic peak potential for the CO oxidation to CO_2 at ~ 0.47 V. A subsequent cyclic voltammogram, performed immediately after CO stripping confirms the complete CO removal and the recovery of the activity of the catalyst. The difference in the areas of voltammogram between the two subsequent sweeps was used to determine the CO stripping charge. The charge obtained, taking into account the scan rate of 10 mV/sec, from the difference in areas between the curves for CSG-Pt(Ru) and JM-Pt(Ru) is ~ 0.0235 C and ~ 0.0753 C, respectively. The ECSA of the CSG-Pt(Ru) and JM-Pt(Ru) has been calculated assuming a monolayer of adsorbed CO is present on the catalyst surface with a charge density of 0.42 mC/cm^2 and normalized with respect to the Pt loading. It was found that the JM-

Pt(Ru) catalyst exhibits a ECSA of ~ 28 m^2/g whereas the CSG -Pt(Ru) catalyst exhibits ECSA of ~ 90 m^2/g which is three times higher than JM-Pt(Ru) catalyst. This clearly indicates that the Pt(Ru) electro-catalyst prepared by the novel CSG method has more active catalytic sites available for selective electrochemical reaction than the commercial JM-Pt(Ru) catalyst though both exhibits similar surface and bulk composition.

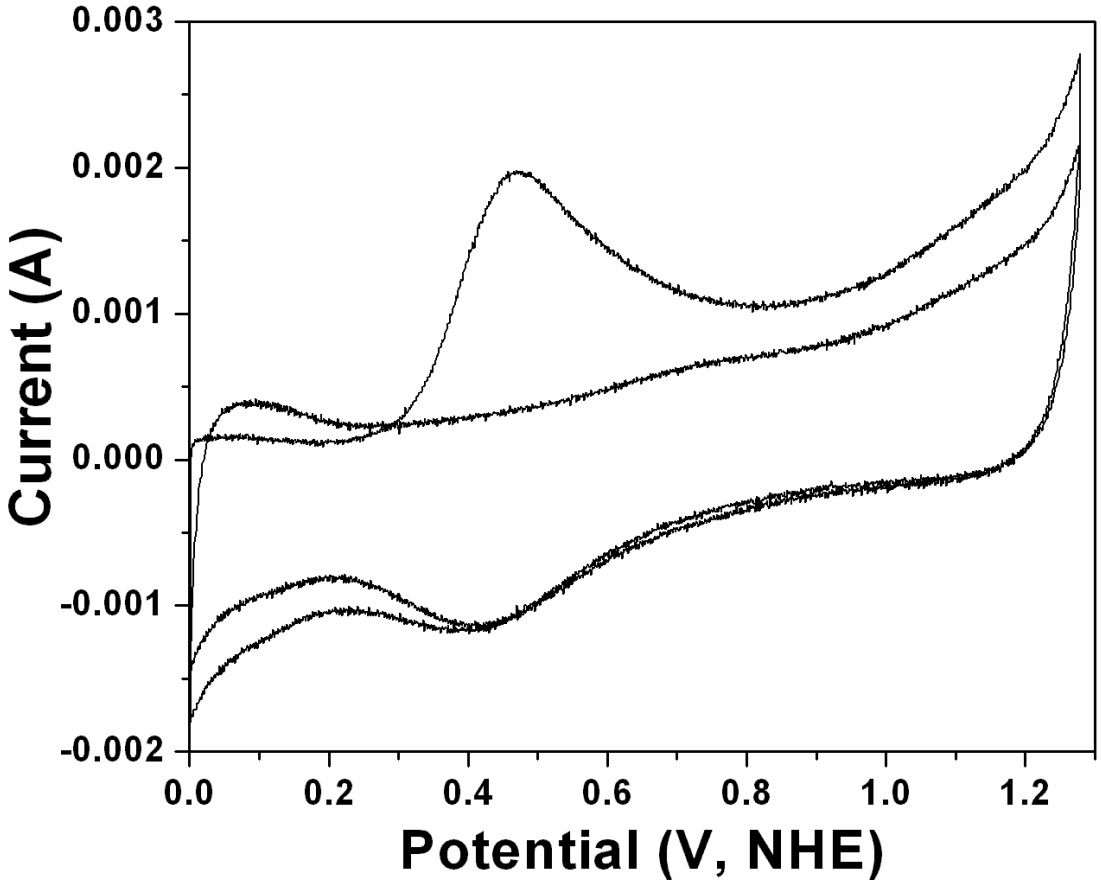

Figure 173. The CO stripping voltammetry curve for CSG-Pt(Ru) in 0.5M H_2SO_4

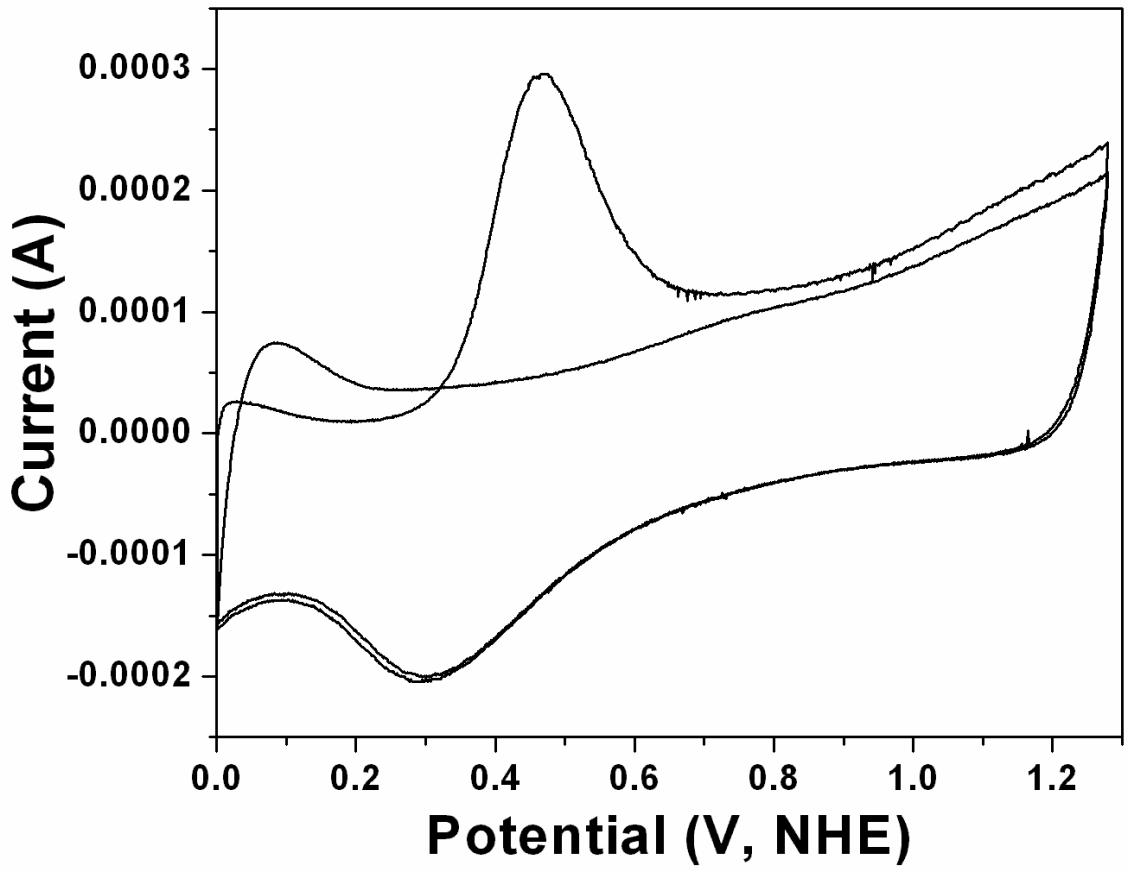

Figure 174. The CO stripping voltammetry curve for JM-Pt(Ru) in 0.5M H_2SO_4

Synthesis of nanocrystalline Pt(Ru) alloy by CSG process, exhibits high BET and ECSA surface area, leads to larger number of Pt active sites available at the surface of the alloy, and as a result excellent electrochemical activity is expected to be achieved. The electrochemical performance such as activity and durability of CSG-Pt(Ru) electro-catalyst has been studied for the methanol oxidation reaction (MOR). In order to measure the electrochemical activity of the CSG-Pt(Ru) and JM-Pt(Ru) catalyst for MOR, the polarization has been performed in the presence of 1 M methanol and 0.5 M sulfuric acid solution as a fuel after pre-conditioning the

catalyst with a catalyst loading ~ 0.2 mg Pt / cm^2. The polarization curve obtained at a scan rate of 10 mV/sec at 40°C is plotted in **Figure 175**. It shows that the CSG-Pt(Ru) catalyst exhibits a current density of ~ 40 mA/cm^2 at ~ 0.65 V *vs.* NHE, whereas the JM-Pt(Ru) catalyst shows a current density of about ~ 27 mA/cm^2 at the same voltage. This indicates that the CSG-Pt(Ru) electro-catalyst which has same bulk and surface composition as commercially available JM-Pt(Ru) shows an increase of ~ 45 % in the catalytic performance. The improved catalytic performance of CSG-Pt(Ru) is expected to arise due to higher BET and ECSA surface area, generated by novel CSG process, in comparison to JM-Pt(Ru) catalyst.

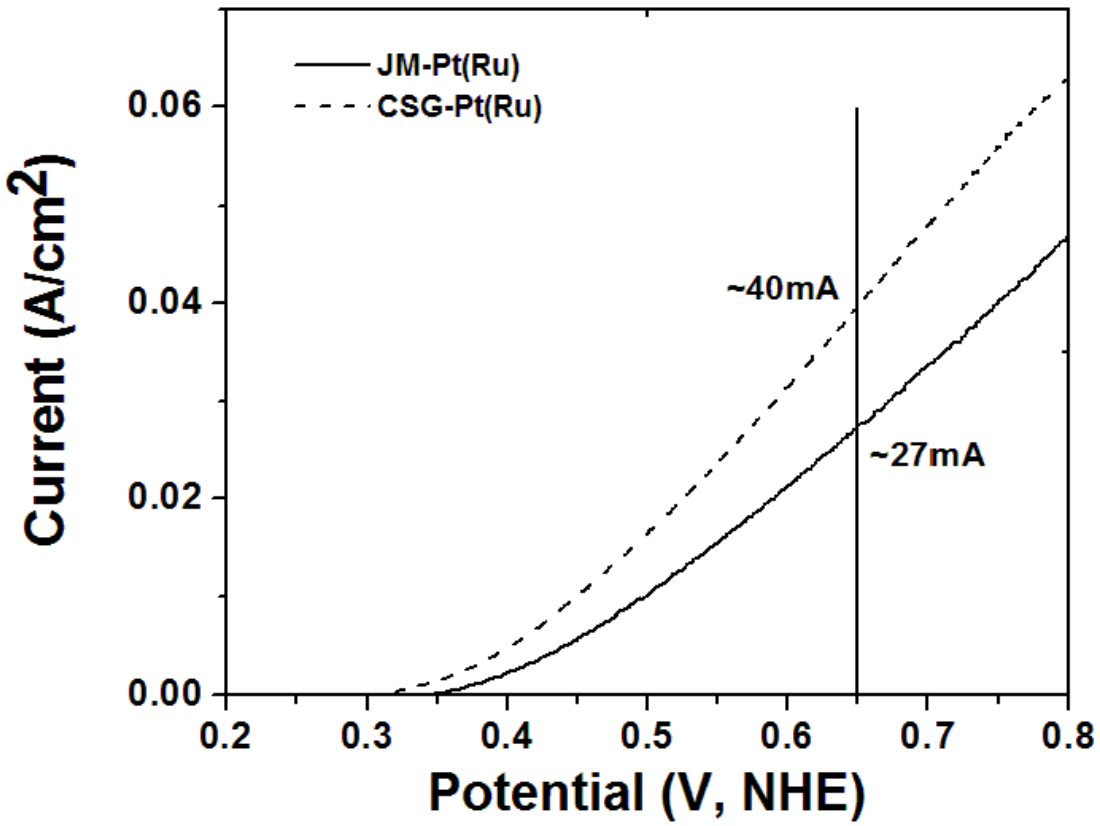

Figure 175. The polarization curve of CSG-Pt(Ru) and JM Pt(Ru) conducted at 40°C with a scan rate of 10 mV/sec

Figure 176 compares the DMFC single cell test performance curves for the CSG-Pt(Ru) catalyst and the JM-Pt(Ru) catalyst with a catalytic loading normalized to ~ 1 mg/cm^2 of Pt on the anode side and ~ 2 mg/cm^2 of Pt black (Alfa Aesar) loading on the cathode side. The DMFC single cell performance, shows the CSG-Pt(Ru) has better catalytic performance than the JM-Pt(Ru) catalyst at temperatures of 40°C, 60°C and 80°C. At a voltage of ~ 0.2 V, the CSG-Pt(Ru) catalyst shows a current density of ~ 140 mA/cm^2 at an operating temperature 80^{o}C which is ~ 40% higher than the JM-Pt(Ru) showing a current density of ~ 100mA/cm^2. At the

corresponding current densities, the CSG-Pt(Ru) catalyst exhibits ~ 40 % higher power density (~ 28 mW/cm^2) than JM-Pt(Ru) catalyst (~ 20 mW/cm^2) at operating temperature 80^oC. The current density is plotted along with the power density in **Figure 177**. **Table 14** shows the current density and power density at 0.2 V (*vs.* NHE) for the CSG-Pt(Ru) and JM-Pt(Ru) catalyst at 40°C, 60°C and 80°C. It is seen that the current density and the power density are increasing gradually with increase in temperature. The maximum power density obtained by CSG-Pt(Ru) and JM-Pt(Ru) at each temperature is tabulated in **Table 15** along with the corresponding voltage and current densities.

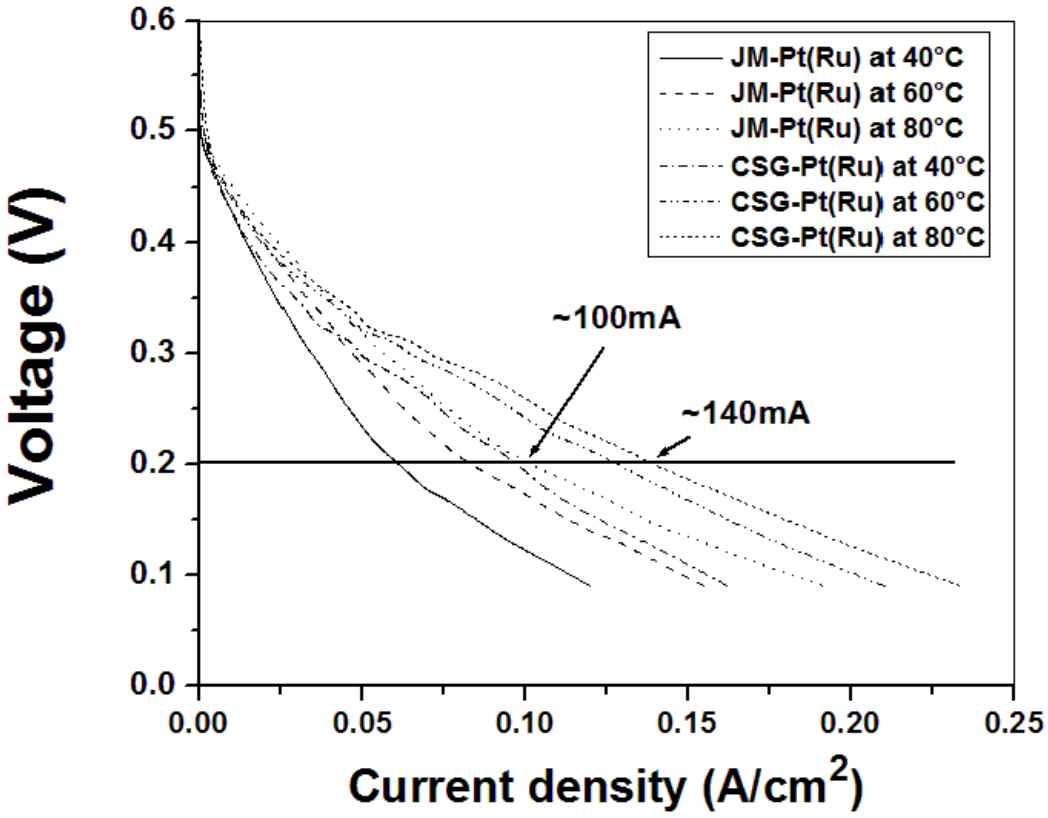

Figure 176. Polarization curve of DMFC single cell at various temperatures for the CSG-Pt(Ru) and JM-Pt(Ru) anode

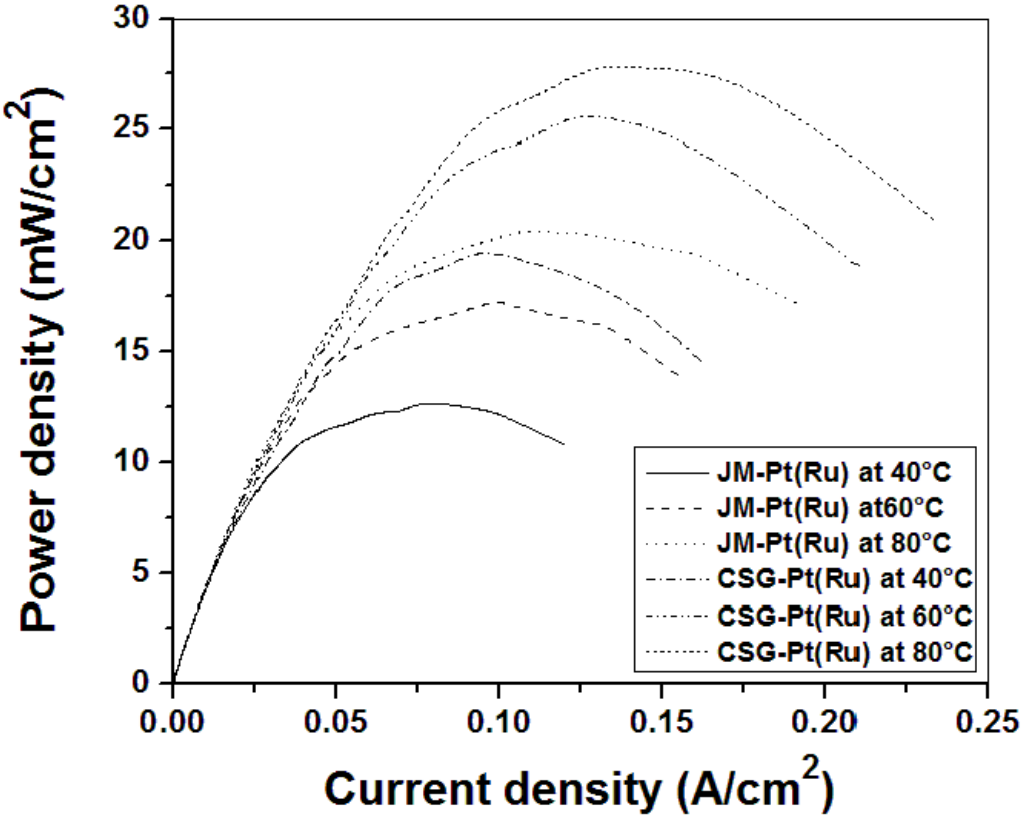

Figure 177. Power density performance of DMFC single cell at various temperatures for the CSG-Pt(Ru) and JM-Pt(Ru) anode

Table 14. The current and power density obtained at 0.2 V for CSG-Pt(Ru) and JM-Pt(Ru)

Temperature ↓	Current density (mA/cm^2)		Power density (mW/cm^2)	
	JM-Pt(Ru)	CSG-Pt(Ru)	JM-Pt(Ru)	CSG-Pt(Ru)
40°C	64	100	12.5	19
60°C	84	132	17	26
80°C	108	140	20	28

Table 15. The maximum power density obtained at various temperatures for CSG-Pt(Ru) and JM-Pt(Ru) along with the corresponding voltage and current densities

Temperature →		40°C	60°C	80°C
Maximum power density (mW/cm^2)	JM-Pt(Ru)	13	17.5	20
	CSG-Pt(Ru)	19	26	28
Current density (mA/cm^2)	JM-Pt(Ru)	78	95	108
	CSG-Pt(Ru)	100	132	140
Corresponding voltage (V)	JM-Pt(Ru)	0.15	0.18	0.2
	CSG-Pt(Ru)	0.2	0.2	0.2

In order to study the durability/stability of the CSG-Pt(Ru) and JM-Pt(Ru) catalyst during MOR reaction, chronoamperometry (current *vs*. time) at a constant voltage of ~ 0.65 V *vs.* NHE at 40^{o}C in 0.5 M H_2SO_4 and 1 M CH_3OH solution has been performed to measure the degradation or loss of activity of the catalyst as a function of time. The chronoamperometry response shown in **Figure 178**, over a period of 2 hours shows that CSG-Pt(Ru) retains ~ 87 % of its initial current density (~ 40 mA/cm^2 to ~ 35 mA/cm^2) whereas JM-Pt(Ru) retains only ~ 66 % of its initial current density (~ 27 mA/cm^2 to ~ 18 mA/cm^2).

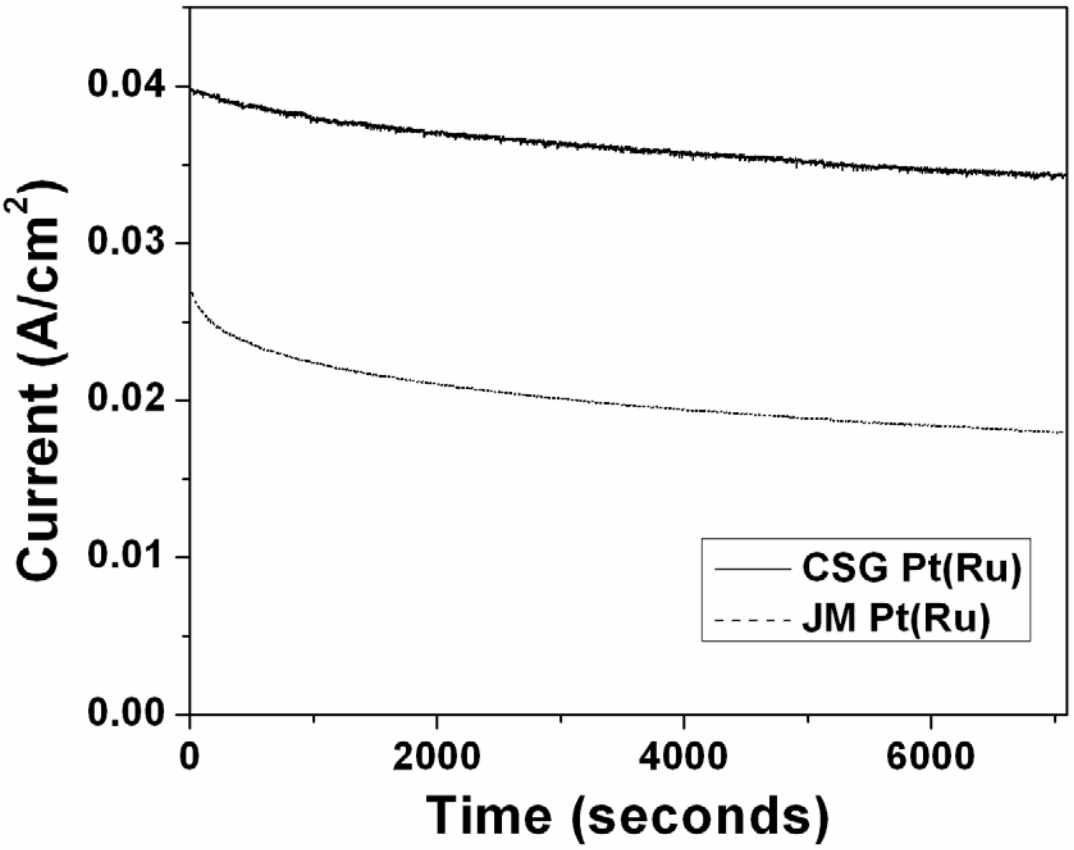

Figure 178. Chronoamperometry plot of CSG-Pt(Ru) and JM-Pt(Ru) measured at 0.65 V *vs.* NHE

In order to quantify the amount of platinum and ruthenium leached in the electrochemical solution, the electrochemical solution after the testing time of 2 hours was collected and run through the inductively coupled plasma optical emission spectroscopy (ICP-OES). It was found that no active Pt leached into the solution for both the catalysts. However, Ru found in the solution for the CSG-Pt(Ru) and JM-Pt(Ru), was ~ 0.064 ppm and ~ 0.084 ppm, respectively. The present study therefore successfully synthesized high ESCA Pt(Ru) based electro-catalyst with the ability to reduce the noble metal oxide loading in the ultra low level with improved electro-catalytic performance and electrochemical stability.

A.4 CONCLUSION

A complexed sol-gel (CSG) approach was used and the catalyst development parameters were optimized in order to develop ultra active highly durable Pt(Ru) alloy catalysts for DMFC anode. The synthesized electro-catalysts by the CSG process had extremely high specific surface area and ECSA, which was ~ 3 times greater than the commercial JM-Pt(Ru) catalyst. This was possible due to controlled removal of the non-conducting carbon in a controlled oxidative environment at ~ 200°C. This ensured that there was no grain growth, and nanocrystalline Pt(Ru) alloy of ~ 3 - 5 nm was formed. The electrochemical properties of CSG-Pt(Ru) were far superior to the JM-Pt(Ru) in terms of current density, power and chemical stability (robustness). To complement the results, the catalysts were tested in a single full cell DMFC configuration for the

methanol oxidation, and current and power densities ~ 40 % higher than that displayed by Johnson Matthey catalyst have been achieved. This novel CSG approach is thus a promising and a viable method to synthesize nanocrystalline high specific surface area unsupported Pt(Ru) based electro-catalyst exhibiting excellent electro-catalytic performance.

APPENDIX B

QUATERNARY ANODE CATALYSTS FOR DMFC

Direct Methanol Fuel Cell (DMFC) is a promising power source for continuous generation of energy without evolution of any toxic by-products and greenhouse gases. Pt-Ru has been the accepted gold standard anode electro-catalyst for DMFC, but significant advances are required to enhance its performance and stability, along with reducing the expensive noble metals. A complexed sol-gel (CSG) approach has been used to develop nanostructured quaternary powder materials. The synthesis method has been optimized to develop reduced noble metal anode catalysts comprising a solid solution alloy of Pt-Ru-Ni-Ti and Pt-Ru-Os-Ir of different compositions. The electro-catalysts are nano-crystalline in nature having high specific surface area, resulting in much more active Pt sites for the methanol oxidation reaction. A reduction in up to ~ 40 at.% of noble metals yields much better electro-catalytic activity and enhanced stability as compared to the commercially used Johnson Matthey $Pt_{50}Ru_{50}$ catalyst. The quaternary electro-catalysts demonstrate immense potential of the CSG approach to synthesize high performance materials for the DMFC anode.

B.1 PLATINUM - RUTHENIUM - NICKEL - TITANIUM

B.1.1 Introduction

Fuel cells have high efficiency, low environmental impact, are inexpensive, and help in distributed power generation. With an ever increasing energy demand and limited fossil fuel resources, efficient energy generation and use become urgent issues. Fuel cells thus play an important role in the future as power sources in the transportation sector, for portable electronics and stationery power generation devices. Cost and durability present two of the most significant challenges affecting the widespread commercialization of fuel cells for diverse applications encompassing stationary power, transportation power, portable power, auxiliary power units, and material handling equipment [141-144]. The use of ion-exchange membrane based fuel cell technology in battery-replacement type applications, such as cell phones, laptops and hand held devices is a market ripe for products that can free users from the aggravation of repetitive recharging and limited usage cycles. A modified Proton exchange membrane fuel cell (PEMFC) in which the direct oxidation of a liquid fuel, methanol, eliminates the near-term availability of hydrogen. The direct methanol fuel cell (DMFC) offers a simple system design and operation since no humidification or reforming of methanol to hydrogen is required [141-144, 171, 172].

To meet the performance and efficiency, durability and cost requirements for fuel cells, significant research has been conducted over the years focusing largely on identifying new materials, and developing novel design and fabrication methods for catalysts and supports. At present, all low temperature DMFCs use supported platinum and platinum alloys as the electro-catalysts [144, 146, 147, 149]. Platinum has the highest catalytic activity for methanol oxidation

at low temperatures and methanol is rapidly oxidized to carbon dioxide on a platinum surface [145-148, 150]. However, carbon monoxide is generated as a by-produce due to which the catalyst surface is poisoned. This reduces the catalytic activity of platinum drastically causing it to become inactive by itself. Therefore, various platinum based binary catalysts incorporating a second metal have been investigated to minimize carbon monoxide poisoning [148-150, 152, 173]. It is known that the 50 - 50 atomic % platinum-ruthenium bimetallic alloys have the most activity for methanol oxidation. This is because according to bifunctional mechanism, oxophilic ruthenium sites covered by various ruthenium oxides constitute the source of oxygen for removal of the adsorbed carbon monoxide on the surface [151, 152, 154, 156-158, 160, 174]. It has also been reported that the electro-catalytic activity of a Pt-Ru catalyst with a Ru-decorated Pt surface in methanol oxidation is twice higher for optimized Ru coverage as compared to Johnson Matthey Pt-Ru black alloy catalysts [145, 150, 157]. Contrary to the Ru-decorated Pt, the structure of Pt-decorated Ru is more attractive for improving mass activity due to the low Pt content in the catalysts [145, 158, 159].

Many bimetallic, trimetallic and quaternary systems investigated used a wide variety of alloying elements with platinum *viz.* ruthenium, tin, cobalt, nickel, osmium, palladium, chromium, titanium and molybdenum [151, 152, 154, 156-160, 173-180]. However, it has been reported that some ternary and quaternary alloy catalyst based on the platinum-ruthenium system have a higher catalytic activity [173, 175-177, 179, 180]. The previous studies therefore clearly demonstrate that design and synthesis of robust electro-catalysts exhibiting high surface area may represent a suitable microstructure that can be expected to improve the catalytic activity, and reduce the loading of the expensive noble metals used as catalysts. Improved anode catalysts should have high surface area with proper alloy design by doping or alloying elements in the

catalyst structure in order to improve the sluggish kinetics of the methanol oxidation reaction [180-182].

In this context, a complex sol-gel process (CSG) has been developed to synthesize unsupported nanocrystalline Pt-Ru-Ni-Ti based quaternary solid solution with reduced noble metal content having high specific surface area (SSA) with excellent electrochemical activity and durable microstructure for the methanol oxidation reaction. In this complex sol-gel process, a homogeneous amorphous gel has been prepared by the complexation reaction between the acetylacetonate complexes of the respective noble metals using tetramethyl ammonium hydroxide (TMAH) as the complexing agent [162-164]. Systematic studies have been done to try and reduce the noble metal content as far as possible without compromising the activity and durability of the catalyst.

B.1.2 Experimental Details

Phase pure and high surface area Pt-Ru-Ni-Ti based catalysts were synthesized using the complexed sol-gel synthesis method. Platinum(II) acetylacetonate [Pt-acac, $Pt(C_5H_7O_2)_2$, Alfa Aesar], ruthenium(III) acetylacetonate [Ru-acac, $Ru(C_5H_7O_2)_3$, Alfa Aesar], nickel(II) acetylacetonate [Ni-acac: $Ni(C_5H_7O_2)_2$, Alfa Aesar] and titanium (IV) isopropoxide [Ti-IPA: $Ti(OCH(CH_3)_2)_4$, Sigma-Aldrich] were used as the sources for Pt, Ru, Ni and Ti, respectively. Pt-acac, Ru-acac, Ni-acac and Ti-IPA of the desired composition (*E.g.* Pt-40 at.%Ru-10 at.%Ni-10 at.%Ti) were dissolved at 50°C in100 ml of acetone. Tetramethylammonium hydroxide [TMAH, $(CH_3)_4NOH$, 25% in methanol, Alfa Aesar], set at TMAH:(Pt + Ru + Ni + Ti) = 1.75:1,

was then added to the solution to serve both as a high molecular weight organic complexing as well as a hydrolyzing agent. Pt-acac, Ru-acac, Ni-acac and Ti-IPA tend to phase separate during drying and evaporation of the solvent. Thus, the addition of the high molecular weight organic reagent (TMAH), and its intended dual role to complex and induce hydrolysis of the starting noble metal precursors was found to be beneficial in yielding homogeneous amorphous gels containing Pt, Ru, Ni and Ti. After stirring for some time, the solvent was evaporated until the solution became viscous, transforming into a thixotropic gel. The viscous gel was dried in air at 120°C for 12 hours.

The dried gels were then transformed to a mortar and pestle and grounded finely to yield the as-prepared powders. This powder was then heat treated in ultra-high purity (UHP) argon at 500°C in order to decompose the amorphous gel structure. The powders were then heat treated multiple times in UHP Ar-1% O_2 gas at a lower temperature of 200°C than that reported earlier [162-164] based on the results of the thermo-gravimetric and differential thermal analysis (TGA-DTA). The powder was grounded finely after every heat treatment in a mortar and pestle. The heat treatments in UHP Ar-1% O_2 helped in removing the carbon in a controlled manner making sure that there is no oxidation of the resultant alloy. Electro-catalysts of compositions $Pt_{40}Ru_{40}Ni_{10}Ti_{10}$, $Pt_{33}Ru_{33}Ni_{21}Ti_{13}$ and $Pt_{30}Ru_{30}Ni_{20}Ti_{20}$ have been reported. The electrochemical performance of the Pt-Ru-Ni-Ti catalyst by this complexed sol-gel (CSG) process has been compared with the Johnson Matthey (JM) bimetallic Pt-Ru commercial catalyst, the gold standard anode catalyst for DMFC.

All the electro-catalyst powders synthesized were analyzed by X-ray diffraction incorporating a state-of-the-art detector (XRD, Philips XPERT PRO system with CuK_α radiation). Typical scans were recorded in the 2θ range of 30° - 90°. The operating voltage and

current were kept constant at 45 kV and 40 mA respectively. The effective particle size was calculated by the Scherrer formula using the X'Pert High Score Plus software.

In order to understand the phase formation and decomposition temperature, thermogravimetric and differential thermal analysis (TGA-DTA) has been conducted on the as-prepared precursors as well as thermally treated powders using a TGA-DTA machine (Netzsch STA 409PC/4/H/Luxx TG-DTA). The TGA-DTA analysis has been carried out employing a heating rate of 10°C/min from room temperature up to 500°C in air.

Specific surface area of the catalyst was measured using the Brunauer-Emmett-Teller (BET) technique. Each sample was first vacuum degassed and then tested using a Micromeritics ASAP 2020. Multipoint BET surface areas are reported for each sample tested. High resolution transmission electron microscopy (HR-TEM) analysis was conducted on the samples using JEOL JEM-2100F to investigate the particle size and morphology.

X-ray photoelectron spectroscopy (XPS) was done on all the samples in order to determine the electronic states of the elements that exist in the alloy. The catalysts analyzed by XPS used a Physical Electronics (PHI) model 32-096 X-ray source control and a 22-040 power supply interfaced to a model 04-548 X-ray source with an Omni Focus III spherical capacitance analyzer (SCA). The system is routinely operated within the pressure range of 10^{-8} to 10^{-9} Torr (1.3×10^{-6} to 1.3×10^{-7} Pa). The system was calibrated in accordance with the manufacturer's procedures utilizing the photoemission lines E_b of Cu $2p_{3/2}$ (932.7 eV), E_b of Au $4f_{7/2}$ (84 eV) and E_b of Ag $3d_{5/2}$ (368.3eV) for a magnesium anode. All reported intensities are experimentally determined peak areas divided by the instrumental sensitivity factors. Charge correction was obtained by referencing the adventitious C 1s peak to 284.8 eV.

Electrochemical characterization was conducted on all the samples using a five port jacketed reaction cell (Ace Glass Inc.) in which was assembled a 3-electrode test system. The testing was done using a VersaSTAT 3 (Princeton Applied Research). A solution of 1 M methanol and 0.5 M sulfuric acid was used as the electrolyte which also served as the fuel. The solution is kept at a constant temperature of 40°C using a Fisher Scientific 3006S Isotemp Refrigerator Circulator. The catalyst ink was prepared for use in polarization and chronoamperometry. The catalyst ink consisted of 85 wt.% catalyst and 15 wt.% Nafion 117 solution [5 wt.% solution in lower aliphatic alcohols, Sigma-Aldrich].The working electrodes were prepared by uniformly spreading the catalyst ink on teflonized carbon papers in an area of 1 cm^2. The platinum loading on the electrodes was ~ 0.2 mg/cm^2. The reference electrode was a XR 200 mercury/mercurous sulfate electrode [Hg/Hg_2SO_4, Radiometer Analytical] that has a potential of ~ + 0.654 V *vs.* NHE. Platinum foil (Alfa Aesar, 0.25 mm thick, 99.95%) was used as the counter electrode.

AFCBP1 Bipotentiostat from Pine Instrument Company was used for getting the stability of the catalyst over time. Chronoamperometry (current signal *vs.* time) was performed in a 3-electrode test system at a constant voltage of ~ 0.65 V *vs.* NHE. The same 3-electrode test system assembly as described above was used with the same electrodes and conditions except for the fact that platinum loading was increased to ~ 0.5 mg/cm^2.

Elemental analysis of the media collected after the stability testing was performed by inductively coupled plasma optical emission spectroscopy (ICP-OES, iCAP 6500 duo Thermo Fisher) in order to determine the amount of ruthenium, nickel and titanium leached in the solution. Standards for getting the calibration lines were procured from Sigma Aldrich (platinum standard for ICP, ruthenium ICP/DCP standard solution, nickel standard for ICP and titanium

standard for ICP). They were then diluted with the stock solution used for electrochemical testing (*i.e.* 1M methanol and 0.5M sulfuric acid).

B.1.3 Results and Discussion

The solid solution alloy systems that were chosen were based upon previous work on binary and ternary alloys of Pt-Ni, Pt-Ru-Ni, Pt-Co, Pt-Ru-Os, Pt-Sn, Pt-Ru-Sn and Pt-Ru-Ti [174, 180, 183-186]. These works show that Ru, Ni, Ti, Os, Sn and Co play a role either in bi-functional mechanism or the ligand effect that helps Pt oxidize methanol while reducing the effects of CO poisoning. The alloy system chosen was similar to the material showing the best quaternary performance by Whitacre *et al.* [180] of Pt-23at.%Ru-31at.%Ni-13at.%Zr ($Pt_{33}Ru_{23}Ni_{31}Zr_{13}$). Since Zirconium (Zr) is well known to be a difficult oxide to reduce the metal, Ti was substituted in its place. The composition was taken such that the atomic % of Pt and Ru were kept same for our quaternary catalyst. The compositions of the quaternary solid solution catalysts synthesized were $Pt_{40}Ru_{40}Ni_{10}Ti_{10}$, $Pt_{33}Ru_{33}Ni_{21}Ti_{13}$ and $Pt_{30}Ru_{30}Ni_{20}Ti_{20}$.

Figure 179 shows the XRD patterns after every stage in the synthesis method. The XRD patterns of the as-prepared gel precursor show an amorphous structure without peaks of any of the starting precursors of Pt, Ru, Ni and Ti. This indicates good chemical homogeneity of the gel powders. It might be due to a possible complexation and hydrolysis of Pt-acac, Ru-acac, Ni-acac and Ti-IPA with TMAH. It also shows the formation of possible aliphatic hydrocarbon or hydrocarbon derivatives due to the complexation and hydrolysis of Pt-acac, Ru-acac, Ni-acac and Ti-IPA with TMAH dissolved in alcohol. The XRD pattern of the dried gel precursor obtained after drying the as-prepared gel in air at 120°C for 12 hours shows that the hydrocarbon

and its derivatives peaks are absent. This is due to the exothermic evaporation, pyrolysis or sublimation of the hydrocarbons and its derivatives in air to form carbon dioxide and water. It does not alter the amorphous nature of our gel. The TGA-DTA analysis of the dried powder performed in UHP-Ar shows that the decomposition is complete at about 500°C as shown in a previous study [164]. The dried gel powder of Pt-Ru-Ni-Ti of different elemental compositions was thus heat treated in UHP-Ar at 500°C for 4 hours in order to decompose the amorphous gel structure. This gives a nano-crystalline Pt-Ru-Ni-Ti based alloy containing a large amount of non-conducting carbon in the alloy. This was confirmed by the TGA-DTA analysis conducted on the powders after heat treatment at 500°C in UHP-Ar. The powder thus obtained after heat treatment in UHP-Ar, will be denoted hereafter as Pt-Ru-Ni-Ti/C. This powder has a very low specific surface area of ($< 10\ m^2/g$) due to the presence of the non-conducting carbon.

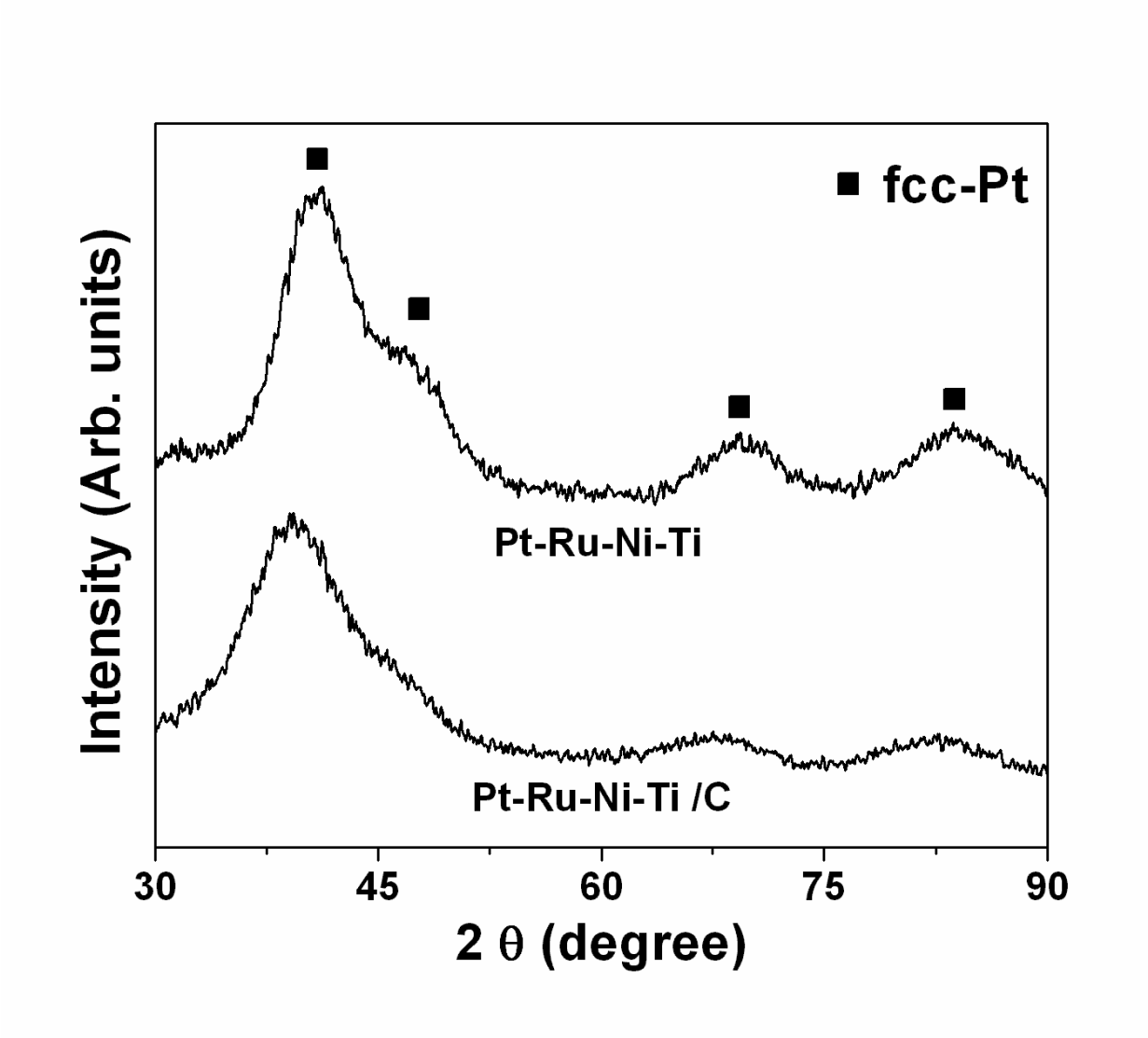

Figure 179. XRD patterns of Pt-Ru-Ni-Ti/C and Pt-Ru-Ni-Ti obtained after heat treatment in UHP-Ar at 500°C and sequential multiple treatments at 200°C in UHP-Ar-1% O_2, respectively

The TGA-DTA trace of Pt-Ru-Ni-Ti/C was done up to 500°C in air, and is shown for a representative catalyst of composition $Pt_{33}Ru_{33}Ni_{21}Ti_{13}$ in **Figure 180**. It shows an enormous weight loss of ~ 35% from ~ 225°C - 300°C. This can be attributed to the oxidation and elimination of the carbon from Pt-Ru-Ni-Ti/C [162-164]. In order to remove this non-conducting

carbon and form phase pure nano-crystalline Pt-Ru-Ni-Ti alloy with high specific surface area, Pt-Ru-Ni-Ti/C was subjected to multiple heat treatments in UHP Ar-1% O_2 gas at 200°C. The 1% oxygen present in the gas helps in controlled removal of carbon without causing any oxidation of the powder finally yielding a single phase Pt-Ru-Ni-Ti alloy. A lower temperature of 200°C was selected because the TGA-DTA trace showed that elimination of carbon at ~ 225°C. Since the TGA-DTA is a dynamic process, we surmise that carbon removal starting at ~ 200°C. Also, a lower heat treatment temperature in presence of 1% oxygen ensures no significant oxidation of the resulting alloy. The TGA-DTA was done after every subsequent heat treatment of the Pt-Ru-Ni-Ti/C in UHP Ar-1% O_2 gas mixture. After the last heat treatment, it is observed that there is almost negligible loss in the TGA-DTA (**Figure 180**) which may be attributed to minimal carbon and/or moisture present in the sample. The DTA trace also does not show any significant exothermic reaction confirming the removal of carbon. This powder is thus our prepared electro-catalyst denoted as Pt-Ru-Ni-Ti alloy. The XRD patterns of Pt-Ru-Ni-Ti show the formation of a nano-crystalline alloy (**Figure 179**). The XRD patterns did not show any additional peaks corresponding to metal oxides arising as a result of the possible oxidation of the other metals *viz.* Ru, Ni and Ti present in the alloy. Heat treatment of the alloy was done in UHP Ar at 600°C to confirm the absence of any oxide and is shown in **Figure 181**. The XRD pattern only shows face centered cubic - Platinum (fcc-Pt) crystalline peaks with no additional peak due to RuO_2, NiO and/or TiO_2, confirming single phase solid solution formation.

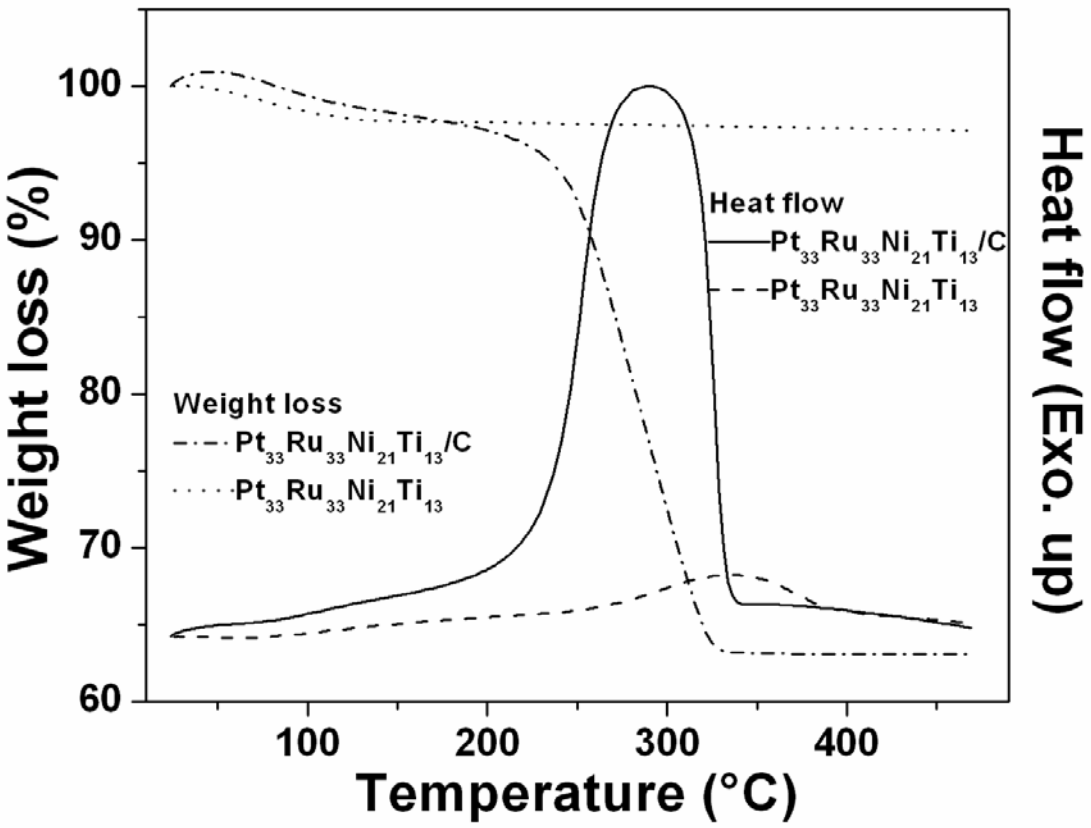

Figure 180. TGA-DTA traces in air of Pt-Ru-Ni-Ti/C and Pt-Ru-Ni-Ti after final heat treatment in UHP Ar - 1% O_2

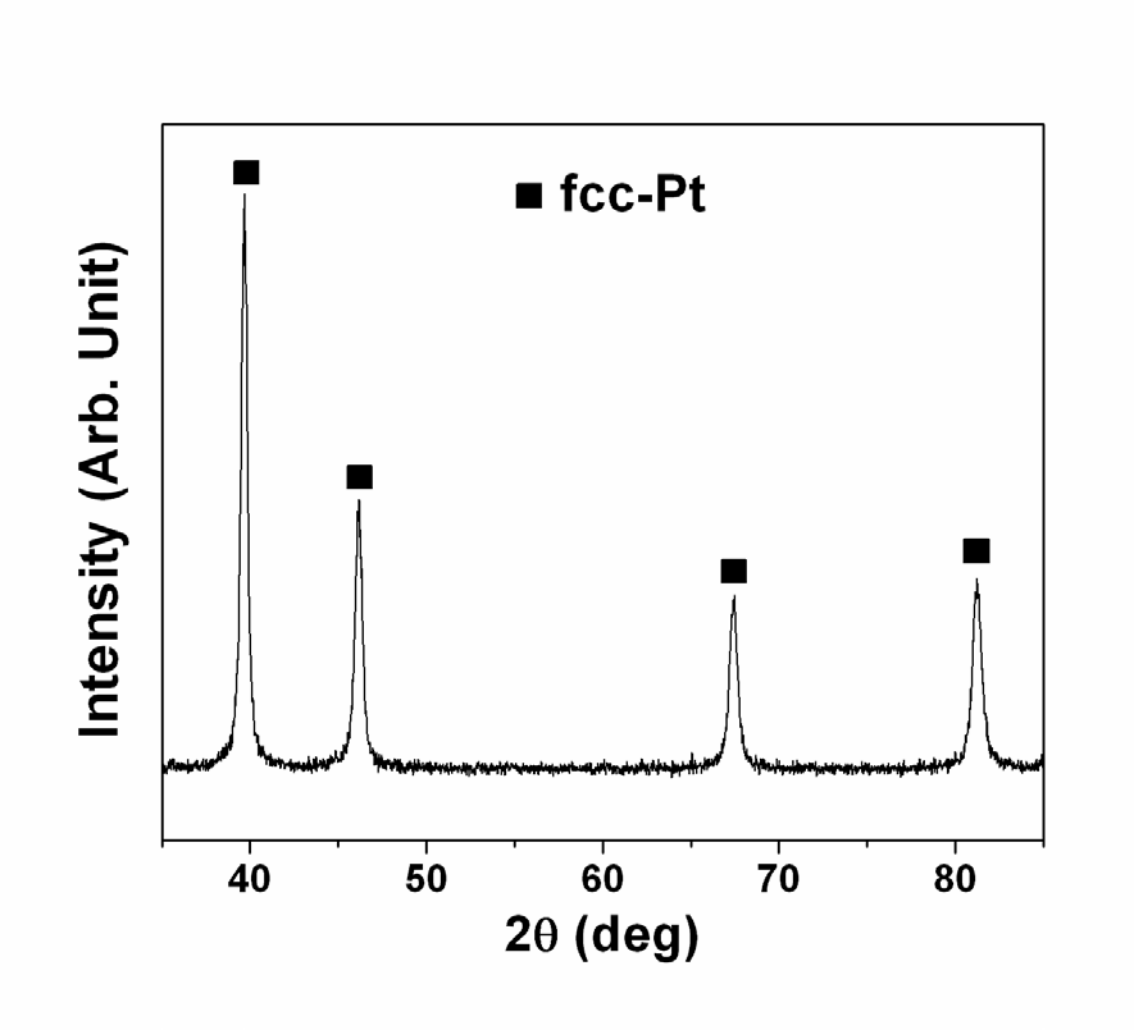

Figure 181. XRD pattern of Pt-Ru-Ni-Ti obtained after heat treatment in UHP-Ar at 600°C

The high resolution transmission electron microscopy (HRTEM) image shown in **Figure 182** confirms the formation of nano-particles of the Pt-Ru-Ni-Ti alloy with a crystallite size of ~ 2 - 4 nm. The most frequently observed lattice fringes in the high resolution image were ~ 0.225 ± 4 nm which can be very well indexed to the interplanar spacing of the (1 1 1) planes of fcc-Pt [165, 166]. The specific surface area of quaternary alloys of compositions $Pt_{40}Ru_{40}Ni_{10}Ti_{10}$, $Pt_{33}Ru_{33}Ni_{21}Ti_{13}$ and $Pt_{30}Ru_{30}Ni_{20}Ti_{20}$ are ~277 m^2/g, 305 m^2/g and 265 m^2/g, respectively. They

are *ca.* 4 times greater than the commercially available Johnson Matthey $Pt_{50}Ru_{50}$ (Alfa Aesar) which has a specific surface area of ~ 75 m^2/g. Thus, the UHP Ar-1% O_2 heat treatments not only led to elimination of the non-conducting carbon from the powder but also no significant grain growth. A higher specific surface area would lead to a larger number of Pt sites available at the surface of the material that would be available to oxidize methanol resulting in greater electrochemical activity.

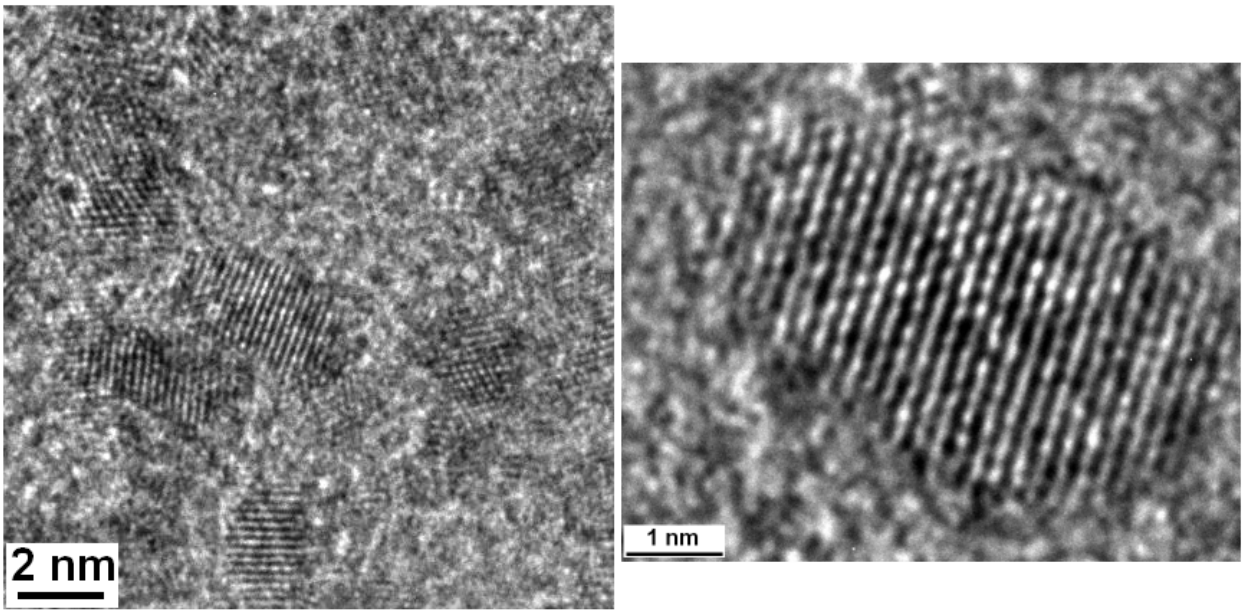

Figure 182. HRTEM images showing the nano-crystalline alloy and lattice fringes of the (111) plane of Pt-Ru-Ni-Ti

In order to determine the surface composition and chemical oxidation states of platinum and ruthenium, x-ray photoelectron spectroscopy (XPS) techniques has been carried out for both the Pt-Ru-Ni-Ti alloys. The Pt 4f doublet peaks are observed at ~ 71.5 eV and ~ 75 eV, corresponding to Pt $4f_{7/2}$ and Pt $4f_{5/2}$ binding energy, respectively, in oxidation state of zero as

shown in **Figure 183**. The shift of Pt $4f_{7/2}$ and Pt $4f_{5/2}$ to slightly higher binding energy might be due to better alloying effect of Ru, Ni and Ti with Pt, which is expected to help in making the CO adsorption weaker [167, 168], and as a result help achieve better electrochemical activity. A shift in the binding energy might also be because of the final state relaxation due to the nanoparticulate size effect as reported by other researchers [169, 170]. In case of ruthenium and titanium, the Ru 3d and Ti 2p spectrum overlaps with the C 1s and Pt 4f spectrum, respectively. This prevents the accurate determination of the oxidation states of ruthenium and titanium. However, the Ru $3p_{3/2}$ spectrum, shown in **Figure 184**, is observed at ~ 462.5 eV which corresponds to metallic Ru [187-189]. **Figure 185** shows the Ni $2p_{3/2}$ spectrum which confirms metallic Ni due to the presence of the peak at ~ 853 eV. Also, high binding energy satellite peaks are observed in the adjacent area due to multi-electron excitation [190-192].

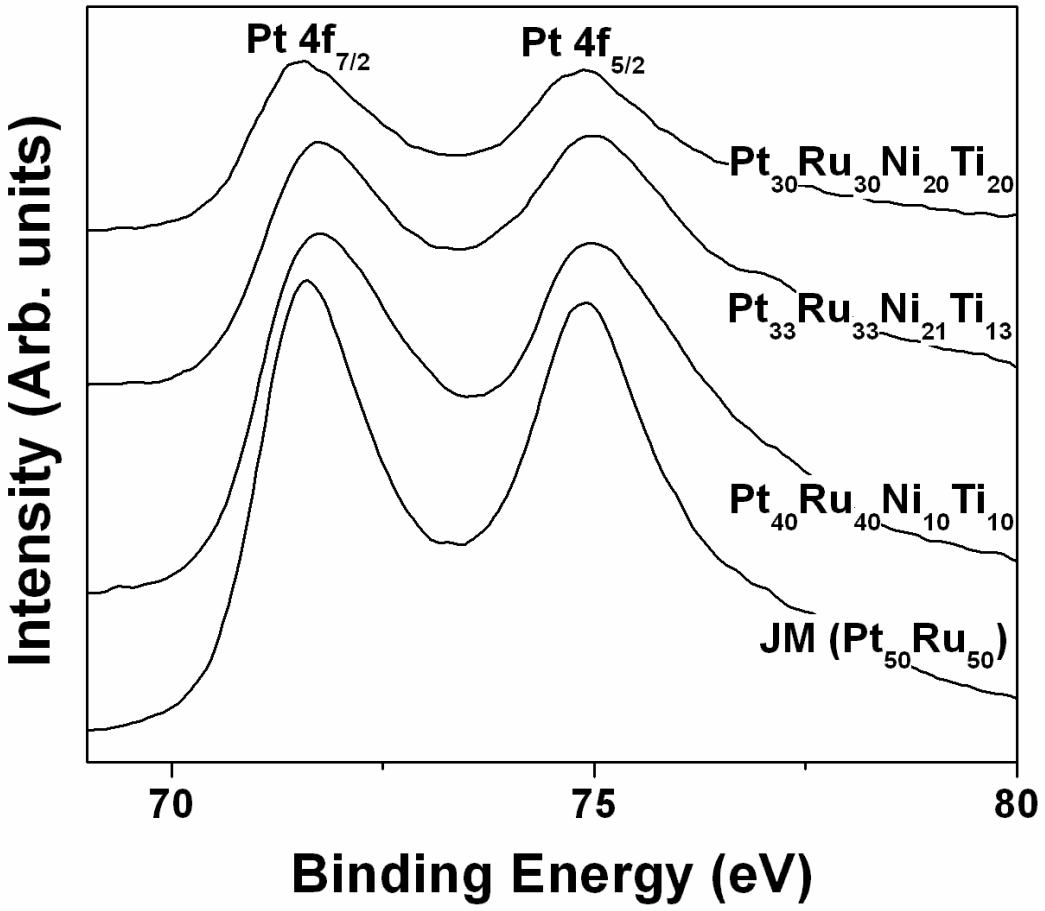

Figure 183. The XPS spectra of Pt $4f_{7/2}$ and Pt $4f_{5/2}$ doublet for Pt-Ru-Ni-Ti and JM catalyst

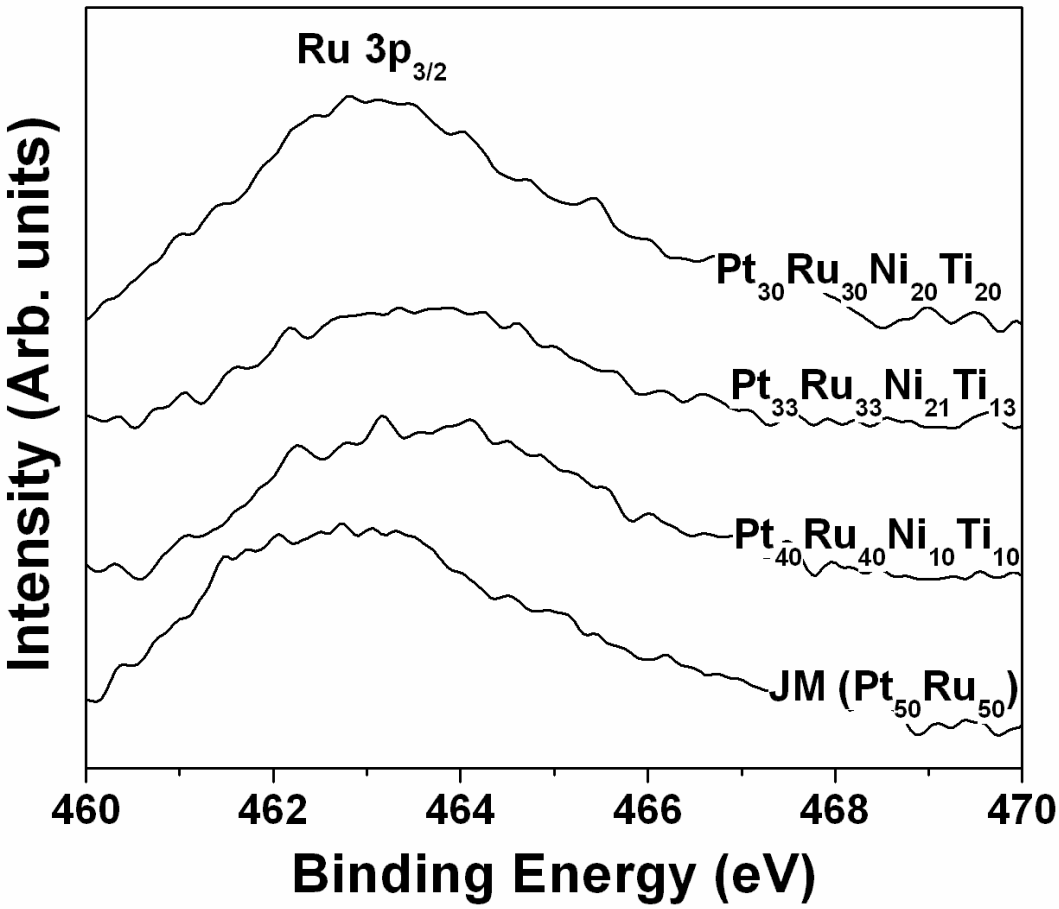

Figure 184. The XPS spectra of Ru $3p_{3/2}$ for Pt-Ru-Ni-Ti and JM catalyst

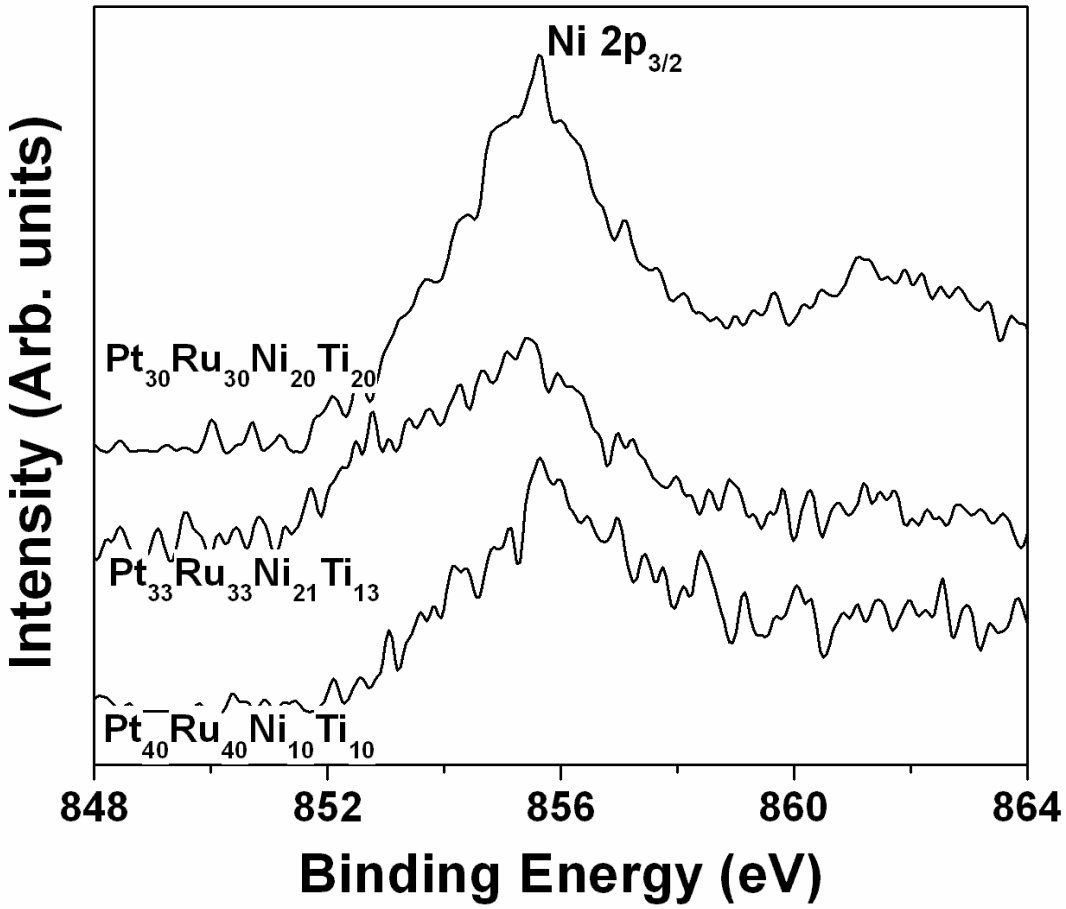

Figure 185. The XPS spectra of Ni $2p_{3/2}$ for Pt-Ru-Ni-Ti catalyst

Electrochemical testing was conducted on all Pt-Ru-Ni-Ti alloys and the JM $Pt_{50}Ru_{50}$ catalyst for comparison. Polarization was conducted in the three electrode cell consisting of 1 M CH_3OH and 0.5 M H_2SO_4 serving as the fuel / electrolyte and the cell was maintained at a temperature of 40°C. **Figure 186** shows the polarization curve for the JM catalyst, along with the CSG prepared $Pt_{40}Ru_{40}Ni_{10}Ti_{10}$, $Pt_{33}Ru_{33}Ni_{21}Ti_{13}$ and $Pt_{30}Ru_{30}Ni_{20}Ti_{20}$. It is observed that the commercial JM catalyst gives ~ 27 mA/cm^2 of current at ~ 0.65 V (*vs.* NHE). All the quaternary

CSG prepared electro-catalysts give higher current density, which is a measure of the electrochemical activity of a catalyst. The high surface area $Pt_{40}Ru_{40}Ni_{10}Ti_{10}$ gives a current of ~ 40 mA/cm^2 at 0.65 V (*vs*. NHE). This implies ~ 48 % increase in the current density even after reducing the noble metal content by 20 at.%. For the quaternary compositions of $Pt_{33}Ru_{33}Ni_{21}Ti_{13}$ and $Pt_{30}Ru_{30}Ni_{20}Ti_{20}$, a current of ~ 37 mA/cm^2 and ~ 32 mA/cm^2 is obtained at 0.65 V (*vs.* NHE), respectively. This corresponds to ~ 18 % and ~ 37 % improved electrochemical performance even after reducing the noble metal content by 34 at.% and 40 at.%, respectively. This increase in electro-catalytic activity can be attributed to the high surface area nano-crystalline electro-catalysts synthesized by the CSG process. This can be attributed to the fact that there will much more catalytically active Pt sites on the surface aiding the methanol oxidation reaction for the CSG prepared powders than the JM catalyst.

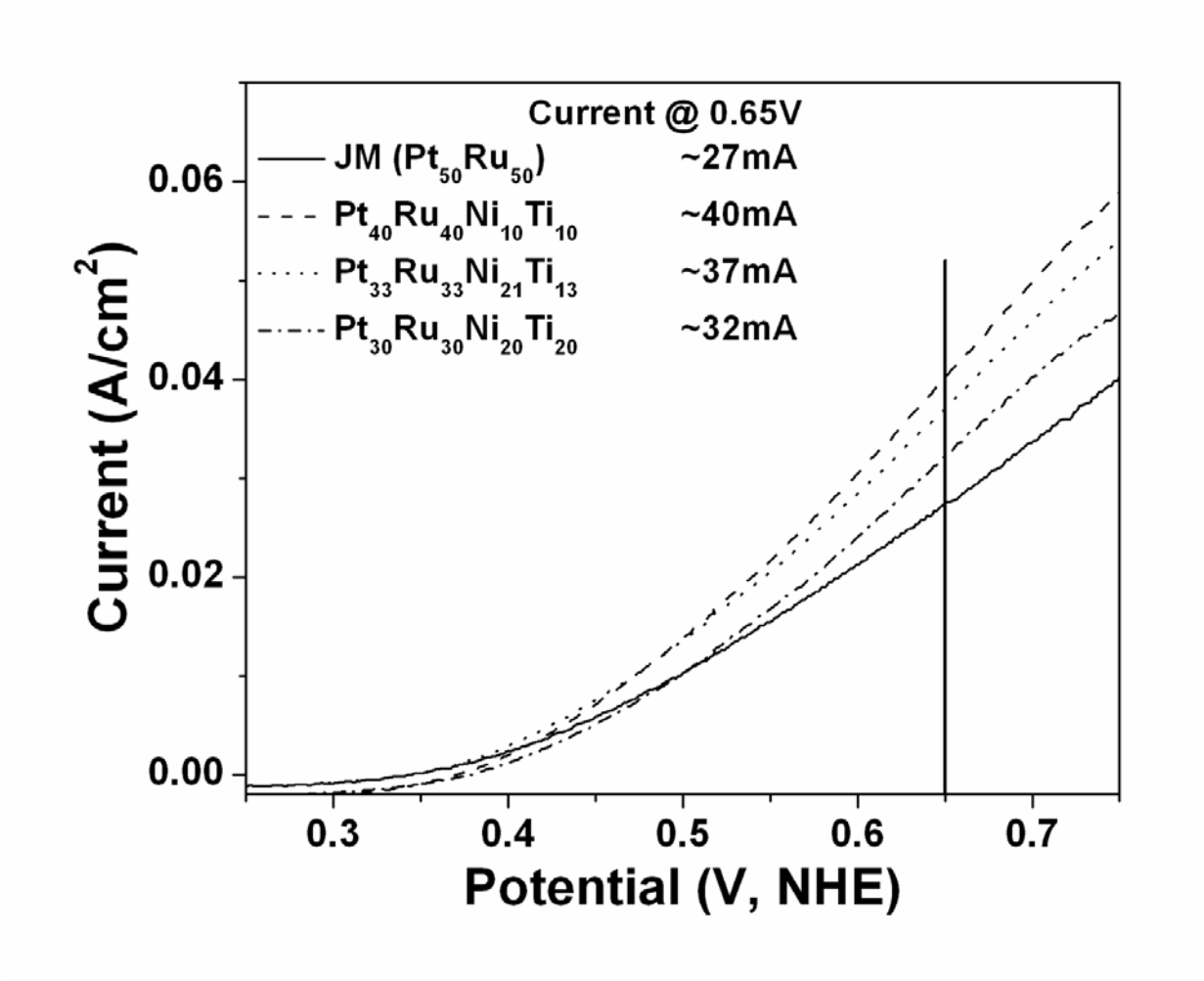

Figure 186. The polarization curve of the quaternary Pt-Ru-Ni-Ti along with the JM catalyst conducted in 1 M CH_3OH and 0.5 M H_2SO_4 at 40°C with a scan rate of 10 mV/sec

In order to study the durability/stability, chronoamperometry (current *vs*. time) measurements have been carried out for all the catalysts in 0.5 M H_2SO_4 and 1 M CH_3OH at a constant voltage of ~ 0.65V (*vs.* NHE) at 40°C for a period of 100 hours. This extended stability tests would help determine the degradation or loss of activity of the catalyst as a function of time. The chronoamperometry response, shown in **Figure 187**, over a period of 100 hours has been normalized with respect to the initial current. It shows that the CSG synthesized reduced noble

metal quaternary electro-catalysts degrades at a much lesser rate than the commercial JM catalyst. The commercial catalyst has current retention of ~ 50 % after 100 hours whereas the quaternary Pt-Ru-Ni-Ti electro-catalysts show current retention of ~ 56 - 61 %.

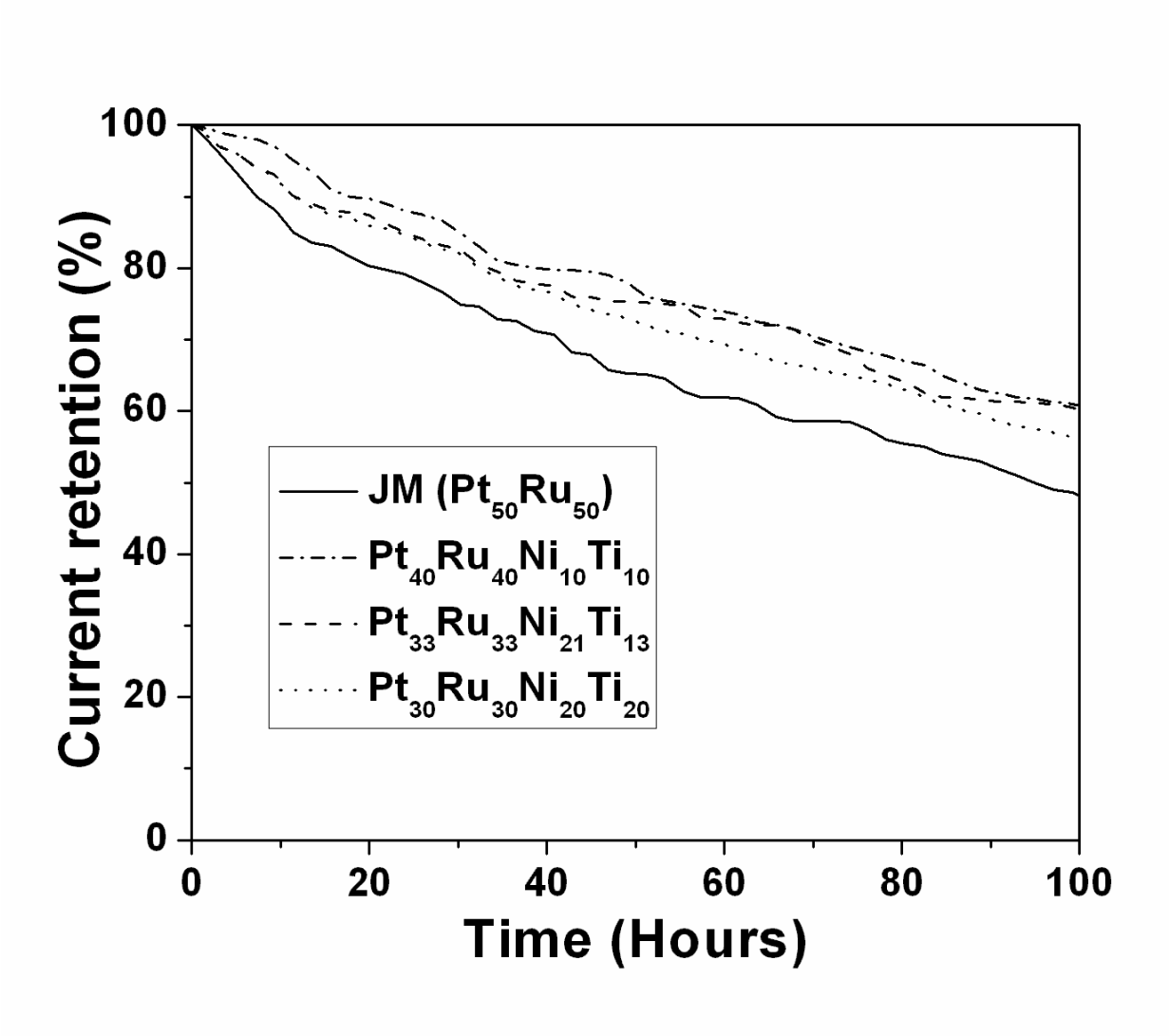

Figure 187. Retention of current in the chronoamperometry plot over a period of 100 hours measured at 0.65 V *vs.* NHE

In order to quantify the amount of platinum, ruthenium, nickel and titanium leached in the electrochemical solution, the electrochemical solution after the testing time of 100 hours was collected and run through the inductively coupled plasma optical emission spectroscopy (ICP-OES). It was found that no active Pt leached into the solution for all the catalysts. However, ruthenium found in the solution for the JM and Pt-Ru-Ni-Ti was ~ 0.85 ppm and ~ 0.64 ppm, respectively. This further elucidates the higher current retention for the quaternary CSG synthesized catalysts. Ni and Ti leached out in the solution for the quaternary catalysts was ~ 0.7 - 0.8 ppm. The present study therefore successfully synthesized nanostructured high surface area Pt-Ru-Ni-Ti solid solution anode electro-catalysts for DMFC, with the ability to reduce the noble metal oxide loading to a very low level and achieve improved electro-catalytic performance and robustness or chemical stability.

B.1.4 Conclusion

In this experimental study, the CSG synthesis has been optimized to yield nanostructured quaternary solid solutions for the DMFC anode. The decomposition of the amorphous gel structure in UHP Ar - 1% O_2 gas mixture at 200°C successfully helped in eliminating the amorphous C without causing any oxidation of the resultant alloy. Phase pure Pt-Ru-Ni-Ti alloys of different compositions with up to 40 at.% reduction in noble metals gave a very high specific surface area of ~ 300 m^2/g. The synthesized materials were tested in a solution of 1 M CH_3OH and 0.5 M H_2SO_4 as an anode for methanol oxidation. The polarization tests confirmed up to ~ 48 % increase in current density for $Pt_{40}Ru_{40}Ni_{10}Ti_{10}$. Even after reducing the noble metal

content of the alloy by ~ 40 at.% ($Pt_{30}Ru_{30}Ni_{20}Ti_{20}$), an improvement of ~ 18 % is achieved. The robustness of the catalysts was evaluated *via* chronoamperometry done over an extended period of 100 hours. It clearly showed that all the quaternary CSG synthesized catalysts have much more current retention than the JM $Pt_{50}Ru_{50}$ catalyst. The results demonstrate that high performance Pt-Ru-Ni-Ti catalysts have the ability to be a potential candidate for use as an anode in DMFC; resulting not only in much better electrochemical performance, but also major reduction in overall costs.

B.2 PLATINUM - RUTHENIUM - OSMIUM - IRIDIUM

B.2.1 Introduction

Direct methanol fuel cells (DMFC) are of interest as suitable power sources for consumer electronic devices as well as remote and auxiliary power units for transportation [193-196]. The main advantage of DMFC is the use of liquid methanol rather than gaseous hydrogen as the operating fuel. The theoretical energy density of methanol that is the amount of energy contained in a given volume of methanol is an order of magnitude greater than even highly compressed hydrogen [193, 194]. However, the currently achieved power densities of DMFC are still significantly below than hydrogen fueled PEM and other fuel cell types which limit its use for commercial application. This mainly arises due to the relatively sluggish kinetics of the electrochemical reactions occurring on the catalyst layers at the electrode surface combined with

the methanol crossover to the cathode compartment [193-199]. There is therefore a critical need to conduct research and develop new and improved electro-catalysts with higher catalytic activity at both the anode and cathode regions in order to enhance the efficiency and power density of DMFC, while lowering the precious metal loadings to realize the much desired cost savings to match the performance. Currently, Pt-Ru alloy of nominal composition Pt - 50 at.% Ru is considered the most suitable catalyst composition yielding the best catalytic activity and is hence widely recognized as the anode catalyst for use in DMFCs [193-195, 198-203].

Improved anode catalysts can be obtained by synthesizing high surface area Pt-Ru based alloy catalysts combined with engineered proper alloy design by modifying the chemical composition of the alloy, and doping or alloying with other elements onto the catalyst structure [151, 164, 182, 193, 199-202, 204]. Several researchers have reported improved performance in ternary or quaternary alloys of Pt-Ru-Os, Pt-Ru-Sn, Pt-Ru-Ni, Pt-Ru-P, Pt-Ru-Os-Ir *etc*. when compared to pure Pt-Ru alloys [164, 180, 182, 204-207]. Out of the different ternary and quaternary systems, it has been reported that Pt-Ru-Os and Pt-Ru-Os-Ir show superior catalytic activity in comparison to other systems [162-164, 179, 204]. There have been reports [182, 204] wherein Pt-Ru-Os and Pt-Ru-Os-Ir based catalysts of specific surface area ~ 31 m^2/g show better catalytic activity in comparison to Pt-Ru alloy despite the higher specific surface area of the latter (~ 65 m^2/g). Synthesis of nano-crystalline Pt-Ru-Os-Ir catalyst of high specific surface area can therefore also be expected to enhance the catalytic activity. Several approaches have been reported for synthesizing high surface area Pt-Ru based nano-particles anode catalysts primarily using halide precursors of respective components, which inevitably require a follow-up washing treatment to remove the undesired secondary residues [177, 205, 207]. As a result, these processes are cumbersome and cost inefficient leading to significant loss of the starting noble

metal precursors. In addition, the use of Vulcan carbon and other high surface area electronic conductors *viz.*, carbon nanotubes have been reported as supports to synthesize high surface area Pt-Ru based anode catalyst to obtain better performance than pure Pt-Ru catalyst [151, 201, 207-210]. However, the relatively low density of carbon leads to a build-up of thick catalyst layers that impede the mass transport of methanol to the catalytic sites.

Our group have demonstrated that the novel sol-gel complexation based chemical process, aptly termed complexed sol-gel (CSG) process, is an attractive alternative route for synthesizing phase pure Pt(Ru) and Pt(Ru,Os) solid solution catalyst possessing a high specific surface area (> 100 m^2/g) with excellent catalytic activity [162-164]. In the present work, the CSG process has been further exploited to synthesize Pt-Ru-Os-Ir based complexes, which were thermally treated at various conditions to synthesize phase pure Pt(Ru,Os,Ir) solid solution catalysts possessing a high specific surface area (SSA) with good catalytic activity. Systematic studies has been conducted to determine the optimal composition in the Pt-Ru-Os-Ir system and it has been identified that the composition containing Pt - 41 at.% Ru - 10 at.% Os - 5 at.% Ir exhibits superior electrochemical performance in comparison to other compositions. Therefore, the synthesis, thermal characteristics and electrochemical performance of the high specific surface area $Pt_{44}Ru_{41}Os_{10}Ir_5$ catalyst has been presented.

B.2.2 Experimental Details

Phase pure and high SSA Pt-Ru-Os-Ir based catalyst powders were synthesized using the CSG process. Platinum (II) acetylacetonate [Pt-acac: $Pt(C_5H_7O_2)_2$, Alfa Aesar], ruthenium (III) acetylacetonate [Ru-acac, $Ru(C_5H_7O_2)_3$, Alfa Aesar], iridium (III) acetylacetonate [Ir-acac,

$Ir(C_5H_7O_2)_3$, Alfa Aesar] and osmium(III) chloride [$OsCl_3$, Sigma Aldrich] were used as the sources for Pt, Ru, Ir and Os, respectively. Pt-acac, Ru-acac, Ir-acac and $OsCl_3$ of the desired composition were dissolved at 50°C in 100 ml of acetone. Tetramethylammonium hydroxide [TMAH, $(CH_3)_4NOH$, 25% in methanol, Alfa Aesar], set at TMAH : (Pt + Ru + Os) = 1.75 : 1, was then added to the solution to serve as a high molecular weight organic complexing as well as a hydrolyzing agent. Since Pt-acac, Ru-acac, Ir-acac and $OsCl_3$ tend to phase separate during drying and evaporation of the solvent, the addition of the high molecular weight organic reagent (TMAH), and its intended dual role to complex and induce hydrolysis of the starting noble metal precursors was found to be beneficial in yielding homogeneous amorphous gels containing Pt, Ru, Ir and Os. After stirring for 10 minutes, the solvent was evaporated until the solution became viscous, transforming into a thixotropic gel. The viscous gel was dried in air at 120°C for 10 hours. The dried gels were then transformed to a mortar and pestle and grounded finely to yield the as-prepared powders. This powder was then heat treated in ultra-high purity (UHP) argon at 500°C in order to decompose the amorphous gel structure. The powders were then heat treated multiple times in UHP Ar-1% O_2 gas at a 300°C to generate high surface area Pt-Ru-Os-Ir catalysts. In order to compare the electrochemical performance of the Pt-Ru-Os-Ir catalyst with Pt-Ru catalyst, the CSG process has also been used to synthesize high specific surface area Pt - 50 at.% Ru alloy.

In order to identify the presence of phase/phases, X-ray diffraction (XRD, Philips XPERT PRO system with CuK_α radiation) study has been conducted on the as prepared precursors as well as the heat treated powders. The effective crystallite sizes of the Pt-Ru and Pt-Ru-Os-Ir catalysts were calculated from the most intense peak by Voigt function using the single line approximation method [88]. Specific surface area of the catalyst has been measured using

the Brunauer - Emmett - Teller (BET) technique (ASAP 2020 Accelerated Surface Area and Porosimetry System, Micromeritics). In order to understand the phase formation and decomposition temperature, thermogravimetric and differential scanning calorimetry (TGA/DSC) has been conducted on the powders. The TGA/DSC analysis has been carried out employing a heating rate of 10ºC/minute from room temperature to 500°C in air. To investigate the particle size and particle morphology, transmission electron microscopy (TEM) analysis was conducted. JEOL 4000EX operating at 400kV was employed for conducting the TEM analysis.

Electrochemical characterization was conducted on selected samples using a three electrode cell. The working electrodes for electrochemical characterization were prepared by spreading the catalyst ink of the respective powders on teflonized carbon papers (applied on 1.5 cm^2 area). The ink consists of 88 wt.% catalyst and 12 wt% Nafion (5 wt.% solution in mixed alcohols, Sigma Aldrich). The Pt loading on the electrode was 0.2 mg / 1.5 cm^2. The working electrodes were electrochemically tested using a Potentiostat (VersaSTAT 3, Princeton Applied Research). A solution containing 1 M methanol and 0.5 M sulfuric acid was used as an electrolyte while also serving as a source of the fuel. A Mercury/Mercurous sulfate electrode that has a potential of ~ + 0.654 V *vs.* NHE was used as the reference electrode.

B.2.3 Results and Discussion

The XRD pattern of the powders at several stages in the synthesis is shown in **Figure 188**. The XRD pattern of the dried gel powder, derived after heating at 120°C for 10 hours in air exhibits an amorphous structure without any peaks corresponding to the starting precursors which indicate the expected good chemical homogeneity of the dried gel powders due to the possible

complexation and hydrolysis of Pt-acac, Ru-acac, Ir-acac and $OsCl_3$ with TMAH. The dried gel powder was heat treated in various conditions to synthesize nano-crystalline phase pure Pt(Ru,Os,Ir) solid solution of nominal composition $Pt_{44}Ru_{41}Os_{10}Ir_5$. The TGA/DSC analysis as seen in **Figure 189** of the dried gel powder performed under ultrahigh purity argon (UHP-Ar) atmosphere shows that the decomposition of the dried gel powder is almost complete at around ~ 450°C. Hence the dried gel powder of Pt-Ru-Os-Ir system was heat treated at 450^{o}C for 6 hours under UHP-Ar atmosphere in order to decompose the amorphous gel structure resulting in the formation of nano-crystalline Pt-Ru-Os-Ir based alloys. The XRD patterns of the heat treated powder [**Figure 188** (b)], obtained after thermal treatment of the dried gel powder at 450°C for 6 hours under UHP-Ar atmosphere, shows the formation of nano-crystalline Pt-Ru-Os-Ir alloy with crystallite size of ~ 2 - 4 nm calculated from the most intense peak using the Voigt function.

However, the presence of large amount of non-conducting carbon has also been detected in the thermally treated Pt-Ru-Os-Ir alloy powders confirmed by the TGA/DSC analysis subsequently conducted on the UHP-Ar treated powders in air. The Pt-Ru-Os-Ir alloy with non-conducting carbon, obtained after thermal treatment of dried gel powder at 450^{o}C under UHP-Ar atmosphere, will be hereafter denoted as Pt-Ru-Os-Ir/C. The Pt-Ru-Os-Ir/C shows a SSA of ~ 8 m^2/g due to the presence of a large amount of low surface area non-conducting carbon. The TGA/DSC traces of Pt-Ru-Os-Ir/C up to 500°C (**Figure 189**), performed under dry air shows a broad exothermic reaction at ~ 290°C with enormous weight loss (~ 40 wt.%) which is expected to arise due to oxidation and elimination of the carbon from Pt-Ru-Os-Ir/C.

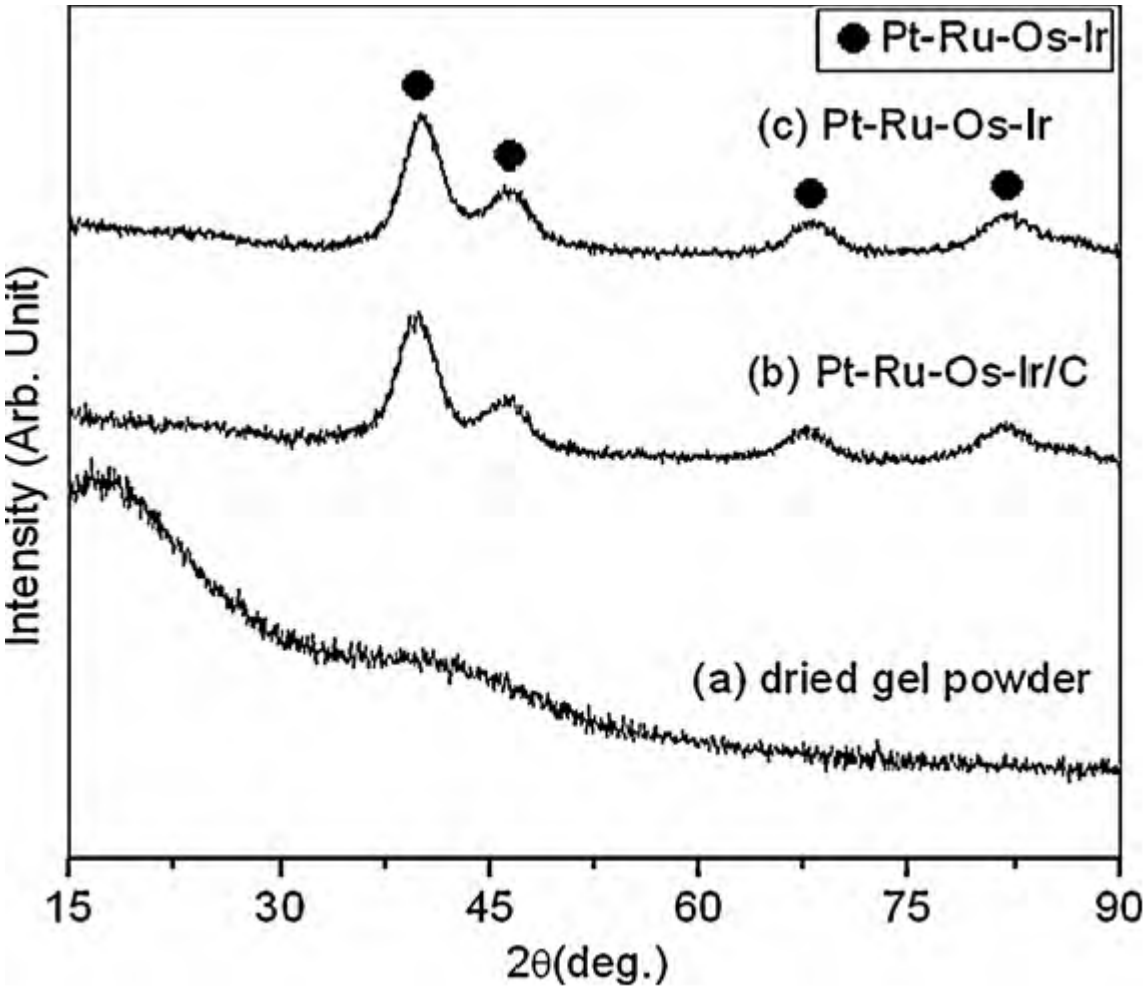

Figure 188. XRD pattern of Pt-Ru-Os-Ir based alloy obtained after drying in air at 120°C (a), further heat treatment in UHP-Ar at 450°C (b), and subsequent thermal treatments in UHP Ar-1% O_2 (c)

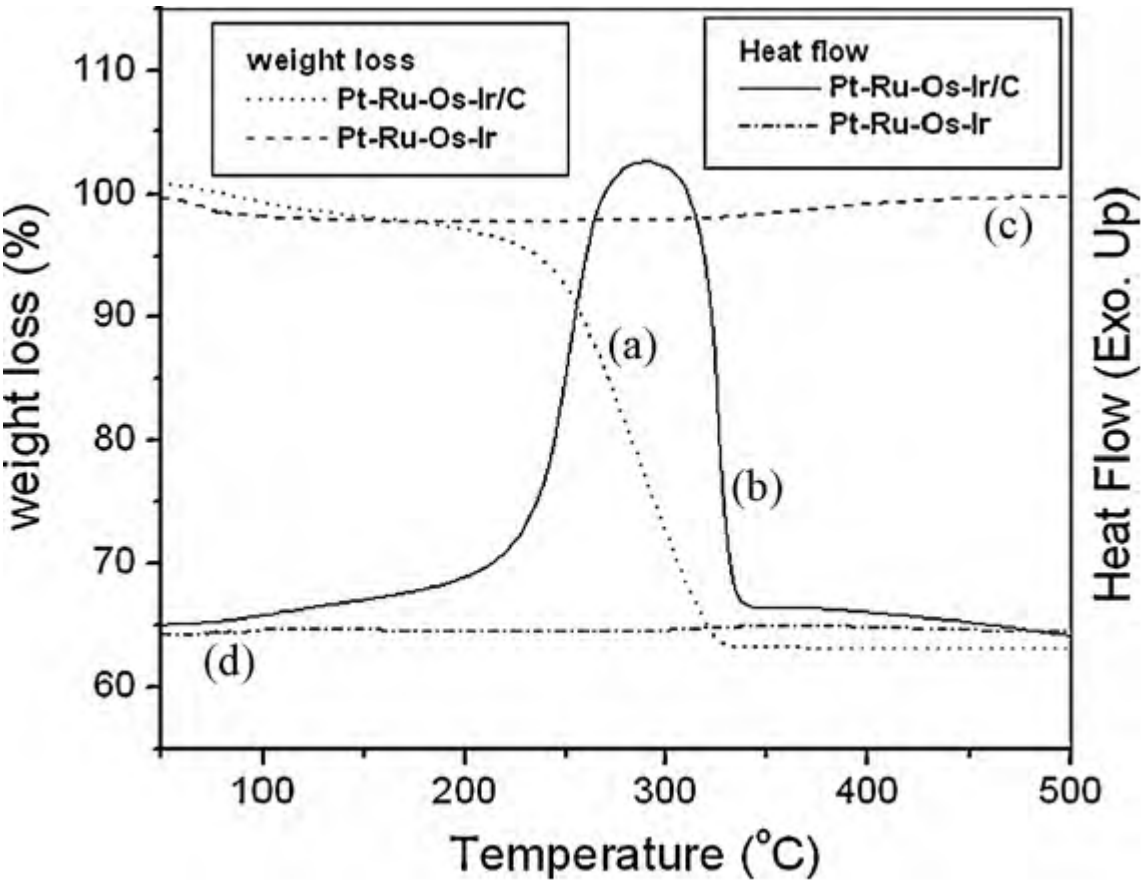

Figure 189. TGA and DSC traces after heat treatement in UHP Ar at 450°C and UHP Ar - 1% O_2 at 300°C

In order to remove the carbon related species present in the Pt-Ru-Os-Ir/C to form the desired nanocrystalline phase pure Pt(Ru,Os,Ir) solid solution with high specific surface area (SSA), the Pt-Ru-Os-Ir/C was further subjected to two sequential thermal treatments at 300°C for 3 hours in the presence of 1 % O_2 balanced by UHP Ar. The 1 % oxygen helps remove the carbon in a controlled fashion thus yielding the single phase Pt-Ru-Os-Ir alloy, denoted as Pt-Ru-Os-Ir, causing minimal or no significant oxidation of the resulting alloys. The XRD patterns of the resulting Pt-Ru-Os-Ir [**Figure 188** (c)] shows the presence of nano-crystalline Pt-Ru-Os-Ir (~

4 nm) alloy suggesting that there is no significant grain growth occurring during the thermal treatment at 300°C. In addition, no significant peaks corresponding to oxides arising as a result of possible oxidation of the metals (*E.g.* RuO_2, IrO_2, OsO_2 or OsO_4) has been observed in the XRD patterns of Pt-Ru-Os-Ir alloy which suggest that no significant oxidation of resulting alloy occurs during thermal treatment of Pt-Ru-Os-Ir alloy under UHP Ar-1% O_2 atmosphere up to 300^{o}C.

The TEM bright field image, shown in **Figure 190**, also confirms the formation of nanoparticles of the Pt-Ru-Os-Ir alloy of crystallite size of ~ 5 - 7 nm. The synthesized Pt(Ru,Os,Ir) solid solution of nominal composition $Pt_{44}Ru_{41}Os_{10}Ir_5$ obtained after controlled heat treatment in Ar-1% O_2 shows a SSA of ~ 95 m^2/g in comparison to ~ 8 m^2/g corresponding to UHP Ar treated Pt-Ru-Os-Ir/C. This result clearly suggests that the significant removal of non-conducting low surface area carbon, facilities the formation of porous structure of Pt-Ru-Os-Ir while also enhancing the specific surface area of the alloy. In addition, removal of carbon also enhances the catalytic activity.

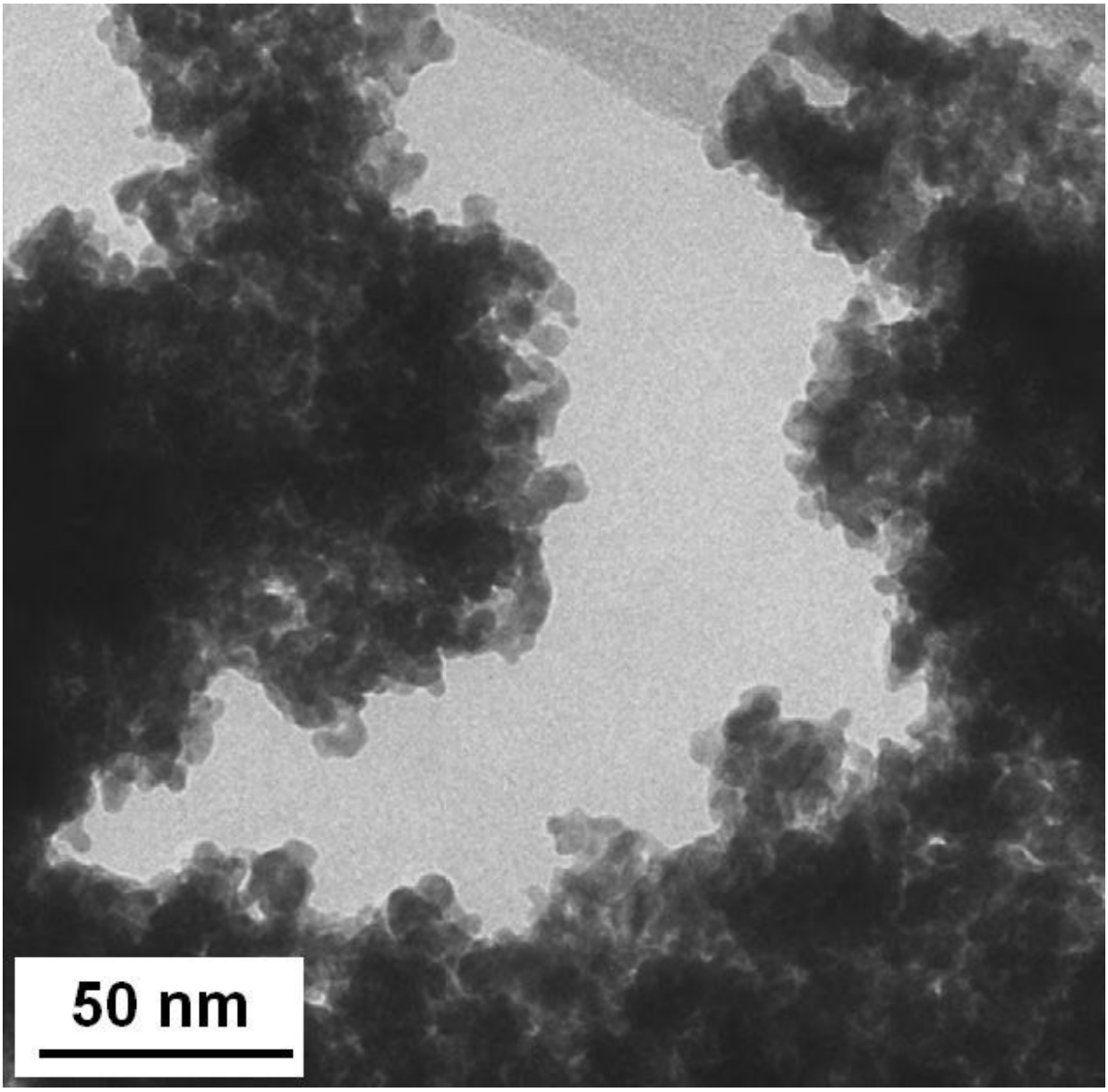

Figure 190. TEM bright field image of Pt-Ru-Os-Ir alloy showing nanoparticles of ~ 5 - 7 nm

Results of electrochemical tests, *i.e.* polarization curve at 40°C and 60°C with a Pt loading 0.2 mg / 1.5 cm^2, conducted on the Pt-Ru-Os-Ir alloy of SSA ~ 95 m^2/g is shown in **Figure 191** and **Figure 192**, respectively. In order to compare the performance of Pt-Ru-Os-Ir alloy, $Pt_{50}Ru_{50}$ of SSA ~ 120 m^2/g with similar Pt loading (~ 0.2 mg / 1.5 cm^2) has also been

plotted. At 40^{o}C and 60^{o}C, $Pt_{50}Ru_{50}$ shows ~ 0.037A and ~ 0.046A current density, respectively at ~ 0 V *vs.* Hg / Hg_2SO_4. On the other hand, Pt-Ru-Os-Ir shows ~ 0.052A and ~ 0.062 A current density, respectively at 40^{o}C and 60^{o}C, which corresponds to ~ 35 - 40 % improved performance in comparison to Pt-Ru synthesized *via* the complexed sol-gel processes. It has also been identified that the current density of the Pt-Ru-Os-Ir catalyst is 20 % higher when the operating temperature is increased from 40^{o}C to 60^{o}C. The above results suggest that the nano-crystalline, high specific surface area, phase pure Pt(Ru,Os,Ir) solid solution of nominal composition $Pt_{44}Ru_{41}Os_{10}Ir_5$ with good chemical homogeneity reveals much improved catalytic activity, demonstrating the potential of the novel complexation based complexed sol-gel (CSG) chemical process for synthesizing high-performance anode catalysts for direct methanol fuel cells.

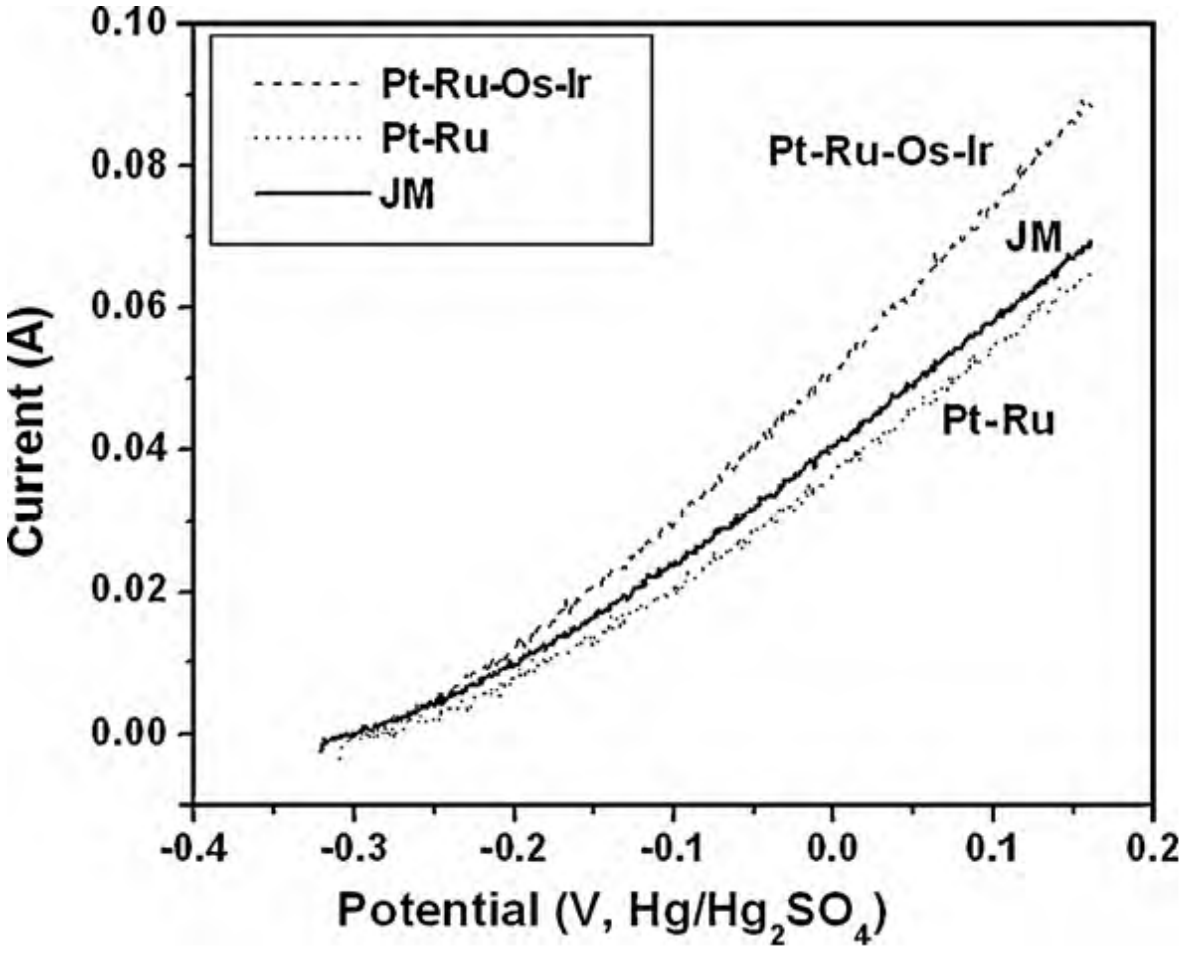

Figure 191. The polarization curves of Pt-Ru-Os-Ir alloy along with Pt-Ru tested at 40°C

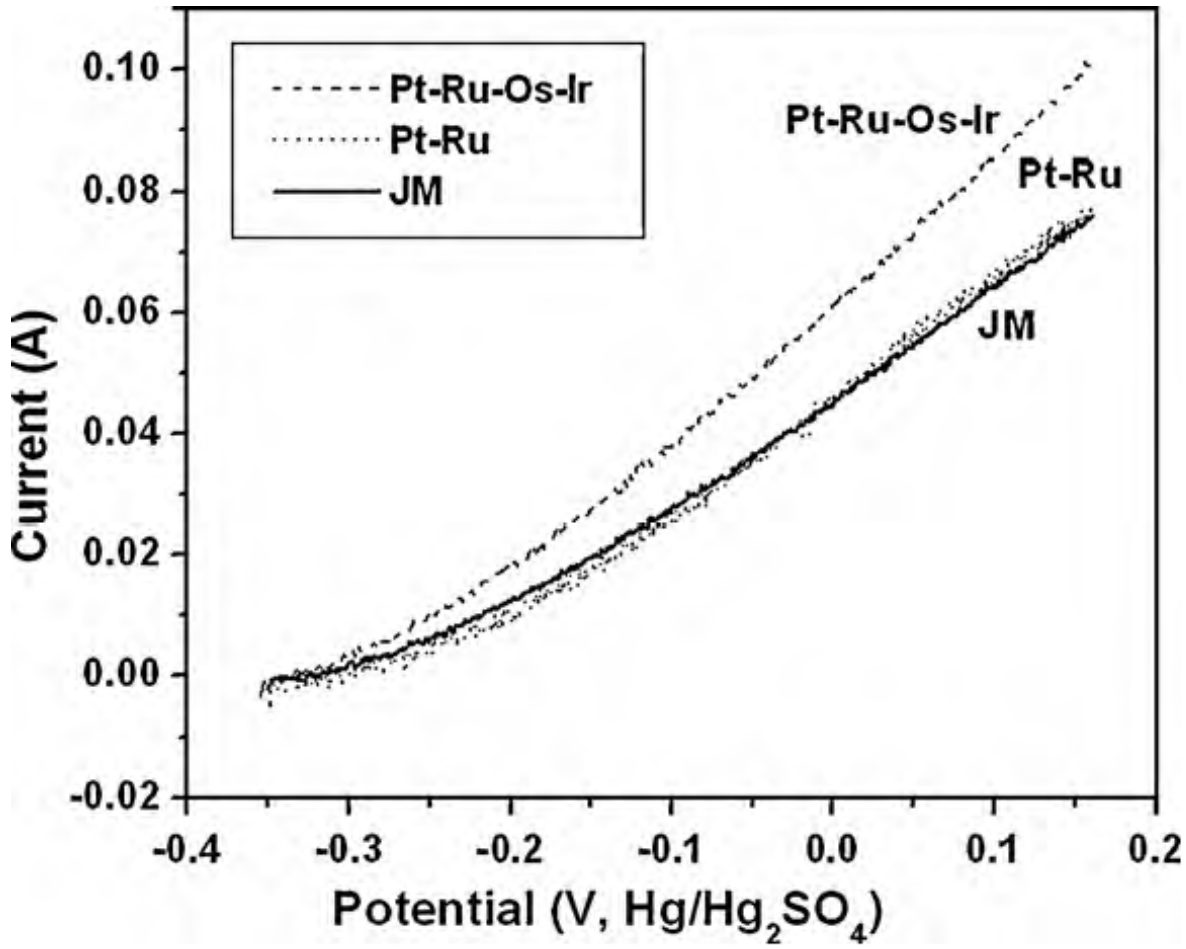

Figure 192.The polarization curves of Pt-Ru-Os-Ir alloy along with Pt-Ru tested at 60°C

B.2.4 Conclusion

A complexed sol-gel (CSG) process has been developed to synthesize Pt-Ru-Os-Ir based anode catalysts possessing high specific surface area (SSA) with good catalytic activity. A homogeneous gel was successfully synthesized by complexing Pt-acac, Ru-acac, Ir-acac and $OsCl_3$ with TMAH serving the dual role of a hydrolysis as well as a complexing agent. Phase pure Pt-Ru-Os-Ir powders possessing SSA of ~ 95 m^2/g was obtained by controlled removal of

the non-conducting carbon generated from the thermally decomposed gel precursor in inert atmosphere. The electrochemical properties of $Pt_{44}Ru_{41}Os_{10}Ir_5$ show ~ 35 - 40 % improved performance in comparison to the pure $Pt_{50}Ru_{50}$ alloy of comparable surface area (also prepared using the CSG approach). It has also been noticed that the catalytic activity of the catalyst increases by ~ 20 % when the operating temperature is increased from 40°C to 60°C. These electrochemical test results demonstrate the potential of the novel complexation based sol-gel process utilizing non-halogen precursors of Pt, Ru, and Ir for synthesizing high performance Pt-Ru-Os-Ir based anode electro-catalysts for DMFC.

APPENDIX C

PEM WATER ELECTROLYSIS SUPPORTS

There is considerable demand for identification of non-noble metal based catalysts and catalyst supports for water electrolysis. Theoretical approaches provide an ideal framework for identifying such systems. In an attempt to identify new electrochemically stable catalyst supports for electrolysis of water, the electronic structures of $MgNb_2O_6$, $MgTa_2O_6$, $ZnNb_2O_6$, and $ZnTa_2O_6$ compounds doped with elements from 3A, 3B, 5B, 6A groups of the Periodic Table as well as F from group VII have been calculated using the Vienna ab-initio simulation package (VASP), within the projector augmented-wave (PAW) method in the general gradient approximation (GGA) for conducting the exchange-correlation corrections. The role of incorporating the additional elements in improving the electronic conductivity as well as the structural and chemical stability is discussed. Based on the calculated values of the cohesive energies for the materials and their type of electronic conductivity, we hypothesize that introduction of group 3A elements (Sc and Y) as well as F contribute drastically to the improvement of the electronic properties as well as the chemical stability of all four Mg and Zn tantalates/niobates based parent oxides. The study indicates that these doped compounds might serve as the most appropriate candidate catalyst supports for water electrolysis.

C.1 AB-INITIO STUDIES

C.1.1 Introduction

Advanced water electrolyzers using proton exchange membranes (PEM) generally utilize expensive noble metal electro-catalysts for the oxygen electrode such as platinum and platinum alloys [15] as well as the equally prohibitively expensive iridium oxide (IrO_2) and ruthenium oxide (RuO_2) catalysts. The tremendous cost associated with the use of noble metal oxides at the current loading levels could be substantially lowered by developing new non-noble metal based catalysts that exhibit comparable or improved catalytic activity as the parent noble metal counterparts or identification of electrochemically stable catalyst supports that can be economically synthesized in high surface area (HSA) forms allowing for reduced levels of catalyst loading without compromising the electro-catalytic activity. Thus, it is desirable that these catalyst supports exhibit high electronic conductivity comparable to the noble metals combined with excellent chemical and electrochemical stability at potentials of 1.8 V - 2.0 V *vs.* normal hydrogen electrode (NHE) wherein electrolysis of water is known to occur.

Very few materials are known to exhibit both the desired electrical conductivity and the much needed electrochemical stability in the desired potential window. In this regard, several researchers have proposed [71, 74, 211, 212] the use of IrO_2 combined with highly corrosive resistant tantalum oxide (Ta_2O_5), tin oxide (SnO_2), niobium oxide (Nb_2O_5), titanium oxide (TiO_2) and non-stoichiometric tungsten oxide (WO_x) for stabilizing the IrO_2 dimensionally stable anode electrode during the service life of the electrolyzer. However, there is a need to further improve

the electronic conductivity to enhance the electro-catalytic activity thus improving the catalyst efficiency and consequently minimizing the catalyst loading.

One approach to achieve this goal would be the introduction of solid solutions of transition metal oxides, such as Nb_2O_5 and Ta_2O_5, with tin oxide, which are known to exhibit the desired high chemical and electrochemical stability but are also well known insulators with poor electronic conductivity. Alloying of the oxides with SnO_2 can likely change their electronic structure, which in turn could positively influence the electronic conductivity. In our recently published first principles theoretical study of different ternary oxides, such as $SnTa_2O_6$, $SnNb_2O_6$, $Sn_2Ta_2O_7$, $Sn_2Nb_2O_7$, doped with small concentration of elements selected from groups 5B and 6A of the Periodic Table, including As, Sb, Bi as well as Cr, Mo, and W [213], it was postulated that $SnTa_2O_6$ doped with As, Sb, or Bi would be the most appropriate material for implementation as catalyst supports with respect to all other materials investigated in the study, both in terms of the electronic conductivity as well as structural / chemical stability.

Besides Sn-Nb/Ta-O oxides there is a large family of bivalent niobates and tantalates [214, 215] which remain largely unexplored for possible use as catalyst supports, however their structural and chemical stability is higher than the tin based oxides. For example, CaO, MgO, SrO oxides have higher formation enthalpy in comparison to SnO, thus one can suggest that tantalates and niobates of Ca, Mg or Sr can also be expected to demonstrate higher structural stability than the tin based systems. Recently, our group investigated a large family of calcium niobates and tantalates doped with small amount of different elements playing the role of donors of additional electrons for improving the electronic conductivity of the material [215]. The results showed that Sc, Y, and F are the best dopants that are able to drastically improve the

conductivity without compromising the structural and electrochemical stability under the aggressive pH and chemical reaction conditions prevalent during operation.

C.1.2 Magnesium and Zinc Tantalates and Niobates

The present study is an attempt to explore Mg- and Zn- based niobates and tantalates as potentially possible candidate materials for use as catalyst supports for water electrolysis and hydrogen fuel cells. We selected $MgNb_2O_6$, $MgTa_2O_6$, $ZnNb_2O_6$, and $ZnTa_2O_6$ compounds for our investigation since these materials are relatively inexpensive, demonstrating high structural and chemical stability and are also well known mostly as promising dielectrics for applications in microwave devices [216, 217] as well as photocatalysts for water splitting and producing hydrogen gas under light illumination [218-220].

Since all the four $MgNb_2O_6$, $MgTa_2O_6$, $ZnNb_2O_6$, and $ZnTa_2O_6$ are semiconductors it would be interesting to investigate the effect of different dopants selected particularly in light of improving the electronic conductivity necessary for achieving high performance of the potential catalyst supports. These elements would likely serve as donors of additional free electrons participating in the charge transfer and thus, increasing the electronic conductivity. Such elements substituting for divalent Mg^{2+} or Zn^{2+} at the corresponding sites in the crystal lattice could belong to 3A, 3B, 5B groups of the Periodic Table, while elements substituting Nb^{5+} and Ta^{5+} in the lattice might belong to 6A group. An additional likely pathway for donating free electrons into the system is to dope the oxides with a small amount of fluorine substituting the corresponding oxygen ions in the crystal structure. An effect of such F doping could be similar to

that observed in fluorine doped tin oxide (FTO) widely investigated experimentally and from first principles [56, 140, 221, 222].

First principles (or *ab-initio*) approaches by definition are based on fundamental laws of quantum mechanics without needs of experimental fitting data, which makes them very attractive for study various properties of materials computationally, without time and cost consuming experimental trials and errors. It makes it possible to rapidly evaluate the effect of compositional modifications of the oxides on their electronic conductivity and structural stability. Based on the above, *ab-initio* calculations of total energies, electronic and optimized crystal structures, and cohesive energies have been carried out in the present study [223] for the following oxides: $MgNb_2O_6$, $MgTa_2O_6$, $ZnNb_2O_6$, and $ZnTa_2O_6$ in both, pure and doped forms with the introduction of a small amount of elements from 3A group - Sc, Y, 3B group - B, Al, Ga, In, 6A group - Cr, Mo, W, 5B group - As, Sb, Bi, as well as F from group 7. The formula units of the doped materials can be written as: $[(Mg/Zn)_{1-x}(3A,\ 3B,\ 5B\ elements)_x](Nb/Ta)_2O_6$, $(Mg/Zn)[(Nb/Ta)_{1-y}(6A\text{-}elements)_y]_2O_6$, and $(Mg/Zn)(Nb/Ta)_2O_{6-x}F_x$, where x = 0.25 and y = 0.125.

C.2 COMPUTATIONAL DETAILS

The total energies, electronic structure and density of electronic states are calculated within density functional theory (DFT) using the generalized gradient approximation (GGA) for the exchange-correlation energy functional in a form suggested by Perdew and Wang [130]. We use the projector augmented wave (PAW) method and a plane wave basis set, as implemented in a

widely used the Vienna Ab initio Simulation Package (VASP) [131-133]. DFT calculations using the common density functionals give adequate values for ground state properties such as total energies and vibrational frequencies. However, excited state properties are not given accurately, for example, the electronic band gap is typically underestimated approximately by a half. Since otherwise DFT approaches are quite accurate and reliable yet faster than other traditional *ab-initio* techniques, such as Hartree - Fock theory and its derivations based on the complex many electron wavefronts, we have chosen VASP package as a main computational tool in present theoretical study.

The atomic positions and the cell parameters, including the cell volume, are optimized by minimizing the forces and stresses *via* the Hellmann - Feynman theorem. Standard PAW potentials were employed for the elemental constituents of all pure and doped compounds in the study. For all the materials considered the plane wave cutoff energy of 520 eV has been chosen to maintain high accuracy of the total energy calculations. The lattice parameters and internal positions of atoms were fully optimized during the double relaxation procedure employed; and consequently, the minima of the total energies with respect to the lattice parameters and internal ionic positions have been determined. This geometry optimization was obtained by minimizing the Hellman - Feynman forces *via* a conjugate gradient method, so that the net forces applied on every ion in the lattice is maintained close to zero. The total electronic energies were converged within 10^{-5} eV/un.cell resulting in the residual force components on each atom to be lower than 0.01 eV/Å/atom, thus allowing for the accurate determination of the internal structural parameters. Since the doped structures contain a small amount of additional elements, it is expected that the equilibrium volume of the basic unit cell is not substantially altered. Hence,

only internal atomic positions have been optimized during the calculations keeping the volumes of the unit cells identical to that of the corresponding undoped parent materials.

The Monkhorst - Pack scheme was used to sample the Brillouin Zone (BZ) and generate the ***k*** point grid for the solids and the different isolated atoms used in the present study. A choice of the appropriate number of ***k*** points in the irreducible part of the BZ was based on convergence of the total energy to be 0.1 meV/atom. For pure and doped forms of $MgNb_2O_6$, $MgTa_2O_6$, $ZnNb_2O_6$ and $ZnTa_2O_6$, the numbers of ***k*** points in the irreducible parts of BZ used were 84, 84, 110 and 110 points, respectively.

$MgNb_2O_6$ and $ZnNb_2O_6$ adopt the orthorhombic columbite crystal structures with Pbcn (#60) space group containing 36 atoms in the conventional unit cell (Z = 4) [224]. The crystal structure of $MgTa_2O_6$ on the other hand belongs to the tetragonal tri-rutile type with $P4_2/mnm$ (#136) space group containing 18 atoms in the unit cell (Z = 2), while $ZnTa_2O_6$ adopts an orthogonal tri-α-PbO_2 type structure with Pbcn (#60) space group containing 36 atoms in the unit cell. To maintain uniformity in all calculations we artificially doubled the 18 atom tri-rutile unit cell of $MgTa_2O_6$ up to 36 atoms per cell to be consistent with the other three parent oxides considered in the study.

C.3 RESULTS AND DISCUSSION

The electronic structures of orthorhombic $MgNb_2O_6$ and tetragonal $MgTa_2O_6$ are almost identical due to the isoelectronic similarity of Nb and Ta. It is also for this reason that orthorhombic $ZnNb_2O_6$ and tetragonal $ZnTa_2O_6$ exhibit similar characteristics. The structural

parameters of the oxides obtained experimentally and derived from the calculations are presented by Velikokhatnyi *et al.* [223]. One can see that the results of the calculations obtained from the structural optimization are in very good agreement with experimental measurements and are characterized by an error of less than 1.2 % for all the four compounds considered in the study. This margin of error is typical for state-of-the-art approximations to density functional theory.

Figure 193 and **Figure 194** show the total (DOS) and partial (PDOS) density of electronic states for all the four parent materials studied. The energy scale has been shifted in such a way that the zero corresponds to the Fermi energy. The occupied bands of $MgNb_2O_6$ and $MgTa_2O_6$ shown in **Figure 193** consist mainly of O 2s, O 2p and to some extent, d-orbitals of Nb or Ta. Mg 3s and Mg 2p states are observed in a very limited amount. The valence band consists primarily of O 2p states with small admixture of transition metal d-orbitals as well as 3s and 2p states of Mg. The conduction bands of the materials are composed of Nb 4d or Ta 5d orbitals hybridized with another part of O 2p states. Similar electronic structure is observed for $ZnNb_2O_6$ and $ZnTa_2O_6$ shown in **Figure 194**. The only difference between Mg- and Zn- based materials is that Mg 3s and 2p are replaced by Zn 3d orbitals hybridized with O 2p and Nb 4d / Ta 5d electronic states comprising the main portions of the valence band of the oxides. Otherwise, the electronic structures of all the four materials are qualitatively very similar. All of the materials demonstrate a forbidden energy gap between the valence and conduction bands. As it was mentioned before, the values of the band gaps (BG) calculated within the DFT methodology are usually underestimated; hence the calculated values of BGs should be taken into consideration only qualitatively.

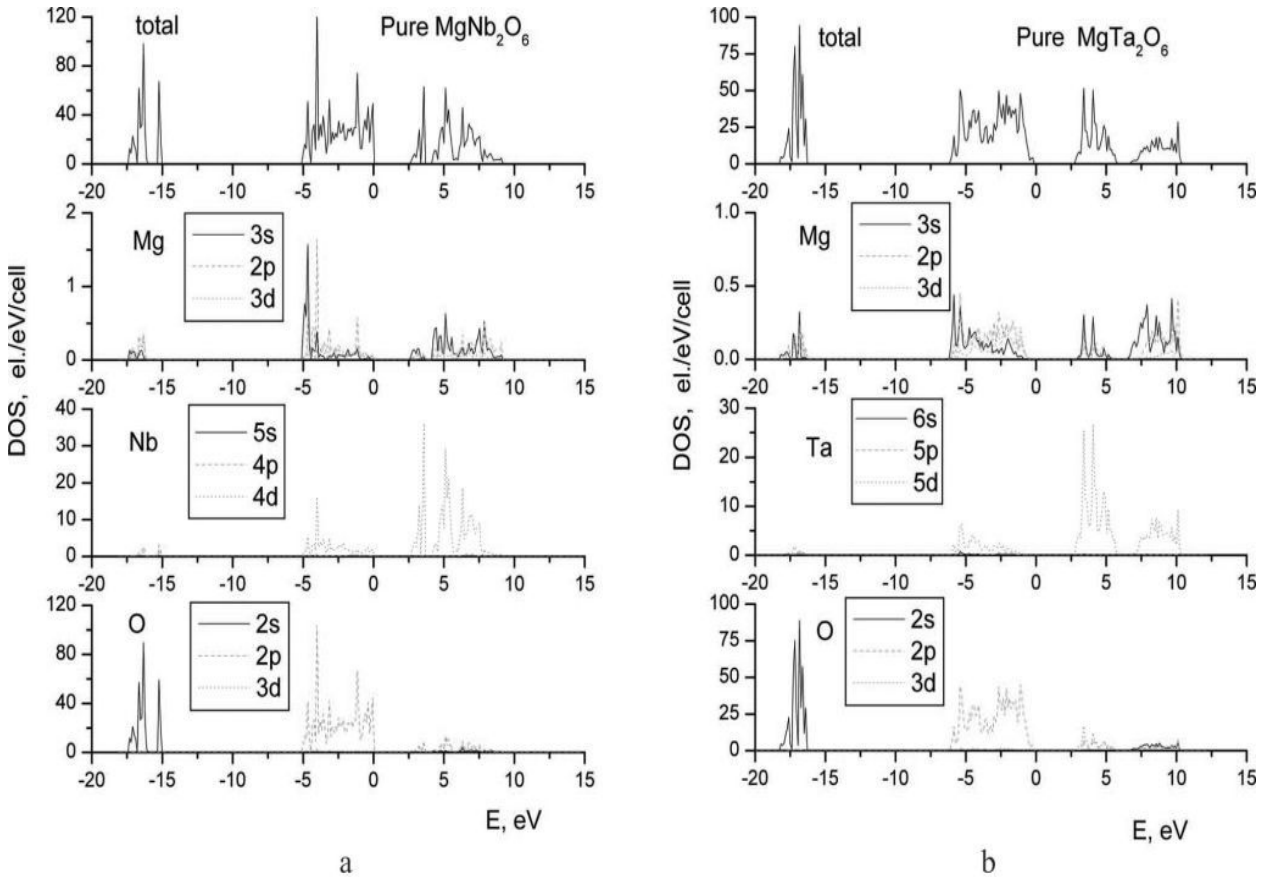

Figure 193. Electronic density of states for $MgNb_2O_6$ (a), and $MgTa_2O_6$ (b)

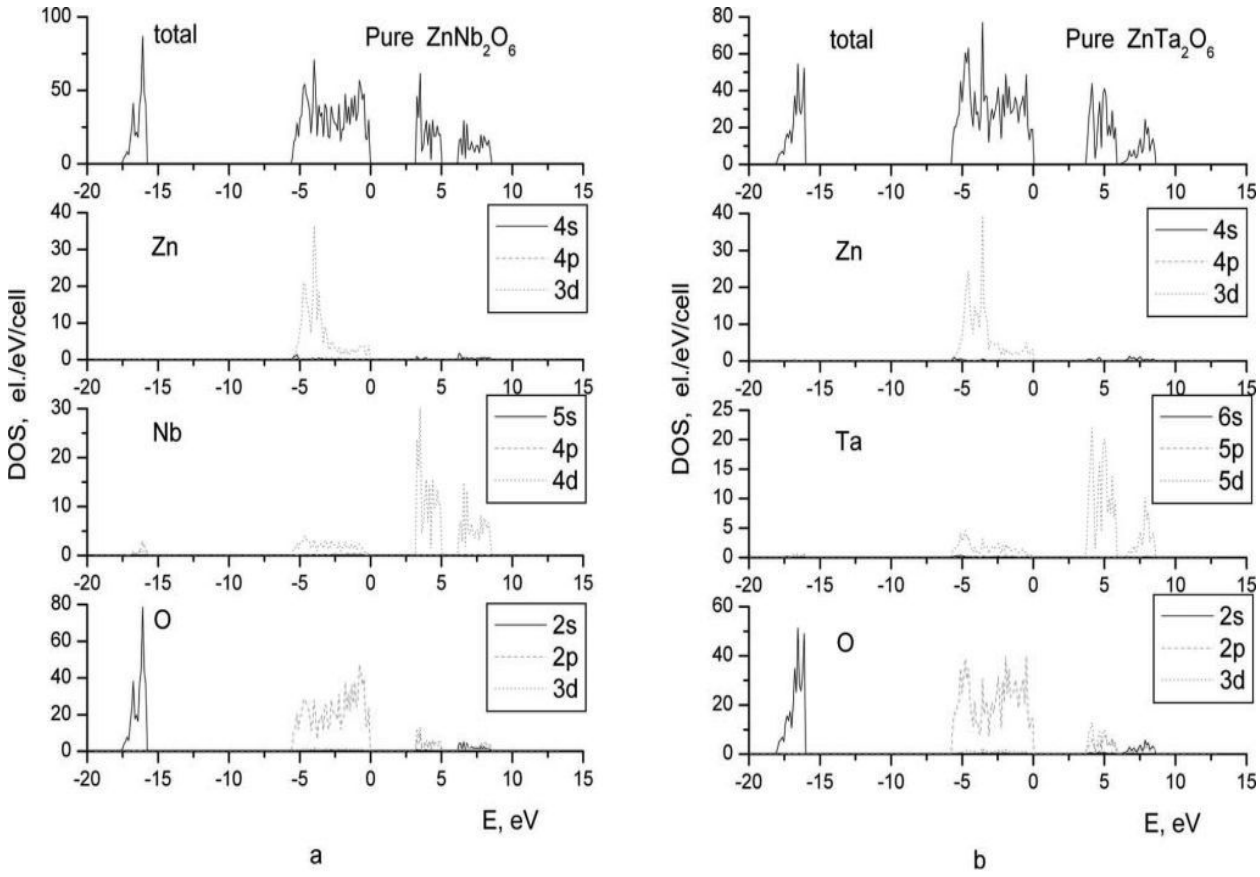

Figure 194. Electronic density of states for $ZnNb_2O_6$ (a), and $ZnTa_2O_6$ (b)

Since all the four oxides are semiconductors, their electronic conductivity is still inadequate for use as electrode materials for electrolysis and needs to be improved further to enhance the charge transfer characteristics critical for lowering the over potential and attaining good catalytic activity. The electronic conductivity could be improved by introducing a small amount of additional elements possessing more valence electrons than Mg / Zn or Nb / Ta. Hence these elements will be capable of serving as donors of free charge carriers, thus increasing the electronic conductivity.

Since the goal of the current study is to unravel the principal role of the introduction of small concentrations of dopants and their corresponding influence on the electronic conductivity

and chemical stability of the parent oxide, only one atom of each dopant has been placed into the elementary cell. Such a selection eliminates any uncertainty in the atomic configurations occurring due to the presence of multiple (two or more) dopant atoms in the unit cell. For example, the 36 atom unit cell of the orthorhombic columbites $(Mg/Zn)Nb_2O_6$ contains 4 Mg or Zn, 8 Nb, and 24 O ions; so that those elements substituting for Mg/Zn in the unit cell will replace one Mg / Zn atom out of the four available. Similarly, only one atom from the 6B group will be substituted for one atom of Nb out of the existing 8 sites and one atom of F will replace one out of 24 oxygen atoms available in the unit cell. The valence electronic configurations of Mg, Zn, Nb, Ta and O atoms are $3s^2 2p^6$, $3d^{10} 4s^2$, $4p^6 5s^1 4d^4$, $6s^2 5d^3$ and $2s^2 2p^4$, respectively. The electronic configurations for Sc and Y are $4s^2 3d^1$ and $4s^2 4p^6 5s^2 4d^1$, respectively; for B, Al, Ga and In are $2s^2 2p^1$, $3s^2 3p^1$, $3d^{10} 4s^2 4p^1$ and $4d^{10} 5s^2 5p^1$, respectively; for As, Sb and Bi are $4s^2 4p^3$, $5s^2 5p^3$ and $6s^2 6p^3$, respectively; for Cr, Mo and W are $3d^5 4s^1$, $4d^5 5s^1$ and $5d^4 6s^2$, respectively; and finally, for F is $2s^2 2p^5$.

Since the niobates and tantalates considered in the present study have similar electronic structures, the main discussion of the results primarily focuses on Mg and Zn niobates doped with the different elements. Moreover, most of the conclusions derived from the present study on doped Mg / Zn niobates can also be applied to the corresponding iso-electronic Mg / Zn tantalates, and hence the results obtained for doped $MgTa_2O_6$ and $ZnTa_2O_6$ will be shown primarily for illustration purposes.

C.3.1 3A and 3B group elements

Due to the isoelectronic nature of elements belonging to the same group of the Periodic Table, the changes in the electronic structure resulting from doping the parent oxides with such elements are qualitatively very similar. Hence we will discuss in detail only one or two representative dopants from each group and mention briefly the results for other members of the particular periodic group.

We chose Sc and Y from 3A group and B, Al, Ga and In from group 3B of the Periodic Table. All the elements have valence +3, and hence they could serve as donors of additional free electrons when they were used as substituents for divalent Mg^{2+} or Zn^{2+}. The total and partial electronic densities of states calculated for $Mg_{0.75}Sc_{0.25}Nb_2O_6$ are shown in **Figure 195** (a). Almost identical results have been obtained for Y doping due to the identical outer electronic configuration. One can therefore see that the doped system demonstrates very similar electronic structure as undoped $MgNb_2O_6$. The only prominent difference is that in the doped system the Fermi level is shifted towards the conduction band rendering this material metallically conductive. It occurs due to the strong hybridization of Sc 3d (or Y 4d) and Nb 4d zones forming the conduction band occupied with additional electrons being supplied to the system by the donor serving Sc- or Y- dopants. It is also worth mentioning that the band gap value between valence and conduction bands is practically not changed during doping and are 2.39 eV and 2.35 eV for Sc- and Y- doping, respectively. Sc- and Y- doping of $MgTa_2O_6$ demonstrate the same results as for $MgNb_2O_6$ discussed above with corresponding band gaps equal to 2.75 eV and 2.9 eV respectively.

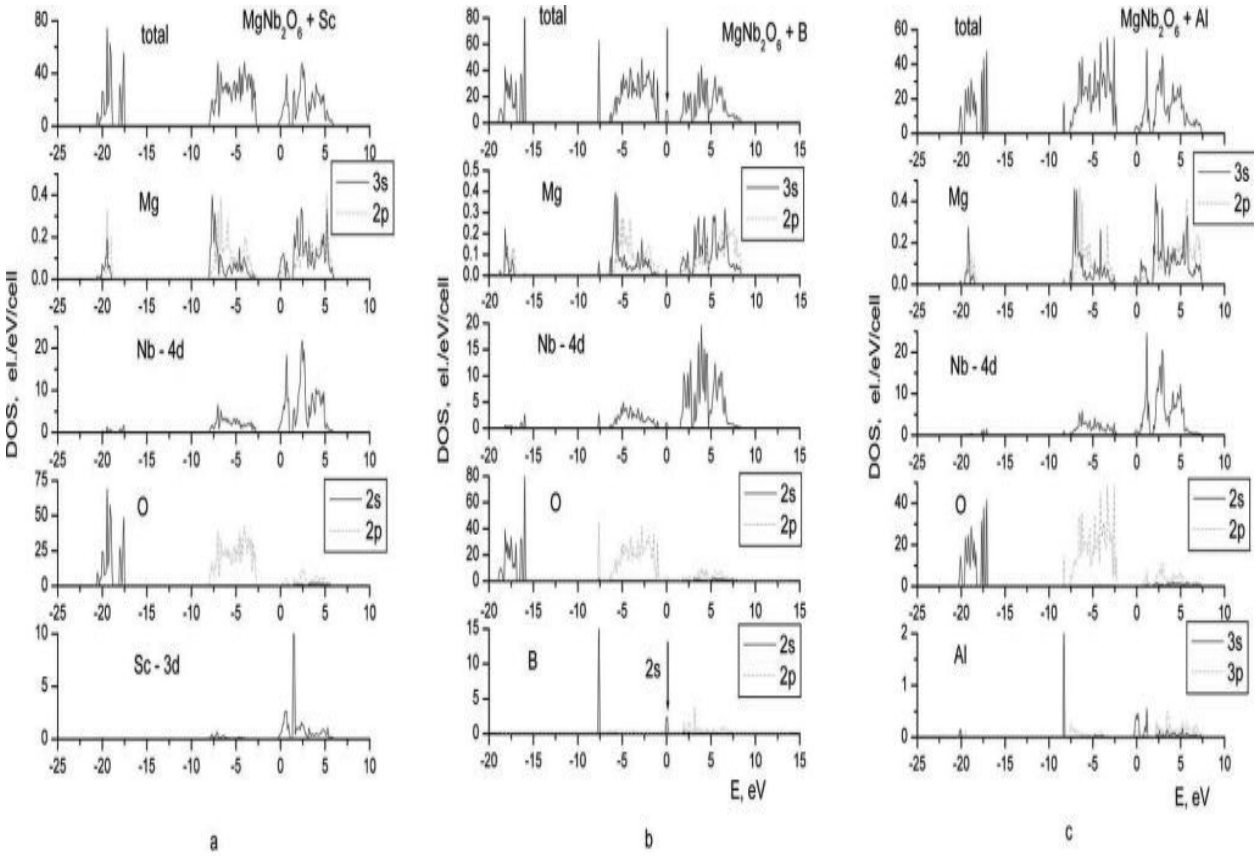

Figure 195. Electronic density of states for $MgNb_2O_6$ with Sc (a), B (b), and Al (c)

As for doping with 3B elements, the results are quite different from those seen for 3A dopants. The total and partial DOS for $MgNb_2O_6$ doped with B and Al are shown on **Figure 195** (b) and (c), respectively. Incorporation of boron introduces a new non-hybridized completely localized impurity zone which is its own valence s states located in the energy gap between the valence and conduction bands (see partial density of states of B denoted by an arrow). This impurity s-zone is separated from the main conduction band by an energy gap of 1.41 eV, which is the value of the activation energy, E_a for the electronic conductivity determined by electron transitions from these localized s-states to the conduction band. Quite similar situation is observed for Ga doped $MgNb_2O_6$ with corresponding E_a equal to 0.54 eV; however, in the case

of Ga doped $MgTa_2O_6$, the Ga 3s orbitals are shifted towards the conduction band, thus hybridizing with Ta 5d states and making the material electronically conductive. This case is very similar to those for Al- and In- doped $MgNb_2O_6$ and $MgTa_2O_6$. Both Al and In s-orbitals hybridize with Nb 4d or Ta 5d conduction bands making these materials also metallically conductive with the activated conductivity $E_a = 0$.

In regards to $ZnNb_2O_6$ and $ZnTa_2O_6$ doped with 3A and 3B elements, the results are very similar to those obtained for Mg niobates and tantalates. **Figure 196** shows the total and partials DOS for $ZnNb_2O_6$ doped with Sc, B and Al. Similar to the Mg niobates and tantalates, Sc and Al improves the electronic conductivity of the parent oxide converting it from the inherent semiconducting state to a metallic form. Similar effect is observed for both $ZnNb_2O_6$ and $ZnTa_2O_6$ doped with Y, Ga and In. Furthermore, B doping of $Zn(Nb/Ta)_2O_6$ demonstrates a similar effect for the electronic conductivity observed in the case of B doped $Mg(Nb/Ta)_2O_6$, wherein the conductivity is improved by significant reduction of the main band gap, while still retaining it in the semiconductor range of 0.8 eV and 1.1 eV for $ZnNb_2O_6$ and $ZnTa_2O_6$, respectively.

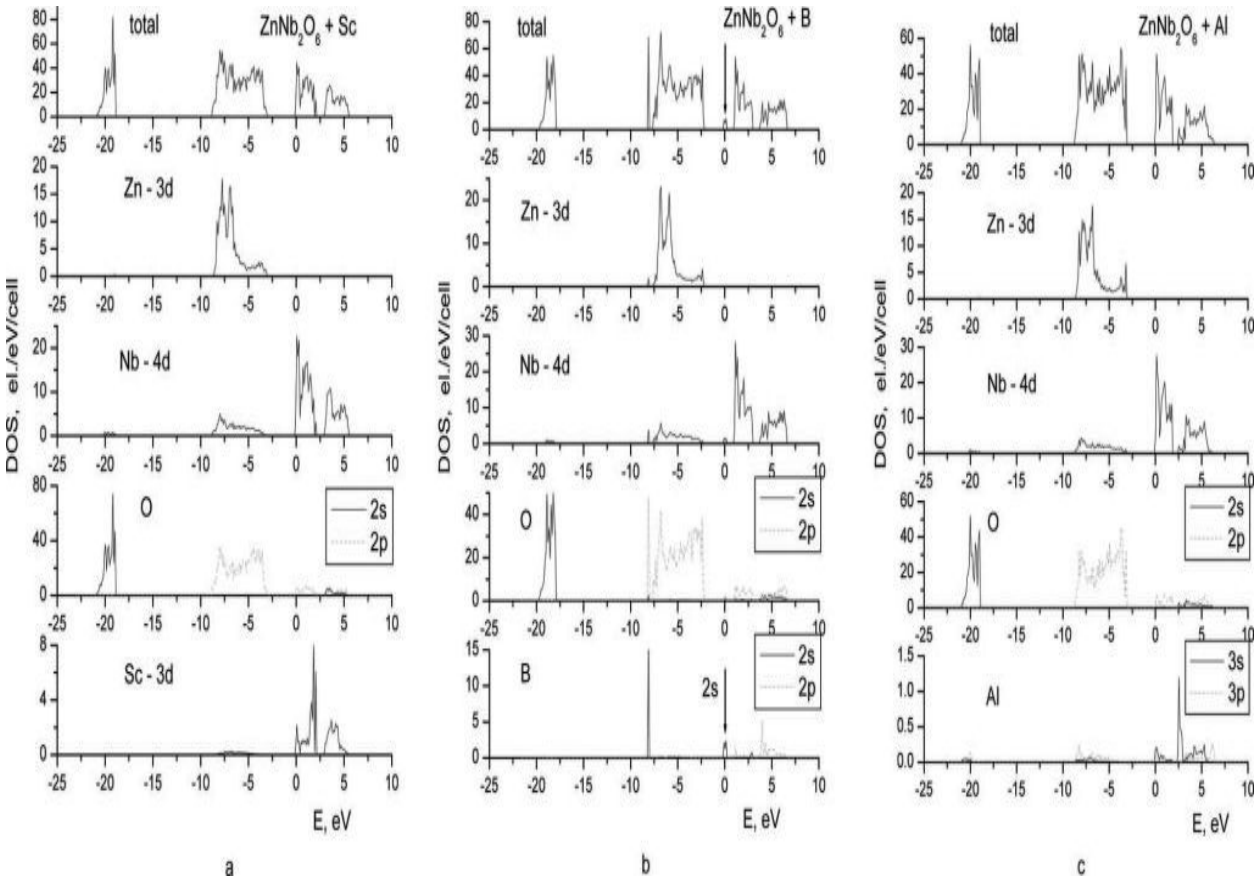

Figure 196. Electronic density of states for $ZnNb_2O_6$ with Sc (a), B (b), and Al (c)

C.3.2 5B and 6A group elements and Fluorine

The total and partial DOS calculated for $Mg_{0.75}As_{0.25}Nb_2O_6$, $Mg[Nb_{0.875}Cr_{0.125}]_2O_6$ and $Mg[Nb_{0.875}W_{0.125}]_2O_6$ are shown in **Figure 197**. In contrast to pure $MgNb_2O_6$, the electronic structures of the doped oxides display several features related to the substituted dopants. The main differences between pure $MgNb_2O_6$ and the structure doped with As, Sb or Bi are the appearance of the s-states of the dopants indicated by arrows hybridized with O 2p states located at the bottom of the valence band and separated from the upper portion of the valence band by an

energy gap of 2.1 eV - 3.0 eV [**Figure 197** (a)]. Also, similar to 3A dopants due to the additional free electrons introduced into the system, the Fermi level of the doped structures is also shifted towards the conduction band resulting in metallic conductivity of the material. The band gap between the valence and conduction bands is ~ 2.1 eV and does not change significantly with respect to that of the undoped oxide (2.4 eV); so that introduction of small amounts of 5B group elements does not noticeably affect the width of the forbidden zone. A similar result is observed for $MgTa_2O_6$ doped with identical 5B elements demonstrating that the values of the energy gap between the valence and conduction bands for all the three dopants are 2.9 eV, 3.0 eV and 2.8 eV for As, Sb and Bi, respectively, which correlates well with the calculated band gap for the pure $MgTa_2O_6$ of 2.75 eV.

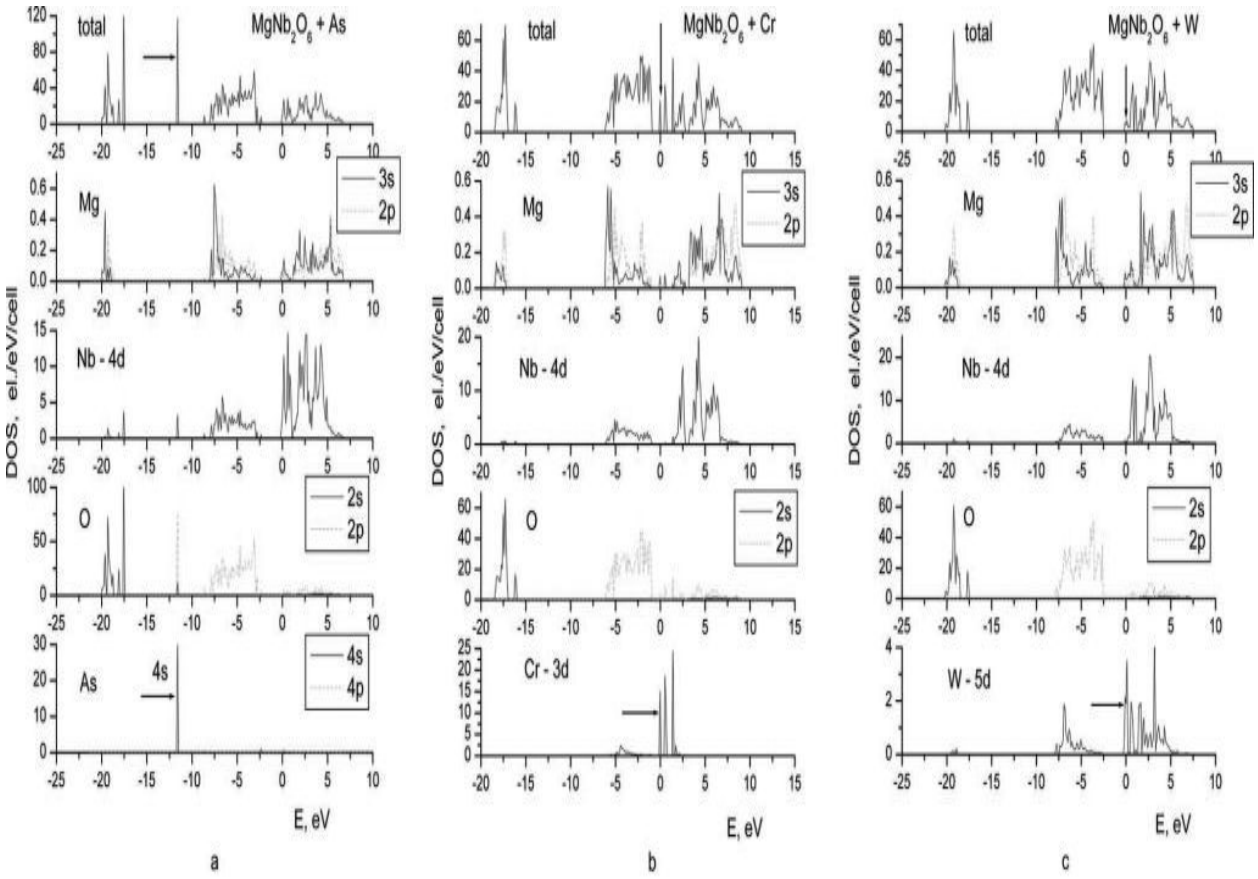

Figure 197. Electronic density of states for $MgNb_2O_6$ with As (a), Cr (b), and W (c)

Incorporation of 6A transition metal, such as Cr, Mo and W demonstrates similar features in the electronic structure as those resulting due to 3B doping. Incorporation of Cr, Mo and W as dopants introduce new states which are their own valence d-states located in the energy gap between valence and conduction bands and marked with arrows in **Figure 197**. In the case of $Mg[Nb_{0.875}Cr_{0.125}]_2O_6$, the partially occupied Cr 3d states are completely localized and separated from the main conduction band by an energy gap of ~ 0.6 eV. Quite a similar situation is observed for Mo doped $MgNb_2O_6$. There is also a partially occupied middle portion of Mo 4d states separated from the upper conduction band by a small energy gap of ~ 0.3 eV that facilitates electron transition to the conduction band and, thus improves the overall electronic

conductivity of the material. Finally, in the case of the W doped oxide, these corresponding W 5d states overlap with the Nb 5d conduction band thus resulting in the activation energy for the conductivity equal to zero. As regards to $MgTa_2O_6$ doped with Cr, Mo and W, all the three doped oxides remain semiconductors and there is no overlap between W 5d states and the Ta 5d conduction band.

Very similar results are obtained for the doping of Zn niobates and tantalates with corresponding dopants. **Figure 198** shows the total and partial DOS calculated for $Zn_{0.75}As_{0.25}Nb_2O_6$, $Zn[Nb_{0.875}Cr_{0.125}]_2O_6$ and $Zn[Nb_{0.875}W_{0.125}]_2O_6$. Apparently, it should be noted that the overall electronic structures of Zn based niobates are almost identical to those of Mg based oxides. The only qualitative difference is that observed in the case of W doped $MgTa_2O_6$ and $ZnTa_2O_6$.

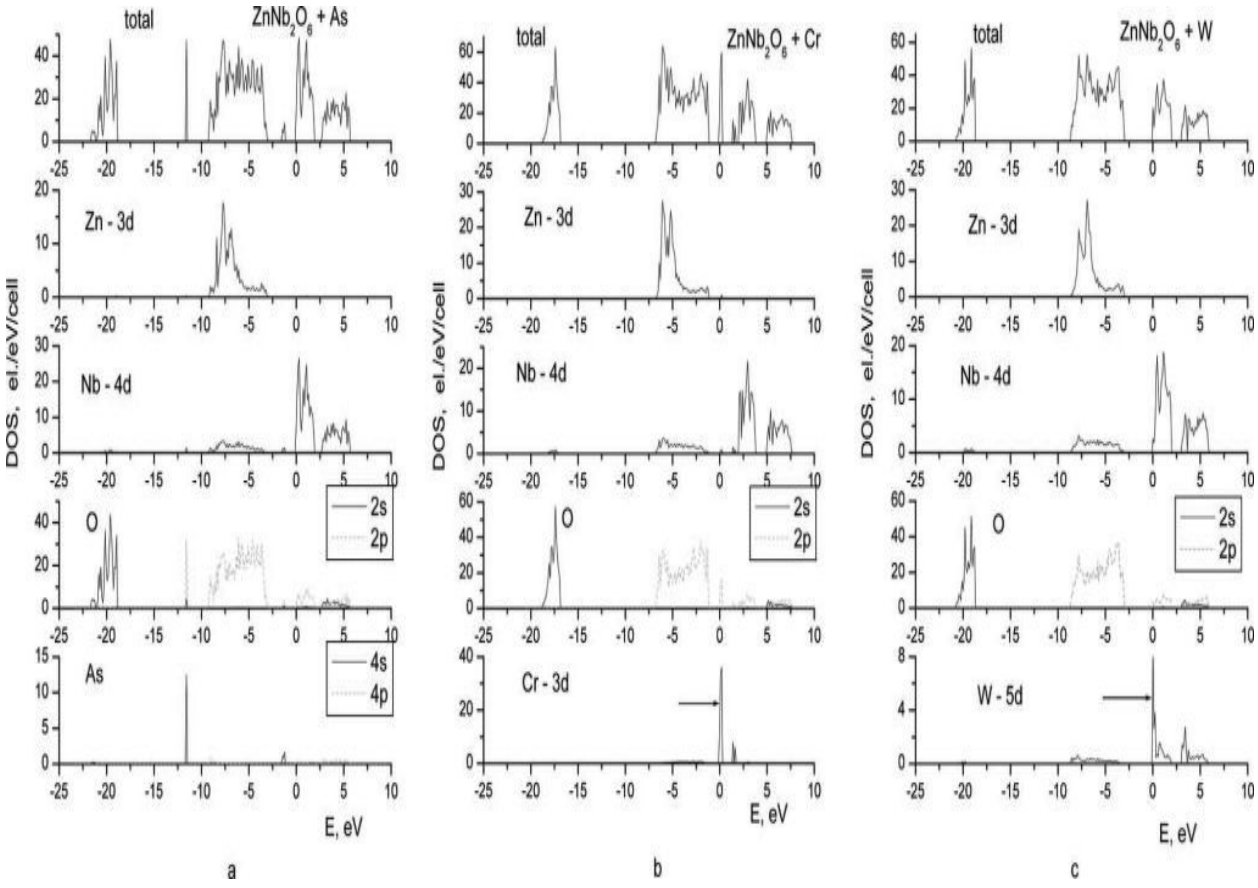

Figure 198. Electronic density of states for $ZnNb_2O_6$ with As (a), Cr (b), and W (c)

Figure 199 demonstrates the electronic DOS calculated for F doped $MgNb_2O_6$ and $ZnNb_2O_6$. As expected, F introduces its own local p-zone located ~ 1 - 2 eV below the main valence zone formed by 2p states of oxygen. Total density of states in the vicinity of the Fermi level is very similar to what one can see in the case of the structure doped with group 3A (Sc) and group 5B (As) elements. No impurity states appear within the band gap so that the Fermi level shifts towards the conduction band resulting in metallic conductivity of the material. Identical result is observed for F doped magnesium and zinc tantalates similar to that calculated for fluorine doped tin oxide (SnO_2:F) systematically investigated and reported by our group [56].

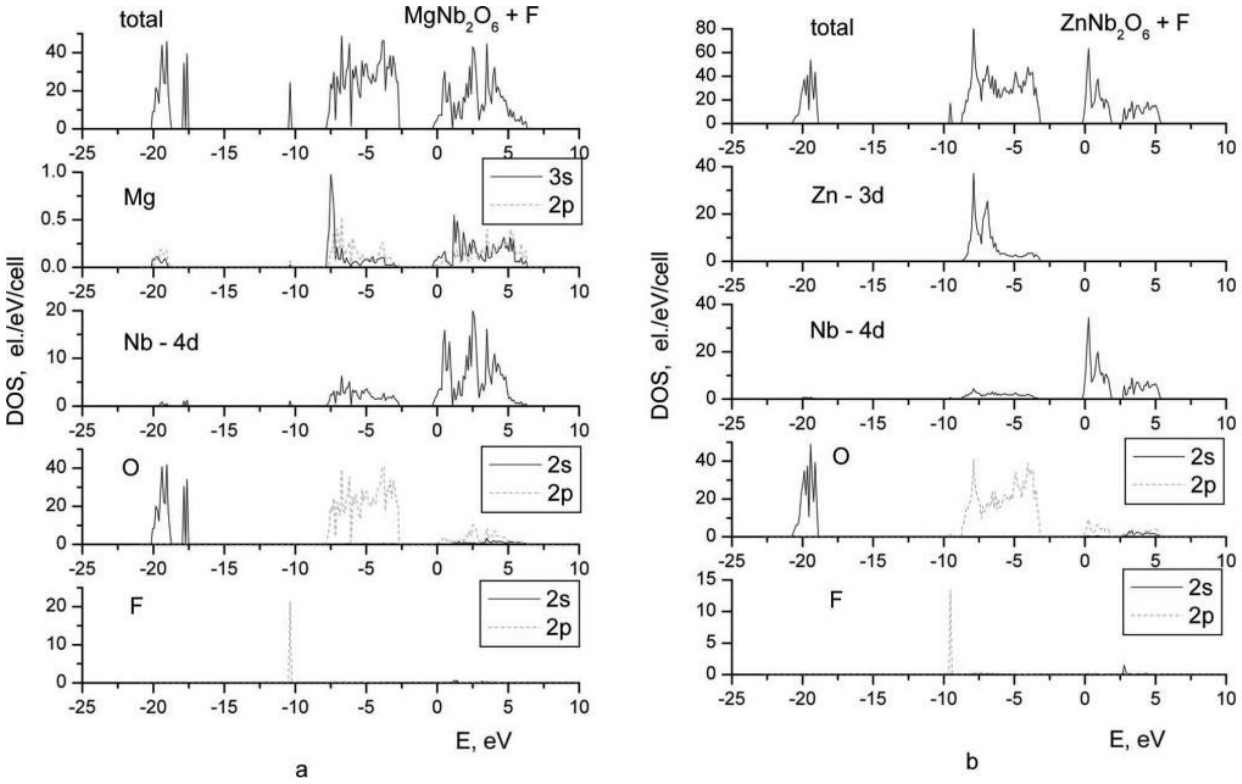

Figure 199. Electronic density of states for $MgNb_2O_6$ (a), and $ZnNb_2O_6$ (b) doped with F

Thus, based on the results obtained on the electronic structure peculiarities demonstrated due to introduction of the small amount of different elements from 3A, 3B, 5B, 6A and 7B periodic groups; one can make a conclusion that introduction of all the dopants do improve the electronic conductivity of doped magnesium and zinc niobates and tantalates, although to different extents. According to the energy values reported by Velikokhatnyi *et al.* [223], one can see that the presence of 3A, 3B (except boron and Ga in the case of $MgNb_2O_6$), 5B and 7B dopants help improve the electronic conductivity much better than those containing 6A. The compounds doped with Sc, Y, Al, Ga (except doped $MgNb_2O_6$), In, As, Sb, Bi, F and W (except doped $MgTa_2O_6$), demonstrate metallic conductivity, while B, Cr, Mo and Ga doped $MgNb_2O_6$ and W doped $MgTa_2O_6$ are characterized by the semiconductor behavior.

C.3.3 Structural and Chemical Stability

The present study is focused at identifying and hierarchically classifying materials in order of their electrochemical stability indicating their ability to withstand the harsh physical, chemical and electrochemical conditions prevalent during water electrolysis. Accordingly, the study is directed at identifying materials that are stable when exposed to acidic or other aggressive environments, and hence the chemical stability in the presence of an electric potential dictated by the cohesive energy is more relevant as opposed to the mechanical strength and is the main focus of the current work. The value of the cohesive energy E_{coh}, thus could serve as a qualitative criterion for comparing and selecting materials that would likely exhibit the most resistance to decomposition when exposed to chemically reactive environments of aggressive acids and bases prevalent during water electrolysis.

The calculated cohesive energies for pure and the doped oxide structures considered in the present study is shown in **Figure 200**. One can see that all the tantalate compounds have higher absolute values of cohesive energy than their corresponding niobium analogs and thus, can be considered to be more stable. This can be expected due to the stronger Ta - O interactions in comparison with the Nb - O bonds in the (Ta/Nb)-O_6 octahedra. Based on the calculated values of cohesive energy per atom in the unit cell, the structural stability of the materials increases as follows: $MgNb_2O_6$ (- 6.30eV/atom) < $ZnNb_2O_6$ (- 6.31 eV/atom) < $ZnTa_2O_6$ (- 6.82 eV/atom) < $MgTa_2O_6$ (- 7.21 eV/atom). Also, it can be seen that basically an introduction of almost all dopants renders the magnesium based compounds less stable than the parent oxides, although to different extents. The only exception is the doping of 3A group elements which renders both $MgNb_2O_6$ and $MgTa_2O_6$ even more stable. This directly relates with the Sc - O and

Y - O bonds which are stronger than the Mg - O bonds of the corresponding parent compounds. Bond dissociation energies of Sc - O, Y - O and Mg - O diatomic molecules are 671.4 kJ/mol, 714.1 kJ/mol and 358.2 kJ/mol respectively [225]. All other dopant elements either do not change or decrease the structural and chemical stability.

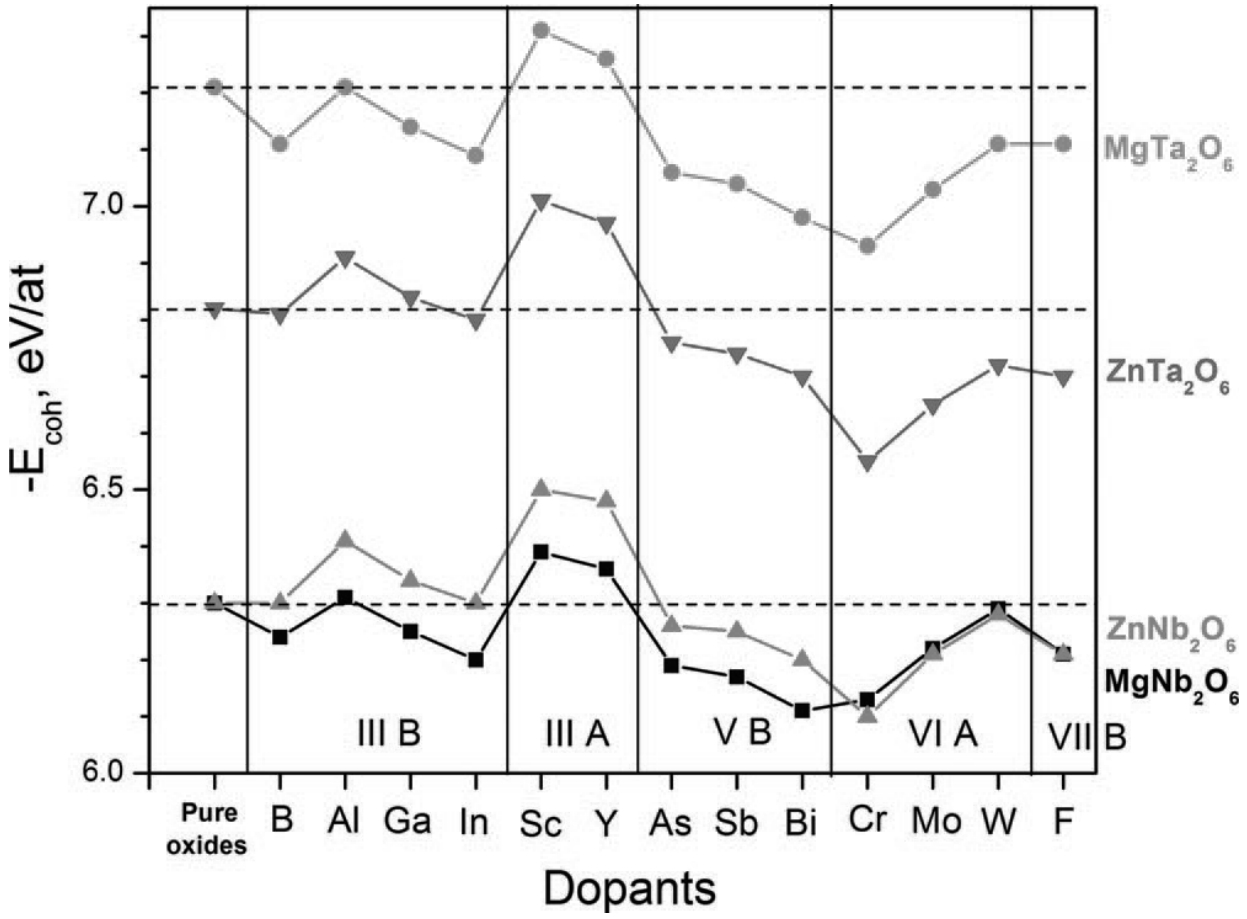

Figure 200. Cohesive energy for all materials studied in eV/at

As for doped $ZnNb_2O_6$ and $ZnTa_2O_6$, not only Sc and Y improve their stability similar to Mg based oxides, but Al and Ga also make these oxides more stable in comparison with the pure undoped parent oxides. Although a substantial amount of doped compounds are less stable in

comparison with the corresponding pure parent oxides, all the doped materials are more stable than pure SnO_2 or F doped SnO_2 that is commonly used as the catalyst support material for water electrolysis (calculated E_{coh} for pure SnO_2 is - 5.08 eV/at and for SnO_2 doped with ~ 6.2 wt.% F is - 4.74 eV/at).

This allows us to conclude that in terms of general stability, the tetragonal trirutile $MgTa_2O_6$ with a cohesive energy of - 7.21 eV/atom can be marked as the most stable compound among the entire four parent oxides considered in the present study. However, $MgTa_2O_6$ doped with Sc and Y render the oxide even more stable with E_{coh} = - 7.31 and -7.26 eV/at, respectively. It is also noteworthy to mention that among all the magnesium and zinc tantalates considered in the study, the least stable is $ZnTa_2O_6$ doped by Cr with E_{coh} = - 6.55 eV/at. However, it demonstrates higher stability in comparison to the most stable niobate $ZnNb_2O_6$ doped with Sc indicating a E_{coh} = - 6.50 eV/at. Hence it could be construed that the tantalite based compounds are more resistant to decomposition and cleavage of the primary bonds when exposed to harsh mechanical or chemical environments such as those likely experienced by these systems when used in highly corrosive acidic environments typically encountered in water electrolysis and the oxygen reduction reactions (ORR) in proton exchange membrane fuel cells.

To validate the theoretical calculations, we synthesized $ZnNb_2O_6$ doped with small amount of yttrium. For these purposes mixtures of powders of zinc oxide (ZnO, Alfa Aesar, 99.9%), niobium oxide (Nb_2O_5, Alfa Aesar, 99.95%) and yttrium oxide (Y_2O_3, Acros, 99.99%) of compositions with yttrium doping up to 1 at. % with a formula unit $(Zn_{0.9}Y_{0.1})Nb_2O_6$ were subjected to a mechano-chemical reaction in a high energy shaker mill (SPEX CertiPrep 8000M) for up to 15 minutes in a stainless steel (SS) vial using 20 SS balls of 2 mm diameter (~ 20 g) with a ball to powder weight ratio 10 : 1. The mechano-chemical miled powders obtained were

sintered in air at 1000°C for 12 hours. Pellets were prepared by compacting the powder using a uniaxial pressure of 7000 lb in a manual press (Carver Inc.).

In order to study the structural stability of the material, chronoamperometry (current signal *vs.* time) has been performed at ~ 1.75 V (*vs.* NHE) for ~ 3 hours using 1 N H_2SO_4 as an electrolyte. The H_2SO_4 solution is kept at a constant temperature of 40°C using a Fisher Scientific 910 Isotemp Refrigerator Circulator. The chronoamperometry (CA) signal was recorded using platinum as a counter electrode and Hg / Hg_2SO_4 as a reference electrode that has a potential of + 0.65V *vs.* NHE. The CA curve for $(Zn_{0.9}Y_{0.1})Nb_2O_6$ is shown in **Figure 201**. The CA curve shows a marked decay of current in the initial period of ~ 30 min with further stabilization of the current. Since this material itself is catalytically inactive (catalyst support only), the CA curve reflects a degree of corrosion occurring at the surface of the electrode. The faster the material degrades, the higher current signal versus time should be detected. It is seen that no increase of current is observed indicating high stability of zinc niobate doped with small amount of yttrium. It is worth to note that according to our calculations, $ZnNb_2O_6$ has lower cohesive energy than those of both zinc and magnesium tantalates (**Figure 200**), which means that $ZnTa_2O_6$ and $MgTa_2O_6$ are expected to demonstrate even higher electrochemical stability than $ZnNb_2O_6$ oxide, thus confirming our theoretical predictions.

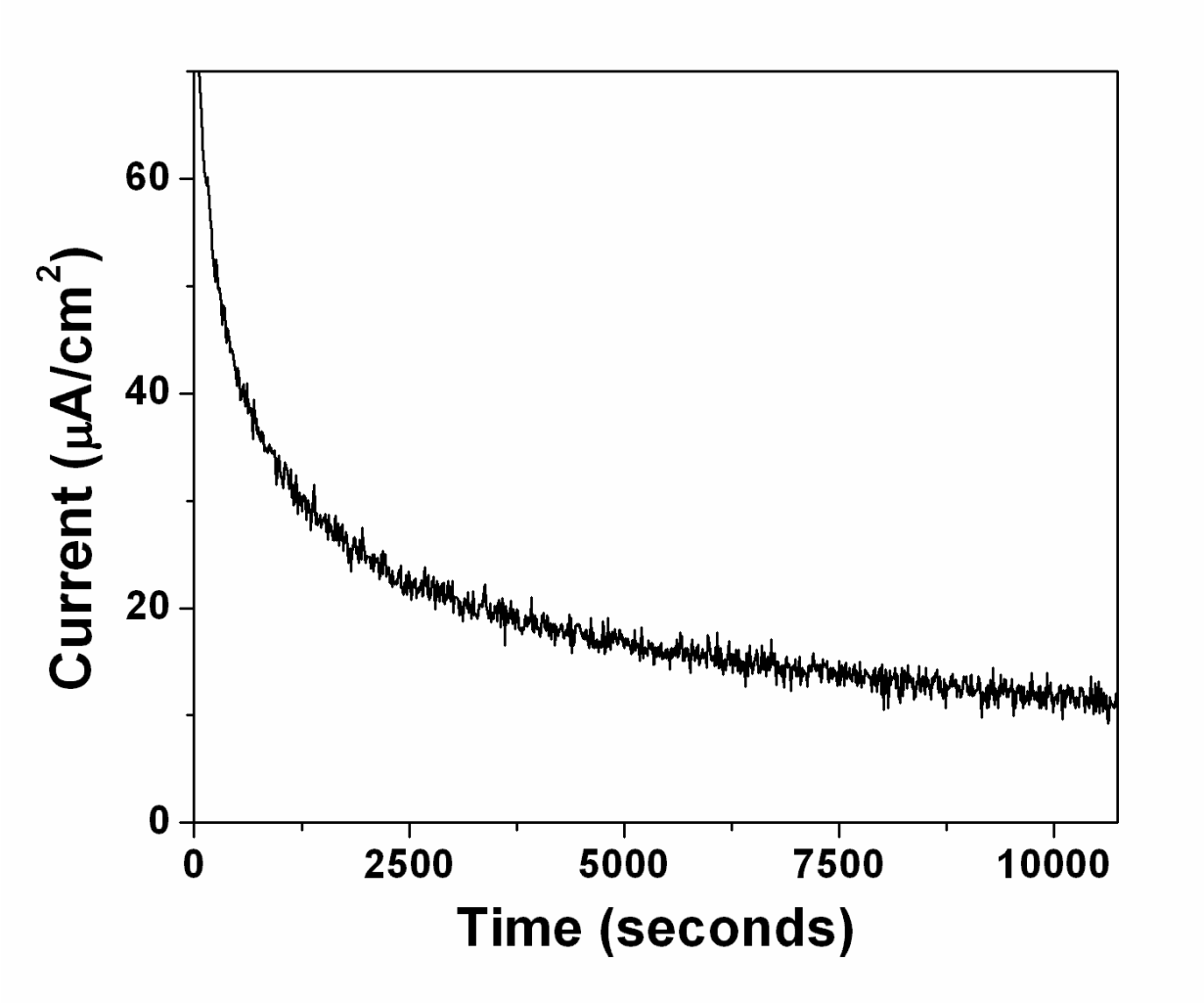

Figure 201. Variation of current vs. time in the chronoamperometry test performed on $(Zn_{0.9}Y_{0.1})Nb_2O_6$ in a 1 N H_2SO_4 solution at 1.75 V (*vs.* NHE)

C.4 CONCLUSION

An attempt to identify new electrochemically stable catalyst supports for PEM water electrolysis using *ab-initio* DFT approach has been undertaken in the present study. Magnesium and zinc

niobates, and magnesium and zinc tantalates, have been chosen for systematic investigation of the influence of small amounts of dopants selected from group 3A, 3B, 5B, 6A and 7B of the Periodic Table on the electronic conductivity and structural stability of the compounds. The study showed that small amounts of 3A, 5B, 7B and the most of 3B group elements noticeably improve the conductivity in comparison to the elements from group 6A of the Periodic Table.

Also, a comparison of the cohesive energies calculated for the pure and doped oxides displayed $MgTa_2O_6$ and Y doped $MgTa_2O_6$ to be the most stable compounds among all materials considered in the study. The study thus allows us to hypothesize based on electronic conductivity and cohesive energy considerations that among all the materials considered in the present study, $MgTa_2O_6$ doped with Sc and Y are the most appropriate candidates for use as a catalyst support in water electrolysis.

APPENDIX D

SUPERCAPACITORS

D.1 VANADIUM OXIDE - CARBON NANOTUBE HETERO-STRUCTURES

D.1.1 Introduction

Rapid progress in electronic device technology in recent years characterized by the widespread proliferation of smart professional and personal gadgets such as smart cell phones, tablets, camcorders, and laptops has provided a major impetus for energy storage devices capable of delivering high power and energy over a sustained period of time. Research in energy storage materials over the past several decades have focused on developing either battery materials capable of very high rate capabilities or supercapacitors with relatively high energy densities [226-228]. Supercapacitors are typically characterized into two classes based on non-Faradaic charge storage that occurs primarily on the surface of electrochemically active materials named aptly as electrochemical double layer capacitors (EDLC). A second class of capacitors is termed as pseudo-capacitors wherein charge transfer is brought about by virtue of Faradaic electrochemical redox reactions undergone by specific electrochemically active elements within

a compound or compounds. With regards to these systems providing high power and energy densities, pseudocapacitor materials fit this bill very well on account of the charge storage mechanism that tends to be a hybrid match of both the battery and supercapacitor worlds [229].

Psuedo-capacitors involve a chain of successive reversible Faradaic reactions occurring at the surface involving one or more electrochemically active elements thus ensuring short charging times and seemingly infinite cyclability. Most commonly studied pseudocapacitors are hydrous ruthenium oxide and manganese oxide, the former limited by the high cost and the latter restricted primarily due to the low capacity occurring as a result of poor electronic conductivity in bulk systems, respectively [230-234]. There is therefore an urgent need for identification of alternate chemistries showing promise as economically viable pseudo-capacitor materials exhibiting reliably high energy densities.

Transition metal oxides are very attractive for this kind of application on account of their ability to accept variable oxidation states. In addition, they tend to exhibit good bulk electronic conductivity and atmospheric stability. Of particular interest to pseudocapacitor applications is the ability of the surface oxide to undergo reversible electrochemical reactions as is the case in Ruthenium oxide [227, 229]. The I-V characteristic of the successive oxidation/reduction reactions at the surface of the electrode resemble that of a capacitor, hence the term pseudocapacitor. Hydrous Ruthenium oxide is an excellent pseudocapacitor material with the ability to maintain stable capacitances of upto 900 Fg^{-1} over a large number of cycles [235]. However, the prohibitive price of noble metal oxides impels the search for alternative oxide materials with similar charge storage characteristics. One such oxide resembling the multiple oxidation states of the metal similar to Ru is vanadium oxide which has previously been studied as a supercapacitor material in non-aqueous electrolytes [236-240]. Vanadium is an element

belonging to Group 5 of the periodic table with a half empty d-shell allowing it to exhibit multiple valence states of + 2 to + 5.

Vanadium oxide has previously been studied as a material for lithium ion battery cathodes. Different morphologies of the oxide including nanotubes have been explored. Amorphous and hydrated vanadium oxide has also been studied widely as a viable supercapacitor electrode in lithium and sodium ion electrolytes [237, 238, 241, 242]. Amorphous vanadium oxide gel/ carbon composites have demonstrated capacities ~ 360 mAh/g with very high intercalation rates. Oxide nanotubes on the other hand, have been studied extensively by Nesper *et al.* [243, 244] as electrode materials using lithium ion electrolytes and have shown great promise. In addition, a class of so called Lithium-ion based aqueous supercapacitors have been identified by Hu *et al.* demonstrating capacitances of upto 740 F/g in aqueous LiCl [245-248]. In all these studies, thin oxide films have shown to result in good electrochemical performance on account of the short diffusion lengths for lithium intercalation. The importance of loading and its influence in achieving attainable capacitance in vanadium nitride based supercapacitor has been highlighted by us in our earlier work [249]. Nanoparticulate materials such as oxides/nitrides of transition metals are very advantageous in terms of achieving desirable electrochemical performance on account of the high specific surface area (SSA) and the enhanced activity that is achievable at the nano-scale dimensions. However, the very nanoparticulate nature which is responsible for enhanced electrochemical activity results in loss of conductivity on account of the large number of grain boundaries. Nanostructured vanadium oxide has a relatively low conductivity [250-252] on the order of 10^{-6} - 10^{-2} $\Omega^{-1}cm^{-1}$. The high electronic conductivity of carbon nanotubes (CNTs) on the other hand, could thus be exploited to create composite 3-D architectures to minimize the oxide–oxide particle contact

leading to efficient electron transport from the current collector to the surface of the vanadium oxide upon which the pseudocapacitance behavior is exhibited. In order to achieve this, architecture similar to that shown by Jampani *et al.* [253] comprising vertically aligned carbon nanotubes (VACNT) covered with electrochemically active vanadium oxide would be ideal to obtain maximum capacitance while allowing for slight expansion/contraction likely as a result of the ensuing possible phase change.

Carbon based hetero-structures have demonstrated improved rate capabilities for various Li-ion and supercapacitor electrode materials including silicon, ruthenium oxide, manganese dioxide and nickel oxide [254-262]. Electrodeposited amorphous hydrated vanadium oxide coatings on CNTs have shown to exhibit capacitances as high as 910 F/g by Kim *et al.* [237] and Balkus *et al.* [263] in lithium electrolyte cells. In a recent report Sathiya *et al.* reported energy storage behavior of oxide coated carbon nanotubes in a Swagelok type cell with a lithium electrolyte and a lithium counter electrode exhibiting capacities as high as 850 mAh/g with up to 60 % of the energy storage coming from a capacitive contribution [264]. Vanadium oxide/CNT composites have also been explored for capacitance behavior in aqueous electrolytes and capacitances as high as 400 F/g have been reported [265]. A similar approach of using a 3-D conducting support to create conductive heterostructures was recently exploited by Yushin *et al.* wherein they demonstrated that vanadium oxide thin films on Al nanowires generated by atomic layer deposition could be used as electrode materials in a Li-ion based supercapacitor [266, 267].

Chemical vapor deposition (CVD) is an ideal and versatile method to obtain uniform architectures on carbon structures [268, 269] while also tailoring the nature of the deposited film depending on the deposition conditions. Various groups have previously reported CVD as a technique for the growth of vanadium oxide thin films [254, 270-276] using both chloride and

metal organic precursors. Oxide films with varying V oxidation states have been reported with ratios of oxides depending on the various deposition conditions including temperature and reagent concentrations [275].

In this work, we have explored an atmospheric pressure chemical vapor deposition (APCVD) method to deposit nanospheres of vanadium oxide on CNTs for use as a supercapacitor electrode in aqueous media. Implementation of CVD as a synthesis method also provides the advantage of avoiding the incorporation of binders for generating the electrodes which can consume upto 50 % of the total weight of the electrode in high surface area systems contributing largely to inactive dead weight [255, 269].

The aim of the current work is to highlight the effects of depositing vanadium oxide on vertically aligned carbon nanotubes serving as an electronically conducting matrix thus enabling the attainment of high capacity in vanadium oxide systems. We have therefore explored the unique morphology of the CVD synthesized VACNT-vanadium oxide nanosphere composite as a viable material for aqueous supercapacitors over an extended voltage window [253]. It is also an attempt to establish that really high capacitances can be achieved in thin film vanadium oxide coated in such a configuration.

D.1.2 Experimental Section

A two step CVD process was used to obtain vanadium oxide nanosphere coated CNT hetero-structures on nickel substrate disks. First, the nickel disks were properly cleaned using dilute acids and acetone, and then weighed. Vertically aligned carbon nanotubes (VACNTs) were then deposited on the Ni disks following a method similar to that reported by Ajayan *et al.* using an

Ar / H_2 mixture [277, 278]. A mixture of ferrocene in m-xylene was used as the carbon source with ferrocene acting as the catalyst for CNT nucleation and growth. The mixture was vaporized and bled into a hot-wall CVD tube maintained at 770 ^oC. A low temperature APCVD setup was then used to deposit the vanadium oxide nanospheres directly on the vertically aligned carbon nanotubes. Vanadium oxide nanospheres were deposited on the VACNTs using vanadium chloride (VCl_4, Sigma Aldrich) and distilled water (Millipore QGARD, 18.2 MΩcm) as the precursors. Both precursors were evaporated and carried into a hot wall CVD reactor wherein the CNT coated nickel (Ni) disks were placed using two independent nitrogen gas streams [275]. Deposition was carried out at 450°C for 45 minutes. The oxide coated disks were then weighed and characterized. Vanadium oxide was also directly deposited on Ni substrate disks by CVD using the same precursors to compare the electrical and electrochemical properties of the plain oxide film with that of the composite heterostructure comprised of oxide nanospheres coated on CNTs.

The nature of the deposition including morphology of the oxide on the CNTs needs to be understood for better understanding of the observed capacitance behavior. To investigate the microstructure of the CVD deposited vanadium oxide nano-spheres and films, scanning electron microscopy (SEM) analysis was conducted on a Philips XL30 machine operating at 20 kV. The atomic composition of the film was also verified using EDAX. To identify the crystalline nature of the oxide coated on the CNTs and to identify any amorphous deposits other than the oxide present on the CNTs, micro-Raman spectroscopy was performed on a Reinshaw inVia Raman microscope. Raman spectra were collected in air at room temperature using a 633 nm laser. Low laser intensities were chosen to avoid heating of the samples and the spectra were collected by averaging multiple scans over a frequency range of 3500-100 cm^{-1}.

To further characterize the oxide-CNT interface, high-resolution transmission electron microscopy (HRTEM) was performed on a JEOL JEM-2100F microscope to observe the morphology of the nanospheres-CNT interface. HRTEM images could also give us an insight into the mechanism of growth of nanospheres on the CNTs. Samples for HRTEM were prepared by scraping off the vanadium oxide deposited CNTs from the Ni substrate and dispersed on 3.05 mm diameter copper grids (JEOL) containing a holey carbon film in methanol by sonication. The grids were then vacuum dried for 24 hours and used for conventional and HRTEM characterization.

To analyze the surface composition, determine the valence state of V ions in the oxide-VACNT composite, x-ray photo electron spectroscopy (XPS) was performed on a Perkin-Elmer PHI-5600 ESCA system. XPS was conducted using a Physical Electronics (PHI) model 32-096 X-ray source control and a 22-040 power supply interfaced to a model 04-548 X-ray source with an Omni Focus III spherical capacitance analyzer (SCA). The system is routinely operated within the pressure range of 10^{-8} to 10^{-9} Torr (1.3×10^{-6} to 1.3×10^{-7} Pa). The system was calibrated in accordance with the manufacturer's procedures utilizing the photoemission lines, E_b of Cu $2p^{3/2}$ - 932.7 eV, E_b of Au $4f^{7/2}$ - 84 eV and E_b of Ag $3d^{5/2}$ - 368.3 eV for a magnesium anode. All the reported intensities are in effect experimentally determined peak areas divided by the instrumental sensitivity factors. Charge correction was obtained by referencing the adventitious C 1s peak to 284.8 eV.

Since the electronic conductivity is a crucial parameter affecting the supercapacitor performance, four point probe conductivity set up was used to measure the conductivity of the vanadium oxide films prepared by CVD. A Veeco FPP 5000 four-probe conductivity instrument (Miller Design & Equipment, Inc.) was used for the measurements and the sheet resistance

values obtained were then converted to electrical conductivity. Four-probe conductivity data is usually obtained by preparing pellets from powders and supporting them on insulators while maintaining contact with four equally spaced probes, two of which supply current while the other two measure voltage across them. The measurement of resistivity of thin films on conducting metal substrates however is a difficult proposition. This is because the flow of electrons from the two current probes would probably occur through the substrate current collector. This current flow does not however occur in the CVD derived oxide and the VACNT-oxide nanosphere composite as the deposit is sufficiently thick and crack free to avoid interference from the substrate.

Cyclic voltammetry was performed on the synthesized oxide and oxide-VACNT heterostructure materials to test their viability as high energy density supercapacitor materials. A three electrode cell configuration was used to perform cyclic voltammetry measurements and electrochemical impedance spectroscopy analysis on the coated Ni disks to both understand the electrochemical mechanisms involved as well as evaluate the specific capacitance of the both the VACNT-vanadium oxide nanosphere composite as well as vanadium oxide thin films prepared by chemical vapor deposition. The cell was assembled with a platinum counter electrode, Ag/AgCl (in 3M KCl) reference electrode, and the active material coated Ni disks described above as the working electrode. An aqueous Na_2SO_4 solution of unit molarity was used as the electrolyte.

Cyclic voltammetry tests were performed on a Princeton Applied Research (PAR) Versastat-3 potentiostat from -1 V to 0.8 V with respect to reference to evaluate the specific capacitance of vanadium oxide thin films and vanadium oxide-VACNT heterostructures generated by CVD. Cycling was performed at different scan rates and area of the cyclic

voltammogram was used to calculate capacitance. Gravimetric capacitance values were evaluated on the basis of both the oxide weight as well as the weight of the total active material.

To further evaluate the supercapacitor response of the CVD-deposited vanadium oxide film as well as vanadium oxide-VACNT heterostructures, electrochemical impedance spectroscopy was performed on the Versastat 3 (Princeton Applied Research) over a frequency range of 0.01Hz-100 KHz. 5 mV amplitude was used and the spectra were collected between -1.0 and 0.8 V at intervals of 100 mV. The impedance spectra were obtained on both the thin film oxide and the VACNT-oxide nanosphere composite heterostructure hybrid electrodes to observe any noticeable changes in charge storage mechanism induced by the presence of carbon nanotubes. ZView (Scribner Associates) software was used for identifying the circuit and the various circuit parameters to match the response of the impedance spectra.

D.1.3 Results and Discussion

Figure 202 shows the scanning electron microscope image of vertically aligned CNTs deposited by chemical vapor deposition on Ni substrate (a), the nature of the oxide film on Ni substrate (b) and the nature of the oxide deposited on the carbon nanotubes (c). The length of each individual tube has been identified to be about 200 µm. It is expected that the prolific length of the CNTs would help create a very good 3-D architecture which could be covered with a thin layer of the oxide to maximize volumetric loading while at the same time ensuring that a very thick film does not cover the carbon nanotubes impeding the proper electronic transport channel. It can be seen that the oxide deposited is in the form of 0.2 - 0.5 µm diameter globules. The globules cover the length of the tube at regular spacing between each globule. This allows for maximum CNT-oxide

electron transport minimizing electron transport through the oxide grain boundaries which naturally will act as a barrier to electron transport. The nanosphere morphology also leads to increased surface exposure of the oxide to the electrolyte *i.e.* maximizing the electrochemical surface area and affording maximum exploitation of the capacitance behavior.

Figure 203 show the EDAX analysis (a) and respective compositions of the oxide film deposited on Ni disk and the VACNT-oxide nanospheres (b). It can clearly be seen that the oxide has a composition of V_2O_{5-x} with x ~ 0.4 in both cases. This indicates that the moderately high temperature of 450°C afforded by the CVD process allows for the synthesis of the oxide at its highest oxidation state with very few defects. A less defective structure at a higher oxidation state is ideal to achieve minimum electron conductivity losses with lower defects, and thus also contributing to better stability of the composition.

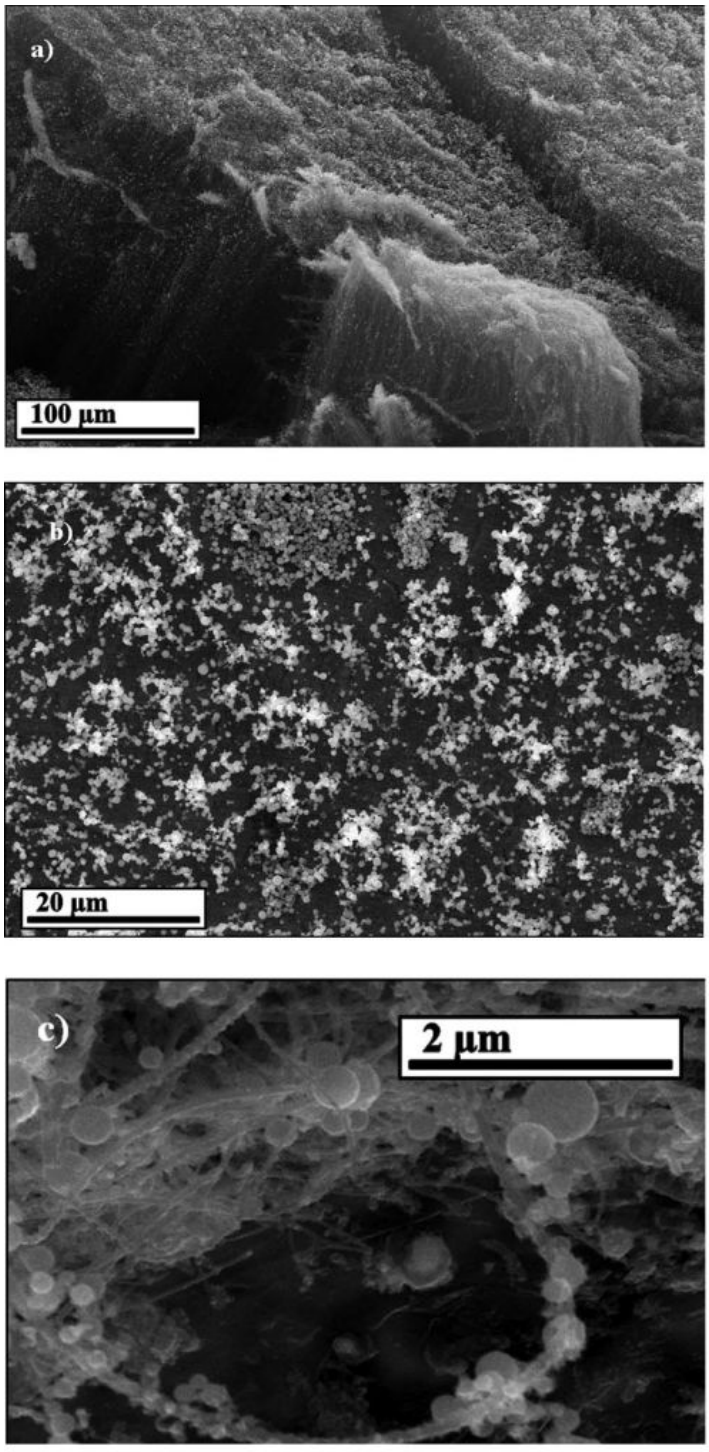

Figure 202. Scanning Electron Microscope images of CVD derived VACNT (a), CVD derived VO_x thin film on Ni (b), and CVD deposited VO_x-VACNT heterostructures (c)

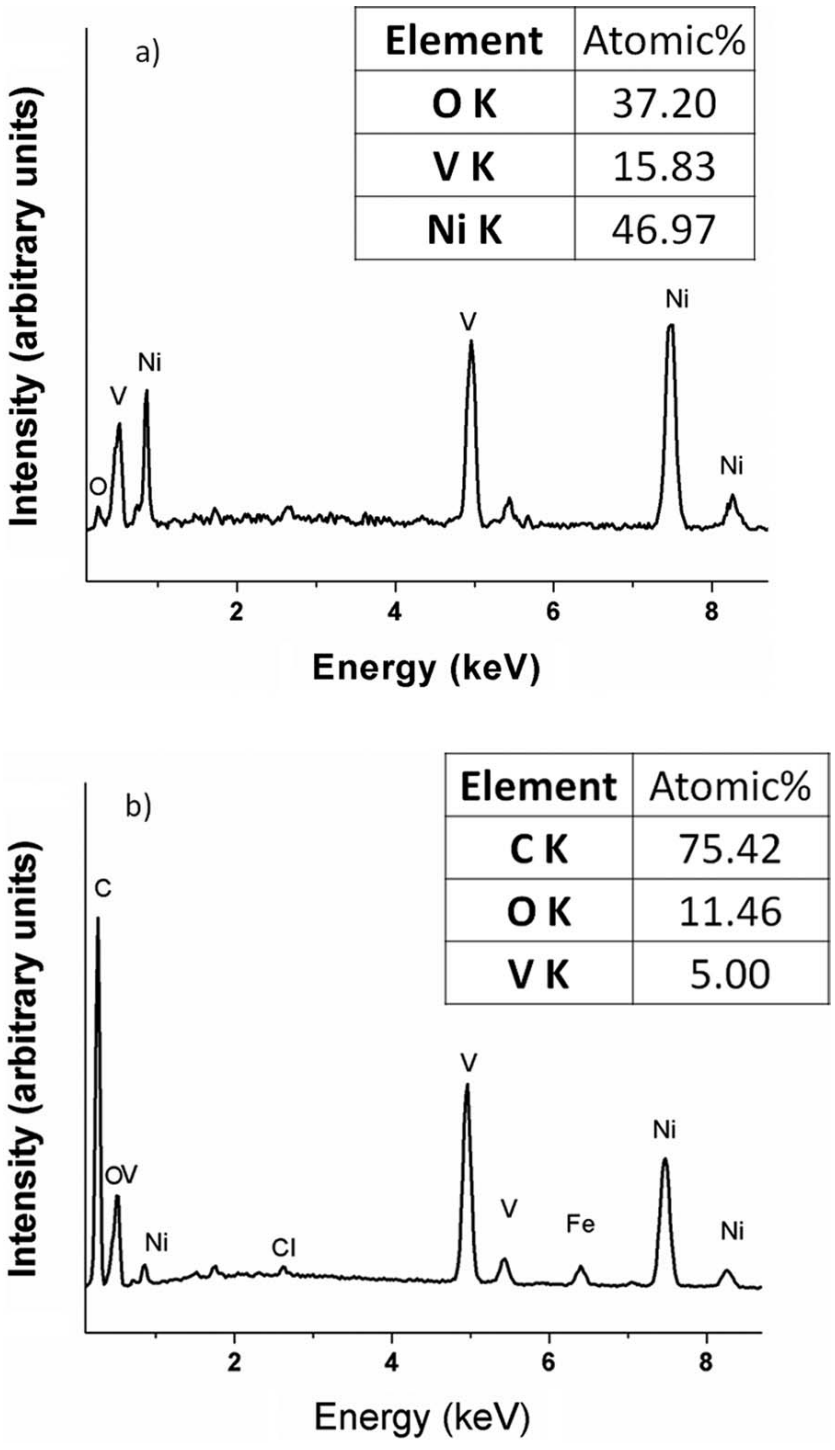

Figure 203. EDX spectra of the CVD deposited thin film on Nickel (a) and CVD deposited-VACNT heterostructures (b)

In order to confirm the composition and nature of the oxide deposit on CNTs, Raman spectroscopic analysis was performed on the material. **Figure 204** shows the Raman spectrum collected on the carbon nanotubes (a) and the vanadium oxide coated on the CNTs (b). The D, G and G' bands are clearly observed at 1250, 1650 and 2650 cm^{-1}, respectively. It is clearly observed that the G/D (I_g/I_d = 1.59) ratio is much greater than one indicating few lattice defects in the graphene layers indicating the MWCNTs would have relatively high conductivity [279, 280]. Several peaks marked have been identified to correspond closest to those of thin filmV_2O_5 [281] and those of vanadium oxide corresponding to VO_x - carbon nanofibers reported previously [282].

In order to confirm the morphology of the nanospheres on the surface of the CNTs, high resolution transmission electron microscopy (HRTEM) was performed on samples scraped off and dispersed onto Cu grids. **Figure 205** shows the image of a vanadium oxide nanosphere covering a carbon nanotube. It can be seen that the diameter of the nanospheres is about 250 nm. Upon closer examination, it can be seen that the oxide nanosphere has an amorphous morphology with no periodic arrangement. The interplanar separation between the CNT layers has been measured to be ~ 0.35 nm. This corresponds to the value reported for that of graphite (d_{002} = 0.35 nm) and multi wall CNTs of diameter 20 nm [283, 284]. The interface of the CNT and the oxide is an important factor that would determine the nature of the electron transport and stability of the oxide particle.

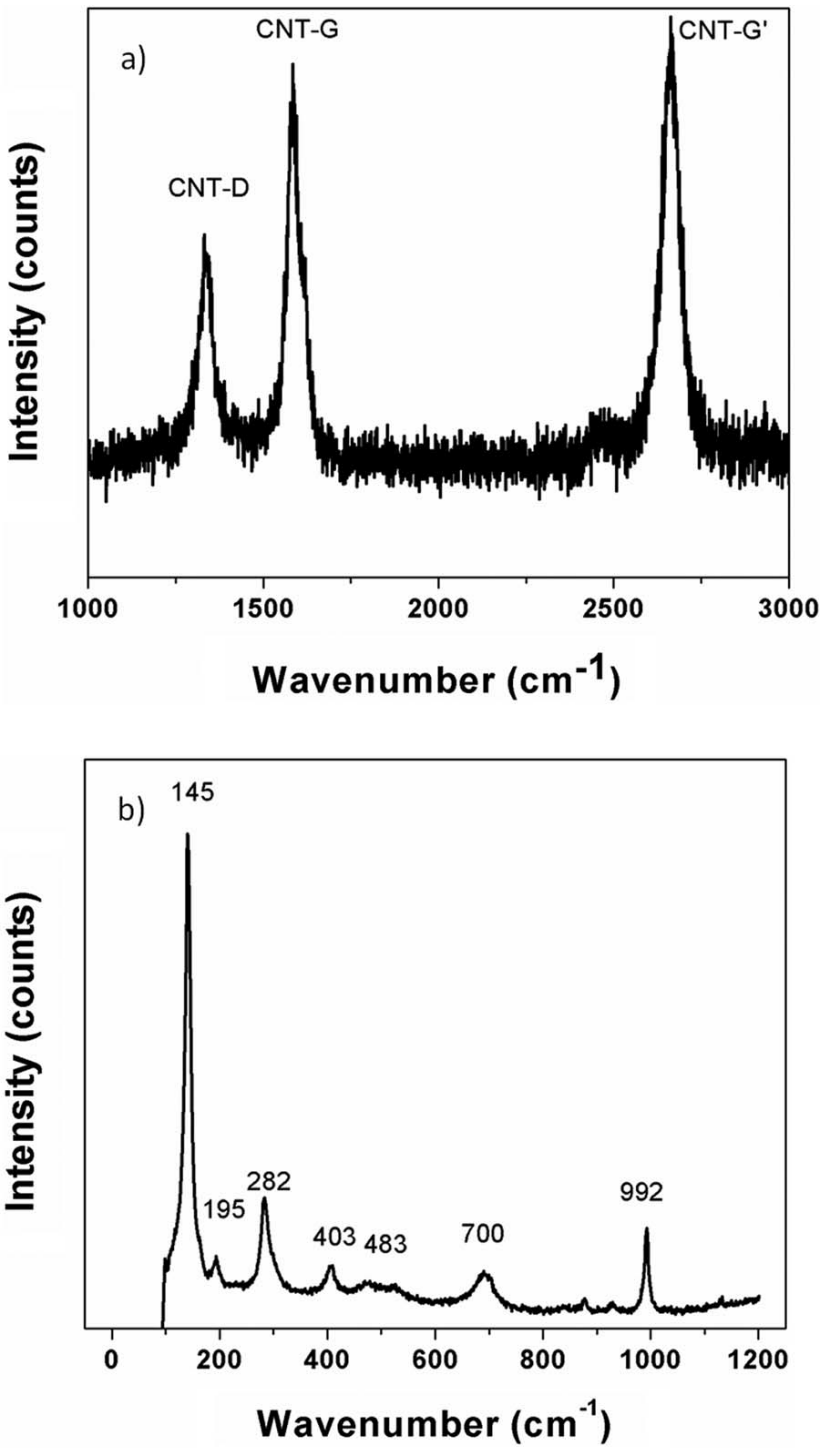

Figure 204. Raman spectra of VACNTs (a) and Vanadium oxide coated on the CNTs (b)

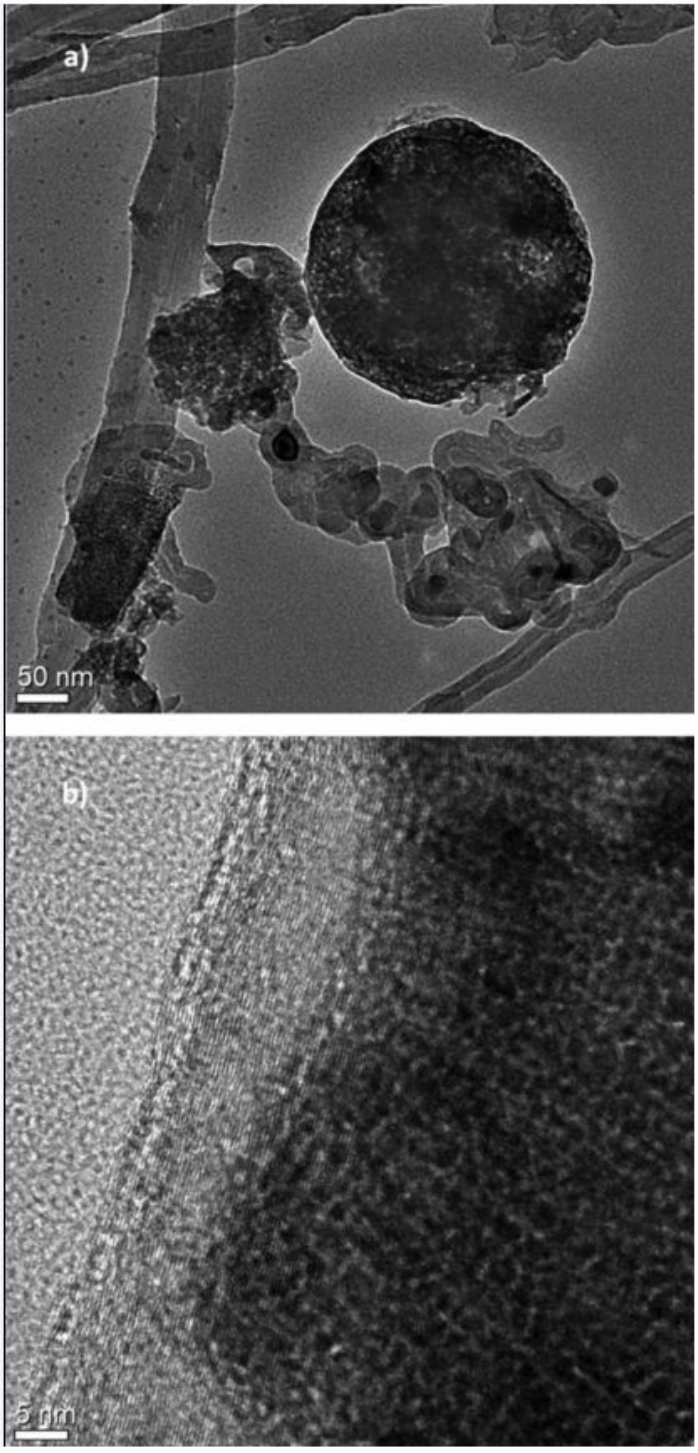

Figure 205. HRTEM images of the vanadium oxide nanospheres coated on Multiwall CNTs

In order to determine the chemical oxidation states of V and O in the VACNT-oxide nanosphere composite electrode, x-ray photoelectron spectroscopy (XPS) techniques has been conducted on a Phillips PHI 5600 system. The XPS spectra of V_{2p} and O_{1s} peak of vanadium oxide are shown in **Figure 206**. The binding energy of vanadium [V $2p^{3/2}$ (517.0 eV) and V $2p^{1/2}$ (524.378 eV)] is indicative of V in the oxidation state between + 4 and + 5 [285, 286]. The binding energy of oxygen O 1s (529.84 eV) corresponds to a high oxidation state of the metal around + 4 / + 5 oxidation state. This binding energy of vanadium corresponds to that of vanadium predominantly being present in a high oxidation state. It has previously been identified that high oxidation state of vanadium in vanadium oxide is amenable for improved supercapacitor performance. The vanadium oxide coated on the VACNTs synthesized by CVD possesses a high oxidation state mixture of V^{5+} / V^{4+} similar to that of other promising oxide materials used in supercapacitors [245, 287].

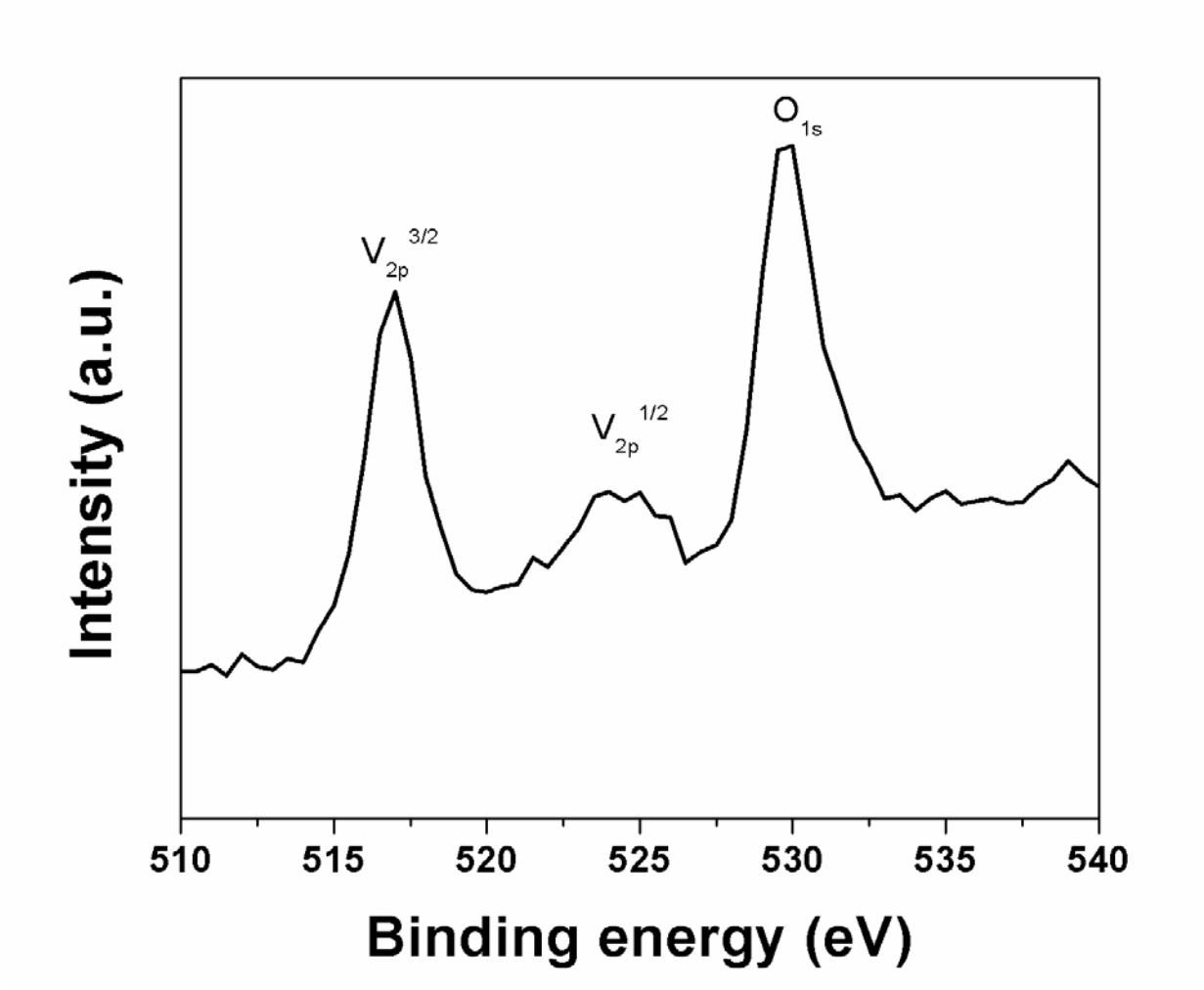

Figure 206. XPS of CVD deposited VACNT-oxide nanosphere heterostructures

Four-probe conductivity measurements were performed on both thin film oxide and VACNT-supported vanadium oxide nanospheres. Sheet conductivity data was obtained using a Veeco - FPP 500 instrument wherein the coated Ni disks were suppressed onto standalone tips and voltage vs. current was measured. Sheet resistance data were multiplied with thickness to obtain bulk resistivity. Bulk resistivity values were averaged and found to be ~ 0.46 Ωcm for the oxide nanospheres coated on CNTs as compared to ~7.5 Ωcm for thin film oxide. Bulk oxide values reported in the literature range between 10^3 and 10^4 Ωcm [252]. The electronic

conductivity of the nickel disk was found to be 9.3 x 10^{-6} Ωcm. This is in agreement with the hypothesis that the four-probe conductivity data does not bear an artifact from the current collector as the conductivity of the VACNT-oxide composite is ~ 5 orders of magnitude lower than that of the nickel disk itself. The deposition of oxide nanospheres on CNTs therefore leads to conductivities similar to those of vanadium oxide nanowires reported previously [288]. This increase in conductivity would thus likely lead to enhanced electron transport and higher rate capability.

Figure 207 shows the cyclic voltammograms of the oxide-nanosphere coated VACNTs (a) and the thin film vanadium oxide (b). The effect of scan rate on both samples is evident in the change of slopes of the I-V curves. As the scan rate increases, the current response on scanning potential undergoes a transition from a flat capacitor type behavior to a resistor - like dependence as is common for most pseudocapacitor materials. Reversible Faradaic peaks are observed at ~ 0.2 V, 0.3 V and 0.6 V on the positive scan and ~ - 0.1 V and 0.3 V on the negative scan in both materials [**Figure 207** (c)]. The potential dependent pseudocapacitance behavior present at these potentials is thought to correspond to a reversible transition of oxidation state of Vanadium from + 5 to + 3 most commonly observed in aqueous systems at the almost neutral pH occurring in a 1 M Na_2SO_4 solution [289, 290]. It can be seen that the Faradaic peak is more pronounced, at higher scan rates, in the VACNT-oxide spheres than in the thin film. This is due to the beneficial effect of the CNTs on the Faradaic capacitor processes occurring in vanadium oxide. The valuable effect of VACNTs is evident in the capacitance plots seen in **Figure 207** (d), in which the capacitance of the oxide nanospheres deposited on both the VACNTs and on Ni substrate are plotted against the cyclic voltammetry scan rates. The effect of the resistance / capacitance behavior previously described is evident from the drop in capacitance with scan rate. This drop

however, is more pronounced in the thin film material as compared to the oxide nanospheres supported on the VACNTs. Capacitances of upto 1400 Fg^{-1} (oxide loading basis) have been observed at scan rates of 2 mV/s in the VACNT-oxide nano-composite material with good capacitance retention at higher rates compared to the oxide thin film on Ni substrates. **Figure 207** (e) shows the dependence of overall capacitance of the VACNT-oxide nano-composite material on scan rate in mFarads/cm^2. Areal capacitance is a very important characteristic when considering materials for industrial applications and it can be seen that the VACNT-oxide nano-composite material has excellent capacitances ranging from 89 mF/cm (at 2 mV/s) to 14 mF/cm (at 200 mV/s) which are superior to those reported for RuO_2 nanotubes reported before [291]. The VACNT-vanadium oxide composite material however does not have areal capacitances as high as highly active ruthenium oxide supercapacitors [292, 293] but is still commercially viable on account of its relatively low cost as compared to ruthenium oxide (~ 0.193 $/g as compared to ~10 $/g). The comparison of a relatively inexpensive vanadium oxide material possessing excellent areal capacitance with that of a well studied noble metal oxide such as ruthenium oxide is meant to provide a basis for contrast rather than to prove superiority in performance. Noble metal based capacitors as already mentioned in the introduction are expensive even though they have excellent charge storage properties. It is therefore the aim of this work to highlight the possibility of vanadium oxide having performance as good as that of a noble metal oxide.

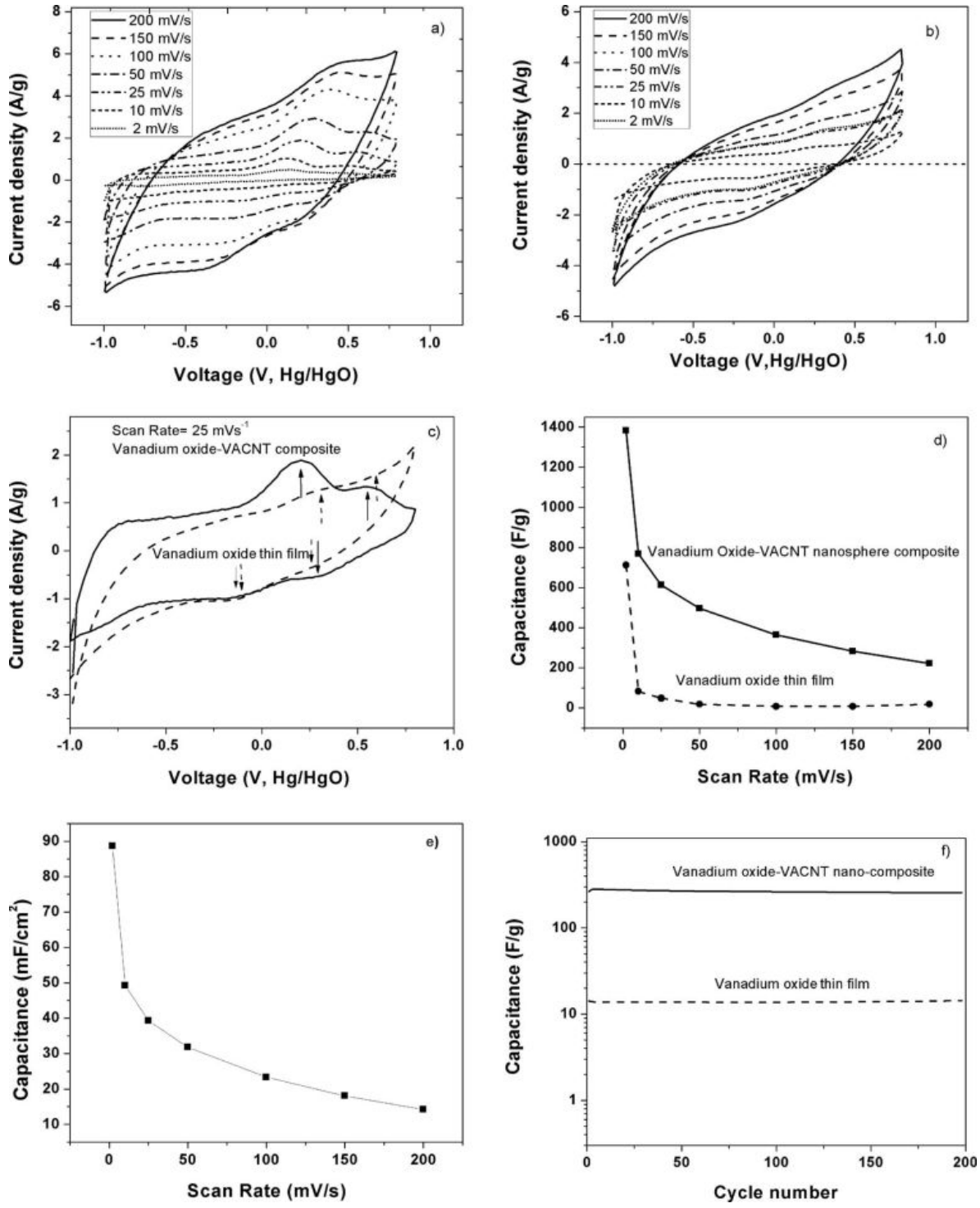

Figure 207. Cyclic voltammograms of the VO_x-VACNT (a), and VO_x thin film (b); Cyclic voltammograms of VO_x-VACNT and VO_x thin film (c), Capacitance behavior of VO_x-VACNT and VO_x thin film (d), Areal capacitance of VO_x-VACNT (e), and cycling behavior of VO_x-VACNT and VO_x thin film.

The synergistic effect of the carbon nanotube-vanadium oxide junction has previously been studied for gas-sensing purposes [282, 294, 295]. It has been suggested that a p-n junction type interaction between the oxide and the CNT leads to increased catalytic response of the oxide while the multi walled CNTs, which acts as a p-type semiconductor help act as fast electron channels. The performance of supercapacitor materials at high rates is most-often limited by the electronic conductivity of the material. The presence of carbon nanotubes as a support structure for the oxide leads to unidirectional electron transfer through the aligned CNTs [296] which then travel through the mini-oxide spheres and interact at the oxide-electrolyte interface where charge is stored. It can be seen that the capacitance of the oxide-VACNT composite is ~ 80 F/g when the total weight of the composite is considered. This drop in capacitance compared to capacitance calculated on the basis of the active oxide material is due to the overwhelming weight of the CNTs which do not exhibit any pseudocapacitance behavior. Though excellent oxide capacitance behavior was demonstrated in the CVD derived vanadium oxide material in the oxide-VACNT composite electrode, the overall capacitance is not very high when compared with other aqueous vanadium oxide supercapacitors [247]. There is therefore a need for further optimization to identify an ideal oxide / CNT ratio so as to maximize capacitance whilst retaining the improvement in rate capability afforded by the high conductivity of the Carbon nanotubes. The fade in capacitance with increase in scan rate is a phenomenon observed in supercapacitor materials as described by Conway *et al.* [227]. This is caused by the change in characteristic of the interface from that of a double layer capacitor to a resistor. This transition is a fundamental feature of all electrochemical double layers. Capacitance changes with scan rate with a factor s which varies from material to material. A similar characteristic in Faradaic

reactions is the kinetic rate constant (k_0) which is a material property in a given electrode / electrolyte assembly. Pseudocapacitance reactions involving charge transfer by tunneling across the electrochemical interface have an inherent rate constant depending on the species involved in the charge transfer which could be limiting in the case of the current oxide coated on the CNTs. It could also be attributed to the nature of the oxide coating on the carbon nanotubes. It is observed that even though the carbon nanotubes have a vertical alignment, the nature of the tethering of the oxide nanoparticles on the carbon nanotubes needs to be improved to achieve better rate capability. In addition, the conductivity of undoped VACNTs themselves is limiting to some extent on account of presence of some amorphous carbon on the CNTs.

Figure 207 (f) shows the ability of the CVD deposited materials to retain charge over large cycles. Both the CVD deposited materials are seen to have exceptional capacitance retention upto 200 cycles, at a scan rate of 150mV/s. This excellent cyclability can be attributed to the reversible nature of the surface pseudocapacitance reactions of the oxide. The thin film oxide has a relatively low capacitance at the high rate at which cycling was performed as seen in **Figure 207** (d) but maintains stability with cycling. The oxidation state of the CVD deposited vanadium oxide is ~ 4.6 consisting predominantly of a + 4 / + 5 oxide. According to the potential - pH diagram, vanadium oxide has stable insoluble phases between the potentials of ~ 0.5 V and - 1 V *vs.* Ag / AgCl [289]. Above 0.5 V, the higher oxidation state oxide is considered soluble to form $H_2VO_4^-$ at a neutral pH. This should be reflected as loss in capacity with cycling. However, the onset potential of electrochemical reactions is known to vary with particle size and microstructure. It is believed that the amorphous nature of the oxide nanoparticles supported on the VACNTs offsets the onset of such dissolution resulting in the very stable performance of the oxide in aqueous Na_2SO_4. It is also possible that the kinetics of the dissolution reaction might be

sluggish and such a fade in capacity would probably be observed if the material were cycled over thousands of cycles.

It is common knowledge that thick films of nanoparticulate oxides especially amorphous oxides would be non-ideal to obtain high capacitances on account of low inherent electronic conductivity, grain boundary diffusion and exposed surface. On the other hand, the use of a relatively thin film on a supported structure affords us the benefits of high surface area, small particle size and direct contact of grains with the highly conductive carbon nanotubes. The accessible capacitance of vanadium oxide thick film is very limited when the material is synthesized as a thick film. However, thin film vanadium oxide has a high capacitance as demonstrated in (**Figure 207**). This is improved even further when the VACNTs are used as a 3 - dimensional support. These results are thus in agreement with trends observed in other pseudo-capacitor materials such as manganese oxide [234]. Though the overall capacitance reported here is lower than that reported in LiCl based systems by Hu *et al.* [245-248], the unique synthesis method, morphology, electrode/electrolyte combination and an in-depth electrochemical characterization provided are original contributions to the best of our knowledge enhancing the understanding of supercapacitor behavior in oxide systems. In addition, the capacitance of the oxide material only when coated on the VACNTs is very high and demonstrates that vanadium oxide is in fact, is a very promising material for aqueous supercapacitors.

In order to further establish the advantages yielded by the CVD deposition of vanadium oxide on CNTs, electrochemical impedance spectra were obtained on the nanospheres as well as oxide film and charge transfer characteristics were compared. **Figure 208** shows the Nyquist plot of the oxide nanosphere-VACNT hybrid (a) and the thin film vanadium oxide (b), at different voltages over the window of interest. It can be observed directly that the impedance behavior of

both materials is different especially at voltages close to the regions of the Faradaic peaks observed at 0.2 V, 0.3 V, 0.6 V and - 0.3 V in the cyclic voltammograms (**Figure 207**). At these potentials corresponding to the Faradaic charge transfer reactions, it can be seen upon comparing the response of oxide film and VACNT-oxide composite that the thin film oxide has a much larger charge transfer resistance. This is inferred from the large semi-circular arcs where one can see the Warburg tail being more prominent as compared to the relatively much smaller semi-circular arcs. The large semi-circular arcs in a Nyquist plot are indicative of high charge transfer resistance which would result in the reduced Faradaic response in thin film oxide at higher scan rates. Pseudocapacitance performance which is usually prevalent in the 10^3 to 10^4 Hz region on account of electrode kinetic rate limitations [229] is much more prominent in the CNT-supported oxide as compared to the thin film oxide.

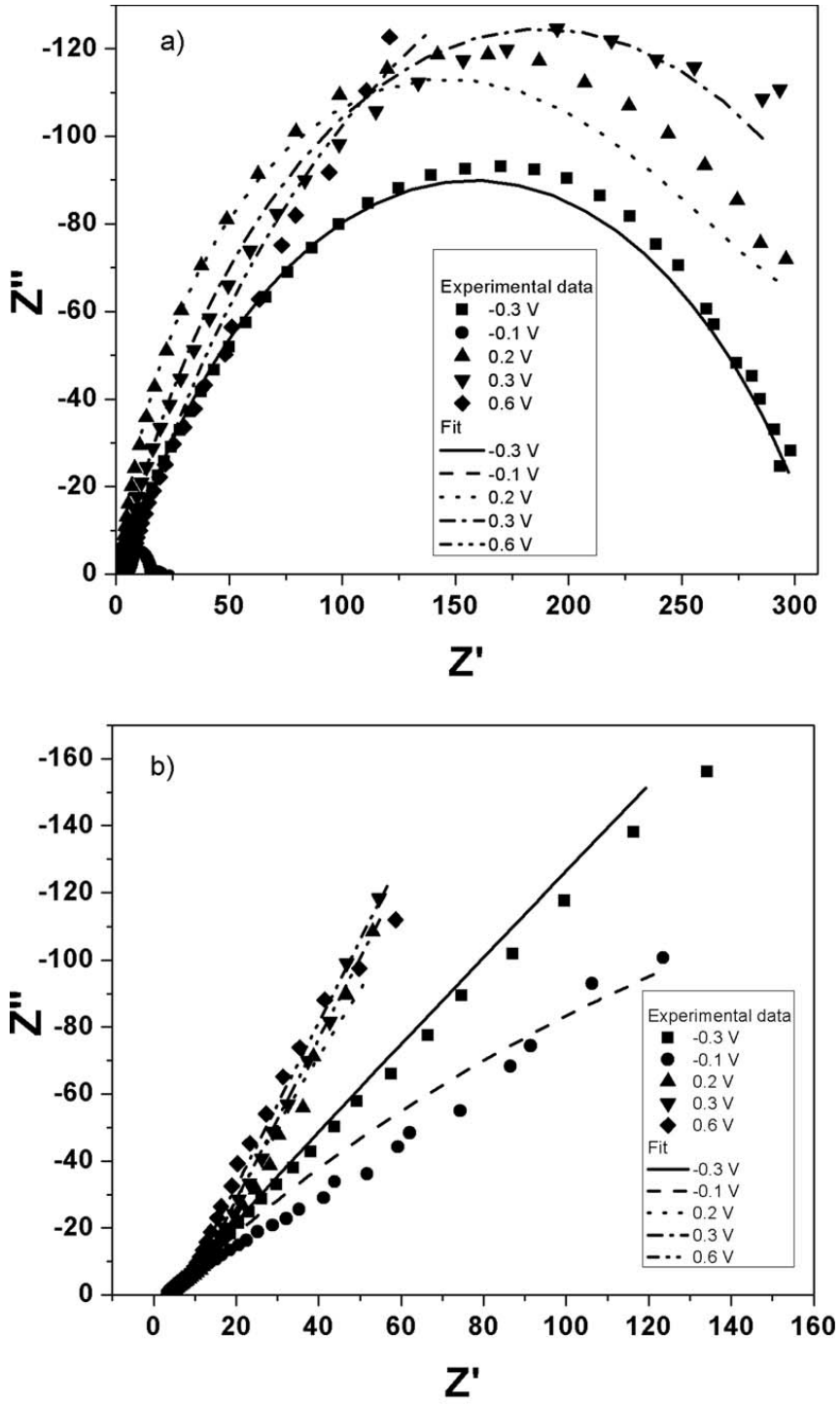

Figure 208. Impedance behavior of thin film vanadium oxide (a) and vanadium oxide nanosphere-VACNT composite heterostructure (b)

Equivalent Circuit modeling was performed using the Z-view software to obtain charge-transfer parameters of the oxides. The underpotential deposition mechanism used considers both the double layer capacitance (usually modeled as a capacitor (C_{dl}) in parallel with a resistor (R_F)) and pseudocapacitance arising from surface reactions (C_p) on the electrode of interest. In addition, an electrochemical series resistance (R_s) common to all electrochemical systems is also considered. However, in porous electrode systems, the capacitor elements are usually modeled as constant phase elements [297, 298]. Constant phase elements are usually used to fit data having depressed semicircular arcs on account of electrode porosity and roughness which leads to fractal character and inhomogeneity in response on account of presence of different crystallographic reaction sites.

It can be seen that the series resistance is fairly constant in both systems and varies between 0.25 and 0.9 Ω/cm^2 which is common in carbon based systems [299]. The most notable difference in behavior between the thin film oxide and the CNT-supported nanospheres is the charge transfer resistance. R_F values are reduced by upto an order on account of the presence of CNTs. This improvement in conductivity is reflected in the high capacitance response observed at high scan rates for the oxide nanosphere-VACNT heterostructures compared to the oxide thin film as seen in **Figure 207** (d).

D.1.4 Conclusion

Hot walled CVD has for the first time been used to create a unique morphology consisting of vanadium oxide nanospheres tethered to carbon nanotubes. Such a CVD derived VACNT supported oxide nanosphere morphologies have been shown to exhibit excellent charge storage

characteristics with capacitances of upto 1400 F/g achieved at a scan rate of 2 mV/s based on the oxide loading. Moreover, the results indicate CNTs to have a strong complimentary effect on the rate capability of oxide capacitance as seen by comparing scan - rate dependent capacitance plots of CNT-oxide hybrid electrodes with pure oxide thin films. One of the highlights of this study is the ease of electrode fabrication. Chemical vapor deposition is a method amenable for continuous production of electrodes in an assembly - chain configuration in contrast with chemical methods used to produce oxides which require batch processes and in turn also involve a second heat treatment step. The need for slurry preparation is eliminated and binder - free electrodes are thus generated. The CVD method could further be optimized to lead to electrodes with a good oxide / CNT ratio so as to maintain excellent capacitance yielded by the thin oxide layer as well as the rate capability enhancement provided by carbon nanotubes.

D.2 NANOSTRUCTURED VANADIUM NITRIDE

D.2.1 Introduction

With the growing interest in alternative energy sources and the cognitive recognition of the benefits of green energy, there is clearly an urgent need for the development of sustainable and clean energy storage systems. This has resulted in a burgeoning of research into novel nanomaterials for energy applications in both industry as well as academia over the last two decades [226, 231, 300]. Supercapacitors are one among a number of such energy storage

devices that are emerging as highly relevant devices for a plethora of mobile and stationary applicationson account of their short charging times and seemingly infinite cyclability. Traditionally, supercapacitors have been classified as electrochemical double layer capacitors (EDLCs) and pseudocapacitors (PC) based on the charge storage mechanisms [229]. High surface area (HSA) activated carbons have been the primary candidates studied as EDLCs wherein charge storage at the electrochemical double layer is the predominant mechanism of charge storage. Unlike conventional batteries, double layer supercapacitors can be cycled at very high rates over millions of cycles without losing much of their charge storage capabilities.

Double layer capacitors however suffer from low energy densities for practical applications since the primary mechanism of charge storage is by the simplistic separation of charge at the electrochemical double layer, a process which is inherently limited by the surface charge coverage even for materials exhibiting very high specific surface area (SSA). The other type of supercapacitors, PC involve a chain of successive reversible Faradaic reactions augmented by additional charge storage reactions induced by the double layer mechanism, thus rendering devices made with these materials to exhibit very high energy densities [227, 229, 298]. Transition metal oxides are very attractive for this kind of application on account of their ability to exhibit variable oxidation states. Of particular interest for PC applications is the ability of the surface oxide to undergo reversible oxidation - reduction with the change in the oxidation states of the primary metal such as Ru in ruthenium oxide capacitor systems [227, 229]. The current - voltage characteristics corresponding to the successive oxidation/reduction reactions occurring at the surface of the electrode have an uncanny resemblance to that of a capacitor and hence the term pseudocapacitor. There is however a critical need to improve power densities of pseudocapacitor materials to make them commercially viable for a number of small and large

scale applications[301]. In addition, pseudocapacitor materials suffer from poor cyclability on account of irreversibility occurring on account of Faradaic charge transfer reactions.

Hydrous ruthenium oxide is a well known pseudocapacitor material with the ability to maintain stable capacitances as high as 900 F/g over a large number of cycles [235]. However, the prohibitive price of the noble metal renders the cost of the capacitors to also be astronomically high thus warranting the search for alternative materials with similar charge storage characteristics. As a result, several other non-noble metal oxides and hydroxyl-oxides of transition metals have been widely explored including those of Mn, Ni and V [230, 233, 238, 302-304]. Additionally, there is a large impetus to improve the energy density of oxide materials to render them commercially viable. There is therefore a need to explore novel chemistries to identify cost effective pseudocapacitor materials with high energy densities and good rate capability. While there has been intense activity in transition metal oxide systems to function as alternative capacitor materials, the corresponding search for non-oxide materials for active application in capacitors is rather limited with relatively few reports [249, 305-318]. There is still much to be explored and understood in this sparsely chartered arena.

Transition metal nitrides are traditionally known for their refractory characteristics primarily due to their high melting point and chemical stability against corrosive acids and bases. Recent work of late by various groups has shown the viability of nitrides for catalysis and energy storage applications. Transition metal nitrides were first shown to have promise as pseudocapacitors by Thompson *et al.* and Liu *et al.* [305-310]. A thorough investigation into transition metal nitride supercapacitors was thus undertaken to explore a simple two step ammonolysis approach exploiting the characteristic nitridation reaction exhibited by the family of transition metal precursors containing identical halide functional groups, Studies by our group

have shown that these nitrides exhibit excellent supercapacitor response in simple aqueous electrolytes [249, 311-313]. Among the various nitrides explored, VN was found to be the most promising, exhibiting a uniquely high capacitance of 1350 F/g albeit under low loading conditions [249, 313]. This exceptional performance at low active material loadings has been attributed to a combination of both double layer type capacitance and pseudo-capacitance response primarily attributed to the presence of a thin surface oxide layer that is grown over the centrally preserved core of the transition metal nitride providing the required electronically conducting platform. The conductivity of bulk vanadium oxide is very low which limits its applicability for supercapacitor electrodes. On the other hand, nitride materials usually possess high electronic conductivities making them viable electrodes capable of good gravimetric capacitances even in thick films. The use of carbon nanotube supported thin film vanadium oxide for aqueous supercapacitors has recently been reported by Jampani *et al.* [253] and capacitances of upto ~1400 F/g have been observed. Such behavior is observed only when a conducting support based composite electrode is prepared. The use of a non-carbon material on which the highly active oxide layer is present is the aim of our studies into nitride based supercapacitors as presented in the current work. Several other groups have subsequently also evaluated the capacitor properties of VN and have reported capacitances of 161 F/g and 186 F/g, respectively [314, 315]. In addition, titanium and vanadium oxy-nitride materials with varying oxygen content were examined and the dependence of capacitance on oxygen / nitrogen ratio have been reported [316, 319].

Traditionally, transition metal nitrides are synthesized by very high temperature gas phase nitridation reaction of the metal or the corresponding oxide which is not only energy inefficient producing coarse and highly crystalline VN with very low surface areas but also

results in characteristic properties that are very undesirable for supercapacitor and energy storage applications. In addition, most methods usually involve the use of very volatile and air sensitive precursors such as chlorides [249, 313, 320], cyanamides [321], dicyanamides [322, 323], C_3N_4 [324] or NH_3 [305, 325, 326]. Foam based methods commonly use organic or carbon based surfactants leading to carbonaceous impurities in the final nitride formed [327, 328]. There is therefore a need for the direct synthesis of nanostructured defect and impurity free transition metal nitrides at low temperatures. In this regard, identification and implementation of a simple, low cost, low temperature approach for the bulk synthesis of VN would certainly complement the recent interest generated in nanostructured VN for capacitor applications.

High energy mechanical milling (HEMM) is one such approach that represent a simple approach commonly used to synthesize a variety of nano-structured materials and nano-composites [329, 330]. Our group has previously utilized this technique extensively for generation of Si based nanostructures for Li-ion applications with considerable success [331-333]. The approach was therefore chosen in this study to explore the solid state synthesis of nano-structured VN on account of the low temperatures involved, simplicity and ease of execution thus enabling bulk synthesis of the nitride in a straightforward and affordable fashion [334]. In addition, the intimate mixing and comminution of the precursors with the milling media leads to a rapid solid state reaction providing much of the energy required to overcome the typical energy barriers needed to induce diffusion and form the metal - nitrogen bonds that ordinarily require high temperature synthesis procedures due to the chemically inert nature of nitrogen. HEMM approach can also be modified to induce chemical reactions between the reacting species *via* mechanical agitation in a process called mechano-chemical reaction wherein the reactive precursors such as vanadium (III) oxide and lithium nitride in the present report, can

spontaneously react *via* the milling action to form the corresponding nitride with the formation of lithium oxide as the sacrificial by product. The approach and precursors are both benign and easily amenable for handling at room temperature thus rendering the approach easily amenable for the large scale synthesis of nitrides at temperatures as low as room temperature. Though lithium nitride is a flammable substance, its handling is relatively much simpler than other nitridation methods which rely on the use of either highly toxic flammable ammonia gas, volatile and toxic halide precursors or formation of dangerous cyanide by-products. This mechano-chemical reaction on a lab scale requires the use of an inert atmosphere glove box or a glove bag which are both much cheaper than the use of other precursors. High energy mechanical milling is a fairly well known technique and is commercially used for a number of applications. The process of high energy mechanical milling is in fact widely scaled up on the industrial scale and success of the process depends on the design of the milling equipment. This report involves the direct synthesis of nanostructured VN at room temperature. We have also attempted herein to compare structural and compositional properties of the nitride thus synthesized with those previously reported to gain an insight into charge storage mechanisms and degradation mechanisms in vanadium nitride [334].

D.2.2 Experimental Section

The precursors for the mechano-chemical reaction were weighed in an inert atmosphere glove box (Vacuum Atmospheres, Inc.) and sealed in a stainless steel vial along with the milling balls. The vial was hermetically sealed and placed in the SPEX high energy mechanical mill. Mixtures of powders of lithium nitride (Li_3N, Alfa Aesar, 99.4%) and vanadium oxide (V_2O_3, Alfa Aesar,

99.7%) of suitable compositions were subjected to mechanical milling in a high energy shaker mill (SPEX CertiPrep 8000 M) for up to 3 hours in a stainless steel (SS) vial using 20 SS balls of 2 mm diameter (~ 20 g) with a ball to powder weight ratio 10 : 1. The resultant milled powders were washed in deionized (DI) water at 40°C to dissolve the lithium oxide formed as a by-product of the mechano-chemical reaction.

In order to perform qualitative phase analysis, the synthesized materials were characterized by X-ray diffraction (XRD) using Philips XPERT PRO system employing CuK_α (λ = 0.15406 nm) radiation with operating voltage and current set at 45kV and 40mA, respectively. The XRD peak profile was analyzed using the Pseudo-Voigt function to determine the Lorentzian and Gaussian contribution of the peaks. The integral breadth of the Lorentzian contribution, determined from peak profile analysis using single line approximation method after eliminating the instrumental broadening and lattice strain contribution, was implemented in the Scherrer formula to calculate the effective crystallite size of VN [335, 336]. The lattice parameter and molar volume of VN has been calculated using least square refinement techniques.

To investigate the microstructure of the milled VN, high resolution transmission electron microscopy (HRTEM) was conducted. HRTEM analysis was conducted on the sample using JEOL JEM-2100F to investigate the particle size and morphology. In addition, the oxygen and nitrogen content in the VN prepared by mechano-chemical reduction were independently analyzed using an inert gas fusion analysis [LECO TC600 analyzer (Alternative Testing Laboratories, Inc.)]. Finally, the specific surface area (SSA) of the VN was also measured using a Micromeritics ASAP 2020 (Accelerated surface area and porosimetry) system. Nitrogen

adsorption and desorption partial pressures was measured and a BET (Brunauer Emmett Teller) type adsorption was assumed to obtain the surface area.

To analyze the surface composition, determine the valence state of V ions in the nitride before, and ascertain any changes in the oxidation state of V upon cycling, x-ray photo electron spectroscopy (XPS) was performed (Perkin-Elmer PHI-5600) before cycling and after electrochemical cycling for 200 cycles in 1M KOH. XPS on the pristine and cycled VN was conducted using a Physical Electronics (PHI) model 32-096 X-ray source control and a 22-040 power supply interfaced to a model 04-548 X-ray source with an Omni Focus III spherical capacitance analyzer (SCA). The system is routinely operated within the pressure range of 10^{-8} to 10^{-9} Torr (1.3×10^{-6} to 1.3×10^{-7} Pa). The system was calibrated in accordance with the manufacturer's procedures utilizing the photoemission lines, E_b of Cu $2p_{3/2}$ - 932.7 eV, E_b of Au $4f_{7/2}$ - 84 eV and E_b of Ag $3d_{5/2}$ - 368.3 for a magnesium anode. All the reported intensities are in effect experimentally determined peak areas divided by the instrumental sensitivity factors. Charge correction was obtained by referencing the adventitious C 1s peak to 284.8 eV.

Since the electronic conductivity of the active material is a crucial parameter affecting the supercapacitor performance, a four point probe was used to measure the electronic conductivity of the mechano-chemically derived VN. To measure the electronic conductivity, pellets were prepared by compacting the VN powder using a uniaxial pressure of 7000 lb in a manual press (Carver Inc.). A FPP 5000 four-probe conductivity instrument (Miller Design & Equipment, Inc.) was used for the measurements. The thickness of the pellets was measured and they were depressed against the four tips on the resistivity meter using a glass slide as a backing plate. Sheet resistance data was obtained in ohm/sq and multiplied with the sample thickness to obtain the resistivity. The flatness and crack-free nature of the pellets was ensured to avoid artifacts in

the measurement of resistivity. The density of the mechano-chemically synthesized VN was measured using a Micromeritics AccuPyc II 1340 gas pycnometer.

Cyclic voltammetry (Princeton Applied Research Versastat 3) and charge-discharge cycling (Arbin BT-2000) were performed on the synthesized VN materials to test their viability as high energy density supercapacitor materials. The process involved preparation of slurry for coating onto pre-weighed nickel current collector disks (1" diameter Nickel disks). The slurry composition consisted of 85 % active nitride, 5 % conductive additive (Super-P Carbon) and 10 % binder poly-vinylidene flouride (PVDF) (Aldrich Chemicals) in a solution of N-methyl 2-pyrollidone (NMP) [Fisher Scientific]. The PVDF was first dissolved in the NMP solvent. The active material and carbon were then dispersed in this solution and allowed to stir till a homogenous mixture was obtained. The slurry coated current collector disks were allowed to dry overnight in a vacuum oven at 120^{o}C before the final weight was recorded. The active material weight was then used to calculate the specific capacitance.

Cyclic voltammetry tests were performed in the -1.2 V to 0 V range with respect to reference to evaluate the specific capacitance of the nanostructured VN generated by high energy milling. Cycling was performed at different rates and the area of the cyclic voltammogram was used to calculate the capacitance. The areal (mF/cm^2) and volumetric capacitance (F/cm^3) of the mechano-chemically synthesized VN were calculated on the basis of both the electrode basis and materials basis. To calculate areal capacitance and volumetric capacitance on the basis of electrode parameters, the area of the working electrode and volume of the material coated on the current collector were used. The areal capacitance on the basis of experimentally observed surface area and material density were also calculated.

In addition, galvanostatic charge-discharge cycling was performed on an Arbin BT-2000 cycler at a current density of 100 mA/g to observe the nature of the V-t characteristic and to carry out long term cycling upto 1000 cycles. Electrochemical impedance spectroscopy (EIS) was performed on the Versastat 3 over a frequency range of 0.01 Hz - 100 KHz. A.C. amplitude of 5 mV was used and the spectra were obtained between 0 and - 1.2 V at intervals of 100 mV. Impedance spectra were obtained before cycling and after 200 cycles to observe any noticeable changes in the charge storage mechanism upon cycling. The Z-View (Scribner Associates) software was used to design the equivalent circuit model of the impedance spectra. Two primary mechanisms of capacitive charge storage described by Conway *et. al.* were studied for the synthesized nitride [229] namely, the under-potential deposition (UPD) and the over-potential deposition (OPD). The under-potential deposition mechanism (UPD) involves charge storage by the classical double layer mechanism along with mono-layer adsorption at the electrode surface. Over-potential deposition (OPD) on the other hand, involves redox reactions occurring over and above the monolayer of adsorbed ions at the surface. This process is also the precursor to gas evolution on the particular electrode, also commonly referred to as the onset potential of electrolysis.

D.2.3 Results and Discussion

The XRD pattern obtained of high energy milling of Li_3N and V_2O_3 as-prepared and after washing the powder is shown in **Figure 209**. It can be seen in **Figure 209** (a) that the x-ray pattern consists of peaks corresponding to those of vanadium nitride, lithium oxide and an unidentified phase. Formation of VN and Li_2O as the by product has been identified which is

expected to arise due to the solid state reaction between Li_3N and V_2O_3 yielding VN and Li_2O according to the reaction stated below.

$$2\ Li_3N + V_2O_3 \rightarrow 3\ Li_2O + 2\ VN$$

However, in addition to the above stated peaks, a third phase is seen to occur in the XRD which is unidentified indicating that a unknown side reaction occurs as a result of the milling process. In order to remove the undesired by-products from the mechanically milled powder, the as-prepared powder was washed in DI water at 40°C. The XRD pattern of the washed powder, displayed in **Figure 209** (b), shows all the peaks corresponding to single phase face centered cubic (fcc) VN which suggest complete removal of Li_2O from the resulting mixture of VN + Li_2O after washing. The unidentified peaks do not match those of the initial reactants or oxide phase. A common contaminant in milling based synthesis is iron abraded from the walls of the milling vials. However, no such contaminant was observed in the case of the nitride made by this method. The reaction between the oxide and the lithium nitride was instantaneous. In fact, nitride formation occurs in 5 minutes as seen in **Figure 209** (c). Even though it is possible that the phase conversion occurring from the time period of 5 - 180 minutes might have involved a change from VO to VN, none of the initial oxide precursors and lithium nitride are observed in the 5 min milled sample. This indicates that the reduction reaction involving the lithium nitride occur rapidly at first and gradually subsequently as indicated by the change in peak width. Lithium nitride is a highly flammable air-sensitive material, but after trying to recover the sample after milling for 5 minutes, no fumes or fire was observed indicating the absence of unreacted lithium nitride. It should be pointed out here that the crystal structures of vanadium nitride (VN) and vanadium monoxide (VO) are almost identical making it difficult to identify when exactly the transition from VO to VN occurs completely. The oxygen and nitrogen content

in the VN prepared by mechano-chemical reduction was thus independently analyzed using an inert gas fusion analyzer (LECO analysis, Alternative Testing Laboratories, Inc.). The oxygen content was evaluated to be ~ 4.83 wt.% and the nitrogen content to be ~ 17.2 wt.%. The final composition of the nitride formed by mechano-chemical reduction was thus found to be $VN_{0.8}O_{0.2}$.

The lattice parameter of the VN obtained after washing of the material milled for 180 minutes, calculated using the least square refinement technique, was found to be ~ 0.4111 ± 0.0002 nm with a molar volume ~ 10.46 cm^3/mol which is in good agreement with the bulk lattice parameter of cubic VN [337, 338]. The effective crystallite size of VN, calculated using the Scherrer formula from the integral breadth of the Lorentzian contribution determined from the peak profile analysis using the single line approximation method after eliminating the instrumental broadening and lattice strain contribution [335, 336], is in the range of ~ 28 nm confirming the nano-crystalline nature of the resultant VN obtained following the mechano-chemical reaction. The crystallite size of VN derived by the mechano-chemical reaction is however much larger than that of the nanoparticulate VN (~ 6.3 nm) reported previously generated by the ammonolysis chemical approach [249]. This is also reflected in the specific surface area (SSA), measured by the BET technique, of the VN synthesized by mechano-chemical reaction (9 m^2/g) which is almost four times lower than the SSA of the nano-particulate nitride (39 m^2/g) generated by the two step ammonolysis chemical approach.

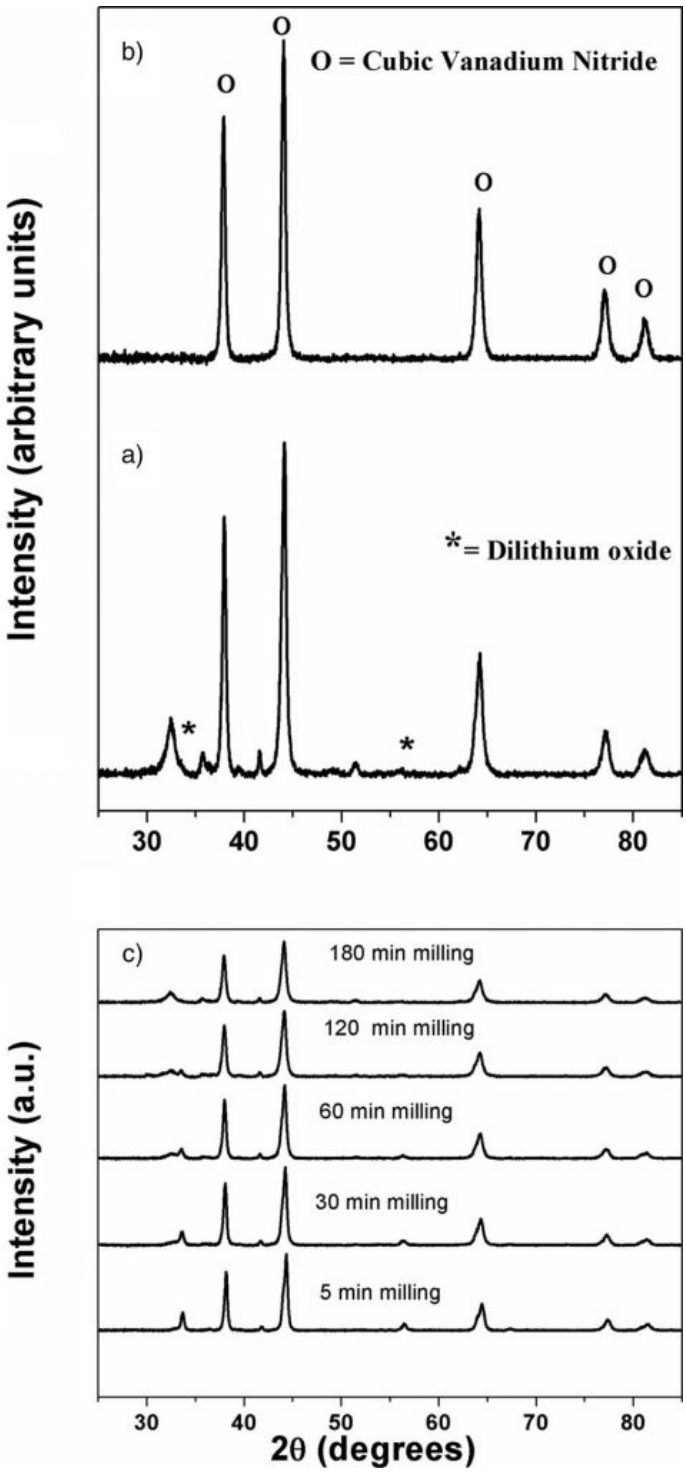

Figure 209. XRD of VN prepared by HEMM taken as-prepared (a), after washing with DI water (b), and as-prepared milling time ranging from 5 to 180 minutes (c)

Figure 210 shows the TEM bright field image along with selected area diffraction (SAD) pattern of VN (a), and the HRTEM image of VN (b). It confirms the formation of nano-sized VN particles with discrete sizes ranging between 30 nm and 150 nm and an average particle size of ~ 50 nm. The HRTEM image shows lattice fringes with a spacing of ~ 0.24 ± 0.002 nm which corresponds to the (1 1 1) interplanar spacing of the face centered cubic VN. The spacing observed between the lattice fringes of (1 1 1) plane of VN in the HRTEM image is also in good agreement with the calculated d_{111} value (~ 0.237 nm) from XRD patterns. Considering the particle size to be ~ 50 nm as indicated by the TEM images (**Figure 210**) and assuming the particles to be spherical, the thickness of the oxide layer can be approximated to be ~ 3.15 nm. Since the lattice constant of vanadium oxide is very similar to that of vanadium nitride, it was not possible to make a distinction between the nitride and the oxide layer in the HRTEM image. It is also possible that the material synthesized by mechano-chemical reduction has the oxygen atoms distributed throughout the bulk nitride lattice, *i.e.* an oxy-nitride instead of a core-shell particle as reported by Choi *et al.* [313].

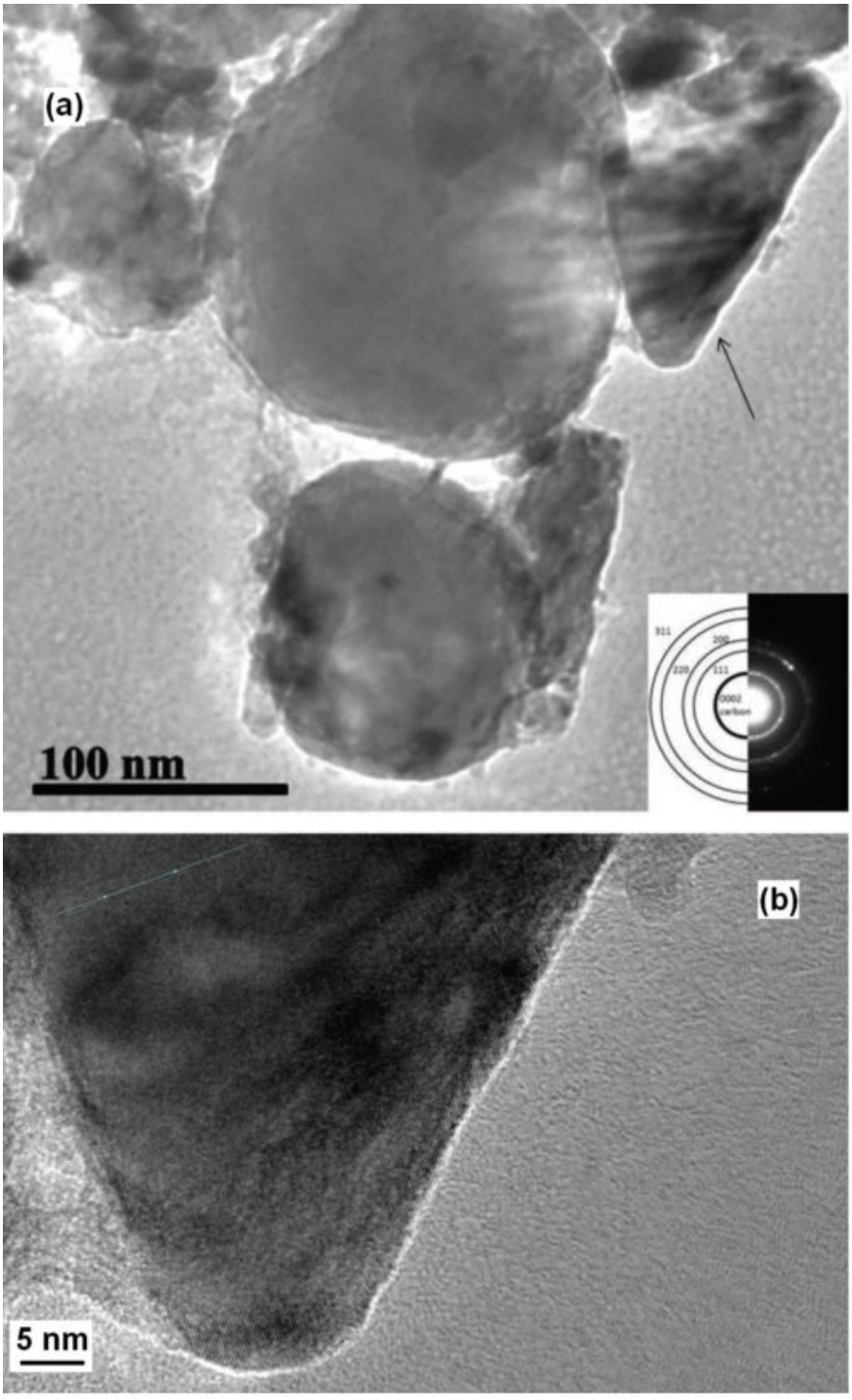

Figure 210. TEM image along with the SAD pattern of VN (a), and the HRTEM image of VN showing lattice fringes with a d spacing of ~0.24 nm

In order to determine the chemical oxidation states of V and N, x-ray photoelectron spectroscopy (XPS) has been conducted on the nano-crystalline VN particles prepared by the mechano-chemical reaction method. **Figure 211** shows the XPS spectra of V 2p (a), N 1s (b) and O 1s (c) of VN. The binding energy of the V $2p^{3/2}$ peaks at 516.7 and 514.4 eV correspond to those of VO_2 and VN respectively [285, 286, 339, 340], indicating the presence of an oxide rich VN surface. O 1s peaks at 530.2 and 532.7 eV correspond to the presence of a mixed oxide (with a predominant + 3 oxidation state of Vanadium) of vanadium and terminal hydroxyl groups respectively [242, 341, 342]. The N 1s peak of VN generated by the mechano-chemical approach before and after 100 cycles with a binding energy of 398.8 eV corresponds well with the binding energy of nano-particulate VN previously reported [249] . This indicates that the VN formed by milling the vanadium oxide and lithium nitride also has a thin surface oxide film as is the case in nano-crystalline VN reported by Choi *et al.* [249].

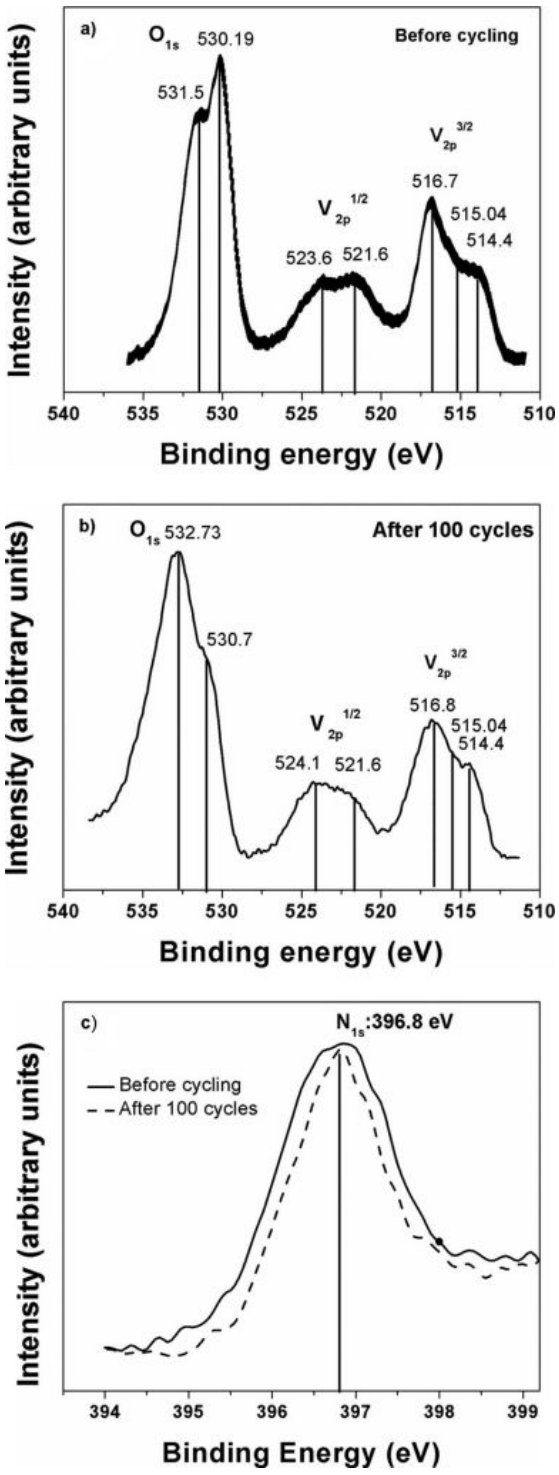

Figure 211. XPS data showing V 2p and O 1s peaks before cycling (a), and after cycling (b); and N 1s peaks before and after cycling (c)

Figure 212 shows the cyclic voltammogram (CV) of VN prepared by mechano-chemical reaction in 1 M KOH over a voltage window of - 1.2 V to 0 V *vs.* Hg/HgO. As it can be seen, both double layer and pseudocapacitor type response is visible in the CV. It can be seen that VN from HEMM exhibits reversible Faradaic reactions much like those of the nanoparticulate VN. Faradaic charge storage occurs at the surface oxide layer covering the nitride. Faradaic peaks are observed at - 0.91 V and - 0.61 V on the anodic scan and at - 0.68 V and - 1.03 V on the cathodic scan [343-345]. It should be noted that the standard electrode potentials reported in the references are *vs.* NHE. Detailed reactions and voltages have been reported by Jampani *et al.* [334]. It must also be noted that the electrode potentials observed in the CV however do not perfectly match the potentials reported in the above references. This can be attributed to the amorphous nature of the surface oxide which will be seen from the XPS spectra. A notable difference in the electrochemical behavior of VN made by mechano-chemical reduction as compared to chemically synthesized nanoparticulate VN reported by Choi *et al.* is the absence of reversible oxidation - reduction peaks at - 0.23 V with respect to Hg / HgO reference electrode on the anodic scan and - 0.32 V on the cathodic scan [249]. This could possibly be attributed to the nature of the surface oxide and the oxidation state of vanadium in the VN synthesized by mechano-chemical reduction

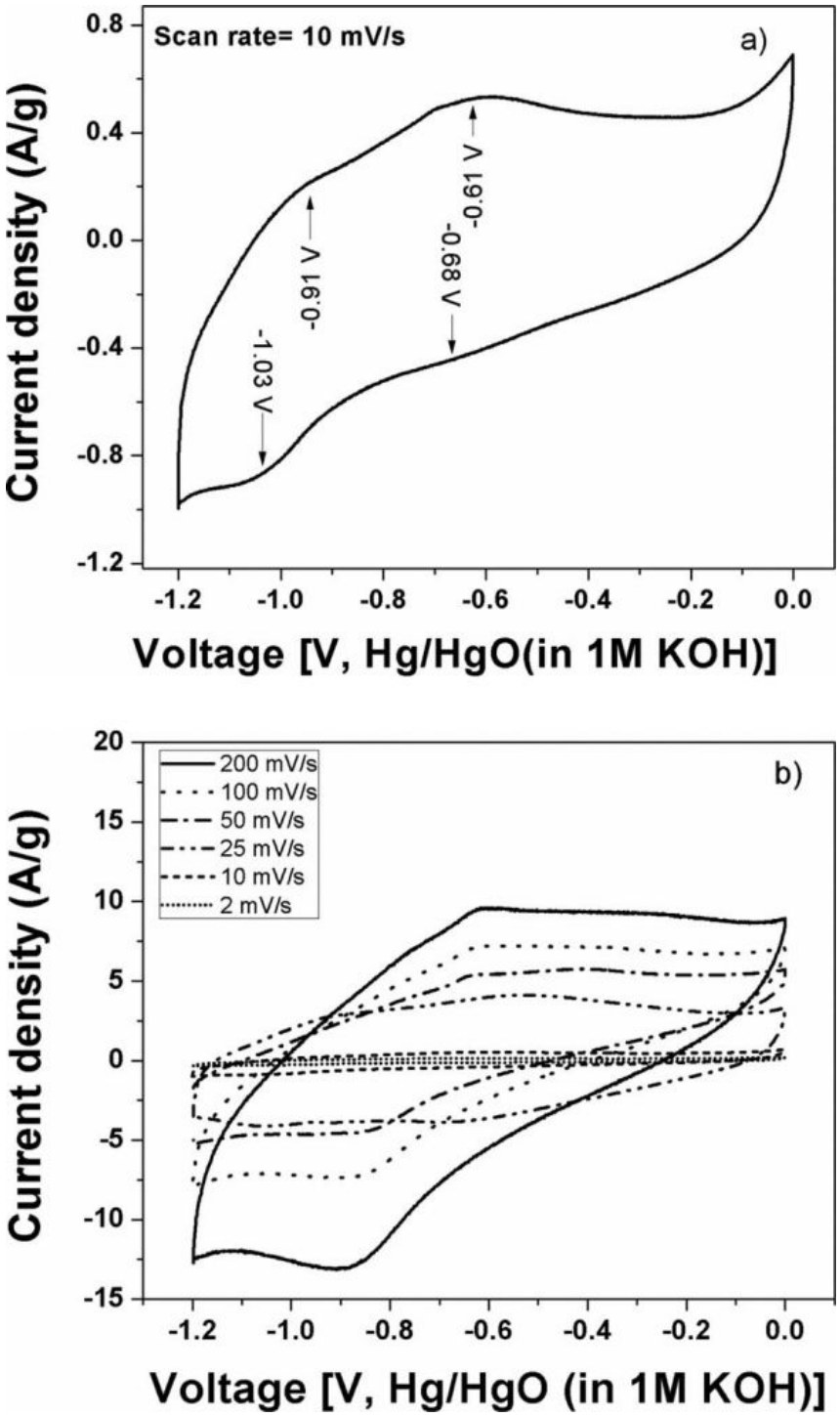

Figure 212. Cyclic voltammogram of VN at a scan rate of 10 mV/s (a), and at different scan rates (b)

The CV of mechano-chemically derived VN at various scan rates [**Figure 212** (b)] varying from 200 mV/s to 2 mV/s (at an active material loading of 0.36 mg/cm^2) shows that the behavior changes from almost square-like behavior to a more distorted parallelogram as scan rate increases. One artifact that sometimes leads to overestimation of capacitance calculated from integration of cyclic voltammograms is the asymmetry of the curve with respect to the horizontal axis. The CV though appearing assymetric in fact has an almost identical area on either side of the current axis possessing a Columbic efficiency of ~ 94 %; indicating that the capacitance calculated by the integration of the I-V curve is not overestimated.

Figure 213 shows the dependence of capacitance of the mechano-chemically obtained VN on both scan rate and active material loading. It can be clearly observed that the capacitance of VN as expected decreases with increasing scan rate as the reaction kinetics of the pseudocapacitance reactions become evidently rate-limited [229]. However, contrary to the trend reported by Choi *et al.* [249], we observed that the capacitance of these mechano-chemically derived nitrides are almost independent of the active material loading. This can be attributed to the much reduced pseudocapacitance contribution, which traditionally is observed to be scan-rate limiting on account of either the inferior electrical conductivity of nano-crystalline nitrides. This is also observed by comparing the decrease in capacitance with increase in scan rate (44 % drop from 2 mV/s to 25 mV/s after which it is stable). The VN reported by Choi *et al.* has a fade of capacitance of ~ 24 % from 25 mV/s to 100 mV/s as a result of the nano-crystalline nature of the VN reported therein. The capacitance drop from 2 mV/s to 25 mV/s occurs as a result of kinetics of the electrochemical reaction. Beyond that point however, there is minimal fade indicating lack of electrical conductivity limitations. Our aim in pointing this out is to draw contrast and point out characteristics of our material which are different and also to point out the result of particle

size on capacitor characteristics. The capacitance values however are less than those reported in the literature for both pure vanadium nitride and oxy-nitride [249, 315, 319, 321, 346, 347]. This could be attributed to the relatively large particle size and low surface area of the mechano-chemically synthesized vanadium nitride. The result nevertheless, indicates that the nano-crystalline VN obtained by the mechano-chemical approach does not remarkably suffer from the electron transport limitations typically seen in the ~ 6 nm VN reported by Choi *et al*. . The milled nitride thus exhibits capacitances between 25 and 55 F/g as compared to 100 - 850 F/g for the chemically synthesized nanoparticulate VN at similar scan rates and loadings of ~ 1 mg/cm^2 [249]. Another remarkable feature of the supercapacitor behavior of mechano-chemically synthesized VN is that there is very good retention in capacity with increasing active material loadings, as a result of higher electronic conductivity, which is reflected in the superior areal and volumetric capacitance of the material.

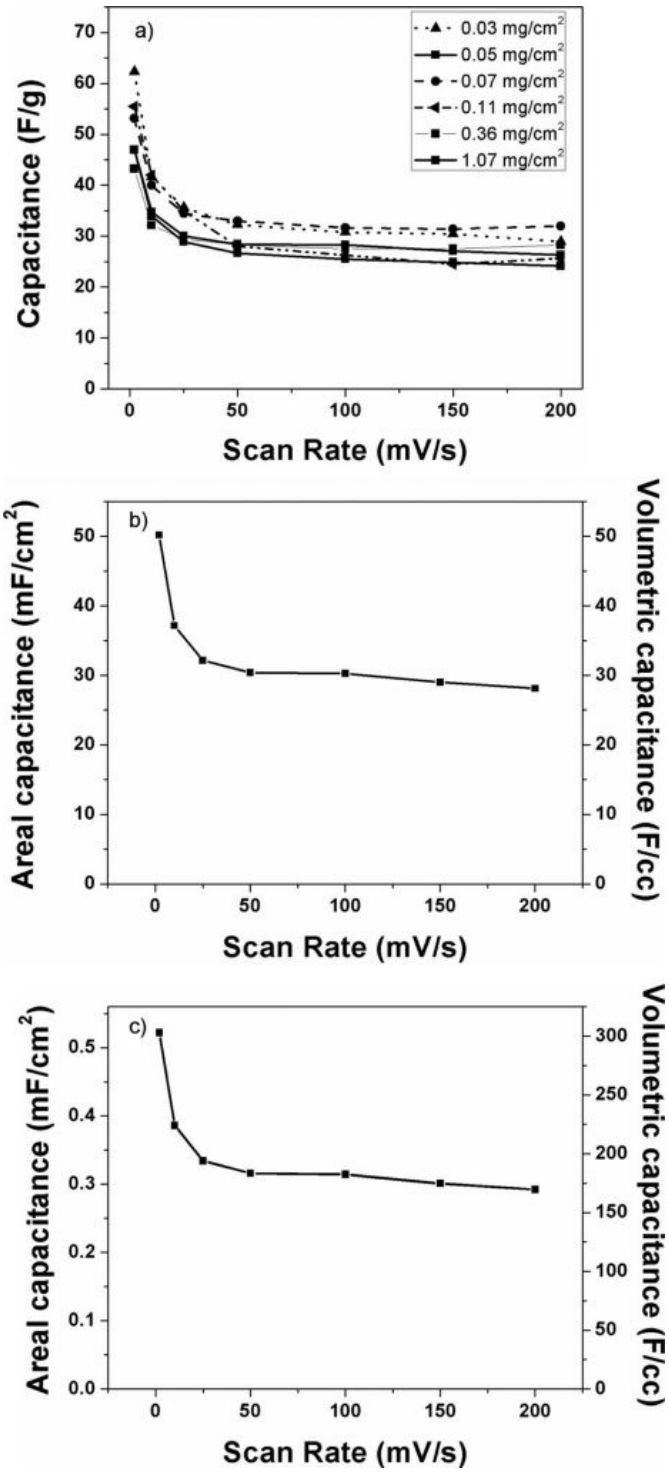

Figure 213. Gravimetric, Areal and Volumetric capacitence of VN as a function of scan rate

Figure 213 also shows the area normalized and volume normalized capacitance of the mechano-chemically synthesized vanadium nitride on the basis of electrode area and thickness (b) and powder surface area and density (c). The powder density was obtained using Micromeritics AccuPyc II 1340 gas pycnometer to be 6.46 g/cm^3 which is comparable to that of commercially obtained VN. Though the gravimetric capacitance of mechano-chemically synthesized VN is low, on account of the loading independence of capacity, the areal capacitance is comparable to that of other capacitor materials such as ruthenium oxide [291]. The nitride material however does not have areal capacitances as high as highly active RuO_2 supercapacitors [292, 293] but is still commercially viable on account of its relatively low cost (~ 2.38 $/g as compared to ~ 10 $/g). The areal capacitance of supercapacitor materials is usually reported on the basis of electrode areas *i.e.* a quantitative measure of the amount of energy stored per electrode area. On the other hand, volumetric capacitance is generally reported on the basis of material volume [348].

Galvanostatic charge-discharge testing was performed on an Arbin BT2000 cycler using a half-cell configuration similar to that used for cyclic voltammetry experiments at a current density of 100 mA/g. **Figure 214** shows the charge-discharge profile (a), and fade in capacity with cycling over 1000 cycles (b). In the charge-discharge profiles, sometimes extended plateaus occur as a result of either of two processes occurring in aqueous electrolytes. One of them, the irreversible conversion of higher oxidation state vanadium into soluble $HV_2O_5^-$ is the root cause of the plateau occurring between - 0.3 V and 0 V [*vs.* Hg / HgO (in 1 M KOH)]. This is indeed an irreversible process seen to occur with higher oxidation state vanadium oxide containing vanadium nitride. However, this phenomenon is minimal in the VN prepared by mechano-chemical reduction as observed in **Figure 214**. The other plateau occurs as a result of the onset

of water electrolysis in aqueous electrolytes. This phenomenon is observed clearly in the charge-discharge profile. The discharge tails off after about - 1 V *vs.* Hg / HgO and the Columbic efficiency drops off to ~ 75 %. As it can be seen, the capacitance is more stable with a fade rate of ~ 0.042 % per cycle as compared to that of ~ 0.1% per cycle seen by Choi *et al.* [249]. It should also be noted that although the VN obtained from HEMM exhibits similar Faradaic response as the nano-particulate VN prepared by ammonolysis of VCl_4, the large observed difference in the supercapacitance values between the two indicates the importance and predominance of the nano-particulate nature necessary for achieving the high capacitive response.

VN prepared by milling can be seen to exhibit both lower specific surface area (~ 9.1 m^2/g) and a much larger crystallite size (~ 26.8 nm) in contrast to VN generated by the chemical approach (SSA 38.8 m^2/g, and crystallite size 6.33 nm). It should also be noted that although the electronic conductivity of the HEMM derived nanostructured VN (473 S/cm) is higher than that of the chemically derived nanoparticulate VN (81.8 S/cm) which is expected of a material possessing higher crystallinity as is the case with the HEMM derived VN; the reduced surface area and the larger particle size more than compensate for the high conductivity thus resulting in a lower capacitance. The synthesis of VN by mechano-chemical milling though yielding a material of lower charge storage capacity nevertheless bears promise on account of the relative ease and cost effectiveness of the procedure.

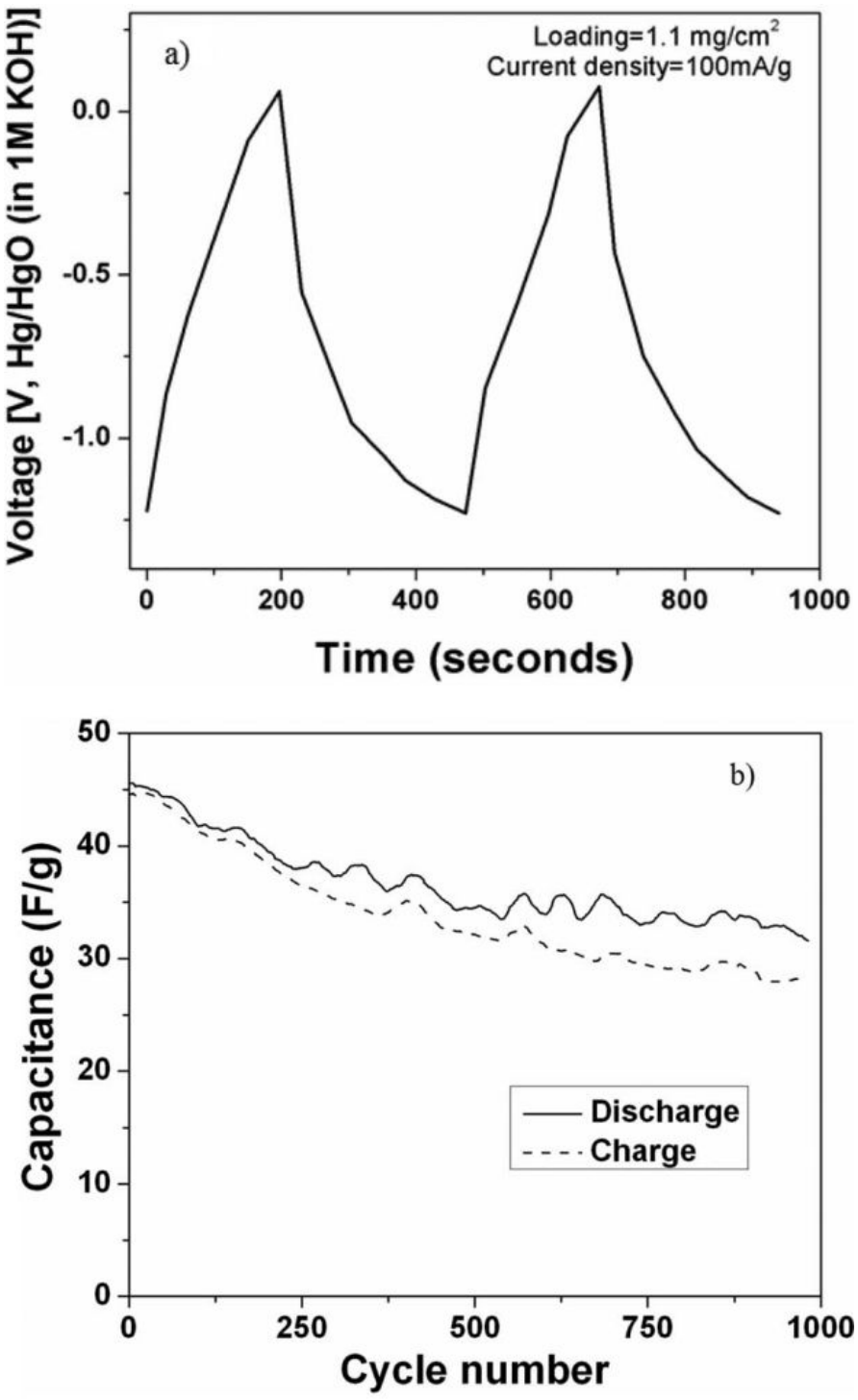

Figure 214. Galvanostatic charge-discharge profile (a), and long term charge - discharge cyclability of HEMM synthesized VN

D.2.4 Conclusion

Milled nitride has been synthesized and shown to have promising capacitance in the range of 25 to 60 F/g. Though the capacitance values are lower than those reported for chemically synthesized nanoparticulate VN, the ease of synthesis involved in milling induced mechano-chemical reduction makes it a very attractive method for synthesis of vanadium nitride. The study has also shown the effect of various materials parameters on VN capacitance. Importance of the reduced crystallite size and high surface area are highlighted in the study. In addition, the nature of the surface oxide has been identified to be vital for pseudocapacitance response of VN. Vanadium nitride synthesized by mechano-chemical reaction exhibits excellent cycling characteristics on account of the absence of Vanadium + 5 oxidation state surface oxide. Furthermore, it has been shown by various characterization techniques that VN derived by the mechano-chemical synthesis has large crystallites leading to better electronic conductivity, lower charge transfer resistance and thus better rate capability as compared to chemically synthesized nanoparticulate VN. The combination of simple low cost synthesis, good rate capability, cycling stability and excellent volumetric capacitance makes VN synthesized by HEMM a very attractive supercapacitor material amenable for scale up and large scale industrial production.

APPENDIX E

BATTERIES

E.1 TIN AND GRAPHITE BASED NANOCOMPOSITES FOR SODIUM ION BATTERIES

E.1.1 Introduction

Renewable energy sources such as solar, wind, geothermal and hydropower can generate electricity without producing carbon dioxide, the undesirable green house pollutant. Hence these systems portend enormous potential for meeting the future energy demands [349, 350]. However, the electricity generated from these intermittent renewable sources requires efficient electrical energy storage (EES) devices for effective delivery of uninterrupted electricity (power storage back up) and load leveling as well as grid energy storage [349-351]. In addition, there is a tremendous global impetus for improved EES devices so that smooth transition from the current hybrid electric vehicle state to that of the much touted plug-in hybrids and the highly desired all-electric vehicles (EVs) is ultimately realized [349-351]. Chemical energy storage technologies based on rechargeable batteries are considered one of the leading EES technologies

to meet this target offering the much desired panacea for both electric vehicles as well as stand-alone stationary power systems [349-353]. Currently Li-ion batteries are the preferred much sought after rechargeable battery systems for most electronic devices and hybrid cars [349-357]. However, in the last few years, a variety of factors have led to considerable interest in Na-ion batteries employing Na^+ to reversibly store power in a compact system offer a compelling economical solution for electrical energy storage [242, 358-361]. In contrast to the Li-ion system that has been researched extensively over the last two decades following its commercialization by Sony in 1990, Na-ion battery is still in a very much developmental research phase. Nevertheless, it has become a target of much debate of late, and is forecasted to be a cheaper (cost equivalent of dollars for bulk metal- Na: 0.075, Li: 0.50), more durable option to store energy compared to the hitherto used Li-ion batteries [242, 358-361]. Moreover, Li is relatively in less abundance (~ 0.0007 % by weight of the earth's crust), whereas Na is much more copiously available (~ 2.6 % by weight of the earth's crust) [225, 242, 358-361]. Na-ion is also chemically more stable compared to Li-ion and more environmentally benign. Consequently, large scale Na-ion EES device have the potential to be easier to engineer and pose less safety concerns [242, 358-360, 362, 363]. If the evolution of Li-ion and Na-ion batteries is assumed to follow a similar trajectory, it is likely that Na-ion batteries will soon emerge an attractive alternative front runner due to the low cost, larger abundance and other environmental combined with socio-economic attributes.

In order for Na-ion to compete with the much researched Li-ion systems, considerable improvement in energy density and rate capability along with performance is required before sodium / liquid organic electrolyte batteries can be considered for practical use as EES devices. Identification of suitable cathodes and anodes which can exhibit high specific capacity, low

irreversible loss, high coulombic efficiency and long cycle life as well as can intercalate / de-intercalate Na^+ at potential above ~ 3 V for the cathode and ~ 0.01 V - 1 V for the anode of Na / Na^+ will be a paradigm shift in the development of high energy density Na-ion rechargeable batteries for EES systems supporting rapid transition to EVs as well as wind and solar energy, distributed energy systems, or 'smart' grid operations. In addition, fundamental studies of alloying / dealloying mechanism of Na^+ with metal alloy anodes and ceramic cathodes will provide valuable information for designing new systems. There is therefore a critical need for significant research to be conducted in the Na-ion battery area, particularly related to identification of new materials and chemistries while also developing cost effective approaches to generate these systems to achieve the much desired radical improvements in energy and power densities. Few studies of candidate negative electrodes for Na-ion battery can be found in the current scientific literature [364-369].

It is now well known that graphite and silicon though well established in the case of the former, and the latter very much researched for Li-ion; however cannot be used as a negative electrode for Na-ion systems since Na atoms do not reversibly alloy / dealloy to form Na-C or Na-Si alloys similar to the Li counterpart (*E.g.* LiC_6 or $Li_{4.4}Si$, respectively) [331, 370]. Recent reports suggest the identification of nanoporous hard carbons as possible negative electrode materials, wherein Na atoms apparently adsorb instead of alloying onto the surfaces or nanoscopic pores throughout the hard carbon particles [364, 366-369]. Doeff *et al*. [364] showed that insertion of Na into petroleum - coke leads to a reversible capacity of ~ 85 mAh/g and proved the feasibility of a rechargeable Na-ion battery with the selection of appropriate electrode materials. Several researchers [364, 366-369] have studied the electrochemical absorption of Na into some hard carbon structures and have found that a reversible capacity ~ 250 mAh/g - 300

mAh/g could be achieved. Such carbons appear to be suitable anodic materials for rechargeable Na-ion batteries. However, deposited Na metal on C surfaces or nanopores appears to form dendrites similar to Li and its safety is further questionable due to its low melting point of 97.7°C compared to 180.5°C for Li. Chevrier *et al.* [370] recently examined theoretically the viability of Na-ion negative electrode materials based on Na alloys (Na-Si, Na-Sn and Na-Pb system) in terms of volumetric energy density and mechanical stability. They have reported formation of different Na-Sn alloy ($NaSn_5$, NaSn, Na_9Sn_4 and $Na_{15}Sn_4$) in the potential window of 0 V - 0.7 V associated with large volume expansion. The calculated volume expansion of different Na-Sn alloys with respect to Sn along with the theoretical specific capacity (mAh/g) associated with the formation of respective phases is tabulated in **Table 16**. Komaba *et al.* [365] has reported a 1^{st} cycle discharge and 1^{st} cycle charge capacity ~ 878 mAh/g and ~ 758 mAh/g, respectively, in a Sn-polyacrylic acid electrode with rapid fade in capacity when cycled in the potential window 0 V - 1.5 V. On the other hand, SnSb/C nanocomposite has been reported to exhibit a reversible capacity ~ 540 mAh/g with 80 % capacity retention after 50 cycles [361]. In spite of the above reports, Na-Sn alloys as negative electrodes have yet to be extensively studied experimentally in order to improve the long term cyclability, coulombic efficiency and specific capacity for future applications in EES devices. In the present study, a homogeneous mixture based on tin and graphite (Sn/C) has been studied as a negative electrode for Na-ion batteries. To demonstrate efficacy, Sn/C nanocomposite has been prepared by high energy mechanical milling (HEMM) for different duration of milling. In order to compare the electrochemical results of Sn/C with pure microcrystalline Sn, the electrochemical properties of pure microcrystalline Sn alone has also been studied. The results indicate feasibility of this system as a potential anode for use in Na batteries [371].

Table 16. Intermetallic sodium stannide (zintl phases) with hteir molar volume, volume expansion and theoretical capacity

Intermetallics	V_m (cm^3/mol)	$(V_m-V_{Sn})/V_{Sn}$	Gravimetric capacity (mAh/g)
$NaSn_5$	21	28 %	45
NaSn	35.8	120	226
Na_9Sn_4	56.7	248	508
$Na_{15}Sn_4$	85.4	424	847

E.1.2 Experimental Section

The mixtures of elemental powders of synthetic graphite (Aldrich, 1 - 2 μm) and Sn (Alfa Aesar, -325 mesh, ≤ 44 μm) of nominal composition C - 70 wt.% Sn were subjected to high energy mechanical milling (HEMM) in a high energy shaker mill (SPEX CeriPrep 8000M) for 5 minutes and 1 hour in a stainless steel (SS) vial using 20 SS balls of 2 mm diameter (~ 20 g) with a ball to powder weight ratio 10 : 1. Graphite (~ 0.6 g) and Sn (~ 1.4 g) were batched in a SS vial in an argon filled glove box (MBraun Unilab Work station - 1200/780) in order to prevent oxidation of the reactive powders during milling.

In order to perform qualitative phase analysis, the milled powders were characterized by x-ray diffraction (XRD) using the Philips PW1830 system employing the CuK_α (λ = 0.15406

nm) radiation. The microstructure of the electrode before and after electrochemical cycling has been carried out using a scanning electron microscope (SEM) equipped with energy dispersive x-ray analysis (EDAX). Philips XL-30FEG equipped with an EDS detector system comprised of an ultrathin beryllium window and Si(Li) detector operating at 25kV was employed for the secondary electron (SE) image. Micro-Raman analyses of the Sn/C have been performed on a multichannel Renishaw InVia Raman microscope. Excitation was provided by the ~ 633 nm line of a diode laser.

In order to evaluate the electrochemical characteristics, electrodes were fabricated by mixing 80 wt.% of the active powder of -325 mesh and 10 wt.% Super P carbon black. A solution containing 10 wt.% polyvinylidene fluoride (PVDF) in N-methylpyrrolidinone was added to the mixture to make a homogeneous solution. The as prepared solution was coated onto a Cu foil and dried at 110°C in vacuum oven. A 2016 coin cell design was used employing sodium foil as a counter electrode, studied electrode as the working electrode and 1 M $NaClO_4$ in ethylene carbonate / dimethyl carbonate (EC / DMC = 1 : 2 by volume) as the electrolyte. All the cells tested in this study were cycled at room temperature within 0.01 V - 1.2 V employing the discharge / charge rates of ~ 50mA/g with a minute rest period between the charge / discharge cycles using a multichannel battery testing system (Arbin BT2000 instrument).

E.1.3 Results and Discussion

Figure 215 shows the variation of specific capacity *vs.* cycle number of pure microcrystalline Sn ($\leq$ 44 μm) cycled at a rate of ~ 50 mA/g in the potential window 0.01 V - 1.2 V. Pure Sn shows a 1^{st} discharge capacity of ~ 856 mAh/g which is close to the theoretical capacity (~ 847 mAh/g)

corresponding to the formation of $Na_{15}Sn_4$ intermetallic or amorphous phase of composition Na - 21 at.% Sn (**Table 16**). The observed 1st discharge capacity in the present study is also in good agreement with the previous reports [361, 365]. The differential capacity plot (dQ/dV *vs.* V) relating to the 1st cycle of pure Sn, shown in **Figure 216**, clearly shows that the alloying reaction (discharge) of Na ion with microcrystalline Sn occurs mainly at a peak potential of ~ 0.18 V, ~ 0.081 V and ~ 0.033 V with an onset potential of ~ 0.21 V, ~ 0.13 V and ~ 0.061 V, respectively. In the present study, the phase/s forming corresponding to the peak potential of ~ 0.18 V, ~ 0.081 V and ~ 0.033 V has been denoted as X-I, X-II and X-III, respectively. The reaction potential and the associated specific capacity, calculated from the deconvolution of the peaks, related to X-I, X-II and X-III phase formation is tabulated in **Table 17**. The composition of the X-I, X-II and X-III phases, estimated based on the associated specific capacity of the respective phases related to the number of reacting sodium ions, is correspondingly close to Na - 50 at.% Sn (NaSn), Na - 30.7 at.% Sn (Na_9Sn_4) and Na - 21 at.% Sn ($Na_{15}Sn_4$), respectively. However, pure Sn shows a 1st charge capacity of ~ 280 mAh/g with an irreversible loss of ~ 67 % (**Figure 215**) which is expected to arise due to the structural failure of Sn particles and / or irreversible alloying / de-alloying processes of Sn with Na very similar to what is known in Li alloying with Si [333, 356]. The differential capacity plot of the 1st charge shows that the de-alloying reaction (charge) of Na ion from X-III phase occurs only at a peak potential of ~ 0.17 V with an onset potential of ~ 0.065 V which suggests alloying and de-alloying reaction of pure microcrystalline Sn with Na ion is irreversible in nature.

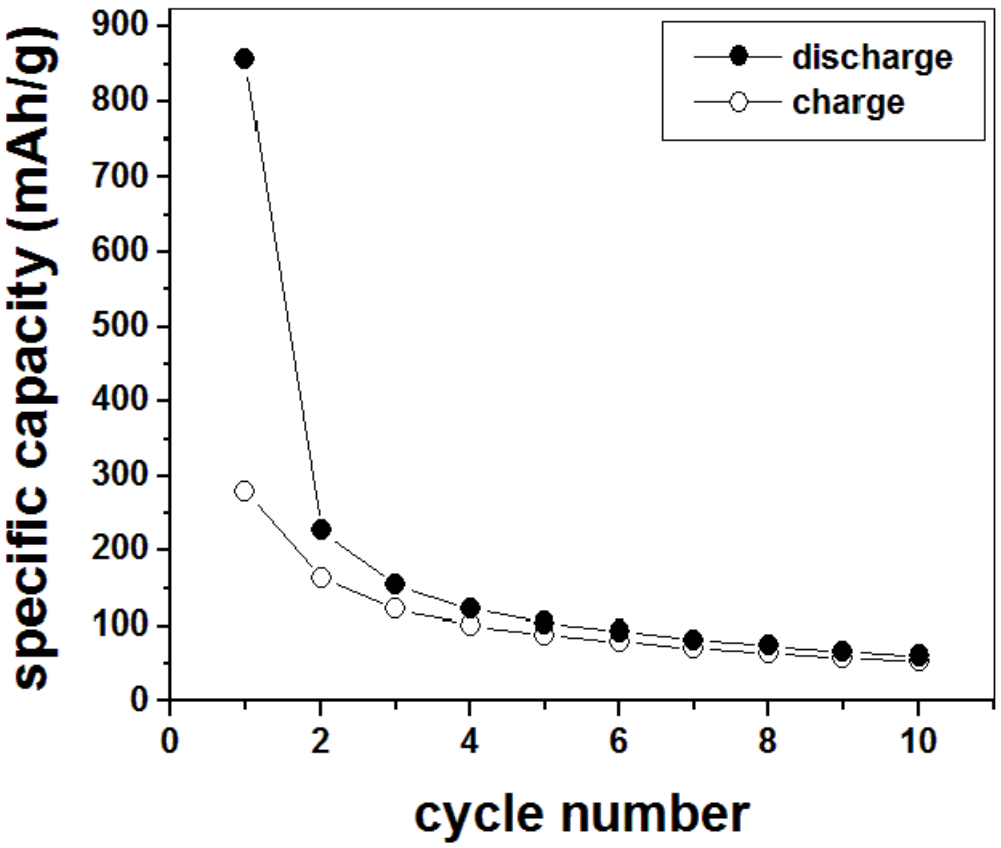

Figure 215. Specific capacity *vs.* cycle number of microcrystalline Sn cycled at a constant current of ~ 50 mA/g in the potential window 0.01 V - 1.2 V

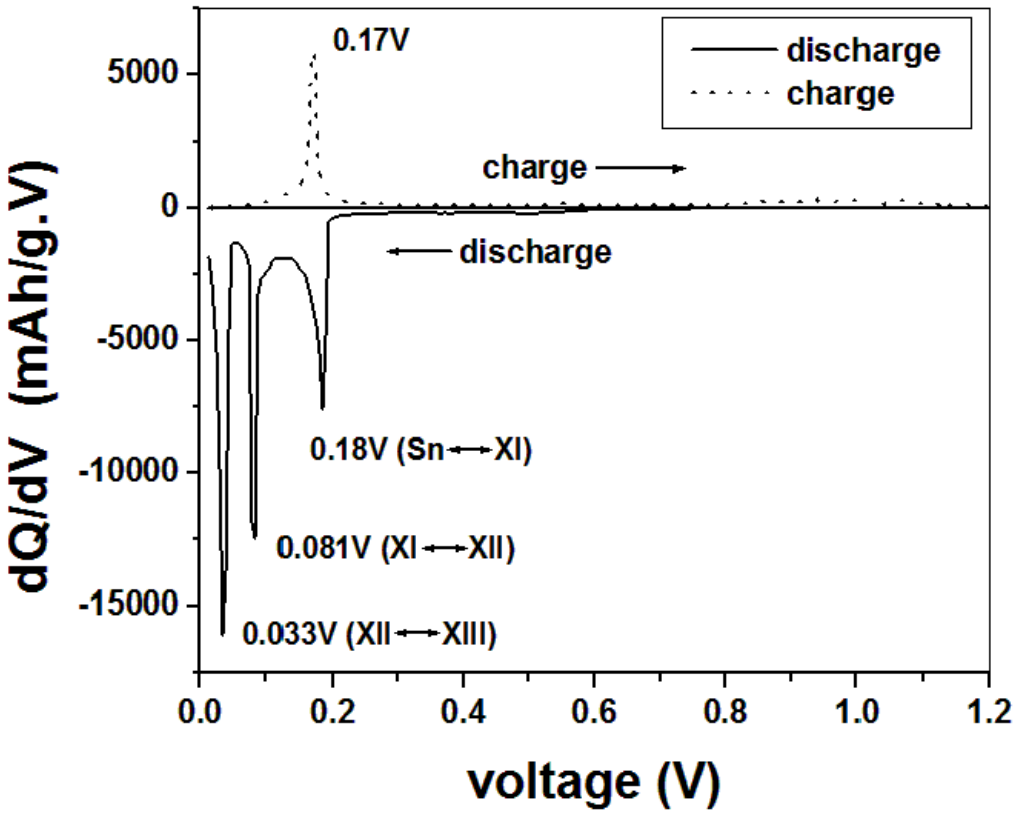

Figure 216. Differential capacity *vs.* cell potential curves of microcrystalline Sn obtained after 1st cycle cycled at ~ 50 mA/g in the potential window 0.01 V - 1.2 V

Table 17. Reaction potential and associated specific capacity of different intermetallics (zintl phases) form during alloying of Na ion with pure Sn

Reaction potential window (V)	Peak potential (V)	Associated specific capacity (mAh/g)	Intermetallic
0.21 - 0.13	0.18	215	X-I (NaSn)
0.13 - 0.063	0.081	260	X-II (Na_9Sn_4)
0.063 - 0.01	0.033	325	X-III ($Na_{15}Sn_4$)

Figure 217 shows the SEM images of pure microcrystalline Sn before cycling (a) and after the 10^{th} cycle (b). It indicates clear evidence of structural failure of the cycled Sn. The mechanical failure of pure Sn during alloying / de-alloying processes is expected to arise due to large volume expansion (~ 420 %) during alloying of Sn with Na to form $Na_{15}Sn_4$; and as a result loss of electrical contact between the cracked and isolated Sn particles, and the current collector as is evident in the case of elemental Si when cycled with Li^+ [333, 356].

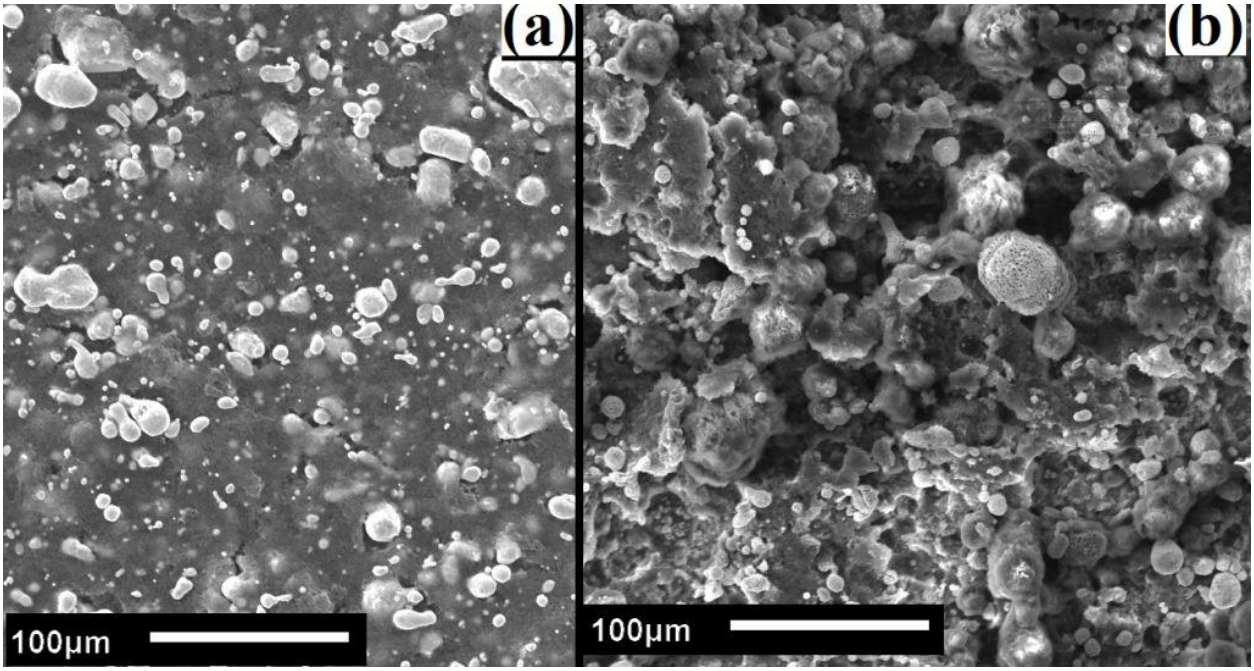

Figure 217. SEM micrograph of pure Sn before (a), and after 10th cycle (b)

In order to improve the structural integrity and cyclability of the Sn based anode, a homogeneous mixture based on Sn and graphite has been synthesized by high energy mechanical milling milled for different duration. The mechanical properties, and as a result the structural stability of Sn/C mixture is expected to be improved due to the presence of graphitic buffer matrix. After 5 minutes and 1 hour of mechanical milling of Sn and graphite of nominal composition C - 70 wt.% Sn, the XRD pattern plotted in **Figure 218**, shows only the presence of pure Sn and graphite without formation of any second phase or oxidation of Sn to SnO_2. This result clearly suggests that graphite and Sn form a homogeneous mixture up to 1 hour of milling without any significant diffusive reaction to form a second phase as also expected from the equilibrium phase diagram which shows immiscibility of Sn and C due to positive heat of reaction [372]. The effective crystallite size of Sn obtained after 1 hour of milling, calculated

using the Scherrer formula from the integral breadth of the Lorentzian contribution determined from peak profile analysis using single line approximation method after eliminating the instrumental broadening and lattice strain contribution [88], is ~ 90 nm; whereas the crystallite size of Sn after 5 minutes of milling is still in the μm range suggesting that HEMM for 1 hour results in the formation of a nanocomposite of Sn and C. On the other hand, the calculated crystallite size of graphite after 5 minutes and 1 hour of milling is ~ 47 nm and ~ 17 nm, respectively.

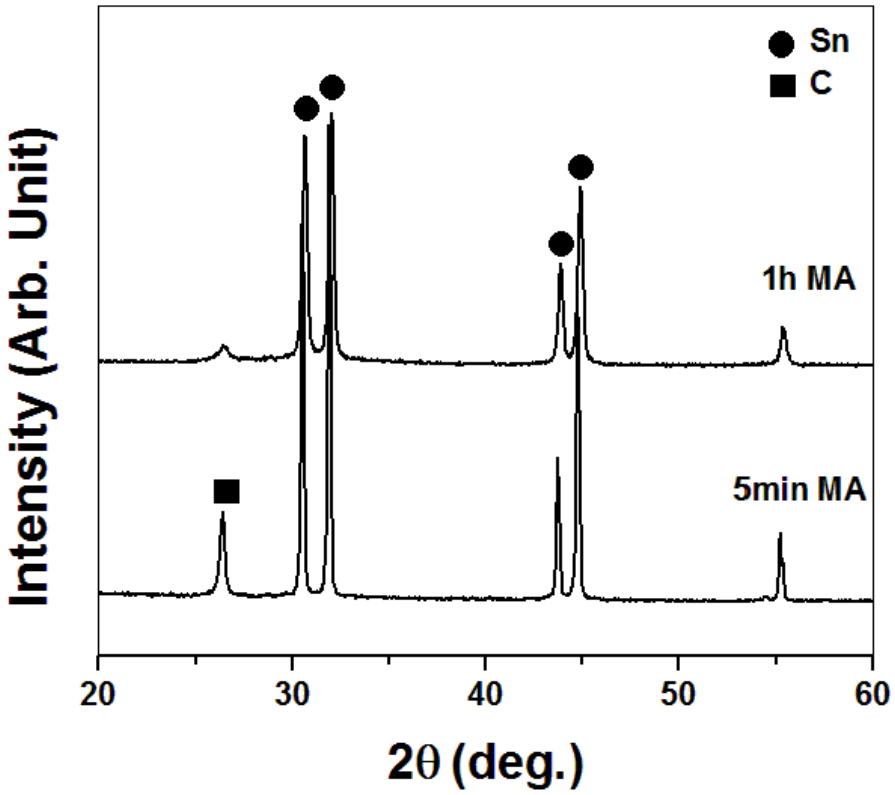

Figure 218. XRD patterns of C - 70 wt.% Sn generated after 5 minutes and 1 hour of milling

In order to investigate the structural order / disorder nature of graphite and possible presence of SnO_2, Raman spectroscopy analysis of Sn/C obtained after 1 hour of milling has been carried out. The Raman spectra of Sn/C, displayed in **Figure 219** along with pure graphite, shows peaks at ~ 1580 cm^{-1} and ~ 1334 cm^{-1} which corresponds to ordered graphite (G band) and the disordered carbon (D band) [373]. The intensity of D band of disordered carbon appears to increase in the Sn/C mixture as compared to graphite which clearly suggests that the crystalline graphite structure collapses to form an amorphous disordered form due to the defect induced melting of crystalline graphite which is commonly observed during HEMM [373, 374]. No significant peaks of crystalline SnO_2, normally seen as characteristic sharp peaks at ~ 474 cm^{-1}, ~ 632 cm^{-1} and ~ 774cm^{-1} corresponding to the E_g, A_{1g} and B_{2g} vibration modes [375] are observed which suggests no oxidation of Sn to SnO_2 during the milling process.

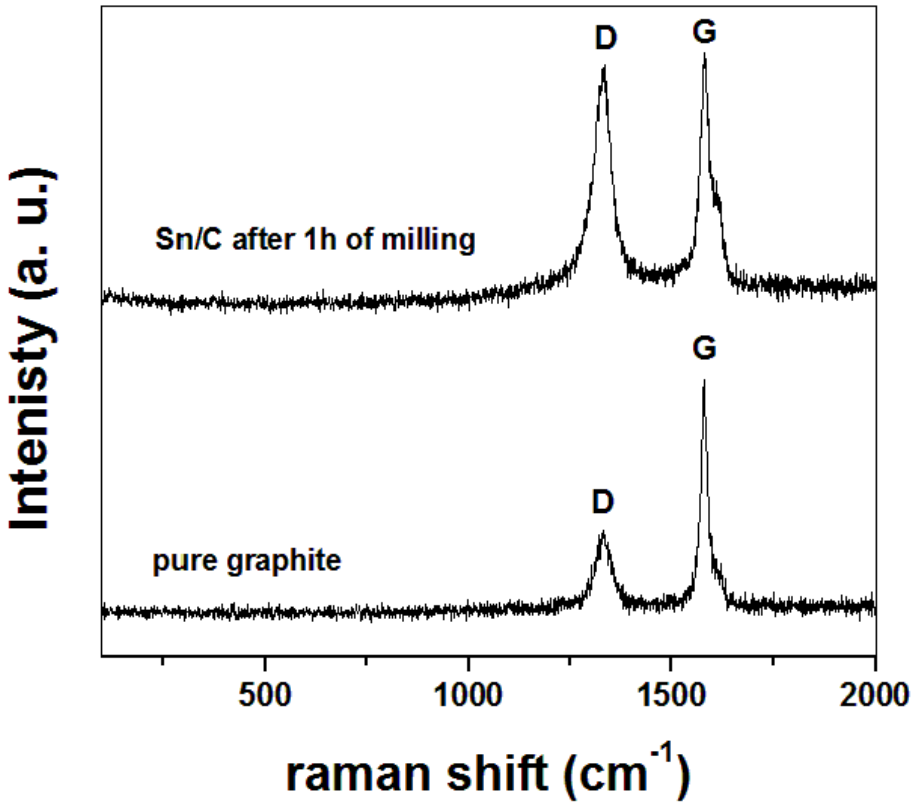

Figure 219. Raman spectra of Sn/C mixture obtained after 1 hour of mechanical milling

Figure 220 shows the variation of specific capacity *vs.* cycle number along with coulombic efficiency of the Sn/C mixture synthesized after 5 min of milling, cycled at a constant current of ~ 50 mA/g in the potential window of 0.01 V - 1.2 V. The 1st discharge and 1st charge capacity of the Sn/C mixture obtained after 5 minutes of milling is ~ 621 mAh/g and ~ 462 mAh/g, respectively, with a 1st cycle irreversible loss of ~ 25 % and the coulombic efficiency above ~ 97 % after the 1st cycle. This result clearly suggests that the presence of graphite as a matrix in the Sn/C mixture improves the structural stability of Sn/C in comparison to pure Sn during the alloying / de-alloying processes with Na. However, a rapid fade in capacity (3.6 % per

cycle) is observed which suggests that HEMM of Sn and C for 5 minutes is not sufficient to generate a strong interfacial bonding in order to improve the mechanical properties and structural integrity of Sn/C for long cycle life.

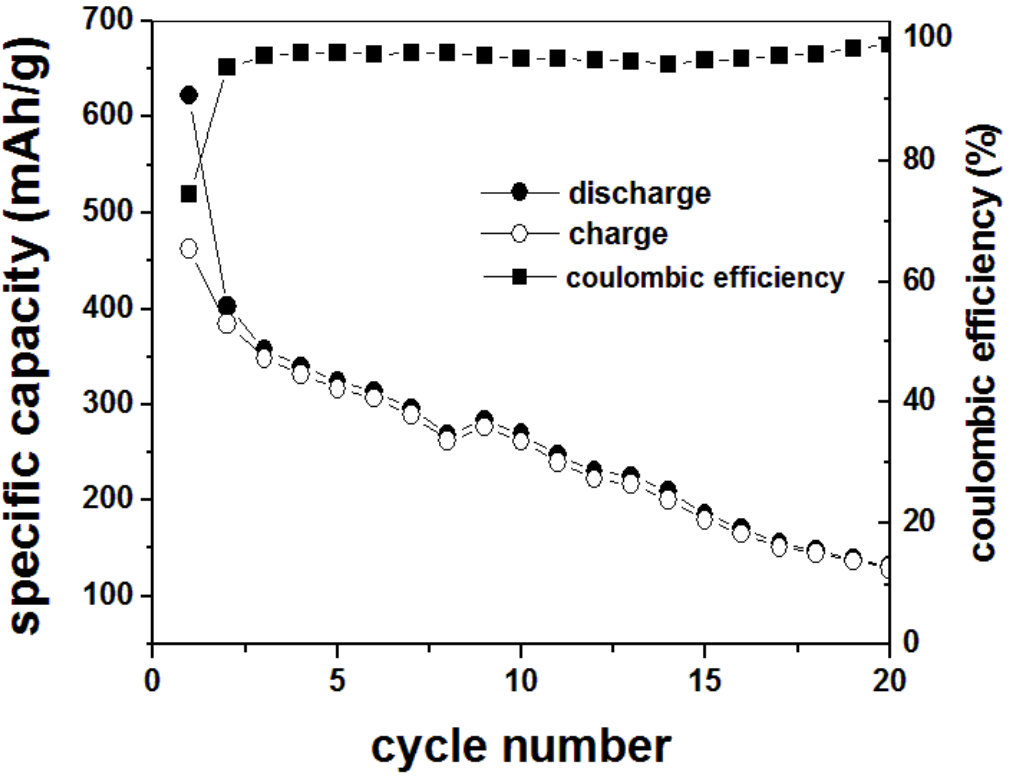

Figure 220. Specific capacity and coulombic efficiency *vs.* cycle number of Sn/C obtained after 5 minutes of HEMM cycled at a constant current of ~ 50 mA/g

On the other hand, the nanocrystalline Sn/C nanocomposite mixture obtained after 1 hour of milling shows a 1st discharge and a 1st charge capacity of ~ 584 mAh/g and ~ 410 mAh/g, respectively, with an irreversible loss of ~ 29 % as seen in **Figure 221**. The coulombic efficiency is above 97 % after the 1st cycle when cycled at an identical current of 50 mA/g in the potential

window of 0.01 V - 1.2 V. The 1st cycle irreversible loss may arise due to electrolyte decomposition at the electrode surface to form a solid electrolyte interphase (SEI) layer rather than the irreversible nature of Na - Sn/C reaction.

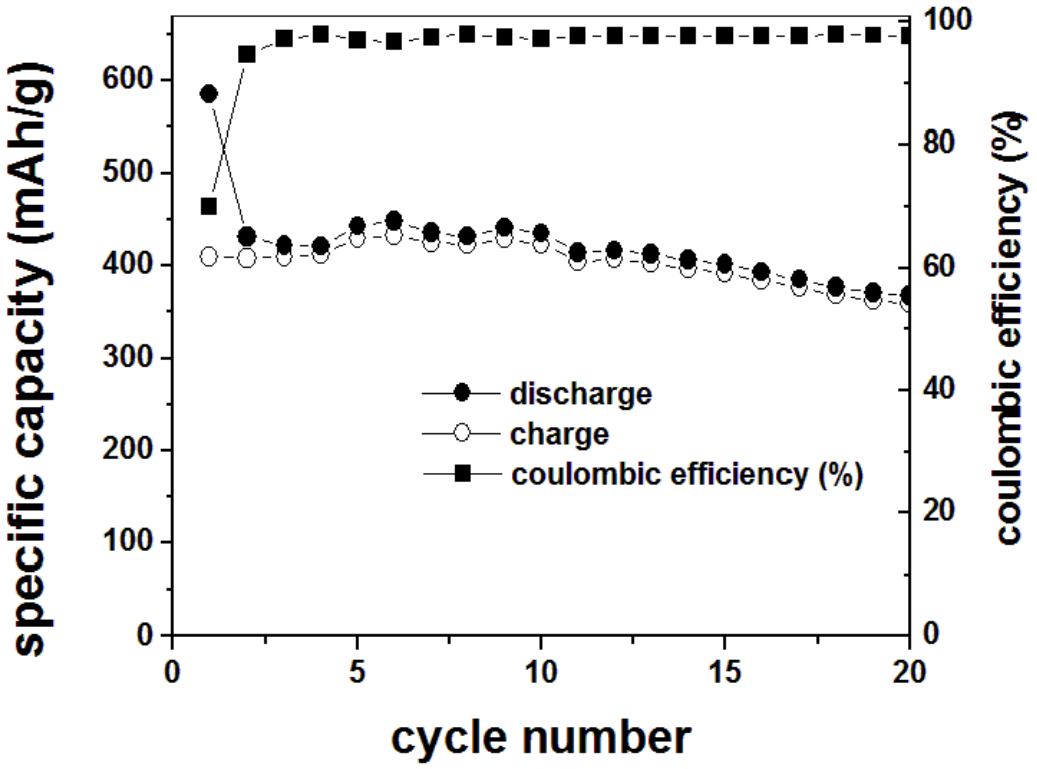

Figure 221. Specific capacity and coulombic efficiency *vs.* cycle number of Sn/C obtained after 1 hour of HEMM cycled at a constant current of ~ 50 mA/g

In comparison to pure Sn and the Sn/C mixture obtained after 5 minutes of milling, the Sn/C nanocomposite mixture obtained after 1 hour of milling shows improvement in cyclability up to 20 cycles with a fade in capacity of ~ 0.7 % loss per cycle. This improvement in the cyclability of Sn/C mixture with increasing milling time is expected due to the likely improvement in mechanical properties of the Sn/C mixture arising from the better interface

adhesion and / or bonding between the Sn and C with increasing milling time which is expected to relieve the stress / strain experienced by Sn to C buffer layer during alloying / de-alloying reaction with Na^+. The improvement of cyclability also may arise due to the nanocrystalline nature of Sn (~ 90 nm) and graphite which are known to exhibit better mechanical properties with respect to their bulk counterpart. The SEM micrograph of the cycled samples of Sn/C electrode cycled at ~ 50 mA/g, shown in **Figure 222**, indicates the excellent structural integrity (devoid of any cracks) even after 20 cycles.

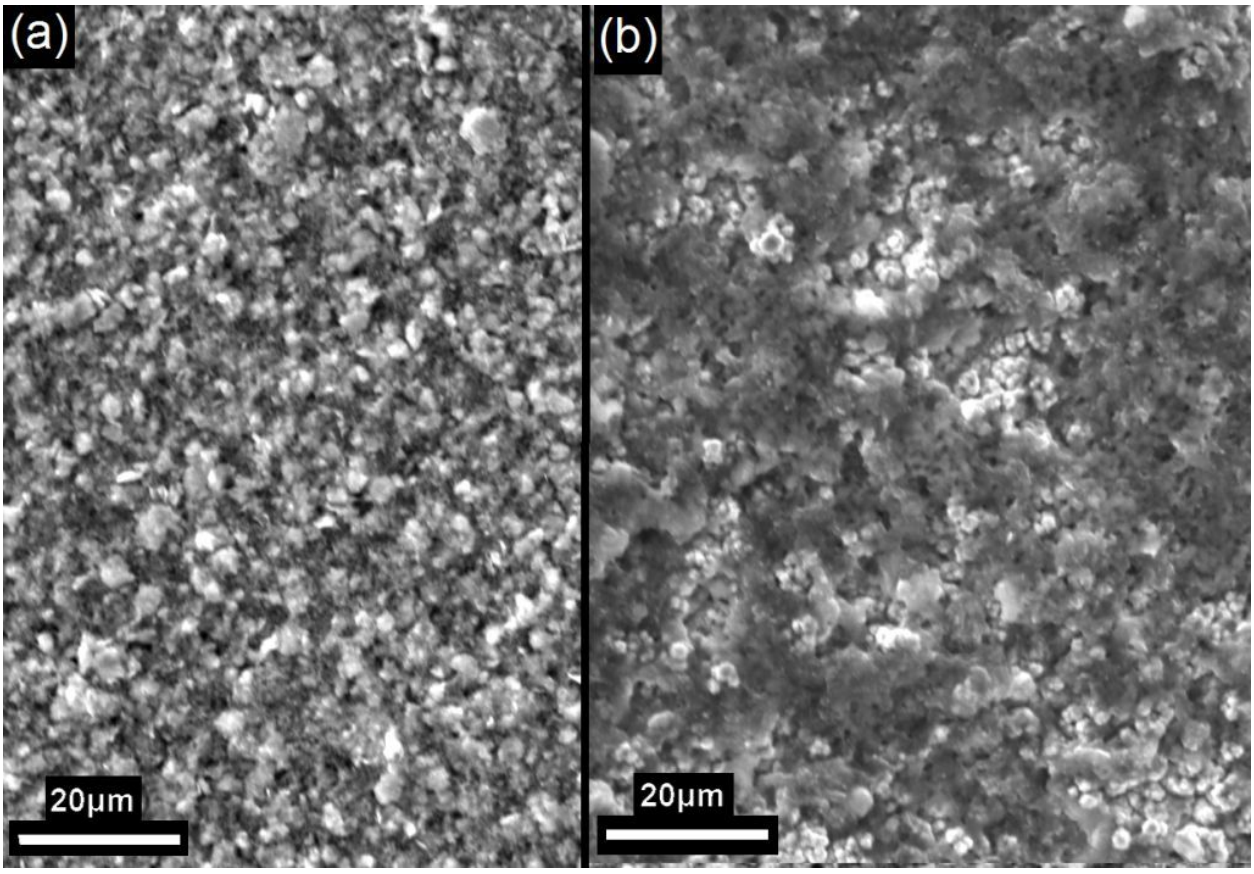

Figure 222. SEM micrograph of Sn/C mixture, obtained after 1 hour of HEMM before (a), and after 20 cycles (b)

These results clearly suggest that the presence of graphite as a buffer matrix significantly improves the structural stability of the Sn/C with respect to pure Sn. This promising result is a reflection for the much research warranted to synthesize nanocomposites exhibiting high strength, high ductility and strong interface of Sn with the matrix. The result also suggests the need for the identification of suitable binders in order to improve the cyclability, rate capability and coulombic efficiency of Sn based electrodes for use as anodes for Na-ion batteries [371].

E.1.4 Conclusion

The present study has been devoted to identify a suitable negative electrode for Na-ion batteries based on a homogeneous mixture of nanocrystalline tin and graphite (Sn/C). Nanocrystalline Sn/C mixture of nominal composition C - 70 wt.% Sn has been synthesized by high energy mechanical milling (HEMM) of pure microcrystalline Sn and graphite. Pure microcryalline Sn exhibits a 1st discharge capacity of ~ 856 mAh/g due to extensive electrochemical reaction of Na^+ with Sn in the peak potential of ~ 0.18 V, ~ 0.08 V and ~ 0.033 V. The phase/s forming at the corresponding peak potentials, determined from the associated specific capacity, are expected to be NaSn, Na_9Sn_4 and $Na_{15}Sn_4$. However, Sn shows a rapid fade in capacity and poor capacity retention due to large volume expansion of Sn to form $Na_{15}Sn_4$ (~ 400 %).

On the other hand, nanocrystalline Sn/C mixture with a crystallite size of Sn ~ 90 nm shows a 1st discharge and 1st charge capacity ~ 546 mAh/g and ~ 410 mAh/g, respectively. The nanocrystalline Sn/C mixture also shows improved capacity retention (0.7 % fade in capacity per cycle) indicating its promise as an anode for Na ion batteries. SEM analysis indicates that the structural integrity combined with microstructural stability of the Sn/C mixture during the

alloying / dealloying process with sodium appear to be the main reasons contributing to the good cyclability in comparison to pure Sn. This buffering capacity of graphite is expected to minimize the volume expansion related cracking of tin enabling its use as anode for sodium ion batteries.

E.2 SILICON - CARBON THIN FILM FOR LITHIUM ION BATTERIES

E.2.1 Introduction

Generation of electricity from renewable energy sources, such as solar or wind, without producing carbon dioxide, an undesirable green house pollutant, offers enormous potential for meeting future energy demands [349, 350]. However, the electricity generated from these intermittent renewable sources requires efficient electrical energy storage (EES) devices for effective delivery of uninterrupted electricity (power storage back up) and load leveling as well as grid energy storage [349-351]. In addition, there is a great need for improved EES devices to transition from today's hybrid electric vehicle state enabling the realization of plug-in hybrids or the much desired all-electric vehicles (EVs) [349-351]. Chemical energy storage technologies based on rechargeable lithium ion batteries are among the leading EES technology, and in recent years have emerged as the flagship battery technologies offering the much desired hope for both electric vehicles as well as stand-alone stationary power systems [349-351, 355, 376]. Portable EES using Li-ion rechargeable batteries have become thus the primary energy storage pulse feeding the wireless revolution for cellular telephones and laptop computers, with hybrid electric

vehicles (HEV) following in close pursuit. However, the performance afforded by current lithium ion battery technologies is very much inferior and is unable to meet the colossal energy storage requirements allowing the efficient use of electrical energy in transportation, commercial, and residential applications. *E.g.* most EES devices based on lithium ion batteries need substantially higher energy and power densities, combined with faster charge/recharge rates if electric / plug-in hybrid vehicles are to be deployed as the universal replacements to gasoline-powered vehicles.

Development of novel electrode materials and electrolytes is essential if Li-ion batteries are to delivery higher energy and power densities. Identification of new systems and improvements in design, architecture and microstructure exhibiting faster recharge times and longer cycle lifetimes than the current state of the art systems is also necessary in order to enable the realization of practical EV transportation and efficient distribution of solar and wind generated electrical power. Rechargeable Li-ion batteries comprised of silicon as an anode in recent years has gained tremendous interest due to its high theoretical specific capacity (~ 4212 mAh/g) which is expected to deliver high energy density in the presence of high specific capacity cathode in the full cell configuration [269, 333, 356, 357, 376, 377]. However, the Si based anodes undergo massive volume expansion and contraction (~ 2 - 4 times) during electrochemical cycling which leads to structural failure of the Si based electrode during repeated alloying and de-alloying processes of Li-ion with Si [269, 333, 356, 357, 376-379]. As a result, the Si based anode materials show poor capacity retention, large 1^{st} cycle irreversible loss and poor coulombic efficiency at each cycle preventing the commercialization of Si based anode for high energy density Li-ion batteries. In order to improve the structural stability, 1^{st} cycle irreversible loss and coulombic efficiency of the Si based electrode, researchers have developed

novel material architectures (*E.g.* nanoporous mesoscopic structures) and refined the structural dimension to nanoscale levels (such as Si nanoparticle, Si nanowire, Si nanotube or thin film amorphous Si) which is expected to improve the electronic conductivity, mass transfer, reaction kinetics and mechanical properties [262, 269, 331, 333, 356, 357, 376, 377, 380-385]. For example, Chan *et al*. [377] has reported that Si nanowire based electrode can accommodate large strain during discharge / charge processes without pulverization; and as a result, the Si nanowire maintains a discharge capacity close to the theoretical capacity of Si with little fading up to 20 cycles. On the other hand, Maranchi *et al*. [382, 386] has reported that amorphous Si thin film of thickness ~ 250 nm exhibits high reversible capacity (~ 3800 mAh g^{-1} at a rate of C/2.5) with improved cyclability (~ 0.09 % fade per cycle) in the potential window of 0.02 V - 1.2 V in contrast to microcrystalline Si which degrades rapidly within few cycles [333].

Despite the nano-scale dimension of the Si anode, Si nanowire, Si nanotube, Si nanoparticle or amorphous Si thin films, all of these systems show a rapid fade in capacity after a few cycles attributed largely to the structural failure of the electrode. In order to improve the structural stability of the Si based electrode for longer lifetimes, the concepts of generating structurally stable nanocomposite materials utilizing nano-crystalline Si powder, Si nanowire, Si nanotube or amorphous Si homogeneously distributed within different types of carbon matrix (*E.g.* graphite, carbon nanotube and disordered carbon) or coated with carbon (core - shell structure) has been explored in great detail primarily to improve the mechanical properties and electronic conductivity of the composite materials [262, 269, 333, 350, 351, 357, 376, 378, 380-385, 387-392]. In this regard, different types of Si/C based composites have recently been generated and investigated [269, 357, 377-380, 384, 385, 387-392] utilizing a variety of synthesis techniques, such as chemical vapor deposition, high energy mechanical milling,

reduction of Si based precursor, thermal decomposition of organic precursors, dispersion of nano-Si in thermally pyrolyzed carbon aerogels *etc*., which show improved cyclability with respect to pure nanostructured Si. Despite these recent reports [350, 351, 355, 376, 380, 382, 385-389, 391], the capacity retention of the Si based nano-composite anode utilizing nanocrystalline or nanostructured silicon as the dispersoid within C matrix or coated with carbon is still not suitable for use in commercial applications due to the high degree of capacity fade per cycle (> 0.01 % loss per cycle), poor cyclability, low columbic efficiency and large 1st cycle irreversible loss. In the present study, the effect of thin amorphous C buffer layer on the structural stability and electrochemical response of amorphous Si thin films (~ 250 nm) has been studied. In this regard, an amorphous C/Si bi-layer thin film (*a*-C/Si) has been prepared by radio frequency (rf) magnetron sputtering where amorphous C of ~ 50 nm thickness is deposited as a buffer layer between the chromium coated copper (Cu) current collector and amorphous Si. In order to compare the electrochemical results of the *a*-C/Si thin film bi-layers with amorphous C/Si/C tri-layers, an amorphous carbon with ~ 50 nm thickness has also been deposited on top of the *a*-C/Si bi-layer thin film. Results of these studies followed by key recommendations of the appropriate nano-scale dimensions that would be needed for the design and low cost large scale manufacturing of amorphous C/Si composites yielding the desired specific capacity along with high energy density and excellent stability have been discussed.

E.2.2 Experimental Section

The *a*-Si, *a*-C/Si bi-layers, and *a*-C/Si/C tri-layered thin film sandwich electrode structures have been deposited on chromium coated high purity oxygen free (HPOFC) 0.0019” thick copper foil

substrates. Due to poor wetting behavior of C with Cu, a ~ 10 nm thick chromium (Cr) has been pre-deposited on the Cu foil, denoted as Cu/Cr. The Cr layer alters the wetting characteristics promoting the adhesion of C to the Cu foil. A ~50nm thick amorphous C film has been deposited on Cu/Cr film using rf magnetron sputtering employing pyrolytic graphite C target. Nanoscale ~ 250 nm thick amorphous Si is deposited on top of the ~ 50 nm C film, denoted as *a*-C/Si thin film bi-layers, by rf magnetron sputtering from a commercial Si target. In the case of tri layered *a*-C/Si/C thin film anode, an additional ~ 50 nm thick amorphous C layer is deposited on top of the *a*-C/Si film. In order to compare the electrochemical properties of *a*-C/Si and *a*-C/Si/C composite with pure *a*-Si, a ~ 250 nm thick amorphous Si (*a*-Si) is also deposited on Cu/Cr substrate without any C buffer layer. The details of the deposition techniques have been described in detail earlier by our group [382, 386].

In order to perform qualitative phase analysis, the as deposited *a*-Si, *a*-Si/C and *a*-C/Si/C films deposited on Cu/Cr substrate were characterized by glancing angle x-ray diffraction (GAXRD) using the Philips PW1830 system employing the CuK_α (λ = 0.15406nm) radiation. The glancing angle x-ray diffraction (GAXRD) analysis has been carried out at various incidence angles in order to minimize the contribution from Cu substrate. The microstructure and elemental analysis of the films before and after electrochemical cycling has also been carried out using a scanning electron microscope (SEM) equipped with energy dispersive x-ray analysis (EDAX). Philips XL-30FEG equipped with an EDS detector system comprised of an ultrathin beryllium window and Si(Li) detector operating at 25 kV was employed for the secondary electron (SE) image and elemental analyses. Micro - Raman analyses of different thin films have been performed on a multichannel Renishaw InVia Raman microscope. Excitation was provided by the 633 nm line of a diode laser. Electrochemical characteristics of the films were analyzed by

utilizing the as deposited structures as electrodes. A 2016 coin cell design was used employing lithium foil as a counter electrode and 1 M $LiPF_6$ in ethylene carbonate / diethyl carbonate (EC / DEC = 1 : 2 by volume) as the electrolyte. All the cells tested in this study were cycled at room temperature within 0.02 V - 1.2 V employing the discharge / charge rates of ~ 100 $\mu A/cm^2$ - 500 $\mu A/cm^2$ with a minute rest period between the charge / discharge cycles using a multichannel battery testing system (Arbin BT2000 instrument).

E.2.3 Results and Discussion

The GAXRD patterns, collected at various incidence angles (0.05° - 0.5°), of *a*-Si/C thin films, synthesized by rf magnetron sputtering, are shown in **Figure 223**. No significant peaks corresponding to Si or carbon have been identified in the GAXRD pattern probably due to the amorphous nature of silicon and carbon. All the peaks, observed in the XRD patterns, correspond to Cu diffracted from the copper foil substrate. The presence of elemental silicon has been confirmed using energy dispersive X-ray spectroscopy analysis attached to the SEM. The SEM image along with EDAX of the as-deposited *a*-Si/C film is shown in **Figure 224**. It indicates the presence of dense silicon on the deposited film. In order to further investigate the structural nature of silicon (order or disorder), Raman spectroscopy analysis of *a*-C/Si thin film has been carried out. The Raman spectra of *a*-C/Si, shown in **Figure 225**, shows a broad transverse optical mode (TO) peak centered at ~ 480 cm^{-1} which is corresponding to amorphous Si. No significant peak corresponding to crystalline Si TO phonon mode, normally seen as a characteristic sharp peak at ~ 520 cm^{-1} is observed which suggests that the *a*-C/Si film synthesized by rf magnetron sputtering possesses only disordered amorphous structure of Si without any significant amount of

crystalline segments. Similar structural analysis (GAXRD, SEM and EDAX) conducted for *a*-Si and tri-layer *a*-C/Si/C thin film, deposited on Cu/Cr substrate shows analogous structural information in comparison to *a*-Si/C thin film.

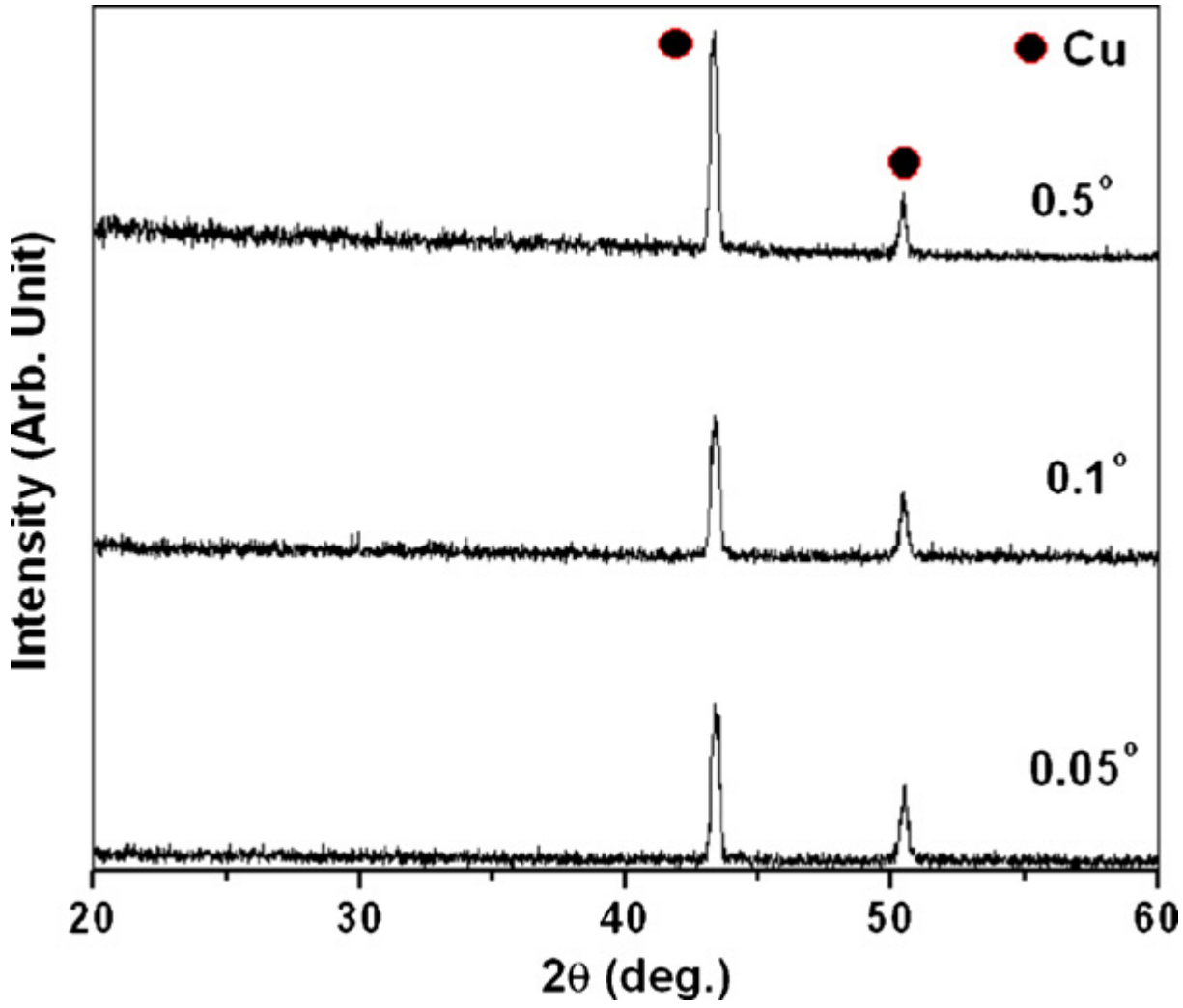

Figure 223. Glancing angle XRD patterns of *a*-C/Si bi-layer thin film generated by rf magnetron sputtering on copper foil

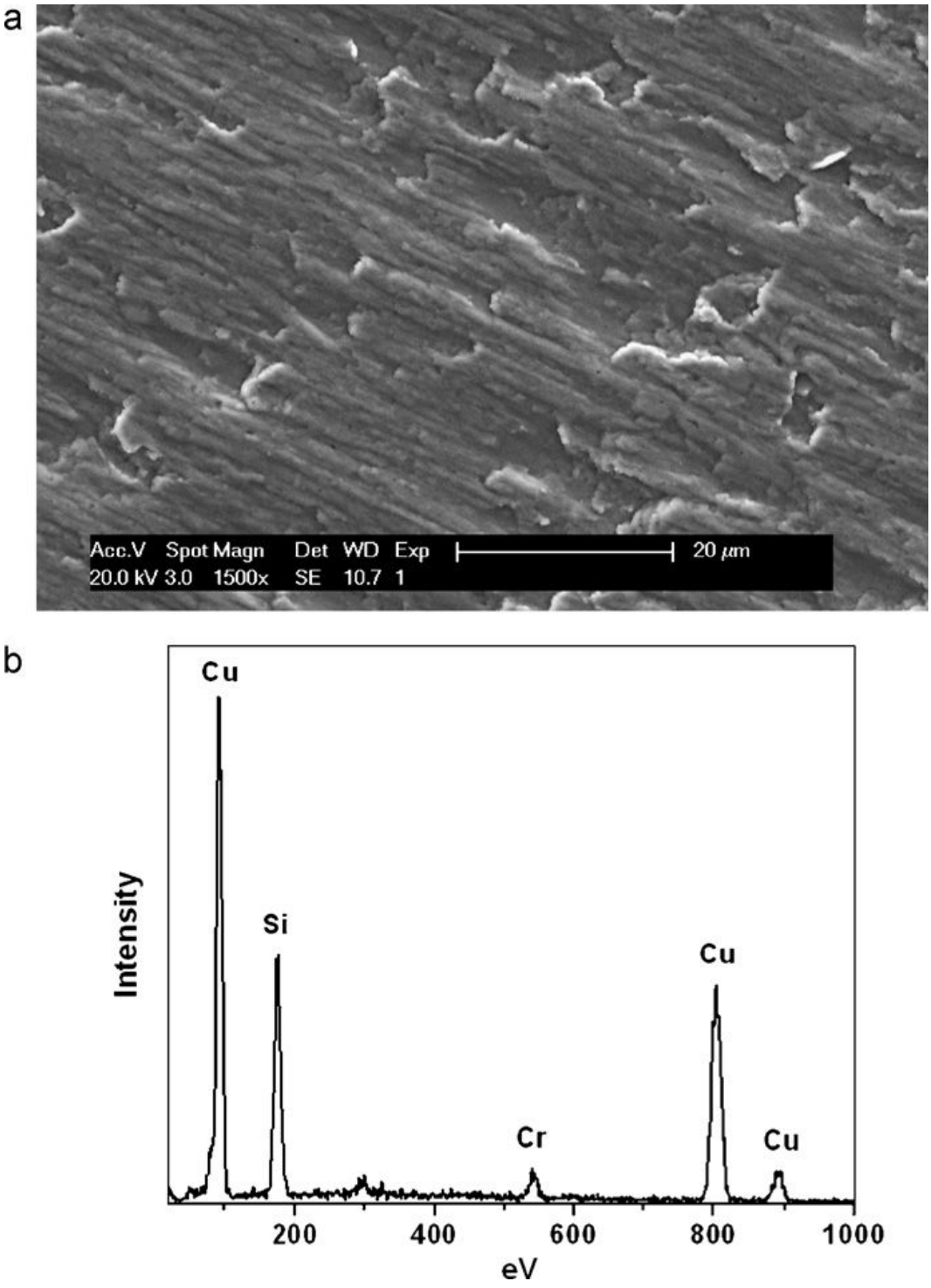

Figure 224. SEM micrograph (a), and EDAX spectra (b) of *a*-C/Si thin film

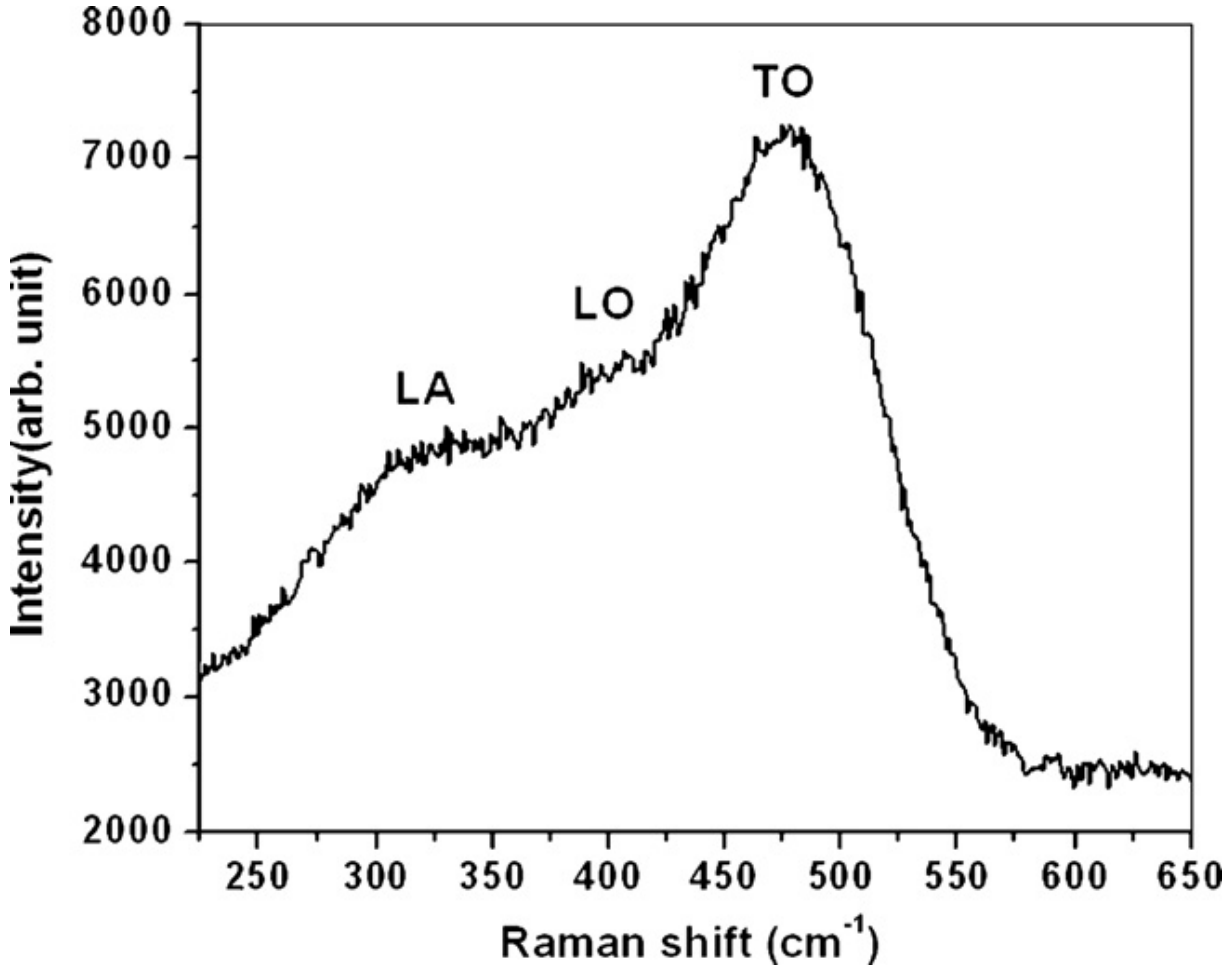

Figure 225. Raman spectra of *a*-C/Si thin film show the presence of amorphous Si

Figure 226 and **Figure 227** show the variation of specific capacity and coulombic efficiency *vs.* cycle number of *a*-Si and *a*-C/Si thin film, respectively, synthesized by rf magnetron sputtering, cycled at a rate of 100 µA/cm^2 (~ C / 2 rate) in the potential window 0.02 V - 1.2 V. The *a*-Si thin film shows a 1st discharge and 1st charge capacity of ~ 8751 mAh/cm^3 and ~ 7084 mAh/cm^3, respectively, with an irreversible loss of only ~ 19 %. The *a*-Si thin film exhibits excellent cyclability with a ~ 0.03 % capacity loss per cycle and excellent coulombic efficiency (~ 99.5 %) up to 30 cycles. However, a rapid fade in capacity and decrease of

coulombic efficiency is observed beyond 30 cycles which is similar in comparison to pure amorphous Si thin film (~ 250 nm thick film) deposited directly on Cu foil as reported previously [382, 386]. On the other hand, *a*-C/Si thin film bi-layer shows a 1st discharge and a 1st charge capacity of ~ 7809 mAh/cm^3 and ~ 6350 mAh/cm^3, respectively, with an irreversible loss of only ~ 18 % (**Figure 227**). The 1st discharge and 1st charge capacity of *a*-C/Si is ~10% lower than *a*-Si thin film due to the presence of ~ 50 nm C buffer layer between Cu/Cr substrate and *a*-Si to form the *a*-C/Si bi-layer film whereas the 1st cycle irreversible loss is quite similar. The bi-layer *a*-C/Si thin film composite anode shows excellent cyclability up to 50 cycles with a fade in capacity of ~ 0.02 % loss per cycle whereas *a*-Si thin film fades rapidly after 30 cycles (**Figure 226**). The coulombic efficiency of *a*-C/Si thin film is ~ 99.5 % up to 50 cycles which decreases with increasing cycle number above 50 cycles. The bi-layer *a*-C/Si thin film nanocomposite shows a higher capacity fade rate after 50 cycles with a fade in capacity of 0.2 % loss per cycle from 50 cycles to 75 cycles. Nevertheless, the above results clearly suggest that the presence of amorphous C buffer layer between Cu/Cr substrate and *a*-Si significantly improves the structural stability of *a*-C/Si thin film with respect to pure thin film amorphous Si. This improvement in the structural stability of the *a*-C/Si nanocomposite film is expected to be due to the likely improvement in mechanical properties of the *a*-C/Si film arising from the interface adhesion and / or bonding between the Si and C which is expected to relieve the stress / strain experienced by Si to C buffer layer during alloying/dealloying reaction with lithium ion and as a result, the delamination of the amorphous Si film from Cu/Cr substrate is prevented.

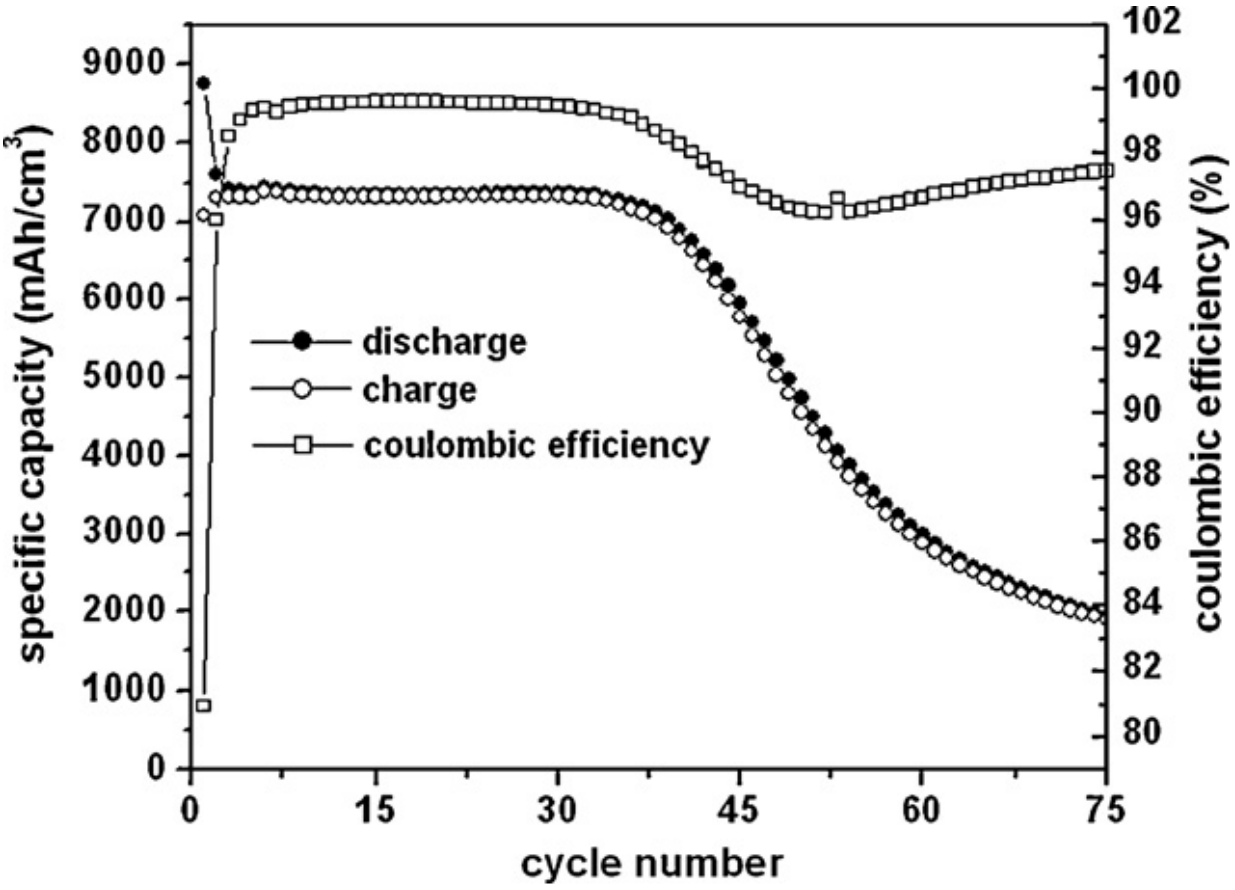

Figure 226. Specific capacity and coulombic efficiency *vs.* cycle number of *a*-Si thin film composite cycled at a constant current of ~ 100 μA/cm^2

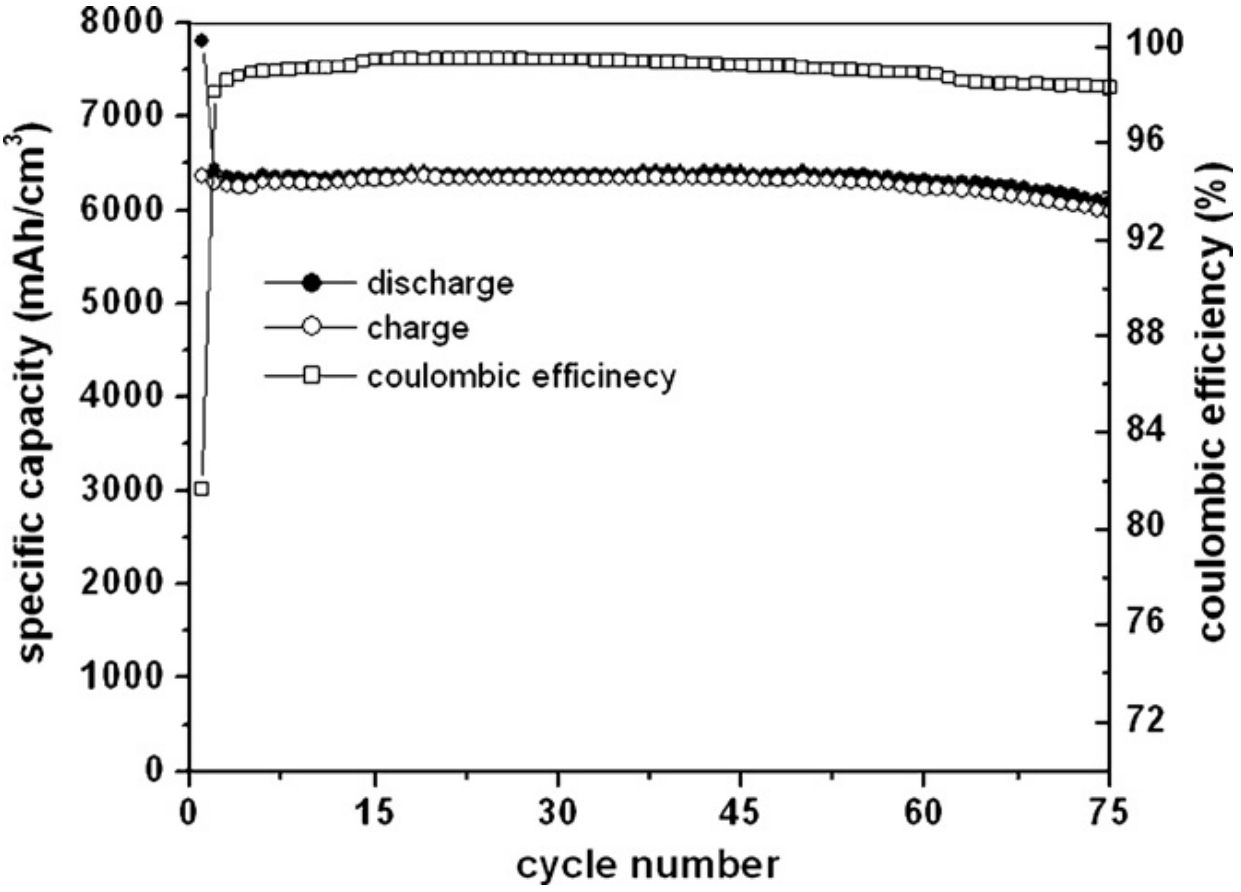

Figure 227. Specific capacity and coulombic efficiency *vs.* cycle number of *a*-C/Si thin film composite cycled at a constant current of ~ 100 µA/cm^2

In order to study the effect of C layer on top of the *a*-C/Si bi layer thin film on the electrochemical performance, the tri layers of *a*-C/Si/C thin film has also been cycled at a rate of 100 µA/cm^2 in the potential window 0.02 V - 1.2 V. The variation of specific capacity and coulombic efficiency *vs.* the cycle numbers of *a*-C/Si/C, shown in **Figure 228**, shows a 1st discharge and a 1st charge capacity of ~ 6430 mAh/cm^3 and ~ 5145 mAh/cm^3, respectively, with an irreversible loss of ~ 20 %. The tri-layered *a*-C/Si/C thin film composite anode also shows excellent cyclability up to 50 cycles with a fade in capacity of ~ 0.03 % loss per cycle and ~ 0.14 % loss per cycle after 50 cycles which is quite similar in nature in comparison to *a*-C/Si bi-layer

film. The coulombic efficiency of *a*-C/Si/C thin film is ~ 99.5 % up to 50 cycles which decreases with increasing cycle number above 50 cycles. The above results clearly indicate that the presence of amorphous C layer on top of the *a*-C/Si does not improve the stability or cyclability significantly compared to the bi-layers of *a*-C/Si whereas the reversible capacity of *a*-C/Si/C is significantly reduced (~ 18 %) in comparison to *a*-C/Si thin film bi-layers.

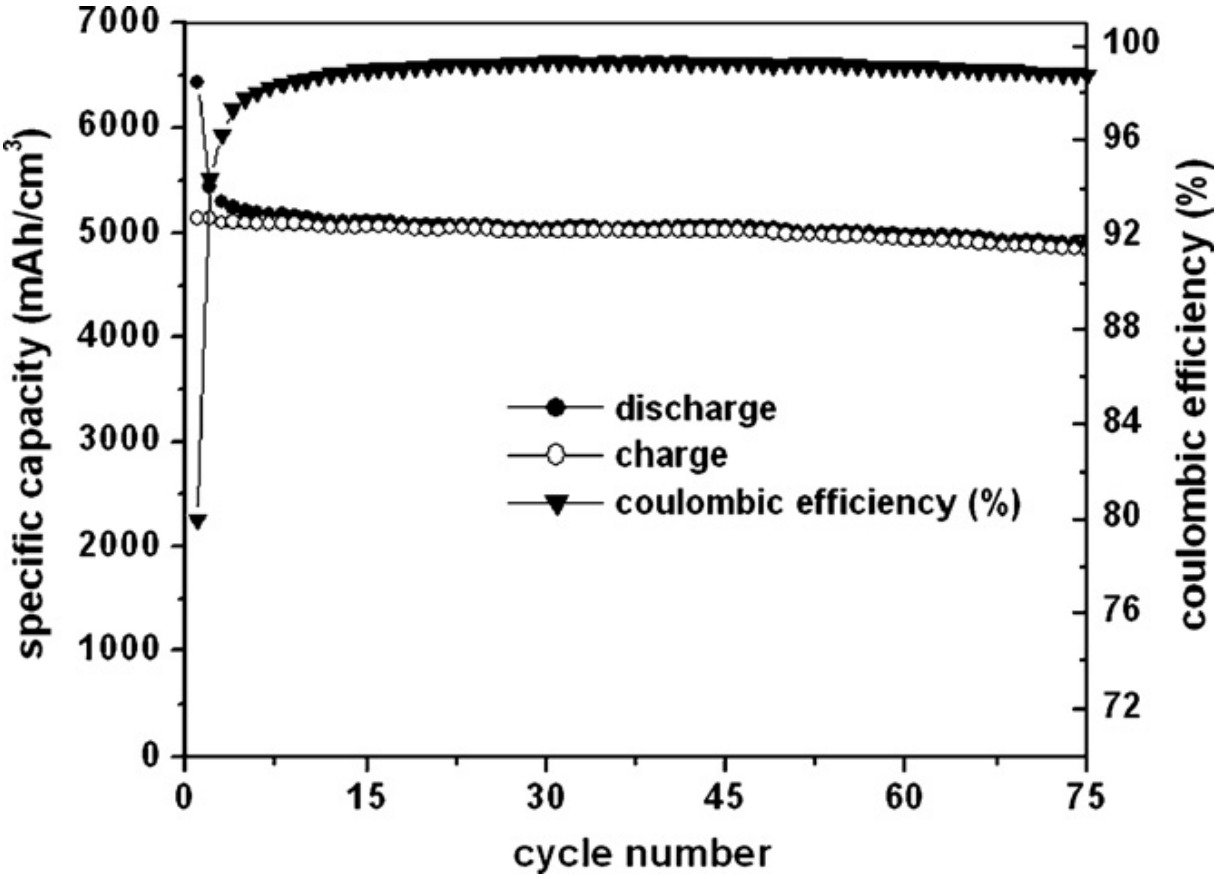

Figure 228. Specific capacity and coulombic efficiency *vs.* cycle number of *a*-C/Si/C thin film composite cycled at a constant current of ~ 100 µA/cm^2

The differential capacity plot (dQ/dV *vs.* V) relating to the 1st cycle of the *a*-C/Si thin film anode cycled at C / 2 rate is shown in **Figure 229**. Several researchers [382, 386, 393, 394]

have also reported similar 1st discharge and 1st charge profile for thin film amorphous Si based anodes cycled at a moderate current rates (< 1C rate). It is clearly evident that the alloying reaction (discharge) of Li ion with amorphous Si (*a*-Si) occurs mainly at a peak potential of ~ 0.24 V and ~ 0.07 V with an onset potential of ~ 0.31 V and ~ 0.15 V, respectively, during the 1st discharge. The present authors recently reported the alloying / dealloying behavior of crystalline Si as well as amorphous Si in significant detail at different potential based on the associated specific capacity observed for the formation of different phases during the discharge / charge processes [333]. The phase forming at a peak potential close to ~ 0.24 V has been reported correspond to the formation of metastable Li-Si based amorphous phase of composition Li-30 at. % Si (P-II) by a solid-state amorphization reaction where the crystallization of the equilibrium intermetallic phases is kinetically forbidden. The phase forming at a peak potential ~ 0.07 V corresponds to the formation of amorphous phase of composition close to Li - 24 at. % Si (P-III) occurs due to solid state reaction of Li ion with P-II phase [333]. The differential capacity plots (dQ/dV *vs.* V) of the 2nd discharge and 2nd charge of the *a*-Si/C composite cycled at a rate of C / 2 in the voltage range of 0.02 V - 1.2 V are also shown in **Figure 229**. It can be construed that from the 2nd cycle onwards, during alloying of lithium ions with *a*-Si/C, nucleation and growth of an amorphous phase (P-I) of composition Li - 50 at.% Si corresponding to the peak potentials of ~ 0.29 V appears to occur in addition to the peak potentials of ~ 0.24 V and ~ 0.07 V that was not originally observed in the first cycle alloying reaction. There is also significant decrease in the intensity of the peaks observed at ~ 0.24 V and ~ 0.07 V indicating the possible change in activation energies of these phases due to the formation of the P-I phase at ~ 0.29 V reducing the driving force for the formation of these phases originally observed in the initial reaction of Li with *a*-Si.

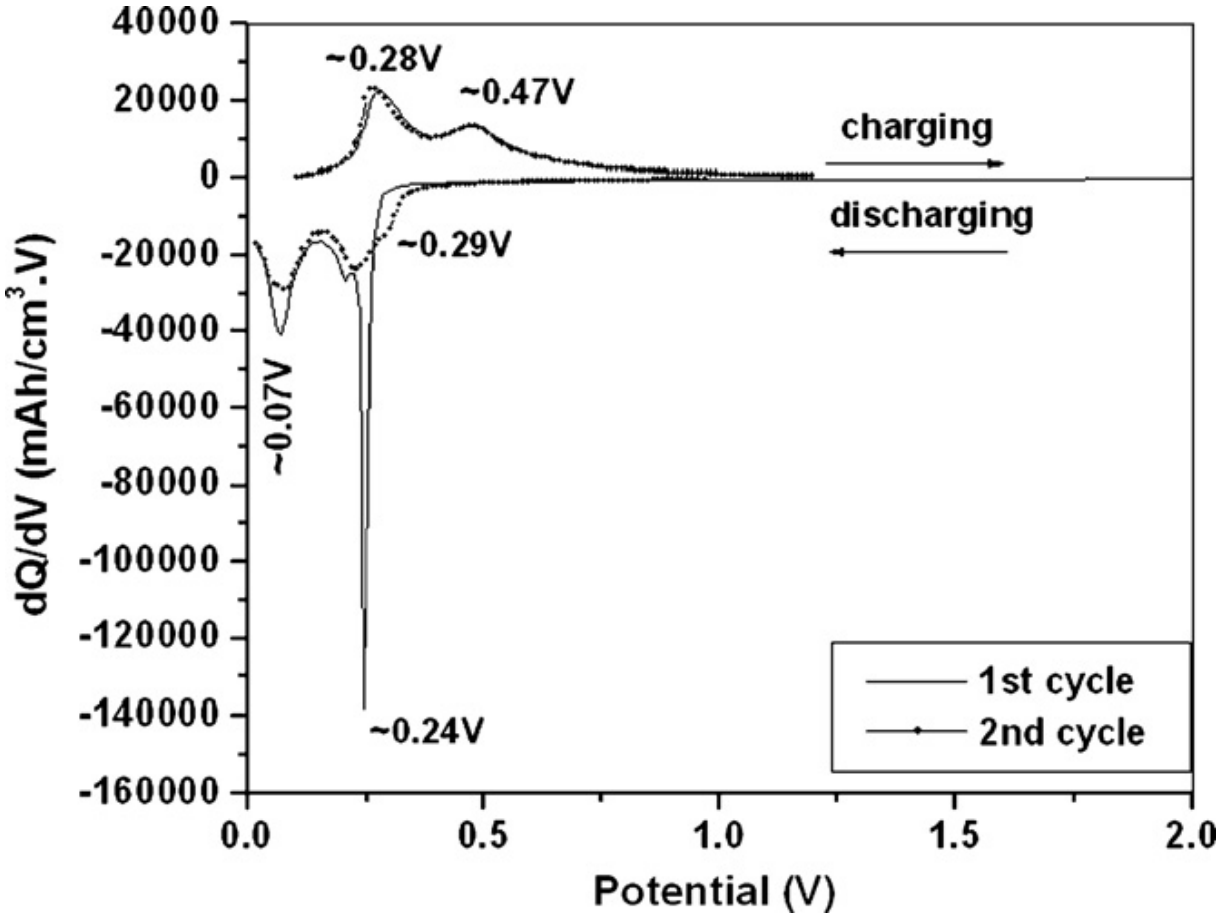

Figure 229. Differential capacity *vs.* cell potential curves of *a*-C/Si thin film electrode obtained after 1st and 2nd cycle cycled at C / 2 rate

The excellent capacity retention of the *a*-C/Si and *a*-C/Si/C thin film nanocomposite is probably due to the maintenance of the structural integrity of the electrode during the alloying and dealloying processes. The SEM micrograph of the cycled samples of *a*-C/Si thin film composite cycled at ~ 100 μA/cm^2 (C / 2 rate), shown in **Figure 230** (a), indicates the excellent structural integrity (devoid of any cracks) even after 75 cycles. Moreover, there appears to be no significant change in the film morphology after cycling, which indicates no new surfaces

generated during cycling. On the other hand, the SEM micrograph of *a*-Si thin film anode, shown in **Figure 230** (b) cycled at ~ 100 μA/cm^2 (C / 2 rate) for 75 cycles shows the structural failure of the electrode during the alloying / dealloying process indicative of one of the main causes of the fade in capacity observed in this composite. The excellent structural integrity of the *a*-Si/C is expected to arise due to the presence of C buffer layer between Si and Cu/Cr substrate which may improve the mechanical properties of the composite by enhancing the interface adhesion / bonding between Si and C for releasing the stress / strain experienced by silicon. Furthermore, adhesion of the *a*-C layer to the Cu by use of Cr could also serve to stabilize the composite and prevent the delamination of the *a*-Si from the Cu substrate with *a*-Si layer essentially gliding on the underlying carbon. The present results clearly suggest that the presence of C buffer layer improves the capacity retention of Si based anode [354]. It is therefore possible that coating of amorphous carbon on *a*-Si or crystalline Si (*c*-Si) could provide similar buffering characteristic allowing the Si/C composite to retain its structural integrity without delamination as shown in earlier publications by our group [269, 331]. Identification of a suitable low cost manufacturing process to generate composites of *a*-Si coated with C buffer layer with excellent interfacial strength will therefore be necessary to exploit the true potential of the thin film structural architectures.

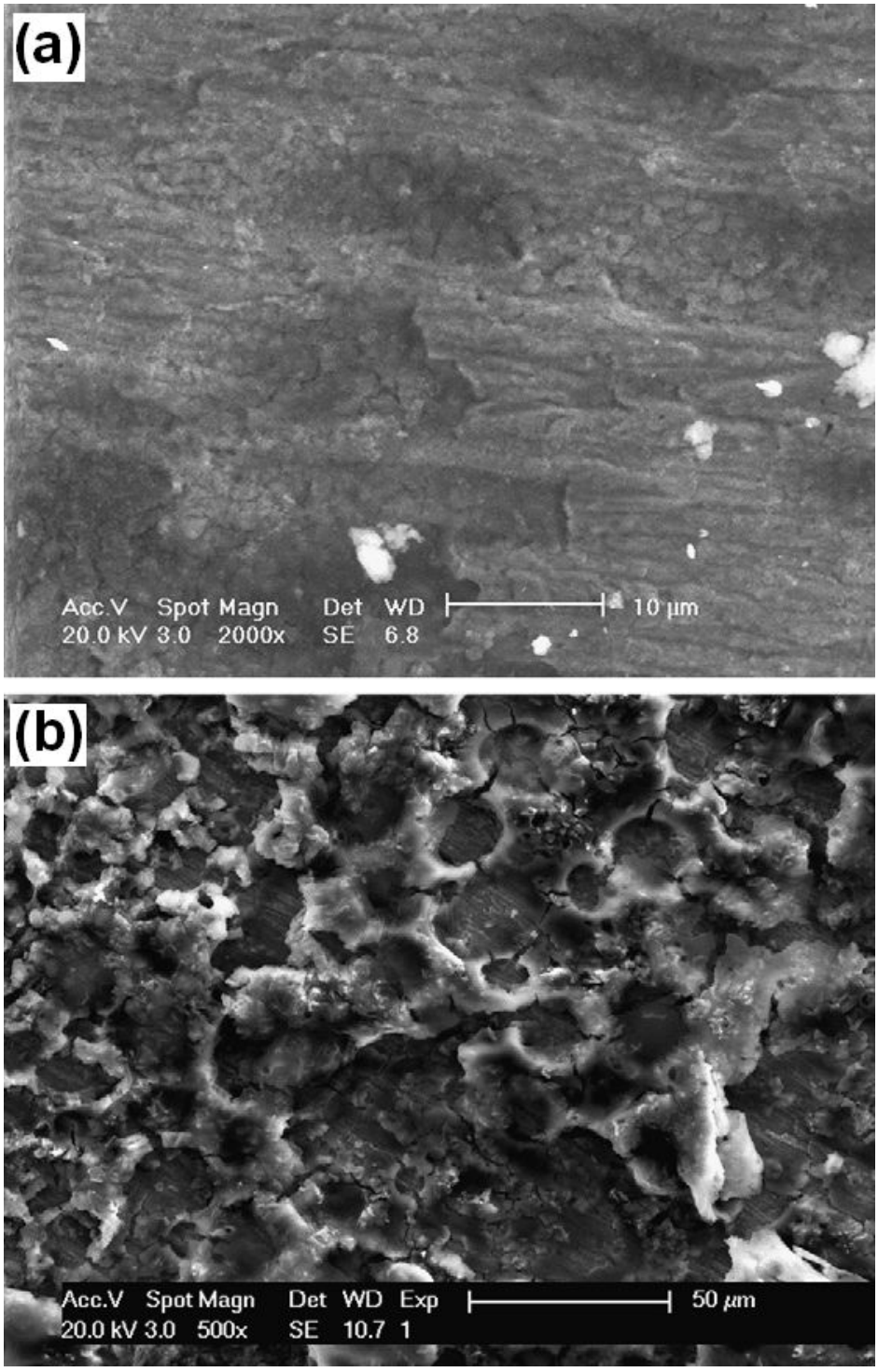

Figure 230. SEM micrograph of *a*-Si/C thin film anode (a), and *a*-Si film (b) after 75 cycles

E.2.4 Conclusion

Bi-layer thin film comprising amorphous carbon (*a*-C) of ~ 50 nm thickness and amorphous silicon (*a*-Si) with a thickness of ~ 250 nm have been deposited by radio frequency magnetron sputtering on chromium coated (~ 10 nm) copper foil to evaluate the buffering effect of *a*-C on the structural stability of *a*-Si anode during electrochemical cycling for Li-ion batteries. The resultant amorphous Si and carbon bi-layer thin film composite (*a*-C/Si) show high reversible capacity (~ 6300 mAh/cm^3) and excellent capacity retention displaying ~ 0.03 % fade in capacity up to 50 cycles when cycled at a rate of 100 μA/cm^2 (~ C / 2), whereas pure amorphous Si thin film (*a*-Si) shows rapid fade in capacity after 30 cycles. The present results also show that the presence of an additional thin amorphous C layer (~ 50 nm) on top of the *a*-C/Si thin film, denoted as tri-layer *a*-C/Si/C thin film, does not improve the cyclability or stability in comparison to bi-layer *a*-C/Si thin film. Results of this study provide evidence that the presence of thin amorphous C layer between the chromium coated Cu substrate and *a*-Si acts as a buffer layer enabling the release of the colossal volume induced stresses ordinarily contained within the *a*-Si during the charge / discharge cycles thus preserving the microstructural stability of the *a*-C/Si based anode. Scanning electron microscopy (SEM) analysis further confirms that the structural integrity of the *a*-C/Si thin film during the alloying / dealloying process with lithium help in contributing to the good cyclability observed in the *a*-C/Si composites. This buffering capacity of the thin C layer between the Cu foil and active Si leads to minimize the volume expansion related cracking of silicon enabling its use in bulk and thin film battery systems.

APPENDIX F

PERMISSIONS

The thesis has text, figures and tables reprinted / reproduced with permission from several publishing companies and societies. All the journal papers listed here have been published in print and electronic form, wherein I (*Karan Sandeep Kadakia*) am a co-author.

The six journal papers listed below have been used in **Section 5.0** and **Section 6.0** :

1. *Karan Kadakia*, Moni K. Datta, Oleg I. Velikokhatnyi, Prashanth Jampani, Prashant N. Kumta, "Fluorine doped (Ir,Sn,Nb)O_2 anode electro-catalyst for oxygen evolution via PEM based water electrolysis", *International Journal of Hydrogen Energy,* 39 (2014) 664-674, Copyright © 2013, Reprinted with permission from Elsevier.
2. *Karan Kadakia*, Moni K. Datta, Oleg I. Velikokhatnyi, Prashanth Jampani, Sung Kyoo Park, Sung Jae Chung, Prashant N. Kumta, "High performance fluorine doped (Sn,Ru)O_2 oxygen evolution reaction electro-catalysts for proton exchange membrane based water electrolysis", *Journal of Power Sources,* 245 (2014) 362-370, Copyright © 2013, Reprinted with permission from Elsevier.

3. *Karan Kadakia*, Moni K. Datta, Prashanth Jampani, Sung Kyoo Park, Prashant N. Kumta, "Novel F-doped IrO_2 oxygen evolution electrocatalyst for PEM based water electrolysis", *Journal of Power Sources,* 222 (2013) 313-317, Copyright © 2012, Reprinted with permission from Elsevier.
4. *Karan Kadakia*, Moni K. Datta, Oleg I. Velikokhatnyi, Prashanth Jampani, Sung Kyoo Park, Partha Saha, James A. Poston, Ayyakkannu Manivannan, Prashant N. Kumta, "Novel (Ir,Sn,Nb)O_2 anode electrocatalysts with reduced noble metal content for PEM based water electrolysis", *International Journal of Hydrogen Energy*, 37 (2012) 3001-3013, Copyright © 2011, Reprinted with permission from Elsevier.
5. Moni K. Datta, *Karan Kadakia*, Oleg I. Velikokhatnyi, Prashanth Jampani, Sung Jae Chung, James A. Poston, Ayyakkannu Manivannan, Prashant N. Kumta, "High performance robust F-doped tin oxide oxygen evolution electro-catalysts for PEM based water electrolysis", *Journal of Materials Chemistry A*, 1 (2013) 4026-4037, Copyright © 2013, Reproduced by permission of The Royal Society of Chemistry (RSC).
6. Oleg I. Velikokhatnyi, *Karan Kadakia*, Moni K. Datta, Prashant N. Kumta, "Fluorine-Doped IrO_2: A potential electrocatalyst for water electrolysis", *Journal of Physical Chemistry C*, 117 (2013) 20542-20547, Copyright © 2013, Reprinted with permission from American Chemical Society.

The journal paper listed below has been used in **Appendix A** :

1. Yousef M. Alyousef, Moni K. Datta, *Karan Kadakia*, Shi Chune Yao, Prashant N. Kumta, "Sol-gel synthesis of Pt-Ru-Os-Ir based anode electro-catalysts for direct

methanol fuel cells", *Journal of Alloys and Compounds*, 506 (2010) 698-702, Copyright © 2010, Reprinted with permission from Elsevier.

The journal paper listed below has been used in **Appendix C** :

1. Oleg I. Velikokhatnyi, *Karan Kadakia*, Sung Kyoo Park, Prashant N. Kumta, "Theoretical study of magnesium and zinc tantalates and niobates as prospective catalyst supports for water electrolysis", *Journal of the Electrochemical Society,* 159[10] (2012) F607-F616, Copyright © 2012, Reproduced by permission of ECS - The Electrochemical Society.

The two journal papers listed below have been used in **Appendix D** :

1. Prashanth Jampani, *Karan Kadakia*, Dae Ho Hong, Rigved Epur, James A. Poston, Ayyakkannu Manivannan, Prashant N. Kumta, "CVD derived vanadium oxide nano-sphere-carbon nanotube (CNT) nano-composite hetero-structures: High energy supercapacitors", *Journal of the Electrochemical Society,* 160[8] (2013) A1-A10, Copyright © 2013, Reproduced by permission of ECS - The Electrochemical Society.
2. Prashanth Jampnai, Moni K. Datta, *Karan Kadakia*, Dae Ho Hong, Sung Jae Chung, Michael C. Tam, James A. Poston, Ayyakkannu Manivannan, Prashant N. Kumta, "A simple low temperature synthesis of nanostructured vanadium nitride for supercapacitor applications", *Journal of the Electrochemical Society*, 160[11] (2013) A2195-A2206, Copyright © 2013, Reproduced by permission of ECS - The Electrochemical Society.

The two journal papers listed below have been used in **Appendix E** :

1. Moni K. Datta, Rigved Epur, Partha Saha, *Karan Kadakia*, Sung Kyoo Park, Prashant N. Kumta, "Tin and graphite based nanocomposites: Potential anode for sodium ion batteries", *Journal of Power Sources*, 225 (2013) 316-322, Copyright © 2012, Reprinted with permission from Elsevier.
2. Moni K. Datta, Jeffrey Maranchi, Sung Jae Chung, Rigved Epur, *Karan Kadakia*, Prashanth Jampani, Prashant N. Kumta, "Amorphous silicon-carbon based nano-scale thin film anode materials for lithium ion batteries", *Electrochimica Acta*, 56 (2011) 4717-4723, Copyright © 2011, Reprinted with permission from Elsevier.

BIBLIOGRAPHY

[1] G.D. Berry, Hydrogen Production, in: J.C. Editor-in-Chief: Cutler (Ed.) Encyclopedia of Energy, Elsevier, New York, 2004, pp. 253-265.

[2] J. Suntivich, K.J. May, H.A. Gasteiger, J.B. Goodenough, Y. Shao-Horn, Science, 334 (2011) 1383-1385.

[3] K. Zeng, D.K. Zhang, Prog. Energy Combust. Sci., 36 (2010) 307-326.

[4] J.M. Ogden, Phys. Today, 55 (2002) 69.

[5] F. Barbir, Chapter 11 - 11. Fuel Cells and Hydrogen Economy, in: PEM Fuel Cells, Academic Press, Burlington, 2005, pp. 399-426.

[6] G.D. Berry, J. Martinez-Frias, F. Espinosa-Loza, S.M. Aceves, Hydrogen Storage and Transportation, in: J.C. Editor-in-Chief: Cutler (Ed.) Encyclopedia of Energy, Elsevier, New York, 2004, pp. 267-281.

[7] H. Wang, D.Y.C. Leung, J. Xuan, International Journal of Hydrogen Energy, 37 (2012) 10002-10009.

[8] M.F. Hordeski, Hydrogen & Fuel Cells: Advances in Transportation and Power, Fairmont Press, 2009.

[9] F. Barbir, Chapter Twelve - Future of Fuel Cells and Hydrogen, in: PEM Fuel Cells (Second Edition), Academic Press, Boston, 2013, pp. 469-508.

[10] B. Sørensen, Chapter 2 - Hydrogen, in: Hydrogen and Fuel Cells, Academic Press, Burlington, 2005, pp. 5-111.

[11] C. Schroeder, Chapter 8 - Hydrogen from Electrolysis, in: S. Daniel, S.C. James (Eds.) The Hydrogen Energy Transition, Academic Press, Burlington, 2004, pp. 121-133.

[12] C.J. Winter, International Journal of Hydrogen Energy, 34 (2009) S1-S52.

[13] M. Conte, F. Di Mario, A. Iacobazzi, A. Mattucci, A. Moreno, M. Ronchetti, Energies, 2 (2009) 150-179.

[14] K. Hedegaard, P. Meibom, Renewable Energy, 37 (2012) 318-324.

[15] F. Barbir, Sol. Energy, 78 (2005) 661-669.

[16] P. Millet, N. Mbemba, S.A. Grigoriev, V.N. Fateev, A. Aukauloo, C. Etievant, International Journal of Hydrogen Energy, 36 (2011) 4134-4142.

[17] M. Carmo, D.L. Fritz, J. Mergel, D. Stolten, International Journal of Hydrogen Energy, 38 (2013) 4901-4934.

[18] M.W. Kanan, D.G. Nocera, Science, 321 (2008) 1072-1075.

[19] R.E. Clarke, S. Giddey, S.P.S. Badwal, International Journal of Hydrogen Energy, 35 (2010) 928-935.

[20] G.W. Crabtree, M.S. Dresselhaus, M.V. Buchanan, Phys. Today, 57 (2004) 39-44.

[21] Q. He, T. Mugadza, X. Kang, X. Zhu, S. Chen, J. Kerr, T. Nyokong, Journal of Power Sources, 216 (2012) 67-75.

[22] J.I. Levene, M.K. Mann, R.M. Margolis, A. Milbrandt, Sol. Energy, 81 (2007) 773-780.

[23] Y.H.P. Zhang, W.-D. Huang, Trends in Biotechnology, 30 (2012) 301-306.

[24] K. Kadakia, M.K. Datta, O.I. Velikokhatnyi, P. Jampani, S.K. Park, P. Saha, J.A. Poston, A. Manivannan, P.N. Kumta, International Journal of Hydrogen Energy, 37 (2012) 3001-3013.

[25] S. Pedrazzi, G. Zini, P. Tartarini, Renewable Energy, 46 (2012) 14-22.

[26] M.W. Kanan, Y. Surendranath, D.G. Nocera, Chem. Soc. Rev., 38 (2009) 109-114.

[27] Y.Y. Liang, Y.G. Li, H.L. Wang, J.G. Zhou, J. Wang, T. Regier, H.J. Dai, Nat. Mater., 10 (2011) 780-786.

[28] S. Malkhandi, B. Yang, A.K. Manohar, A. Manivannan, G.K.S. Prakash, S.R. Narayanan, J. Phys. Chem. Lett., 3 (2012) 967-972.

[29] C.P. De Pauli, S. Trasatti, Journal of Electroanalytical Chemistry, 538–539 (2002) 145-151.

[30] J.M. Hu, H.M. Meng, J.Q. Zhang, C.N. Cao, Corrosion Sci., 44 (2002) 1655-1668.

[31] A.T. Marshall, S. Sunde, M. Tsypkin, R. Tunold, International Journal of Hydrogen Energy, 32 (2007) 2320-2324.

[32] A. Marshall, B. Borresen, G. Hagen, M. Tsypkin, R. Tunold, Electrochimica Acta, 51 (2006) 3161-3167.

[33] S.D. Song, H.M. Zhang, X.P. Ma, Z.G. Shao, R.T. Baker, B.L. Yi, International Journal of Hydrogen Energy, 33 (2008) 4955-4961.

[34] K. Kadakia, M.K. Datta, P.H. Jampani, S.K. Park, P.N. Kumta, Journal of Power Sources, 222 (2013) 313-317.

[35] Y. Takasu, N. Yoshinaga, W. Sugimoto, Electrochem. Commun., 10 (2008) 668-672.

[36] X. Wu, K. Scott, International Journal of Hydrogen Energy, 36 (2011) 5806-5810.

[37] B. Sørensen, Chapter 2 - Hydrogen, in: Hydrogen and Fuel Cells (Second Edition), Academic Press, Boston, 2012, pp. 5-94.

[38] R.L. LeRoy, International Journal of Hydrogen Energy, 8 (1983) 401-417.

[39] P. Millet, S. Grigoriev, Chapter 2 - Water Electrolysis Technologies, in: L.M. Gandía, G. Arzamendi, P.M. Diéguez (Eds.) Renewable Hydrogen Technologies, Elsevier, Amsterdam, 2013, pp. 19-41.

[40] J.C. Ganley, International Journal of Hydrogen Energy, 34 (2009) 3604-3611.

[41] S. Marini, P. Salvi, P. Nelli, R. Pesenti, M. Villa, M. Berrettoni, G. Zangari, Y. Kiros, Electrochimica Acta, 82 (2012) 384-391.

[42] T. Smolinka, FUELS – HYDROGEN PRODUCTION | Water Electrolysis, in: J. Garche (Ed.) Encyclopedia of Electrochemical Power Sources, Elsevier, Amsterdam, 2009, pp. 394-413.

[43] S.-D. Kim, J.-H. Yu, D.-W. Seo, I.-S. Han, S.-K. Woo, International Journal of Hydrogen Energy, 37 (2012) 78-83.

[44] C. Yang, A. Coffin, F. Chen, International Journal of Hydrogen Energy, 35 (2010) 3221-3226.

[45] N. Li, M. Keane, M.K. Mahapatra, P. Singh, International Journal of Hydrogen Energy, 38 (2013) 6298-6303.

[46] S. Siracusano, V. Baglio, N. Briguglio, G. Brunaccini, A. Di Blasi, A. Stassi, R. Ornelas, E. Trifoni, V. Antonucci, A.S. Aricò, International Journal of Hydrogen Energy, 37 (2012) 1939-1946.

[47] F.I. Mattos-Costa, P. de Lima-Neto, S.A.S. Machado, L.A. Avaca, Electrochimica Acta, 44 (1998) 1515-1523.

[48] E. Rasten, G. Hagen, R. Tunold, Electrochimica Acta, 48 (2003) 3945-3952.

[49] A. Damjanovic, A. Dey, J.O.M. Bockris, Journal of The Electrochemical Society, 113 (1966) 739-746.

[50] R.L. LeRoy, C.T. Bowen, D.J. LeRoy, Journal of The Electrochemical Society, 127 (1980) 1954-1962.

[51] N. Krstajic, S. Trasatti, Journal of Applied Electrochemistry, 28 (1998) 1291-1297.

[52] A. Minguzzi, F.-R.F. Fan, A. Vertova, S. Rondinini, A.J. Bard, Chemical Science, 3 (2012) 217-229.

[53] J. Rossmeisl, Z.W. Qu, H. Zhu, G.J. Kroes, J.K. Norskov, Journal of Electroanalytical Chemistry, 607 (2007) 83-89.

[54] J. Rossmeisl, A. Logadottir, J.K. Nørskov, Chemical Physics, 319 (2005) 178-184.

[55] O.I. Velikokhatnyi, K. Kadakia, M.K. Datta, P.N. Kumta, The Journal of Physical Chemistry C, 117 (2013) 20542-20547.

[56] O.I. Velikokhatnyi, P.N. Kumta, Physica B: Condensed Matter, 406 (2011) 471-477.

[57] M.K. Datta, K. Kadakia, O.I. Velikokhatnyi, P.H. Jampani, S.J. Chung, J.A. Poston, A. Manivannan, P.N. Kumta, Journal of Materials Chemistry A, 1 (2013) 4026-4037.

[58] K. Kadakia, M.K. Datta, O.I. Velikokhatnyi, P. Jampani, S.K. Park, S.J. Chung, P.N. Kumta, Journal of Power Sources, 245 (2014) 362-370.

[59] K. Kadakia, M.K. Datta, O.I. Velikokhatnyi, P.H. Jampani, P.N. Kumta, International Journal of Hydrogen Energy, 39 (2014) 664-674.

[60] A. Marshall, B. Borresen, G. Hagen, M. Tsypkin, R. Tunold, Materials Chemistry and Physics, 94 (2005) 226-232.

[61] S.A. Grigoriev, V.I. Porembsky, V.N. Fateev, International Journal of Hydrogen Energy, 31 (2006) 171-175.

[62] K.M. Papazisi, A. Siokou, S. Balomenou, D. Tsiplakides, International Journal of Hydrogen Energy, 37 (2012) 16642-16648.

[63] G.H. Chen, X.M. Chen, P.L. Yue, Journal of Physical Chemistry B, 106 (2002) 4364-4369.

[64] G.Y. Chen, C.C. Waraksa, H.G. Cho, D.D. Macdonald, T.E. Mallouk, Journal of the Electrochemical Society, 150 (2003) E423-E428.

[65] S. Ardizzone, C.L. Bianchi, G. Cappelletti, M. Ionita, A. Minguzzi, S. Rondinini, A. Vertova, Journal of Electroanalytical Chemistry, 589 (2006) 160-166.

[66] C.P. Depauli, S. Trasatti, Journal of Electroanalytical Chemistry, 396 (1995) 161-168.

[67] E. Mayousse, F. Maillard, F. Fouda-Onana, O. Sicardy, N. Guillet, International Journal of Hydrogen Energy, 36 (2011) 10474-10481.

[68] M. Morimitsu, R. Otogawa, M. Matsunaga, Electrochimica Acta, 46 (2000) 401-406.

[69] A.V. Nikiforov, A.L.T. Garcia, I.M. Petrushina, E. Christensen, N.J. Bjerrum, International Journal of Hydrogen Energy, 36 (2011) 5797-5805.

[70] F.M. Sapountzi, S.C. Divane, E.I. Papaioannou, S. Souentie, C.G. Vayenas, Journal of Electroanalytical Chemistry, 662 (2011) 116-122.

[71] A.J. Terezo, J. Bisquert, E.C. Pereira, G. Garcia-Belmonte, Journal of Electroanalytical Chemistry, 508 (2001) 59-69.

[72] A.J. Terezo, E.C. Pereira, Electrochimica Acta, 44 (1999) 4507-4513.

[73] A.J. Terezo, E.C. Pereira, Electrochimica Acta, 45 (2000) 4351-4358.

[74] G.P. Vercesi, J.Y. Salamin, C. Comninellis, Electrochimica Acta, 36 (1991) 991-998.

[75] E. Elangovan, K. Ramamurthi, Thin Solid Films, 476 (2005) 231-236.

[76] H. Kim, R.C.Y. Auyeung, A. Piqué, Thin Solid Films, 516 (2008) 5052-5056.

[77] E. Shanthi, A. Banerjee, V. Dutta, K.L. Chopra, Journal of Applied Physics, 53 (1982) 1615-1621.

[78] W.S. Choi, S.S.A. Seo, K.W. Kim, T.W. Noh, M.Y. Kim, S. Shin, Physical Review B, 74 (2006).

[79] J.S. de Almeida, R. Ahuja, Physical Review B, 73 (2006).

[80] M.A. Aegerter, Solar Energy Materials and Solar Cells, 68 (2001) 401-422.

[81] N. Özer, T. Barreto, T. Büyüklimanli, C.M. Lampert, Solar Energy Materials and Solar Cells, 36 (1995) 433-443.

[82] M.H.P. Santana, L.A. De Faria, J.F.C. Boodts, Electrochimica Acta, 49 (2004) 1925-1935.

[83] R. Kötz, S. Stucki, Electrochimica Acta, 31 (1986) 1311-1316.

[84] R. Adams, R.L. Shriner, Journal of the American Chemical Society, 45 (1923) 2171-2179.

[85] J. Cheng, H. Zhang, G. Chen, Y. Zhang, Electrochimica Acta, 54 (2009) 6250-6256.

[86] Y. Wang, C. Ma, X. Sun, H. Li, Journal of Colloid and Interface Science, 286 (2005) 627-631.

[87] N. Uekawa, T. Kudo, F. Mori, Y.J. Wu, K. Kakegawa, Journal of Colloid and Interface Science, 264 (2003) 378-384.

[88] T.H. de Keijser, J.I. Langford, E.J. Mittemeijer, A.B.P. Vogels, Journal of Applied Crystallography, 15 (1982) 308-314.

[89] R. Jiang, D. Chu, Electrochimica Acta, 45 (2000) 4025-4030.

[90] K.J.J. Mayrhofer, D. Strmcnik, B.B. Blizanac, V. Stamenkovic, M. Arenz, N.M. Markovic, Electrochimica Acta, 53 (2008) 3181-3188.

[91] T.J. Schmidt, H.A. Gasteiger, G.D. Stäb, P.M. Urban, D.M. Kolb, R.J. Behm, Journal of The Electrochemical Society, 145 (1998) 2354-2358.

[92] S. Gottesfeld, I.D. Raistrick, S. Srinivasan, Journal of The Electrochemical Society, 134 (1987) 1455-1462.

[93] K.E. Gubbins, R.D. Walker, Journal of The Electrochemical Society, 112 (1965) 469-471.

[94] R.N. Itoe, G.D. Wesson, E.E. Kalu, Journal of The Electrochemical Society, 147 (2000) 2445-2450.

[95] E. Lust, E. Härk, J. Nerut, K. Vaarmets, Electrochimica Acta, 101 (2013) 130-141.

[96] J.L. Cohen, D.J. Volpe, H.D. Abruna, Physical Chemistry Chemical Physics, 9 (2007) 49-77.

[97] L.M. Da Silva, D.V. Franco, L.A. De Faria, J.F.C. Boodts, Electrochimica Acta, 49 (2004) 3977-3988.

[98] E.M. Garcia, H.A. Tarôco, T. Matencio, R.Z. Domingues, J.A.F. dos Santos, International Journal of Hydrogen Energy, 37 (2012) 6400-6406.

[99] M.M. Hefny, S. Abdel-Wanees, Electrochimica Acta, 41 (1996) 1419-1422.

[100] A.A. Shaltout, H.H. Afify, S.A. Ali, Journal of Electron Spectroscopy and Related Phenomena, 185 (2012) 140-145.

[101] J.-M. Hu, J.-Q. Zhang, C.-N. Cao, International Journal of Hydrogen Energy, 29 (2004) 791-797.

[102] A. Damjanovic, Journal of Electroanalytical Chemistry, 355 (1993) 57-77.

[103] R. Jiang, F.C. Anson, Journal of Electroanalytical Chemistry and Interfacial Electrochemistry, 305 (1991) 171-184.

[104] L.M. Da Silva, L.A. De Faria, J.F.C. Boodts, Electrochimica Acta, 48 (2003) 699-709.

[105] A. Mills, H.L. Davies, Electrochimica Acta, 37 (1992) 1217-1225.

[106] S. Siracusano, V. Baglio, A. Di Blasi, N. Briguglio, A. Stassi, R. Ornelas, E. Trifoni, V. Antonucci, A.S. Aricò, International Journal of Hydrogen Energy, 35 (2010) 5558-5568.

[107] S. Ardizzone, M. Falciola, S. Trasatti, Journal of The Electrochemical Society, 136 (1989) 1545-1550.

[108] H. Tamura, C. Iwakura, International Journal of Hydrogen Energy, 7 (1982) 857-865.

[109] J. Ribeiro, M. Moats, A. Andrade, Journal of Applied Electrochemistry, 38 (2008) 767-775.

[110] M. Ito, Y. Murakami, H. Kaji, K. Yahikozawa, Y. Takasu, Journal of The Electrochemical Society, 143 (1996) 32-36.

[111] C. Iwakura, K. Hirao, H. Tamura, Electrochimica Acta, 22 (1977) 329-334.

[112] I.T. Weber, R. Andrade, E.R. Leite, E. Longo, Sensors and Actuators B: Chemical, 72 (2001) 180-183.

[113] B.S. Murty, M.K. Datta, S.K. Pabi, Sadhana-Academy Proceedings in Engineering Sciences, 28 (2003) 23-45.

[114] E.J.W. Whittaker, R. Muntus, Geochimica et Cosmochimica Acta, 34 (1970) 945-956.

[115] N. Todorova, T. Giannakopoulou, G. Romanos, T. Vaimakis, J. Yu, C. Trapalis, International Journal of Photoenergy, 2008 (2008).

[116] C. Papadopoulou, A. Lycourghiotis, P. Grange, B. Delmon, Applied Catalysis, 38 (1988) 255-271.

[117] A.K. Ghosh, R.A. Kydd, Catalysis Reviews, 27 (1985) 539-589.

[118] J. Ramirez, R. Cuevas, A.L. Agudo, S. Mendioroz, J.L.G. Fierro, Applied Catalysis, 57 (1990) 223-240.

[119] A.A. Bolzan, C. Fong, B.J. Kennedy, C.J. Howard, Acta Crystallographica Section B: Structural Science, 53 (1997) 373-380.

[120] J.C. Cruz, S. Rivas, D. Beltran, Y. Meas, R. Ornelas, G. Osorio-Monreal, L. Ortiz-Frade, J. Ledesma-García, L.G. Arriaga, International Journal of Hydrogen Energy, 37 (2012) 13522-13528.

[121] V. Natarajan, S. Basu, K. Scott, International Journal of Hydrogen Energy, 38 (2013) 16623-16630.

[122] Z.B. Zhou, R.Q. Cui, G.M. Hadi, W.Y. Li, Z.M. Ding, Journal of Materials Science: Materials in Electronics, 12 (2001) 417-421.

[123] T.H. Dekeijser, J.I. Langford, E.J. Mittemeijer, A.B.P. Vogels, Journal of Applied Crystallography, 15 (1982) 308-314.

[124] F.M. Amanullah, K.J. Pratap, V. Hari Babu, Materials Science and Engineering: B, 52 (1998) 93-98.

[125] B. Hammer, J.K. Nørskov, Theoretical surface science and catalysis—calculations and concepts, in: H.K. Bruce C. Gates (Ed.) Advances in Catalysis, Academic Press, 2000, pp. 71-129.

[126] T. Bligaard, J.K. Nørskov, Electrochimica Acta, 52 (2007) 5512-5516.

[127] H. Dau, C. Limberg, T. Reier, M. Risch, S. Roggan, P. Strasser, ChemCatChem, 2 (2010) 724-761.

[128] S. Kandoi, A. Gokhale, L. Grabow, J. Dumesic, M. Mavrikakis, Catalysis Letters, 93 (2004) 93-100.

[129] P. Atkins, J. de Paula, Physical Chemistry, W. H. Freeman, 2006.

[130] J.P. Perdew, W. Yue, Physical Review B, 33 (1986) 8800-8802.

[131] G. Kresse, J. Furthmüller, Physical Review B, 54 (1996) 11169-11186.

[132] G. Kresse, J. Furthmüller, Computational Materials Science, 6 (1996) 15-50.

[133] G. Kresse, D. Joubert, Physical Review B, 59 (1999) 1758-1775.

[134] G. Henkelman, A. Arnaldsson, H. Jónsson, Computational Materials Science, 36 (2006) 354-360.

[135] A.J. Bard, R. Parsons, J. Jordan, Standard Potentials in Aqueous Solution, Taylor & Francis, 1985.

[136] B. Hamad, The European Physical Journal B, 70 (2009) 163-169.

[137] N.D. Landolt-Bornstein, Group, 3 (1982) 12.

[138] J.E. Dominguez, X.Q. Pan, L. Fu, P.A. Van Rompay, Z. Zhang, J.A. Nees, P.P. Pronko, Journal of Applied Physics, 91 (2002) 1060.

[139] B. Gottlieb, R. Koropecki, R. Arce, R. Crisalle, J. Ferron, Thin Solid Films, 199 (1991) 13-21.

[140] D. Zaouk, R. al Asmar, J. Podlecki, Y. Zaatar, A. Khoury, A. Foucaran, Microelectronics Journal, 38 (2007) 884-887.

[141] J. Milliken, F. Joseck, M. Wang, E. Yuzugullu, Journal of Power Sources, 172 (2007) 121-131.

[142] S. Satyapal, J. Petrovic, C. Read, G. Thomas, G. Ordaz, Catalysis Today, 120 (2007) 246-256.

[143] N.L. Garland, D.C. Papageorgopoulos, J.M. Stanford, Energy Procedia, 28 (2012) 2-11.

[144] D.P. Wilkinson, J. Zhang, R. Hui, J. Fergus, X. Li, Proton exchange membrane fuel cells: materials properties and performance, CRC Press, 2009.

[145] X. Zhao, M. Yin, L. Ma, L. Liang, C. Liu, J. Liao, T. Lu, W. Xing, Energy & Environmental Science, 4 (2011) 2736-2753.

[146] J. Zhang, PEM fuel cell electrocatalysts and catalyst layers: fundamentals and applications, Springer, 2008.

[147] C. Wang, M. Waje, X. Wang, J.M. Tang, R.C. Haddon, Yan, Nano Letters, 4 (2003) 345-348.

[148] E. Proietti, F. Jaouen, M. Lefèvre, N. Larouche, J. Tian, J. Herranz, J.-P. Dodelet, Nature communications, 2 (2011) 416.

[149] C. Zhou, F. Peng, H. Wang, H. Yu, C. Peng, J. Yang, Electrochem. Commun., 12 (2010) 1210-1213.

[150] S. Alayoglu, A.U. Nilekar, M. Mavrikakis, B. Eichhorn, Nat. Mater., 7 (2008) 333-338.

[151] A.C. Garcia, V.A. Paganin, E.A. Ticianelli, Electrochimica Acta, 53 (2008) 4309-4315.

[152] V.R. Stamenkovic, B.S. Mun, M. Arenz, K.J. Mayrhofer, C.A. Lucas, G. Wang, P.N. Ross, N.M. Markovic, Nat. Mater., 6 (2007) 241-247.

[153] A. Velázquez-Palenzuela, F. Centellas, J.A. Garrido, C. Arias, R. María Rodríguez, E. Brillas, P.-L.s. Cabot, The Journal of Physical Chemistry C, 114 (2010) 4399-4407.

[154] A. Murthy, A. Manthiram, Electrochem. Commun., 13 (2011) 310-313.

[155] Z.-G. Shao, F. Zhu, W.-F. Lin, P.A. Christensen, H. Zhang, Journal of Power Sources, 161 (2006) 813-819.

[156] T. Maiyalagan, T.O. Alaje, K. Scott, The Journal of Physical Chemistry C, 116 (2011) 2630-2638.

[157] F. Maillard, G.Q. Lu, A. Wieckowski, U. Stimming, The Journal of Physical Chemistry B, 109 (2005) 16230-16243.

[158] A.S. Aricò, V. Baglio, A.D. Blasi, E. Modica, G. Monforte, V. Antonucci, Journal of Electroanalytical Chemistry, 576 (2005) 161-169.

[159] D. Kaplan, M. Alon, L. Burstein, Y. Rosenberg, E. Peled, Journal of Power Sources, 196 (2011) 1078-1083.

[160] A.S. Aricò, V. Baglio, E. Modica, A. Di Blasi, V. Antonucci, Electrochem. Commun., 6 (2004) 164-169.

[161] X. Cheng, C. Peng, M. You, L. Liu, Y. Zhang, Q. Fan, Electrochimica Acta, 51 (2006) 4620-4625.

[162] Y.M. Alyousef, M.K. Datta, K. Kadakia, S.C. Yao, P.N. Kumta, Journal of Alloys and Compounds, 506 (2010) 698-702.

[163] Y.M. Alyousef, M.K. Datta, S.C. Yao, P.N. Kumta, Journal of Physics and Chemistry of Solids, 70 (2009) 1019-1023.

[164] J.Y. Kim, Z.G. Yang, C.C. Chang, T.I. Valdez, S.R. Narayanan, P.N. Kumta, Journal of The Electrochemical Society, 150 (2003) A1421-A1431.

[165] S. Chen, K. Kimura, The Journal of Physical Chemistry B, 105 (2001) 5397-5403.

[166] M.R. Kim, S.J. Kim, D.-J. Jang, Crystal Growth & Design, 10 (2009) 257-261.

[167] G.F. Cabeza, P. Légaré, N.J. Castellani, Surface Science, 465 (2000) 286-300.

[168] M. Wakisaka, S. Mitsui, Y. Hirose, K. Kawashima, H. Uchida, M. Watanabe, The Journal of Physical Chemistry B, 110 (2006) 23489-23496.

[169] R. Ahmadi, M.K. Amini, J.C. Bennett, Journal of Catalysis, 292 (2012) 81-89.

[170] Y.-T. Kim, T. Mitani, Journal of Catalysis, 238 (2006) 394-401.

[171] A. Hamnett, Catalysis Today, 38 (1997) 445-457.

[172] X. Ren, P. Zelenay, S. Thomas, J. Davey, S. Gottesfeld, Journal of Power Sources, 86 (2000) 111-116.

[173] B. Gurau, R. Viswanathan, R. Liu, T.J. Lafrenz, K.L. Ley, E.S. Smotkin, E. Reddington, A. Sapienza, B.C. Chan, T.E. Mallouk, S. Sarangapani, The Journal of Physical Chemistry B, 102 (1998) 9997-10003.

[174] V. Radmilovic, H.A. Gasteiger, P.N. Ross, Journal of Catalysis, 154 (1995) 98-106.

[175] H.A. Gasteiger, N. Markovic, P.N. Ross, E.J. Cairns, The Journal of Physical Chemistry, 98 (1994) 617-625.

[176] B.N. Grgur, N.M. Markovic, P.N. Ross, The Journal of Physical Chemistry B, 102 (1998) 2494-2501.

[177] J.-H. Choi, K.-W. Park, B.-K. Kwon, Y.-E. Sung, Journal of The Electrochemical Society, 150 (2003) A973-A978.

[178] C. Lamy, A. Lima, V. LeRhun, F. Delime, C. Coutanceau, J.-M. Léger, Journal of Power Sources, 105 (2002) 283-296.

[179] K.L. Ley, R. Liu, C. Pu, Q. Fan, N. Leyarovska, C. Segre, E.S. Smotkin, Journal of The Electrochemical Society, 144 (1997) 1543-1548.

[180] J.F. Whitacre, T. Valdez, S.R. Narayanan, Journal of The Electrochemical Society, 152 (2005) A1780-A1789.

[181] N.M. Marković, P.N. Ross, Electrochimica Acta, 45 (2000) 4101-4115.

[182] E. Reddington, A. Sapienza, B. Gurau, R. Viswanathan, S. Sarangapani, E.S. Smotkin, T.E. Mallouk, Science, 280 (1998) 1735-1737.

[183] F. Colmati, E. Antolini, E.R. Gonzalez, Journal of Power Sources, 157 (2006) 98-103.

[184] J.F. Drillet, A. Ee, J. Friedemann, R. Kötz, B. Schnyder, V.M. Schmidt, Electrochimica Acta, 47 (2002) 1983-1988.

[185] V. Radmilovic, T.J. Richardson, S.J. Chen, P.N. Ross Jr, Journal of Catalysis, 232 (2005) 199-209.

[186] Q. Yi, J. Zhang, A. Chen, X. Liu, G. Xu, Z. Zhou, Journal of Applied Electrochemistry, 38 (2008) 695-701.

[187] M.A. Ernst, W.G. Sloof, Surface and Interface Analysis, 40 (2008) 334-337.

[188] C. Cattaneo, M.I. Sanchez de Pinto, H. Mishima, B.A. López de Mishima, D. Lescano, L. Cornaglia, Journal of Electroanalytical Chemistry, 461 (1999) 32-39.

[189] A.S. Arico, E. Modica, E. Passalacqua, V. Antonucci, P.L. Antonucci, Journal of Applied Electrochemistry, 27 (1997) 1275-1282.

[190] J. YangáLee, Journal of Materials Chemistry, 13 (2003) 2555-2560.

[191] K.-W. Park, J.-H. Choi, B.-K. Kwon, S.-A. Lee, Y.-E. Sung, H.-Y. Ha, S.-A. Hong, H. Kim, A. Wieckowski, The Journal of Physical Chemistry B, 106 (2002) 1869-1877.

[192] Y. Liang, H. Zhang, Z. Tian, X. Zhu, X. Wang, B. Yi, The Journal of Physical Chemistry B, 110 (2006) 7828-7834.

[193] U.A. Icardi, S. Specchia, G.J.R. Fontana, G. Saracco, V. Specchia, Journal of Power Sources, 176 (2008) 460-467.

[194] S.K. Kamarudin, F. Achmad, W.R.W. Daud, International Journal of Hydrogen Energy, 34 (2009) 6902-6916.

[195] B.D. McNicol, D.A.J. Rand, K.R. Williams, Journal of Power Sources, 83 (1999) 15-31.

[196] R. Rashidi, I. Dincer, G.F. Naterer, P. Berg, Journal of Power Sources, 187 (2009) 509-516.

[197] H.S. Liu, C.J. Song, L. Zhang, J.J. Zhang, H.J. Wang, D.P. Wilkinson, Journal of Power Sources, 155 (2006) 95-110.

[198] G. Hoogers, Fuel Cell Technology Handbook, Taylor & Francis, 2002.

[199] J. Larminie, A. Dicks, Fuel Cell Systems Explained, J. Wiley, 2003.

[200] E. Antolini, T. Lopes, E.R. Gonzalez, Journal of Alloys and Compounds, 461 (2008) 253-262.

[201] T.-Y. Jeon, K.-S. Lee, S.J. Yoo, Y.-H. Cho, S.H. Kang, Y.-E. Sung, Langmuir, 26 (2010) 9123-9129.

[202] C. Roth, N. Benker, R. Theissmann, R.J. Nichols, D.J. Schiffrin, Langmuir, 24 (2008) 2191-2199.

[203] C. Xu, A. Faghri, X. Li, T. Ward, International Journal of Hydrogen Energy, 35 (2010) 1769-1777.

[204] D. Chu, R.Z. Jiang, Solid State Ionics, 148 (2002) 591-599.

[205] J. Liu, J. Cao, Q. Huang, X. Li, Z. Zou, H. Yang, Journal of Power Sources, 175 (2008) 159-165.

[206] Q. Yi, L. Li, W. Yu, Z. Zhou, X. Liu, G. Xu, Journal of Alloys and Compounds, 466 (2008) 52-58.

[207] W.D. King, J.D. Corn, O.J. Murphy, D.L. Boxall, E.A. Kenik, K.C. Kwiatkowski, S.R. Stock, C.M. Lukehart, Journal of Physical Chemistry B, 107 (2003) 5467-5474.

[208] W. Li, X. Wang, Z. Chen, M. Waje, Y. Yan, Journal of Physical Chemistry B, 110 (2006) 15353-15358.

[209] C. Yang, D. Wang, X. Hu, C. Dai, L. Zhang, Journal of Alloys and Compounds, 448 (2008) 109-115.

[210] C. Zhou, H. Wang, F. Peng, J. Liang, H. Yu, J. Yang, Langmuir, 25 (2009) 7711-7717.

[211] S. Trasatti, Electrochimica Acta, 36 (1991) 225-241.

[212] S. Trasatti, Electrochimica Acta, 45 (2000) 2377-2385.

[213] O.I. Velikokhatnyi, P.N. Kumta, Physica B: Condensed Matter, 404 (2009) 1737-1745.

[214] D.R. Lide, H.V. Kehiaian, CRC Handbook of Thermophysical and Thermochemical Data, Taylor & Francis, 1994.

[215] O.I. Velikokhatnyi, P.N. Kumta, Journal of Power Sources, 202 (2012) 190-199.

[216] R.C. Pullar, Journal of the American Ceramic Society, 92 (2009) 563-577.

[217] W.-S. Xia, L.-X. Li, P. Zhang, P.-F. Ning, Materials Letters, 65 (2011) 3317-3319.

[218] Z. Ding, W. Wu, S. Liang, H. Zheng, L. Wu, Materials Letters, 65 (2011) 1598-1600.

[219] S.M. Ji, S.H. Choi, J.S. Jang, E.S. Kim, J.S. Lee, J. Phys. Chem. C, 113 (2009) 17824-17830.

[220] H. Kato, A. Kudo, Chem. Phys. Lett., 295 (1998) 487-492.

[221] A.V. Moholkar, S.M. Pawar, K.Y. Rajpure, C.H. Bhosale, J.H. Kim, Applied Surface Science, 255 (2009) 9358-9364.

[222] J. Xu, S. Huang, Z. Wang, Solid State Communications, 149 (2009) 527-531.

[223] O.I. Velikokhatnyi, K. Kadakia, S.K. Park, P.N. Kumta, Journal of The Electrochemical Society, 159 (2012) F607-F616.

[224] M. Waburg, H. Mullerbuschbaum, Zeitschrift Fur Anorganische Und Allgemeine Chemie, 508 (1984) 55-60.

[225] D.R. Lide, CRC Handbook of Chemistry and Physics, 85th Edition, Taylor & Francis, 2004.

[226] P. Simon, Y. Gogotsi, Nat. Mater., 7 (2008) 845-854.

[227] B.E. Conway, Journal of the Electrochemical Society, 138 (1991) 1539-1548.

[228] A.S. Arico, P. Bruce, B. Scrosati, J.M. Tarascon, W. Van Schalkwijk, Nat. Mater., 4 (2005) 366-377.

[229] B.E. Conway, Electrochemical Supercapacitors: Scientific Fundamentals and Technological Applications, Kluwer Academic/Plenum Publishers, New York, 1999.

[230] C.C. Hu, T.W. Tsou, Electrochem. Commun., 4 (2002) 105-109.

[231] R. Kotz, M. Carlen, Electrochimica Acta, 45 (2000) 2483-2498.

[232] J.M. Miller, B. Dunn, T.D. Tran, R.W. Pekala, Journal of the Electrochemical Society, 144 (1997) L309-L311.

[233] M. Toupin, T. Brousse, D. Belanger, Chemistry of Materials, 14 (2002) 3946-3952.

[234] M. Toupin, T. Brousse, D. Bélanger, Chemistry of Materials, 16 (2004) 3184-3190.

[235] J.W. Long, K.E. Swider, C.I. Merzbacher, D.R. Rolison, Langmuir, 15 (1999) 780-785.

[236] Z. Chen, Y. Qin, D. Weng, Q. Xiao, Y. Peng, X. Wang, H. Li, F. Wei, Y. Lu, Advanced Functional Materials, 19 (2009) 3420-3426.

[237] I.H. Kim, J.H. Kim, B.W. Cho, Y.H. Lee, K.B. Kim, Journal of the Electrochemical Society, 153 (2006) A989-A996.

[238] T. Kudo, Y. Ikeda, T. Watanabe, M. Hibino, M. Miyayama, H. Abe, K. Kajita, Solid State Ionics, 152 (2002) 833-841.

[239] K.-W. Nam, K.-H. Kim, E.-S. Lee, W.-S. Yoon, X.-Q. Yang, K.-B. Ki, Journal of Power Sources, 182 (2008) 642-652.

[240] S. Suzuki, M. Hibino, M. Miyayama, Journal of Power Sources, 124 (2003) 513-517.

[241] S.D. Perera, B. Patel, J. Bonso, M. Grunewald, J.P. Ferraris, K.J. Balkus, ACS Appl. Mater. Interfaces, 3 (2011) 4512-4517.

[242] S. Tepavcevic, H. Xiong, V.R. Stamenkovic, X. Zuo, M. Balasubramanian, V.B. Prakapenka, C.S. Johnson, T. Rajh, ACS Nano, 6 (2011) 530-538.

[243] M.E. Spahr, P. Bitterli, R. Nesper, M. Muller, F. Krumeich, H.U. Nissen, Angewandte Chemie-International Edition, 37 (1998) 1263-1265.

[244] M.E. Spahr, P. Stoschitzki-Bitterli, R. Nesper, O. Haas, P. Novak, Journal of the Electrochemical Society, 146 (1999) 2780-2783.

[245] C.C. Hu, C.M. Huang, K.H. Chang, Journal of Power Sources, 185 (2008) 1594-1597.

[246] C.M. Huang, C.C. Hu, K.H. Chang, J.M. Li, Y.F. Li, Journal of the Electrochemical Society, 156 (2009) A667-A671.

[247] J.M. Li, K.H. Chang, C.C. Hu, Electrochem. Commun., 12 (2010) 1800-1803.

[248] J.M. Li, K.H. Chang, T.H. Wu, C.C. Hu, Journal of Power Sources, 224 (2013) 59-65.

[249] D. Choi, G.E. Blomgren, P.N. Kumta, Advanced Materials, 18 (2006) 1178-+.

[250] J.C. Badot, N. Baffier, Journal of Materials Chemistry, 2 (1992) 1167-1174.

[251] Y. Wang, G. Cao, Chemistry of Materials, 18 (2006) 2787-2804.

[252] F. Coustier, J. Hill, B.B. Owens, S. Passerini, W.H. Smyrl, Journal of the Electrochemical Society, 146 (1999) 1355-1360.

[253] P.H. Jampani, K. Kadakia, D.H. Hong, R. Epur, J.A. Poston, A. Manivannan, P.N. Kumta, Journal of The Electrochemical Society, 160 (2013) A1118-A1127.

[254] T. Szorenyi, K. Bali, I. Hevesi, Journal of Non-Crystalline Solids, 35-6 (1980) 1245-1248.

[255] S.D. Perera, B. Patel, N. Nijem, K. Roodenko, O. Seitz, J.P. Ferraris, Y.J. Chabal, K.J. Balkus, Advanced Energy Materials, 1 (2011) 936-945.

[256] C.Y. Lee, H.M. Tsai, H.J. Chuang, S.Y. Li, P. Lin, T.Y. Tseng, Journal of the Electrochemical Society, 152 (2005) A716-A720.

[257] A.L.M. Reddy, M.M. Shaijumon, S.R. Gowda, P.M. Ajayan, Nano Letters, 9 (2009) 1002-1006.

[258] S.R. Sivakkumar, J.M. Ko, D.Y. Kim, B.C. Kim, G.G. Wallace, Electrochimica Acta, 52 (2007) 7377-7385.

[259] Z. Fan, J. Chen, K. Cui, F. Sun, Y. Xu, Y. Kuang, Electrochimica Acta, 52 (2007) 2959-2965.

[260] I.H. Kim, J.H. Kim, K.B. Kim, Electrochemical and Solid State Letters, 8 (2005) A369-A372.

[261] I.H. Kim, J.H. Kim, Y.H. Lee, K.B. Kim, Journal of the Electrochemical Society, 152 (2005) A2170-A2178.

[262] W. Wang, P.N. Kumta, Journal of Power Sources, 172 (2007) 650-658.

[263] S.D. Perera, B. Patel, N. Nijem, K. Roodenko, O. Seitz, J.P. Ferraris, Y.J. Chabal, K.J. Balkus, Advanced Energy Materials, 1 (2011) 936-945.

[264] M. Sathiya, A.S. Prakash, K. Ramesha, J.M. Tarascon, A.K. Shukla, Journal of the American Chemical Society, 133 (2011) 16291-16299.

[265] Z. Chen, Y.C. Qin, D. Weng, Q.F. Xiao, Y.T. Peng, X.L. Wang, H.X. Li, F. Wei, Y.F. Lu, Advanced Functional Materials, 19 (2009) 3420-3426.

[266] J. Benson, S. Boukhalfa, A. Magasinski, A. Kvit, G. Yushin, ACS Nano, 6 (2011) 118-125.

[267] S. Boukhalfa, K. Evanoff, G. Yushin, Energy & Environmental Science, 5 (2012) 6872-6879.

[268] W. Wang, R. Epur, P.N. Kumta, Electrochem. Commun., 13 (2011) 429-432.

[269] W. Wang, P.N. Kumta, ACS Nano, 4 (2010) 2233-2241.

[270] D. Vernardou, P. Paterakis, H. Drosos, E. Spanakis, I.M. Povey, M.E. Pemble, E. Koudoumas, N. Katsarakis, Solar Energy Materials and Solar Cells, 95 (2011) 2842-2847.

[271] L. Michailovits, K. Bali, T. Szorenyi, I. Hevesi, Acta Physica Academiae Scientiarum Hungaricae, 49 (1980) 217-221.

[272] R. Binions, G. Hyett, C. Piccirillo, I.P. Parkin, Journal of Materials Chemistry, 17 (2007) 4652-4660.

[273] T.D. Manning, I.P. Parkin, Polyhedron, 23 (2004) 3087-3095.

[274] M.N. Field, I.P. Parkin, Journal of Materials Chemistry, 10 (2000) 1863-1866.

[275] T.D. Manning, I.P. Parkin, R.J.H. Clark, D. Sheel, M.E. Pemble, D. Vernadou, Journal of Materials Chemistry, 12 (2002) 2936-2939.

[276] I.P. Parkin, G.S. Elwin, Journal of Materials Chemistry, 11 (2001) 3120-3124.

[277] S.K. Pal, S. Talapatra, S. Kar, L. Ci, R. Vajtai, T. Borca-Tasciuc, L.S. Schadler, P.M. Ajayan, Nanotechnology, 19 (2008).

[278] S. Talapatra, S. Kar, S.K. Pal, R. Vajtai, L. Ci, P. Victor, M.M. Shaijumon, S. Kaur, O. Nalamasu, P.M. Ajayan, Nature Nanotechnology, 1 (2006) 112-116.

[279] A.C. Ferrari, J. Robertson, Physical Review B, 61 (2000) 14095-14107.

[280] A.C. Ferrari, J. Robertson, Physical Review B, 64 (2001).

[281] E. Cazzanelli, G. Mariotto, S. Passerini, W.H. Smyrl, A. Gorenstein, Solar Energy Materials and Solar Cells, 56 (1999) 249-258.

[282] S. Santangelo, G. Messina, G. Faggio, M.G. Willinger, N. Pinna, A. Donato, A. Arena, N. Donato, G. Neri, Diam. Relat. Mat., 19 (2010) 590-594.

[283] T. Belin, F. Epron, Materials Science and Engineering: B, 119 (2005) 105-118.

[284] C.H. Kiang, M. Endo, P.M. Ajayan, G. Dresselhaus, M.S. Dresselhaus, Physical Review Letters, 81 (1998) 1869-1872.

[285] E. Hryha, E. Rutqvist, L. Nyborg, Surface and Interface Analysis, 44 (2012) 1022-1025.

[286] A.V. Naumkin, A. Kraut-Vass, S.W. Gaarenstroom, C.J. Powell, in: NIST Standard Reference database 20, National Institute of Standards & Technology, 2012.

[287] M. Sathiya, A.S. Prakash, K. Ramesha, J.M. Tarascon, A.K. Shukla, Journal of the American Chemical Society, 133 (2011) 16291-16299.

[288] J. Muster, G.T. Kim, V. Krstic, J.G. Park, Y.W. Park, S. Roth, M. Burghard, Advanced Materials, 12 (2000) 420-+.

[289] M. Pourbaix, Atlas of electrochemical equilibria in aqueous solutions, Pergamon Press, Oxford, 1966.

[290] N. Takeno, Atlas of Eh-pH diagrams, National Institute of Advanced Industrial Science & Technology, 2005.

[291] C.-C. Liu, D.-S. Tsai, D. Susanti, W.-C. Yeh, Y.-S. Huang, F.-J. Liu, Electrochimica Acta, 55 (2010) 5768-5774.

[292] K.-H. Chang, C.-C. Hu, Applied Physics Letters, 88 (2006) 193102-193103.

[293] C.-C. Hu, K.-H. Chang, M.-C. Lin, Y.-T. Wu, Nano Letters, 6 (2006) 2690-2695.

[294] M.-G. Willinger, G. Neri, A. Bonavita, G. Micali, E. Rauwel, T. Herntrich, N. Pinna, Physical Chemistry Chemical Physics, 11 (2009) 3615-3622.

[295] L. Niinisto, M. Ritala, M. Leskela, Mater. Sci. Eng. B-Solid State Mater. Adv. Technol., 41 (1996) 23-29.

[296] M. Zhang, M. Yudasaka, S. Bandow, S. Iijima, Chem. Phys. Lett., 369 (2003) 680-683.

[297] G.J. Brug, A.L.G. Vandeneeden, M. Sluytersrehbach, J.H. Sluyters, Journal of Electroanalytical Chemistry, 176 (1984) 275-295.

[298] P.S. Germain, W.G. Pell, B.E. Conway, Electrochimica Acta, 49 (2004) 1775-1788.

[299] C. Portet, G. Yushin, Y. Gogotsi, Carbon, 45 (2007) 2511-2518.

[300] J.R. Miller, Science, 335 (2012) 1312-1313.

[301] P. Jampani, A. Manivannan, P.N. Kumta, Electrochemical Society Interface, 19 (2010) 57-62.

[302] V. Subramanian, H.W. Zhu, R. Vajtai, P.M. Ajayan, B.Q. Wei, Journal of Physical Chemistry B, 109 (2005) 20207-20214.

[303] H. Wang, H.S. Casalongue, Y. Liang, H. Dai, Journal of the American Chemical Society, 132 (2010) 7472-7477.

[304] K.W. Nam, K.B. Kim, Journal of the Electrochemical Society, 149 (2002) A346-A354.

[305] H. Kwon, S. Choi, L.T. Thompson, Journal of Catalysis, 184 (1999) 236-246.

[306] T.C. Liu, W.G. Pell, B.E. Conway, S.L. Roberson, Journal of the Electrochemical Society, 145 (1998) 1882-1888.

[307] L.T. Thompson Jr, M.R. Wixom, J.M. Parker, in, Google Patents, 1997.

[308] L.T. Thompson Jr, M.R. Wixom, in, Google Patents, 1999.

[309] M. Wixom, D. Tarnowski, J. Parker, J. Lee, P. Chen, I. Song, L. Thompson, in: Materials Research Society Symposium Proceedings, Cambridge Univ Press, 1998, pp. 643-654.

[310] L. Owens, L.T. Thompson Jr, M.R. Wixom, in, Google Patents, 1998.

[311] D. Choi, P.N. Kumta, Journal of the American Ceramic Society, 90 (2007) 3113-3120.

[312] D. Choi, P.N. Kumta, Journal of the Electrochemical Society, 153 (2006) A2298-A2303.

[313] D.W. Choi, P.N. Kumta, Electrochemical and Solid State Letters, 8 (2005) A418-A422.

[314] A.M. Glushenkov, D. Hulicova-Jurcakova, D. Llewellyn, G.Q. Lu, Y. Chen, Chemistry of Materials, 22 (2010) 914-921.

[315] X.P. Zhou, H.Y. Chen, D. Shu, C. He, J.M. Nan, Journal of Physics and Chemistry of Solids, 70 (2009) 495-500.

[316] C.Z. Deng, K.C. Tsai, D. Ghantous, in, Google Patents, 1999.

[317] X. Lu, M. Yu, T. Zhai, G. Wang, S. Xie, T. Liu, C. Liang, Y. Tong, Y. Li, Nano Letters, 13 (2013) 2628-2633.

[318] C.M. Ghimbeu, E. Raymundo-Pinero, P. Fioux, F. Beguin, C. Vix-Guterl, Journal of Materials Chemistry, 21 (2011) 13268-13275.

[319] R.L. Porto, R. Frappier, J.B. Ducros, C. Aucher, H. Mosqueda, S. Chenu, B. Chavillon, F. Tessier, F. Cheviré, T. Brousse, Electrochimica Acta, 82 (2012) 257-262.

[320] G. Hyett, M.A. Green, I.P. Parkin, Chemical Vapor Deposition, 14 (2008) 309-312.

[321] Y.X. Du, M. Lei, H. Yang, Journal of Materials Science & Technology, 24 (2008) 737-741.

[322] M. Lei, H.Z. Zhao, H. Yang, P.G. Li, H.L. Tang, B. Song, W.H. Tang, Diam. Relat. Mat., 16 (2007) 1974-1981.

[323] M. Lei, H.Z. Zhao, H. Yang, B. Song, P.G. Li, W.H. Tang, Materials Letters, 62 (2008) 1539-1542.

[324] P.G. Li, M. Lei, H.Z. Zhao, H.L. Tang, H. Yang, W.H. Tang, Materials Chemistry and Physics, 105 (2007) 234-239.

[325] R. Kapoor, S.T. Oyama, Journal of Solid State Chemistry, 99 (1992) 303-312.

[326] S.T. Oyama, R. Kapoor, H.T. Oyama, D.J. Hofmann, E. Matijevic, Journal of Materials Research, 8 (1993) 1450-1454.

[327] P. Krawiec, P.L. De Cola, R. Glaser, J. Weitkamp, C. Weidenthaler, S. Kaskel, Advanced Materials, 18 (2006) 505-+.

[328] P. Krawiec, S. Kaskel, Topics in Catalysis, 52 (2009) 1549-1558.

[329] I.S. Kim, G.E. Blomgren, P.N. Kumta, Journal of Power Sources, 130 (2004) 275-280.

[330] I. Kim, P.N. Kumta, G.E. Blomgren, Electrochemical and Solid State Letters, 3 (2000) 493-496.

[331] M.K. Datta, P.N. Kumta, Journal of Power Sources, 158 (2006) 557-563.

[332] M.K. Datta, P.N. Kumta, Journal of Power Sources, 165 (2007) 368-378.

[333] M.K. Datta, P.N. Kumta, Journal of Power Sources, 194 (2009) 1043-1052.

[334] P.J. Hanumantha, M.K. Datta, K.S. Kadakia, D.H. Hong, S.J. Chung, M.C. Tam, J.A. Poston, A. Manivannan, P.N. Kumta, Journal of The Electrochemical Society, 160 (2013) A2195-A2206.

[335] J.I. Langford, D. Louer, P. Scardi, Journal of Applied Crystallography, 33 (2000) 964-974.

[336] H. Toraya, Journal of Applied Crystallography, 23 (1990) 485-491.

[337] T. Suszko, W. Gulbinski, A. Urbanowicz, Materials Letters, 65 (2011) 2146-2148.

[338] M.A. Roldan, V. Lopez-Flores, M.D. Alcala, A. Ortega, C. Real, J. Eur. Ceram. Soc., 30 (2010) 2099-2107.

[339] C.D. Wagner, G.E. Muilenberg, Handbook of x-ray photoelectron spectroscopy: a reference book of standard data for use in x-ray photoelectron spectroscopy, Physical Electronics Division, Perkin-Elmer Corp., 1979.

[340] D. Briggs, P. Seah, Practical Surface Analysis: Auger and X-ray photoelectron spectroscopy, Wiley, 1990.

[341] C.W. Zou, X.D. Yan, J. Han, R.Q. Chen, W. Gao, J. Phys. D-Appl. Phys., 42 (2009).

[342] D.L. Legrand, H.W. Nesbitt, G.M. Bancroft, American Mineralogist, 83 (1998) 1256-1265.

[343] G.H. Kelsall, I. Thompson, P.A. Francis, Journal of Applied Electrochemistry, 23 (1993) 417-426.

[344] A.J. Bard, R. Parsons, J. Jordan, Standard potenitals in aqueous solution, New York, 1985.

[345] M. Pourbaix, Atlas of electrochemical equilibria in aqueous solutions, National Association of Corrosion Engineers, 1974.

[346] L. Zhang, C.M.B. Holt, E.J. Luber, B.C. Olsen, H.T. Wang, M. Danaie, X.W. Cui, X.H. Tan, V.W. Lui, W.P. Kalisvaart, D. Mitlin, J. Phys. Chem. C, 115 (2011) 24381-24393.

[347] E. Eustache, R. Frappier, R.L. Porto, S. Bouhtiyya, J.-F. Pierson, T. Brousse, Electrochem. Commun., 28 (2013) 104-106.

[348] H. Kim, B.N. Popov, Journal of Power Sources, 104 (2002) 52-61.

[349] H.D. Abruña, Y. Kiya, J.C. Henderson, Phys. Today, 61 (2008) 43-47.

[350] M.S. Whittingham, Mrs Bulletin, 33 (2008) 411-419.

[351] C. Liu, F. Li, L.-P. Ma, H.-M. Cheng, Advanced Materials, 22 (2010) E28-+.

[352] F. Cheng, J. Liang, Z. Tao, J. Chen, Advanced Materials, 23 (2011) 1695-1715.

[353] T. Reddy, D. Linden, Linden's Handbook of Batteries, 4th Edition, McGraw-Hill Education, 2010.

[354] M.K. Datta, J. Maranchi, S.J. Chung, R. Epur, K. Kadakia, P. Jampani, P.N. Kumta, Electrochimica Acta, 56 (2011) 4717-4723.

[355] B. Kang, G. Ceder, Nature, 458 (2009) 190-193.

[356] U. Kasavajjula, C. Wang, A.J. Appleby, Journal of Power Sources, 163 (2007) 1003-1039.

[357] R. Teki, M.K. Datta, R. Krishnan, T.C. Parker, T.-M. Lu, P.N. Kumta, N. Koratkar, Small, 5 (2009) 2236-2242.

[358] Y. Cao, L. Xiao, W. Wang, D. Choi, Z. Nie, J. Yu, L.V. Saraf, Z. Yang, J. Liu, Advanced Materials, 23 (2011) 3155-+.

[359] S.-W. Kim, D.-H. Seo, X. Ma, G. Ceder, K. Kang, Advanced Energy Materials, 2 (2012) 710-721.

[360] N. Yabuuchi, M. Kajiyama, J. Iwatate, H. Nishikawa, S. Hitomi, R. Okuyama, R. Usui, Y. Yamada, S. Komaba, Nat. Mater., 11 (2012) 512-517.

[361] L. Xiao, Y. Cao, J. Xiao, W. Wang, L. Kovarik, Z. Nie, J. Liu, Chemical Communications, 48 (2012) 3321-3323.

[362] J.F. Whitacre, A. Tevar, S. Sharma, Electrochem. Commun., 12 (2010) 463-466.

[363] J.F. Whitacre, T. Wiley, S. Shanbhag, Y. Wenzhuo, A. Mohamed, S.E. Chun, E. Weber, D. Blackwood, E. Lynch-Bell, J. Gulakowski, C. Smith, D. Humphreys, Journal of Power Sources, 213 (2012) 255-264.

[364] M.M. Doeff, Y.P. Ma, S.J. Visco, L.C. Dejonghe, Journal of The Electrochemical Society, 140 (1993) L169-L170.

[365] S. Komaba, Y. Matsuura, T. Ishikawa, N. Yabuuchi, W. Murata, S. Kuze, Electrochem. Commun., 21 (2012) 65-68.

[366] S. Komaba, W. Murata, T. Ishikawa, N. Yabuuchi, T. Ozeki, T. Nakayama, A. Ogata, K. Gotoh, K. Fujiwara, Advanced Functional Materials, 21 (2011) 3859-3867.

[367] D.A. Stevens, J.R. Dahn, Journal of The Electrochemical Society, 148 (2001) A803-A811.

[368] K. Tang, L. Fu, R.J. White, L. Yu, M.-M. Titirici, M. Antonietti, J. Maier, Advanced Energy Materials, 2 (2012) 873-877.

[369] X. Xia, J.R. Dahn, Journal of The Electrochemical Society, 159 (2012) A515-A519.

[370] V.L. Chevrier, G. Ceder, Journal of The Electrochemical Society, 158 (2011) A1011-A1014.

[371] M.K. Datta, R. Epur, P. Saha, K. Kadakia, S.K. Park, P.N. Kumta, Journal of Power Sources, (2012).

[372] T.B. Massalski, Binary Alloy Phase Diagrams, ASM International, 1990.

[373] J. Nanda, M.K. Datta, J.T. Remillard, A. O'Neill, P.N. Kumta, Electrochem. Commun., 11 (2009) 235-237.

[374] C. Ettl, K. Samwer, Materials Science and Engineering a-Structural Materials Properties Microstructure and Processing, 178 (1994) 245-254.

[375] S.H. Sun, G.W. Meng, G.X. Zhang, T. Gao, B.Y. Geng, L.D. Zhang, J. Zuo, Chem. Phys. Lett., 376 (2003) 103-107.

[376] A. Magasinski, P. Dixon, B. Hertzberg, A. Kvit, J. Ayala, G. Yushin, Nat. Mater., 9 (2010) 353-358.

[377] C.K. Chan, H. Peng, G. Liu, K. McIlwrath, X.F. Zhang, R.A. Huggins, Y. Cui, Nature Nanotechnology, 3 (2008) 31-35.

[378] L.Y. Beaulieu, K.W. Eberman, R.L. Turner, L.J. Krause, J.R. Dahn, Electrochemical and Solid State Letters, 4 (2001) A137-A140.

[379] J.H. Ryu, J.W. Kim, Y.E. Sung, S.M. Oh, Electrochemical and Solid State Letters, 7 (2004) A306-A309.

[380] L.-F. Cui, Y. Yang, C.-M. Hsu, Y. Cui, Nano Letters, 9 (2009) 3370-3374.

[381] H. Kim, J. Cho, Nano Letters, 8 (2008) 3688-3691.

[382] J.P. Maranchi, A.F. Hepp, A.G. Evans, N.T. Nuhfer, P.N. Kumta, Journal of The Electrochemical Society, 153 (2006) A1246-A1253.

[383] M.-H. Park, M.G. Kim, J. Joo, K. Kim, J. Kim, S. Ahn, Y. Cui, J. Cho, Nano Letters, 9 (2009) 3844-3847.

[384] J. Saint, M. Morcrette, D. Larcher, L. Laffont, S. Beattie, J.-P. Peres, D. Talaga, M. Couzi, J.-M. Tarascon, Advanced Functional Materials, 17 (2007) 1765-1774.

[385] A. Timmons, A.D.W. Todd, S.D. Mead, G.H. Carey, R.J. Sanderson, R.E. Mar, J.R. Dahn, Journal of The Electrochemical Society, 154 (2007) A865-A874.

[386] J.P. Maranchi, A.F. Hepp, P.N. Kumta, Electrochemical and Solid State Letters, 6 (2003) A198-A201.

[387] J. Rong, C. Masarapu, J. Ni, Z. Zhang, B. Wei, ACS Nano, 4 (2010) 4683-4690.

[388] L.-F. Cui, L. Hu, J.W. Choi, Y. Cui, ACS Nano, 4 (2010) 3671-3678.

[389] J. Guo, A. Sun, C. Wang, Electrochem. Commun., 12 (2010) 981-984.

[390] R. Huang, X. Fan, W. Shen, J. Zhu, Applied Physics Letters, 95 (2009).

[391] C. Martin, M. Alias, F. Christien, O. Crosnier, D. Belanger, T. Brousse, Advanced Materials, 21 (2009) 4735-+.

[392] Q. Si, K. Hanai, T. Ichikawa, A. Hirano, N. Imanishi, Y. Takeda, O. Yamamoto, Journal of Power Sources, 195 (2010) 1720-1725.

[393] V. Baranchugov, E. Markevich, E. Pollak, G. Salitra, D. Aurbach, Electrochem. Commun., 9 (2007) 796-800.

[394] J.B. Kim, B.S. Jun, S.M. Lee, Electrochimica Acta, 50 (2005) 3390-3394.